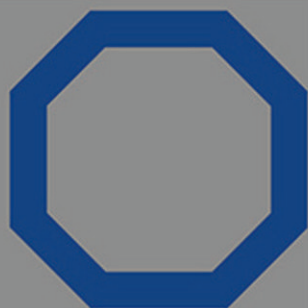


J.-C.G. Bünzli and V.K. Pecharsky
Editors



HANDBOOK ON THE
PHYSICS AND CHEMISTRY OF
RARE EARTHS



Volume 45

North-Holland

Including Actinides



Handbook on the Physics and Chemistry of Rare Earths

Including Actinides

Volume 45

HANDBOOK ON THE PHYSICS AND CHEMISTRY
OF RARE EARTHS

Including Actinides

Advisory Editorial Board

GIN-YA ADACHI

Kobe, Japan

WILLIAM J. EVANS

Irvine, USA

YURI GRIN

Dresden, Germany

SUZAN M. KAUZLARICH

Davis, USA

MICHAEL F. REID

Canterbury, New Zealand

CHUNHUA YAN

Beijing, P.R. China

Editors Emeritus

KARL A. GSCHNEIDNER, JR

Ames, USA

LEROY EYRING✠

Tempe, USA

✠*Deceased (2005)*

Handbook on the Physics and Chemistry of Rare Earths

Including Actinides

Volume 45

Editors

Jean-Claude G. Bünzli

Swiss Federal Institute of Technology, Lausanne (EPFL)
Institute of Chemical Sciences and Engineering
BCH 1402
CH-1015 Lausanne
Switzerland

Vitalij K. Pecharsky

The Ames Laboratory, U.S. Department of Energy, and
Department of Materials Science and Engineering
Iowa State University,
Ames, Iowa 50011-3020,
USA



Amsterdam • Boston • Heidelberg • London • New York • Oxford
Paris • San Diego • San Francisco • Singapore • Sydney • Tokyo
North-Holland is an imprint of Elsevier



North-Holland is an imprint of Elsevier
Radarweg 29, PO Box 211, 1000 AE Amsterdam, The Netherlands
The Boulevard, Langford Lane, Kidlington, Oxford OX5 1GB, UK

Copyright © 2014 Elsevier B.V. All rights reserved.

No part of this publication may be reproduced, stored in a retrieval system or transmitted in any form or by any means electronic, mechanical, photocopying, recording or otherwise without the prior written permission of the publisher.

Permissions may be sought directly from Elsevier's Science & Technology Rights Department in Oxford, UK: phone (+44) (0) 1865 843830; fax (+44) (0) 1865 853333; email: permissions@elsevier.com. Alternatively you can submit your request online by visiting the Elsevier web site at <http://elsevier.com/locate/permissions>, and selecting, *Obtaining permission to use Elsevier material*.

Notice

No responsibility is assumed by the publisher for any injury and/or damage to persons or property as a matter of products liability, negligence or otherwise, or from any use or operation of any methods, products, instructions or ideas contained in the material herein. Because of rapid advances in the medical sciences, in particular, independent verification of diagnoses and drug dosages should be made.

British Library Cataloguing in Publication Data

A catalogue record for this book is available from the British Library

Library of Congress Cataloguing-in-Publication Data

A catalog record for this book is available from the Library of Congress

ISBN: 978-0-444-63256-2

ISSN: 0168-1273

For information on all North-Holland publications
visit our website at store.elsevier.com

Printed and Bound in Great Britain

14 15 16 13 12 11 10 9 8 7 6 5 4 3 2 1



Working together
to grow libraries in
developing countries

www.elsevier.com • www.bookaid.org

Preface

These elements perplex us in our reaches [sic], baffle us in our speculations, and haunt us in our very dreams. They stretch like an unknown sea before us—mocking, mystifying, and murmuring strange revelations and possibilities.

Sir William Crookes (February 16, 1887)

Volume 45 of the *Handbook on the Physics and Chemistry of Rare Earths* features four chapters covering subjects ranging from gas-phase chemistry, to inorganic clusters and complexes, optical refrigeration, and organolanthanide chemistry.

The first chapter ([Chapter 263](#)) is devoted to an unusual aspect of f-element chemistry, gas-phase chemistry. Thanks to the development of sensitive mass spectrometry techniques, many new rare-earth and actinide molecular and cluster species have been identified; this in turn deepened knowledge of the basic chemistry of these elements and provided clues for understanding condensed-phase processes. Two strong features of this review are the discussion of experimental thermodynamic parameters obtained for several atomic and molecular ions and the validation of computational methods applied to the challenging f-elements. The following review ([Chapter 264](#)) deals with clusters formed by rare-earth elements with endohedral transition metal atoms. These heteroatomic species contain 6–10 rare-earth ions and are usually surrounded by halide ligands, building large $\{TR_r\}X_x$ entities. The chapter focuses on the synthesis and crystal growth of these stunning “anti-Werner” complexes by comproportionation of rare-earth trihalides in presence of the transition metal at elevated temperature and on the detailed description of their structure. Semiconductor optical detectors largely benefit from cryogenic technologies to improve their signal-to-noise ratio; present techniques have definite limitations and [Chapter 265](#) presents an alternative, optical (laser) cooling. Indeed, some luminescent materials emit light of higher energy than the excitation source, anti-Stokes emission, and a few lanthanide ions doped into transparent matrices, such as trivalent erbium, thulium, and ytterbium, are ideal candidates for optical refrigeration. The final chapter ([Chapter 266](#)) describes arene-bridged rare-earth complexes with emphasis on compounds obtained by reduction reactions; this aspect of organolanthanide chemistry exemplifies the remarkable advances made by this field that started 60 years ago. Bimetallic lanthanide complexes bridged by ligands derived from arenes and complexes of

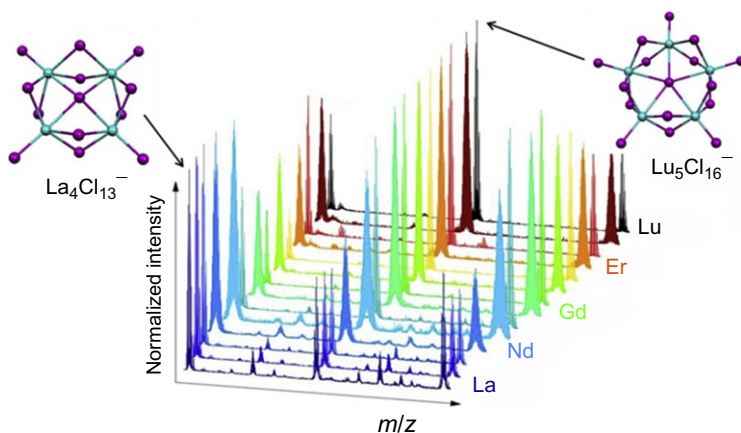
ferrocene-based diamide ligands constitute a major subtheme in the chapter. Detailed discussions then follow on compounds derived from fused rings and their reactivity with white phosphorus.

We thank Professor William Evans, member of the Advisory Editorial board, for suggesting the authors of the last chapter and for his help in writing the preface.

CHAPTER 263. GAS-PHASE ION CHEMISTRY OF RARE EARTHS AND ACTINIDES

By Joaquim Marçalo and John K. Gibson

Universidade de Lisboa, Portugal, and Lawrence Berkeley National Laboratory, USA



Gas-phase chemistry studies of atomic and molecular rare-earth and actinide ions have a deep-rooted history of more than three decades. In gas phase, physical and chemical properties of elementary and molecular species can be studied in absence of external perturbations. Due to the relative simplicity of gas-phase systems compared to condensed-phase systems, solutions or solids, it is possible to probe in detail the relationships between electronic structure, reactivity, and energetics. Most of this research involves the use of a variety of mass spectrometry techniques, which allows one exerting precise control over reactants and products. Many new rare earth and actinide molecular and cluster species have been identified that have expanded knowledge of the basic chemistry of these elements and provided clues for understanding condensed-phase processes. Key thermodynamic parameters have been obtained for numerous atomic and molecular ions. Such fundamental physicochemical studies have provided opportunities for the refinement and validation of computational methods as applied to the particularly challenging lanthanide and actinide elements. Among other applications, the roles of

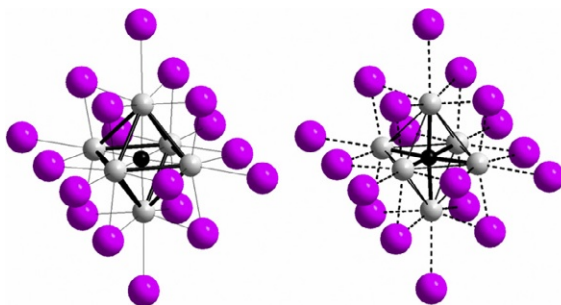
ligands, solvent molecules, and counter ions have been examined at a molecular level. A deeper understanding of plasma chemistry, flame chemistry, radiolysis, and interstellar chemistry stems from these gas-phase studies. Important applications in analytical and biomedical mass spectrometry have also benefited from discoveries in this area.

The chapter starts with an introduction on gas-phase chemistry and associated experimental techniques as well as on electronic structures and energetics of lanthanide and actinide ions. It then focuses on reactions of these ions with oxidants, inorganic molecules, small hydrocarbons, and organic molecules. The review ends with considerations on hydrolysis, solvation, complexation, and interactions with biologically relevant molecules.

CHAPTER 264. SYMBIOSIS OF INTERMETALLIC AND SALT: RARE-EARTH METAL CLUSTER COMPLEXES WITH ENDOHEDRAL TRANSITION METAL ATOMS

By Gerd Meyer

Universität zu Köln, Germany, and Iowa State University, USA



Rare-earth elements, R, form clusters with endohedral transition metal atoms, T, featuring six to eight R atoms. These heteroatomic species, $\{TR_r\}$ where r is the coordination number (CN) of T (6–8), are surrounded by halide ligands, X, building larger entities, $\{TR_r\}X_x$. Examples are the prolific $\{TR_6\}X_{12}R$ and $\{TR_6\}X_{10}$ compound types. Edge- and face-sharing of (mainly) octahedral clusters constitute a small number of oligomers, dimers to pentamers, with the tetrameric $\{T_4R_{16}\}$ oligomers being the most abundant. Further connection of clusters via common edges leads to a variety of chains with numerous $\{TR_3\}X_3$ -type compounds, exhibiting a surprising structural diversity. CNs of the endohedral atom of seven and eight are also observed in $\{TR_7\}$ and $\{TR_8\}$ clusters. Similar coordination environments are also seen in $\{T_rR_r\}$ polar intermetallic compounds, for example, CN=8–10 in $\{Ru_{11}Lu_{20}\}$. Thus, $\{TR_r\}X_x$ clusters—also coined as metal-rich halides or as anti-Werner complexes—may be understood as a symbiotic arrangement of (polar) intermetallics and salts. Consequently, bonding in both polar

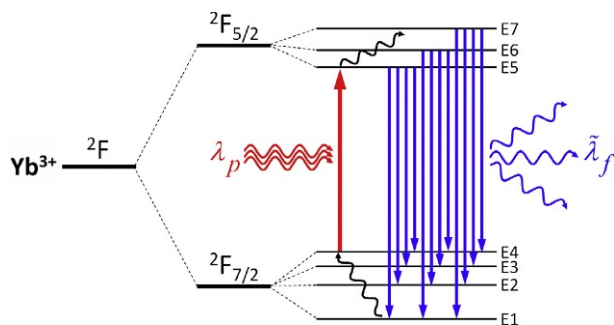
intermetallics and heterocluster complexes is mainly heteroatomic with minor homoatomic contributions. Synthesis and crystal growth is mostly accomplished by comproportionation of RX_3 and R in the presence of T at high temperatures in refractory metal containers (mostly niobium or tantalum) followed by controlled cooling.

After presenting the components and synthesis of the cluster complexes described in this review, the chapter focuses on detailed descriptions of their crystal chemistry before ending with a discussion on their electronic structure. So far, not much is known about the physical properties, such as conductivity or magnetism, of these compounds, an issue that requires closer inspection in the immediate future.

CHAPTER 265. SOLID-STATE OPTICAL REFRIGERATION

By Markus P. Hehlen, Mansoor Sheik-Bahae, and Richard I. Epstein

Los Alamos National Laboratory, University of New Mexico, Albuquerque, and ThermoDynamic Films, Santa Fe, USA



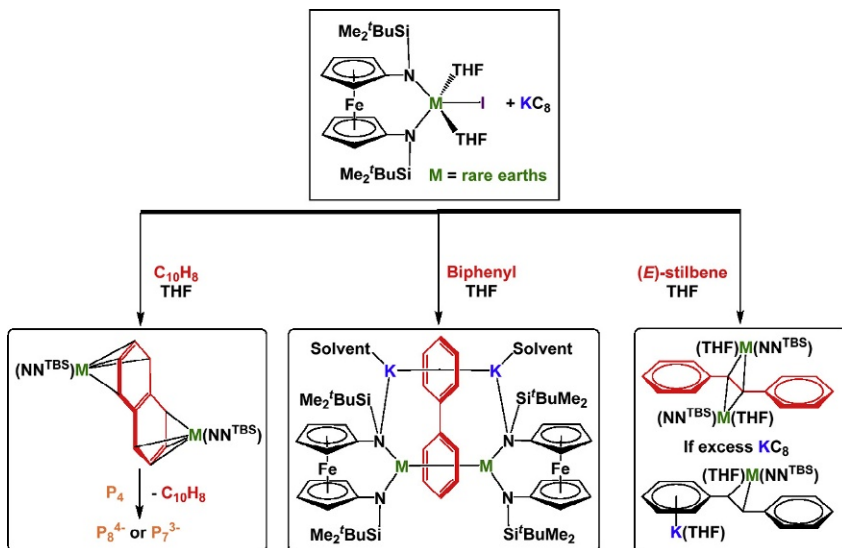
Refrigeration is a technique almost as old as humanity. Until the middle of the nineteenth century, collecting of ice and snow, evaporating water, or dissolving salts into it were the major cooling technologies. The discovery of cyclic refrigeration was a major breakthrough, and vapor compression, vapor absorption, and gas cycle refrigerators meet most of everyday refrigeration needs with a few new technologies such as magnetocaloric, electrocaloric, and elastocaloric refrigeration emerging as promising tools. Semiconductor optical detectors largely benefit from cryogenic technologies to improve their signal-to-noise ratio. Their cooling is however challenging in view of constraints in size, weight, power, and especially vibrations. Present techniques, which include liquid helium and thermoelectric coolers, have definite limitations so that optical cooling may be a viable alternative. The latter phenomenon is based on the observation that some luminescent materials emit light of higher energy than the excitation source, the energy difference being supplied by vibrational levels. Lanthanide ions doped into inorganic matrices, in particular trivalent erbium, thulium, and ytterbium, have excited states with large

quantum efficiencies, which make them ideal candidates for optical refrigeration. Although the efficiency remains small, laser-induced cooling allows one to reach lower temperatures (100 K) compared to thermoelectric cooling (170 K) and it is therefore an exciting technology with appreciable potential for solid-state optical devices.

The chapter starts with a brief history of refrigeration and solid-state cooling before concentrating on the description of experimental techniques, followed by a presentation of lanthanide-doped laser-cooling materials. It concludes on considerations aiming at improving the cooling efficiency and requirements for the design of practical lanthanide-based optical containing devices. It is anticipated that cooling temperatures down to liquid nitrogen temperature could be reached with Yb-doped YLiF_4 .

CHAPTER 266. RARE EARTH ARENE-BRIDGED COMPLEXES OBTAINED BY REDUCTION OF ORGANOMETALLIC PRECURSORS

By Wenlian Huang and Paula L. Diaconescu
University of California, Los Angeles, USA



Rare earth organometallic chemistry has witnessed remarkable advances since the first paper that appeared 60 years ago on cyclopentadienyl compounds, authored by Wilkinson and Birmingham. In particular, ancillary ligands other than cyclopentadienyl derivatives have been introduced and their complexes exhibit distinct reactivity and properties compared to the metallocene or half-sandwiched analogues. The chapter reviews arene-bridged rare-earth complexes with emphasis on compounds obtained by reduction

reactions. A particular accent is placed on rare-earth complexes supported by 1,1'-ferrocenediyl diamides since they have the most diverse chemistry with arenes: fused arenes, such as naphthalene and anthracene, form inverse-sandwiched complexes in which the arene is dianionic; weakly conjugated arenes, such as biphenyl, *p*-terphenyl, and 1,3,5-triphenylbenzene, are unexpectedly reduced by four-electron processes and lead to 6-carbon, 10- π electron aromatic systems; on the contrary, (*E*)-stilbene can only be reduced by two electrons, which are located on the carbon-carbon double bond instead of the phenyl rings. The reactivity of some rare earth arene-bridged complexes is discussed, for instance activation of white phosphorus by rare-earth naphthalene complexes.

The review begins with a selective summary of the history of organometallic and reductive rare-earth chemistry as an introduction to bimetallic lanthanide complexes bridged by ligands derived from arenes and to complexes of ferrocene-based diamide ligands, a major subtheme in the chapter. Detailed discussions then follow on complexes derived from fused rings and their reactivity with phosphorus and on complexes derived from biphenyl and stilbene as substrates, with emphasis on ferrocene-based diamide complexes.

Jean-Claude G. Bünzli
Vitalij K. Pecharsky

Contents

Preface	v
Contents	xi
Contents of Volumes 1–44	xiii
Index of Contents of Volumes 1–45	xxvii
263. Gas-Phase Ion Chemistry of Rare Earths and Actinides	1
<i>Joaquim Marçalo and John K. Gibson</i>	
264. Symbiosis of Intermetallic and Salt: Rare-Earth Metal Cluster Complexes with Endohedral Transition Metal Atoms	111
<i>Gerd Meyer</i>	
265. Solid-State Optical Refrigeration	179
<i>Markus P. Hehlen, Mansoor Sheik-Bahae, and Richard I. Epstein</i>	
266. Rare Earth Arene-Bridged Complexes Obtained by Reduction of Organometallic Precursors	261
<i>Wenliang Huang and Paula L. Diaconescu</i>	
Index	331

This page intentionally left blank

Contents of Volumes 1–44

VOLUME 1: Metals

1978, 1st repr. 1982, 2nd repr. 1991; ISBN 0-444-85020-1

1. Z.B. Goldschmidt, *Atomic properties (free atom)* 1
 2. B.J. Beaudry and K.A. Gschneidner Jr, *Preparation and basic properties of the rare earth metals* 173
 3. S.H. Liu, *Electronic structure of rare earth metals* 233
 4. D.C. Koskenmaki and K.A. Gschneidner Jr, *Cerium* 337
 5. L.J. Sundström, *Low temperature heat capacity of the rare earth metals* 379
 6. K.A. McEwen, *Magnetic and transport properties of the rare earths* 411
 7. S.K. Sinha, *Magnetic structures and inelastic neutron scattering: metals, alloys and compounds* 489
 8. T.E. Scott, *Elastic and mechanical properties* 591
 9. A. Jayaraman, *High pressure studies: metals, alloys and compounds* 707
 10. C. Probst and J. Wittig, *Superconductivity: metals, alloys and compounds* 749
 11. M.B. Maple, L.E. DeLong and B.C. Sales, *Kondo effect: alloys and compounds* 797
 12. M.P. Dariel, *Diffusion in rare earth metals* 847
- Subject index 877

VOLUME 2: Alloys and intermetallics

1979, 1st repr. 1982, 2nd repr. 1991; ISBN 0-444-85021-X

13. A. Iandelli and A. Palenzona, *Crystal chemistry of intermetallic compounds* 1
 14. H.R. Kirchmayr and C.A. Poldy, *Magnetic properties of intermetallic compounds of rare earth metals* 55
 15. A.E. Clark, *Magnetostrictive RFe_2 intermetallic compounds* 231
 16. J.J. Rhyne, *Amorphous magnetic rare earth alloys* 259
 17. P. Fulde, *Crystal fields* 295
 18. R.G. Barnes, *NMR, EPR and Mössbauer effect: metals, alloys and compounds* 387
 19. P. Wachter, *Europium chalcogenides: EuO, EuS, EuSe and EuTe* 507
 20. A. Jayaraman, *Valence changes in compounds* 575
- Subject index 613

VOLUME 3: Non-metallic compounds – I

1979, 1st repr. 1984; ISBN 0-444-85215-8

21. L.A. Haskin and T.P. Paster, *Geochemistry and mineralogy of the rare earths* 1
22. J.E. Powell, *Separation chemistry* 81
23. C.K. Jørgensen, *Theoretical chemistry of rare earths* 111
24. W.T. Carnall, *The absorption and fluorescence spectra of rare earth ions in solution* 171
25. L.C. Thompson, *Complexes* 209
26. G.G. Libowitz and A.J. Maeland, *Hydrides* 299
27. L. Eyring, *The binary rare earth oxides* 337
28. D.J.M. Bevan and E. Summerville, *Mixed rare earth oxides* 401

29. C.P. Khattak and F.F.Y. Wang, *Perovskites and garnets* 525
30. L.H. Brixner, J.R. Barkley and W. Jeitschko, *Rare earth molybdates (VI)* 609
Subject index 655

VOLUME 4: Non-metallic compounds – II

1979, 1st repr. 1984; ISBN 0-444-85216-6

31. J. Flahaut, *Sulfides, selenides and tellurides* 1
32. J.M. Haschke, *Halides* 89
33. F. Hulliger, *Rare earth pnictides* 153
34. G. Blasse, *Chemistry and physics of R-activated phosphors* 237
35. M.J. Weber, *Rare earth lasers* 275
36. F.K. Fong, *Nonradiative processes of rare-earth ions in crystals* 317
37A. J.W. O’Laughlin, *Chemical spectrophotometric and polarographic methods* 341
37B. S.R. Taylor, *Trace element analysis of rare earth elements by spark source mass spectroscopy* 359
37C. R.J. Conzemius, *Analysis of rare earth matrices by spark source mass spectrometry* 377
37D. E.L. DeKalb and V.A. Fassel, *Optical atomic emission and absorption methods* 405
37E. A.P. D’Silva and V.A. Fassel, *X-ray excited optical luminescence of the rare earths* 441
37F. F.W.V. Boynton, *Neutron activation analysis* 457
37G. S. Schuhmann and J.A. Philpotts, *Mass-spectrometric stable-isotope dilution analysis for lanthanides in geochemical materials* 471
38. J. Reuben and G.A. Elgavish, *Shift reagents and NMR of paramagnetic lanthanide complexes* 483
39. J. Reuben, *Bioinorganic chemistry: lanthanides as probes in systems of biological interest* 515
40. T.J. Haley, *Toxicity* 553
Subject index 587

VOLUME 5

1982, 1st repr. 1984; ISBN 0-444-86375-3

41. M. Gasgnier, *Rare earth alloys and compounds as thin films* 1
42. E. Gratz and M.J. Zuckermann, *Transport properties (electrical resistivity, thermoelectric power thermal conductivity) of rare earth intermetallic compounds* 117
43. F.P. Netzer and E. Bertel, *Adsorption and catalysis on rare earth surfaces* 217
44. C. Boulesteix, *Defects and phase transformation near room temperature in rare earth sesquioxides* 321
45. O. Greis and J.M. Haschke, *Rare earth fluorides* 387
46. C.A. Morrison and R.P. Leavitt, *Spectroscopic properties of triply ionized lanthanides in transparent host crystals* 461
Subject index 693

VOLUME 6

1984; ISBN 0-444-86592-6

47. K.H.J. Buschow, *Hydrogen absorption in intermetallic compounds* 1
48. E. Parthé and B. Chabot, *Crystal structures and crystal chemistry of ternary rare earth–transition metal borides, silicides and homologues* 113
49. P. Rogl, *Phase equilibria in ternary and higher order systems with rare earth elements and boron* 335

50. H.B. Kagan and J.L. Namy, *Preparation of divalent ytterbium and samarium derivatives and their use in organic chemistry* 525
Subject index 567

VOLUME 7

1984; ISBN 0-444-86851-8

51. P. Rogl, *Phase equilibria in ternary and higher order systems with rare earth elements and silicon* 1
52. K.H.J. Buschow, *Amorphous alloys* 265
53. H. Schumann and W. Genthe, *Organometallic compounds of the rare earths* 446
Subject index 573

VOLUME 8

1986; ISBN 0-444-86971-9

54. K.A. Gschneidner Jr and F.W. Calderwood, *Intra rare earth binary alloys: phase relationships, lattice parameters and systematics* 1
55. X. Gao, *Polarographic analysis of the rare earths* 163
56. M. Leskelä and L. Niinistö, *Inorganic complex compounds I* 203
57. J.R. Long, *Implications in organic synthesis* 335
Errata 375
Subject index 379

VOLUME 9

1987; ISBN 0-444-87045-8

58. R. Reisfeld and C.K. Jørgensen, *Excited state phenomena in vitreous materials* 1
59. L. Niinistö and M. Leskelä, *Inorganic complex compounds II* 91
60. J.-C.G. Bünzli, *Complexes with synthetic ionophores* 321
61. Zhiqian Shen and Jun Ouyang, *Rare earth coordination catalysis in stereospecific polymerization* 395
Errata 429
Subject index 431

VOLUME 10: High energy spectroscopy

1987; ISBN 0-444-87063-6

62. Y. Baer and W.-D. Schneider, *High-energy spectroscopy of lanthanide materials – An overview* 1
63. M. Campagna and F.U. Hillebrecht, *f-electron hybridization and dynamical screening of core holes in intermetallic compounds* 75
64. O. Gunnarsson and K. Schönhammer, *Many-body formulation of spectra of mixed valence systems* 103
65. A.J. Freeman, B.I. Min and M.R. Norman, *Local density supercell theory of photoemission and inverse photoemission spectra* 165
66. D.W. Lynch and J.H. Weaver, *Photoemission of Ce and its compounds* 231
67. S. Hüfner, *Photoemission in chalcogenides* 301
68. J.F. Herbst and J.W. Wilkins, *Calculation of 4f excitation energies in the metals and relevance to mixed valence systems* 321
69. B. Johansson and N. Mårtensson, *Thermodynamic aspects of 4f levels in metals and compounds* 361
70. F.U. Hillebrecht and M. Campagna, *Bremsstrahlung isochromat spectroscopy of alloys and mixed valent compounds* 425

71. J. Röhler, *X-ray absorption and emission spectra* 453
 72. F.P. Netzer and J.A.D. Matthew, *Inelastic electron scattering measurements* 547
 Subject index 601

VOLUME 11: Two-hundred-year impact of rare earths on science

1988; ISBN 0-444-87080-6

H.J. Svec, *Prologue* 1

73. F. Szabadváry, *The history of the discovery and separation of the rare earths* 33
 74. B.R. Judd, *Atomic theory and optical spectroscopy* 81
 75. C.K. Jørgensen, *Influence of rare earths on chemical understanding and classification* 197
 76. J.J. Rhyne, *Highlights from the exotic phenomena of lanthanide magnetism* 293
 77. B. Bleaney, *Magnetic resonance spectroscopy and hyperfine interactions* 323
 78. K.A. Gschneidner Jr and A.H. Daane, *Physical metallurgy* 409
 79. S.R. Taylor and S.M. McLennan, *The significance of the rare earths in geochemistry and cosmochemistry* 485
 Errata 579
 Subject index 581

VOLUME 12

1989; ISBN 0-444-87105-5

80. J.S. Abell, *Preparation and crystal growth of rare earth elements and intermetallic compounds* 1
 81. Z. Fisk and J.P. Remeika, *Growth of single crystals from molten metal fluxes* 53
 82. E. Burzo and H.R. Kirchmayr, *Physical properties of $R_2Fe_{14}B$ -based alloys* 71
 83. A. Szytuła and J. Leciejewicz, *Magnetic properties of ternary intermetallic compounds of the RT_2X_2 type* 133
 84. H. Maletta and W. Zinn, *Spin glasses* 213
 85. J. van Zytveld, *Liquid metals and alloys* 357
 86. M.S. Chandrasekharaiah and K.A. Gingerich, *Thermodynamic properties of gaseous species* 409
 87. W.M. Yen, *Laser spectroscopy* 433
 Subject index 479

VOLUME 13

1990; ISBN 0-444-88547-1

88. E.I. Gladyshevsky, O.I. Bodak and V.K. Pecharsky, *Phase equilibria and crystal chemistry in ternary rare earth systems with metallic elements* 1
 89. A.A. Eliseev and G.M. Kuzmichyeva, *Phase equilibrium and crystal chemistry in ternary rare earth systems with chalcogenide elements* 191
 90. N. Kimizuka, E. Takayama-Muromachi and K. Siratori, *The systems R_2O_3 – M_2O_3 – $M'O$* 283
 91. R.S. Houk, *Elemental analysis by atomic emission and mass spectrometry with inductively coupled plasmas* 385
 92. P.H. Brown, A.H. Rathjen, R.D. Graham and D.E. Tribe, *Rare earth elements in biological systems* 423
 Errata 453
 Subject index 455

VOLUME 14

1991; ISBN 0-444-88743-1

93. R. Osborn, S.W. Lovesey, A.D. Taylor and E. Balcar, *Intermultiplet transitions using neutron spectroscopy* 1
94. E. Dormann, *NMR in intermetallic compounds* 63
95. E. Zirngiebl and G. Güntherodt, *Light scattering in intermetallic compounds* 163
96. P. Thalmeier and B. Lüthi, *The electron–phonon interaction in intermetallic compounds* 225
97. N. Grewe and F. Steglich, *Heavy fermions* 343
- Subject index 475

VOLUME 15

1991; ISBN 0-444-88966-3

98. J.G. Sereni, *Low-temperature behaviour of cerium compounds* 1
99. G.-Y. Adachi, N. Imanaka and Zhang Fuzhong, *Rare earth carbides* 61
100. A. Simon, H.J. Mattausch, G.J. Miller, W. Bauhofer and R.K. Kremer, *Metal-rich halides* 191
101. R.M. Almeida, *Fluoride glasses* 287
102. K.L. Nash and J.C. Sullivan, *Kinetics of complexation and redox reactions of the lanthanides in aqueous solutions* 347
103. E.N. Rizkalla and G.R. Choppin, *Hydration and hydrolysis of lanthanides* 393
104. L.M. Vallarino, *Macrocyclic complexes of the lanthanide(III), yttrium(III), and dioxouranium (VI) ions from metal-templated syntheses* 443
- Errata 513
- Subject index 515

CUMULATIVE INDEX, Vols. 1–15

1993; ISBN 0-444-89965-0

VOLUME 16

1993; ISBN 0-444-89782-8

105. M. Loewenhaupt and K.H. Fischer, *Valence-fluctuation and heavy-fermion 4f systems* 1
106. I.A. Smirnov and V.S. Oskotski, *Thermal conductivity of rare earth compounds* 107
107. M.A. Subramanian and A.W. Sleight, *Rare earth pyrochlores* 225
108. R. Miyawaki and I. Nakai, *Crystal structures of rare earth minerals* 249
109. D.R. Chopra, *Appearance potential spectroscopy of lanthanides and their intermetallics* 519
- Author index 547
- Subject index 579

VOLUME 17: Lanthanides/Actinides: Physics – I

1993; ISBN 0-444-81502-3

110. M.R. Norman and D.D. Koelling, *Electronic structure, Fermi surfaces, and superconductivity in f electron metals* 1
111. S.H. Liu, *Phenomenological approach to heavy-fermion systems* 87
112. B. Johansson and M.S.S. Brooks, *Theory of cohesion in rare earths and actinides* 149
113. U. Benedict and W.B. Holzapfel, *High-pressure studies – Structural aspects* 245

114. O. Vogt and K. Mattenberger, *Magnetic measurements on rare earth and actinide mononictides and monochalcogenides* 301
115. J.M. Fournier and E. Gratz, *Transport properties of rare earth and actinide intermetallics* 409
116. W. Potzel, G.M. Kalvius and J. Gal, *Mössbauer studies on electronic structure of intermetallic compounds* 539
117. G.H. Lander, *Neutron elastic scattering from actinides and anomalous lanthanides* 635
Author index 711
Subject index 753

VOLUME 18: Lanthanides/Actinides: Chemistry

1994; ISBN 0-444-81724-7

118. G.T. Seaborg, *Origin of the actinide concept* 1
119. K. Balasubramanian, *Relativistic effects and electronic structure of lanthanide and actinide molecules* 29
120. J.V. Beitz, *Similarities and differences in trivalent lanthanide- and actinide-ion solution absorption spectra and luminescence studies* 159
121. K.L. Nash, *Separation chemistry for lanthanides and trivalent actinides* 197
122. L.R. Morss, *Comparative thermochemical and oxidation – reduction properties of lanthanides and actinides* 239
123. J.W. Ward and J.M. Haschke, *Comparison of 4f and 5f element hydride properties* 293
124. H.A. Eick, *Lanthanide and actinide halides* 365
125. R.G. Haire and L. Eyring, *Comparisons of the binary oxides* 413
126. S.A. Kinkead, K.D. Abney and T.A. O'Donnell, *f-Element speciation in strongly acidic media: lanthanide and mid-actinide metals, oxides, fluorides and oxide fluorides in superacids* 507
127. E.N. Rizkalla and G.R. Choppin, *Lanthanides and actinides hydration and hydrolysis* 529
128. G.R. Choppin and E.N. Rizkalla, *Solution chemistry of actinides and lanthanides* 559
129. J.R. Duffield, D.M. Taylor and D.R. Williams, *The biochemistry of the f-elements* 591
Author index 623
Subject index 659

VOLUME 19: Lanthanides/Actinides: Physics – II

1994; ISBN 0-444-82015-9

130. E. Holland-Moritz and G.H. Lander, *Neutron inelastic scattering from actinides and anomalous lanthanides* 1
131. G. Aeppli and C. Broholm, *Magnetic correlations in heavy-fermion systems: neutron scattering from single crystals* 123
132. P. Wachter, *Intermediate valence and heavy fermions* 177
133. J.D. Thompson and J.M. Lawrence, *High pressure studies – Physical properties of anomalous Ce, Yb and U compounds* 383
134. C. Colinet and A. Pasturel, *Thermodynamic properties of metallic systems* 479
Author index 649
Subject index 693

VOLUME 20

1995; ISBN 0-444-82014-0

135. Y. Önuke and A. Hasegawa, *Fermi surfaces of intermetallic compounds* 1
136. M. Gasgnier, *The intricate world of rare earth thin films: metals, alloys, intermetallics, chemical compounds,...* 105
137. P. Vajda, *Hydrogen in rare-earth metals, including RH_{2+x} phases* 207
138. D. Gignoux and D. Schmitt, *Magnetic properties of intermetallic compounds* 293
Author index 425
Subject index 457

VOLUME 21

1995; ISBN 0-444-82178-3

139. R.G. Bautista, *Separation chemistry* 1
140. B.W. Hinton, *Corrosion prevention and control* 29
141. N.E. Ryan, *High-temperature corrosion protection* 93
142. T. Sakai, M. Matsuoka and C. Iwakura, *Rare earth intermetallics for metal–hydrogen batteries* 133
143. G.-y. Adachi and N. Imanaka, *Chemical sensors* 179
144. D. Garcia and M. Faucher, *Crystal field in non-metallic (rare earth) compounds* 263
145. J.-C.G. Bünzli and A. Milicic-Tang, *Solvation and anion interaction in organic solvents* 305
146. V. Bhagavathy, T. Prasada Rao and A.D. Damodaran, *Trace determination of lanthanides in high-purity rare-earth oxides* 367
Author index 385
Subject index 411

VOLUME 22

1996; ISBN 0-444-82288-7

147. C.P. Flynn and M.B. Salamon, *Synthesis and properties of single-crystal nanostructures* 1
148. Z.S. Shan and D.J. Sellmyer, *Nanoscale rare earth–transition metal multilayers: magnetic structure and properties* 81
149. W. Suski, *The $ThMn_{12}$ -type compounds of rare earths and actinides: structure, magnetic and related properties* 143
150. L.K. Aminov, B.Z. Malkin and M.A. Teplov, *Magnetic properties of nonmetallic lanthanide compounds* 295
151. F. Auzel, *Coherent emission in rare-earth materials* 507
152. M. Dolg and H. Stoll, *Electronic structure calculations for molecules containing lanthanide atoms* 607
Author index 731
Subject index 777

VOLUME 23

1996; ISBN 0-444-82507-X

153. J.H. Forsberg, *NMR studies of paramagnetic lanthanide complexes and shift reagents* 1
154. N. Sabbatini, M. Guardigli and I. Manet, *Antenna effect in encapsulation complexes of lanthanide ions* 69
155. C. Görller-Walrand and K. Binnemans, *Rationalization of crystal-field parameterization* 121
156. Yu. Kuz'ma and S. Chykhrij, *Phosphides* 285

157. S. Boghosian and G.N. Papatheodorou, *Halide vapors and vapor complexes* 435
158. R.H. Byrne and E.R. Sholkovitz, *Marine chemistry and geochemistry of the lanthanides* 497
Author index 595
Subject index 631

VOLUME 24

1997; ISBN 0-444-82607-6

159. P.A. Dowben, D.N. McIlroy and Dongqi Li, *Surface magnetism of the lanthanides* 1
160. P.G. McCormick, *Mechanical alloying and mechanically induced chemical reactions* 47
161. A. Inoue, *Amorphous, quasicrystalline and nanocrystalline alloys in Al- and Mg-based systems* 83
162. B. Elschner and A. Loidl, *Electron-spin resonance on localized magnetic moments in metals* 221
163. N.H. Duc, *Intersublattice exchange coupling in the lanthanide-transition metal intermetallics* 339
164. R.V. Skolozdra, *Stannides of rare-earth and transition metals* 399
Author index 519
Subject index 559

VOLUME 25

1998; ISBN 0-444-82871-0

165. H. Nagai, *Rare earths in steels* 1
166. R. Marchand, *Ternary and higher order nitride materials* 51
167. C. Görrler-Walrand and K. Binnemans, *Spectral intensities of f-f transitions* 101
168. G. Bombieri and G. Paolucci, *Organometallic π complexes of the f-elements* 265
Author index 415
Subject index 459

VOLUME 26

1999; ISBN 0-444-50815-1

169. D.F. McMorrow, D. Gibbs and J. Bohr, *X-ray scattering studies of lanthanide magnetism* 1
170. A.M. Tishin, Yu.I. Spichkin and J. Bohr, *Static and dynamic stresses* 87
171. N.H. Duc and T. Goto, *Itinerant electron metamagnetism of Co sublattice in the lanthanide-cobalt intermetallics* 177
172. A.J. Arko, P.S. Riseborough, A.B. Andrews, J.J. Joyce, A.N. Tahvildar-Zadeh and M. Jarrell, *Photo-electron spectroscopy in heavy fermion systems: Emphasis on single crystals* 265
Author index 383
Subject index 405

VOLUME 27

1999; ISBN 0-444-50342-0

173. P.S. Salamakha, O.L. Sologub and O.I. Bodak, *Ternary rare-earth-germanium systems* 1
174. P.S. Salamakha, *Crystal structures and crystal chemistry of ternary rare-earth germanides* 225
175. B. Ya. Kotur and E. Gratz, *Scandium alloy systems and intermetallics* 339
Author index 535
Subject index 553

VOLUME 28

2000; ISBN 0-444-50346-3

176. J.-P. Connerade and R.C. Karnatak, *Electronic excitation in atomic species* 1
177. G. Meyer and M.S. Wickleder, *Simple and complex halides* 53
178. R.V. Kumar and H. Iwahara, *Solid electrolytes* 131
179. A. Halperin, *Activated thermoluminescence (TL) dosimeters and related radiation detectors* 187
180. K.L. Nash and M.P. Jensen, *Analytical separations of the lanthanides: basic chemistry and methods* 311
Author index 373
Subject index 401

VOLUME 29: The role of rare earths in catalysis

2000; ISBN 0-444-50472-9

P. Maestro, *Foreword* 1

181. V. Paul-Boncour, L. Hilaire and A. Percheron-Guégan, *The metals and alloys in catalysis* 5
182. H. Imamura, *The metals and alloys (prepared utilizing liquid ammonia solutions) in catalysis II* 45
183. M.A. Ulla and E.A. Lombardo, *The mixed oxides* 75
184. J. Kašpar, M. Graziani and P. Fornasiero, *Ceria-containing three-way catalysts* 159
185. A. Corma and J.M. López Nieto, *The use of rare-earth-containing zeolite catalysts* 269
186. S. Kobayashi, *Triflates* 315
Author index 377
Subject index 409

VOLUME 30: High-Temperature Superconductors – I

2000; ISBN 0-444-50528-8

187. M.B. Maple, *High-temperature superconductivity in layered cuprates: overview* 1
188. B. Raveau, C. Michel and M. Hervieu, *Crystal chemistry of superconducting rare-earth cuprates* 31
189. Y. Shiohara and E.A. Goodilin, *Single-crystal growth for science and technology* 67
190. P. Karen and A. Kjekshus, *Phase diagrams and thermodynamic properties* 229
191. B. Elschner and A. Loidl, *Electron paramagnetic resonance in cuprate superconductors and in parent compounds* 375
192. A.A. Manuel, *Positron annihilation in high-temperature superconductors* 417
193. W.E. Pickett and I.I. Mazin, *RBa₂Cu₃O₇ compounds: electronic theory and physical properties* 453
194. U. Staub and L. Soderholm, *Electronic 4f-state splittings in cuprates* 491
Author index 547
Subject index 621

VOLUME 31: High-Temperature Superconductors – II

2001; ISBN 0-444-50719-1

195. E. Kaldis, *Oxygen nonstoichiometry and lattice effects in YBa₂Cu₃O_x. Phase transitions, structural distortions and phase separation* 1
196. H.W. Weber, *Flux pinning* 187
197. C.C. Almasan and M.B. Maple, *Magnetoresistance and Hall effect* 251
198. T.E. Mason, *Neutron scattering studies of spin fluctuations in high-temperature superconductors* 281

199. J.W. Lynn and S. Skanthakumar, *Neutron scattering studies of lanthanide magnetic ordering* 315
200. P.M. Allenspach and M.B. Maple, *Heat capacity* 351
201. M. Schabel and Z.-X. Shen, *Angle-resolved photoemission studies of untwinned yttrium barium copper oxide* 391
202. D.N. Basov and T. Timusk, *Infrared properties of high- T_c superconductors: an experimental overview* 437
203. S.L. Cooper, *Electronic and magnetic Raman scattering studies of the high- T_c cuprates* 509
204. H. Sugawara, T. Hasegawa and K. Kitazawa, *Characterization of cuprate superconductors using tunneling spectra and scanning tunneling microscopy* 563
- Author index 609
- Subject index 677

VOLUME 32

2001; ISBN 0-444-50762-0

205. N.H. Duc, *Giant magnetostriction in lanthanide-transition metal thin films* 1
206. G.M. Kalvius, D.R. Noakes and O. Hartmann, *μ SR studies of rare-earth and actinide magnetic materials* 55
207. Rainer Pöttingen, Dirk Johrendt and Dirk Kußmann, *Structure–property relations of ternary equiatomic YbTX intermetallics* 453
208. Kurima Kobayashi and Satoshi Hirotsawa, *Permanent magnets* 515
209. I.G. Vasilyeva, *Polysulfides* 567
2010. Dennis K.P. Ng, Jianzhuang Jiang, Kuninobu Kasuga and Kenichi Machida, *Half-sandwich tetrapyrrole complexes of rare earths and actinides* 611
- Author index 655
- Subject index 733

VOLUME 33

2003; ISBN 0-444-51323-X

211. Brian C. Sales, *Filled skutterudites* 1
212. Oksana L. Sologub and Petro S. Salamakha, *Rare earth – antimony systems* 35
213. R.J.M. Konings and A. Kovács, *Thermodynamic properties of the lanthanide (III) halides* 147
214. John B. Goodenough, *Rare earth – manganese perovskites* 249
215. Claude Piguet and Carlos F.G.C. Geraldes, *Paramagnetic NMR lanthanide induced shifts for extracting solution structures* 353
216. Isabelle Billard, *Lanthanide and actinide solution chemistry as studied by time-resolved emission spectroscopy* 465
217. Thomas Tröster, *Optical studies of non-metallic compounds under pressure* 515
- Author index 591
- Subject index 637

VOLUME 34

2004; ISBN 0-444-51587-9

218. Yaroslav M. Kalychak, Vasyl' I. Zaremba, Rainer Pöttingen, Mar'yana Lukachuk and Rolf-Dieter Hoffman, *Rare earth–transition metal–indides* 1
219. P. Thalmeier and G. Zwicknagl, *Unconventional superconductivity and magnetism in lanthanide and actinide intermetallic compounds* 135
220. James P. Riehl and Gilles Muller, *Circularly polarized luminescence spectroscopy from lanthanide systems* 289

221. Oliver Guillou and Carole Daiguebonne, *Lanthanide-containing coordination polymers* 359
222. Makoto Komiyama, *Cutting DNA and RNA* 405
 Author index 455
 Subject index 493

VOLUME 35

2005; ISBN 0-444-52028-7

223. Natsuko Sakai, Katsuhiko Yamaji, Teruhisa Horita, Yue Ping Xiong and Harumi Yokokawa, *Rare-earth materials for solid oxide fuel cells (SOFC)* 1
224. Mathias S. Wickleder, *Oxo-selenates of rare-earth elements* 45
225. Koen Binnemans, *Rare-earth beta-diketonates* 107
226. Satoshi Shinoda, Hiroyuki Miyake and Hiroshi Tsukube, *Molecular recognition and sensing via rare-earth complexes* 273
 Author index 337
 Subject index 377

VOLUME 36

2006; ISBN 0-444-52142-9

227. Arthur Mar, *Bismuthides* 1
228. I. Aruna, L.K. Malhotra and B.R. Mehta, *Switchable metal hydride films* 83
229. Koen Binnemans, *Applications of tetravalent cerium compounds* 281
230. Robert A. Flowers II and Edamana Prasad, *Samarium (II) based reductants* 393
 Author index 475
 Subject index 511

VOLUME 37: Optical Spectroscopy

2007; ISBN 978-0-444-52144-6

231. Kazuyoshi Ogasawara, Shinta Watanabe, Hiroaki Toyoshima and Mikhail G. Brik, *First-principles calculations of $4f^n \rightarrow 4f^{n-1} 5d$ transition spectra* 1
232. Gary W. Burdick and Michael F. Reid, *$4f^n-4f^{n-1} 5d$ transitions* 61
233. Guokui Liu and Xueyuan Chen, *Spectroscopic properties of lanthanides in nanomaterials* 99
234. Takuya Nishioka, Kôichi Fukui and Kazuko Matsumoto, *Lanthanide chelates as luminescent labels in biomedical analyses* 171
235. Steve Comby and Jean-Claude G. Bünzli, *Lanthanide near-infrared luminescence in molecular probes and devices* 217
 Author index 471
 Subject index 503

VOLUME 38

2008; ISBN 978-0-444-52143-9

236. Z.C. Kang, *Lanthanide higher oxides: The contributions of Leroy Eyring* 1
237. Rainer Pöttgen and Ute Ch. Rodewald, *Rare earth–transition metal–plumbides* 55
238. Takao Mori, *Higher borides* 105
239. K.-H. Müller, M. Schneider, G. Fuchs and S.-L. Drechsler, *Rare-earth nickel borocarbides* 175
240. Michael T. Pope, *Polyoxometalates* 337
 Author index 383
 Subject index 431

VOLUME 39

2009; ISBN 978-0-444-53221-3

241. W.M. Temmerman, L. Petit, A. Svane, Z. Szotek, M. Lüders, P. Strange, J.B. Staunton, I.D. Hughes, and B.L. Gyorffy, *The dual, localized or band-like, character of the 4f-states* 1
242. L. Vasylechko, A. Senyshyn, and U. Bismayer, *Perovskite-type aluminates and gallates* 113
243. Toshihiro Yamase, *Luminescence of polyoxometallolanthanoates and photochemical nano-ring formation* 297
- Author index 357
- Subject index 381

VOLUME 40

2010; ISBN 978-0-444-53220-6

244. Christiane Görller-Walrand and Linda Fluyt, *Magnetic circular dichroism of lanthanides* 1
245. Z. Zheng, *Cluster compounds of rare-earth elements* 109
246. François Nief, *Molecular chemistry of the rare-earth elements in uncommon low-valent states* 241
247. Claude Piguet and Jean-Claude G. Bünzli, *Self-Assembled lanthanide helicates: From basic thermodynamics to applications* 301
- Author index 555
- Subject index 583

VOLUME 41

2011; ISBN 978-0-444-53590-0

248. Pieter Thyssen and Koen Binnemans, *Accommodation of the rare earths in the periodic table: A historical analysis* 1
249. Hisanori Shinohara and Yahachi Saito, *Metallofullerenes* 95
250. Lubomir D. Gulay and Marek Daszkiewicz, *Ternary and quaternary chalcogenides of Si, Ge, Sn, Pb, and In* 157
251. Chun-Hua Yan, Zheng-Guang Yan, Ya-Ping Du, Jie Shen, Chao Zhang, and Wei Feng, *Controlled synthesis and properties of rare earth nanomaterials* 275
- Author index 473
- Subject index 517

VOLUME 42

2012; ISBN 978-0-444-54316-5

252. Y. Uwatoko, I. Umehara, M. Ohashi, T. Nakano, and G. Oomi, *Thermal and electronic properties of rare earth compounds at high pressure* 1
253. Alexander D. Chervonnyi, *Thermodynamic properties of lanthanide fluorides and chlorides in the gaseous and condensed states* 165
- Author index 485
- Subject index 507

VOLUME 43

2013; ISBN 978-0-444-59536-2

254. Koen Binnemans, *Lanthanidomesogens* 1
255. Mikiya Tanaka, Tatsuya Oki, Kazuya Koyama, Hirokazu Narita, and Tetsuo Oishi, *Recycling of rare earths from scrap* 159
256. Isabelle Billard, *Ionic liquids: New hopes for efficient lanthanide/actinide extraction and separation?* 213
257. Gopi K. Samudrala and Yogesh K. Vohra, *Structural properties of lanthanides at ultra high pressure* 275
258. John W. Arblaster, *Selected values of the thermodynamic properties of scandium, yttrium, and the lanthanide elements* 321
- Author index 567
- Subject index 591

VOLUME 44

2014; ISBN 978-0-444-62711-7

259. Sophie M. Guillaume, Laurent Maron, and Peter W. Roesky, *Catalytic Behavior of Rare-Earth Borohydride Complexes in Polymerization of Polar Monomers* 1
260. Yasuhiko Iwadate, *Structures and Properties of Rare-Earth Molten Salts* 87
261. Jean-Claude G. Bünzli and Anne-Sophie Chauvin, *Lanthanides in Solar Energy Conversion* 169
262. Yaroslav Mudryk, Vitalij K. Pecharsky, and Karl A. Gschneidner, Jr., *R₅T₄ Compounds: An Extraordinary Versatile Model System for the Solid State Science* 283
- Index 451

This page intentionally left blank

Index of Contents of Volumes 1–45

4f excitation energies, calculations
of **10**, ch. 68, p. 321
4f levels, thermodynamic aspects
10, ch. 69, p. 361
4f state splittings in cuprates **30**,
ch. 194, p. 491
4f states, character of **39**, ch. 241, p. 1
4fⁿ-4fⁿ⁻¹5d transitions **37**, ch. 231,
p. 1; **37**, ch. 232, p. 61

A

ab-initio calculation of energy
levels **37**, ch. 231, p. 1
absorption spectra of ions in
solution **3**, ch. 24, p. 171; **18**,
ch. 120, p. 159
actinides origin of concept **18**,
ch. 118, p. 1
– extraction of **43**, ch. 256, p. 213
– separation from lanthanides **43**,
ch. 256, p. 213
activated phosphors **4**, ch. 34, p. 237
activated thermoluminescence **28**,
ch. 179, p. 187
activation
– of P₄ by rare earths **45**, ch. 266, p. 261
aluminates **39**, ch. 242, p. 113
amorphous alloys **7**, ch. 52, p. 265
– Al- and Mg-based **24**, ch. 161, p. 83
– magnetic **2**, ch. 16, p. 259
anion interaction in organic solvents **21**,
ch. 145, p. 305
antimony alloy systems **33**,
ch. 212, p. 35
An-Ln separation using ionic liquids **43**,
ch. 256, p. 213
Atomic ions
– actinides in gas phase **45**, ch. 263, p. 1
– rare-earth ions in gas phase **45**, ch. 263,
p. 1
arene-bridged complexes **45**, ch. 266, p. 261

atomic properties (free atom) **1**, ch. 1, p. 1
atomic theory **11**, ch. 74, p. 81

B

batteries, recycling of **43**, ch. 255, p. 159
beta-diketonates **35**, ch. 225, p. 107
– mesogenic complexes **43**, ch. 254, p. 1
Belousov-Zhabotinsky reactions **36**,
ch. 229, p. 281
biochemistry **18**, ch. 129, p. 591
bioinorganic chemistry **4**, ch. 39, p. 515
biological systems **13**, ch. 92, p. 423
bioprobes **40**, ch. 247, p. 301
biphenyl complexes **45**, ch. 266, p. 261
bis(benzimidazole)pyridine
– mesogenic complexes **43**, ch. 254, p. 1
– self-assembled complexes **40**, ch. 247,
p. 303
bismuth alloy systems **36**, ch. 227, p. 1
borides **6**, ch. 48, p. 113; **6**, ch. 49,
p. 335; **38**, ch. 238, p. 105; **38**,
ch. 239, p. 175
borohydride complexes **44**, ch. 259, p. 1

C

carbides **15**, ch. 99, p. 61; **38**, ch. 239, p. 175
Carnall, William T. **37**, dedication, p. xiii
catalysis **29**, foreword, p. 1
– arene-bridged complexes **45**, ch. 266,
p. 261
– borohydrides **44**, ch. 259, p. 1
– ceria-containing three-way **29**,
ch. 184, p. 159
– metals and alloys **29**, ch. 181, p. 5
– metals and alloys in liquid ammonia
solutions **29**, ch. 182, p. 45
– stereospecific polymerization **9**, ch. 61,
p. 395; **44**, ch. 262, p. 283
– mixed oxides **29**, ch. 183, p. 75
– zeolites **29**, ch. 185, p. 269
catalysts, recycling of **43**, ch. 255, p. 159

- cerimetry **36**, ch. 229, p. 281
- cerium **1**, ch. 4, p. 337
- cerium compounds
- low-temperature behavior **15**, ch. 98, p. 1
 - tetravalent **36**, ch. 229, p. 281
- cerium(IV)
- catalysts **36**, ch. 229, p. 281
 - mediated reactions **36**, ch. 229, p. 281
 - redox properties **36**, ch. 229, p. 281
- chalcogenides,
- magnetic measurements on mono- **17**, ch. 114, p. 301
 - quaternary **41**, ch. 250, p. 157
 - ternary **41**, ch. 250, p. 157
- chemical analysis by
- atomic emission with inductively coupled plasmas **13**, ch. 91, p. 385
 - mass spectrometry, *see* spectroscopy, mass
 - neutron activation **4**, ch. 37F, p. 457
 - optical absorption **4**, ch. 37D, p. 405
 - optical atomic emission **4**, ch. 37D, p. 405
 - polarography **4**, ch. 37A, p. 341; **8**, ch. 55, p. 163
 - spectrophotometry **4**, ch. 37A, p. 341
 - trace determination in high-purity oxides **21**, ch. 146, p. 367
 - x-ray excited optical luminescence **4**, ch. 37E, p. 441
- chemical sensors **21**, ch. 143, p. 179
- chemical understanding and classification **11**, ch. 75, p. 197
- chirality sensing **35**, ch. 226, p. 273
- chlorides, thermodynamic properties of **42**, ch. 253, p. 165
- cluster compounds **40**, ch. 245, p. 109
- produced from solids and solutions **45**, ch. 263, p. 1
- cluster halides
- structure of **45**, ch. 264, p. 111
 - synthesis of **45**, ch. 264, p. 111
- coherent emission **22**, ch. 151, p. 507
- cohesion, theory of **17**, ch. 112, p. 149
- complexes (also see lanthanide chelates) **3**, ch. 25, p. 209
- antenna effect **23**, ch. 154, p. 69
 - arene-bridged **45**, ch. 266, p. 261
 - beta-diketonates **35**, ch. 225, p. 107
 - biphenyl **45**, ch. 266, p. 261
 - borohydrides in catalysis **44**, ch. 259, p. 1
 - encapsulation **23**, ch. 154, p. 69
 - group 3 stilbene **45**, ch. 266, p. 261
 - half-sandwich tetrapyrrole **32**, ch. 210, p. 611
 - inorganic **8**, ch. 56, p. 203; **9**, ch. 59, p. 91
 - low-valent state **40**, ch. 246, p. 241
 - macrocycles **15**, ch. 104, p. 443
 - molecular recognition in **35**, ch. 226, p. 273
 - organometallic π type **25**, ch. 168, p. 265
 - polyoxometalates **38**, ch. 240, p. 337
 - sensing in **35**, ch. 226, p. 273
 - with synthetic ionophores **9**, ch. 60, p. 321
- coordination in organic solvents **21**, ch. 145, p. 305
- coordination polymers **34**, ch. 221, p. 359
- corrosion
- prevention and control **21**, ch. 140, p. 29
 - protection **21**, ch. 141, p. 93
- cosmochemistry **11**, ch. 79, p. 485
- crystal chemistry
- of aluminates **39**, ch. 242, p. 113
 - of elements at ultra high pressure **43**, ch. 257, p. 275
 - of gallates **39**, ch. 242, p. 113
 - of higher borides **38**, ch. 238, p. 105
 - of intermetallic compounds **2**, ch. 13, p. 1
 - of quaternary systems with chalcogenides **41**, ch. 250, p. 157
 - of R_5T_4 intermetallic compound **44**, ch. 262, p. 283
 - of ternary germanides **27**, ch. 174, p. 225
 - of ternary systems with chalcogenides **13**, ch. 89, p. 191; **41**, ch. 250, p. 157
 - of ternary systems with metallic elements **13**, ch. 88, p. 1
 - of ternary transition metal borides **6**, ch. 48, p. 113
 - of ternary transition metal plumbides **38**, ch. 237, p. 55
 - of ternary transition metal silicides **6**, ch. 48, p. 113
 - of $ThMn_{12}$ -type compounds **22**, ch. 149, p. 143
- crystal field **2**, ch. 17, p. 295
- in non-metallic compounds **21**, ch. 144, p. 263
 - parametrization, rationalization of **23**, ch. 155, p. 121
- crystal structures, *see* crystal chemistry
- cuprates
- 4f state splittings **30**, ch. 194, p. 491
 - crystal chemistry **30**, ch. 188, p. 31

- electron paramagnetic resonance (EPR) **30**, ch. 191, p. 375
- electronic theory **30**, ch. 193, p. 453
- flux pinning **31**, ch. 196, p. 187
- Hall effect **31**, ch. 197, p. 251
- heat capacity **31**, ch. 200, p. 351
- infrared properties **31**, ch. 202, p. 437
- magnetoresistance **31**, ch. 197, p. 251
- neutron scattering
- – magnetic ordering **31**, ch. 199, p. 315
- – spin fluctuations **31**, ch. 198, p. 281
- overview **30**, ch. 187, p. 1
- oxygen nonstoichiometry and lattice effect **31**, ch. 195, p. 1
- phase equilibria **30**, ch. 190, p. 229
- – of R_5T_4 intermetallic compounds **44**, ch. 262, p. 283
- phase transitions, structural distortions and phase separation **31**, ch. 195, p. 1
- – in R_5T_4 intermetallic compounds **44**, ch. 262, p. 283
- photoemission, angle-resolved studies **31**, ch. 201, p. 391
- physical properties **30**, ch. 193, p. 453
- – of R_5T_4 intermetallic compounds **44**, ch. 262, p. 283
- positron annihilation **30**, ch. 192, p. 417
- Raman scattering **31**, ch. 203, p. 509
- scanning tunneling microscopy **31**, ch. 204, p. 563
- single crystals, growth of **30**, ch. 189, p. 67
- superconductivity **30**; **31**
- thermochemical properties **30**, ch. 190, p. 229
- tunneling spectra **31**, ch. 204, p. 563

D

- dedications
- F. H. Spedding **11**, p. 1
- Friedrich Hund **14**, p. ix
- LeRoy Eyring **36**, p. xi
- William T. Carnall **37**, p. xiii
- diffraction techniques
- at high pressure **42**, ch. 242, p. 4
- for molten salts structure determination
- diketonates, *see* beta-diketonates
- diffusion in metals **1**, ch. 12, p. 847
- divalent samarium in organic chemistry **6**, ch. 50, p. 525; **36**, ch. 230, p. 393
- divalent ytterbium in organic chemistry **6**, ch. 50, p. 525
- DNA, cutting of **34**, ch. 222, p. 405

- dye-sensitized solar cells, lanthanides in **44**, ch. 261, p. 169
- dynamical screening of core holes in intermetallic compounds **10**, ch. 63, p. 75

E

- elastic and mechanical properties of metals **1**, ch. 8, p. 591
- electron paramagnetic resonance (EPR) **2**, ch. 18, p. 387; **24**, ch. 162, p. 221
- in cuprate superconductors **30**, ch. 191, p. 375
- electronic excitation in atomic species **28**, ch. 176, p. 1
- electronic properties of compounds at high pressure **42**, ch. 252, p. 1
- electronic structure
- of actinide atomic ions in gas phase **45**, ch. 263, p. 1
- calculations for molecules **22**, ch. 152, p. 607
- of chalcogenides **39**, ch. 241, p. 1
- of metals **1**, ch. 3, p. 233; **17**, ch. 110, p. 1; **39**, ch. 241, p. 1
- of oxides **39**, ch. 241, p. 1
- of rare-earth atomic ions in gas phase **45**, ch. 263, p. 1
- of pnictides **39**, ch. 241, p. 1
- electronic theory of cuprates **30**, ch. 193, p. 453
- electron-phonon interaction in intermetallic compounds **14**, ch. 96, p. 225
- electron-spin resonance, *see* electron paramagnetic resonance
- emission spectra (also *see* fluorescence and luminescence)
- in solution **3**, ch. 24, 172
- X-ray excited **10**, ch. 71, p. 453
- energetics
- of actinide ions in gas phase **45**, ch. 263, p. 1
- of rare-earth ions in gas phase **45**, ch. 263, p. 1
- enthalpy of atomization
- of fluorides **42**, ch. 253, p. 429
- of monochlorides **42**, ch. 253, p. 412
- of RX^+ ions **42**, ch. 253, p. 436
- enthalpy of formation
- calculation with Born-Haber cycle **42**, ch. 253, p. 324
- of crystalline dichlorides **42**, ch. 253, p. 318

- of crystalline trichlorides **42**, ch. 253, p. 271
- of trichlorides, from mass spectra **42**, ch. 253, p. 306
- of trichlorides, from saturated vapor data **42**, ch. 253, p. 306
- enthalpy of phase transition
 - of crystalline trichlorides **42**, ch. 253, p. 256
- enthalpy of reaction involving RF, RF₂, and RCl **42**, ch. 253, p. 403
- enthalpy of sublimation
 - of dichlorides **42**, ch. 253, p. 354
 - of elements **43**, ch. 258, p. 321
 - of trichlorides **42**, ch. 253, p. 274
- enthalpy, standard of the elements **43**, ch. 258, p. 321
- entropy, standard, of the elements **43**, ch. 258, p. 321
- equilibrium constant
 - calculation for trichlorides **42**, ch. 253, p. 290
 - calculation for RF, RF₂, and RCl **42**, ch. 253, p. 403
- europium chalcogenides **2**, ch. 19, p. 507
- exchange coupling in transition metal intermetallics **24**, ch. 163, p. 339
- excited state phenomena in vitreous materials **9**, ch. 58, p. 1
- extraction, of rare earths and actinides **43**, ch. 256, p. 213
- Eyring, L.
 - dedication **36**, p. xi
 - contributions of, higher oxides **38**, ch. 236, p. 1

F

- f-electron hybridization **39**, ch. 241, p. 1
- in intermetallic compounds **10**, ch. 63, p. 75
- f-element speciation in strongly acidic media (superacids) **18**, ch. 126, p. 507
- f-f transitions, spectral intensities **25**, ch. 167, p. 101
- f-states: dual, localized, band-like character **39**, ch. 241, p. 1
- fast-atom bombardment mass spectrometry **45**, ch. 263, p. 1
- Fermi surfaces
 - of intermetallic compounds **20**, ch. 135, p. 1

- of metals **17**, ch. 110, p. 1
- ferrocene-based ligands **45**, ch. 266, p. 261
- fluorescence spectra of ions in solution **3**, ch. 24, p. 171
- fluorescence, anti-Stokes **45**, ch. 265, p. 179
- fluoride glasses **15**, ch. 101, p. 287; **45**, ch. 265, p. 179
- fluorides
 - properties **5**, ch. 45, p. 387
 - thermodynamic properties **42**, ch. 253, p. 165
- flux pinning in cuprates **31**, ch. 196, p. 187
- fullerenes **41**, ch. 249, p. 95

G

- gallates **39**, ch. 242, p. 113
- garnets **3**, ch. 29, p. 525
- gas-phase ion chemistry **45**, ch. 263, p. 1
- geochemistry **3**, ch. 21, p. 1; **11**, ch. 79, p. 485; **23**, ch. 158, p. 497
- germanium, ternary systems **27**, ch. 173, p. 1
- glow-discharge mass spectrometry **45**, ch. 263, p. 1
- giant magnetocaloric effect, see magnetocaloric effect
- guided ion beam mass spectrometry **45**, ch. 263, p. 1

H

- halides **4**, ch. 32, p. 89; **18**, ch. 124, p. 365
 - metal-rich **15**, ch. 100, p. 191
- Molten salts **44**, ch. 260, p. 87
 - simple and complex **28**, ch. 177, p. 53
 - thermodynamic properties **18**, ch. 122, p. 239; **33**, ch. 213, p. 147
 - vapors and vapor complexes **23**, ch. 157, p. 435
- Hall effect in cuprates **31**, ch. 197, p. 251
- heat capacity
 - of cuprates **31**, ch. 200, p. 351
 - of metals **1**, ch. 5, p. 379; **43**, ch. 258, p. 321
- heavy fermions **14**, ch. 97, p. 343; **16**, ch. 105, p. 1; **19**, ch. 132, p. 177
 - phenomenological approach **17**, ch. 111, p. 87
 - photoelectron spectroscopy **26**, ch. 172, p. 265
- helicates **40**, ch. 247, p. 301

- high pressure studies **1**, ch. 9, p. 707
- anomalous Ce, Yb and U compounds **19**, ch. 133, p. 383
 - diffraction techniques **42**, ch. 252, p. 4
 - electronic properties **42**, ch. 252, p. 82
 - heat capacity **42**, ch. 252, p. 45
 - mass spectra **42**, ch. 252, p. 18
 - magnetic properties **42**, ch. 252, p. 44
 - optical studies of non-metallic compounds **33**, ch. 217, p. 515
 - physical properties **42**, ch. 252, p. 4
 - structural aspects **17**, ch. 113, p. 245; **42**, ch. 252, p. 4
 - thermal expansion **42**, ch. 252, p. 33
- high temperature superconductors **30**; **31**
- history
- of the discovery and separation of rare earths **11**, ch. 73, p. 33
 - of the positioning of rare earths in the periodic table **41**, ch. 248, p. 1
- Hund, F. **14**, dedication, p. ix
- hydration **15**, ch. 103, p. 393; **18**, ch. 127, p. 529; **45**, ch. 263, p. 1
- hydrides **3**, ch. 26, p. 299; **18**, ch. 123, p. 293
- borohydrides **44**, ch. 259, p. 1
 - switchable films **36**, ch. 228, p. 83
- hydrogen absorption in intermetallic compounds **6**, ch. 47, p. 1
- hydrogen in metals, including
- RH_{2+x} phases **20**, ch. 137, p. 207
- hydrolysis **15**, ch. 103, p. 393; **18**, ch. 127, p. 529; **40**, ch. 245, p. 109; **45**, ch. 263, p. 1
- hyperfine interactions **11**, ch. 77, p. 323
- I**
- inelastic electron scattering **10**, ch. 72, p. 547
- infrared properties
- of cuprates **31**, ch. 202, p. 437
 - of molten salts **44**, ch. 260, p. 87
- inorganic complex compounds **8**, ch. 56 p. 203; **9**, ch. 59, p. 91
- Intermetallic compounds
- amorphous magnetic alloys **2**, ch. 16, p. 259
 - binary and pseudo-binary R₅T₄ compounds **44**, ch. 262, p. 283
 - chalcogenides **2**, ch. 19, p. 507
 - crystal chemistry **2**, ch. 13, p. 1
 - crystal fields in **2**, ch. 17, p. 295
 - dynamical screening of core holes **10**, ch. 63, p. 75
 - electron-phonon interaction **14**, ch. 96, p. 225
 - exchange coupling **24**, ch. 163, p. 339
 - f-electron hybridization **10**, ch. 63, p. 75
 - Fermi surfaces **20**, ch. 135, p. 1
 - growth of **12**, ch. 80, p. 1
 - hydrogen absorption **6**, ch. 47, p. 1
 - itinerant electron metamagnetism in cobalt compounds **26**, ch. 171, p. 177
 - light scattering **14**, ch. 95, p. 163
 - magnetic properties **2**, ch. 14, p. 55; **12**, ch. 83, p. 133; **20**, ch. 138, p. 293
 - magnetocaloric effect in R₅T₄ compounds **44**, ch. 262, p. 283
 - magnetostriction - in RFe₂ compounds **2**, ch. 15, p. 231
 - in R₅T₄ compounds **44**, ch. 262, p. 283
 - Mössbauer effect in **17**, ch. 116, p. 539
 - nuclear magnetic resonance in **2**, ch. 18, p. 387; **14**, ch. 94, p. 63
 - scandium alloy systems **27**, ch. 175, p. 339
 - ternary RT₂X₂ type compounds **12**, ch. 83, p. 133
 - ternary equiatomic YbTX **32**, ch. 207, 453
 - transport properties **5**, ch. 42, p. 117; **17**, ch. 115, p. 409
 - valence changes in **2**, ch. 20, p. 575
- intermediate valence **19**, ch. 132, p. 177
- ion cyclotron resonance
- mass spectrometry **45**, ch. 263, p. 1
- ionic liquids (also see molten salts), in
- An-Ln extraction and separation **43**, ch. 256, p. 213
- itinerant electron metamagnetism in cobalt intermetallics **26**, ch. 171, p. 177
- K**
- kinetics of complexation in aqueous solutions **15**, ch. 102, p. 347
- Kondo effect **1**, ch. 11, p. 797
- L**
- lanthanide-induced shifts **4**, ch. 38, p. 483; **23**, ch. 153, p. 1; **33**, ch. 215, p. 353
- lanthanide chelates (also see complexes)
- for sensitizing NIR luminescence **37**, ch. 234, p. 171
 - in biomedical analyses **37**, ch. 235, p. 217
- lanthanidomesogens **43**, ch. 254, p. 1

laser-ablation mass spectrometry **45**, ch. 263, p. 1
 laser cooling cycle **45**, ch. 265, p. 179
 laser spectroscopy **12**, ch. 87, p. 433
 lasers **4**, ch. 35, p. 275
 light scattering in intermetallic compounds **14**, ch. 95, p. 163
 liquid crystalline complexes **43**, ch. 254, p. 1
 liquid salts **44**, ch. 260, p. 87
 liquid metals and alloys **12**, ch. 85, p. 357
 LIS, *see* lanthanide-induced shifts
 luminescence
 – antenna effect **23**, ch. 154, p. 69
 – in biomedical analyses **37**, ch. 234, p. 171; **40**, ch. 247, p. 301
 – in NIR molecular probes and devices **37**, ch. 235, p. 217
 – polyoxometalates **39**, ch. 243, p. 297
 – studies of ions **18**, ch. 120, p. 159
 – spectra of ions in solution **3**, ch. 24, p. 171
 – thermometry **45**, ch. 265, p. 179
 luminescent solar concentrators, lanthanides in **44**, ch. 261, p. 169

M

μ SR studies of magnetic materials **32**, ch. 206, p. 55
 magnetic circular dichroism **40**, ch. 244, p. 1
 magnetic and transport properties of metals **1**, ch. 6, p. 411
 magnetic correlations in heavy-fermion systems **19**, ch. 131, p. 123
 magnetic properties (also *see* physical properties)
 – at high pressure **42**, ch. 252, p. 1
 – of borides **38**, ch. 238, p. 105
 – of intermetallic compounds **2**, ch. 14, p. 55; **20**, ch. 138, p. 293
 – of nickel borocarbides **38**, ch. 239, p. 175
 – of nonmetallic compounds **22**, ch. 150, p. 295
 – of R_5T_4 pseudobinary intermetallic compounds **44**, ch. 262, p. 283
 – of ternary RT_2X_2 type intermetallic compounds **12**, ch. 83, p. 133
 – of $ThMn_{12}$ -type compounds **22**, ch. 149, p. 143
 magnetic structures **1**, ch. 7, p. 489
 magnetism **34**, ch. 219, p. 135
 – exotic phenomena **11**, ch. 76, p. 293
 – surface **24**, ch. 159, p. 1
 magnetocaloric effect, in R_5T_4 compounds **44**, ch. 262, p. 283

magnetostriction
 – in R_5T_4 intermetallic compounds **44**, ch. 262, p. 283
 – RFe_2 **2**, ch. 15, p. 231
 – transition metal thin films **32**, ch. 205, p. 1
 marine chemistry **23**, ch. 158, p. 497
 mass spectra
 – of actinide ions in gas phase **45**, ch. 263, p. 1
 – calculation of enthalpy of formation from **42**, ch. 253, p. 299
 – of $EuCl_3$ and Eu_2Cl_6 **42**, ch. 253, p. 313
 – of rare-earth ions in gas phase **45**, ch. 263, p. 1
 mechanical alloying **24**, ch. 160, p. 47
 mechanically induced chemical reactions **24**, ch. 160, p. 47
 metal cluster complexes **45**, ch. 264, p. 111
 metal-hydrogen batteries **21**, ch. 142, p. 133
 metallofullerenes **41**, ch. 249, p. 95
 mineralogy **3**, ch. 21, p. 1
 minerals, crystal structures **16**, ch. 108, p. 249
 mixed valence systems
 – bremsstrahlung isochromat spectroscopy **10**, ch. 70, p. 425
 – calculation of $4f$ excitation energies **10**, ch. 68, p. 321
 – many-body formulation of spectra **10**, ch. 64, p. 103
 molecular recognition **35**, ch. 226, p. 273
 molten salts
 electrolysis **43**, ch. 255, p. 159
 – structure of halides **44**, ch. 260, p. 87
 molybdates (VI) **3**, ch. 30, p. 609
 multilayers
 – negative magnetoresistance in Fe/Tb **42**, ch. 252, p. 145
 – transition metals **42**, ch. 148, p. 81
 Mössbauer effect **2**, ch. 18, p. 387
 – of intermetallic compounds **17**, ch. 116, p. 539

N

nanostructures and nanomaterials
 – Al- and Mg-based systems **24**, ch. 161, p. 83
 – ceria **41**, ch. 249, p. 95
 – halides **41**, ch. 249, p. 95
 – hydroxides **41**, ch. 249, p. 95

- metallofullerenes **41**, ch. 249, p. 95
- oxides **41**, ch. 249, p. 95
- oxysalts **41**, ch. 249, p. 95
- properties **22**, ch. 147, p. 1; **41**, ch. 251, p. 275
- photochemical ring formation **39**, ch. 243, 297
- synthesis **22**, ch. 147, p. 1; **41**, ch. 251, p. 275
- spectroscopic properties **37**, ch. 233, p. 99
- sulfates **41**, ch. 249, p. 95
- transition metal multilayers **22**, ch. 148, p. 81
- negative magnetoresistance in multilayer Fe/Tb **42**, ch. 252, p. 145
- neutron scattering
 - elastic **17**, ch. 117, p. 635
 - inelastic **1**, ch. 7, p. 489
 - intermultiple transitions **14**, ch. 93, p. 1
 - inelastic of anomalous lanthanides **19**, ch. 130, p. 1
 - in heavy-fermion systems **19**, ch. 131, p. 123
 - of magnetic ordering in cuprates **31**, ch. 199, p. 315
 - of molten salts **44**, ch. 260, p. 87
 - of spin fluctuations in cuprates **31**, ch. 198, p. 281
- near-infrared luminescence in molecular probes and devices **37**, ch. 235, p. 217
- nitride materials, ternary and higher order **24**, ch. 166, p. 51
- NMR **2**, ch. 18, p. 387
 - in intermetallic compounds **14**, ch. 94, p. 63
 - lanthanide induced shifts for extracting solution structures **33**, ch. 215, p. 353
 - of complexes **23**, ch. 153, p. 1
 - of paramagnetic complexes **4**, ch. 38, p. 483
 - solution structure by paramagnetic NMR analysis **33**, ch. 215, p. 353
- nonradiative processes in crystals **4**, ch. 36, p. 317
- nuclear magnetic resonance, *see* NMR

O

- optical glasses, recycling of **43**, ch. 255, p. 159
- optical refrigeration **45**, ch. 265, p. 179
- organic synthesis **8**, ch. 57, p. 335
- organometallic compounds **7**, ch. 53, p. 446
 - arene-bridged compounds **45**, ch. 266, p. 261
 - divalent samarium, in **6**, ch. 50, p. 525; **36**, ch. 230, p. 393
 - divalent ytterbium, in **6**, ch. 50, p. 525
 - low valent **40**, ch. 246, p. 241
 - tetravalent cerium, in **36**, ch. 229, p. 281
- oxidation – reduction properties **18**, ch. 122, p. 239
- oxides
 - aluminates **39**, ch. 242, p. 113
 - binary **3**, ch. 27, p. 337; **18**, ch. 125, p. 413
 - gallates **39**, ch. 242, p. 113
 - higher **38**, ch. 236, p. 1
 - mixed **3**, ch. 28, p. 401
 - sesqui, defects in **5**, ch. 44, p. 321
 - sesqui, phase transformation in **5**, ch. 44, p. 321
 - ternary systems, R_2O_3 - M_2O_3 - $M'O$ **13**, ch. 90, p. 283
- oxo-selenates **35**, ch. 224, p. 45
- oxygen nonstoichiometry and lattice effect in $YBa_2Cu_3O_x$ **31**, ch. 195, p. 1

P

- permanent magnets **12**, ch. 82, p. 71; **32**, ch. 208, p. 515
 - recycling of **43**, ch. 255, p. 159
- periodic table
 - influence of rare earths on **11**, ch. 75, p. 197
 - position of rare earths in **41**, ch. 248, p. 1
- perovskites **3**, ch. 29, p. 525
 - aluminates **39**, ch. 242, p. 113
 - gallates **39**, ch. 242, p. 113
 - manganese **33**, ch. 214, p. 249
- phase equilibria
 - in binary R_5T_4 intermetallic compounds **44**, ch. 262, p. 283
 - in cuprates **30**, ch. 190, p. 229
 - in ternary systems with boron **6**, ch. 49, p. 335; **38**, ch. 238, p. 105
 - in ternary systems with chalcogenides **13**, ch. 89, p. 191
 - in ternary systems with metallic elements **13**, ch. 88, p. 1
 - in ternary systems with lead **38**, ch. 237, p. 55
 - in ternary systems with silicon **7**, ch. 51, p. 1
 - in rare earth binary alloys **8**, ch. 54, p. 1

phase transitions

- structural distortions and phase separation in $\text{YBa}_2\text{Cu}_3\text{O}_x$ **31**, ch. 195, p. 1
- in the elements at ultra high pressure **43**, ch. 257, p. 275
- in R_5T_4 intermetallic compounds **44**, ch. 262, p. 283

phosphides **23**, ch. 156, p. 285

phosphors, recycling of **43**, ch. 255, p. 159

photochemical, nano-ring formations in polyoxometalates **39**, ch. 243, p. 297

photoemission

- angle-resolved studies of untwinned $\text{YBa}_2\text{Cu}_3\text{O}_x$ **31**, ch. 201, p. 391
- in chalcogenides **10**, ch. 67, p. 301
- inverse spectra, local density supercell theory **10**, ch. 65, p. 165
- of Ce and its compounds **10**, ch. 66, p. 231
- spectra, local density supercell theory **10**, ch. 65, p. 165
- theory of **39**, ch. 241, p. 1

Photovoltaics, lanthanides in **44**, ch. 261, p. 169

physical metallurgy **11**, ch. 78, p. 409

physical properties (also see magnetic properties)

- at high pressure **42**, ch. 252, p. 1
- of cuprates **30**, ch. 193, p. 453
- of metals **1**, ch. 2, p. 173
- of metals at ultra high pressure **43**, ch. 257, p. 275
- of $\text{R}_2\text{Fe}_{14}\text{B}$ -based alloys **12**, ch. 82, p. 71
- of R_5T_4 intermetallic compounds **44**, ch. 262, p. 283

pnictides **4**, ch. 33, p. 153

- magnetic measurements on mono- **17**, ch. 114, p. 301

polishing powders, recycling of **43**, ch. 255, p. 159

Polymerization, stereospecific catalysis

- with borohydride complexes **44**, ch. 259, p. 1
- with coordination complexes **9**, ch. 61, p. 395

polyoxometalates **38**, ch. 240, p. 337

- luminescence of **39**, ch. 243, p. 297

positron annihilation in high-temperature superconductors **30**, ch. 192, p. 417

preparation and purification of metals **1**, ch. 2, p. 173

pressure-induced

- cross-over **42**, ch. 252, p. 83
- electronic transitions **42**, ch. 252, p. 82
- magnetic order **42**, ch. 252, p. 129
- structural transitions **43**, ch. 257, p. 275; **44**, ch. 262, p. 283
- superconductivity **42**, ch. 252, p. 96

pyrochlores **16**, ch. 107, p. 225

pyrometallurgy, in rare-earth recycling **43**, ch. 255, p. 159

Q

quasicrystalline, Al- and Mg-based systems **24**, ch. 161, p. 83

R

Raman scattering of cuprates **31**, ch. 203, p. 509

recycling of rare earths **43**, ch. 255, p. 159

redox reactions

- arene-bridged complexes **45**, ch. 266, p. 261
- in aqueous solutions **15**, ch. 102, p. 347
- Ce(IV)/Ce(III) **36**, ch. 229, p. 347
- Sm(III)/Sm(II) **36**, ch. 230, p. 393

relativistic effects and electronic structure **18**, ch. 119, p. 29

Ring opening polymerization (ROP) **44**, ch. 259, p. 1

RNA, cutting of **34**, ch. 222, p. 405, **36**, ch. 229, p. 392

S

samarium(II) reductants **36**, ch. 230, p. 393

scandium

- alloy systems and intermetallics **27**, ch. 175, p. 339
- arene complexes **45**, ch. 266, 261

scanning tunneling microscopy of cuprates **31**, ch. 204, p. 563

Schiff's base complexes **43**, ch. 254, p. 1

selenates **35**, ch. 224, p. 45

selenides **4**, ch. 31, p. 1

selenites **35**, ch. 224, p. 45

self-assembly of helicates **40**, ch. 247, p. 301

separation chemistry **3**, ch. 22, p. 81; **18**, ch. 121, p. 197; **21**, ch. 139, p. 1; **43**, ch. 256, p. 213

- analytical, basic chemistry and methods **28**,
ch. 180, p. 311
- silicon solar cells, lanthanides in **44**,
ch. 261, p. 169
- shift reagents **4**, ch. 38, p. 483; **23**,
ch. 153, p. 1; **33**, ch. 215, p. 353; **35**,
ch. 225, p. 107
- single crystals
 - growth from molten metal fluxes **12**,
ch. 81, p. 53
 - growth of cuprates **30**, ch. 189, p. 67
 - growth of metals and intermetallic
compounds **12**, ch. 80, p. 1
 - skutterudites, filled **33**, ch. 211, p. 1
 - Solar energy conversion, lanthanides in **44**,
ch. 261, p. 169
 - solid electrolytes **28**, ch. 178, p. 131; **35**,
ch. 223, p. 1
 - solid oxide fuel cells (SOFC) **35**, ch. 223,
p. 1
 - solution chemistry **15**, ch. 103, p. 393; **18**,
ch. 127, p. 529; **18**, ch. 128, p. 559; **21**,
ch. 145, 305
 - solvation in organic solvents **21**,
ch. 145, p. 305
 - spectroscopic properties
 - in solution **3**, ch. 24, p. 172
 - in transparent crystals **5**, ch. 46, p. 461
 - nanomaterials **37**, ch. 233, p. 99
 - spectroscopy
 - absorption and fluorescence of R ions **3**,
ch. 22, p. 172
 - appearance potential **16**, ch. 109, p. 519
 - bremsstrahlung isochromat **10**, ch. 70,
p. 425
 - circularly polarized luminescence **34**,
ch. 220, p. 289
 - high-energy **10**, ch. 62, p. 1
 - magnetic circular dichroism **40**,
ch. 244, p. 1
 - magnetic resonance **11**, ch. 77, p. 323
 - mass
 - spark source matrices **4**,
ch. 37C, p. 377
 - spark source trace element analysis **4**,
ch. 37B, p. 359
 - stable-isotope dilution analysis **4**,
ch. 37G, p. 471
 - with inductively coupled plasmas
analysis **13**, ch. 91, p. 385
 - optical **3**, ch. 24, p. 172; **5**, ch. 46, p. 461;
11, ch. 74, p. 81; **33**, ch. 216, p. 465; **37**,
ch. 233, p. 99; ch. 234, p. 171; **37**,
ch. 235, p. 217; **39**, ch. 243, p. 297
 - photoelectron in heavy fermion systems **26**,
ch. 172, p. 265
 - time-resolved emission in
 - solution chemistry **33**, ch. 216, p. 465
 - Spedding, F. H., **11**, prologue, p. 1
 - spin glasses **12**, ch. 84, p. 213
 - stannides, transition metal ternary
systems **24**, ch. 164, p. 399
 - steels **25**, ch. 165, p. 1
 - Stokes shift **45**, ch. 265, p. 179
 - stresses, static and dynamic **26**, ch. 170, p. 87
 - structural properties, lanthanides at high
pressure **43**, ch. 257, p. 275
 - sublimation enthalpy
 - of metals **43**, ch. 258, p. 321
 - of trichlorides **42**, ch. 253, p. 274
 - of trifluorides **42**, ch. 253, p. 235
 - sulfides **4**, ch. 31, p. 1
 - poly **32**, ch. 209, 567
 - superconductivity **1**, ch. 10, p. 749; **34**,
ch. 219, p. 135
 - at high pressure **42**, ch. 252, p. 96
 - crystal chemistry of cuprates **30**,
ch. 188, p. 31
 - in metals **17**, ch. 110, p. 1
 - high-temperature layered cuprates:
overview **30**, ch. 187, p. 1
 - nickel borocarbides **38**, ch. 239, p. 175
 - unconventional and magnetism **34**,
ch. 219, p. 135
 - surfaces
 - adsorption on **5**, ch. 43, p. 217
 - catalysis on **5**, ch. 43, p. 217
 - switchable metal hydride films **36**,
ch. 228, p. 83
 - synthesis of cluster halides
 - disproportionation **45**, ch. 264, p. 111
 - metallothermic reduction **45**, ch. 264, p. 111
 - systematics, intra rare earth binary
alloys **8**, ch. 54, p. 1

T

 - tellurides **4**, ch. 31, p. 1
 - ternary equiatomic YbTX intermetallics **32**,
ch. 207, p. 453
 - tetravalent cerium compounds **36**, ch. 229,
p. 281
 - theoretical chemistry **3**, ch. 23, p. 111
 - thermal conductivity of compounds **16**,
ch. 106, p. 107

- thermal properties of compounds at high pressure **42**, ch. 252, p. 1
- thermodynamic functions
- of dichlorides **42**, ch. 253, p. 198
 - of difluorides **42**, ch. 253, p. 207
 - of dimeric trichlorides **42**, ch. 253, p. 296
 - of metals **43**, ch. 258, p. 321
 - of monochlorides **42**, ch. 253, p. 381
 - of monofluorides **42**, ch. 253, p. 381
 - of trichlorides **42**, ch. 253, p. 176
 - of trifluorides **42**, ch. 253, p. 196
- thermochemical properties **18**, ch. 122, p. 239
- of chlorides **42**, ch. 253, p. 165
 - of cuprates **30**, ch. 190, p. 229
 - of dimeric trichlorides **42**, ch. 253, p. 214
 - of fluorides **42**, ch. 253, p. 165
 - of gaseous species **12**, ch. 86, p. 409
 - of metallic systems **19**, ch. 134, p. 479
 - of metals **43**, ch. 258, p. 321
 - of trichlorides **42**, ch. 253, p. 176
 - of trifluorides **42**, ch. 253, p. 196
- thin films **5**, ch. 41, p. 1; **20**, ch. 136, p. 105
- switchable metal hydrides **36**, ch. 228, p. 83
- time-of-flight mass spectrometry **45**, ch. 263, p. 1
- toxicity **4**, ch. 40, p. 553
- transition metal-indides **34**, ch. 218, p. 1
- transport properties
- at high pressure **42**, ch. 252, p. 68
 - of intermetallics **5**, ch. 42, p. 117; **17**, ch. 115, p. 409
- triflates **29**, ch. 186, p. 315
- tunneling spectra of cuprates **31**, ch. 204, p. 563
- ## U
- ultra high pressure (also see high pressure studies)
- elements at **43**, ch. 258, p. 321
 - structural properties at **43**, ch. 257, p. 275
- ## V
- valence fluctuations **2**, ch. 20, p. 575; **16**, ch. 105, p. 1; **39**, ch. 241, p. 1
- vapor pressure of halides **42**, ch. 253, p. 441
- ## X
- x-ray absorption and emission spectra **10**, ch. 71, p. 453
- x-ray scattering **26**, ch. 169, p. 1

Chapter 263

Gas-Phase Ion Chemistry of Rare Earths and Actinides

Joaquim Marçalo* and John K. Gibson†

**Centro de Ciências e Tecnologias Nucleares, Instituto Superior Técnico, Universidade de Lisboa, Bobadela LRS, Portugal*

†*The Glenn T. Seaborg Center, Chemical Sciences Division, Lawrence Berkeley National Laboratory, Berkeley, California, USA*

Chapter Outline

1 Introduction	1	2.4 Hydrolysis, Hydration, Solvation, and Complexation	59
1.1 Gas-Phase Ion Chemistry	1	2.5 Experiments with Biologically Relevant Molecules	69
1.2 Experimental Methods	3	2.6 Clusters Produced from Solids and Solutions	70
1.3 Electronic Structures and Energetics of Sc, Y, Lanthanide, and Actinide Atomic Ions	5	2.7 Miscellaneous Studies and Ions	77
2 Chemistry of Atomic and Molecular Ions	13	3 Energetics of Key Species	88
2.1 Reactions with Oxidants and Inorganic Molecules	15	3.1 Rare Earths	88
2.2 Reactions with Small Hydrocarbons	38	3.2 Actinides	89
2.3 Reactions with Other Organic Molecules	49	4 Conclusions and Future Prospects	94
		Acknowledgments	96
		References	97

1 INTRODUCTION

1.1 Gas-Phase Ion Chemistry

In the gas phase, physical and chemical properties of elementary species can be studied in the absence of external perturbations, while in condensed phases, solution or solid, the dense environments formed by the solvent or the lattice have important effects on chemical processes. Due to the relative simplicity of gas-phase systems, it is possible to probe the relationships between electronic structure, reactivity, and energetics, and the information obtained can be compared directly with the results from theoretical models.

Most of the research in this area involves the use of a variety of mass spectrometry (MS) techniques, which provide the capacity to exert control over reactants and products. Among other advantages, the roles of ligands, solvent molecules, and counterions can be examined at a molecular level. Fundamental insights into the intrinsic properties of ion/molecule reactions with analogs in solution, like metal ion complexation, are amenable with these studies. Moreover, extensive thermodynamic information about ions, including standard enthalpies of formation and bond dissociation energies of ligated species, and electron affinities, ionization energies, and proton affinities (PAs) of neutral molecules can be obtained. A deeper understanding of plasma chemistry, flame chemistry, radiolysis, and interstellar chemistry has relied on these types of studies. Important applications in analytic and biomedical MS continue to benefit from discoveries in the area.

The underlying principles of gas-phase ion chemistry, covering aspects such as ion/molecule collisions, potential energy surfaces, ion spectroscopy, collisional activation and dissociation, ion mobility, ion thermochemistry, solvation, and cluster studies, have been fully described in the literature, particularly in the first volume of *The Encyclopedia of Mass Spectrometry* (Armentrout et al., 2003); concise overviews of the fundamentals of gas-phase ion chemistry by one of the main contributors to the field are also available (Armentrout, 2004, 2013). Theoretical methods play an important role in the elucidation of gas-phase ion reactivity and, at the same time, strongly rely on these types of studies for obtaining experimental validation; a comprehensive review of theoretical methods related to gas-phase ion chemistry studies has appeared (Mercero et al., 2005). Gas-phase metal ion chemistry, with a focus on experimental studies, has been the subject of several excellent reviews since the late 1980s. These have mainly addressed organometallic chemistry topics with emphasis on methane/hydrocarbon activation and reaction mechanisms (Allison, 1986; Armentrout, 1989; Armentrout and Beauchamp, 1989; Beauchamp and van Koppen, 1992; Buckner and Freiser, 1988; Eller and Schwarz, 1991; Fisher, 2001; Freiser, 1996; Operti and Rabezzana, 2006; Richardson and Plattner, 2007; Roithova and Schröder, 2010; Schlangen and Schwarz, 2009; Schröder and Schwarz, 1995, 2008; Schröder et al., 2000b,c,d; Schwarz, 2003, 2011; Weisshaar, 1993) and other more specialized topics such as gas-phase catalysis (Bohme and Schwarz, 2005; Schlangen and Schwarz, 2012) or the chemistry of multiply charged metal cations (Roithova and Schröder, 2007; Roth and Freiser, 1991; Schröder and Schwarz, 1999; Stace, 2002; Weisshaar, 1993).

Gas-phase chemistry studies of atomic and molecular rare earth and actinide ions now have a well-founded history of more than three decades. Several fundamental aspects of f-element chemistry have been examined based on these studies. An important advantage of these types of studies is that only submilligram amounts of material are required and radiation is not detrimental, which has rendered some of the more radioactive actinides amenable to

inspection. Whereas rare earth studies have effectively excluded only promethium (as there have been no studies of reactions of Pm ions, reference in this chapter to “all of the lanthanides” implicitly excludes Pm), initial studies on actinides unsurprisingly focused on naturally occurring U and Th and were only later, starting in the 1990s, extended to Pa and several of the more abundant members of the transuranium series, Np through Es.

There have been no previous reviews of the entire rare earth gas-phase ion chemistry field, and the extensive work with Sc and Y has to be found in the general reviews cited above; lanthanide ion chemistry has, however, been finely reviewed approximately 8 years ago by Bohme (2005). In the case of the actinides, three successive, broad reviews have appeared in the last 12 years (Gibson, 2002b; Gibson and Marçalo, 2006; Heaven et al., 2010). Most of the gas-phase metal ion chemistry reviews mentioned above include references to rare earths and actinides and can be instructively consulted as they place the rare earth and actinide studies in an appropriate perspective. In this review, an extensive account of the basic gas-phase ion chemistry of rare earths and actinides is provided, and only brief references will be made to related MS studies of rare earth and actinide compounds. As this is a review in gas-phase metal *ion* chemistry, reactions of neutral species such as neutral metal atoms, an interesting topic on its own, are not included.

1.2 Experimental Methods

Studies of gas-phase ion chemistry are greatly facilitated by the presence of charged species, and, therefore, most of the research has involved the use of a variety of MS techniques. Three main types of instruments have been employed: flow/drift tubes, ion traps, and ion beams. Flow/drift techniques like the selected-ion flow tube (SIFT), and ion traps, for example, Fourier transform ion cyclotron resonance (FTICR) or quadrupole ion trap (QIT), are best suited for studies of ion/molecule reactions at room temperature, including kinetics measurements, while ion beam or guided ion beam (GIB) techniques permit studies of ion/molecule reactions over a broad range of collision energies, due to the ability to accurately control the kinetic energy of the reactant ions. The two groups of techniques are essentially complementary and can provide detailed kinetic, mechanistic, and thermochemical information. Both commercial and specially designed tandem mass spectrometers have been used along the years, and descriptions of the main types of equipment can be found in the first volume of *The Encyclopedia of Mass Spectrometry* (Armentrout et al., 2003) or in a detailed review by McLuckey and Wells (2001). Descriptions of other specialized experimental setups can be found in the original references cited in the following pages; of note is a special MS technique designated laser ablation (LA) with prompt reaction and detection (LAPRD), which was very important in the extension of ion chemistry studies to the more radioactive members of the actinide series (Gibson, 2002b).

Associated methods of relevance in gas-phase ion chemistry comprise ion activation/dissociation (McLuckey and Mentinova, 2011), where collision-induced dissociation (CID) stands out due to its generalized use, and ion spectroscopy (Baer and Dunbar, 2010; Polfer, 2011; Roithova, 2012); again, key descriptions of these methods also appear in the first volume of *The Encyclopedia of Mass Spectrometry* (Armentrout et al., 2003). The related aspects pertaining to ion thermochemistry will be referenced in Section 3.

As kinetics measurements are extensively covered in the subsequent sections, they deserve a brief discussion at this point. In a simplified classical view of a gas-phase ion/molecule reaction, a long-range attractive force is established between an ion and a neutral molecule, due to ion-induced dipole interaction and, depending on the specific case, ion–permanent dipole and/or ion–quadrupole interaction. This attractive force induces an initial well in the potential energy surface that may confer to the nascent ion/neutral complex enough energy to overcome barriers and proceed to reaction products. The net result is that ion/molecule reactions are among the fastest chemical reactions known; an exothermic ion/molecule reaction proceeding without an activation barrier is 1–2 orders of magnitude faster than an exothermic molecule/molecule reaction proceeding without an activation barrier. The reaction rate constant, k , is normally compared with a theoretical collisional rate constant, k_{COL} , whose magnitude depends on the physical properties of the particular ion/neutral pair, namely, the polarizability and permanent dipole of the neutral reactant, the charge of the ion, and the reduced mass of the reactants. The ratio of the two constants, k/k_{COL} , defines the reaction efficiency, which represents the reaction probability, that is, the fraction of ion/neutral collisions that are effective in the formation of products; these efficiencies are useful measures of the relative reactivity of ions. Ion/molecule reactions that are endothermic or have an activation barrier typically exhibit a threshold with increasing ion kinetic energy, rapidly increase in reaction rate as the kinetic energy initially increases, and then slow down again at higher kinetic energies; the analysis of the kinetic energy dependence of the reaction cross section can provide thermodynamic information about the system.

The other chief component of a mass spectrometer, the ion source, determines the types of ions that can be examined when starting from a specific sample (Gross and Caprioli, 2007). Laser-based methods, variably dubbed ablation, ionization, and desorption/ionization supposedly depending on the involved laser power, have played an important role from initial studies of bare metal ions to the widespread sought-after production of cluster ions; for these latter species, the development of the so-called cluster sources was key to progress (Duncan, 2012). In more recent years, electrospray ionization (ESI) has played a central role due to its capacity to transfer/produce ions from solutions under mild conditions. Besides yielding new types of ions for chemical probing, ESI became a method of choice for the identification of solution species (speciation) and for direct observation of reaction

intermediates in solution, although with limitations that arise from chemical processes occurring during electrospray that can influence the sampling, as addressed by several authors (Agrawal and Schröder, 2011; Di Marco and Bombi, 2006; Richardson and Plattner, 2007; Santos et al., 2005; Schröder, 2012a,b; Stewart, 1999). Rare earth and actinide ion chemistry has profited from all of these developments in ionization methods, as it will be seen in the following pages.

1.3 Electronic Structures and Energetics of Sc, Y, Lanthanide, and Actinide Atomic Ions

The electronic configurations of monovalent and divalent rare earth and actinide atomic ions are provided in Tables 1 and 2, respectively; the ground-state (GS) and relevant excited-state configurations are included. As discussed below, these electronic configurations and energies have been extensively employed to evaluate the reactivity of rare earth and actinide cations, as well as molecular bonding of these elements. It has been revealed, since the early work on transition metal ion chemistry (Armentrout et al., 1981), that much of the chemical behavior of bare metal cations can be understood and predicted based on the number of valence electrons at the metal center that are available to participate in chemical bonding.

In the case of Sc and Y, as d-transition elements, the availability and importance of s and/or d valence electrons in the corresponding cations is evident. For the 4f-element lanthanides and 5f-element actinides, the quasivalence f electrons are generally—but not necessarily—chemically inert such that it is the population of non-f valence electrons, primarily those in the valence Ln/An 6s/7s and 5d/6d orbitals, which principally govern many key aspects of their chemistry. Accordingly, the excited-state configurations of primary interest are those in which a 4f or 5f electron has been promoted into a 5d/6d or 6s/7s orbital, thereby making available an additional non-f electron for participation in chemical bonding. There are at least a few important cases where evidence for the participation of f electrons, particularly 5f electrons, in bonding is revealed by a deviation from the predicted correlation between the reactivity and the promotion energy (PE) to a prepared divalent state with two non-f electrons. The PEs of the Ln⁺ and An⁺ ions to both d¹s¹ and d² configurations are plotted in Figs. 1 and 2, respectively. Large variations across the lanthanide and actinide series are clearly evident, an effect that is manifested in much of the gas-phase ion chemistry discussed below.

Other atomic properties like the second ionization energies can also play an important role, particularly in the chemistry of doubly charged cations, which can induce electron transfer reactions as discussed below. The third ionization energies, which display a variation across the lanthanide series that correlates with the variation of the PEs shown in Fig. 1, have been used as a measure of the relative stability of the 2+ and 3+ oxidation states of these

TABLE 1 Ground-State (GS) and Selected Excited-State Electronic Configurations of Rare Earth Cations^a

Rare Earth (R)	R ⁺		R ²⁺	
	<i>Configuration</i>	<i>Energy</i>	<i>Configuration</i>	<i>Energy</i>
Sc	3d ¹ 4s ¹	0/GS	3d ¹	0/GS
	3d ²	0.60	4s ¹	3.17
	4s ²	1.46		
Y	5s ²	0/GS	4d ¹	0/GS
	4d ¹ 5s ¹	0.15	5s ¹	0.93
	4d ²	1.05		
La	5d ²	0/GS	5d ¹	0/GS
	5d ¹ 6s ¹	0.24	4f ¹	0.89
	6s ²	0.92	6s ¹	1.69
	4f ¹ 6s ¹	1.75		
	4f ¹ 5d ¹	2.13		
Ce	4f ¹ 5d ²	0/GS	4f ²	0/GS
	4f ¹ 5d ¹ 6s ¹	0.32	4f ¹ 5d ¹	0.47
	4f ² 6s ¹	0.48	4f ¹ 6s ¹	2.38
	4f ² 5d ¹	0.88	5d ²	5.01
	4f ¹ 6s ²	1.21	5d ¹ 6s ¹	7.85
Pr	4f ³ 6s ¹	0/GS	4f ³	0/GS
	4f ³ 5d ¹	0.48	4f ² 5d ¹	1.66
	4f ² 5d ²	0.73	4f ² 6s ¹	3.52
	4f ² 5d ¹ 6s ¹	0.97		
Nd	4f ⁴ 6s ¹	0/GS	4f ⁴	0/GS
	4f ⁴ 5d ¹	0.55	4f ³ 5d ¹	1.89
	4f ³ 5d ²	1.14	4f ³ 6s ¹	3.8 ± 0.3*
	4f ³ 5d ¹ 6s ¹	1.40		
Pm	4f ⁵ 6s ¹	0/GS	4f ⁵	0/GS
	4f ⁵ 5d ¹	0.66	4f ⁴ 5d ¹	2.0 ± 0.3
	4f ⁴ 5d ²	1.2 ± 0.4*	4f ⁴ 6s ¹	3.7 ± 0.4
	4f ⁴ 5d ¹ 6s ¹	1.4 ± 0.3*		

TABLE 1 Ground-State (GS) and Selected Excited-State Electronic Configurations of Rare Earth Cations—Cont'd

Rare Earth (R)	R ⁺		R ²⁺	
	Configuration	Energy	Configuration	Energy
Sm	4f ⁶ 6s ¹	0/GS	4f ⁶	0/GS
	4f ⁶ 5d ¹	0.88	4f ⁵ 5d ¹	3.26
	4f ⁷	2.27	4f ⁵ 6s ¹	4.5 ± 0.3*
	4f ⁵ 5d ²	2.4 ± 0.1*		
	4f ⁵ 5d ¹ 6s ¹	2.67		
Eu	4f ⁷ 6s ¹	0/GS	4f ⁷	0/GS
	4f ⁷ 5d ¹	1.23	4f ⁶ 5d ¹	4.20
	4f ⁷ 6p ¹	2.95	4f ⁶ 6s ¹	5.72
	4f ⁶ 5d ¹ 6s ¹	3.74		
	4f ⁶ 5d ²	4.54		
Gd	4f ⁷ 5d ¹ 6s ¹	0/GS	4f ⁷ 5d ¹	0/GS
	4f ⁷ 6s ²	0.43	4f ⁸	0.30
	4f ⁷ 5d ²	0.50	4f ⁷ 6s ¹	1.14
	4f ⁸ 6s ¹	0.99		
	4f ⁸ 5d ¹	2.28		
Tb	4f ⁹ 6s ¹	0/GS	4f ⁹	0/GS
	4f ⁸ 5d ¹ 6s ¹	0.40	4f ⁸ 5d ¹	1.11
	4f ⁸ 6s ²	0.73	4f ⁸ 6s ¹	2.19
	4f ⁸ 5d ²	1.10		
	4f ⁹ 5d ¹	1.40		
Dy	4f ¹⁰ 6s ¹	0/GS	4f ¹⁰	0/GS
	4f ⁹ 5d ¹ 6s ¹	1.31	4f ⁹ 5d ¹	~2.1
	4f ⁹ 6s ²	1.53	4f ⁹ 6s ¹	3.1 ± 0.2*
	4f ¹⁰ 5d ¹	1.84		
	4f ⁹ 5d ²	2.42		

Continued

TABLE 1 Ground-State (GS) and Selected Excited-State Electronic Configurations of Rare Earth Cations—Cont'd

Rare Earth (R)	R ⁺		R ²⁺	
	Configuration	Energy	Configuration	Energy
Ho	4f ¹¹ 6s ¹	0/GS	4f ¹¹	0/GS
	4f ¹⁰ 6s ²	1.2 ± 0.3*	4f ¹⁰ 5d ¹	2.24
	4f ¹⁰ 5d ¹ 6s ¹	1.43*	4f ¹⁰ 6s ¹	2.71
	4f ¹¹ 5d ¹	2.02		
	4f ¹⁰ 5d ²	2.9 ± 0.1*		
Er	4f ¹² 6s ¹	0/GS	4f ¹²	0/GS
	4f ¹¹ 6s ²	0.85	4f ¹¹ 5d ¹	2.10
	4f ¹¹ 5d ¹ 6s ¹	1.32	4f ¹¹ 6s ¹	2.39
	4f ¹² 5d ¹	2.05		
	4f ¹¹ 5d ²	2.71		
Tm	4f ¹³ 6s ¹	0/GS	4f ¹³	0/GS
	4f ¹² 6s ²	1.54	4f ¹² 5d ¹	2.84
	4f ¹² 5d ¹ 6s ¹	2.05	4f ¹² 6s ¹	3.14
	4f ¹³ 5d ¹	2.19		
	4f ¹² 5d ²	3.82		
Yb	4f ¹⁴ 6s ¹	0/GS	4f ¹⁴	0/GS
	4f ¹³ 6s ²	2.66	4f ¹³ 5d ¹	4.14
	4f ¹⁴ 5d ¹	2.85	4f ¹³ 6s ¹	4.30
	4f ¹³ 5d ¹ 6s ¹	3.32		
	4f ¹³ 5d ²	5.58		
Lu	4f ¹⁴ 6s ²	0/GS	4f ¹⁴ 6s ¹	0/GS
	4f ¹⁴ 5d ¹ 6s ¹	1.46	4f ¹⁴ 5d ¹	0.71
	4f ¹⁴ 5d ²	3.65		

^aThe configurations exclude the 18 electrons in the closed-shell Ar core, [Ar], for Sc; the 36 electrons in the closed-shell krypton core, [Kr], for Y; and the 54 electrons in the closed-shell xenon core, [Xe], for the Ln. Energies are in eV (1 eV = 96.485 kJ mol⁻¹) and correspond to the lowest-lying term for the indicated configuration relative to the GS configuration at 0 eV. Values are from the following: Sc, Moore (1971a); Y, Moore (1971b); and Ln, Martin et al. (1978); values marked with an asterisk are estimates from Brewer (1971); values for the singly ionized metals can also be found in a more recent compilation (Sansone and Martin, 2005).

TABLE 2 Ground-State (GS) and Selected Excited-State Electronic Configurations of Actinide Cations^a

Actinide (An)	An ⁺		An ²⁺	
	Configuration	Energy	Configuration	Energy
Ac	7s ²	0/GS	7s ¹	0/GS
	6d ¹ 7s ¹	0.59	6d ¹	0.10
	6d ²	1.64	5f ¹	2.91
	5f ¹ 7s ¹	3.70		
Th	6d ² 7s ¹	0/GS	5f ¹ 6d ¹	0/GS
	6d ¹ 7s ²	0.23	6d ²	0.01
	5f ¹ 7s ²	0.56	5f ¹ 7s ¹	0.31
	5f ¹ 6d ¹ 7s ¹	0.76	6d ¹ 7s ¹	0.68
			5f ²	1.88
Pa	5f ² 7s ²	0/GS	5f ² 6d ¹	0/GS
	5f ² 6d ¹ 7s ¹	0.10	5f ² 7s ¹	0.5 ± 0.1
	5f ¹ 6d ² 7s ¹	0.59	5f ³	0.6 ± 0.1
	5f ² 6d ²	0.92	5f ¹ 6d ²	1.2 ± 0.7
			5f ¹ 6d ¹ 7s ¹	2.1 ± 0.5
U	5f ³ 7s ²	0/GS	5f ⁴	0/GS
	5f ³ 6d ¹ 7s ¹	0.04	5f ³ 6d ¹	0.03
	5f ³ 6d ²	0.57	5f ³ 7s ¹	0.46
	5f ² 6d ² 7s ¹	1.71	5f ² 6d ²	2.41
			5f ² 6d ¹ 7s ¹	3.35
Np	5f ⁴ 6d ¹ 7s ¹	0/GS	5f ⁵	0/GS
	5f ⁴ 7s ²	0.003	5f ⁴ 6d ¹	0.7 ± 0.4
	5f ⁵ 7s ¹	0.01	5f ⁴ 7s ¹	1.2 ± 0.5
	5f ⁴ 6d ²	0.9 ± 0.4	5f ³ 6d ²	4.2 ± 0.7
			5f ³ 6d ¹ 7s ¹	5.1 ± 0.6
Pu	5f ⁶ 7s ¹	0/GS	5f ⁶	0/GS
	5f ⁵ 7s ²	1.02	5f ⁵ 6d ¹	1.6 ± 0.4
	5f ⁵ 6d ¹ 7s ¹	1.08	5f ⁵ 7s ¹	2.1 ± 0.5

Continued

TABLE 2 Ground-State (GS) and Selected Excited-State Electronic Configurations of Actinide Cations—Cont'd

Actinide (An)	An ⁺		An ²⁺	
	Configuration	Energy	Configuration	Energy
	5f ⁶ 6d ¹	1.49	5f ³ 6d ²	6.2±0.5
	5f ⁵ 6d ²	2.14	5f ⁴ 6d ¹ 7s ¹	7.1±0.6
Am	5f ⁷ 7s ¹	0/GS	5f ⁷	0/GS
	5f ⁷ 6d ¹	1.76	5f ⁶ 6d ¹	3.0±0.4
	5f ⁶ 7s ²	2.3±0.1	5f ⁶ 7s ¹	3.3±0.5
	5f ⁶ 6d ¹ 7s ¹	2.5±0.1	5f ⁶ 6d ²	8.7±0.6
	5f ⁶ 6d ²	3.6±0.2	5f ⁵ 6d ¹ 7s ¹	9.6±0.6
Cm	5f ⁷ 7s ²	0/GS	5f ⁸	0/GS
	5f ⁸ 7s ¹	0.26	5f ⁷ 6d ¹	0.6±0.4
	5f ⁷ 6d ¹ 7s ¹	0.50	5f ⁷ 7s ¹	0.6±0.6
	5f ⁷ 6d ²	1.84	5f ⁶ 6d ²	7.8±0.9
	5f ⁸ 6d ¹	2.13	5f ⁵ 6d ¹ 7s ¹	8.3±0.9
Bk	5f ⁹ 7s ¹	0/GS	5f ⁹	0/GS
	5f ⁸ 7s ²	0.87	5f ⁸ 7s ¹	1.4±0.7
	5f ⁸ 6d ¹ 7s ¹	1.53	5f ⁸ 6d ¹	1.7±0.6
	5f ⁹ 6d ¹	2.03	5f ⁷ 6d ²	6.9±0.9
	5f ⁸ 6d ²	2.7±0.4	5f ⁷ 6d ¹ 7s ¹	6.9±0.9
Cf	5f ¹⁰ 7s ¹	0/GS	5f ¹⁰	0/GS
	5f ⁹ 7s ²	1.5±0.5	5f ⁹ 7s ¹	2.4±0.7
	5f ¹⁰ 6d ¹	2.40	5f ⁹ 6d ¹	3.0±0.6
	5f ⁹ 6d ¹ 7s ¹	3.00	5f ⁸ 6d ¹ 7s ¹	9.4±0.9
	5f ⁹ 6d ²	4.2±0.5	5f ⁸ 6d ²	9.7±0.9
Es	5f ¹¹ 7s ¹	0/GS	5f ¹¹	0/GS
	5f ¹⁰ 7s ²	1.5±0.6	5f ¹⁰ 7s ¹	2.5±0.7
	5f ¹¹ 6d ¹	2.7±0.2	5f ¹⁰ 6d ¹	3.3±0.6
	5f ¹⁰ 6d ¹ 7s ¹	2.9±0.2	5f ⁹ 6d ¹ 7s ¹	10.9±0.9
	5f ¹⁰ 6d ²	4.7±0.6	5f ⁹ 6d ²	11.4±0.9

TABLE 2 Ground-State (GS) and Selected Excited-State Electronic Configurations of Actinide Cations—Cont'd

Actinide (An)	An ⁺		An ²⁺	
	Configuration	Energy	Configuration	Energy
Fm	5f ¹² 7s ¹	0/GS	5f ¹²	0/GS
	5f ¹¹ 7s ²	1.1 ± 0.6	5f ¹¹ 7s ¹	2.1 ± 0.7
	5f ¹¹ 6d ¹ 7s ¹	2.9 ± 0.6	5f ¹¹ 6d ¹	3.3 ± 0.6
	5f ¹² 6d ¹	3.0 ± 0.2	5f ¹⁰ 6d ¹ 7s ¹	11.3 ± 0.9
	5f ¹¹ 6d ²	5.0 ± 0.9	5f ¹⁰ 6d ²	12.2 ± 0.9
Md	5f ¹³ 7s ¹	0/GS*	5f ¹³	0/GS*
	5f ¹⁴	0.7 ± 0.6*	5f ¹² 7s ¹	3.0 ± 0.7*
	5f ¹² 7s ²	2.1 ± 0.6*	5f ¹² 6d ¹	4.6 ± 0.6*
	5f ¹³ 6d ¹	3.2 ± 0.2*	5f ¹⁰ 6d ¹ 7s ¹	12.4 ± 0.9*
	5f ¹² 6d ¹ 7s ¹	4.1 ± 0.6*	5f ¹⁰ 6d ²	13.6 ± 0.9*
No	5f ¹⁴ 7s ¹	0/GS*	5f ¹⁴	0/GS*
	5f ¹³ 7s ²	3.1 ± 0.7*	5f ¹³ 7s ¹	3.8 ± 0.7*
	5f ¹⁴ 6d ¹	3.7 ± 0.1*	5f ¹³ 6d ¹	5.8 ± 0.6*
	5f ¹³ 6d ¹ 7s ¹	5.3 ± 0.6*	5f ¹² 6d ¹ 7s ¹	14.8 ± 0.9*
	5f ¹³ 6d ²	8.2 ± 0.9*	5f ¹² 6d ²	16.4 ± 0.9*
Lr	5f ¹⁴ 7s ²	0/GS*	5f ¹⁴ 7s ¹	0/GS*
	5f ¹⁴ 6d ¹ 7s ¹	2.9 ± 0.4*	5f ¹⁴ 6d ¹	2.5 ± 0.2*
	5f ¹⁴ 6d ²	6.1 ± 0.5*	5f ¹³ 7s ²	10.7 ± 0.6*
	5f ¹³ 6d ¹ 7s ²	11.3 ± 1.1*	5f ¹³ 6d ¹ 7s ¹	12.2 ± 0.7*
	5f ¹³ 6d ² 7s ¹	13.6 ± 1.1*	5f ¹³ 6d ²	14.3 ± 0.7*

^aThe configurations exclude the 86 electrons in the closed-shell radon core, [Rn]. Energies are in eV (1 eV = 96.485 kJ mol⁻¹) and correspond to the lowest-lying term for the indicated configuration relative to the GS configuration at 0 eV. Values are from *Blaise and Wyart (1992)*, as available at <http://www.lac.u-psud.fr/Database/Contents.html>, except for those marked with an asterisk, which are estimates from *Brewer (1971)*; values for the singly ionized metals can also be found in a more recent compilation (*Sansonetti and Martin, 2005*).

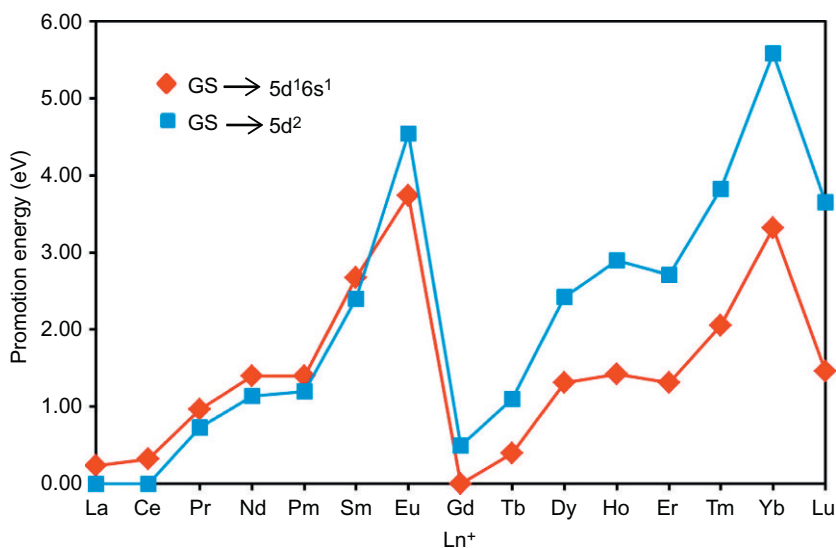


FIGURE 1 Promotion energies of the Ln⁺ ions from the ground states to configurations with two non-4f electrons, [Xe]4fⁿ⁻²5d¹6s¹ (red diamonds) (dark gray in print) and [Xe]4fⁿ⁻²5d² (blue squares) (light gray in print); data are from Table 1.

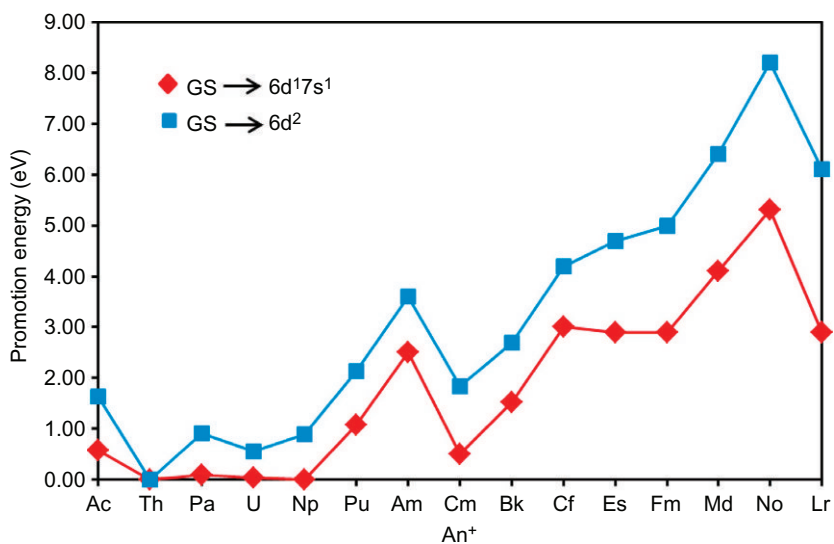


FIGURE 2 Promotion energies of the An⁺ ions from the ground states to configurations with two non-5f electrons, [Rn]5fⁿ⁻²6d¹7s¹ (red diamonds) (dark gray in print) and [Rn]5fⁿ⁻²6d² (blue squares) (light gray in print); data are from Table 2.

metals. Sources for these quantities for the rare earths and actinides are also the atomic energy level compilations indicated in the footnotes to [Tables 1 and 2](#) or, together with other relevant thermodynamic information, Morss' chapter in this handbook ([Morss, 1994](#)); for the case of the actinides, a more recent source of information is also available ([Konings et al., 2006](#)).

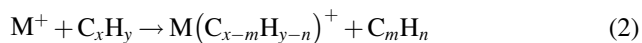
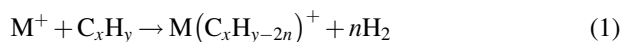
2 CHEMISTRY OF ATOMIC AND MOLECULAR IONS

The early 1980s witnessed the first systematic studies of the gas-phase reactivity of mostly singly charged transition metal atomic cations, initially comprising Sc. Until the end of that decade, studies involving Y, La, Lu, and a few other lanthanides also appeared, and in the mid-1990s, the first systematic studies of all the Ln cations were reported.

Except for a study of a few reactions of Pu^+ , most early work with the actinide cations was limited to long-lived naturally occurring Th and U. Beginning in the mid-1990s, specialized mass spectrometers with unique sample-handling capabilities were developed to enable systematic studies of ion chemistry for all of the actinides from Th to Es. The actinides beyond Es—Fm, Md, No, and Lr—are available in insufficient quantities ($<1 \mu\text{g}$) to effectively produce gas-phase ion sources; the short half-lives of these transeinsteinium isotopes (<1 day) further hinder progress in the extension of gas-phase ion chemistry studies beyond Es by conventional approaches.

The activation of dihydrogen to form the hydride MH^+ is the simplest reaction of an M^+ ion, and this was one of the first reactions examined. Numerous studies of bare and ligated rare earth and actinide ions with a variety of small inorganic molecules followed, particularly with O-atom donors, with the purpose of obtaining oxide ions and characterizing their energetics.

Small hydrocarbons, alkanes, and alkenes in particular, are convenient substrates to establish correlations between the electronic configurations of the reactant ions and the reaction products and mechanisms, and were extensively investigated with both singly and doubly charged rare earth and actinide cations. Hydrocarbon activation by metal ions generally proceeds by oxidative insertion into a C—H or C—C bond, as indicated in [Eqs. \(1\) and \(2\)](#), which requires two chemically active valence electrons at the metal center, such as in $\{\text{C}-\text{M}^+-\text{H}\}$ or $\{\text{C}-\text{M}^+-\text{C}\}$ intermediates:



Early examinations of the reactions of Ln^+ ions with these substrates demonstrated the utility of this type of chemical reactivity in elucidating the role of the electronic structures of 4f-element ions in inducing bond activation. Subsequent studies with the An^+ ions also provided important insights

into the roles of electronic structure, and particularly of the quasivalence 5f electrons, in C—H and C—C bond activation.

Many different organic molecules have been used as reagents, expanding the observed chemistry. Reactions with O-containing organic molecules provided direct comparisons with the results of oxidation reactions with inorganics. Part of the motivation for the studies with more elaborate organic molecules was the drawing of parallels with condensed-phase chemistry, obtaining evidence for elusive species and eventually helping in the design of synthetic strategies.

The advent of ESI in the 1990s opened the door to a more effective approach to condensed-phase/solution chemistry and allowed for the examination of hydration, solvation, and complexation of rare earths and actinides, including with multiply charged metal ions. By controlling the composition of the solution, it is possible to produce a variety of metal ion complexes coordinated by diverse covalently and datively bound neutral ligands, as well as by various counterions. In the case of the actinides, the robust and important uranyl ion, UO_2^{2+} , has been a prime focus in the studies of actinide chemistry in solution and gas as explored by ESI. Ion spectroscopy, profiting from new powerful light sources, accompanied the development of ion chemistry studies based on ESI.

ESI has also increased the, until recently limited, investigations of the interactions of rare earth cations with biologically relevant molecules, for example, amino acids (AAs), peptides, and other biomolecules, by ion chemistry methods. These elements are not as important as many others in biological processes, but both the toxicity, through interference with the activity of Ca^{2+} , and the potential therapeutic uses of these cations are attracting more attention. Curiously, the biocoordination behavior of uranyl and other actinide cations, which could reveal specific molecular interactions involved in transport and chemical toxicity, is relatively unexplored, including via MS/gas-phase approaches.

In contrast to the “soft” ESI ion formation technique, LA/ionization of solids as a means to produce metal cluster ions is a high-energy process that can provide various types of species, generally with strong covalent bonds, such as in oxides or carbides, as opposed to the weaker bonding exhibited in species produced by ESI. Cluster ion chemistry studies with rare earths and actinides have developed a “solid” history, with metallofullerenes playing an important role.

As confirmation of the mature nature of the field of rare earth and actinide ion chemistry, [Section 2](#) concludes with references to a number of studies that address topics as diverse as metal–metal bonding, new species from the fragmentation of complex ions, flame chemistry and chemi-ionization, and analytic applications in elemental MS.

In the description of rare earth and actinide gas-phase ion chemistry that follows, relevant literature has been covered until August 2013. Mention will

be often made to the associated energetics and kinetics; as for the former, [Section 3](#) will present an overview with indication of key references, while for the latter, besides the original references included below, two comprehensive compilations by [Anicich \(1993, 2003\)](#) are available.

2.1 Reactions with Oxidants and Inorganic Molecules

2.1.1 Rare Earths

The first gas-phase study of the reaction of a rare earth metal ion with dihydrogen was performed by [Tolbert and Beauchamp \(1984\)](#) in the case of Sc^+ using an ion beam instrument. The formation of ScH^+ is endothermic, and the analysis of the threshold for the reaction provided the first experimental Sc^+-H bond energy, $D_0(\text{Sc}^+-\text{H})=226\pm 18\text{kJ mol}^{-1}$. The reactions of Sc^+ with H_2 and its isotopomers HD and D_2 were subsequently examined by Armentrout and coworkers using guided ion beam mass spectrometry (GIB-MS) ([Elkind and Armentrout, 1987](#); [Elkind et al., 1989](#)). The enhanced capabilities of the instrument used by Armentrout and coworkers allowed the scrutiny of specific populations of electronic states of the metal ions and a more precise determination of the 0 K Sc^+-H bond energy, $D_0(\text{Sc}^+-\text{H})=235\pm 9\text{kJ mol}^{-1}$. The reactions of Y^+ , La^+ , and Lu^+ with dihydrogen were also studied in this work and the respective M^+-H bond energies determined for the first time. Differences in the reaction mechanism were uncovered for Lu^+ as compared with the other three rare earth ions. The reactions of Y^+ were later reexamined by Armentrout and coworkers with concordant results ([Sievers et al., 1996b](#)).

The interaction of Sc^+ with H_2 was also the object of study by Bowers and coworkers ([Bowers, 1994](#); [Bushnell et al., 1994](#)) in what became the first example of cluster-mediated σ -bond activation. By examining the energetics of H_2 loss from $\text{Sc}^+(\text{H}_2)_{1-5}$ clusters through temperature-dependent equilibrium experiments, supported by theoretical computations, evidence was obtained for the insertion of Sc^+ into the first H_2 ligand.

Armentrout and coworkers were the first to study oxidation reactions in detail, using GIB techniques. [Fisher et al. \(1990\)](#) examined the reaction of Sc^+ with O_2 , together with all other first-row transition metal ions. The formation of ScO^+ is exothermic and only a lower limit for the Sc^+-O bond energy could be obtained, in agreement with known literature values. A succeeding study of the formation of ScO^+ through the endothermic reaction of Sc^+ with CO provided the first direct experimental determination of $D_0(\text{Sc}^+-\text{O})$ ([Clemmer et al., 1991](#)). The authors recommended the bond energy value $D_0(\text{Sc}^+-\text{O})=689\pm 11\text{kJ mol}^{-1}$ based on their own and other experimental results, reported in detail below, for the reactions of ScO^+ with D_2 to form Sc^+ ([Clemmer et al., 1993](#)) and Sc^+ with D_2O to form ScO^+ ([Chen et al., 1994](#)); these two studies also allowed the examination of the formation and energetics of Sc^+ hydroxide. The reaction of Sc^+ with CO also

yielded the carbide ScC^+ , and the threshold of the reaction cross section indicated $D_0(\text{Sc}^+ - \text{C}) = 322 \pm 6 \text{ kJ mol}^{-1}$ (Clemmer et al., 1991); this value is substantially smaller than the $\text{Sc}^+ - \text{O}$ bond energy and was discussed by the authors on the basis of the nature of the bonding in the two species. The oxidation reactions of Y^+ were also examined, namely, the exothermic reaction with O_2 and the endothermic reaction with CO (Sievers et al., 1996a); the CO results provided experimental values for the $\text{Y}^+ - \text{O}$ and $\text{Y}^+ - \text{C}$ 0 K bond energies. CO_2 was later employed as an oxidant and its reactions with Y^+ and YO^+ . The reverse reactions of YO^+ and YO_2^+ with CO , were investigated (Sievers and Armentrout, 1999); the energies for CO binding to Y^+ , YO^+ , and YO_2^+ , and CO_2 to YO^+ could be determined in experiments that also involved collisional activation with Xe . Neutral and cationic metal dioxides had been previously studied for the first time as formed in endothermic reactions of ScO^+ , YO^+ , and LaO^+ with NO_2 (Clemmer et al., 1992), allowing for the determination of the second bond dissociation energies of the dioxides.

Several oxidation studies of lanthanide cations besides the above-mentioned oxidation of La^+ have been performed. Murad (1984) carried out an early investigation of the exothermic reaction of Sm^+ with O_2 to give SmO^+ in an ion beam instrument and obtained an estimated thermal rate constant of $\sim 2 \times 10^{-10} \text{ cm}^3 \text{ molecule}^{-1} \text{ s}^{-1}$. Schilling and Beauchamp (1988) used an ion beam instrument and NO as the reagent to examine the oxidation of Pr^+ and Gd^+ ions; the corresponding monoxides were the only products formed. Matsuo et al. (1993) studied the reactivity of Lu^+ with O_2 in a radio-frequency (RF) ion trap and observed efficient formation of the monoxide ion. The reaction of Er^+ with O_2 was studied by Backe et al. (2005) in a setup that used a pulsed ion beam from a tandem accelerator introduced in an argon buffer gas cell; the measured rate constant for the formation of ErO^+ was found to be in agreement with reference measurements by Fourier transform ion cyclotron resonance mass spectrometry (FTICR-MS). Schwarz and coworkers (Cornehl et al., 1997a) investigated the reactions of Ce^+ and Nd^+ and the corresponding monoxides with O_2 , CO_2 , N_2O , and H_2O by FTICR-MS, in a comparative study with the actinide ions Th^+ and U^+ ; the formation of the Ce and Nd monoxide cations was observed with all the oxidants studied and, additionally, LnOH^+ was formed in the case of H_2O and CeN^+ in the case of N_2O ; however, none of these oxidizing reagents were able to yield the dioxide cations. The same group (Heinemann et al., 1996) examined in more detail the formation of Ce oxides and showed that CeO_2^+ could be produced by the reaction of CeO^+ with NO_2 but not with N_2O , O_2 , or NO . The structure and properties of CeO_2^+ were studied experimentally by CID and reactivity and by theoretical calculations that specified a linear cerium dioxide with a resonating π -bond. Two other lanthanide ions, Gd^+ and Lu^+ , were investigated by Gibson et al. (2008) using FTICR-MS as part of a comparative

study with Cm^+ ; the examined inorganic oxidants were O_2 , CO_2 , N_2O , NO , and H_2O , and the formation of LnO^+ was observed in all cases except for the unreactive pair Lu^+/NO .

In 2001, Bohme and coworkers initiated a comprehensive study of the reactions of inorganic oxidants with some 60 different atomic cations, with a particular focus on the lanthanides. These extensive studies were made possible by the development of a novel inductively coupled plasma/selected-ion flow tube (ICP/SIFT) mass spectrometer (Koyanagi et al., 2000). Reactions of Sc^+ , Y^+ , and the lanthanides from La^+ to Lu^+ (except Pm^+) with O_2 (Koyanagi and Bohme, 2001; Koyanagi et al., 2002), CO_2 (Cheng et al., 2006b; Koyanagi and Bohme, 2006), N_2O (Koyanagi and Bohme, 2001; Lavrov et al., 2004), NO (Blagojevic et al., 2005a, 2006), NO_2 (Jarvis et al., 2010, 2013), and D_2O (Cheng et al., 2006c, 2007) were examined. Products, reaction efficiencies, and individual references to the original work can be found in Table 3. Periodicities in the reaction efficiencies of metal cations with the different oxidants were analyzed by Bohme and coworkers in terms of factors such as reaction exothermicity, the presence of activation barriers in the reaction coordinates, and the conservation of spin. The periodic behavior in the specific case of the lanthanide series was examined in detail and uncovered an intriguing difference between early and late lanthanide cations through a correlation between N_2O reactivity and the PEs from the GS to the $4f^{n-1}5d^16s^1$ configuration (see Table 1 and Fig. 1), as illustrated in Fig. 3 (Koyanagi and Bohme, 2001).

A few reactions of ligated rare earth ions with oxygen, besides those of the monoxide ions, have also been investigated. Schröder and Schwarz (1993) used FTICR-MS to examine the reactivity of $\text{Sc}(\text{C}_2\text{H}_4)^+$ and found that it could be ascribed to the high oxophilicity of the metal ion; the formation of ScO^+ , $\text{Sc}(\text{O}_2)^+$, and $\text{ScO}(\text{C}_2\text{H}_4)^+$ was observed, with no evidence for the activation of the ethylene ligand. Mono- and bisadducts of benzene of the type $\text{R}(\text{C}_6\text{H}_6)_{1,2}^+$, including for $\text{R} = \text{Sc}$, Y , and La , were generated, and their reactivity toward O_2 measured by Bohme and coworkers in a SIFT apparatus (Caraiman and Bohme, 2002); oxygen activation by the examined rare earth metal cations was preserved upon the addition of one benzene ligand but was observed with two benzene ligands only in the case of La . Oxygen and NO and H_2O were found to produce ScO^+ in the reactions of another ligated rare earth ion, ScC_6H_4^+ (scandium-benzyne), while N_2O , CO_2 , and CO were unreactive (Huang et al., 1991b).

Reactions of a few of the much less studied doubly charged rare earth cations with inorganic oxidants were examined by Gibson et al. (2008) using FTICR-MS. The reactions of the lanthanide ions Gd^{2+} and Lu^{2+} with O_2 , CO_2 , N_2O , NO , and H_2O were investigated in a comparative study with Cm^{2+} ; the reaction of La^{2+} with N_2O was also studied. The formation of LnO^{2+} , with the metal centers apparently in an unusual, but only formally

TABLE 3 Reactions of Bare Rare-Earth Singly-Charged Cations with Oxidants by Bohme and co-workers^a

Reactants	Products ^b	$k/k_{\text{COL}}^{\text{c}}$	Reactants	Products ^b	$k/k_{\text{COL}}^{\text{c}}$
$\text{Sc}^+ + \text{O}_2$	$\text{ScO}^+ + \text{O}$	0.54	$\text{Gd}^+ + \text{O}_2$	$\text{GdO}^+ + \text{O}$	0.86
$\text{Y}^+ + \text{O}_2$	$\text{YO}^+ + \text{O}$	0.67	$\text{Tb}^+ + \text{O}_2$	$\text{TbO}^+ + \text{O}$	0.67
$\text{La}^+ + \text{O}_2$	$\text{LaO}^+ + \text{O}$	0.75	$\text{Dy}^+ + \text{O}_2$	$\text{DyO}^+ + \text{O}$	0.47
$\text{Ce}^+ + \text{O}_2$	$\text{CeO}^+ + \text{O}$	0.88	$\text{Ho}^+ + \text{O}_2$	$\text{HoO}^+ + \text{O}$	0.42
$\text{Pr}^+ + \text{O}_2$	$\text{PrO}^+ + \text{O}$	0.75	$\text{Er}^+ + \text{O}_2$	$\text{ErO}^+ + \text{O}$	0.44
$\text{Nd}^+ + \text{O}_2$	$\text{NdO}^+ + \text{O}$	0.57	$\text{Tm}^+ + \text{O}_2$	$\text{Tm}^+ \cdot \text{O}_2 + \text{He}$	0.003 ^d
$\text{Sm}^+ + \text{O}_2$	$\text{SmO}^+ + \text{O}$	0.48	$\text{Yb}^+ + \text{O}_2$	$\text{Yb}^+ \cdot \text{O}_2 + \text{He}$	≤ 0.0006
$\text{Eu}^+ + \text{O}_2$	$\text{Eu}^+ \cdot \text{O}_2 + \text{He}$	≤ 0.0006	$\text{Lu}^+ + \text{O}_2$	$\text{LuO}^+ + \text{O}$	0.14 ^d
$\text{Sc}^+ + \text{CO}_2$	$\text{ScO}^+ + \text{CO}$	0.087	$\text{Gd}^+ + \text{CO}_2$	$\text{GdO}^+ + \text{CO}$	0.50
$\text{Y}^+ + \text{CO}_2$	$\text{YO}^+ + \text{CO}$	0.80	$\text{Tb}^+ + \text{CO}_2$	$\text{TbO}^+ + \text{CO}$	0.056
$\text{La}^+ + \text{CO}_2$	$\text{LaO}^+ + \text{CO}$	0.61/0.64	$\text{Dy}^+ + \text{CO}_2$	$\text{Dy}^+(\text{CO}_2)$	0.004
$\text{Ce}^+ + \text{CO}_2$	$\text{CeO}^+ + \text{CO}$	0.66	$\text{Ho}^+ + \text{CO}_2$	$\text{Ho}^+(\text{CO}_2)$	0.0015
$\text{Pr}^+ + \text{CO}_2$	$\text{PrO}^+ + \text{CO}$	0.23	$\text{Er}^+ + \text{CO}_2$	$\text{Er}^+(\text{CO}_2)$	0.00089
$\text{Nd}^+ + \text{CO}_2$	$\text{NdO}^+ + \text{CO}$	0.054	$\text{Tm}^+ + \text{CO}_2$	$\text{Tm}^+(\text{CO}_2)$	0.0010
$\text{Sm}^+ + \text{CO}_2$	$\text{Sm}^+(\text{CO}_2)$	0.00073	$\text{Yb}^+ + \text{CO}_2$	$\text{Yb}^+(\text{CO}_2)$	0.0010

$\text{Eu}^+ + \text{CO}_2$	$\text{Eu}^+(\text{CO}_2)$	0.0012	$\text{Lu}^+ + \text{CO}_2$	$\text{LuO}^+ + \text{CO}$	0.049
$\text{Sc}^+ + \text{N}_2\text{O}$	$\text{ScO}^+ + \text{N}_2$	0.73	$\text{Eu}^+ + \text{N}_2\text{O}$	$\text{EuO}^+ + \text{N}_2$	0.097
$\text{Y}^+ + \text{N}_2\text{O}$	$\text{YO}^+ + \text{N}_2$	0.82	$\text{Gd}^+ + \text{N}_2\text{O}$	$\text{GdO}^+ + \text{N}_2$	0.75
$\text{La}^+ + \text{N}_2\text{O}$	$\text{LaO}^+ + \text{N}_2$ (96/98%)	0.76/0.82	$\text{Tb}^+ + \text{N}_2\text{O}$	$\text{TbO}^+ + \text{N}_2$	0.17
	$\text{LaN}^+ + \text{NO}$ (4/2%)		$\text{Dy}^+ + \text{N}_2\text{O}$	$\text{DyO}^+ + \text{N}_2$	0.038
$\text{Ce}^+ + \text{N}_2\text{O}$	$\text{Ce}^+ + \text{N}_2$ (75%)	0.72	$\text{Ho}^+ + \text{N}_2\text{O}$	$\text{HoO}^+ + \text{N}_2$	0.024
	$\text{CeN}^+ + \text{NO}$ (25%)		$\text{Er}^+ + \text{N}_2\text{O}$	$\text{ErO}^+ + \text{N}_2$	0.018
$\text{Pr}^+ + \text{N}_2\text{O}$	$\text{PrO}^+ + \text{N}_2$	0.39	$\text{Tm}^+ + \text{N}_2\text{O}$	$\text{TmO}^+ + \text{N}_2$	0.0062
$\text{Nd}^+ + \text{N}_2\text{O}$	$\text{NdO}^+ + \text{N}_2$	0.40	$\text{Yb}^+ + \text{N}_2\text{O}$	$\text{YbO}^+ + \text{N}_2$	0.00093
$\text{Sm}^+ + \text{N}_2\text{O}$	$\text{SmO}^+ + \text{N}_2$	0.19	$\text{Lu}^+ + \text{N}_2\text{O}$	$\text{LuO}^+ + \text{N}_2$	0.37
$\text{Sc}^+ + \text{NO}$	$\text{ScO}^+ + \text{N}$	0.043	$\text{Tb}^+ + \text{NO}$	$\text{TbO}^+ + \text{N}$	0.072
$\text{Y}^+ + \text{NO}$	$\text{YO}^+ + \text{N}$	0.12	$\text{Dy}^+ + \text{NO} + \text{NO}$	$\text{DyO}^+ + \text{N}_2\text{O}$	0.045
$\text{La}^+ + \text{NO}$	$\text{LaO}^+ + \text{N}$	0.40	$\text{Ho}^+ + \text{NO} + \text{NO}$	$\text{HoO}^+ + \text{N}_2\text{O}$	0.027
$\text{Ce}^+ + \text{NO}$	$\text{CeO}^+ + \text{N}$	0.89	$\text{Er}^+ + \text{NO} + \text{NO}$	$\text{ErO}^+ + \text{N}_2\text{O}$	0.027
$\text{Pr}^+ + \text{NO}$	$\text{PrO}^+ + \text{N}$	0.32	$\text{Tm}^+ + \text{NO} + \text{NO}$	$\text{TmO}^+ + \text{N}_2\text{O}$	0.020
$\text{Nd}^+ + \text{NO}$	$\text{NdO}^+ + \text{N}$	0.060	$\text{Yb}^+ + \text{NO} + \text{NO}$	$\text{YbO}^+ + \text{N}_2\text{O}$ (95%)	0.0092
$\text{Sm}^+ + \text{NO} + \text{NO}$	$\text{SmO}^+ + \text{N}_2\text{O}$	0.034		$\text{NO}^+ + \text{YbNO}$ (5%)	
$\text{Eu}^+ + \text{NO} + \text{NO}$	$\text{EuO}^+ + \text{N}_2\text{O}$	0.017	$\text{Lu}^+ + \text{NO} + \text{NO}$	$\text{LuO}^+ + \text{N}_2\text{O}$	0.020

Continued

TABLE 3 Reactions of Bare Rare-Earth Singly-Charged Cations with Oxidants by Bohme and co-workers—Cont'd

Reactants	Products	k/k_{COL}	Reactants	Products	k/k_{COL}
$\text{Gd}^+ + \text{NO}$	$\text{GdO}^+ + \text{N}$	0.41			
$\text{Sc}^+ + \text{NO}_2$	$\text{ScO}^+ + \text{NO}$ (95%)	1.1	$\text{Eu}^+ + \text{NO}_2$	$\text{EuO}^+ + \text{NO}$	0.75
	$\text{NO}^+ + \text{ScO}$ (5%)		$\text{Gd}^+ + \text{NO}_2$	$\text{GdO}^+ + \text{NO}$ (98%)	1.1
$\text{Y}^+ + \text{NO}_2$	$\text{YO}^+ + \text{NO}$	0.98		$\text{NO}^+ + \text{GdO}$ (2%)	
$\text{La}^+ + \text{NO}_2$	$\text{LaO}^+ + \text{NO}$ (99%)	0.97	$\text{Tb}^+ + \text{NO}_2$	$\text{TbO}^+ + \text{NO}$	0.96
	$\text{NO}^+ + \text{LaO}$ (1%)		$\text{Dy}^+ + \text{NO}_2$	$\text{DyO}^+ + \text{NO}$	0.88
$\text{Ce}^+ + \text{NO}_2$	$\text{CeO}^+ + \text{NO}$ (99%)	0.95	$\text{Ho}^+ + \text{NO}_2$	$\text{HoO}^+ + \text{NO}$	0.84
	$\text{NO}^+ + \text{CeO}$ (1%)		$\text{Er}^+ + \text{NO}_2$	$\text{ErO}^+ + \text{NO}$	0.92
$\text{Pr}^+ + \text{NO}_2$	$\text{PrO}^+ + \text{NO}$ (99%)	0.96	$\text{Tm}^+ + \text{NO}_2$	$\text{TmO}^+ + \text{NO}$	0.84
	$\text{NO}^+ + \text{PrO}$ (1%)		$\text{Yb}^+ + \text{NO}_2$	$\text{YbO}^+ + \text{NO}$	0.30
$\text{Nd}^+ + \text{NO}_2$	$\text{NdO}^+ + \text{NO}$	0.97	$\text{Lu}^+ + \text{NO}_2$	$\text{LuO}^+ + \text{NO}$	1.0
$\text{Sm}^+ + \text{NO}_2$	$\text{SmO}^+ + \text{NO}$	1.0			
$\text{Sc}^+ + \text{D}_2\text{O}$	$\text{ScO}^+ + \text{D}_2$	0.00068	$\text{Eu}^+ + \text{D}_2\text{O}$	$\text{Eu}^+(\text{D}_2\text{O})$	<0.00024
$\text{Y}^+ + \text{D}_2\text{O}$	$\text{YO}^+ + \text{D}_2$	0.44	$\text{Gd}^+ + \text{D}_2\text{O}$	$\text{GdO}^+ + \text{D}_2$	0.11

La ⁺ + D ₂ O	LaO ⁺ + D ₂ (80%)	0.14	Tb ⁺ + D ₂ O	TbO ⁺ + D ₂	0.040
	LaOD ⁺ + D (20%)		Dy ⁺ + D ₂ O	Dy ⁺ (D ₂ O)	<0.00024
Ce ⁺ + D ₂ O	CeO ⁺ + D ₂	0.095	Ho ⁺ + D ₂ O	Ho ⁺ (D ₂ O)	<0.00024
Pr ⁺ + D ₂ O	PrO ⁺ + D ₂ (95%)	0.0043	Er ⁺ + D ₂ O	Er ⁺ (D ₂ O)	<0.00024
	PrOD ⁺ + D (5%)		Tm ⁺ + D ₂ O	Tm ⁺ (D ₂ O)	<0.00024
Nd ⁺ + D ₂ O	NdO ⁺ + D ₂	0.0010	Yb ⁺ + D ₂ O	YbOD ⁺ + D	0.0025
Sm ⁺ + D ₂ O	SmO ⁺ + D ₂	0.00067	Lu ⁺ + D ₂ O	LuO ⁺ + D ₂	0.035

^aSc⁺, Y⁺, La⁺/O₂ (Koyanagi et al., 2002); Ln⁺/O₂ (Koyanagi and Bohme, 2001); Sc⁺, Y⁺, La⁺/CO₂ (Koyanagi and Bohme, 2006); Ln⁺/CO₂ (Cheng et al., 2006b); Sc⁺, Y⁺, La⁺/N₂O (Lavrov et al., 2004); Ln⁺/N₂O (Koyanagi and Bohme, 2001); Sc⁺, Y⁺, La⁺/NO (Blagojevic et al., 2005a); Ln⁺/NO (Blagojevic et al., 2006); Sc⁺, Y⁺, La⁺/NO₂ (Jarvis et al., 2013); Ln⁺/NO₂ (Jarvis et al., 2010); Sc⁺, Y⁺, La⁺/D₂O (Cheng et al., 2007); Ln⁺/D₂O (Cheng et al., 2006c).

^bWhere more than one product is given the percentages in parentheses are relative branching ratios.

^cReaction efficiencies, k/k_{COL} , are pseudo-first order rate constants k relative to the collisional rate constant, k_{COL} . Values of k/k_{COL} greater than unity indicate uncertainties in the experimental rate constant k , and/or calculated k_{COL} .

^dValues corrected due to apparent error in k/k_{COL} calculation in the original publication; see also Bandura et al. (2006).

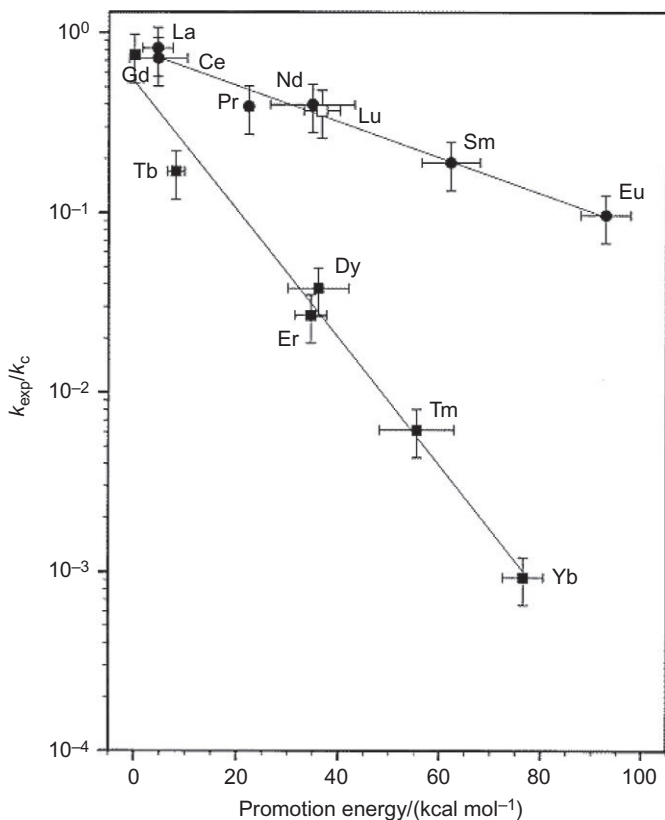


FIGURE 3 Correlation of reaction efficiency with the electron promotion energy from the ground state to the first $5d^1 6s^1$ configuration that is proposed to be required for $\text{Ln}^+ - \text{O}$ bond formation in the reactions of early (solid circles) and late (solid squares) Ln^+ ions with N_2O . Lu^+ (open square) clearly is an exception to the trend observed for the late Ln^+ ions. *Reproduced with permission from Koyanagi and Bohme (2001). Copyright 2001 American Chemical Society.*

so, tetravalent oxidation state, was observed in the reactions with N_2O . GdOH^{2+} and LuOH^{2+} were produced in the reactions with H_2O and reacted further with H_2O by proton transfer. Electron transfer to form the singly charged metal ions was the only reaction channel of the Ln^{2+} with NO , the oxidant with the lowest ionization energy (IE); no reactions were observed with O_2 and CO_2 . The examination of the kinetics of electron transfer from N_2O , CO_2 , and CO to the three LnO^{2+} ions allowed estimations of the second LnO ionization energies and the $\text{Ln}^{2+} - \text{O}$ bond energies for the studied lanthanides.

In their study, Gibson et al. (2008) demonstrated that the LnO^{2+} ions catalyzed the oxidation of CO to CO_2 concomitant with the reduction of N_2O to N_2 . The thermodynamic requirement for O-atom transport from N_2O to CO

mediated by an $MO^{+/2+}$ ion is that its oxygen dissociation energy is intermediate between $D(N_2-O)$ and $D(OC-O)$. Bohme and coworkers studied this process in detail for several monovalent metal ions that met the above requirement (Blagojevic et al., 2005b). Among the metal ions that effected O-atom transport catalysis in the reduction of N_2O by CO were Eu^+ and Yb^+ , as illustrated in Fig. 4; Tm^+ and Lu^+ were also examined but the corresponding monoxides reacted too slowly with CO such that they did not act as catalysts. In a subsequent study, Blagojevic et al. (2008) investigated the oxidation of H_2 by N_2O for several metal ions, including Eu^+ , Tm^+ , and Yb^+ , but their monoxides reacted too slowly with H_2 to produce H_2O .

Several other inorganic molecules have been used as reagents in reactivity experiments with rare earth metal cations. COS can act as an oxidant but is also an S-atom donor, and it was used in the investigation of the formation of metal sulfide ions, sometimes in conjunction with the sulfur-transfer reagent CS_2 . Kretzschmar et al. (2000) used GIB and FTICR-MS to study the reactions of bare Sc^+ ions with COS and CS_2 and of the metal sulfide ScS^+ with oxygen-transfer substrates (CO, CO_2 , COS, and H_2O) and with Xe to examine its CID; an assessment of the results of ion/molecule reactions, CID, and equilibrium measurements resulted in $D_0(Sc^+ - S) = 480 \pm 5 \text{ kJ mol}^{-1}$. The same approach was later used to examine the thermochemistry of Y^+ , yielding similar results and $D_0(Y^+ - S) = 530 \pm 17 \text{ kJ mol}^{-1}$ (Kretzschmar et al., 2006).

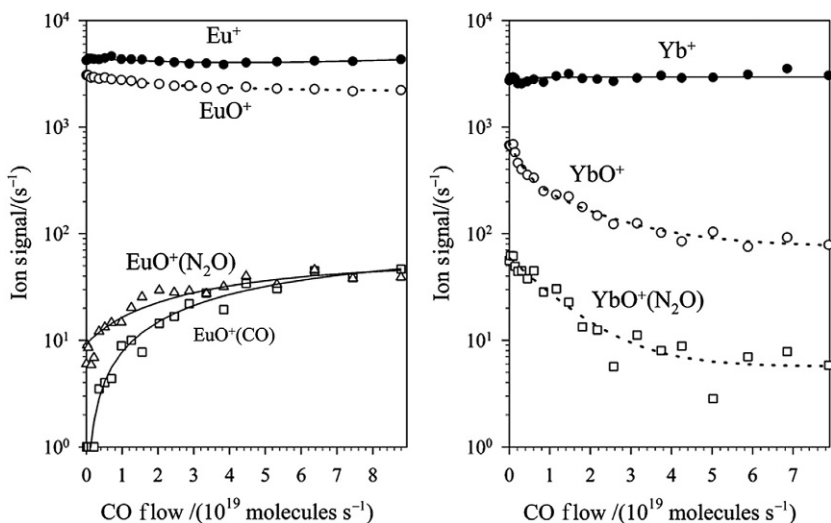


FIGURE 4 Ion profiles recorded for the chemistry initiated by EuO^+ and YbO^+ with carbon monoxide at 295 K in helium buffer gas at 0.35 Torr. The flows of N_2O added upstream are 3 and 4×10^{17} molecules s^{-1} . The initial slopes in the decays of RO^+ were used to fit the formation of product ions (solid lines). Reproduced with permission from Blagojevic et al. (2005b). Copyright 2005 American Chemical Society.

Bohme and coworkers extended their comprehensive reactivity studies to CS_2 and examined the reactions of Sc^+ , Y^+ , and La^+ (Cheng et al., 2006a), as well as the remaining lanthanide series cations (Cheng et al., 2006b). Very efficient formation of the sulfide ions was observed for the more reactive metal ions and the periodicity in the reaction efficiencies observed for the Ln^+ cations and the oxidants appeared to be attenuated in the case of CS_2 , an effect that was attributed to the much higher polarizability of CS_2 as compared to CO_2 . The reactions of Sc^+ , Y^+ , and La^+ with COS were also studied in Bohme's laboratory, with the observation of both RS^+ and RO^+ ions as primary products; however, as of this writing, only a summary of these results is available, in the group's Web site (<http://www.chem.yorku.ca/profs/bohme/research/molecule/OCS.html>).

The formation of rare earth metal sulfide ions, particularly polysulfides, in reactions of the singly charged metal cations with S_8 was studied by Dance, Fisher, and Willett using FTICR-MS. The authors examined Sc^+ (Dance et al., 1995, 1996), Y^+ (Dance et al., 1996), La^+ (Dance et al., 1996; Fisher et al., 1998), and the lanthanide ions Ln^+ (Fisher et al., 1998). A series of $[\text{RS}_n]^+$ product ions were formed, with n starting at 2–4 and increasing up to 21 for longer reaction times, as observed for the cases of La and Pr ; the reaction rates correlated approximately with the occurrence of a ground or low excited state with two unpaired non-f electrons, as observed with other substrates.

The activation of NH_3 with the formation of the metal–imido ion MNH^+ was observed by Freiser and coworkers using FTICR-MS in the case of Sc^+ (Buckner et al., 1988) and Y^+ (Ranatunga et al., 1996). Using GIB-MS, Clemmer et al. (1990) examined the interaction of Sc^+ with NH_3 (and ND_3) and also observed the exothermic dehydrogenation of ammonia to form ScNH^+ ; the endothermic products ScH^+ and ScNH_2^+ were also identified and the thermochemistries of ScNH^+ and ScNH_2^+ were established for the first time. Bohme and coworkers also studied NH_3 in their ICP/SIFT instrument and reported the results obtained for the Ln^+ cations (Koyanagi et al., 2010); these ions reacted by H_2 elimination to form LnNH^+ in the case of La^+ , Ce^+ , Gd^+ , and Tb^+ or by NH_3 addition with the remaining lanthanide ions, reflecting the different accessibility of $5d^1 6s^1$ configurations of the lanthanide cations. The reactions of Sc^+ and Y^+ were also measured by Bohme and coworkers, and the formation of the metal–imido ions also observed; although the results were not yet published at the time of this writing, a summary of the results can be retrieved from the group's Web site (<http://www.chem.yorku.ca/profs/bohme/research/molecule/NH3.html>). Quemet et al. (2013) have recently examined the reactions of La^+ , Sm^+ , Eu^+ , and Gd^+ with NH_3 and ND_3 with concordant results. Schwarz and coworkers (Kretschmer et al., 2012) observed the formation of ScNH_2^+ and parallel H_2 elimination in a recent study of the reaction of ScH^+ with NH_3 at thermal energies, in a mass spectrometer of quadrupole–hexapole–quadrupole configuration

equipped with an ESI source. No scrambling processes were seen in the product ions generated in experiments with the couples ScH^+/ND_3 and ScD^+/NH_3 , suggesting a nonreversible σ -bond metathesis mechanism.

Silane and germane were other main-group hydrides that were the object of reactivity studies with the rare earth cations. Geribaldi and coworkers used FTICR-MS to investigate the reactions of Sc^+ (Azzaro et al., 1992), Y^+ (Azzaro et al., 1992; Decouzon et al., 1989), and Lu^+ (Azzaro et al., 1992) with silane. Lu^+ was unreactive, Y^+ formed the metal silylene ion YSiH_2^+ as the single primary product in an exothermic process, while the reaction of Sc^+ to form ScH^+ and ScSiH_2^+ was slow and considered endothermic by the authors; the primary products of Sc^+ and Y^+ reacted further to result in the oligomerization of silane. Armentrout and coworkers later examined the reactions of Sc^+ , Y^+ , La^+ , and Lu^+ with SiH_4 with their GIB technique (Kickel and Armentrout, 1995). The formation of MH^+ , MH_2^+ , and MSiH_x^+ ($x=0-3$) was observed and the 0 K bond energies for M^+-SiH_x ($x=0-3$) were determined. The formation of MSiH_2^+ for $\text{M}=\text{Y}$ and La appeared to be exothermic and efficient, while for the inefficient reactions of Lu^+ and Sc^+ , the interpretation of the results was not definitive. Germane, GeH_4 , was incidentally examined by Gibson (2002a) in its reactions with Ce^+ , Tb^+ , and Tm^+ using the LAPRD technique; this work was performed within a comparison with the reactivity of An^+ ions; the formation of LnGeH_2^+ was observed for Ce^+ and Tb^+ , while Tm^+ was unreactive.

Sulfur hexafluoride is the last, clearly inorganic molecule to be mentioned in this first part of the summary of reactions of the rare earth ions; reactions with related fluorocarbons will be described in Section 2.3. Jiao and Freiser used FTICR-MS to study reactions of SF_6 with several transition metal ions, including Sc^+ , Y^+ , and La^+ (Jiao and Freiser, 1993). The MF^+ and MF_2^+ ions were observed as primary products, together with several SF_n^+ ions, with the reactions involving Sc^+ having been examined in particular detail. Heinemann et al. (1995b) obtained similar results with Pr^+ , also by FTICR-MS. Gibson (1996c) also observed the formation of LnF^+ and LnF_2^+ ions in the cases of Tb^+ and Ho^+ , using LAPRD. The definitive survey of the reactions of SF_6 with rare earth metal cations was again performed by Bohme and coworkers, who investigated the lanthanide series cations (Cheng and Bohme, 2006), as well as Sc^+ and Y^+ (Cheng et al., 2009). In the case of the Ln^+ ions, multiple F-atom abstraction was observed, in very fast reactions, as the primary products were mostly LnF_n^+ and SF_n^+ (where $n=1-3$), with $n=2$ for LnF_n^+ and $n=3$ for SF_n^+ dominant; similar results were obtained for Sc^+ and Y^+ ions. As in other cases, the reaction efficiencies and the product distributions of the Ln^+ ions correlated with the electron PE required to achieve two unpaired valence electrons in the Ln^+ cation; again, differences were observed between early and late lanthanide cations.

2.1.2 Actinides

The diatomic hydrides, UH^+ and PuH^+ , were among the first actinide molecular ions to be systematically prepared by reactions of the actinide cations U^+ and Pu^+ with neutral H-atom donors, H_2 (D_2), H_2O (D_2O), and H_2S (Moreland et al., 1970). These authors obtained the first estimate for $D_0(\text{U}^+ - \text{H}) = 320 \pm 50 \text{ kJ mol}^{-1}$ from the threshold energies in the ion beam apparatus for these endothermic reactions. Armentrout et al. subsequently performed a precise study of the energy dependence of reactions of U^+ with D_2 and CD_4 to produce the UD^+ , which provided $D_0(\text{U}^+ - \text{D}) = 280 \pm 10 \text{ kJ mol}^{-1}$, in accord with the earlier value (Armentrout et al., 1977a,b); these early GIB results for an actinide ion/molecule reaction are illustrated in Fig. 5. An ancillary result of this latter work was the assignment of the PA of U, $\text{PA}(\text{U})$, as $238 \pm 5 \text{ kJ mol}^{-1}$, revealing that the U atom is more basic than Li and Mg. Other reported monohydrides include AmH^+ from the reaction of Am^{2+} with ethylene oxide, $\text{C}_2\text{H}_4\text{O}$; UH^+ was also formed in the reaction of U^{2+} with formaldehyde, CH_2O (Gibson et al., 2005).

Among the most extensively studied reactions of bare and ligated actinide ions are those with O-atom donors, with a central goal of synthesizing and characterizing elementary monoxide and dioxide ions, particularly AnO^+ ,

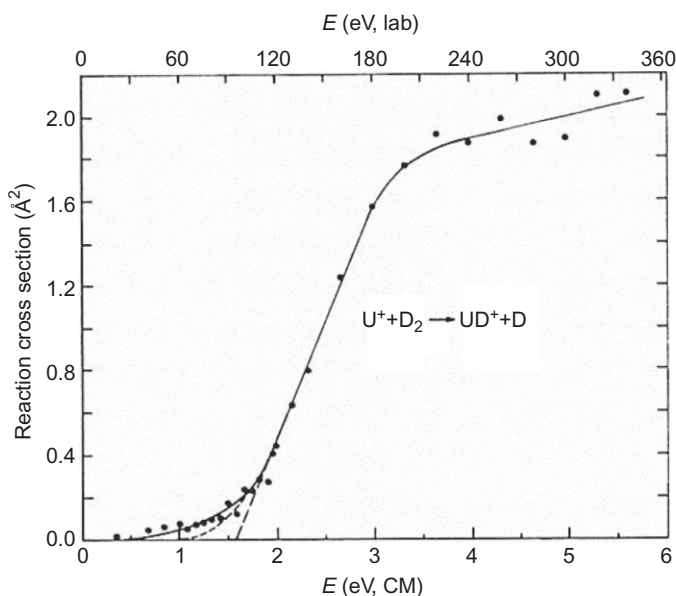


FIGURE 5 Guided ion beam results for the abstraction of D from D_2 by U^+ . The straight dashed line is the extrapolation in the threshold onset region. Reproduced with permission from Armentrout et al. (1977b). Copyright 1977 American Chemical Society.

AnO_2^+ , AnO^{2+} , and AnO_2^{2+} . There have been several reports of the spontaneous exothermic reaction of U^+ with O_2 to produce UO^+ , starting with that by [Johnsen and Biondi \(1972\)](#), in which a thermal pseudo-first-order rate constant of $k = 8.5 \times 10^{-10} \text{ cm}^3 \text{ molecule}^{-1} \text{ s}^{-1}$ was reported ($k_{\text{COL}} = 5.5 \times 10^{-10}$, where k_{COL} is the calculated collisional rate constant); subsequent reported rate constants were $k = 5.6 \times 10^{-10}$ ([Armentrout and Beauchamp, 1980](#)), $k = 6.4 \times 10^{-10}$ ([Cornehl et al., 1997a](#)), $k = 4.0 \times 10^{-10}$ ([Santos et al., 2002](#)), and $k = 9.2 \times 10^{-10}$ ([Jackson et al., 2002c, 2004b](#)) (all rate constants are in units of $\text{cm}^3 \text{ molecule}^{-1} \text{ s}^{-1}$). These five values are in reasonable agreement and indicate that for reaction An^+/XO with $\text{An}=\text{U}$ and $\text{X}=\text{O}$, the rate is close to the collisional rate. In Eqs. (3) and (4), XO designates O-atom donors such as O_2 ($\text{X}=\text{O}$), NO ($\text{X}=\text{N}$), and CO_2 ($\text{X}=\text{CO}$):



Ensuing reactivity studies revealed large variations in oxidation kinetics across the actinide series from Th^+ to Cm^+ . These kinetics are summarized in [Table 4](#) as pseudo-first-order rate constants relative to the estimated collisional rate, k/k_{COL} , for a variety of O-atom donors XO. In general, for a given O-atom donor molecule, faster kinetics are associated with more exothermic oxidation reactions; the thermodynamics of these reactions are derived from the thermodynamic data presented in [Section 3](#). For example, Eq. (3) for O_2 is exothermic by 276 kJ mol^{-1} for U^+ and occurs near the collisional rate, whereas it is exothermic by 153 kJ mol^{-1} for Pu^+ and occurs at $\sim 30\%$ of the collisional rate. Kinetic constraints to O-atom transfer result in important exceptions to thermodynamic generalizations based on rate constants, particularly when comparing different O-atom donors. For example, despite that N_2O is thermodynamically a much more facile O-atom donor ($D(\text{N}_2-\text{O}) = 167 \text{ kJ mol}^{-1}$) than is O_2 ($D(\text{O}-\text{O}) = 498 \text{ kJ mol}^{-1}$), Am^+ is oxidized to AmO^+ at $\sim 30\%$ of the collisional rate by O_2 but at only 0.4% of the collisional rate by N_2O ; there is clearly a substantial kinetic barrier for O-atom transfer from N_2O to metal cations. The transcurium oxide ions BkO^+ , CfO^+ , and EsO^+ were produced by LA of solids ([Gibson and Haire, 2000, 2001b, 2003](#)), but their formation by gas-phase reactions of the An^+ ions with O-atom donors have not been systematically and quantitatively studied.

The AnO_2^+ ions have been produced by reaction (4) for $\text{An}=\text{Th}$, Pa , U , Np , Pu , and Am , with kinetics as summarized in [Table 5](#). The CmO_2^+ ion, which has the lowest OAn^+-O bond dissociation energy (BDE) of the studied actinides, was not observed under thermal reaction conditions with any of the employed oxidants but was produced in the hyperthermal reaction of CmO^+ with O_2 . The ThO_2^+ ion was produced under thermal conditions with the kinetically and thermodynamically facile oxidant $\text{C}_2\text{H}_4\text{O}$ (ethylene oxide) and also with the kinetically hindered oxidant N_2O . The reaction of ThO^+

TABLE 4 Reactions of Bare Actinide Singly-Charged Cations with Oxidants^a

Reactants	Products	k/k_{COL} ^b	Reactants	Products	k/k_{COL} ^b
Th ⁺ + O ₂	ThO ⁺ + O	1.1; ^c 1.12; ^d 0.82 ^e	Pu ⁺ + O ₂	PuO ⁺ + O	0.27 ^e
Pa ⁺ + O ₂	PaO ⁺ + O	0.66 ^f	Am ⁺ + O ₂	AmO ⁺ + O	0.32 ^k
U ⁺ + O ₂	UO ⁺ + O	1.5; ^g 1.0; ^h 1.2; ^d 0.71; ^e 1.6 ^{i,j}	Cm ⁺ + O ₂	CmO ⁺ + O	0.37 ^l
Np ⁺ + O ₂	NpO ⁺ + O	0.68 ^e			
Th ⁺ + H ₂ O	ThO ⁺ + OH (65%)	0.57; ^d 0.20 ^e	Np ⁺ + H ₂ O	NpO ⁺ + OH	0.10 ^e
	ThOH ⁺ + H (35%)		Pu ⁺ + H ₂ O	PuO ⁺ + OH	0.004 ^e
Pa ⁺ + H ₂ O	PaO ⁺ + OH (70%)	0.26 ^f	Am ⁺ + H ₂ O	AmO ⁺ + OH	0.001 ^k
	PaOH ⁺ + H (30%)		Cm ⁺ + H ₂ O	CmO ⁺ + OH	0.05 ^l
U ⁺ + H ₂ O	UO ⁺ + OH	0.47; ^d 0.13 ^e			
	UOH ⁺ + H ^{h,i}				
Th ⁺ + N ₂ O	ThO ⁺ + N ₂ (65%; 50%)	1.02; ^d 0.68 ^e	Np ⁺ + N ₂ O	NpO ⁺ + N ₂ (25%)	0.48 ^e
	ThN ⁺ + NO (35%; 50%)			NpN ⁺ + NO (75%)	
Pa ⁺ + N ₂ O	PaO ⁺ + N ₂ (60%)	0.49 ^f	Pu ⁺ + N ₂ O	PuO ⁺ + N ₂	0.02 ^e
	PaN ⁺ + NO (40%)		Am ⁺ + N ₂ O	AmO ⁺ + N ₂	0.004 ^k
U ⁺ + N ₂ O	UO ⁺ + N ₂ (70%)	1.25; ^d 0.47 ^e	Cm ⁺ + N ₂ O	CmO ⁺ + N ₂	0.17 ^l
	UN ⁺ + NO (30%)				

TABLE 4 Reactions of Bare Actinide Singly-Charged Cations with Oxidants—**Cont'd**

Reactants	Products	k/k_{COL}	Reactants	Products	k/k_{COL}
$\text{Th}^+ + \text{C}_2\text{H}_4\text{O}$	$\text{ThO}^+ + \text{C}_2\text{H}_4$	0.61 ^e	$\text{Pu}^+ + \text{C}_2\text{H}_4\text{O}$	$\text{Pu}^+ + \text{C}_2\text{H}_4$	0.21 ^e
$\text{Pa}^+ + \text{C}_2\text{H}_4\text{O}$	$\text{PaO}^+ + \text{C}_2\text{H}_4$	0.44 ^f	$\text{Am}^+ + \text{C}_2\text{H}_4\text{O}$	$\text{Am}^+ + \text{C}_2\text{H}_4$	0.21 ^k
$\text{U}^+ + \text{C}_2\text{H}_4\text{O}$	$\text{UO}^+ + \text{C}_2\text{H}_4$	0.34 ^e	$\text{Cm}^+ + \text{C}_2\text{H}_4\text{O}$	$\text{Cm}^+ + \text{C}_2\text{H}_4$	0.26 ^l
$\text{Np}^+ + \text{C}_2\text{H}_4\text{O}$	$\text{Np}^+ + \text{C}_2\text{H}_4$	0.32 ^e			
$\text{Th}^+ + \text{CO}_2$	$\text{ThO}^+ + \text{CO}$	0.95 ^d	$\text{Np}^+ + \text{CO}_2$	$\text{NpO}^+ + \text{CO}$	0.30 ^e
$\text{Pa}^+ + \text{CO}_2$	$\text{PaO}^+ + \text{CO}$	0.35 ^e	$\text{Pu}^+ + \text{CO}_2$	$\text{PuO}^+ + \text{CO}$	0.003 ^e
$\text{U}^+ + \text{CO}_2$	$\text{UO}^+ + \text{CO}$	0.38; ^f 1.02; ^d 0.29 ^e	$\text{Am}^+ + \text{CO}_2$	$\text{AmO}^+ + \text{CO}$	0.001 ^k
	$\text{UO}_2^+ + \text{C}$		$\text{Cm}^+ + \text{CO}_2$	$\text{CmO}^+ + \text{CO}$	0.08 ^l
$\text{Th}^+ + \text{NO}$	$\text{ThO}^+ + \text{N}$	1.4; ^c 0.49 ^e	$\text{Pu}^+ + \text{NO}$	$\text{PuO}^+ + \text{N}$	0.17 ^e
$\text{Pa}^+ + \text{NO}$	$\text{PaO}^+ + \text{N}$	0.51 ^f	$\text{Am}^+ + \text{NO}$	$(\text{AmO}^+ + \text{N})$	<0.001 ^k
$\text{U}^+ + \text{NO}$	$\text{UO}^+ + \text{N}$	0.46 ^e	$\text{Cm}^+ + \text{NO}$	$\text{CmO}^+ + \text{N}$	0.013 ^l
$\text{Np}^+ + \text{NO}$	$\text{NpO}^+ + \text{N}$	0.45 ^e			
$\text{Th}^+ + \text{CH}_2\text{O}$	$\text{ThO}^+ + \text{CH}_2$	0.61 ^e	$\text{Np}^+ + \text{CH}_2\text{O}$	$\text{NpO}^+ + \text{CH}_2$	0.28 ^e
$\text{Pa}^+ + \text{CH}_2\text{O}$	$\text{PaO}^+ + \text{CH}_2$	0.48 ^f	$\text{Pu}^+ + \text{CH}_2\text{O}$	$(\text{PuO}^+ + \text{CH}_2)$	<0.001 ^e
$\text{U}^+ + \text{CH}_2\text{O}$	$\text{UO}^+ + \text{CH}_2$	0.53 ^e	$\text{Cm}^+ + \text{CH}_2\text{O}$	$(\text{CmO}^+ + \text{CH}_2)$	<0.001 ^l
$\text{U}^+ + \text{CO}$	$\text{UO}^+ + \text{C}^{\text{h}}$	-			
	$\text{UC}^+ + \text{O}^{\text{h}}$				
$\text{Th}^+ + \text{OCS}$	$\text{ThO}^+ + \text{CS}$ (60%)	0.87 ^m	$\text{Np}^+ + \text{OCS}$	$\text{NpO}^+ + \text{CS}$ (60%)	0.83 ^m
	$\text{ThS}^+ + \text{CO}$ (40%)			$\text{NpS}^+ + \text{CO}$ (40%)	
$\text{Pa}^+ + \text{OCS}$	$\text{PaO}^+ + \text{CS}$ (60%)	0.83 ^m	$\text{Pu}^+ + \text{OCS}$	$\text{PuS}^+ + \text{CO}$	0.25 ^m
	$\text{PaS}^+ + \text{CO}$ (40%)		$\text{Am}^+ + \text{OCS}$	$\text{AmS}^+ + \text{CO}$	0.022 ^m

Continued

TABLE 4 Reactions of Bare Actinide Singly-Charged Cations with Oxidants—Cont'd

Reactants	Products	k/k_{COL}	Reactants	Products	k/k_{COL}
$U^+ + OCS$	$UO^+ + CS^h$		$Cm^+ + OCS$	$CmS^+ + CO$	0.42^m
	$US^+ + CO^h$				
	$UO^+ + CS$ (60%)	0.92^m			
	$US^+ + CO$ (40%)				

^aProducts of reactions which are endothermic and observed only for energetic collisions are in italics. Where more than one product is given the percentages in parentheses are relative branching ratios. Products in parentheses were not observed under thermal conditions.

^bReaction efficiencies, k/k_{COL} , are pseudo-first order rate constants k relative to the collisional rate constant, k_{COL} . Values of k/k_{COL} greater than unity indicate uncertainties in the experimental rate constant k , and/or calculated k_{COL} . Where a value for k/k_{COL} is not provided either k was not measured or the reaction is endothermic and does not proceed spontaneously.

^c(Johnsen et al., 1974)

^d(Cornehl et al., 1997a)

^e(Santos et al., 2002)

^f(Santos et al., 2006b)

^g(Johnsen and Biondi, 1972)

^h(Armentrout and Beauchamp, 1980a)

ⁱ(Jackson et al., 2002c)

^j(Jackson et al., 2004b)

^k(Santos et al., 2003)

^l(Gibson et al., 2008)

^m(Pereira et al., 2011).

with H_2O results in the oxide hydroxide $ThO(OH)^+$ in which the prevalent Th(IV) oxidation state is exhibited. As with the oxidation reactions of the bare An^+ ions, there is a general correlation of reaction efficiency with exothermicity. Thus, with the oxidant C_2H_4O , the oxidation of PaO^+ to PaO_2^+ occurs at 43% of the collisional rate, whereas the oxidation of AmO^+ to AmO_2^+ occurs at only 0.3% of the collisional rate; this difference can be attributed to the much greater $D(OPa^+ - O) \approx 780 \text{ kJ mol}^{-1}$ versus $D(OAm^+ - O) \approx 410 \text{ kJ mol}^{-1}$.

Studied reactions of dipositive An^{2+} and AnO^{2+} with O-atom donors are summarized in Table 6. All of the AnO^{2+} for $An = Th - Cm$ have been synthesized. In a seminal work, Cornehl et al. (1996a) synthesized the bare uranyl ion, UO_2^{2+} , by the sequential reaction of laser-ablated U^{2+} ions with two molecules of O_2 or N_2O . As is common for small dipositive ions such as UO_2^{2+} , electron transfer from the oxidant also resulted in charge reduction to UO_2^+ . Measured electron transfer rates increase as the difference

TABLE 5 Reactions of Singly-Charged Actinide Monoxide Cations with Oxidants^a

Reactants	Products	k/k_{COL}^b	Reactants	Products	k/k_{COL}^b
ThO ⁺ + O ₂	ThO ₂ ⁺ + O	0.04; ^{c,d} <0.001 ^e	PuO ⁺ + O ₂	PuO ₂ ⁺ + O	0.07 ^e
PaO ⁺ + O ₂	PaO ₂ ⁺ + O	0.65 ^f	AmO ⁺ + O ₂	(AmO ₂ ⁺ + O)	<0.001 ⁱ
UO ⁺ + O ₂	UO ₂ ⁺ + O	0.95; ^g 0.45; ^e 1.6 ^h	CmO ⁺ + O ₂	(CmO ₂ ⁺ + O)	<0.001 ^j
NpO ⁺ + O ₂	NpO ₂ ⁺ + O	0.28 ^e		CmO ₂ ⁺ + O ^j	
ThO ⁺ + H ₂ O	ThO ₂ H ⁺ + OH	0.36; ^g 0.11 ^e	NpO ⁺ + H ₂ O	NpO ₂ ⁺ + OH	0.004 ^e
PaO ⁺ + H ₂ O	PaO ₂ ⁺ + H ₂ (40%)	0.19 ^f	PuO ⁺ + H ₂ O	PuO ₂ ⁺ + OH	0.002 ^e
	PaO ₂ H ⁺ + OH (60%)		AmO ⁺ + H ₂ O	AmO ₂ H ₂ ⁺	0.001 ⁱ
UO ⁺ + H ₂ O	UO ₂ ⁺ + OH	0.04; ^g 0.009; ^e 0.006 ^h	CmO ⁺ + H ₂ O	CmO ₂ H ₂ ⁺ ^j	-
ThO ⁺ + N ₂ O	ThO ₂ ⁺ + N ₂	0.71; ^g 0.31 ^e	PuO ⁺ + N ₂ O	PuO ₂ ⁺ + N ₂	0.003 ^e
PaO ⁺ + N ₂ O	PaO ₂ ⁺ + N ₂	0.48 ^f	AmO ⁺ + N ₂ O	(AmO ₂ ⁺ + N ₂)	<0.001 ⁱ
UO ⁺ + N ₂ O	UO ₂ ⁺ + N ₂	0.49; ^g 0.08 ^e	CmO ⁺ + N ₂ O	(CmO ₂ ⁺ + N ₂)	<0.001 ^j
NpO ⁺ + N ₂ O	NpO ₂ ⁺ + N ₂	0.07 ^e			
ThO ⁺ + C ₂ H ₄ O	ThO ₂ ⁺ + C ₂ H ₄	0.34 ^e	AmO ⁺ + C ₂ H ₄ O	AmO ₂ ⁺ + C ₂ H ₄ (10%)	0.03 ⁱ

Continued

TABLE 5 Reactions of Singly-Charged Actinide Monoxide Cations with Oxidants—Cont'd

Reactants	Products	k/k_{COL}	Reactants	Products	k/k_{COL}
$\text{PaO}^+ + \text{C}_2\text{H}_4\text{O}$	$\text{PaO}_2^+ + \text{C}_2\text{H}_4$	0.43 ^f		$\text{AmO}_2\text{H}_2^+ + \text{C}_2\text{H}_3$ (20%)	
$\text{UO}^+ + \text{C}_2\text{H}_4\text{O}$	$\text{UO}_2^+ + \text{C}_2\text{H}_4$	0.30 ^e		$\text{AmO}_2\text{C}_2\text{H}_2^+ + \text{H}_2$ (60%)	
$\text{NpO}^+ + \text{C}_2\text{H}_4\text{O}$	$\text{NpO}_2^+ + \text{C}_2\text{H}_4$	0.28 ^e		$\text{AmO}_2\text{C}_2\text{H}_4^+$ (10%)	
$\text{PuO}^+ + \text{C}_2\text{H}_4\text{O}$	$\text{PuO}_2^+ + \text{C}_2\text{H}_4$	0.15 ^e	$\text{CmO}^+ + \text{C}_2\text{H}_4\text{O}$	$(\text{CmO}_2^+ + \text{C}_2\text{H}_4)$	<0.001 ^j
$\text{ThO}^+ + \text{CO}_2$	$(\text{ThO}_2^+ + \text{CO})$	<0.001 ^e	$\text{PuO}^+ + \text{CO}_2$	$(\text{PuO}_2^+ + \text{CO})$	<0.001 ^e
$\text{PaO}^+ + \text{CO}_2$	$\text{PaO}_2^+ + \text{CO}$	0.41 ^f	$\text{AmO}^+ + \text{CO}_2$	$(\text{AmO}_2^+ + \text{CO})$	<0.001 ⁱ
$\text{UO}^+ + \text{CO}_2$	$\text{UO}_2^+ + \text{CO}$	0.002; ^g 0.004 ^e	$\text{CmO}^+ + \text{CO}_2$	$(\text{CmO}_2^+ + \text{CO})$	<0.001 ^j
$\text{NpO}^+ + \text{CO}_2$	$(\text{NpO}_2^+ + \text{CO})$	<0.001 ^e			
$\text{ThO}^+ + \text{NO}$	$\text{ThO}_2^+ + \text{N}$	0.01; ^{c,d} <0.001 ^e	$\text{PuO}^+ + \text{NO}$	$(\text{PuO}_2^+ + \text{N})$	<0.001 ^e
$\text{PaO}^+ + \text{NO}$	$\text{PaO}_2^+ + \text{N}$	0.33 ^f	$\text{AmO}^+ + \text{NO}$	$(\text{AmO}_2^+ + \text{N})$	<0.001 ⁱ
$\text{UO}^+ + \text{NO}$	$\text{UO}_2^+ + \text{N}$	0.11 ^e	$\text{CmO}^+ + \text{NO}$	$(\text{CmO}_2^+ + \text{N})$	<0.001 ^j
$\text{NpO}^+ + \text{NO}$	$(\text{NpO}_2^+ + \text{N})$	<0.001 ^e			
$\text{ThO}^+ + \text{OCS}$	ThOS^+	0.67 ^k	$\text{NpO}^+ + \text{OCS}$		<0.005 ^k

PaO ⁺ + OCS	PaO ₂ ⁺ + CS (40%)	0.88 ^k	PuO ⁺ + OCS		<0.005 ^k
	PaOS ⁺ + CO (60%)		AmO ⁺ + OCS		<0.005 ^k
UO ⁺ + OCS	UOS ⁺ + CO ^l	0.51 ^k	CmO ⁺ + OCS	CmS ⁺ + CO ₂	0.23 ^k
	UO ₂ ⁺ + CS ^l				
	UOS ⁺ + CO (85%)				
	UO ₂ ⁺ + CS (15%)				

^aProducts of reactions which are endothermic and observed only for energetic collisions are in italics. Where more than one product is given the percentages in parentheses are relative branching ratios. Products in parentheses were not observed under thermal conditions.

^bReaction efficiencies, k/k_{COL} , are pseudo-first order rate constants k relative to the collisional rate constant, k_{COL} . Values of k/k_{COL} greater than unity indicate uncertainties in the experimental rate constant k , and/or calculated k_{COL} . Where a value for k/k_{COL} is not provided either k was not measured or the reaction is endothermic and does not proceed spontaneously.

^cAccording to the thermodynamics presented in Section 3.2 this reaction should be endothermic.

^d(Johnsen et al., 1974)

^e(Santos et al., 2002)

^f(Santos et al., 2006b)

^g(Cornehl et al., 1997a)

^h(Jackson et al., 2002c)

ⁱ(Santos et al., 2003)

^j(Gibson et al., 2008)

^k(Pereira et al., 2011)

^l(Armentrout and Beauchamp, 1980a).

TABLE 6 Selected reactions of An^{2+} and AnO^{2+} with Oxidants^a

Reactants	Products	k/k_{COL} ^b	Reactants	Products	k/k_{COL} ^b
$Th^{2+} + O_2$	$ThO^{2+} + O$	0.56 ^c	$Pu^{2+} + O_2$	$PuO^{2+} + O$	<0.001 ^c
$Pa^{2+} + O_2$	$PaO^{2+} + O$	0.55 ^d	$Am^{2+} + O_2$	$AmO^{2+} + O$	<0.001 ^c
$U^{2+} + O_2$	$UO^{2+} + O$	1; ^e 1.6; ^f 0.53 ^c	$Cm^{2+} + O_2$	$CmO^{2+} + O$	<0.001 ^c
$Np^{2+} + O_2$	$NpO^{2+} + O$	0.48 ^c			
$U^{2+} + H_2O$	$UO^{2+} + OH$	0.22 ^f			
$Th^{2+} + N_2O$	$ThO^{2+} + N_2$ (45%)	0.41 ^c	$U^{2+} + N_2O$	$UO^{2+} + N_2$ (55%)	0.40 ^c
	$ThN^{+} + NO^{+}$ (55%)			$UN^{+} + NO^{+}$ (45%)	
$Pa^{2+} + N_2O$	$PaO^{2+} + N_2$ (60%)	0.40 ^d	$Np^{2+} + N_2O$	$NpO^{2+} + N_2$	0.25 ^c
	$PaN^{+} + NO^{+}$ (40%)		$Pu^{2+} + N_2O$	$PuO^{2+} + N_2$	0.17
			$Cm^{2+} + N_2O$	$CmO^{2+} + N_2$	0.22 ^{g,c}
$Am^{2+} + C_2H_4O$	$AmO^{2+} + C_2H_4$	0.01 ^c			
$ThO^{2+} + O_2$	$(ThO_2^{2+} + O)$	<0.001 ^c	$NpO^{2+} + O_2$	$NpO_2^{2+} + O$	0.01 ^c
$UO^{2+} + O_2$	$UO_2^{2+} + O$	0.04; ^e 0.03; ^f 0.03 ^c	$PuO^{2+} + O_2$	$(PuO_2^{2+} + O)$	<0.001 ^c
$ThO^{2+} + N_2O$	$(ThO_2^{2+} + N_2)$	<0.001 ^c	$NpO^{2+} + N_2O$	$NpO_2^{2+} + N_2$	0.28 ^c
$PaO^{2+} + N_2O$	$PaO_2^{2+} + N_2$	0.34 ^d	$PuO^{2+} + N_2O$	$PuO_2^{2+} + N_2$	0.19 ^c
$UO^{2+} + N_2O$	$UO_2^{2+} + N_2$	0.31 ^c			

^aWhere more than one product is given the percentages in parentheses are relative branching ratios. Products in parentheses were not observed under thermal conditions.

^bReaction efficiencies, k/k_{COL} , are pseudo-first order rate constants k relative to the collisional rate constant, k_{COL} . Values of k/k_{COL} greater than unity indicate uncertainties in the experimental rate constant k , and/or calculated k_{COL} . Where a value for k/k_{COL} is not provided either k was not measured or the reaction is endothermic and does not proceed spontaneously.

^c(Gibson et al., 2005)

^d(Santos et al., 2006b)

^e(Cornehl et al., 1996a)

^f(Jackson et al., 2002c, 2004b)

^g(Gibson et al., 2008).

between the ionization energies of the neutral and dipositive ion increase such that they can be employed to estimate the ionization energies of UO_2^+ and other monovalent cations. In later work, the other prevalent condensed-phase dipositive actinyl ions, NpO_2^{2+} and PuO_2^{2+} , were similarly synthesized by the oxidation of Np^{2+} and Pu^{2+} (Gibson et al., 2005). Although the dipositive protactinyl ion, PaO_2^{2+} , is not known to exist in condensed phase, it was produced in gas phase by the rather efficient oxidation of PaO^{2+} using N_2O (Santos et al., 2006b); this is one of many examples of exotic actinide chemistry that is accessible in the gas phase but not in condensed phases. The instability of PaO_2^{2+} in condensed phase reflects the instability of oxidation states above closed-shell Pa(V); it should not be supposed that hexavalent protactinium is present in PaO_2^{2+} . Inherently stable isolated species such as PaO_2^{2+} can be very reactive and thus prepared only under rarified gas-phase conditions where interactions with reactants are excluded. The PaO_2^{2+} ion is one of several metal oxide ions that fulfill the thermodynamic and kinetic requirements for catalyzing the gas-phase oxidation of CO to CO_2 by N_2O according to Eqs. (5) and (6), a process that was experimentally demonstrated:



The thermodynamic requirement for this O-atom transfer from N_2O to CO is $D(\text{N}_2 - \text{O}) < D(\text{OPa}^{2+} - \text{O}) < D(\text{OC} - \text{O})$. Both constituent reactions are fairly efficient—that is, $>10\%$ —but the catalytic cycle is quenched by electron transfer to PaO_2^{2+} from both N_2O and CO to produce PaO_2^+ , which is a thermodynamically reticent O-atom donor. Americyl, AmO_2^{2+} , is a known albeit uncommon condensed-phase species, but is much more challenging to synthesize than the preceding actinyl ions. It has been predicted that bare AmO_2^{2+} should be minimally stable in the gas phase, but its synthesis has not been reported (Gibson et al., 2005).

Studies of actinide nitride and sulfide ions are more limited than for the oxides. Johnsen and Biondi (1972) reported that the reaction of U^+ with N_2 did not exothermically produce UN^+ . Subsequently, Armentrout et al. (1977a) examined the endothermic reaction of U^+ with N_2 to produce UN^+ and determined that $D_0(\text{U}^+ - \text{N}) = 454 \pm 19 \text{ kJ mol}^{-1}$. The ThN^+ , PaN^+ , and UN^+ ions are produced by direct reaction of An^+ ions with N_2O (Cornehl et al., 1997a; Santos et al., 2002, 2006b) or by charge-reduction reactions of the dipositive An^{2+} ions with N_2O (Cornehl et al., 1996a; Gibson et al., 2005; Santos et al., 2006b). Armentrout and Beauchamp reported the exothermic synthesis of US^+ by the reaction of U^+ with COS and USO^+ by the reaction of UO^+ with COS (Armentrout and Beauchamp, 1980). More recently, the series of diatomic AnS^+ molecular ions, for $\text{An} = \text{Th}$ through Cm, was synthesized by

exothermic reactions of An^+ with COS or CS_2 (Pereira et al., 2011). Reactions of AnO^+ with COS produced $ThOS^+$, $PaOS^+$, and UOS^+ ; the result that $AnOS^+$ were not produced for $An = Np, Pu, Am, \text{ or } Cm$ indicates weaker $OAn^+ - S$ bonds beyond uranium.

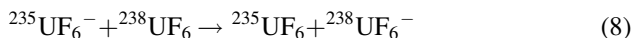
Largely due to the importance of volatile UF_6 and other actinide halides in nuclear processing, there have been several studies of gas-phase reactions of actinide ions with halogenated molecules. Reactions of U^+ with CH_3F , SiF_4 , CH_3Cl , and CCl_4 resulted in the formation of UF^+ , UF_2^+ , UCl^+ , and UCl_2^+ ; the collisional energy dependence of these reactions provided bond energies (Armentrout and Beauchamp, 1981). A study of the reactions of U^+ and UF^+ with SF_6 under thermal conditions revealed exothermic transfer of up to three F atoms in single ion/molecule reactions to produce the UF_n^+ ions for $n = 1-4$ (Jackson et al., 2004a); the ability to readily oxidize uranium is apparent from these results. In contrast, UF_2^+ and UF_3^+ were inert toward SF_6 , which is not attributed to endothermicity of F-atom abstraction by UF_2^+ and UF_3^+ , but rather to a repulsive barrier for the fluorinated uranium center to approach SF_6 and abstract an additional F atom. The reaction of Pa^+ with SF_6 resulted in facile fluorination to PaF_4^+ in which Pa is in its highest oxidation state under normal conditions (Gibson and Haire, 2002). Reaction with hexafluoropropene oxidized Bk^+ to BkF_2^+ (Gibson and Haire, 2001b), but Es^+ only to EsF^+ , reflecting the greater stability of the divalent oxidation state of Es (Gibson and Haire, 2003). The UF_5^+ ion comprising hexavalent uranium was produced by the exothermic reaction of UF^+ and UF_6 to give UF_2 and UF_5^+ by an unusual F^- -transfer process (Beauchamp, 1976b). Noble gas cations, He^+ , Ne^+ , Ar^+ , and Kr^+ , react with neutral UF_6 to exothermically abstract an electron to produce $UF_n^+ + nF$ ($n = 3 - 5$) (Streit and Babcock, 1987). It was possible by this approach to produce appreciable UF_6^+ , which is a low-stability species with a weak $F_5U^+ - F$ bond, only by the interaction of UF_6 with excited-state $Ne(^3P_2)$. In the same work, the first heteroligand uranium ion, UOF_3^+ , was produced by the reaction of UF_6 with H_2O^+ (Streit and Babcock, 1987). McAskill reported the formation of $U_2F_{11}^+$ and $U_2F_{10}^+$ by the association reactions of UF_6 with UF_5^+ and UF_4^+ , respectively, and of $U_3F_{16}^+$ by the association of UF_6 with $U_2F_{10}^+$ (McAskill, 1975).

The relatively high electron affinity of UF_6 (Beauchamp, 1976a), ~ 5 eV, has motivated studies of various uranium fluoride anions. Beauchamp produced UF_6^- by surface ionization on a rhenium filament and studied its reactions with neutral UF_6 as a function of collision energy from 0 to 35 eV (Beauchamp, 1976a). It was determined that Eq. (7) occurs with an endothermicity of 2.7 ± 0.2 eV:



Reaction (7) also occurred with internally excited UF_6^- ions produced by electron attachment to neutral UF_6 (Beauchamp, 1976b). The fluoride dissociation energy for UF_7^- , $D(UF_6 - F^-) = 192 \pm 42$ kJ mol $^{-1}$, is rather large albeit

much less than $D(\text{UF}_5 - \text{F}^-) = 452 \pm 25 \text{ kJ mol}^{-1}$. The UF_7^- molecular anion is quite stable considering the requirement for seven fluoride ligands in such close proximity around the uranium metal center. It was also shown that the electron transfer reaction given by Eq. (8) is not barrierless and thus does not spontaneously proceed:



Compton studied the formation of both positive and negative ions by electron ionization and electron attachment in UF_6 (Compton, 1977). The cross section for the electron ionization of UF_6 from the threshold electron energy, $\sim 14 \text{ eV}$, to 1 keV exhibited a maximum of $\sim 18 \text{ \AA}^2$ at $\sim 160 \text{ eV}$. Reactions of UF_6 with electrons and alkali metal atoms to produce uranium fluoride anions confirmed the high electron affinity of UF_6 and demonstrated that $D(\text{UF}_5^- - \text{F})$ and $D(\text{UF}_5 - \text{F}^-)$ are similar, to within $\sim 1 \text{ eV}$, but are both $\sim 2 \text{ eV}$ greater than $D(\text{UF}_5 - \text{F})$. That the U—F bonds are stronger in UF_6^- than in UF_6 reflects the large electron affinity of UF_6 . Streit and Newton reported that exothermic electron transfer from halide anions and SF_6^- to UF_6 occurs close to the collisional rate (Streit and Newton, 1980), a result that renders particularly intriguing the nonoccurrence of thermoneutral Eq. 8 due to an unanticipated barrier.

Bonds between the highly nucleophilic actinides and electrophilic fluorine are particularly strong; the degree of fluorination of different actinide ions provides a means to evaluate the comparative stabilities of actinide oxidation states. Abstraction of F atoms from perfluorinated hydrocarbons such as $\text{C}_{14}\text{F}_{24}$ by An^+ and AnO^+ ions ($\text{An} = \text{Th}, \text{U}, \text{Np}, \text{Pu}, \text{Am}$) resulted in a series of AnF_n^+ and AnOF_n^+ ions (Gibson, 1999b). As an example of fluorination revealing relative oxidation state stabilities, the oxidation of Am terminated at $\text{Am}^{\text{III}}\text{F}_2^+$, whereas both $\text{Np}^{\text{IV}}\text{F}_3^+$ and $\text{Np}^{\text{V}}\text{OF}_2^+$ were produced. In contrast to polyoxides in which there may be O—O bonding, the metal oxidation states can be confidently assigned in simple actinide fluoride species such as these.

In contrast to methane, the Si—H and Ge—H bonds of silane and germane are relatively fragile. Despite that the combustion of CH_4 is highly exothermic, it is inert at room temperature, whereas SiH_4 spontaneously ignites in air to produce SiO_2 and H_2O . In accord with the relatively precarious nature of SiH_4 , it is readily activated by actinide ions toward which CH_4 is inert. The U^+ , Np^+ , and Pu^+ ions each dehydrogenate SiH_4 to produce the respective AnSiH_2^+ ions (Gibson, 2002a). Germane exhibited a similar reactivity as silane; an exceptional result was the complete dehydrogenation of three and four GeH_4 molecules by Th^+ to produce ThGe_3^+ and ThGe_4^+ , the structures of which are indeterminate.

Whereas most oxidation studies have focused on O-atom donation to bare or ligated actinide ions, the oxidation of U(V) to U(VI) by the association of

molecular O₂ to gas-phase uranyl coordination complexes has recently been observed. Groenewold et al.(2006a) reported the addition of O₂ to [UO₂(L)_{2,3}]⁺ complexes to produce the adducts [UO₂(L)_{2,3}(O₂)]⁺, where L is acetone and/or water. Such molecular oxygen addition was not observed for hexavalent uranyl complexes, [UO₂(OH)(L)_n]⁺. It was inferred that the addition of O₂ to uranyl(V) complexes results in superoxo complexes in which the uranium metal center is oxidized to U(VI), a conclusion that was later substantiated by computations that showed these to be side-on η²-O₂ superoxo complexes, as shown in Fig. 6 (Bryantsev et al., 2008; Leavitt et al., 2009). It was subsequently found that the dimethyl sulfoxide (DMSO) ligand coordinated to uranyl(V) enhances oxidation to uranyl(VI) by the addition of O₂, an effect attributed to the greater electron density at the uranium metal center due to charge donation from more basic DMSO (Leavitt et al., 2009). In a comparative study of the actinyl(V) ions, it was found that [UO₂(H₂O)₂]⁺ inefficiently adds O₂, whereas the O₂ addition reaction is much more efficient for [UO₂(H₂O)₃]⁺, consistent with oxidation from uranyl(V) to uranyl(VI) being favored by an additional electron-donating ligand (Rios et al., 2012a). In contrast to uranyl(V), the corresponding neptunyl(V) and plutonyl(V) complexes did not add O₂ under the same experimental conditions. Density functional theory (DFT) confirmed that superoxo formation is exothermic for uranyl but not neptunyl, a result that can be attributed to the greater reduction potential for neptunyl(VI) as compared to uranyl(VI).

2.2 Reactions with Small Hydrocarbons

2.2.1 Rare Earths

Rare earth metal monocations did not react with methane under the thermal, low-pressure conditions of FTICR-MS: Sc⁺, Y⁺, and La⁺ (Huang et al., 1987) and La⁺–Lu⁺ (Cornehl et al., 1995). In an ion beam instrument at low energy, Sc⁺ (Schilling and Beauchamp, 1988; Tolbert and Beauchamp, 1984) and Gd⁺ (Schilling and Beauchamp, 1988) were also unreactive. Under the multicollision conditions of a fast flow reactor at 0.75 Torr of He buffer gas, Weisshaar and coworkers (Tonkyn et al., 1988) observed clustering reactions of Sc⁺, to form Sc(CH₄)_n⁺ ions (n=1–3). In the SIFT apparatus of Bohme and coworkers (Shayesteh et al., 2009), at room temperature in a helium bath gas at 0.35 Torr, methane adducts R(CH₄)⁺ were identified as primary products for Sc⁺, Y⁺, La⁺, Ce⁺, and Gd⁺; the remaining lanthanide ions were unreactive under these conditions. Using GIB-MS, where the translational energy of the reactant metal ions is varied, Sunderlin and Armentrout (1989) observed the endothermic formation of RCH₂⁺ at low energy, and RCH₃⁺ and RH⁺ at higher energies, for Sc⁺, Y⁺, La⁺, and Lu⁺, as illustrated in Fig. 7 for the case of La⁺; the R⁺–CH₂ and R⁺–CH₃ bond energies were determined in this study.

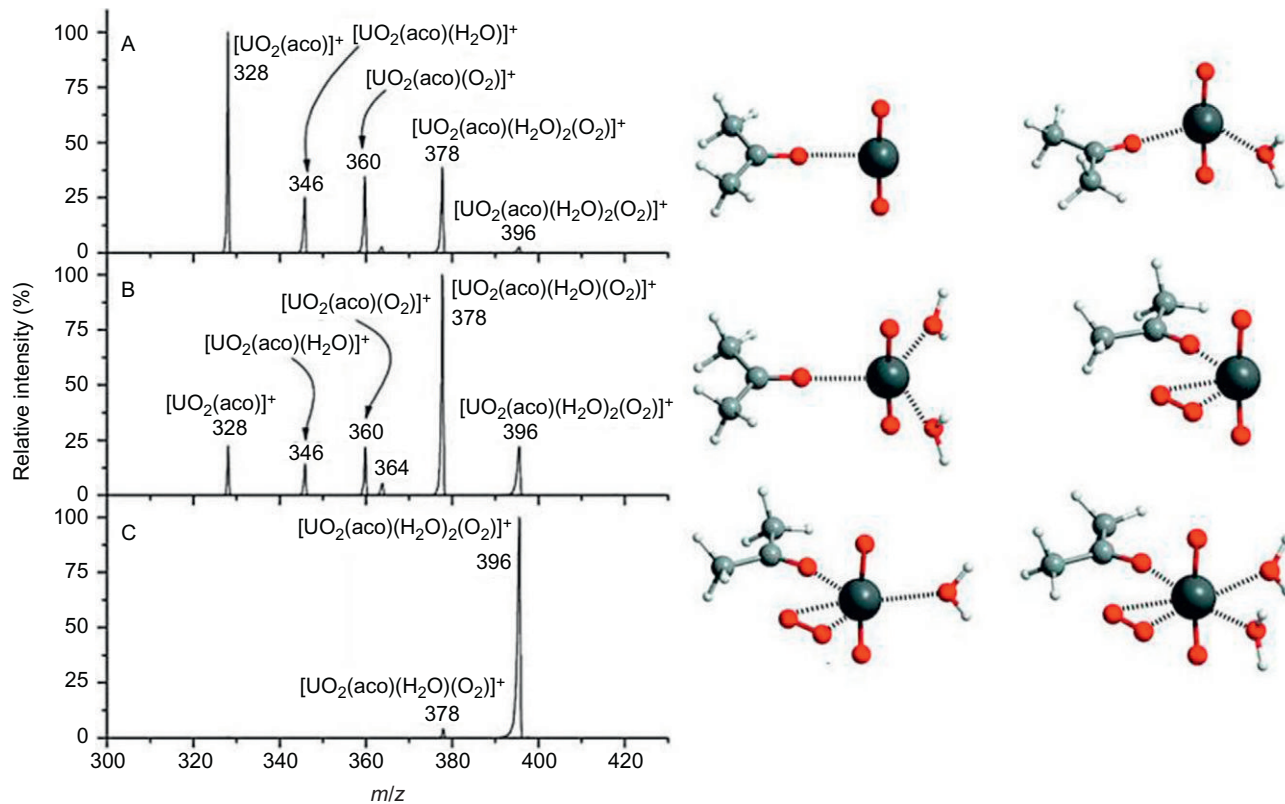


FIGURE 6 Mass spectra of isolated $[\text{UO}_2(\text{aco})]^+$ reacting in a mixed atmosphere containing H_2O and O_2 for (a) 10 ms, (b) 100 ms, and (c) 1000 ms and the computed structures of the key species; aco is acetone. *Reproduced with permission from Leavitt et al. (2009). Copyright 2009 American Chemical Society.*

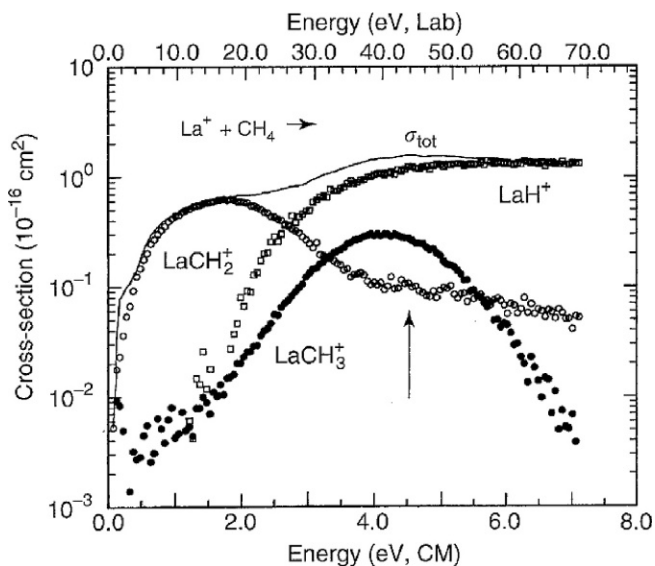


FIGURE 7 Variation of product cross sections with translational energy for the reaction of La^+ with CH_4 ; the arrow indicates $D_0(\text{H}-\text{CH}_3)$ at 4.54 eV. Reproduced with permission from *Sunderlin and Armentrout (1989)*. Copyright 1989 American Chemical Society.

The overall reactivity picture changes when moving from methane to ethane, as activation becomes exothermic for some rare earth cations. Single dehydrogenation and double dehydrogenation of ethane by Sc^+ ions, to form ScC_2H_4^+ and ScC_2H_2^+ , respectively, were observed in most of the experimental setups mentioned above for the case of methane (*Huang et al., 1987; Sunderlin and Armentrout, 1989; Sunderlin et al., 1987; Tonkyn and Weisshaar, 1986; Tonkyn et al., 1988*). Single dehydrogenation and double dehydrogenation were also observed in the case of Y^+ and La^+ in GIB experiments (*Sunderlin and Armentrout, 1989*), but only single dehydrogenation by FTICR-MS (*Huang et al., 1987*). Gd^+ also induced single elimination and double elimination of dihydrogen in low-energy ion beam experiments (*Schilling and Beauchamp, 1988*). *Cornehl et al. (1995)* studied all the lanthanide cations by FTICR-MS and observed only very inefficient single dehydrogenation for La^+ and Ce^+ .

Several other alkanes and alkenes, linear, branched, and cyclic, were examined with the different techniques mentioned above: Sc^+ (*Huang et al., 1987; Lech and Freiser, 1988; Seemeyer et al., 1995; Sunderlin and Armentrout, 1990; Tolbert and Beauchamp, 1984; Tonkyn et al., 1988*), Y^+ (*Huang et al., 1987*), and La^+ – Lu^+ (*Cornehl et al., 1995; Heinemann et al., 1994; Huang et al., 1987; Schilling and Beauchamp, 1988*). For alkanes larger than ethane, increased reactivity was observed, which included also the activation of C–C bonds as indicated by the elimination of methane or other small hydrocarbons. Alkenes were also generally more reactive than alkanes, which

was interpreted as a result of an enhanced interaction of the alkene π -system with the metal ion. The reactions of several Ln^+ ions with alkenes, with emphasis on cycloalkenes, were also investigated by Gibson and Haire using the LAPRD technique, in part for comparison with transuranium An^+ ions (Gibson, 1996a, 1997b, 1998b,c,d; Gibson and Haire, 1998, 2000, 2001b).

The structures of several primary product ions were probed by CID experiments, and their reactivity with hydrocarbons was also studied, profiting from the multistage capabilities of FTICR-MS (Cornehl et al., 1995; Heinemann et al., 1994; Huang et al., 1987; Lech and Freiser, 1988). A feature of the reactivity of rare earth metal ions with linear and branched alkanes larger than C_3 was the formation of metal-dialkyl ions, such as $\text{CH}_3\text{-R}^+\text{-CH}_3$, identified on the basis of deuterium labeling and CID experiments in some of the cited studies. These observations prompted further studies, using FTICR-MS, where the reactivity of $\text{Sc}(\text{CH}_3)_2^+$ and $\text{Sc}(\text{CH}_3)(\text{CH}_2\text{CH}_3)^+$ ions with alkanes and alkenes was examined and the σ -bond metathesis mechanism, considered to be prevalent for these ligated d^0 metal ions, was interrogated (Crellin et al., 1994, 1995, 1996; Huang et al., 1992). Similar studies were performed with the YCH_3^+ ion (Huang et al., 1991a), the YNH^+ ion (Ranatunga et al., 1996), and MCHCN^+ ions where $\text{M}=\text{Sc}$ and Y (Wilson et al., 1993).

Schilling and Beauchamp (1988), in their study of Pr^+ , Eu^+ , and Gd^+ , presented the first experimental evidence for the relevance of the electron configuration of the lanthanide cations in enabling the effective activation of C—H and/or C—C bonds of hydrocarbons (see Table 1 and Fig. 1). The accessibility of configurations with two non-f valence electrons was proposed as a requirement and confirmed by the observation of a much higher reactivity of Gd^+ compared with Pr^+ and by the nonreactivity of Eu^+ . Cornehl et al. (1995) extended these studies to all the lanthanide cations and confirmed the model showing that the reactivity along the series increased for substrates in which the energy demand for bond activation was lower. Figure 8 features a plot that summarizes the relative reactivity of the Ln^+ ions as a function of the electronic PEs from the GSs to the lowest-lying states with $4f^n5d^16s^1$ configurations; the relative reactivity was defined as the sum of the relative reaction rates of the Ln^+ cations with propane, butane, cyclohexane, propene, 1-butene, and 1,4-cyclohexadiene, normalized to the reactivity of La^+ , the most reactive Ln^+ ion.

The effect of simple oxo ligation of rare earth cations on their reactivities with hydrocarbons was also examined in detail by Schwarz and coworkers using FTICR-MS (Cornehl et al., 1997b). While only the more reactive lanthanide cations (La^+ , Ce^+ , Pr^+ , Gd^+ , Tb^+ , and Lu^+) were able to activate buta-1,3-diene, the corresponding LnO^+ became inert. In contrast, the monoxides of the unreactive metal cations Eu^+ , Dy^+ , Ho^+ , Er^+ , Tm^+ , and Yb^+ either transferred an oxygen atom to the substrate (Eu^+ and Yb^+) or activated butadiene with the loss of acetylene and other products. Based on a correlation of the reaction rates with the ionization energies of the LnO molecules,

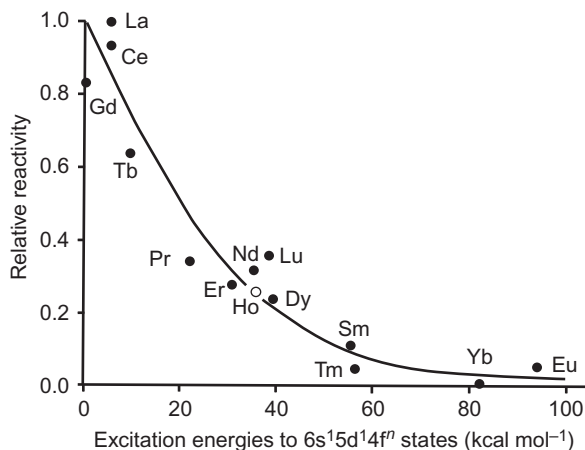


FIGURE 8 Relative reactivity of Ln^+ cations with hydrocarbons as a function of the promotion energy from the ground state to the lowest-lying state with a $4f^n 5d^1 6s^1$ configuration. *Reproduced with permission from Cornehl et al. (1995). Copyright 1995 American Chemical Society.*

the authors proposed a mechanism for the initial activation step in which, following an electrophilic attack of LnO^+ on the π -system of the diene, a cationic metallaoxa cyclohexene is formed as the key intermediate; the mechanism was further tested and validated by studying reactions of LnO^+ with isoprene and of Ln^+ with dihydrofuran and tetrahydrofuran (THF).

The reactivity of the early lanthanide oxide cations CeO^+ (Heinemann et al., 1996) and NdO^+ (Cornehl et al., 1997a) was also examined with several alkanes and alkenes, but no reactions were observed by FTICR-MS. On the contrary, CeO_2^+ was quite reactive with linear and branched alkanes by C—H bond activation and with simple alkenes and aromatic compounds by both oxygen-atom transfer and C—H bond activation (Heinemann et al., 1996); the high reactivity was ascribed to the radical nature of the CeO_2^+ ion, which has one unpaired electron based on theoretical calculations. CeO_2^+ was also observed to mediate the catalytic oxidation of ethene in the presence of NO_2 , as illustrated in Fig. 9.

The reactivity of doubly charged rare earth cations with small hydrocarbons was also investigated by FTICR-MS. In early studies, Freiser and coworkers examined reactions of Sc^{2+} and Y^{2+} (Hill et al., 1997), as well as La^{2+} (Ranasinghe et al., 1992), with linear C_1 – C_6 alkanes; combinations of electron transfer, hydride transfer, carbanion transfer, dehydrogenation, and alkane-loss products were observed. None of the metal ions reacted with methane, and La^{2+} was also unreactive with ethane. Since the metal dications have only one valence electron, oxidative addition to form two covalent bonds to the metal center is not possible, and alternative multicentered mechanisms were proposed. Another interesting aspect of these studies was the observation

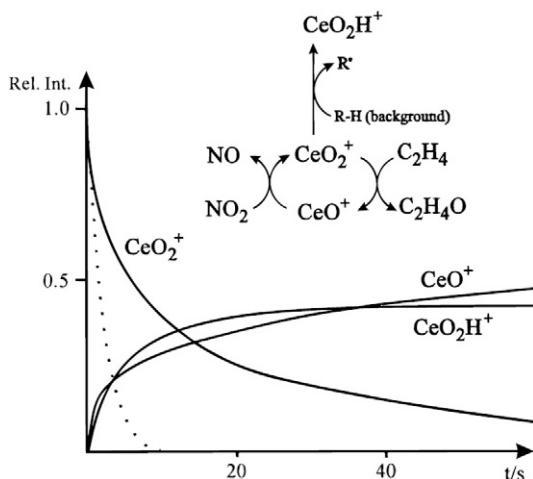


FIGURE 9 Reaction scheme and time dependency of the relative ion intensities in the catalytic oxidation of ethene by CeO_2^+ , in the presence of NO_2 ; the dotted line shows the decay of the CeO_2^+ signal for the noncatalytic reaction. Reproduced with permission from *Heinemann et al. (1996)*. Copyright 1996 American Chemical Society.

that C_n alkanes displaced C_{n-1} alkenes in $\text{Y}(\text{alkene})^{2+}$ ions due to the greater polarizability, indicating an electrostatic bonding character in $\text{Y}(\text{alkene})^{2+}$ complexes that was corroborated by theoretical calculations (*Hill et al., 1991, 1997*). More recently, *Marçalo et al. (2008)* surveyed the reactivity of all the lanthanide series dications, La^{2+} – Lu^{2+} , with linear alkanes (C_1 – C_4) and alkenes (C_2 – C_4), confirming and extending the previous work. The only lanthanide cations that were capable of activating hydrocarbons to form doubly charged organometallic ions were La^{2+} , Ce^{2+} , Gd^{2+} , and Tb^{2+} , which have GS or low-lying $5d^1$ electronic configurations; Lu^{2+} , with an accessible $5d^1$ electronic configuration but a high electron affinity, reacted only through charge-transfer channels, while the remaining Ln^{2+} ions reacted via charge-transfer channels or adduct formation (a summary of the observed reactivities is presented in *Fig. 10*; see *Table 1* for the GS and low-lying electronic configurations of the Ln^{2+} ions).

2.2.2 Actinides

The U^+ ion was shown to endothermically react with CD_4 to produce UD^+ (*Armentrout et al., 1977a,b*). Most subsequent studies of reactions of actinide ions with hydrocarbons have focused on exothermic reactions under thermal conditions since under these conditions intrinsic actinide reactivities and the roles of electronic structures are revealed. *Heinemann et al. (1995a)* reported reactions of U^+ with several small hydrocarbons, finding that U^+ is essentially inert toward CH_4 but becomes increasingly reactive toward larger

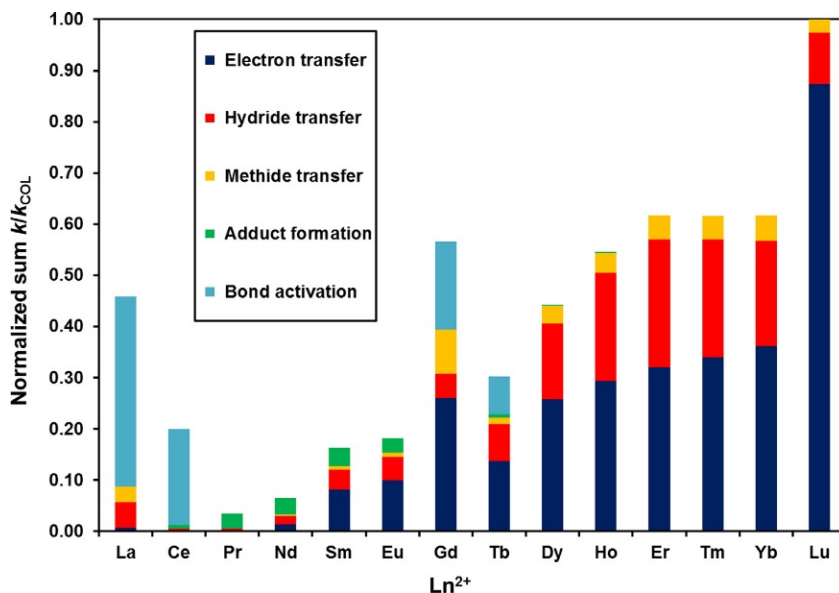
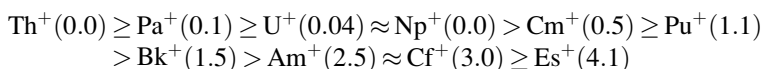


FIGURE 10 Chart showing the normalized sum of the fractions of the k/k_{COL} values corresponding to the five different types of reaction channels of Ln^{2+} ions for all studied hydrocarbons; the normalization was relative to Lu^{2+} that had the greatest sum of reaction efficiencies. The chart was prepared from the data in [Marçalo et al. \(2008\)](#).

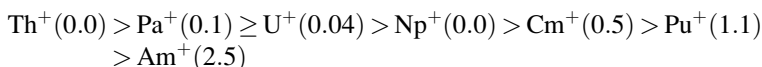
alkanes and alkenes. The U^+ ion reacts at $\sim 20\%$ of the collisional rate with butane, inducing single dehydrogenation and double dehydrogenation, as well as C—C bond activation. A particularly intriguing observation was the sequential dehydrogenation of three ethylene molecules to produce a U^+ -benzene complex ([Heinemann et al., 1995a](#)). Shortly thereafter, [Marçalo et al. \(1996a\)](#) studied the activation of alkanes and alkenes by Th^+ . As for U^+ , the Th^+ ion was found to activate small hydrocarbons with increasing efficiency as the number of carbon atoms increase. A particularly notable result was the finding that Th^+ is more reactive than U^+ ; even CH_4 was activated by Th^+ to produce ThCH_2^+ , albeit at only 2% efficiency. This was the first demonstration of a difference in gas-phase organometallic chemistry between actinides and set the stage for subsequent systematic studies of reactivity across the series.

Based on the results for Th^+ and U^+ , and the known GS and low-lying electronic configurations of the An^+ ions, [Marçalo et al. \(1996a\)](#) predicted trends in actinide ion reactivity that would later be experimentally substantiated. In the first of a series of studies of comparative actinide ion reactivities, the expectation that Pu^+ would exhibit a reduced reactivity in comparison with U^+ was confirmed ([Gibson, 1998d](#)). Comparative propensities for hydrocarbon activation by bare An^+ ions from Th^+ to Es^+ established the following

ordering of reactivities (Gibson, 1998b,d; Gibson and Haire, 1998, 2000, 2001b, 2002, 2003; Gibson and Marçalo, 2006; Santos et al., 2002):



The numbers in parentheses are the PEs (in eV) to the $[\text{Rn}]5f^{n-2}6d^17s^1$ electronic configurations (Table 2), as discussed below. For the actinide ions Th^+ through Cm^+ , these qualitative comparisons of the activation of small hydrocarbon molecules by monpositive actinide ions were largely substantiated by measured reaction rate constants and derived reaction efficiencies, as seen from the representative values in Table 7 (Gibson et al., 2007). From the results in Table 7, the similar trends noted above for the lanthanides of greater reactivity as the size and polarizability of the hydrocarbon increase, as well as greater reactivities of alkenes versus alkanes, are apparent. These quantitative studies provide the following refined reactivity ordering for the first seven actinide ions:



If the 5f electrons do not participate in C—H or C—C bond activation, then it follows that two non-5f valence electrons are necessary to enable

TABLE 7 Reaction Efficiencies, k/k_{COL} , for Monpositive Actinide Ions with Alkanes and Alkenes^a

M ⁺	CH ₄	C ₂ H ₆	C ₃ H ₈	<i>n</i> -C ₄ H ₁₀	C ₂ H ₄	C ₃ H ₆	1-C ₄ H ₈
Th ⁺	0.01	0.12	0.18	0.18	0.34	0.30	0.30
Pa ⁺	<0.001	<0.001	0.05	0.10	0.27	0.25	0.39
U ⁺	<0.001	<0.001	0.01	0.08	0.23	0.25	0.29
Np ⁺	<0.001	<0.001	<0.001	0.01	0.10	0.28	0.27
Cm ⁺	<0.001	<0.001	<0.001	<0.001	<0.001	0.02	0.20
Pu ⁺	<0.001	<0.001	<0.001	<0.001	<0.001	<0.001	0.16
Am ⁺	<0.001	<0.001	<0.001	<0.001	<0.001	<0.001	<0.001
Ta ⁺	0.07	0.31	0.28	0.22	0.26	0.29	0.34

^aValues from Gibson et al. (2007) are k/k_{COL} where k is the measured pseudo-first-order rate constant and k_{COL} is the collisional rate constant. Efficiencies for Ta⁺ (Gibson, Marçalo, et al., unpublished) are included for comparison of the An⁺ with a reactive d-block transition metal. C—H activation and H₂ elimination are dominant; some C—C activation occurs for *n*-C₄H₁₀, C₃H₆, and 1-C₄H₈.

insertion and formation of two covalent bonds in the C–An⁺–H or C–An⁺–C activated intermediate. The ground and low-lying electronic states for the An⁺ ions are given in Table 2. The ions Np⁺ and Cm⁺ both have [Rn] 5f^{*n*–2}7s² GS configurations; the observation that the reactivity of Cm⁺ is significantly lower than that of Np⁺ suggests that the reactive configuration is not [Rn]5f^{*n*–2}7s², but is rather [Rn]5f^{*n*–2}6d¹7s¹ in which the two non-5f valence electrons are unpaired and thus available to form two covalent bonds (Gibson, 2003). It is these PEs to the [Rn]5f^{*n*–2}6d¹7s¹ ([Rn]5f^{*n*–2}6d²7s¹ for Th⁺) that are specified in parentheses in the above comparisons of An⁺ ion reactivities. The PE for Cm⁺ of 0.5 eV thus explains its lower reactivity as compared with Np⁺. The reactivity trend is seen to generally relate to the PEs from the GS An⁺ configurations to the [Rn]5f^{*n*–2}6d¹7s¹ configuration, with a good correlation from Np⁺ to Am⁺. However, for Th⁺, Pa⁺, U⁺, and Np⁺, the PEs are all 0.1 eV or less, yet the reactivities decrease across this region of the actinide ion series. The particularly high reactivity of Th⁺ can be attributed to its quartet [Rn]6d²7s¹ GS configuration in which there are three valence electrons available to participate in bond activation; the even higher reactivity of Ta⁺ (Table 7) can similarly be attributed to its quintet [Xe]5d³7s¹ GS. The decrease in reactivity from Pa⁺ to Np⁺ may indicate some participation of the 5f electrons in bond activation for the early members of the series, in which participation decreases across the An⁺ series. This interpretation is supported by the anomalously high reactivity of PaO⁺, as discussed below. Given that the PE for Ac⁺, 0.59 eV, is similar to that of Cm⁺, 0.50 eV, similar reactivities would be predicted for these two ions; the challenging experiments with very scarce and highly radioactive ²²⁷Ac have yet to be performed.

Reactions of doubly charged actinide cations, An²⁺, with hydrocarbons provide a means to further explore the relationships between actinide electronic configurations and organometallic bond activation. The reactions of Th²⁺ and U²⁺ with methane, ethane, and propane were studied experimentally and by DFT in an effort to provide a firm theoretical basis for the semi-empirical interpretation that two non-5f valence electrons are needed for effective hydrocarbon activation by actinide cation insertion into a C–H or C–C bond (Di Santo et al., 2011). Both Th²⁺ and U²⁺ were found to activate C₂H₆ and C₃H₈ with comparable efficiencies; in contrast, Th²⁺ activates CH₄, whereas U²⁺ does not. The computed potential energy profiles for the reactions of Th²⁺ and U²⁺ with methane are shown in Fig. 11. Based on the very small PE of 0.01 eV to the reactive Th²⁺ [Rn]6d² configuration and the large PE of 2.4 eV to the U²⁺ [Rn]5f²6d² configuration, a substantially greater activation efficiency of Th²⁺ versus U²⁺ is anticipated, as is observed with the CH₄ reaction substrate. The result that U²⁺ dehydrogenates ethane and propane is attributed to a general lowering of the entire potential energy surface as the size of the alkane substrate increases; for example, dehydrogenation by U²⁺ is computed to be endothermic for CH₄ by ~100 kJ mol^{–1}, but

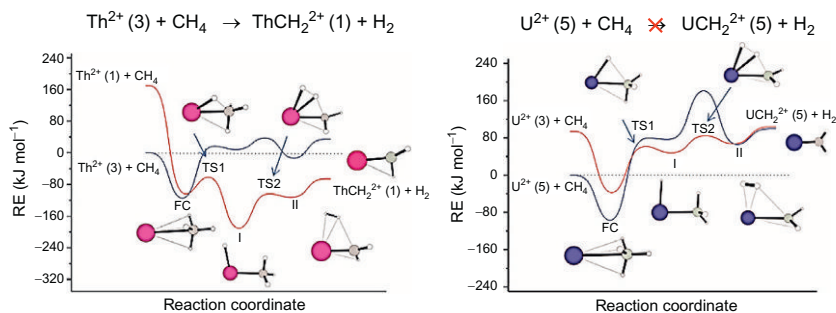
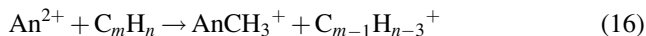
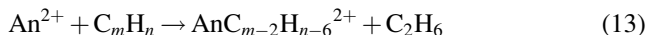
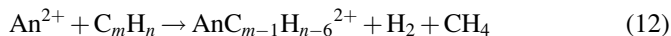
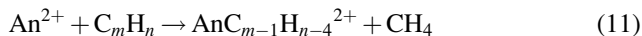
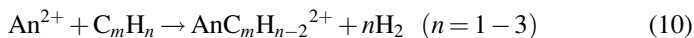
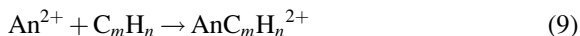


FIGURE 11 Computed potential energy profiles for the reactions of Th^{2+} and U^{2+} with CH_4 . The experimental observation that Th^{2+} activates CH_4 whereas U^{2+} does not is consistent with these profiles. *Reproduced with permission from Di Santo et al. (2011). Copyright 2011 American Chemical Society.*

exothermic for C_2H_6 and C_3H_8 by ~ 30 and ~ 60 kJ mol^{-1} , respectively. The computed energies for the insertion of Th^{2+} into C—H and C—C bonds are 2.2 ± 0.3 eV lower than those for the insertion of U^{2+} . This value is in good agreement with the 2.4 eV difference between PEs to the $[\text{Rn}]6d^2$ (for Th^{2+}) and $[\text{Rn}]5f^26d^2$ (for U^{2+}) reactive electronic states, providing validation of the PE model for rationalizing actinide ion reactivities.

Marçalo et al. (2011) performed a systematic study of the reactivities of the dipositive actinide ions Th^{2+} to Cm^{2+} with methane, ethane, propane, *n*-butane, ethene, propene, and 1-butene. All of the studied An^{2+} exhibited significant net reactivities with at least some of the hydrocarbons, with the observed reactions given by Eqs. (9)–(16), where (9) is adduct formation, (10)–(13) are bond activation, (14) is electron transfer, (15) is hydride transfer, and (16) is methide transfer:



The results are summarized graphically in Fig. 12. With the exceptions of CH_4 and C_2H_6 , the first ionization energies of the hydrocarbons are smaller

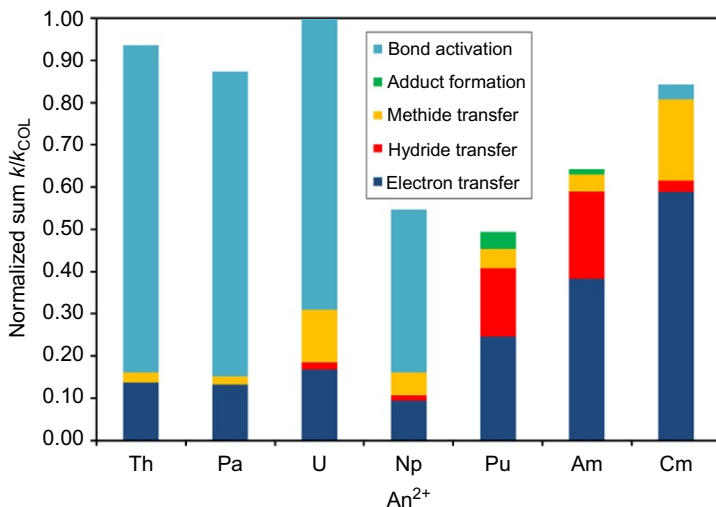


FIGURE 12 Chart showing the normalized sum of the fractions of the k/k_{COL} values corresponding to the five different types of reaction channels of An^{2+} ions for all studied hydrocarbons; the normalization was relative to U^{2+} that had the greatest sum of reaction efficiencies. Reproduced from *Marçalo et al. (2011)* with permission from the PCCP Owner Societies.

than the second ionization energies of all of the An^+ such that Eq. (14) is exothermic. Figure 12 reveals that bond activation according to Eqs. (10)–(13) is dominant for Th^{2+} to Np^{2+} , whereas charge transfer according to Eqs. (14)–(16) is dominant for Pu^{2+} , Am^{2+} , and Cm^{2+} . The results indicate that bond activation dominates for An^{2+} ions with PEs to the $[\text{Rn}]5f^{n-2}6d^2$ divalent configuration within ~ 4 eV of the GS; the reactivity decreases as the PE increases in this range, with Np^{2+} (PE ≈ 4 eV) substantially less reactive than Th^{2+} (PE ≈ 0 eV). For dipositive actinide ions with higher PEs, in the range of ~ 6 – 9 eV for Pu^{2+} , Am^{2+} , and Cm^{2+} , direct bond activation by insertion is minor and charge-transfer processes become dominant. Although the higher charge on dipositive An^{2+} ions facilitates activation by insertion for higher PEs as compared with monositive An^+ ions, the PE model for bond activation remains applicable.

The effects of oxo ligation on the reactivity of metal centers, as in AnO^+ and AnO_2^+ ions, provide further insights into the nature of activation processes and the inherent electronic structures of actinides. *Cornehl et al. (1997a)* studied the reactions of ThO^+ , ThO_2^+ , UO^+ , and UO_2^+ with several hydrocarbons. The two monoxide cations were unreactive with small alkanes, CH_4 to $n\text{-C}_4\text{H}_{10}$, and the smallest alkenes, C_2H_4 and C_3H_6 , but did activate 1- C_4H_8 (butene) and C_6H_8 (1,4-cyclohexadiene). The radical-like reactivity of ThO^+ , which abstracts a $\cdot\text{CH}_3$ radical from butene, was attributed to one unpaired 7s electron at the metal center; it was demonstrated that the

reactivities of ThO^+ and ZrO^+ are similar, suggesting that ThO^+ should be considered as a d-block transition metal oxide ion, at least in the context of hydrocarbon activation. A particularly intriguing aspect of this study was the observation that butene and cyclohexadiene are dehydrogenated upon interacting with UO^+ , in which the metal center has a $[\text{Rn}]5f^3$ configuration. The reactivity of UO^+ was attributed to the participation of the 5f electrons in bond activation; this is evidently the first demonstration of such chemical activity of 5f electrons. The UO_2^+ ion, with only one compact 5f electron, is inert, while ThO_2^+ predominantly abstracts a H atom from hydrocarbons to produce $\text{ThO}(\text{OH})^+$ in which Th is in its stable tetravalent oxidation state. A subsequent study of the reactivities of AnO^+ ions ($\text{An}=\text{Th}$ to Cm) with small alkanes and alkenes ($\text{C}_1\text{--C}_4$) revealed that most AnO^+ were inert, ThO^+ and UO^+ exhibited limited reactivity only with 1- C_4H_8 , and PaO^+ exhibited a relatively high reactivity toward all substrates except methane and ethane (Gibson et al., 2007). The high reactivity of the PaO^+ ion revealed unexpectedly facile C—H and C—C bond activation, indicating the insertion of the Pa metal center into hydrocarbon bonds. To understand the nature of the insertion process, computations showed that the electronic GS configuration is $\text{Pa}(5f^1 6d^1)\text{O}^+$ and that all excited states up to at least 1.8 eV have this configuration or $\text{Pa}(5f^1 7s^1)\text{O}^+$. The ability of a $\text{Pa}(5f^1 6d^1)$ metal center to insert into C—H and C—C bonds indicates that the 5f electron is chemically active. The substantial reactivity of PaO^+ , much lower reactivity of UO^+ , and inert nature of NpO^+ and later AnO^+ ions indicate an active role of the 5f electrons for Pa, a lesser role for U, and inert 5f character for Np and beyond; this is consistent with increasingly compact and inert 5f orbitals upon proceeding across the series.

2.3 Reactions with Other Organic Molecules

2.3.1 Rare Earths

The first systematic study of all the lanthanide monocations with the same organic molecule, 1,3,5-tri-*t*-butylbenzene, using FTICR-MS, was reported by Yin et al. (1994); Sc^+ and Y^+ were also examined in this study. The formation of bis(arene) complex ions by successive coordination of intact ligands was mainly observed for those rare earth cations, namely, Sm^+ , Eu^+ , Tm^+ , and Yb^+ , with GS to d^1s^1 PEs too high to permit facile activation of the *t*-butyl group of the arene to form product ions with the elimination of hydrogen, methane, and other neutral species. This work was extended to the study of the reactivity of the lanthanide cations with other arenes, namely, benzene, naphthalene, toluene, mesitylene, and hexamethylbenzene, but was reported only in a preliminary form (Marçalo and Pires de Matos, 2002). Again, different yields of bis(arene) ionic species were obtained depending on the PEs and also on the strength of the C—H bonds in the different arenes. Another

observation was the enhancement of the reactivity of some of the Ln^+ ions after the addition of one arene, probably due to changes in the electronic configuration of the metal ion upon bonding to the arene ligand.

In another early study by FTICR-MS, Freiser and coworkers had observed the formation of the scandium–benzyne ion ScC_6H_4^+ from the dehydrogenation of benzene by Sc^+ (Huang et al., 1991b); this product ion displayed interesting chemistry, which included an unusual hydrogenation reaction to give the Sc^+ –benzene ion and a wide variety of products in reactions with several alkanes and alkenes. The formation of YC_6H_4^+ was also detected in the reactions of Y^+ ions with small benzene clusters by a LA-molecular beam method (Higashide et al., 1990). Gibson performed several reactivity studies of Ln^+ ions with benzene by LAPRD in which LnC_6H_4^+ ions were identified for some of the more reactive Ln^+ ions, namely, Gd^+ (Gibson, 1996a) and Ce^+ (Gibson, 1997b). Dehydrogenation of benzene by the Ce^+ cation was also observed by FTICR-MS (Heinemann et al., 1996); in this study, direct comparisons with the oxide ions CeO^+ and CeO_2^+ were made, with the monoxide being utterly unreactive, while the dioxide efficiently yielded CeO^+ , presumably transferring one oxygen atom to benzene to form phenol. Another rare earth monoxide ion, ScO^+ , formed only the benzene adduct in an FTICR-MS study (Ryan et al., 1994); exchange reactions of the product with C_6D_6 without H/D scrambling indicated that benzene and oxygen were coordinated as separate, intact ligands. The same technique was later employed to examine the reactions of Sc^+ and ScO^+ with toluene (Bjarnason and Ridge, 1998); while ScO^+ formed only the adduct, dehydrogenation was the main reaction channel for Sc^+ , producing ScC_7H_6^+ for which CID and ligand exchange reactions provided evidence that the structure is Cp-Sc-CCH^+ ($\text{Cp} = \text{cyclo-C}_5\text{H}_5^-$). Gapeev and Dunbar (2002) also used FTICR-MS to investigate the association reactions of benzene to ScX_n^+ ions ($\text{X} = \text{Cl}, \text{Br}, \text{I}; n = 1, 2$), concluding that binding of the first benzene molecule was enhanced by specific chemical interactions, while binding of the second benzene molecule was more electrostatic.

The so-called superbenzene, coronene, was used as a substrate by Pozniak and Dunbar (1997) in an FTICR-MS study of the formation kinetics of monomer and dimer association complexes with Sc^+ and Y^+ , together with several other main-group and transition metal cations. The formation of coronene adducts was also observed for RO^+ and R(OH)_2^+ ions, for both Sc and Y, with rates similar to the attachment rates for the corresponding bare metal ions; the same ions were produced by the reaction of R(coronene)^+ with background oxygen/water. In a different approach, Duncan and coworkers used covaporization of Nd oxide and pyrene in a laser plasma source with time-of-flight mass spectrometry (TOF-MS) detection to produce NdO(pyrene)_n^+ ions, with $n = 1, 2$ (Ayers et al., 2004).

Halogenated arenes were also used as reagents with rare earth cations. The four phenyl halides were first examined by Bjarnason (1991) in their reactions

with the Sc^+ ion using FTICR-MS, with dehydrohalogenation to form ScC_6H_4^+ as the primary reaction channel observed; consecutive eliminations of HX to yield $\text{Sc}(\text{C}_6\text{H}_4)_n^+$ occurred, with n ranging from 2 for $\text{X}=\text{F}$ to 5 for $\text{X}=\text{I}$. Similar experiments with Sc^+ and naphthalene halides were later performed by Bjarnason (1994, 1996) with concurrent results. Cornehl et al. (1996b) used FTICR-MS to study the reactivity of all the lanthanide series cations with fluorobenzene with the objective of probing the ability of Ln^+ ions to activate the rather strong $\text{C}-\text{F}$ bonds. The formation of LnF^+ ions by F -atom abstraction was the main reaction channel along the series, but the most reactive lanthanides, La^+ , Ce^+ , Gd^+ , Tb^+ , and Lu^+ , exhibited additional $\text{C}-\text{H}$ and $\text{C}-\text{C}$ bond activation pathways, namely, dehydrohalogenation and the loss of C_2H_2 . Experimental evidence was given for a “harpoon”-like mechanism for the F -atom abstraction process; reactions of selected lanthanide cations with other fluorinated hydrocarbons, including CH_3F and C_6F_6 , were also examined in this study. The reactivity of Pr^+ had been previously investigated by the same group (Heinemann et al., 1995b); Schwarz’s group also reported the reactions of Sc^+ and Y^+ with CH_3F (Harvey et al., 1997). Several fluorinated hydrocarbons were also used by Gibson (1996c, 1999b) in LAPRD studies of the lanthanide ions.

Systematic studies by Bohme and coworkers of the reactivity of rare earth cations were performed with halogenated hydrocarbons, specifically C_6F_6 with Sc^+ , Y^+ , and La^+ (Caraiman et al., 2004); CH_3F with all the Ln^+ ions (Koyanagi et al., 2005) as well as Sc^+ , Y^+ , and La^+ (Zhao et al., 2006); and CH_3Cl with all the Ln^+ ions (Zhao et al., 2005) and Sc^+ and Y^+ (retrievable from the group’s Web page <http://www.chem.yorku.ca/profs/bohme/research/molecule/CH3Cl.html>). The results were in overall agreement with the previous studies in terms of product ions, but the “harpoon”-like abstraction mechanism was put in doubt based on the periodicity of the reaction efficiencies along the lanthanide series, which seemed to indicate that a $\text{C}-\text{X}$ bond insertion mechanism was operative.

Nitrogen-containing organic molecules have been sparingly studied. Buckner and coworkers (Wilson et al., 1993) used FTICR-MS to show that Sc^+ and Y^+ activate acetonitrile to form the presumed carbene ions RCHCN^+ . Gibson and Haire (Gibson, 1999a; Gibson and Haire, 1998, 2000, 2001b) examined the reactions of a few Ln^+ ions with acetonitrile and other nitriles as well as butylamine in comparative studies with actinide cations. Pope and Buckner (1993) observed that Sc^+ and Y^+ activated pyridine, quinoline, and isoquinoline with the elimination of HCN as the dominant pathway, while the corresponding monoxide ions formed only the adducts; in the reaction of Sc^+ with 2-picoline, the presence of the methyl group rendered dehydrogenation as the main channel and also made the loss of CH_3CN competitive with the loss of HCN . Rodgers and coworkers used GIB-MS to prepare Sc^+ monoadducts with pyridine (Rodgers et al., 2000), pyrimidine (Amunugama and

Rodgers, 2001), and imidazole (Rannulu et al., 2004) and evaluated the corresponding binding energies using threshold CID.

In the case of oxygen-containing organic molecules, a significant number of studies involving all the rare earth cations have appeared, particularly for the case of alcohols. G ribaldi and coworkers used FTICR-MS to examine in detail several aspects of the reactivities of Sc^+ , Y^+ , and Lu^+ with aliphatic alcohols, namely, methanol, ethanol, *n*-propanol, *i*-propanol, and *t*-butanol (Azzaro et al., 1993; Geribaldi et al., 1996). The overall reactivity appeared to be controlled by the high oxophilicity of the metal ions, with the primary products being mainly oxygenated species; however, differences were found depending on the chain length and ramification of the alcohol, as well as between Sc^+ and Y^+ , which were supposed to react by bond insertion mechanisms, and Lu^+ , which evidently reacted by direct abstraction or by multicentered mechanisms. In related studies by G ribaldi and coworkers, the σ -bond metathesis reactions of $\text{Sc}(\text{OCD}_3)_2^+$ with water, ethanol, and *n*-propanol (Crellin et al., 1999) and the diastereoisomeric differentiation of *cis*- and *trans*-2-methylcyclohexanol mediated by Sc^+ (Antonczak et al., 2003) were investigated. Gibson (1999c) examined by LAPRD the reactions of Tb^+ , Tm^+ , and their monoxide ions with several aliphatic alcohols. Zhao et al. (2001) used FTICR-MS to study the reactions of Sc^+ with propargyl alcohol.

A systematic study of the reactions of all the Ln^+ cations with methanol clusters was performed by a LA-molecular beam method, also designated as a “pickup technique” (Lu and Yang, 1998). The Sm^+ , Eu^+ , Dy^+ , Tm^+ , and Yb^+ ions did not react with methanol, whereas the remaining Ln^+ ions formed dehydrogenation products LnCH_2O^+ and LnCH_3O^+ ; for clusters that resulted from reactions with multiple methanol molecules, the dehydrogenation products were $\text{Ln}(\text{OCH}_3)_2(\text{CH}_3\text{OH})_{n-2}^+$ for most Ln^+ and $\text{Ln}(\text{OCH}_3)(\text{CH}_3\text{OH})_{n-1}^+$ for $\text{Ln}=\text{Eu}$. The relative reactivities across the series showed a dependence on the PEs similar to that observed with other reagents, as described in previous sections. Reactions of LnO^+ with the methanol clusters led to water elimination; preliminary results obtained for the LaO^+ cation were previously reported (Lu et al., 1995).

The FTICR-MS examination of the reactivity of rare earth cations with methanol, ethanol, and *i*-propanol was later extended to all the lanthanide series cations by Carretas et al. (2004). All the lanthanide ions reacted to form LnO^+ and LnOH^+ ions as main primary products, showing strong similarities with the results obtained by G ribaldi and coworkers with the same alcohols. The primary product ions participated in subsequent reactions, which through intermediate species such as $\text{Ln}(\text{OH})_2^+$ and $\text{Ln}(\text{OH})(\text{OR})^+$ led mainly to $\text{Ln}(\text{OR})_2(\text{HOR})_n^+$ ions, where $n=0-3$; as is often the case, Eu^+ constituted an exception as it only formed $\text{Eu}(\text{OR})(\text{HOR})_n^+$ species, due to the stability of its formal oxidation state 2+. The overall efficiency of the reactions along

the series showed a dependence on the PEs like that observed in studies with the methanol clusters and with other reagents.

Another related study encompassed the examination of the reactions of Sc^+ , Y^+ , and Ln^+ ions with phenol (Carretas et al., 1998). All the ions except Yb^+ were observed to react, activating O—H, C—O, and/or C—H bonds, with the formation of RO^+ , ROH^+ , and/or ROC_6H_4^+ ions as primary products; the reaction sequences were also investigated and displayed results in concurrence with those obtained for aliphatic alcohols. The primary product distributions and reaction efficiencies revealed the existence of important differences in the relative reactivities of the rare earth metal cations, which apparently depend on the electron configurations of the metal ions (as illustrated in Fig. 13), their oxophilicity, and the second ionization energies of the metals.

The efficient formation of dialkoxy metal species $\text{M}(\text{OR})_2^+$ in the reactions of rare earth metal cations with alcohols, coupled with the knowledge that trialkylorthoformates, $\text{HC}(\text{OR})_3$, easily lose an alkoxy group under electron or chemical ionization, leading to the electronically stabilized ion $\text{HC}(\text{OR})_2^+$, suggested that the reaction of M^+ with $\text{HC}(\text{OR})_3$ could lead to $\text{M}(\text{OR})_2^+$ species that would then act as chemical ionization reagents toward $\text{HC}(\text{OR})_3$, forming $\text{HC}(\text{OR})_2^+$ and neutral $\text{M}(\text{OR})_3$. Geribaldi et al. (1995) initially tested this hypothesis with Sc^+ ions in an FTICR-MS study and

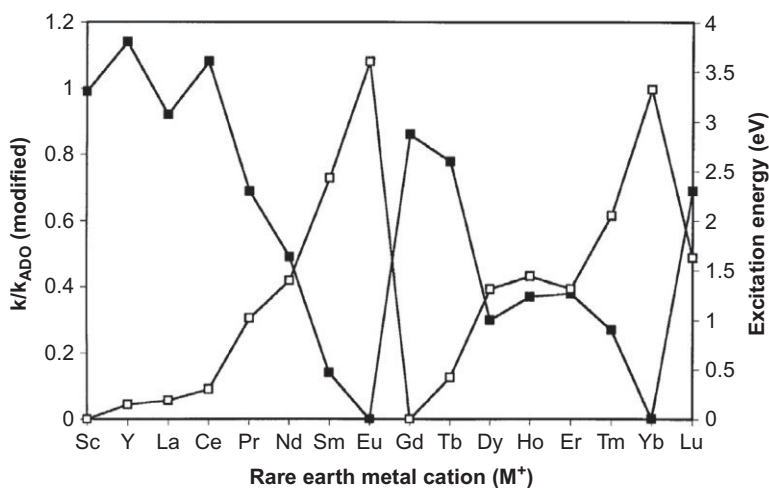
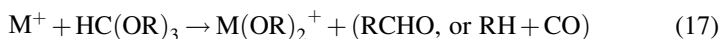
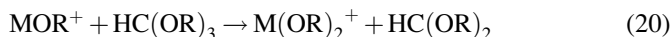
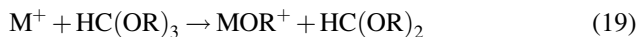


FIGURE 13 Efficiencies of the reactions of rare earth metal cations with phenol (filled squares, left axis; modified to account only for bond insertion channels) and ground to d^1s^1 state promotion energies of the metal cations (open squares, right axis). Reproduced with permission from Carretas et al. (1998). Copyright 1998 Springer.

confirmed that the processes depicted in Eqs. (17) and (18) could lead to the envisaged neutral metal trisalkoxides (R = Me, Et, *n*-Pr; M = Sc):



In a subsequent work, G ribaldi, Maralo, and coworkers (Marchande et al., 2000) extended the investigation to the remaining rare earth ions, verifying that also in the cases of Y⁺ and the Ln⁺ ions, except Eu⁺ and Yb⁺, the presumed neutral metal trisalkoxides could be obtained. The reactions given by Eqs. (19) and (20) were also observed such that together with the process in Eq. (18), sequential reactions of bare M⁺ with HC(OR)₃ could yield the neutral metal trisalkoxides:



Studies of various other oxygen-containing organic molecules have included Sc⁺ and formaldehyde, acetaldehyde, and acetone (Tolbert and Beauchamp, 1984); Pr⁺ and Gd⁺ with the same carbonyl compounds (Schilling and Beauchamp, 1988); Sc⁺, Y⁺, and La⁺ with dimethyl peroxide (Wesendrup et al., 1995); Pr⁺, Tb⁺, and Tm⁺ with dimethyl ether (Gibson, 1999c; Gibson and Haire, 2000); Tb⁺ and Tm⁺ with ethylene oxide (Gibson, 2001); Sc⁺ with furan (Grimm et al., 2004); and Gd⁺ and Lu⁺ with ethylene oxide and formaldehyde (Gibson et al., 2008). With few exceptions, the main products of these reactions were the metal monoxide ions, reflecting the high oxophilicity of the rare earth cations; exceptions of note are the RH₂⁺ ions formed in the reactions of Sc⁺ and Gd⁺ with formaldehyde and the LnOCH₃⁺ ions formed with dimethyl ether. The only doubly charged rare earth cations to have been examined in reactions with oxygen-containing organic molecules were Gd²⁺ and Lu²⁺ (Gibson et al., 2008); with ethylene oxide, oxidation concomitant with electron transfer to produce LnO⁺ dominated, while with formaldehyde, the formation of LnH⁺ for both Gd²⁺ and Lu²⁺, as well as GdO⁺ and Lu⁺, was observed.

The only examples of sulfur-containing organic molecules used as reagents were propanethiol and ethanedithiol, examined by Gibson (1999c) in reactions with Tb⁺ and Tm⁺ ions as part of a comparison with the reactivity of An⁺ ions. With propanethiol, LnS⁺ ions were the main reaction products, whereas with ethanedithiol, LnS₂⁺ ions were formed.

The extensive condensed-phase organo-rare earth chemistry developed with the 1,2,3,4,5-pentamethylcyclopentadienyl anion, C₅Me₅⁻, was accompanied by some studies in the gas phase that were initiated with the examination of the behavior of Sm(C₅Me₅)₂ by Maralo et al. (1996b) using FTICR-MS. Electron ionization spectra showed the formation of Sm(C₅Me₅)₂⁺,

$\text{Sm}(\text{C}_5\text{Me}_5)^+$, and Sm^+ , with all the three ions reacting with neutral $\text{Sm}(\text{C}_5\text{Me}_5)_2$ by electron transfer to produce $\text{Sm}(\text{C}_5\text{Me}_5)_2^+$. The $\text{Sm}(\text{C}_5\text{Me}_5)^+$ reactant ion also formed the $\text{Sm}_2(\text{C}_5\text{Me}_5)_3^+$ ion, a presumed triple-decker species, in a condensation reaction with neutral $\text{Sm}(\text{C}_5\text{Me}_5)_2$, as illustrated in Fig. 14. In that study, it was also observed that the $\text{Sm}(\text{C}_5\text{Me}_5)_2^+$ ion could be obtained by the reaction of the Sm^+ ion with $\text{C}_5\text{Me}_5\text{H}$, 1,2,3,4,5-pentamethylcyclopentadiene, in a two-step process involving an intermediate tetramethylfulvenide species, $\text{Sm}(\text{C}_5\text{Me}_4\text{CH}_2)^+$. These reactivity experiments with $\text{C}_5\text{Me}_5\text{H}$ were later expanded to the remaining Ln^+ , Sc^+ , Y^+ , and the corresponding monoxide ions (Marçalo et al., 1997b). The reactivity of Eu^+ , Tm^+ , and Yb^+ was found to be similar to that observed previously for Sm^+ , namely, the formation of the tetramethylfulvenide ion as the main primary product and of the metallocene ion $\text{Ln}(\text{C}_5\text{Me}_5)_2^+$ as the main secondary product. Several other species were observed in the primary reactions of Sc^+ , Y^+ , and the remaining Ln^+ ions, corresponding to single and multiple losses of small molecules such as H_2 and CH_4 . The differences in reactivity were correlated with the accessibility

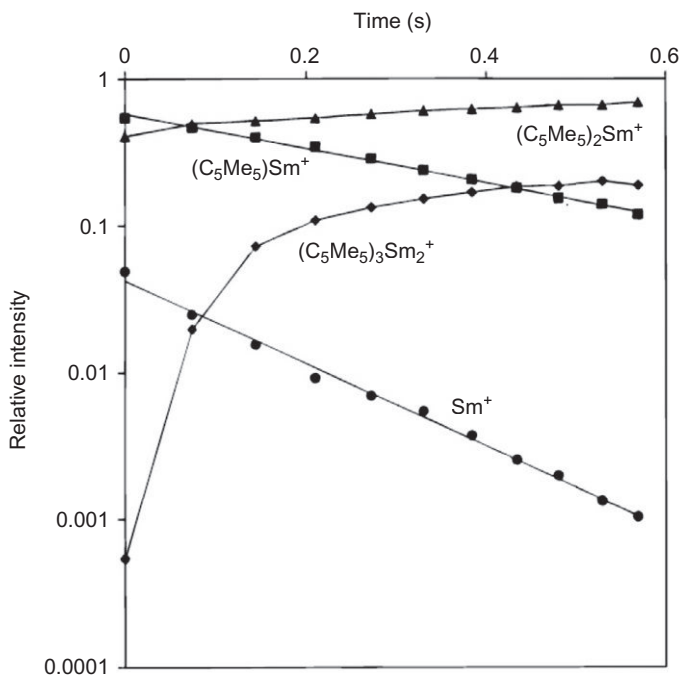


FIGURE 14 Temporal variation of positive ion intensities in 7×10^{-8} Torr of $(\text{C}_5\text{Me}_5)_2\text{Sm}$ following 70 eV electron ionization. Reproduced with permission from Marçalo et al. (1996b). Copyright 1996 American Chemical Society.

of reactive excited-state electron configurations of the metal ions, as previously observed with other organic reagents. In the reactions of the RO^+ cations with $\text{C}_5\text{Me}_5\text{H}$, the reactivity appeared to be determined by the strength of the R^+-O bonds: The ions with the strongest bonds, LaO^+ , CeO^+ , PrO^+ , and NdO^+ , formed $\text{Ln}(\text{C}_5\text{Me}_5)(\text{OH})^+$ as the primary product, which reacted further to give $\text{Ln}(\text{C}_5\text{Me}_5)_2^+$ and H_2O as secondary products; ScO^+ , YO^+ , SmO^+ , GdO^+ to TmO^+ , and LuO^+ yielded $\text{RO}(\text{C}_5\text{Me}_4\text{CH}_2)^+$, $\text{R}(\text{C}_5\text{Me}_4\text{CH}_2)^+$, and $\text{R}(\text{C}_5\text{Me}_5)(\text{OH})^+$ as primary products and $\text{R}(\text{C}_5\text{Me}_4\text{CH}_2)_2^+$ and $\text{R}(\text{C}_5\text{Me}_5)_2^+$ as secondary products; and the ions with the weakest Ln^+-O bonds, EuO^+ and YbO^+ , formed LnOH^+ as the primary product and $\text{Ln}(\text{C}_5\text{Me}_5)^+$ as the secondary product. These product distributions reflect the stability of the +2 oxidation states of Eu and Yb, with their monoxide cations behaving similarly to the alkaline-earth oxide ions CaO^+ , SrO^+ , and BaO^+ , also examined in this work. Gibson and Haire (Gibson, 2000; Gibson and Haire, 2005) also studied the reactions of several Ln^+ ions with $\text{C}_5\text{Me}_5\text{H}$ in their LAPRD experimental setup for comparisons with An^+ ions, with results in overall agreement with the FTICR-MS results.

The formation of other lanthanide metallocenes in the gas phase, through reactions of Ln^+ ions with indene and cyclooctatetraene (COT), was reported only in a summarized form by Marçalo and Pires de Matos (2002). As in the case of $\text{C}_5\text{Me}_5\text{H}$, different abilities were found along the Ln series to activate the bonds of the substrates, influencing the access to metallocene species. The reactivity of COT with several Ln^+ cations ($\text{Ln} = \text{Ce}, \text{Pr}, \text{Sm}, \text{Eu}, \text{Gd}, \text{Tb}, \text{Dy}, \text{Ho}, \text{Tm}, \text{Lu}$) had been previously examined by Gibson (1997b) by LAPRD. Substantial yields of the condensation product $\text{Ln}(\text{COT})^+$ were found and attributed to the particularly strong organolanthanide bonding in the adduct; for some of Ln^+ cations, dehydrogenation to form LnC_8H_6^+ was also observed. The formation of $\text{Ln}(\text{COT})^+$ complexes was also observed in reactions of the Ln^+ ions with cyclooctadiene through double dehydrogenation.

2.3.2 Actinides

In a study of reactions of bare and oxo-ligated thorium and uranium cations with arenes, Marçalo et al. (1997a) revealed several key aspects of the chemistry of these two actinides. Bare Th^+ and U^+ reacted with all of the studied arenes—benzene, naphthalene, toluene, mesitylene, hexamethylbenzene, and 1,3,5-tri-*tert*-butylbenzene—inducing C—H and/or C—C bond cleavage. The Th^+ ion was consistently more reactive than U^+ , in accord with results obtained with small linear hydrocarbons, as discussed above. It was found that the reaction efficiencies with benzene- d_6 were significantly greater than with normal benzene, an effect consistent with adduct stabilization due to lower C—D vibrational frequencies. Whereas only C—H cleavage (H_2 loss) was observed for benzene, additional reaction pathways, including C_2H_2 loss, appeared for the more polarizable substituted arenes; 13 reaction pathways,

in addition to adduct formation, were observed for the $\text{Th}^+/1,3,5\text{-tri-}t\text{-tert-butylbenzene}$ reaction pair. All of the arenes formed adducts with ThO^+ and UO^+ , with the efficiency increasing as the size and vibrational degrees of freedom of the arene increase. The two AnO^+ additionally induced H_2 elimination from hexamethylbenzene and CH_4 elimination from 1,3,5-tri-*tert*-butylbenzene; the mechanisms of these reactions are uncertain. The UO_2^+ ion was inert and only produced adducts with the arenes. The dipositive Th^{2+} and U^{2+} ions reacted with all of the arenes, primarily by electron transfer from the neutral arene to the An^{2+} . Smaller yields of dipositive and monopositive bond cleavage products were the first demonstration of hydrocarbon activation by dipositive actinide cations (Marçalo et al., 1997a), the systematics of which was later elaborated by Marçalo et al. (2011). A contemporary report of the reactions of Th^+ , U^+ , ThO^+ , and UO^+ with benzene and COT (Gibson, 1997b) essentially corroborated the results of Marçalo et al. In particular, Th^+ , U^+ , ThO^+ , and UO^+ were found to induce dehydrogenation of benzene and COT; adduct formation was enhanced for the larger COT substrate.

Szric and coworkers (Kazazic et al., 2005, 2006; Szric et al., 1997a,b) reported qualitative studies of reactions of U^+ with polyaromatic hydrocarbons (PAHs). The results were complicated by competition between oxidation and adduct formation, but an intriguing observation was the addition of multiple PAH molecules to U^+ , such as in $[\text{U}(\text{phenanthrene})_3]^+$; dehydrogenation of PAHs was also observed. Duncan and coworkers also examined the formation of uranium cationic complexes with PAHs using covaporization of uranyl acetate and pyrene (Ayers et al., 2004) or corannulene (Ayers et al., 2005) in a laser plasma source with TOF-MS detection, observing the formation of $\text{UO}_x(\text{PAH})_y^+$ species with $x=0\text{--}2$ and $y=1, 2$.

The An^+ and AnO^+ ions for $\text{An}=\text{Th}\text{--}\text{Am}$ were reacted with small nitriles (Gibson, 1999a). The terminal N: group resulted in substantially enhanced adduct formation in comparison with hydrocarbons. Among the actinide oxide cations, only ThO^+ was reactive, activating propionitrile, $:\text{N}=\text{C}_3\text{H}_5$. The comparative efficiencies of the bare metal cations at activating C—H bonds and dehydrogenating the nitriles were similar to results for alkenes. For example, Np^+ was more reactive than Am^+ , in accord with the necessity for two non-f valence electrons to enable insertion into a C—H bond. An unexpected result was that AnO^+ ions, including NpO^+ and AmO^+ , reacted with butylamine to induce dehydrogenation. A multicentered intermediate was postulated with the coordination of the metal center to the :N electron donor enabling the observed bond activation.

Reactivities of the actinide ions U^+ , Np^+ , Pu^+ , and Am^+ with alcohols and thiols have been reported (Gibson, 1999c). The U^+ and Np^+ ions were substantially more reactive with alcohols than Pu^+ and Am^+ . Although the structures of the product compositions were somewhat uncertain, the

comparative reactivities of the An^+ ions suggest that two non-5f valence electrons in the ground (or very low-lying) electronic configuration are required for alcohol activation. Reactions of bare or oxo-ligated actinide cations with propanethiol resulted in UOS^+ , PuS_2^+ , $NpOS^+$, NpS_2^+ , and AmS^+ . The reaction of Am^+ with ethanedithiol also produced AmS_2^+ , presumably by a bimolecular reaction in which two S atoms are abstracted from a single dithiol molecule. The reaction of An^+ ions with propanethiol and/or ethanedithiol produced the hydrosulfides $Np(SH)^+$, $Np(SH)_2^+$, $Am(SH)^+$, and $Am(SH)_2^+$, and the sulfide hydrosulfide $NpS(SH)^+$. The reactions of AnO^+ with propanethiol produced the hydroxide hydrosulfides, $An(OH)(SH)^+$ for $An = U^+ - Np^+$. It is reasonable that all of the observed reactions should be exothermic. Additional products were apparent but, as with the alcohol reactions, the pathways and compositions were indeterminate.

The 1,2,3,4,5-pentamethylcyclopentadiene molecule, $C_5(Me)_5H(HCp^*)$, is particularly susceptible to activation, by both insertion and “direct” (noninsertion) mechanisms, and thus provides a means to induce chemistry for otherwise inert metal ions (Marçalo et al., 1997b). As expected, both Th^+ and U^+ exhibited a high reactivity with HCp^* , inducing extensive bond cleavage (Jackson et al., 2002a). A particularly interesting result was that ThO^+ and UO^+ induced the elimination of CH_3 and H_2 , which is characteristic of bare metal ions with one chemically active valence electron and is thus indicative of a direct mechanism. A comparison of the reactions of Np^+ , Pu^+ , and Am^+ with HCp^* revealed insertion–activation for the former two and direct activation by Am^+ , which has a much higher PE to the prepared divalent state (Table 2). In contrast to their reactions with small alkanes and alkenes, Cf^+ and Es^+ were found to efficiently activate HCp^* (Gibson and Haire, 2005). A comparison of reactivities revealed three types of activation of HCp^* that correlate with the increasing electronic PEs, with Cm^+ and Bk^+ exhibiting insertion–activation, Am^+ and Cf^+ exhibiting direct activation, and Es^+ exhibiting another type of direct activation seen only for metal cations with especially large PEs (>3 eV). The products of the reaction of Es^+ with HCp^* are the only known organoeinsteinium compounds.

Primary and sequential reactions of four small uranium oxide/hydroxide anions, UO_2^- , UO_3^- , UO_4^- , and $UO_3(OH)^-$, with methanol, were studied; the experimental observations were evaluated by DFT, with the validity of the computational results—structures and reaction mechanisms—confirmed by isotopic labeling experiments (Michelini et al., 2010). The UO_2^- ion was inert, whereas the other three oxoanions reacted with three methanol molecules via the addition or elimination of formaldehyde, water, or dihydrogen to ultimately produce inert uranyl methoxide anion complexes, $[U^V O_2(OCH_3)_2]^-$ or $[U^{VI} O_2(OCH_3)_3]^-$. The structure of the UO_4^- ion reveals four discrete U—O bonds with no O—O bonding. Another notable feature of the DFT results that was verified by isotopic labeling is that the structure of

$[\text{UO}_3\text{H}_2]^-$ is a hydride hydroxide, $[\text{HUO}_2(\text{OH})]^-$, rather than a bishydroxide, $[\text{UO}(\text{OH})_2]^-$. This result is consistent with the retention of the $\text{O}=\text{U}=\text{O}$ uranyl moiety in all intermediates and products. The inert character of $[\text{O}=\text{U}=\text{O}]^-$ can be attributed to the stability of the uranyl structure, an interpretation supported by the computations.

2.4 Hydrolysis, Hydration, Solvation, and Complexation

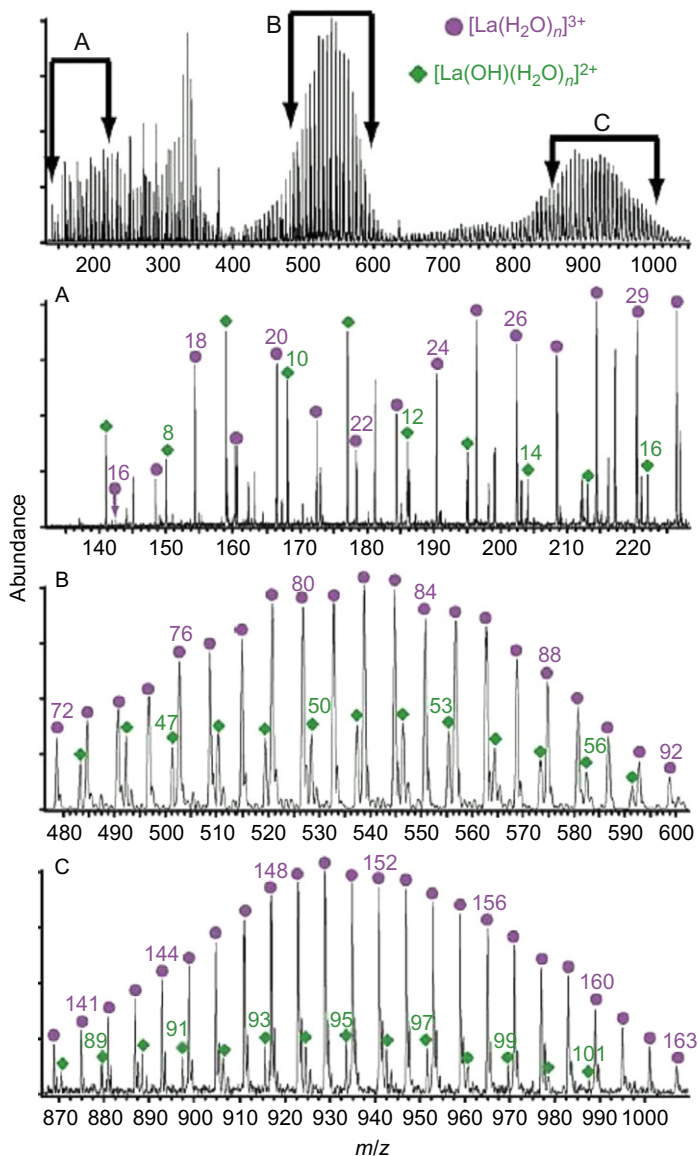
2.4.1 Rare Earths

Kebarle and coworkers (Blades et al., 1990) were the first to show that triply charged complexes of the type $[\text{RL}_n]^{3+}$ could be obtained by ESI-MS of salts of trivalent rare earth metals, namely, Y, La, Ce, Nd, and Sm, using the highly polar aprotic solvents DMSO and dimethylformamide (DMF); the $[\text{RL}_n]^{3+}$ ion intensities were low, which made determinations of ion–solvent binding energies difficult. No triply charged hydrates, $[\text{R}(\text{H}_2\text{O})_n]^{3+}$, could be observed as the species were always in the form of the charge-reduced variant, $\text{ROH}(\text{H}_2\text{O})_n^{2+}$. In accord with these results, Cheng et al. (1992) found that with protic solvents, such as H_2O and CH_3OH , and the rare earth metal salts of Sc, Y, La, Ce, Pr, Nd, and Yb, only the charge-reduced, solvent-derived oxide species were observed; again, it was found that aprotic solvents, like DMSO and CH_3CN , were capable of producing $[\text{RL}_n]^{3+}$ complexes. Following on the results from previous studies, $[\text{RL}_n]^{3+}$ complexes for $\text{R}=\text{Sc}$, Y, La, Ce, and Yb were prepared in the gas phase by electrospray and laser spray using DMSO and hexamethylphosphoramide as ligands (Kojima et al., 1999); laser spray was found to be more suitable for the observation of ions with larger solvation energies. Stewart and Horlick (1994), in a comprehensive ESI-MS study of lanthanide metal salt solutions, observed no $[\text{RL}_n]^{3+}$ complexes in the common protic solvents H_2O and CH_3OH ; the differences in the observed chemistry along the lanthanide series were interpreted in terms of the trends in the difference in IE between metal and solvent and the ease with which the metal ion forms an oxide/hydroxide. In a recent study of water solutions of the entire lanthanide series nitrates by ESI-MS (Oikawa et al., 2011), the relative peak intensities of the species $\text{Ln}(\text{OH})(\text{H}_2\text{O})_j^{2+}$ and $\text{Ln}(\text{OH})_2(\text{H}_2\text{O})_k^+$ were related to changes in the hydration number of the Ln^{3+} ions along the series. A low-energy CID study of presumed $\text{Ln}(\text{OH})_2^+$ ions ($\text{Ln}=\text{La}$, Pr) produced by ESI, forming LnO^+ and H_2O , was used to address the charge-reduction processes occurring in ESI mode, from $\text{Ln}(\text{H}_2\text{O})_n^{3+}$, to $\text{LnOH}(\text{H}_2\text{O})_{n-1}^{2+}$, to $\text{Ln}(\text{OH})_2^+$ (Vukomanovic and Stone, 2000). Complexes containing CeOH^{2+} ligated by three and four acetone molecules were generated by ESI and characterized using wavelength-selective infrared multiphoton dissociation (IRMPD) by Groenewold et al. For the complex $\text{CeOH}(\text{acetone})_3^{2+}$, two dissociation channels were

identified, an initial elimination of acetone and elimination of acetone concurrent with a charge separation process to produce $\text{CeO}(\text{acetone})^+$.

[Shvartsburg \(2002a\)](#) examined in detail the stability of triply charged rare earth ions upon coordination by acetonitrile, $\text{R}(\text{CH}_3\text{CN})_n^{3+}$, for Y and all the Ln except Dy, Er, and Tm; Sc complexes could not be detected. The tricationic species were probed by CID, and the fragmentation pathways involving charge reduction by electron and proton transfers were compared with equivalent processes studied previously for acetonitrile complexes of metal dications. The author used the same CID approach to study DMSO complexes of Sc^{3+} , La^{3+} , and Yb^{3+} , together with other trivalent metal ions ([Shvartsburg, 2002b](#)); characteristic sizes for the charge reduction in $\text{R}(\text{DMSO})_n^{3+}$ and $\text{R}(\text{DMSO})_n^{2+}$ complexes were examined as a function of the elemental IE, revealing no intrinsic gap between the stabilities of dication and trication complexes. [Shvartsburg \(2002c\)](#) was also able to prepare trication complexes for Y and all the Ln except Nd, Dy, Er, and Tm (not investigated) using the distinctive protic ligand diacetone alcohol (DAA), which comprises both a strongly complexing carbonyl group and an alcohol group; the stability of the tricationic complexes was again investigated by CID.

Williams and coworkers ([Bush et al., 2006](#)) showed for the first time that it was possible to form $\text{Ln}(\text{H}_2\text{O})_n^{3+}$ complexes, where Ln = La, Ce, and Eu, using ESI coupled to FTICR-MS with an ion cell cooled to -140°C , in a method dubbed “nanodrop mass spectrometry.” Clusters with n ranging from 16 to over 160 could be readily produced; their structures were probed in the case of La by infrared (IR) photodissociation, which indicated that a minimum of 17 water molecules are necessary to stabilize the clusters under the low-energy ion excitation conditions and long time frame of the experiments ([Fig. 15](#)). The same authors later extended this study to Y and all the Ln elements ([Bush et al., 2008](#)); the structures and reactivities of the $\text{R}(\text{H}_2\text{O})_n^{3+}$ ions containing 17–21 water molecules were probed using black-body IR radiative dissociation, with observation of an abrupt transition in the dissociation pathway from the exclusive loss of a single neutral water molecule to the exclusive loss of a small protonated water cluster via a charge separation process. The authors produced evidence that the charge-reduction chemistry does not depend directly on the IE of the metal but rather correlates with the first hydrolysis constant in bulk aqueous solution. The ability to prepare hydrated multiply charged cations demonstrated by Williams and coworkers was the basis of a new method for measuring absolute standard hydrogen electrode potentials ([Donald and Williams, 2011](#); [Donald et al., 2009](#)), initially demonstrated using the reduction energies of gaseous nanodrops of $\text{Eu}(\text{H}_2\text{O})_n^{3+}$, with $n = 55\text{--}140$, and directly relating them to the reduction energy of the Eu^{3+} ion in bulk aqueous solution. Another use of the metal–water clusters produced by Williams and coworkers was to provide the energetics of electron hydration via electron capture by $\text{La}(\text{H}_2\text{O})_n^{3+}$



Triply charged, highly solvated metal ions $\text{Ln}(\text{H}_2\text{O})_n^{3+}$ ($\text{Ln}=\text{La, Tb, Lu}$) were also generated using a commercial mass spectrometer under the so-called cold-flooding conditions required to produce protonated water clusters by ESI (McQuinn et al., 2007). CID studies allowed for the detailed examination of the solvent/ion evaporation process, with the small ($n < 15$) $\text{Ln}(\text{H}_2\text{O})_n^{3+}$ clusters being unstable and producing charge-reduced $\text{Ln}(\text{OH})(\text{H}_2\text{O})_n^{2+}$ ions upon decomposition. The same group later extended the study to Y and all the Ln (Pape et al., 2011), confirming by CID that the hydrated tricationic metal ions $\text{R}(\text{H}_2\text{O})_n^{3+}$ decomposed by proton transfer to form $\text{R}(\text{OH})(\text{H}_2\text{O})_{n-(x+1)}^{2+}$ and $\text{H}(\text{H}_2\text{O})_x^+$ ($x = 3, 4, \dots$) when n was reduced below a cluster size that correlated with the solution acidity of the metal ion.

An alternative method to ESI for forming triply charged metal–solvent clusters was employed by Stace and coworkers (Walker et al., 1999): ligated neutral clusters were formed and subsequently ionized by electron ionization. With this technique, $\text{Ho}(\text{L})_n^{3+}$ clusters could be prepared for $\text{L}=\text{acetone}$ or acetonitrile, but no such clusters could be observed for $\text{L}=\text{water}$ or methanol, as charge reduction occurred instead.

Other approaches to hydration and solvation may involve the use of ion/molecule reactions under different experimental conditions, or CID or photodissociation of water or solvent adducts of the metal cations. In early work, Magnera et al. (1989) used CID in a triple quadrupole to obtain the water and hydroxyl binding energies to Sc^+ ions, ca. 131 and 367 kJ mol^{-1} , respectively. The sequential addition of H_2O , NH_3 , CH_3CN , DMF, and THF to ScO^+ and YO^+ ions was examined by Wilson and Buckner (1993) by FTICR-MS. Singly and doubly charged Sc–water complexes, produced in a supersonic molecular beam by laser vaporization and mass analyzed in a TOF spectrometer, were probed by vibrational spectroscopy using IR laser photodissociation and the method of rare gas atom predissociation to investigate the influence of the electronic structure of an early transition metal on the cation–water interactions (Carnegie et al., 2011). Shi et al. (2007a) used ESI to produce tricationic nitrile complexes of La, $\text{La}(\text{CH}_3\text{CN})_n^{3+}$ ($n=6-9$) and $\text{La}\{\text{NC}(\text{CH}_2)_4\text{CN}\}_n^{3+}$ ($n=3-4$), and studied the reactions with water at low collision energies in triple quadrupole or hybrid quadrupole–TOF mass spectrometers, obtaining evidence for a preferred coordination number of eight for La^{3+} . Hydration of Yb(III) halide/hydroxide ions, YbX_2^+ and $\text{YbX}(\text{OH})^+$ ($\text{X}=\text{OH, Cl, Br, or I}$), produced by ESI was studied in a QIT-MS by Gibson and coworkers (Rutkowski et al., 2011a); the Yb ions were found to coordinate from one to four water molecules. It was determined that the second hydration was faster than both the first and the third hydrations, and the fourth hydration was the slowest.

2.4.2 Actinides

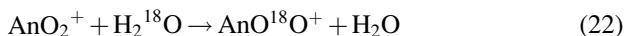
The elementary uranyl ions UO_2^+ and $\text{UO}_2(\text{OH})^+$ produced by ESI were found to add up to four and three water molecules, respectively, in the gas

phase (Gresham et al., 2003). It was subsequently confirmed by DFT that these are coordination number six complexes, $\text{UO}_2(\text{H}_2\text{O})_4^+$ and $\text{UO}_2(\text{OH})(\text{H}_2\text{O})_3^+$, and are the highest inner sphere hydrates in gas phase, such that the gas-phase coordination number is one less than in solution (Rios et al., 2012a). The initial conclusion that UO_2^+ hydrates more efficiently than $\text{UO}_2(\text{OH})^+$ (Gresham et al., 2003) was subsequently modified based on direct rate measurements (Rios et al., 2012a), with the ultimate conclusion that $\text{UO}_2(\text{OH})^+$ hydrates much more rapidly than UO_2^+ being in accord with the greater degrees of freedom in the hydroxide ion to dissipate energy and stabilize the nascent hydrate against dissociation prior to collisional cooling (Rutkowski et al., 2011a). This effect was also seen in the increase in efficiency of water addition to the monohydrate $\text{UO}_2(\text{H}_2\text{O})^+$ by a factor of $\sim 20\times$ as compared with bare UO_2^+ . The hydration behaviors of NpO_2^+ and PuO_2^+ are very similar to that of UO_2^+ , terminating in the tetrahydrates (Rios et al., 2012a); $\text{NpO}_2(\text{OH})^+$ and $\text{PuO}_2(\text{OH})^+$ were not produced in detectable amounts by ESI due to the relatively low stabilities of the Np(VI) and Pu(VI) oxidation states. The comparative hydration rates for $[\text{UO}_2\text{A}]^+$ complexes (A = acetate, nitrate, or hydroxide) were rationalized based on both the differences in electron donation to the uranium metal center and the differences in ligand degrees of freedom to dissipate energy in the nascent monohydrates (Chien et al., 2004).

Actinyl ions can react with water to exchange an oxygen atom according to Eq. (21):



This process is considered here in the context of hydration because the initial step in the exchange process must be the association of a water molecule to the actinyl ion. Oxo exchange for monopositive actinyl ions was studied using labeled water-18 (Eq. 22) where O represents the naturally dominant (99.8%) ^{16}O isotope and An = U, Np, or Pu (Rios et al., 2012b):



Equation (22) was observed to occur for UO_2^+ but not for NpO_2^+ or PuO_2^+ , a result that indicated that exchange occurs at least $20\times$ faster for uranyl(V) as compared with neptunyl(V) and plutonyl(V). Notably, the same relationship of much faster exchange of UO_2^+ is observed in solution, a result considered enigmatic given that uranyl exhibits substantially stronger oxo bonds than do neptunyl and plutonyl. DFT computations (the results of which are shown in Fig. 16) revealed higher barriers for exchange of UO_2^+ versus NpO_2^+ and PuO_2^+ . An explanation for the unexpected increasing resistance of actinyl bonds to disruption in oxo exchange upon proceeding from uranyl to plutonyl could be increasing covalency, which would disfavor the formation of the ionic bishydroxide $\text{OAn}(\text{OH})_2^+$ oxo exchange intermediates.

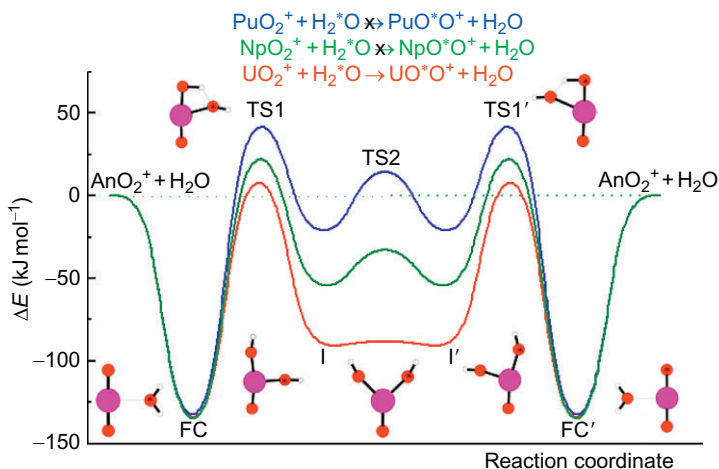
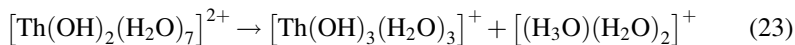


FIGURE 16 DFT-computed potential energy profiles for oxo exchange of H_2O with UO_2^+ (red, lower), NpO_2^+ (green, middle), and PuO_2^+ (blue, upper). The energy profiles are consistent with the nonobservation of exchange for NpO_2^+ and PuO_2^+ . *Reproduced with permission from Rios et al. (2012b). Copyright 2012 American Chemical Society.*

Hydration of dipositive thorium hydroxide revealed that $[\text{Th}(\text{OH})_2(\text{H}_2\text{O})_6]^{2+}$ is a stable dication complex but that Eq. (23) occurs spontaneously upon the addition of another water molecule (Rutkowski et al., 2013):



This result reveals that spontaneous hydrolysis of $\text{Th}(\text{OH})_2^{2+}$ to $\text{Th}(\text{OH})_3^+$ requires a minimum of two second-sphere water molecules to enable charge separation. The proposed proton-transfer process is illustrated in Fig. 17, where proton transfer from an inner sphere water molecule in $[\text{Th}(\text{OH})_2(\text{H}_2\text{O})_7]^{2+}$ results in hydrated $\text{Th}(\text{OH})_3^+$ and the hydronium ion trimer, $[(\text{H}_3\text{O})(\text{H}_2\text{O})_2]^+$. In aqueous solution, the product ions are fully hydrated and the corresponding proton-transfer process is suppressed by the presence of $(\text{H}_3\text{O})_{\text{aq}}^+$ at low pH. The results are a case where a seemingly obvious and important solution process that cannot be directly observed, hydrolysis of Th(IV), is demonstrated on a different scale in gas phase. It is notable that whereas inner shell hydration stabilizes $\text{Th}(\text{OH})_2^{2+}$ from solution to gas, the addition of second-shell water molecules then enables charge separation, with the implication that the formation of nanodroplets containing $\text{Th}(\text{OH})_2^{2+}$ cannot be achieved by the bottom-up approach of addition of water molecules but must rather be achieved by the top-down approach of the evaporation of water from larger droplets.

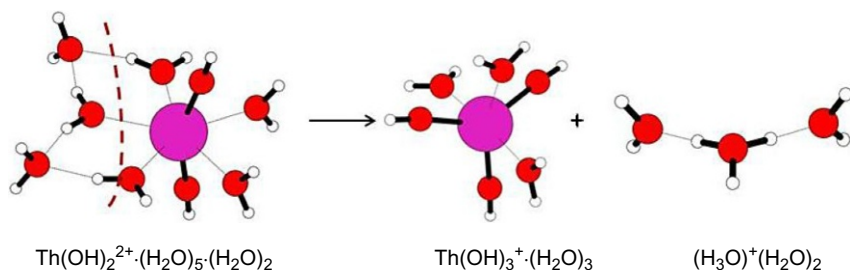


FIGURE 17 Charge separation model for the observed hydrolysis of $[\text{Th(OH)}_2(\text{H}_2\text{O})_7]^{2+}$ to $[\text{Th(OH)}_3(\text{H}_2\text{O})_3]^+ + [(\text{H}_3\text{O})(\text{H}_2\text{O})_2]^+$. The structures were computed by DFT. *Reproduced with permission from Rutkowski et al. (2013). Copyright 2013 American Chemical Society.*

Using ESI to probe speciation in solutions of uranyl and citrate, $\text{C}_3\text{H}_4(\text{OH})(\text{COO})_3^{3-}$, Pasislis and Pemberton (2003) produced several gas-phase uranyl citrate complexes that were taken to support the proposed solution speciation. The gas-phase chemistries of these complexes were explored (Somogyi et al., 2007), with CID of polynuclear species resulting in clusters such as U_4O_n^- ($n = 11-13$); the $\text{U}_4\text{O}_{13}^-$ cluster is particularly intriguing as it presumably incorporates O—O bonding and/or O^* radical character such that the U(VI) oxidation state is not exceeded. Schröder and coworkers have explored the use of ESI to infer solution speciation from observed gas-phase compositions, with a focus on uranyl nitrate hydrolysis revealed by $[\text{U}_m\text{O}_{2m}(\text{X},\text{Y})_{2m-1}(\text{H}_2\text{O})_n]^+$ ($\text{X},\text{Y} = \text{OH}, \text{NO}_3$) (Tsierkezos et al., 2009). The essential conclusion was that gas-phase speciation can provide clues to solution speciation but that quantitative inferences require caution. Walther and coworkers have produced a variety of thorium(IV), uranyl(VI), and plutonyl(VI) hydroxide ions by ESI as a route to explore the experimentally challenging determination of solution hydrolysis mechanisms and species (Steppert and Walther, 2013; Steppert et al., 2012; Walther et al., 2008, 2009). Although a correlation between hydroxide ions in solution and those observed in the gas phase by ESI was established, a quantitative relationship was not definitively demonstrated, largely because there is no means to directly probe the compositions and concentrations of actinide hydroxide ions in solution. Despite that the nano-ESI technique used in the hydrolysis speciation studies is relatively mild and less disruptive to speciation, the production of gas-phase hydroxide ions from aqueous solution by ESI necessarily introduces the possibility for redox processes and reactions in nanodroplets during evaporation. The conclusion is that ESI is a useful tool to probe solution speciation but cannot generally be employed alone to definitively identify solution species. The work of Walther and coworkers provided a more detailed examination of the solution speciation and hydrolysis of uranyl and thorium as previously studied by ESI by Moulin and coworkers (Moulin et al., 2000, 2001).

Although ESI species in the gas phase may in some cases provide a means to infer precursor solution speciation, a broader area of interest lies in the ability to produce and study novel gas-phase complexes by ESI and subsequent gas-phase chemistry, such as in the case of the $\text{U}_4\text{O}_{13}^-$ cluster mentioned above. In the realm of actinides, the focus in this research effort has largely been on the key uranyl(VI) ion, with much of the seminal work having been performed by Van Stipdonk, Groenewold, and coworkers (Anbalagan et al., 2004; Bryantsev et al., 2008; Chien et al., 2004; Gresham et al., 2003, 2011; Groenewold et al., 2004, 2006a,b, 2008a,b,c, 2010a,b, 2011; Leavitt et al., 2009; Van Stipdonk et al., 2003, 2004a,b, 2006). The hydration behaviors of actinyl ions produced by ESI were discussed above (Section 2.5.2) (Gresham et al., 2003; Rios et al., 2012a). Whereas only monocationic actinyl ions were observed for ESI from aqueous solutions, the addition of a stronger Lewis base ligand such as acetone and acetonitrile enabled transfer of dicationic uranyl from solution to gas, such as for the $[\text{UO}_2(\text{CH}_3\text{COCH}_3)_4]^{2+}$ and $[\text{UO}_2(\text{CH}_3\text{CN})_4]^{2+}$ complexes (Van Stipdonk et al., 2004a, 2006). When less than four acetonitrile ligands coordinate and protect the uranyl ion, charge-reduction hydrolysis to $\text{UO}_2(\text{OH})^+$ occurs in the gas phase. However, in the absence of sufficient background water, $[\text{UO}_2(\text{CH}_3\text{COCH}_3)_{2,3}]^{2+}$ can be produced (Groenewold et al., 2006b), revealing that as few as two base ligands can stabilize dicationic uranyl from solution to gas. It was later shown that PuO_2^{2+} could similarly be transferred from solution to gas by ESI when stabilized by the base ligands acetone and acetonitrile, albeit substantially less efficiently than UO_2^{2+} , which is attributed to the lower U(VI/V) reduction potential (0.17 eV) as compared with that for Pu(VI/V) (1.02 eV) (Rios et al., 2011b). ESI of solutions containing the stronger Lewis base DMF was employed to obtain the dicationic neptunyl complex $[\text{NpO}(\text{DMF})_4]^{2+}$ (Rutkowski et al., 2011b). The necessity for a stronger base to stabilize dicationic neptunyl(VI) is in accord with the even higher Np(VI/V) reduction potential (1.24 eV) as compared with plutonyl. An important ancillary result of the more recent study of actinyl acetone complexes was the observation of gas-phase complexes apparently comprising more than five acetone ligands, specifically $[\text{UO}_2(\text{CH}_3\text{COCH}_3)_{6,7,8}]^{2+}$ (Rios et al., 2011b). Such apparently “hypercoordinated” complexes would presumably comprise second-sphere acetone molecules, which should be too weakly bound to be observed under the experimental conditions, in agreement with the result that the maximum coordination in the case of acetonitrile was that in $[\text{UO}_2(\text{CH}_3\text{CN})_4]^{2+}$. Dicationic uranyl complexes with isotopically labeled acetone and DAA revealed that the apparently “hypercoordinated” acetone complexes actually comprised DAA ligands, which are isobaric with two acetones (Rios et al., 2012c). Because DAA is a strong base and can bind in a bidentate mode, as little as 0.1% of DAA in acetone could account for the prevalent DAA complexes. A further indication of DAA was the loss of

H₂O to produce mesityl oxide as can be induced by either CID (Rios et al., 2011b, 2012c) or exothermic addition of a basic ligand (Rios and Gibson, 2012).

Given that effective Lewis base ligands are necessary to stabilize dipositive actinyl and other dipositive metal ions from solution to gas, transferring even more highly charged metal ions to the gas phase presents a challenge. The key to achieving this is to encapsulate the metal in a cavity that stabilizes the highly charged metal ion by electron donation from several donor sites. Using this approach, it has been possible to transfer the Th⁴⁺ ion from solution to gas by ESI as [Th(TMOGA)₃]⁴⁺ (TMOGA = tetramethyl-3-oxa-glutaramide), in which the tetrapositive thorium ion is coordinated by nine oxygen atoms from the three TMOGA ligands (Gong et al., 2013). This accomplishment is facilitated in the case of thorium because its fourth IE is the lowest of all those in the periodic table, with the possible exceptions of transactinide elements not available for such studies.

As the structural information provided by MS is necessarily limited, a major advance in gas-phase actinide chemistry has been the determination of IR vibrational spectra of actinide complexes, specifically uranyl coordination complexes produced by ESI (Gresham et al., 2011; Groenewold et al., 2006b, 2008a,b,c, 2010a,b, 2011). DFT computations are often employed to assist in the interpretations of the IR spectra. An IR study of [UO₂(CH₃COCH₃)_n]²⁺ ($n=2-4$) and [UO₂(CH₃CN)_n]²⁺ ($n=3-5$) complexes revealed systematic red shifting of the asymmetrical O=U=O stretching frequency as the number of ligands, n , increases, consistent with increasing donation of electron density to the metal center—the results for uranyl acetone complexes are shown in Fig. 18 (Groenewold et al., 2006b). Compared with the dipositive complexes having several neutral donor ligands, the O=U=O frequency was shifted to lower wave numbers upon the addition of a single anion ligand—that is, in [UO₂X]⁺ complexes where X = OH, OCH₃, or OOCCH₃—indicating even greater charge donation to uranyl in the monopositive complexes (Groenewold et al., 2008a). IR spectra of the [UO₂(NO₃)₃]⁻ anion complex revealed a splitting of the nitrate frequency consistent with the expected tris-bidentate coordination and with solution spectra (Groenewold et al., 2008b). The spectrum of the NO₂-loss product upon CID indicates a [UO₂(NO₃)₂(O[•])]⁻ structure with a radical O atom in the equatorial plane. The IR spectrum for the nitrate dimer [(UO₂)₂(NO₃)₅]⁻ indicates a single bridging nitrate ligand between the uranyl moieties and a higher asymmetrical O=U=O frequency compared with [UO₂(NO₃)₃]⁻, consistent with less electron donation to uranyl from the bridging nitrate anion (Groenewold et al., 2011). Vibrational spectra of [UO₂(ROH)]⁺ complexes where ROH is water or an alcohol revealed that the asymmetrical O=U=O stretching frequency is some 20 cm⁻¹ lower than for [UO₂(ligand)]²⁺ complexes but very similar to that in [UO₂(NO₃)₃]⁻ (Groenewold et al., 2008c). This comparison suggests that the nature of the UO₂ moiety in [UO₂(NO₃)₃]⁻

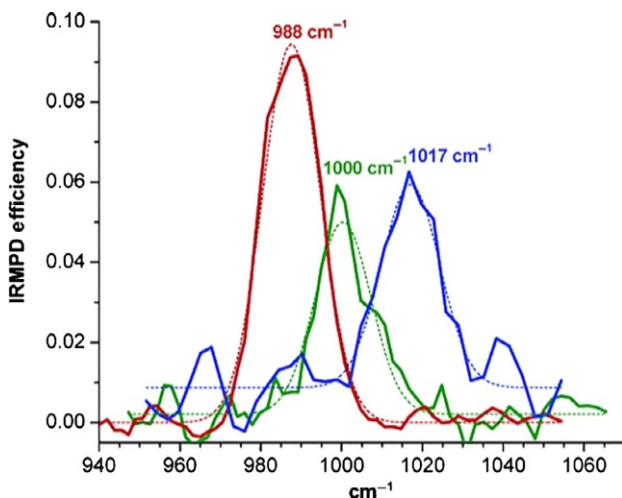


FIGURE 18 O=U=O asymmetrical stretching region of the IRMPD spectra of $[\text{UO}_2(\text{CH}_3\text{COCH}_3)_n]^{2+}$. Dotted lines are Gaussian fits, and solid lines are data, for complexes having $n=4$ (red, 988 cm^{-1}), 3 (green, 1000 cm^{-1}), and 2 (blue, 1017 cm^{-1}). Reproduced with permission from Groenewold et al. (2006b). Copyright 2006 American Chemical Society.

is essentially that of uranyl(V) rather than an anion complex of uranyl(VI). For the uranyl acetate and benzoate complexes, $[\text{UO}_2(\text{OOC}-\text{R})_3]^-$ where $\text{R}=\text{CH}_3$ or *cyclo*- C_6H_5 , the IR spectra indicate predominant structures with two bidentate and one monodentate carboxylate ligands (Groenewold et al., 2010a), this in contrast to three bidentate ligands in the tris-nitrate anion complex. Whereas the $[\text{UO}_2(\text{X})(\text{CH}_3\text{COCH}_3)_3]^+$ complexes exhibited little change in the O=U=O asymmetrical stretch frequency for $\text{X}=\text{Cl}$, Br , and I , this frequency decreases from $\text{X}=\text{I}$ to Cl in the $[\text{UO}_2\text{X}_3]^-$ anion complexes (Groenewold et al., 2010b), indicating that stronger bonding between the metal center and the halide weakens the oxo bonds. A notable feature of this work was that the IR-inactive symmetrical stretch in linear $\text{O}=\text{U}=\text{O}^{2+}$ becomes active in the $[\text{UO}_2(\text{X})(\text{CH}_3\text{COCH}_3)_3]^+$ complexes, appearing around 880 cm^{-1} , consistent with the slight ($\sim 7^\circ$) deviation from linearity predicted by DFT; this is a clear example of IR spectroscopy revealing a predicted structural feature of a gas-phase complex.

To date, IR spectroscopy of actinide complexes has been limited to uranyl. It should be anticipated that in the future this approach will be applied to U(IV) and Th(IV) complexes. Although it is regrettably unlikely that a facility capable of performing these experiments with other actinides will soon become available, it would be desirable to similarly characterize neptunyl, plutonyl, and other transuranic complexes to establish variations in structural and bonding features across the actinide series.

2.5 Experiments with Biologically Relevant Molecules

2.5.1 Rare Earths

Complexes of La^{3+} with peptides, including a peptide with no basic residues, were produced without charge reduction using ESI (Shvartsburg and Jones, 2004); some of the complexes fragmented along pathways that differed from those for protonated analogs and this could be of analytic utility. In a related study, Hopkinson and coworkers used La^{3+} to obtain $[\text{La}(\text{peptide})]^{3+}$ complexes by ESI, with the peptides containing four, three, or only two residues (Shi et al., 2007b); relying on previous work referenced in Section 2.4.1 (Shi et al., 2007a), the authors were able to deduce the number of binding sites provided by each peptide. In a subsequent study, Hopkinson and coworkers made the first observation of small, protonated dipositive $(\text{a}_3 + \text{H})^{2+}$ and $(\text{a}_2 + \text{H})^{2+}$ ions (a_3 and a_2 are iminium ions that occur as fragments in the MS/gas-phase sequencing of protonated peptides), produced in CID of a $[\text{La}(\text{GGG})(\text{CH}_3\text{CN})_2]^{3+}$ complex, where GGG is triglycine (Shi et al., 2008). The same group, together with Oomens and coworkers, was able to obtain the first gas-phase IR spectra of a triply charged complex, La^{3+} complexed to a derivative of tryptophan, and evaluated the binding sites of the metal ion (Verkerk et al., 2012). The preference for La^{3+} in this type of studies derives from it having the lowest third IE of all trivalent metals, as well as having an electronic structure and chemical behavior somewhat similar to those of biologically relevant alkaline-earth metal ions.

Previously, the groups of Williams and Oomens (Prell et al., 2010) performed the first IRMPD studies of trivalent metal-cationized peptide complexes with La^{3+} , Eu^{3+} , and Ho^{3+} , produced by ESI, but could only examine doubly charged complexes; the variation of the size of the metal ion induced only minor structural changes. Comparisons were made with protonated and alkali metal or alkaline-earth metal-cationized peptide complexes investigated previously with IRMPD. Williams and coworkers (Flick et al., 2013) performed a thorough ESI study of the complexation of lanthanide cations (La, Pr, Sm, Eu, Tb, Ho, Tm, Yb, or Lu) with peptides, which predominantly resulted in the formation of $[\text{Ln}(\text{peptide-H})]^{2+}$ for small peptides (below or close to 1000 Da) and $[\text{Ln}(\text{peptide})]^{3+}$ for larger peptides. Electron-capture dissociation (ECD) of the doubly charged complexes resulted in significantly higher electron-capture efficiency and sequence coverage than peptide-divalent metal ion complexes that have the same net charge. Flick and Williams (2012) also examined by ESI and ECD the effect of the interaction of La^{3+} with proteins, as a potential tool for obtaining structural information in native MS.

Few studies with other biologically related molecules have been reported. Kojima et al. (1999) investigated the ion chemistry of the triply charged rare earth metal ions Sc^{3+} , Y^{3+} , La^{3+} , Ce^{3+} , and Yb^{3+} with glucose, sucrose, raffinose, cyclodextrin, and ginsenoside Rb1 by ESI and laser spray and observed

the formation of $R(\text{ligand})_n^{3+}$ species. [Rodgers and Armentrout \(2002\)](#) used threshold CID in a GIB-MS to study $\text{Sc}(\text{adenine})^+$ ions, observing intact ligand loss in competition with the elimination of purine, HCN, and ammonia; this work complemented other experiments by Rodgers and coworkers on the energetics of Sc^+ monoadducts with N-donor bases, cited in [Section 2.3.1](#).

2.5.2 Actinides

Fast-atom bombardment mass spectrometry (FAB-MS) experiments with uranyl and several AAs and two dipeptides (PEP) showed that species up to $[\text{UO}_2(\text{AA})_5]^+$ or $[\text{UO}_2(\text{PEP})_5]^+$ could be obtained ([Kemp and Read, 1996](#)). The dissociation of the AA ligands and ligand fragmentation, with the carboxyl group being retained, were observed; fragmentation of the dipeptide complexes occurred mainly via carbon-(amide)nitrogen cleavage, indicating a role of uranyl in steering molecular breakdown to give amide- or carboxyl-containing fragments. Uranyl complexes with the peptides Asp-Ala-His-Lys and Gly-Gly-His were examined by ESI-MS ([Huang et al., 2005](#)); CID of the $[\text{UO}_2(\text{Asp-Ala-His-Lys})]^+$ complex gave rise to H_2O loss and to fragments associated with the dissociation of AA residues.

The binding of UO_2^{2+} ion to selected 8-mer and/or 12-mer oligonucleotides was studied by ESI-FTICR-MS, profiting from the high-resolution and MS^n capabilities of the technique ([Wu et al., 1996](#)). CID experiments with the uranyl oligonucleotide complex ions indicated that the uranyl ion (as well as Mg^{2+} and Na^+ ions, which were also examined) preferentially bound to the central thymine region of the sequence; a high site and sequence specificity in the binding was observed for the uranyl ion. The authors concluded that the utility of ESI combined with high-performance MS/MS to study the interactions of metal ions with oligonucleotides provides complementary information to results from solution.

Desferrioxamine (DEF) is a siderophore produced by fungi and bacteria that has three hydroxamate groups available to bind metal ions, preferentially not only iron for biological systems but also other metal ions, including uranyl. Due to the prevalence of siderophores in natural environments, it is important to understand their potential roles in actinide transport. The complex of uranyl(VI) and singly deprotonated DEF siderophore, $[\text{UO}_2(\text{DEF-H})]^+$, was produced by ESI and subjected to CID ([Groenewold et al., 2004](#)). The primary CID pathway was cleavage of the hydroxamate linkage, consistent with its role in metal binding. The result that the complex did not hydrate was interpreted to indicate that the uranium metal center is fully coordinated in the complex.

2.6 Clusters Produced from Solids and Solutions

2.6.1 Rare Earths

Although ESI is a method that can straightforwardly yield cluster ions, for example, from solutions of simple metal salts, only one dedicated study

involving the rare earths has been reported. Recently, [Rutkowski et al. \(2012\)](#) produced anionic lanthanide chloride clusters, $\text{Ln}_n\text{Cl}_{3n+1}^-$, for the whole lanthanide series by ESI of LnCl_3 in isopropanol; bromide and iodide clusters were also obtained for selected LnBr_3 ($\text{Ln}=\text{La}, \text{Ce}, \text{Pr}, \text{Nd}, \text{Sm}, \text{Lu}$) and LnI_3 ($\text{Ln}=\text{La}, \text{Lu}$). The clusters were characterized in a QIT-MS and “magic numbers” were apparent at $n=4$ for La–Sm, $\text{La}_4\text{Cl}_{13}^-$, and at $n=5$ for Dy–Lu, $\text{Lu}_5\text{Cl}_{16}^-$, as illustrated in [Fig. 19](#). Multiply charged anion clusters with z down to -5 appeared in the spectra for the early lanthanides (La–Eu). Partial hydrolysis to $\text{Ln}_n\text{Cl}_{3n+1-y}(\text{OH})_y^-$ with $y=1, 2$ was prevalent for the late lanthanides but only for small clusters with $n=2$ or 3. DFT computations were employed to determine the structures and energetics of selected clusters.

Conversely, several reports on the formation of rare earth oxide cluster cations using desorption/ionization methods have appeared over the course of several years. FAB-MS was used in a number of studies in which different rare earth (Y and Ln) precursor compounds were used, namely, oxides, simple salts, and complexes ([Kahwa et al., 1988a,b](#); [Kemp and Read, 1995](#); [Kemp et al., 1995b](#)). Ligated lanthanide cluster ions could also be obtained, as could oxide clusters containing two different lanthanides; in two of these studies, the structures, stabilities, and CID patterns of the clusters were investigated in detail for the case of Y ([Kahwa et al., 1988a](#)) and several Ln ([Kemp and Read, 1995](#)). A single study of La oxide cluster cations generated using an uncommon plasma desorption/ionization with a ^{252}Cf fission source, coupled to TOF-MS, was also reported ([Van Stipdonk et al., 1999](#)).

LA of rare earth oxides (Sc, Y, and several Ln), along with other metal oxides, was examined by [Michiels and Gijbels \(1984\)](#); the distributions of

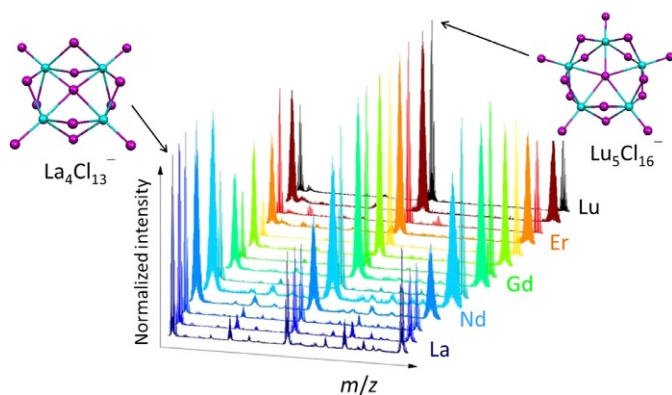


FIGURE 19 ESI mass spectra of $\text{Ln}_n\text{Cl}_{3n+1}^-$ clusters ($\text{Ln}=\text{La-Lu}$ except Pm and $n=4-6$) showing the predominance of $\text{La}_4\text{Cl}_{13}^-$ and $\text{Lu}_5\text{Cl}_{16}^-$ and the corresponding structures from DFT computations. *Reproduced from Rutkowski et al. (2012) with permission from the PCCP Owner Societies.*

the cluster cations formed were convincingly correlated with the valence electron configuration of the metal in the oxide and the RO^+ BDE. LA coupled to TOF-MS was also used by [Mele et al. \(1989, 1990\)](#) to produce Sc, Y, and La cluster oxide cations from solid oxides. Y and La oxide cations were produced by laser vaporization in a pulsed nozzle source and detected with TOF-MS, with $\text{RO}(\text{R}_2\text{O}_3)_x^+$ species being particularly abundant ([Reed and Duncan, 2008](#)); photodissociation experiments indicated common dissociation channels for both metals and a special stability for the $\text{RO}(\text{R}_2\text{O}_3)_x^+$ ions.

Gibson performed detailed studies of the generation of lanthanide oxide cluster cations by LA with TOF-MS detection, from oxide and oxalate precursors ([Gibson, 1994a,b, 1995](#)). Different series of Ln_mO_n^+ ions were identified, with prevalence of what could be described as $\text{LnO}^+(\text{Ln}_2\text{O}_3)_x$ species for the trivalent Ln; however, the observed cluster stoichiometry distributions clearly depended on the relative accessibilities of the +2, +3, and +4 oxidation states. The work was later expanded to include heterovalent metals in ternary oxide cluster ions, namely, Ca or Sr and Ta, Zr, or Hf ([Gibson, 1996b](#)); examples of mixed La or Ce and Pu oxide clusters were also obtained ([Gibson and Haire, 2004](#)). Related experiments involving mixtures of Ln oxides (Ln = Ho, Lu) and selenium resulted in the formation of binary, LnSe_n^+ , and ternary ions, LnOSe_n^+ , but no species with more than one metal ion were observed ([Gibson, 1999d](#)).

The formation of anionic rare earth oxide clusters using LA has been reported for the case of Ce, using CeO_2 as solid precursor ([Aubriet et al., 2009](#)). However, cerium oxyhydroxide cluster anions, $[\text{Ce}_x\text{O}_y(\text{OH})_z]^-$, dominated the mass spectra, and only negligible amounts of hydrogen-free clusters were observed in the primary spectrometer used in this work, an FTICR-MS with external ion source and accumulation hexapole; however, the abundance of $[\text{Ce}_x\text{O}_y]^-$ ions increased when a TOF-MS was used for analysis. The authors proposed that anhydrous $[\text{Ce}_x\text{O}_y]^-$ ions and neutral species were initially formed in the LA process and that these species then reacted with water present along the ion path, yielding the observed oxohydroxy species in which all the Ce atoms are in the IV oxidation state; concurrent reaction with O_2 to form superoxide species was also observed in the experiments, which included CID studies. DFT modeling of the cluster structures showed that they contain one-to-multiple hydroxide moieties, but not datively bound water.

The aforementioned studies of rare earth oxide cluster ions focused on formation and structural aspects, and apart from the supposed ion chemistry occurring during synthesis, only recently have reactivity experiments with different small molecules been pursued, mainly due to the work of Ding's group, following inventive work by Castleman and coworkers with transition metal oxide clusters ([Castleman, 2011; Johnson et al., 2008](#)). Rare earth oxides are widely used as catalysts or catalyst supports; investigating the bonding

and reactivity of metal oxide clusters under controlled conditions is generally considered a means to understand elementary reactions on metal oxide surfaces. Ding and coworkers have used LA coupled to a fast flow reactor and TOF-MS detection to examine the reactivity of both cationic and anionic rare earth oxide clusters with important substrates like small hydrocarbons and CO (Ding et al., 2011; Tian et al., 2012; Wu et al., 2010; Xu et al., 2011; Xua et al., 2013; Zhao et al., 2011b). Accounts of the work put in perspective with related studies with transition metal oxide cluster ions have also been published recently (Ding et al., 2012; Zhao et al., 2011a). The rationale for the enhanced reactivity of some of the metal oxide clusters, as based on the MS experiments and accompanying DFT studies, is the presence of oxygen-centered radicals ($O^{\cdot-}$). Two major factors can apparently influence C—H bond activation, spin and charge; the clusters can be negatively or positively charged, or neutral overall, and the local charge distribution around the $O^{\cdot-}$ centers can also significantly affect the reactivity. The use of yttrium as dopant in vanadium oxide clusters, and its role in methane activation, was also examined by Ding and coworkers (Li et al., 2011). Castleman and coworkers examined theoretically the role of Sc as dopant in Zr oxide clusters to provide one less electron and thus induce the formation of O-centered radicals (Nöblier et al., 2010).

In related efforts by FTICR-MS, Schwarz and coworkers (Ma et al., 2012) also used yttrium as a dopant in aluminum oxide cluster cations, $Al_2O_3^+$, which had been previously shown to enable the direct conversion of CH_4 into CH_2O (Wang et al., 2012); the net result was that in the thermal reactions of $YAlO_3^+$ with methane, there was an increase in the reactivity of $Y_2O_3^+$ (unreactive with methane) and the selectivity of $Al_2O_3^+$. Schwarz and coworkers also examined recently the $YAlO_2^+/YAlO_3^+$ and $Y_2O_2^+/Y_2O_3^+$ couples in the context of CO/ N_2O conversion and observed rather low catalytic activities (Ma et al., 2013).

The other main-group element of particular relevance for the theme of this section is carbon. Soon after their discovery of the fullerenes, Smalley and coworkers used MS methods to demonstrate that metallofullerene species could be generated in the gas phase—one of the metals studied was lanthanum (Heath et al., 1985; Weiss et al., 1988). This was the beginning of the burgeoning field of metallofullerenes, particularly important for rare earths, that was recently reviewed in this handbook (Shinohara and Saito, 2011) and elsewhere (Lu et al., 2012, 2013). In the initial work by Smalley and coworkers, the structures of the La-fullerene species were probed by photodissociation, and the exceptional stability of LaC_{60}^+ led to the suggestion that the La atom was trapped inside the fullerene cage; this was a controversial hypothesis, as challenged by Cox et al. also using MS-based experiments (Cox et al., 1986, 1988). Freiser and coworkers investigated the reaction of La^+ ions with C_{60} by FTICR-MS, obtaining LaC_{60}^+ for which CID yielded La^+ indicating the

formation of an externally bound metallofullerene (Huang and Freiser, 1991). Subsequent developments clearly demonstrated the existence and fascinating chemistry and physics of endohedral metallofullerenes. Interestingly, laser desorption and thermal desorption MS studies of metallofullerenes of the rare earth elements found in arc-produced soots showed the formation of two distinct groups, a trivalent group comprising Sc, Y, La, Ce, Pr, Nd, Gd, Tb, Ho, Er, and Lu and a divalent group comprising Sm, Eu, and Yb (Moro et al., 1993).

These metallofullerenes may not be strictly rare earth clusters as those discussed above in this section, but much of the investigation around this topic revealed the existence and stability of rare earth carbide cluster ions. McElvany (1992) used laser vaporization coupled to FTICR-MS to generate yttrium–fullerene ions, $Y_xC_n^+$ ($x=1, 2$ with even number $n=60-100$), from samples containing yttrium oxide, graphite, and fullerenes. CID and oxidation reactions with H_2O or N_2O were used to compare these species with externally bound ions, for example, YC_{60}^+ , generated by gas-phase association reactions, with the stability toward fragmentation and oxidation suggesting that the laser-generated species had endohedral structures, $Y_x@C_n^+$; laser vaporization of yttrium oxide and graphite mixtures yielded only Y^+ , YO^+ , YO_2^+ , and minor amounts of YC_2^+ and YC_4^+ . Freiser and coworkers also studied the formation of yttrium–carbon clusters using laser ionization of yttrium metal in a He/CH_4 atmosphere within a cluster source coupled to FTICR-MS (Kan et al., 1996). Motivation was the newly discovered metallo-carbohedrenes or “Met-Cars” (Guo et al., 1992a; Leskiw and Castleman, 2002), but although a broad range of $Y_xC_y^+$ cluster ions were generated, no evidence was obtained for a “magic” $M_8C_{12}^+$ composition. The $Y_4C_7^+$ cluster was relatively abundant, and its CID behavior and reactivity with CH_3Br , H_2O , and NH_3 were examined, in comparison with $Y_4C_{8,9}^+$ and $Y_3C_{7,8}^+$, to evaluate the effects of the yttrium-to-carbon ratio.

The synthesis of metallofullerenes was also attempted with different precursors in LA FTICR-MS experiments. Hopwood et al. (1997) found that mixtures of lanthanum oxide and carbon black readily produced fullerene and metallofullerene cations, namely, LaC_n^+ with $n=44-96$, at laser powers much lower than usually required for graphite. Pyrolyzed coal-tar pitch samples consisting mainly of PAHs were similarly studied and metallofullerene formation also occurred (Zhang et al., 1999). The elements Y, La, Ce, Pr, Nd, Gd, and Sm, as oxides or sulfides, were examined, with C_{60}^+ , $M@C_{60}^+$, and $M@C_{70}^+$ being the most abundant product ions, although dimetallofullerene ions, $M_2@C_{2n}^+$, were also identified. High laser powers resulted only in the formation of small metal carbide cluster ions, such as LaC_n^+ ($n=2-10$) and $La_2C_m^+$ ($m=4-9$). CID experiments were used to study the structures of the small La carbide ions and the metallofullerene ion $La@C_{60}^+$; the CID results and the observation that $La@C_{60}^+$ was unreactive with methanol, benzene, and carbon disulfide

indicated the endohedral nature of this La metallofullerene. The same group later investigated the reactivity of small yttrium and lanthanum carbide cations, YC_n^+ and LaC_n^+ for $n=2, 4,$ and $6,$ produced as before from mixtures of carbonaceous material and metal oxide, with benzene and cyclohexane (Zhang et al., 2005). The MC_2^+ ions reacted similarly to the “bare” metal cations, inducing dehydrogenation of the hydrocarbon molecules, whereas the MC_4^+ and MC_6^+ ions exhibited reduced reactivity and only formation of addition products; DFT calculations revealed “fan” structures for the GSs of the LaC_n^+ ions. The reactions of ScC_n^+ ($n=2-6$) with O_2 had been previously studied using an RF ion trap (Watanabe et al., 1993); the carbide ions were produced by LA of a mixed sample of graphite and scandium. Major product ions were ScO^+ for all ScC_n^+ and ScO_2^+ for ScC_n^+ with odd $n,$ and the estimated rate constants were found to be much lower for species with even $n.$ The observation of small rare earth carbide cations is also common in elemental MS employing laser and spark ionizations, with the intensities of the dicarbide ions of the lanthanides correlating with the dissociation energies of the MC_2 molecules (Becker and Dietze, 1985, 1995, 1997).

Other MS-based techniques have been especially valuable in the study of the structures of metallofullerenes and other metal carbide clusters. The mobility of a gas-phase ion through an inert buffer gas under the influence of a weak electric field depends on the ion’s average collision cross section, which in turn depends on its geometry. This is the basis of the ion mobility measurements that, as developed by Jarrold and coworkers, have unveiled several structural features of metallofullerenes, particularly for the case of lanthanum (Clemmer and Jarrold, 1997; Clemmer et al., 1994a,b; Shelimov and Jarrold, 1996; Shelimov et al., 1994, 1995, 1996). The main findings were the existence of several isomers for the LaC_n^+ metallofullerene ions, depending on the number of carbon atoms, including a variety of isomers in which La is bound to polycyclic polyene rings or to a cage; a minimum size for the fullerene cage to be able to accommodate a lanthanum atom; the spontaneous conversion of ring isomers to the endohedral metallofullerene upon annealing, which indicated that the lanthanum atom acts as a nucleation center; and the formation of dilanthanum fullerenes existing as a mixture of both one and two endohedral lanthanum atoms even though the fullerene cages were large enough to accommodate two lanthanum atoms.

Using a combination of laser vaporization and molecular beam methods with TOF-MS analysis, plus photoionization, photoelectron spectroscopy, and reactions with small molecules for characterization, Kaya and coworkers were able to produce and characterize several intriguing rare earth organometallic clusters with network structures (Nakajima and Kaya, 2000). These studies employed C_{60} as a ligand; the $M-C_{60}$ clusters formed for $M=Sc$ had chain or ring structures in which metal atoms and C_{60} were alternately

connected (Nagao et al., 1998), whereas Eu and Ho could also form pyramidal structures (Nagao et al., 1999). This approach was also used with benzene as a substrate, with which Sc formed multiple-decker sandwich structures (Kurikawa et al., 1999b). Similar extended stacking structures were obtained for COT and lanthanide metal atoms (Ce, Nd, Eu, Ho, and Yb), with MS showing a pattern of peaks corresponding to $[\text{Ln}_n(\text{COT})_{n+1}]^+$ (Kurikawa et al., 1998, 1999a; Miyajima et al., 1999); the Ln-COT clusters were described as consisting of positively charged Ln and negatively charged COT. A direct spectroscopic examination of the structures of these Ln-COT clusters was later performed by Duncan and coworkers through photodissociation experiments with $[\text{Ln}_n(\text{COT})_{n+1}]^+$ ions for Ln = Nd, Sm, and Dy, which provided evidence for sandwich and multiple-decker sandwich structures (Scott et al., 2007).

2.6.2 Actinides

Marçalo et al. (2009) reported that LA of solid samples of UO_3 and $\text{U}_2(\text{NH}_4)_2\text{O}_7$ resulted in a series of negative and positive cluster ions with compositions $[\text{U}_x\text{O}_m]^-$ ($x=2-13$) and $[\text{U}_y\text{O}_n]^+$ ($y=2-9$). The small anion clusters ($x < 5$) exhibit compositions close to $[\text{U}_x\text{O}_{3x}]^-$ in which the average uranium oxidation state is VI, whereas the larger anion clusters exhibit oxygen substoichiometry with compositions closer to $[\text{U}_x\text{O}_{(2.5)x}]^-$ in which the uranium oxidation state is closer to V. The cation clusters generally exhibit lower oxidation states, with a propensity for U(V) in $[\text{U}_y\text{O}_{2y}]^+$. Cationic uranium oxide clusters had been previously observed in several studies using either FAB of uranyl salts (Brown and Ismail, 1990; Jennings et al., 1989; Kemp et al., 1995a) or laser desorption/ionization/LA of uranium oxides and other uranium compounds (Gibson, 1997b, 1999d; Michiels and Gijbels, 1984; Soto-Guerrero et al., 2001; Tench et al., 1991); in one of these earlier studies, a detailed examination of the CID of these clusters was performed (Kemp et al., 1995a). The formation of cationic thorium oxide clusters was also described in two of these reports, one using FAB (Kemp et al., 1995a) and the other LA (Michiels and Gijbels, 1984).

LA of plutonium oxalate resulted in $\text{Pu}_x\text{O}_y(\text{OH})_z^+$ clusters with values of x up to 18 (Gibson and Haire, 2001c). In contrast to uranium oxide clusters, a wide range of oxygen/hydroxide compositions were exhibited, indicating plutonium in oxidation states of III, IV, V, and VI. A “magic number” high-abundance cluster appeared at the composition $\text{Pu}_{16}\text{O}_{22-z}(\text{OH})_z$ ($0 \leq z \leq 4$); speculation as to the structure of this cluster remains to be evaluated. LA of mixtures of plutonium and another metal oxalate resulted in small mixed clusters $\text{M}_x\text{Pu}_y\text{O}_z^+$ ($x+y \leq 3$) where M = La, Ce, U, Sr, or Zr (Gibson and Haire, 2004). The range of observed compositions revealed the comparative stabilities of oxidation states and specifically that Pu(IV) is favored over Ce(IV).

U, Np, and Pu selenide and oxide–selenide molecular and cluster cations were synthesized by LA of dilute mixtures of An oxides in a selenium matrix (Gibson, 1999d); binary ions, AnSe_n^+ , and ternary cluster ions, $\text{An}_x\text{O}_m\text{Se}_n^+$, were observed, with the compositions of the mixed O/Se clusters suggesting the aggregation of AnO_m^+ with Se_n , the presence of Se^{2-} ions in analogy with O^{2-} , or the presence of structures involving O–Se bonding.

LA of the actinides U to Cf embedded in polyimide matrices resulted in small organoactinide ions, providing a distinctive opportunity to probe variations in elementary organometallic chemistry in this region of the periodic table (Gibson, 1997a, 1998a,e; Gibson and Haire, 1999, 2001a). The organoactinide ion product distributions were found to reveal the same correlation with atomic energetics as demonstrated in hydrocarbon activation by An^+ ions, as discussed above. Dominant products were AnC_2^+ for $\text{An}=\text{U}$, Np, Pu, and Cm and AnC_2H^+ for $\text{An}=\text{Am}$, Bk, and Cf. It is presumed that there are two An–C bonds in $\text{An}=(\text{C}_2)^+$ with C_2 in an η^2 side-on bonding configuration and a single An–C bond in $\text{An}-\text{C}\equiv\text{CH}^+$. Accordingly, it is precisely those An^+ that most effectively insert into C–H and C–C bonds that produce predominantly AnC_2^+ and those An^+ that are comparatively inert toward insertion that produce predominantly AnC_2H^+ .

The formation of thorium and uranium carbide ions, AnC_n^+ , with $n=1-6$, has been observed in MS studies involving plasma and thermal ionization sources (Becker and Dietze, 1997; Kraiem et al., 2010). Recently, laser ionization of solid Th and U carbides resulted in molecular actinide carbide clusters as examined by FTICR-MS (Pereira et al., 2013). Intriguing high abundances for both ThC_{13}^+ and UC_{13}^+ and for $\text{Th}_{13}\text{C}_n^+$ were observed, and a disparity between $\text{An}=\text{Th}$ and U in the relative abundances of the bimetallic ions An_2C_3^+ and An_2C_4^+ was apparent and elucidated by DFT-based computations.

Smalley and coworkers (Guo et al., 1992b) used a laser vaporization cluster source, coupled to FTICR-MS, and a UO_2 –graphite mixed sample to produce a series of $\text{U}@C_n$ species, as illustrated in Fig. 20, and reveal the stabilization of C_{28} as $\text{U}@C_{28}$; evidence for the formation of $\text{U}_2@C_n$, beginning with $\text{U}_2@C_{50}$, was also presented. Recently, Marshall, Kroto, and coworkers (Dunk et al., 2012) also used a cluster source and FTICR-MS to reexamine the formation of $\text{U}@C_{28}$ as a dominant species and precursor for larger $\text{U}@C_n$ structures.

2.7 Miscellaneous Studies and Ions

2.7.1 Rare Earths

Freiser and coworkers developed a method to generate by FTICR-MS mixed bimetallic cations via reactions of a bare metal cation with a neutral, volatile transition metal carbonyl like $\text{Fe}(\text{CO})_5$, followed by consecutive CID of the

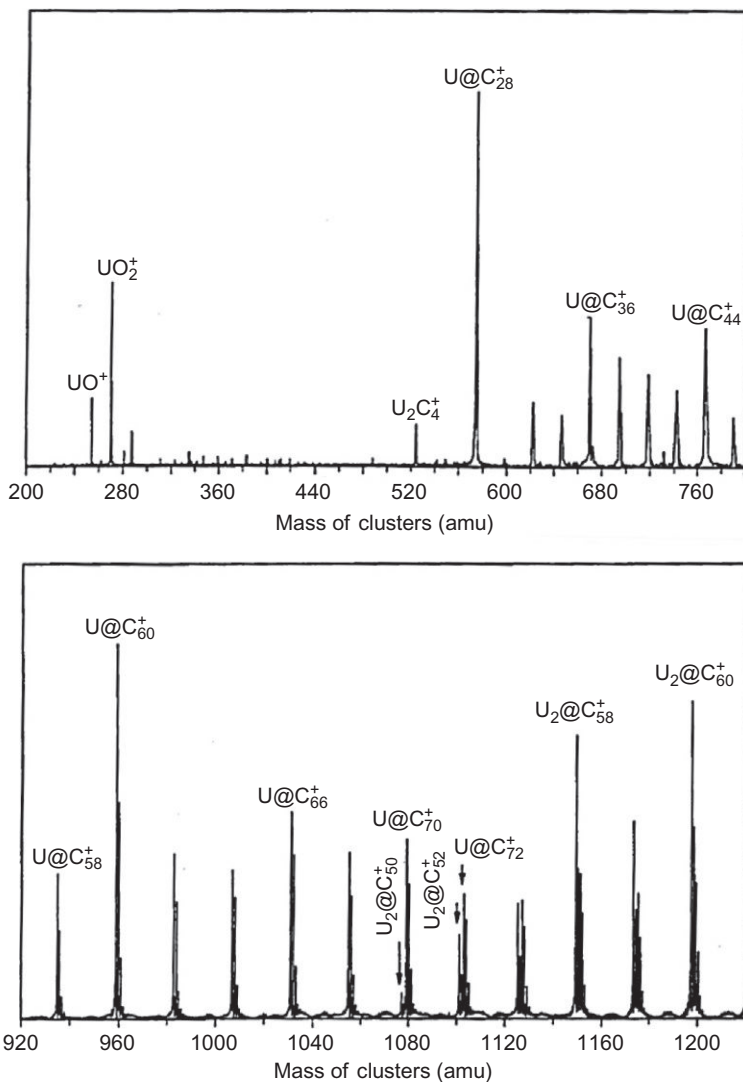


FIGURE 20 FTICR mass spectrum of carbon–uranium cluster cations produced by laser vaporization of a graphite– UO_2 composite disk. Reproduced with permission from Guo *et al.* (1992b). Copyright 1992 American Association for the Advancement of Science.

$\text{MFe}(\text{CO})_{5-x}^+$ product ions. $\text{MFe}^{+/2+}$ ions were produced in this way for the cases of Sc^+ (Lech *et al.*, 1989), La^+ (Huang and Freiser, 1988b), and La^{2+} (Huang and Freiser, 1988a); for the case of Y^+ , there was only mention of these products (Lech *et al.*, 1989). The reactivity of these bimetallic ions with numerous hydrocarbons was examined in detail and compared with the

reactivity of the bare metal ions. Pires de Matos and coworkers later used FTICR-MS to extend this approach to all the Ln series cations (Vieira et al., 2001). The observed primary products of the reactions with $\text{Fe}(\text{CO})_5$ were of the type $\text{LnFe}(\text{CO})_x^+$ (Ln=La, Ce, Pr, Nd, Gd, Tb: $x=3$; Ln=Ho, Er, Lu: $x=3, 4$; and Ln=Sm, Eu, Dy, Tm, Yb: $x=4$), and LnFe^+ species could be obtained in all cases by CID of the primary product ions; the product distributions and the reaction efficiencies obtained in kinetics studies revealed a close relation with the relative stability of the accessible formal oxidation states of the lanthanide cations. In this same work, the reactivity of the Ln^+ cations with ferrocene, $\text{Fe}(\text{C}_5\text{H}_5)_2$, was also investigated in another quest for the formation of Ln—Fe bonds; however, the majority of the Ln^+ cations reacted by metal exchange, yielding the biscyclopentadienyl ions $\text{Ln}(\text{C}_5\text{H}_5)_2^+$, while the less reactive Ln^+ cations, Sm^+ , Eu^+ , Tm^+ , and Yb^+ , formed the adduct ions $\text{LnFe}(\text{C}_5\text{H}_5)_2^+$, the nature of which was established based on CID experiments that mostly showed the loss of neutral ferrocene. Interestingly, these rather “exotic” reagents revealed trends in the reactivity of the Ln^+ cations with strong similarities to the reactivity trends observed with simple organic and inorganic molecules, as described in previous sections.

Other fragmentation studies of metal ion complexes have also led to new species with new types of bonding. CID experiments with $\text{M}(\text{NO}_3)_4^-$ ions, generated by ESI for $\text{M}=\text{Sc}$ and Y , were performed in a tandem MS of quadrupole–octupole–quadrupole geometry (Li et al., 2003). The main observed fragmentations corresponded to NO_2 elimination, with consecutive formation of $\text{MO}(\text{NO}_3)_3^-$ and $\text{MO}_2(\text{NO}_3)_2^-$ ions; in these oxo species, one of O atoms can probably be presented as ionic O^- or radical O^\bullet , such that Sc and Y retain their very stable +3 oxidation states.

A rather peculiar rare earth ion chemistry topic is the behavior of these metals in flames; different ionization mechanisms may occur in different flames (hydrocarbon, $\text{H}_2\text{—O}_2\text{—N}_2$, $\text{H}_2\text{—O}_2\text{—Ar}$, etc.), which can include chemical ionization by H_3O^+ , thermal (collisional) ionization, and chemi-ionization. The experiments mainly involve MS detection and modeling of the neutral and ionic species present. Goodings and coworkers have investigated for several years the behavior of a number of rare earth elements, namely, Sc, Y, and a few Ln, in various flames (Chen and Goodings, 1998, 1999; Chow and Goodings, 1995; Goodings et al., 1988, 1994; Guo and Goodings, 2002a,b; Patterson and Goodings, 1995, 1996). The specific process of chemi-ionization in oxidation has been examined by Dyke and coworkers for several Ln metals (Cockett et al., 1989, 1990, 1991a,b).

Another particular but interesting observation of new rare earth ionic species has been made in the ion sources of elemental analytic MS instruments. Rare earth argide ions, MAr^+ , have been detected in plasma MS (ICP-MS, LA-ICP-MS, and glow discharge mass spectrometry (GD-MS)), with the

intensity of these species being of the order of a few per cent in GD-MS (Becker et al., 1996). A correlation between the intensities of the metal argide ions and the bond dissociation energies of diatomic ions was revealed, and the distribution of diatomic argide ions of the lanthanides in ICP-MS was found to be comparable to the distribution of lanthanide oxide ions.

In elemental MS, ion chemistry does not occur only in the ion sources. The use of collision/reaction cells in ICP-MS, with the purpose of resolving or eliminating isobaric interferences through chemical reactions, has led to the exploration of differences in reactivity of metal cations of interest and has been interrelated with fundamental studies of gas-phase reactivity. One of the motivations for the comprehensive work of Bohme's group, described in previous sections, was the identification of reagents that can help resolve interferences in ICP-MS. The significant differences in reactivity of the lanthanide series cations with several small molecules may be used for chemical separation, with separation factors that contrast with generally much less efficient solution-based separations for ions in the same oxidation state. In solution, there is a statistical distribution among chemical states as determined by the equilibrium constant, that is, ΔG . In contrast, bimolecular gas-phase reactions must be exothermic or thermoneutral to occur, that is, $\Delta H \leq 0$, with the result that the use of a gas-phase reaction that is exothermic for one metal ion and endothermic for another can readily provide enormous separation factors, hypothetically infinite, between the two metal ions. This separation approach can be readily applied in mass spectrometric analysis but is not practical for bulk separations due to low throughput. A few comprehensive reviews of the topic by practitioners of the field are available (Bandura et al., 2006; Olesik and Jones, 2006; Tanner et al., 2002), and there, one can find specific references to the use of some of the ion/molecule reactions described in previous sections for analytic purposes.

Another potential analytic application of gas-phase metal-ion chemistry was suggested by Freiser and coworkers but apparently as yet with no practical consequences. Pattern recognition methods were used to evaluate and demonstrate the efficacy of the rare earth metal ions Sc^+ , Y^+ , and La^+ as chemical ionization reagents for molecular MS; a large number of organic molecules were examined by FTICR-MS, comprising six classes: alkanes, alkenes, ketones, aldehydes, ethers, and alcohols (Forbes et al., 1986a,b, 1987).

On the other extreme of the spectrum, as compared to the above applications, recent ion mobility experiments in Ar with several lanthanides (Eu^+ , Gd^+ , Tb^+ , Dy^+ , Ho^+ , and Yb^+) open up the possibility of examining intrinsic effects of the electronic configurations on the interactions with neutral species (Laatiaoui et al., 2012). The results indicated that Gd^+ had a lower mobility than the remaining Ln^+ that was attributed to the occupation of a d-orbital instead of an f-orbital in its GS. This is an interesting extension of the seminal

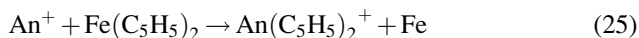
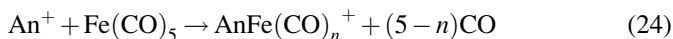
work performed by Bowers and coworkers in the early 1990s on metal ion chromatography (Bowers et al., 1993; Kemper and Bowers, 1991).

2.7.2 Actinides

In view of the central role of the uranyl moiety in actinide chemistry, there has been a special effort to synthesize and characterize species that are isoelectronic with uranyl. Heinemann and Schwarz (1995) produced the UN^+ ion by the reaction of U^+ with N_2O ; the reaction of UN^+ with O_2 , CO_2 , SO_2 , and COS resulted in $[\text{NUO}]^+$, a monopositive ion isoelectronic with dipositive UO_2^{2+} . The computed electronic structures of UO_2^{2+} and $[\text{NUO}]^+$ are similar, with the latter exhibiting lesser stabilization due to relativistic effects.

A route to actinide–transition metal bonding is LA of alloys of actinides and transition metals. Using this approach, Marçalo and coworkers prepared the following binary intermetallic ions: ThPt^+ , PaPt^+ , UPt^+ , NpPt^+ , PuPt^+ , AmPt^+ , CmPt^+ , UAu^+ , and UIr^+ (Santos et al., 2006a). A study of the uranium–transition metal cations, UM^+ , with C_2H_6 , indicated no reactivity. This is in contrast to the bare M^+ , which dehydrogenate ethane, and reveals that the $\text{An}-\text{M}$ bonding “shuts off” the transition metal ion reactivity. Based on the theoretical prediction that Ir is chemically analogous to N, it follows that $[\text{IrUO}]^+$ should be isoelectronic with $[\text{NUO}]^+$ and UO_2^{2+} (Gagliardi and Pyykkö, 2004). The $[\text{IrUO}]^+$ ion was synthesized by the oxidation of $[\text{IrU}]^+$ using N_2O . The inert character of $[\text{IrU}]^+$ is consistent with a triple $\text{Ir}\equiv\text{U}$ bond and the prediction that $[\text{Ir}\equiv\text{U}=\text{O}]^+$ is indeed isoelectronic with $[\text{N}\equiv\text{U}=\text{O}]^+$ and $[\text{O}=\text{U}=\text{O}]^{2+}$ (Gagliardi and Pyykkö, 2004).

Reactions of Th^+ and U^+ with iron pentacarbonyl, $\text{Fe}(\text{CO})_5$, and ferrocene, $\text{Fe}(\text{C}_5\text{H}_5)_2$, produced $\text{AnFe}(\text{CO})_{2,3}^+$ and $\text{An}(\text{C}_5\text{H}_5)^+$ according to reactions (24) and (25) (Vieira et al., 2001):



The actinide/iron carbonyl complexes can be considered as partially ionic $[\text{An}]^{3+}[\text{Fe}(\text{CO})_3]^{2-}$ and $[\text{An}]^{4+}[\text{Fe}(\text{CO})_2]^{3-}$, in which there is $\text{An}-\text{Fe}$ bonding as evidenced by CID elimination of CO molecules to ultimately yield AnFe^+ . These reactions thus provided a route to actinide–transition metal bonding. In the reactions with $\text{Fe}(\text{C}_5\text{H}_5)_2$, the actinide ion replaces the iron atom to produce the An^{III} cyclopentadienylide complexes, $[\text{An}]^{3+}[(\text{C}_5\text{H}_5)_3]^{2-}$, providing a new route to actinide metallocenes. The ThO^+ and UO^+ ions reacted with $\text{Fe}(\text{CO})_5$ to yield formally $[\text{ThO}]^{2+}[\text{Fe}(\text{CO})_4]^-$, $[\text{UO}]^{3+}[\text{Fe}(\text{CO})_3]^{2-}$, and $[\text{ThO}]^{3+}[\text{Fe}(\text{CO})_3]^{2-}$; the formal oxidation state of Th(V) in the last of these species indicates that the purely ionic bonding scenario is not valid. The stable

UO_2^+ ion produced only the adduct, $[\text{UO}_2]^+[\text{Fe}(\text{CO})_5]$. Additional reactions of ligated Th and U cations with the two iron complexes were also reported (Vieira et al., 2001).

In the above experiments, no evidence was obtained for the bonding of carbonyl to Th or U. Recently, Ricks et al. (2010) were able to produce uranium and uranium dioxide carbonyl cations by laser vaporization of uranium metal coincident with carbon monoxide gas pulses and study them with mass-selected-ion IR spectroscopy in the C—O stretching region. The mass spectra presented in Fig. 21 illustrate the formation of complexes containing up to 10–15 CO ligands bound to U^+ , UO^+ , or UO_2^+ ions; the ions contain both strongly bound ligands and weakly bound “excess” ligands that condense because of the cold supersonic beam conditions. Dissociation patterns, spectra, and quantum chemical calculations established that the abundant

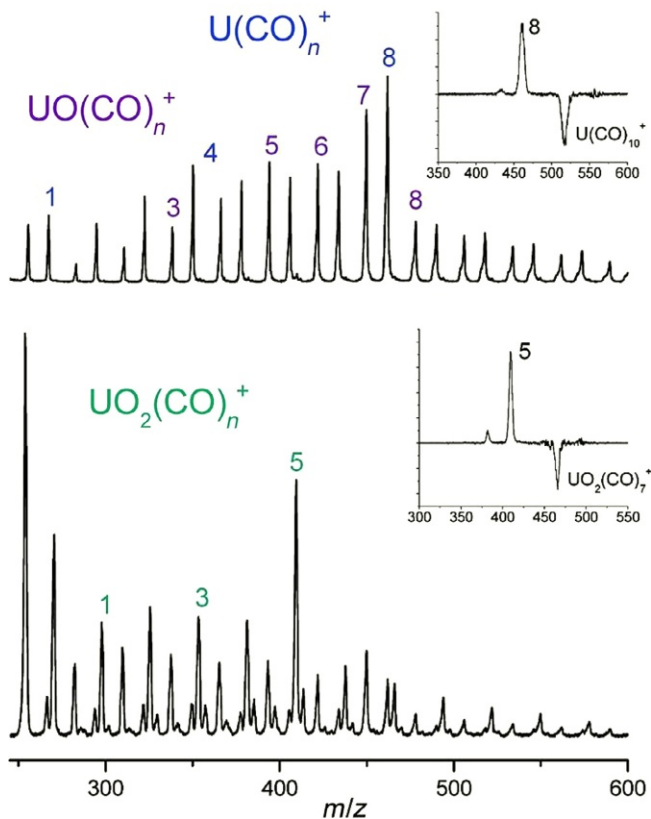


FIGURE 21 Mass spectra of U^+ ($n=1, 4, 8$), UO^+ ($n=3, 5, 6, 7, 8$), and UO_2^+ ($n=1, 3, 5$) carbonyl ions. The insets show representative fragmentation of clusters with second-shell coordination, as examined by photodissociation experiments. *Reproduced with permission from Ricks et al. (2010). Copyright 2010 American Chemical Society.*

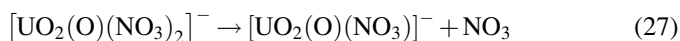
$\text{U}(\text{CO})_8^+$ and $\text{UO}_2(\text{CO})_5^+$ species corresponded to fully coordinated ions with D_{4d} square antiprism and D_{5h} pentagonal bipyramid structures, respectively; $\text{U}(\text{CO})_8^+$ appears to be the first example of an eight-coordinate homoleptic carbonyl. The authors used the same methodology to produce and characterize UO_4^+ and UO_6^+ cations (Ricks et al., 2011). UO_4^+ was found to have a central UO_2 core with an additional η^2 -coordinated oxygen molecule, with the character of a $\text{UO}_2^{2+}-\text{O}_2^-$ ion pair; UO_6^+ presented the same core structure, with an additional weakly bound oxygen molecule with η^1 coordination.

Neutral uranium tetraborohydride, $\text{U}(\text{BH}_4)_4$, which can be envisioned as $\text{U}(\text{IV})$ coordinated by four BH_4^- ligands, is of interest as a volatile uranium compound that could serve as a source of U atoms due to the relatively weak binding of the BH_4 ligands; its ionization/fragmentation behavior has accordingly been examined by electron impact (Armentrout and Beauchamp, 1979) and electron transfer to He^+ (Babcock et al., 1984a), with both approaches providing similar results. Dominant processes upon energetic ionization of $\text{U}(\text{BH}_4)_4$ are formal loss of neutral BH_4 ligands, which are of inherently low stability toward the loss of a H atom to produce the stable BH_3 molecule. Accordingly, the especially high intensity of $\text{U}(\text{BH}_4)_2^+$ at large fragmentation energies is attributed to the stability of the neutral $\text{B}_2\text{H}_6 + \text{H}_2$ products. The uranocene complex in which uranium(IV) is coordinated by two cyclooctatetraenyl anion ligands, $\text{U}(\text{C}_8\text{H}_8)_2$, was similarly ionized by transfer of an electron from the complex to He^+ , a process that is exothermic by ~ 18 eV (Babcock et al., 1984b). The resulting fragmentation of the energetic cation complex produced primarily the half-sandwich cation complex $[\text{U}(\text{C}_8\text{H}_8)]^+$ by the loss of a C_8H_8 ligand and the complex $[\text{U}(\text{C}_6\text{H}_6)]^+$ by the loss of C_8H_8 and C_2H_2 , both of which correspond to primary pathways for electron impact ionization of C_8H_8 .

As discussed above, bare U^+ is substantially more reactive toward hydrocarbon activation than is oxo-ligated UO^+ . Duncan and coworkers demonstrated that the uranium metal center plays a similar role in bond activation in complexes of benzene with bare and oxo-ligated uranium cations (Pillai et al., 2005). Photodissociation of the cation complex $[\text{U}(\text{C}_6\text{H}_6)]^+$ resulted in both ligand loss and fragmentation to produce $[\text{U}(\text{C}_2\text{H}_2)]^+$ and $[\text{U}(\text{C}_4\text{H}_2)]^+$, whereas $[\text{U}(\text{C}_6\text{H}_6)_{2,3}]^+$ exhibited only the elimination of intact ligands to give $[\text{U}(\text{C}_6\text{H}_6)]^+$. Both $[\text{UO}(\text{C}_6\text{H}_6)]^+$ and $[\text{UO}(\text{C}_6\text{H}_6)_2]^+$ exhibit only ligand loss to give UO^+ , such that the oxo ligand in the complex has rendered the uranium metal center inert toward the activation of coordinated benzene, in direct analogy with reactions of hydrocarbons with U^+ and UO^+ . The results for $[\text{U}(\text{C}_6\text{H}_6)_{1-3}]^+$ suggest that U^+ —benzene bonding, like the U^+ —O bond, renders the uranium metal center inert.

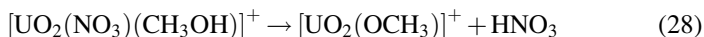
CID of metal nitrate complexes provides opportunities for rich redox chemistry both at the metal center and at oxygen ligands due to the possibility

for the loss of the stable NO_2 molecule. In the case of uranyl nitrate anion complexes, the CID fragmentation pathways given by Eqs. (26) and (27) have been reported (Pasilis et al., 2006):



For uranium, it is valid to assume that oxidation states above U(VI) are inaccessible so that the O-atom ligand in the product of Eq. (26) is presumably O^- and that it in the product of Eq. (27) is presumably O^{2-} . These results with uranyl illustrate the utility of the NO_3^- ligand as a source of O atoms in CID. These studies should be extended to transuranium actinides, specifically NpO_2^{2+} and PuO_2^{2+} , where higher oxidation states may be accessed by replacement of NO_3^- by O^{2-} .

CID experiments of $[\text{UO}_2(\text{NO}_3)_3]^-$, $[\text{UO}_2(\text{ClO}_4)_3]^-$, or $[\text{UO}_2(\text{CH}_3\text{COO})_3]^-$ ions in a Q-TOF instrument produced fragmentations equivalent to the ones depicted by Eqs. (26) and (27), with subsequent CID eventually leading to UO_4^- ions (Sokalska et al., 2010). In cationic nitrate complexes with a neutral alcohol ligand, CID elimination of HNO_3 can result in alkoxides, such as the methoxide and ethoxide products in Eqs. (28) and (29) (Van Stipdonk et al., 2003):



Uranyl ethoxides and propoxides produced by HNO_3 elimination exhibited sequential CID chemistry corresponding to the elimination of alkenes as in Eqs. (30) and (31) (Van Stipdonk et al., 2003):

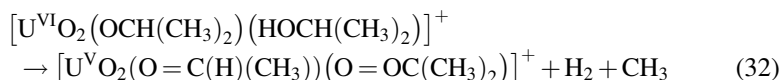


In the sequence given by Eqs. (29) and (30), the NO_3^- ligand and the uranyl metal center facilitate the conversion of ethanol to ethylene.

The $[\text{UO}_2\text{X}(\text{H}_2\text{O})_3]^+$ ($\text{X} = \text{Cl}^-, \text{Br}^-, \text{I}^-, \text{ClO}_4^-$) complexes were subjected to CID with a goal of producing $[\text{UO}_2\text{X}]^+$ by water elimination (Anbalagan et al., 2004). Although the anticipated uranyl bromide and perchlorate complexes were produced, HX elimination resulted in $[\text{UO}_2(\text{OH})]^+$ for $\text{X} = \text{Cl}$ or I . The result that the intermediate halide Br should behave differently than Cl and I was rationalized based on the propensities for intracomplex proton transfer in the $[\text{UO}_2\text{X}(\text{H}_2\text{O})]^+$ species, which it was inferred could be diminished for $\text{X} = \text{Br}$ based on the relative PAs of the three neutral UO_2X_2 molecules. CID of the $[\text{UO}_2\text{X}(\text{HOR})]^+$ ($\text{R} = \text{CH}_3$ or C_2H_5) complexes resulted in enhanced HX elimination with the formation of the alkoxides, $[\text{UO}_2(\text{OR})]^+$.

This latter result may be related to the relative acidities of the alcohols and/or stronger binding of the alkoxide ligands to uranyl.

The reduction of uranyl(VI) to uranyl(V) presents the possibility for the oxidation of ligands under energetic CID fragmentation conditions. [Van Stipdonk et al. \(2004b\)](#) demonstrated the oxidation of 2-propanol to acetone, concomitant with the reduction of U(VI) to U(V) in sequential CID of the uranyl(VI) propoxide complex, $[\text{UO}_2(\text{OCH}(\text{CH}_3)_2)(\text{HOCH}(\text{CH}_3)_2)]^+$, from which H_2 and then CH_3 were eliminated according to the net reaction given by Eq. (32):



CID of the uranium complex product of Eq. (32) first eliminates the acetaldehyde ligand and then the more strongly bound acetone ligand to give bare UO_2^+ . The mechanism of this net reaction was not fully elaborated but was confirmed by deuterium substitution. That this process does not occur for the corresponding Ni^{2+} , Co^{2+} , Pb^{2+} , or Ca^{2+} complexes substantiates the key role of the reduction of uranyl(VI) to uranyl(V), showing a correlation of gas-phase redox chemistry with the utility of solid uranium oxides as redox-active catalytic substrates.

The fragmentation of complexes can provide routes to new types of bonding and ligation. A recent example is the formation of a uranyl- SO_2 complex by CID of a uranyl(V) sulfinate complex (Eq. 33) ([Gong and Gibson, 2013](#)):



Both the SO_2CH_3^- and the radical $^*\text{SO}_2^-$ ligands exhibit bidentate $\eta^2\text{-O}_2$ binding to the uranyl center in the equatorial plane, a novel bonding motif for uranyl. The loss of CH_3 from the uranyl complex contrasts with the loss of SO_2 from the $[\text{Cu}(\text{SO}_2\text{CH}_3)_2]^-$ complex to produce the organometallic $[\text{Cu}(\text{SO}_2\text{CH}_3)(\text{CH}_3)]^-$ ion, a difference that can be attributed to the more oxophilic character of uranium. The SO_2 ligand is spontaneously replaced by O_2 concomitant with oxidation of uranium, Eq. (34):

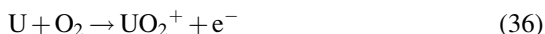


In the peroxide product complex of Eq. (34), the oxygen is η^2 side-on bonded to uranium. The observed spontaneous replacement of SO_2 by O_2 is computed to be exothermic by only 18 kJ mol^{-1} .

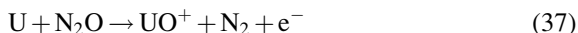
A means to deposit energy in multiply charged cation complexes is by the exothermic addition of an electron. The technique of electron transfer dissociation (ETD) employs as an electron donor the polycyclic aromatic hydrocarbon fluoranthene anion, $\text{C}_{16}\text{H}_{10}^-$, the electron binding energy for which is only $\sim 0.6 \text{ eV}$. An important characteristic of ETD when applied to metal ion complexes is that the process results in both charge reduction and chemical reduction. ETD of $[\text{An}^{\text{VI}}\text{O}_2(\text{CH}_3\text{C}(\text{O})\text{CH}_3)_4]^{2+}$ and $[\text{An}^{\text{VI}}\text{O}_2(\text{CH}_3\text{CN})_4]^{2+}$

resulted in the loss of two or more ligands ($L = \text{acetone}$ or acetonitrile) to produce $[\text{An}^{\text{V}}\text{O}_2(\text{L})_{0,1,2}]^+$ (Rios et al., 2011a). The bis-ligated uranyl(V) products added O_2 to produce the superoxides $[\text{U}^{\text{VI}}\text{O}_2(\text{O}_2)(\text{L})_2]^+$, whereas the plutonyl(V) complex exhibited only water addition with no change in oxidation state, reflecting the higher Pu(VI/V) redox potential. Due to the accessibility of the actinyl(V) oxidation states, ETD of actinyl(VI) complexes does not exhibit extraordinary chemistry, with ligand loss as the primary process. In contrast, the application of this approach to Th(IV) complexes, for example, would be expected to result in more distinctive fragmentation processes because the resulting Th(III) oxidation state is inherently unstable.

The chemi-ionization reactions given by Eqs. (35) and (36) were reported and characterized by Fite et al. (Fite and Irving, 1972; Fite et al., 1974):



As a result of the strong binding between U and O, and the low ionization energies of UO and UO_2 , these reactions are substantially exothermic, by greater than 200 kJ mol^{-1} , and proceed spontaneously under low-energy conditions. Associative reactions between U and O_2 proceed at approximately the collisional rate, but the chemi-ionization processes account for only $\sim 1\%$ of the products, with neutral $\text{UO} + \text{O}$ as the dominant products. In the case of the reaction of U and O, where no neutral channel is accessible, the chemi-ionization process proceeds with a rate close to the collisional limit. Dyke et al. (1988) studied the chemi-ionization reaction of U with O_2 (Eq. 36) and that of U with N_2O , Eq. (37), by chemielectron spectroscopy:



Because N_2O is an even more facile O-atom donor than O_2 — $D(\text{N}_2\text{O}) = 167 \text{ kJ mol}^{-1}$ versus $D(\text{O} - \text{O}) = 498 \text{ kJ mol}^{-1}$ —Eq. (37) is more exothermic than Eq. (35). The quite different chemielectron spectra for Eqs. (35) and (36) were employed to derive potential energy surfaces for the two processes.

A general challenge in gas-phase chemistry is to produce small multiply charged molecular cations, particularly those that are thermodynamically stable rather than metastable. Cations comprising an actinide are promising candidates due to the low ionization energies of the actinides, a characteristic employed to produce the Th^{4+} complex discussed above (Gong et al., 2013). With a focus on smaller molecular ions, Schröder et al. (1999) proposed and demonstrated the existence of UF^{3+} as an example of such a multiply charged species, the stability of which was predicted due to the moderate ionization energies of uranium, and the high ionization of fluorine along with its propensity to form strong polarized covalent bonds to metals. The UF^{3+}

ion was produced by charge stripping of UF^{2+} whereby the dication is ionized by high-energy collisions with inert gas atoms. A key conclusion of this work is that UF^{3+} is a thermodynamically stable trication, not metastable toward Coulomb explosion to yield U^{2+} and F^+ . This inherent stability is a result of the modest ionization energies of U and the favorable U—F bonding interactions. This conclusion is all the more remarkable given that the formal charge on uranium in UF^{3+} is +3.4 due to the electron-withdrawing fluorine ligands.

As a counterpart to the previous fundamental study, it should be stressed that, as indicated above for the lanthanides, the exploration of the differences in reactivity of metal cations has found direct applications in elemental MS with the generalized use of collision/reaction cells in ICP-MS for the resolution of isobaric interferences. In the case of the actinides, and as described in previous sections, differences in reaction efficiencies can provide large mass separations for such important isobaric nuclides as $^{238}\text{U}/^{238}\text{Pu}$ and $^{241}\text{Pu}/^{241}\text{Am}$. The measured oxidation efficiency of U^+ with CH_2O is at least 500 times greater than that of Pu^+ so that $^{238}\text{U}^+$ can be oxidized to produce primarily $^{238}\text{UO}^+$ at mass 254, while $^{238}\text{Pu}^+$ remains essentially unreacted. Similarly, the use of NO as the oxidant would result in more efficient oxidation of Pu^+ versus Am^+ by at least a factor of 170 based on the experimentally determined reaction rate limit for Am^+ . It should be emphasized that these are only lower limits to the separation factors because the studied oxidation reactions of Pu^+ with CH_2O , and of Am^+ with NO, were below the experimental detection limits. Thermodynamic considerations reveal that the oxidation of Pu^+ by CH_2O , and of Am^+ by NO, is substantially endothermic such that these reactions should not occur under thermal conditions; accordingly, the actual achievable separation factors are ideally infinite and realistically should be much greater than $1000\times$. Fluorination is also a relatively straightforward means to separate isobaric actinides for analysis using reaction thermodynamics. Using an F-atom donor, XF, with a $D(\text{X}-\text{F})$ BDE that is intermediate between those for two metal fluoride ions, it is possible to simultaneously oxidize actinides to different oxidation states, as, for example, to $^{238}\text{UF}_5^+$ (mass 333) and $^{238}\text{PuF}_4^+$ (mass 314) or to $^{241}\text{PuF}_3^+$ (mass 295) and $^{241}\text{AmF}_2^+$ (mass 279). Some of the fundamental results involving An ions, described in the previous sections, have effectively been put to practice in analytic studies by ICP-MS, as referenced in comprehensive reviews of the field (Bandura et al., 2006; Olesik and Jones, 2006; Tanner et al., 2002).

Like in the case of the previous subsection on rare earths, a long jump from applications to fundamental studies is taken to close this section. Drift-time measurements in an argon-filled buffer gas cell related ion mobility with ionic size for plutonium and americium singly charged cations and for plutonium metal and oxide ions (Backe et al., 2005); these experiments are part of highly demanding investigations of the electronic properties of late actinides and transactinides.

3 ENERGY OF KEY SPECIES

The determination of gas-phase ion thermochemistry has closely accompanied ion chemistry experiments. As indicated in [Section 1](#), gas-phase experiments provide direct relationships between the electronic structures of reactants and the energetics of reactions. Additionally, information about neutral species can be obtained from ion chemistry measurements. Besides generating fundamental data on ionic and neutral species, ion thermochemistry is of great practical importance to MS. It is a consolidated field and the experimental techniques were comprehensively reviewed by Ervin some 10 years ago ([Ervin, 2001](#)). Reviews on the more specific topic of organometallic ion thermochemistry are available ([Martinho Simões and Beauchamp, 1990](#); [Operti and Rabezzana, 2003](#)). Several compilations and overviews of the thermodynamics of ions, including those of the rare earths and actinides, are available, some dedicated (incidentally, most dealing with the actinides), some of a more general nature, sometimes including also the thermodynamics of related neutral species ([Chandrasekharaiah and Gingerich, 1989](#); [Hildenbrand et al., 1985](#); [Konings et al., 2006](#); [Lias et al., 1988](#); [Luo, 2007](#); [Morss, 1994](#); [Schofield, 2006](#)). The annually revised *CRC Handbook of Chemistry and Physics* (the 94th edition was published in 2013; this is also available online at <http://www.hbcpnetbase.com/>) also contains a great deal of relevant information. Last but not least, the NIST online database at <http://webbook.nist.gov> contains a wealth of thermodynamic data and is a key, convenient source ([Linstrom and Mallard, 2013](#)). The classic field of high-temperature MS, specifically the Knudsen effusion method coupled to the MS study of vaporization products of inorganic compounds, has contributed significantly to the known thermodynamics of gaseous neutral species.

3.1 Rare Earths

Many bond dissociation energies have been determined by the GIB-MS technique developed by Armentrout and coworkers since the early 1980s ([Ervin and Rodgers, 2013](#)). The methods have included threshold energy measurements of both endoergic bimolecular reactions and endoergic CID as a function of the reactant kinetic energy ([Armentrout, 2002](#)). These experiments have yielded a large, accurate database in particular for metal ions, which include metal hydrides, metal methyls, metal carbonyls, metal oxides, metal sulfides, metal amides, and other systems ([Armentrout, 2003](#); [Armentrout and Kickel, 1996](#); [Rodgers and Armentrout, 2000](#)). Sc, Y, La, and Lu are the rare earths that have been examined by Armentrout and coworkers, and [Table 8](#) presents a selection of bond dissociation energies of the monocationic species. Periodic trends in the bond energies for the transition metals were uncovered and assessed in terms of the atomic electronic configurations and PEs, and this was an early seminal contribution of Armentrout and

Beauchamp (Armentrout, 1990, 2003; Armentrout and Beauchamp, 1989; Armentrout and Clemmer, 1992; Armentrout and Georgiadis, 1988; Armentrout and Kickel, 1996; Armentrout et al., 1981, 1989; Kretzschmar et al., 2001). Some of these trends/correlations are illustrated by the examples presented in Figs. 22 and 23: in the former, the first-row (including Sc^+) and the second-row (including Y^+) transition metal ion hydride bond energies are plotted as a function of the atomic metal ion PE to an s^1d^n spin-decoupled state; in the latter, the bond energies of Sc^+ to isoelectronic series of ligands, CH_3 , NH_2 , and OH or CH_2 , NH , and O , are plotted as a function of the number of electron lone pairs on the ligands or the presumed bond order.

In the case of the lanthanide cations, and apart from the values for La^+ and Lu^+ in Table 8, dissociation energies for the whole series are available for Ln^+ —oxygen and Ln^+ —halide bonds, as evaluated by Chandrasekharaiah and Gingerich (1989) and Kaledin et al. (1999), respectively, mostly based on high-temperature MS results. The Ln^+ —O and Ln —O dissociation energies were assessed by Gibson (2003), based on correlations with the electronic structures and energetics of the isolated metal atoms and ions. The intriguing conclusion was that the bonding between the Ln metal cation or atom and oxygen requires two unpaired valence 5d electrons and not one 6s and one 5d, as illustrated in Fig. 24 where the $D(\text{Ln}^+—\text{O})$ are plotted as a function of the PEs of the Ln^+ cations from the GS to the lowest $5d^2$ and $5d^16s^1$ configurations.

Some final references to other examples of MS-based energetics determinations involving rare earth cations are the following: Freiser and coworkers employed photodissociation to measure metal ion—ligand bond dissociation energies in singly and doubly charged organometallic ions that included Sc, Y, and La (Hettich and Freiser, 1987; Ranasinghe and Freiser, 1992; Ranasinghe et al., 1992); Jackson et al. examined the effects of bond strength and mass in the determination of $\text{M}^+—\text{O}$ dissociation energies by CID in a QIT for Y^+ and several Ln^+ (Jackson et al., 2002b); and charge-stripping experiments in sector instruments were used to determine bond energies in doubly charged Sc hydroxide cations (Dai et al., 1995; McCullough-Catalano and Lebrilla, 1993) and the second ionization energies of LaO and LaOH (Schröder et al., 2000a).

3.2 Actinides

Knowledge of thermodynamic properties of even small elementary actinide molecular ions (and neutral species) are severely limited, particularly for the actinides other than Th and U. Some reported bond dissociation energies have been noted in the preceding sections; the focus here is on the few systematic studies of actinide molecular ion thermochemistry. The most comprehensive set of experimental results are available for actinide monoxides and dioxides for Th through Cm, with little additional data available since the 2009 evaluation by Marçalo and Gibson (2009); the derived bond dissociation enthalpies

TABLE 8 Bond Dissociation Energies $D_0(M^+-X)$ of Monopositive Rare Earth Cations, as Determined by Armentrout and Coworkers^a

M	M ⁺ -H	M ⁺ -CH ₃	M ⁺ -CH ₂	M ⁺ -NH ₂	M ⁺ -NH	M ⁺ -OH	M ⁺ -O	M ⁺ -S
Sc	235 ± 9	233 ± 10	402 ± 23	347 ± 5 ^b	483 ± 10 ^b	499 ± 9 ^c	689 ± 6	480 ± 5
Y	256 ± 8	236 ± 5	388 ± 13	–	–	–	699 ± 17	530 ± 8
La	239 ± 9	217 ± 15	401 ± 7	–	–	–	–	–
Lu	204 ± 15	176 ± 20	–	–	–	–	–	–

^aValues in kJ mol^{-1} from Armentrout (2003) except where indicated.

^bArmentrout and Kickel (1996).

^cClemmer et al. (1993).

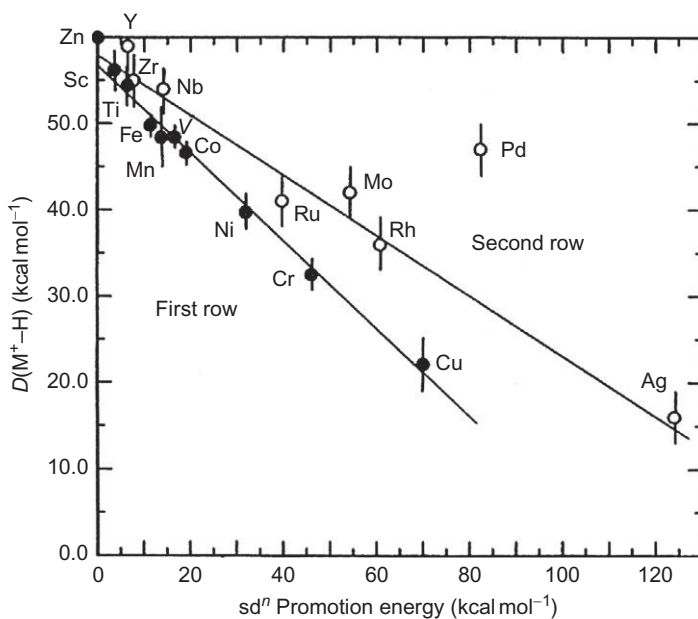


FIGURE 22 First-row (closed symbols) and second-row (open symbols) transition metal ion hydride bond energies versus the atomic metal ion promotion energy to an sd^n spin-decoupled state; the lines are linear regression fits to the first- and second-row data excluding Pd. *Reproduced with permission from Armentrout and Georgiadis (1988). Copyright 1988 Elsevier.*

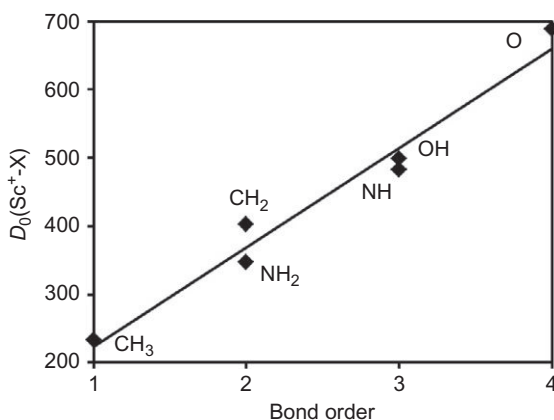


FIGURE 23 Plot of Sc^+-X bond dissociation energies as a function of the presumed bond order, following Armentrout and Clemmer (1992); the BDE data (in $kJ\ mol^{-1}$) are from Table 8.

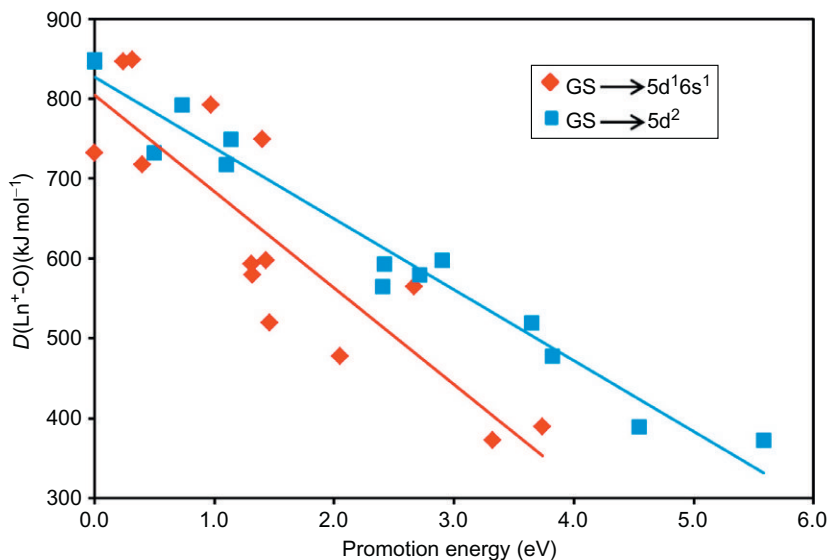


FIGURE 24 Plot of $D(\text{Ln}^+-\text{O})$ from Chandrasekharaiah and Gingerich (1989) as a function of the promotion energies of the Ln^+ cations from the ground state to the lowest $5d^2$ (blue squares (light gray in print); linear fit $R^2=0.96$) and $5d^16s^1$ (red diamonds (dark gray in print); linear fit $R^2=0.76$) configurations from Table 1. The $D(\text{Ln}^+-\text{O})$ values (in kJ mol^{-1}) are the following: La 847; Ce 849, Pr 792, Nd 749, Sm 565, Eu 389, Gd 732, Tb 718, Dy 593, Ho 598, Er 579, Tm 478, Yb 372, and Lu 520.

are compiled in Table 9. The average bond dissociation enthalpies for the AnO_2 , AnO_2^+ , and AnO_2^{2+} are presented graphically in Fig. 25. With the distinct exception of $\text{ThO}_2^{+/2+}$, in which the *formal* oxidation states are unstable Th(V/VI), the An—O bond energies generally decrease across the series, with maxima for $\text{Pa}^{\text{V}}\text{O}_2^+$ and $\text{U}^{\text{VI}}\text{O}_2^{2+}$. This is in accord with predictions based on the actinide atomic electronic structures and energetics; these predictions furthermore provide estimates for oxide bond energies for the actinides beyond Cm (Gibson, 2003).

A key fundamental property of small molecules is the IE, which allows thermodynamic properties of neutral species to be derived from those of cations, and vice versa. Only a few actinide molecular ionization energies have been accurately measured by spectroscopic techniques, specifically by Heaven and coworkers: $\text{IE}(\text{UO})=6.03107 \pm 0.00003 \text{ eV}$ (Goncharov et al., 2006), $\text{IE}(\text{UO}_2)=6.127 \pm 0.001 \text{ eV}$ (Merritt et al., 2008), $\text{IE}(\text{ThO})=6.60263 \pm 0.00003 \text{ eV}$ (Goncharov and Heaven, 2006), and $\text{IE}(\text{ThF})=6.3952 \pm 0.0037 \text{ eV}$ (Barker et al., 2012). Marçalo and coworkers have employed electron transfer of actinide cations with neutral species to

TABLE 9 Bond Dissociation Enthalpies of Neutral, Monopositive, and Dipositive Actinide Monoxides and Dioxides^a

An	$D(\text{An}-\text{O})$	$D(\text{An}^+-\text{O})$	$D(\text{An}^{2+}-\text{O})$	$D(\text{OAn}-\text{O})$	$D(\text{OAn}^+-\text{O})$	$D(\text{OAn}^{2+}-\text{O})$
Th	872 ± 25	843 ± 25	829 ± 80	684 ± 14	462 ± 14	0 ± 170
Pa	801 ± 59	800 ± 50	781 ± 30	780 ± 48	780 ± 29	317 ± 110
U	758 ± 13	774 ± 13	706 ± 45	750 ± 14	741 ± 14	529 ± 31
Np	744 ± 21	760 ± 10	524 ± 36	632 ± 43	610 ± 22	504 ± 10
Pu	658 ± 10	651 ± 19	439 ± 49	599 ± 22	509 ± 38	403 ± 95
Am	582 ± 34	560 ± 28	367 ± 13	509 ± 65	410 ± 56	256 ± 129
Cm	709 ± 43	670 ± 38	342 ± 12	405 ± 70	202 ± 60	0 ± 150

^aValues in kJ mol^{-1} from Marçalo and Gibson (2009).

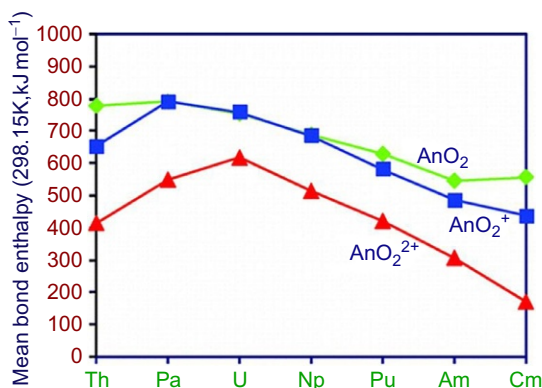


FIGURE 25 Mean bond dissociation enthalpies for neutral, monopositive, and dipositive actinide dioxide molecules. Reproduced with permission from Marçalo and Gibson (2009). Copyright 2009 American Chemical Society.

bracket the ionization energies of several actinide oxides, particularly transuranic oxides, providing values with relatively large uncertainties that are nonetheless refinements of previous estimates (Marçalo and Gibson, 2009).

As essentially no thermodynamic values were available for actinide sulfides, the homologues of the actinide oxides, Pereira et al. (2011) recently obtained experimental values for An^+-S bond dissociation energies by studying reactions of bare and ligated actinide cations with S-atom donors

TABLE 10 Bond Dissociation Energies of Actinide Monosulfides^a

An	$D(\text{An}^+-\text{S})$	$D(\text{An}-\text{S})$
Ac	465 ± 48	505 ± 68
Th	570 ± 75	608 ± 77
Pa	525 ± 86	545 ± 91
U	500 ± 60	510 ± 63
Np	491 ± 52	494 ± 55
Pu	420 ± 23	446 ± 30
Am	334 ± 27	375 ± 33
Cm	455 ± 16	504 ± 25

^aValues in kJ mol^{-1} from *Pereira et al. (2011)*.

and other neutral molecules, with the key values summarized in [Table 10](#). These results reveal that the $D(\text{An}^+-\text{S})$ are lower than the corresponding $D(\text{An}^+-\text{O})$, by some 200–300 kJ mol^{-1} , and follow similar trends along the actinide series.

4 CONCLUSIONS AND FUTURE PROSPECTS

Gas-phase ion chemistry and thermochemistry of rare earths and actinides, as apparent from this chapter, is now a mature field albeit with many areas for future development. Reactivity studies with numerous elementary substrates have revealed key underlying principles that relate observed behavior to the electronic structures and energetics of the atomic metal ions. Many new rare earth and actinide molecular and cluster species have been identified that expanded the knowledge of the basic chemistry of these elements. Studies of clusters have enabled experiments that provide some links to condensed-phase processes, though these connections generally remain somewhat limited in scope. Several key thermodynamic values, including bond dissociation energies and/or ionization energies, have been obtained for numerous elementary molecules; these are fundamental physical properties. Such physical properties furthermore provide opportunities for the refinement and validation of computational methods as applied to demanding lanthanides and actinides, where relativistic and multiconfigurational effects challenge conventional theoretical methodologies.

As in other regions of the periodic table, there remain many areas ripe for investigation of the rare earths and actinides by gas-phase ion chemistry

approaches. The knowledge of the thermochemistry of elementary molecules should be expanded and refined beyond the rather limited collection of accurately determined bond dissociation energies. An issue that is not fully understood, and should be more carefully addressed in the future, is the role of the 5f electrons of the actinide elements in bond activation and bonding. As reactivity studies alone may not resolve this issue, it will be beneficial to spectroscopically examine details of the electronic structures of molecular actinide species; due to the ability to produce, manipulate, and detect charged species, it is anticipated that forefront spectroscopic endeavors will be most effectively applied to actinide molecular and complex ions. Advances in the study of metal–ligand interactions, including with biomolecules and other coordinating ligands, may be expected in forthcoming investigations and will contribute to fundamental understanding of the physiological behavior of actinides and the transport of actinides in the ecosphere, and developing from first-principles perspectives advanced lanthanide recovery and separations processes that are becoming increasingly critical. The study of transeinsteinium actinides using specialized online techniques at high-energy ion accelerator facilities where these elements are produced may also be expected in the near future. In view of the inability to study the condensed-phase chemistry of the heaviest of the actinide elements, Fm, Md, No, and Lr, gas-phase ion reactivity studies that can be performed using single-atom approaches promise to be particularly fruitful in revealing fundamental aspects of their chemistry, such as whether they behave as divalent or trivalent metals.

An increasingly important goal of gas-phase metal ion chemistry in general, and that of the rare earths and actinides in particular, is to provide better understanding of these metal ions in condensed-phase systems. As has been discussed here, ESI offers a means to transfer complexes directly from solution to gas. Soft ESI conditions have already enabled the study of nanodroplets that contain Ln^{3+} ions, which has provided the first opportunity to distinctly follow the transition from bare lanthanide metal ions to fully solvated ions and directly probe on a microscopic level solution processes such as reduction and hydrolysis. The expansion of this line of inquiry will result in substantial advances in understanding the behavior of metal ions in solution. In addition to those phenomena that have already been studied, areas to be pursued using nanodroplet experimental approaches with the rare earths and actinides include solvation and complexation and the dynamics of these processes. Another link to condensed-phase chemistry is the formation of new types of chemical transformations and bonding that may be elusive using conventional synthetic approaches. This has been demonstrated on a limited scale with the production of new bonding motifs by fragmentation of gas-phase complexes. The goal of these types of studies is not to supplant condensed-phase molecular chemistry, but rather to complement it and potentially provide guidance toward new synthetic approaches. New species produced in gas phase furthermore provide opportunities for spectroscopic

characterization of novel metal—ligand bonds, the results of which can be deciphered using state-of-the-art theoretical methodologies.

ACKNOWLEDGMENTS

The work of J. M. has benefited from the financial support from Fundação para a Ciência e a Tecnologia particularly through the National Mass Spectrometry Network (RNEM—Rede Nacional de Espectrometria de Massa). The work of J. K. G. is funded by the U.S. Department of Energy, Office of Basic Energy Sciences, Heavy Element Chemistry, at LBNL under Contract No. DE-AC02-05CH11231. The authors are indebted to Drs. António Pires de Matos and Richard G. Haire for the early and ongoing support of the *f*-element gas-phase ion chemistry programs in Portugal and the United States.

ABBREVIATIONS AND SYMBOLS

AA	amino acid
An	actinide (Ac–Lr)
BDE	bond dissociation energy
CID	collision-induced dissociation
COT	cyclooctatetraene
Cp	cyclopentadienyl anion (C ₅ H ₅ [−])
DAA	diacetone alcohol
DEF	desferrioxamine
DMF	dimethylformamide
DMSO	dimethyl sulfoxide
<i>D</i>	298.15 K bond dissociation energy (kJ mol ^{−1})
<i>D</i>₀	0 K bond dissociation energy (kJ mol ^{−1})
DFT	density functional theory
ECD	electron-capture dissociation
ESI	electrospray ionization
ETD	electron transfer dissociation
FAB-MS	fast-atom bombardment mass spectrometry
FTICR	Fourier transform ion cyclotron resonance
FTICR-MS	Fourier transform ion cyclotron resonance mass spectrometry
GD-MS	glow discharge mass spectrometry
GGG	triglycine
GIB	guided ion beam
GIB-MS	guided ion beam mass spectrometry
GS	ground-state electronic configuration
HCp	cyclopentadiene
HCp*	1,2,3,4,5-pentamethylcyclopentadiene
ICP	inductively coupled plasma
ICP/SIFT	inductively coupled plasma/selected-ion flow tube
IE	ionization energy

IR	infrared
IRMPD	infrared multiphoton dissociation
<i>k</i>	rate constant
<i>k</i> _{COL}	collisional rate constant
LA	laser ablation
LAPRD	laser ablation with prompt reaction and detection
Ln	lanthanide (La–Lu)
M	metal (sometimes used as replacement for R in case of ambiguity)
MS	mass spectrometry
MS²	see MS/MS
MS/MS	tandem mass spectrometry
PA	proton affinity (kJ mol ⁻¹)
PAH	polyaromatic hydrocarbon
PE	promotion energy between electronic configurations
Q-TOF	quadrupole time of flight
QIT	quadrupole ion trap
R	rare earth (Sc, Y, and La–Lu)
RF	radiofrequency
SIFT	selected-ion flow tube
THF	tetrahydrofuran
TMOGA	tetramethyl-3-oxa-glutaramide
TOF-MS	time-of-flight mass spectrometry

REFERENCES

- Agrawal, D., Schröder, D., 2011. *Organometallics* 30, 32.
- Allison, J., 1986. *The Gas-Phase Chemistry of Transition-Metal Ions with Organic Molecules*. Progress in Inorganic Chemistry, Vol. 34. John Wiley & Sons, Inc, New York, p. 627.
- Amunugama, R., Rodgers, M.T., 2001. *J. Phys. Chem. A* 105, 9883.
- Anbalagan, V., Chien, W., Gresham, G.L., Groenewold, G.S., Van Stipdonk, M.J., 2004. *Rapid Commun. Mass Spectrom.* 18, 3028.
- Anicich, V.G., 1993. *J. Phys. Chem. Ref. Data* 22, 1469.
- Anicich, V.G., 2003. *An Index of the Literature for Bimolecular Gas Phase Cation-Molecule Reaction Kinetics*. Jet Propulsion Laboratory—California Institute of Technology, Pasadena, CA, USA, p.1194, JPL-Publication-03-19.
- Antonczak, S., Marchande, N., Cabrol-Bass, D., Geribaldi, S., 2003. *Int. J. Mass Spectrom.* 222, 383.
- Armentrout, P.B., 1989. Reactions of atomic metal ions with H₂, CH₄, and C₂H₆: electronic requirements for H–H, C–H, and C–C bond activation. In: Russell, D.H. (Ed.), *Gas Phase Inorganic Chemistry*. Plenum, New York, pp. 1–42.
- Armentrout, P.B., 1990. *Int. Rev. Phys. Chem.* 9, 115.
- Armentrout, P.B., 2002. *J. Am. Soc. Mass Spectrom.* 13, 419.
- Armentrout, P.B., 2003. *Int. J. Mass Spectrom.* 227, 289.
- Armentrout, P.B., 2004. *J. Anal. At. Spectrom.* 19, 571.
- Armentrout, P.B., 2013. *J. Am. Soc. Mass Spectrom.* 24, 173.
- Armentrout, P.B., Beauchamp, J.L., 1979. *Inorg. Chem.* 18, 1349.

- Armentrout, P.B., Beauchamp, J.L., 1980. *Chem. Phys.* 50, 27.
- Armentrout, P.B., Beauchamp, J.L., 1981. *J. Phys. Chem.* 85, 4103.
- Armentrout, P.B., Beauchamp, J.L., 1989. *Acc. Chem. Res.* 22, 315.
- Armentrout, P.B., Clemmer, D.E., 1992. Guided ion beam studies of the energetics of organometallic species. In: Martinho Simões, J.A. (Ed.), *Energetics of Organometallic Species*, vol. 367. Springer, Netherlands, p. 321.
- Armentrout, P.B., Georgiadis, R., 1988. *Polyhedron* 7, 1573.
- Armentrout, P.B., Gross, M.L., Caprioli, R.M., 2003. In: Armentrout, P.B., Gross, M.L., Caprioli, R.M. (Eds.), *The Encyclopedia of Mass Spectrometry. Theory and Ion Chemistry*, vol. 1. Elsevier, Amsterdam.
- Armentrout, P.B., Halle, L.F., Beauchamp, J.L., 1981. *J. Am. Chem. Soc.* 103, 6501.
- Armentrout, P.B., Hodges, R.V., Beauchamp, J.L., 1977a. *J. Chem. Phys.* 66, 4683.
- Armentrout, P.B., Hodges, R.V., Beauchamp, J.L., 1977b. *J. Am. Chem. Soc.* 99, 3162.
- Armentrout, P.B., Kickel, B.L., 1996. Gas-phase thermochemistry of transition metal ligand systems: reassessment of values and periodic trends. In: Freiser, B.S. (Ed.), *Organometallic Ion Chemistry*, vol. 15. Springer, Netherlands, p. 1.
- Armentrout, P.B., Sunderlin, L.S., Fisher, E.R., 1989. *Inorg. Chem.* 28, 4436.
- Aubriet, F., Gaumet, J.-J., de Jong, W.A., Groenewold, G.S., Gianotto, A.K., McIlwain, M.E., Van Stipdonk, M.J., Leavitt, C.M., 2009. *J. Phys. Chem. A* 113, 6239.
- Ayers, T.M., Westlake, B.C., Duncan, M.A., 2004. *J. Phys. Chem. A* 108, 9805.
- Ayers, T.M., Westlake, B.C., Preda, D.V., Scott, L.T., Duncan, M.A., 2005. *Organometallics* 24, 4573.
- Azzaro, M., Breton, S., Decouzon, M., Geribaldi, S., 1992. *Rapid Commun. Mass Spectrom.* 6, 306.
- Azzaro, M., Breton, S., Decouzon, M., Geribaldi, S., 1993. *Int. J. Mass Spectrom. Ion Process.* 128, 1.
- Babcock, L.M., Herd, C.R., Streit, G.E., 1984a. *Chem. Phys. Lett.* 112, 169.
- Babcock, L.M., Herd, C.R., Streit, G.E., 1984b. *Chem. Phys. Lett.* 112, 173.
- Backe, H., Dretzke, A., Horn, R., Kolb, T., Lauth, W., Repnow, R., Sewtz, M., Trautmann, N., 2005. *Hyperfine Interact.* 162, 77.
- Baer, T., Dunbar, R.C., 2010. *J. Am. Soc. Mass Spectrom.* 21, 681.
- Bandura, D.R., Baranov, V.I., Litherland, A.E., Tanner, S.D., 2006. *Int. J. Mass Spectrom.* 255–256, 312.
- Barker, B.J., Antonov, I.O., Heaven, M.C., Peterson, K.A., 2012. *J. Chem. Phys.* 136, 104305.
- Beauchamp, J.L., 1976a. *J. Chem. Phys.* 64, 929.
- Beauchamp, J.L., 1976b. *J. Chem. Phys.* 64, 718.
- Beauchamp, J.L., van Koppen, P.A.M., 1992. Fundamental gas phase studies of the mechanism and thermochemistry of organometallic reactions. In: Martinho Simões, J.A. (Ed.), *Energetics of Organometallic Species*, vol. 367. Springer, Netherlands, p. 287.
- Becker, J.S., Dietze, H.-J., 1995. *J. Anal. At. Spectrom.* 10, 637.
- Becker, J.S., Dietze, H.-J., 1997. *Fresenius J. Anal. Chem.* 359, 338.
- Becker, J.S., Seifert, G., Saprykin, A.I., Dietze, H.-J., 1996. *J. Anal. At. Spectrom.* 11, 643.
- Becker, S., Dietze, H.J., 1985. *Int. J. Mass Spectrom. Ion Process.* 67, 57.
- Bjarnason, A., 1991. *Organometallics* 10, 1244.
- Bjarnason, A., 1994. *Rapid Commun. Mass Spectrom.* 8, 366.
- Bjarnason, A., 1996. *Organometallics* 15, 3275.
- Bjarnason, A., Ridge, D.P., 1998. *Organometallics* 17, 1889.
- Blades, A.T., Jayaweera, P., Ikonomou, M.G., Kebarle, P., 1990. *Int. J. Mass Spectrom. Ion Process.* 101, 325.

- Blagojevic, V., Bozovic, A., Orlova, G., Bohme, D.K., 2008. *J. Phys. Chem. A* 112, 10141.
- Blagojevic, V., Flaim, E., Jarvis, M.J.V., Koyanagi, G.K., Bohme, D.K., 2005a. *J. Phys. Chem. A* 109, 11224.
- Blagojevic, V., Flaim, E., Jarvis, M.J.Y., Koyanagi, G.K., Bohme, D.K., 2006. *Int. J. Mass Spectrom.* 249, 385.
- Blagojevic, V., Orlova, G., Bohme, D.K., 2005b. *J. Am. Chem. Soc.* 127, 3545.
- Blaise, J., Wyart, J.F., 1992. *Energy Levels and Atomic Spectra of Actinides. Tables Internationales de Constantes*, Paris.
- Bohme, D.K., 2005. Gas-phase reactivity of lanthanide cations. In: Nibbering, N., Gross, M.L., Caprioli, R.M. (Eds.), *The Encyclopedia of Mass Spectrometry. Fundamentals of and Applications to Organic (and Organometallic) Compounds*, vol. 4. Elsevier, Amsterdam, p. 638.
- Bohme, D.K., Schwarz, H., 2005. *Angew. Chem. Int. Ed.* 44, 2336.
- Bowers, M.T., 1994. *Acc. Chem. Res.* 27, 324.
- Bowers, M.T., Kemper, P.R., Vonhelden, G., Van Koppen, P.A.M., 1993. *Science* 260, 1446.
- Brewer, L., 1971. *J. Opt. Soc. Am.* 61, 1666.
- Brown, D.A., Ismail, S., 1990. *Inorg. Chim. Acta* 171, 41.
- Bryantsev, V.S., de Jong, W.A., Cossel, K.C., Diallo, M.S., Goddard, W.A., Groenewold, G.S., Chien, W., Van Stipdonk, M.J., 2008. *J. Phys. Chem. A* 112, 5777.
- Buckner, S.W., Freiser, B.S., 1988. *Polyhedron* 7, 1583.
- Buckner, S.W., Gord, J.R., Freiser, B.S., 1988. *J. Am. Chem. Soc.* 110, 6606.
- Bush, M.F., Saykally, R.J., Williams, E.R., 2006. *Int. J. Mass Spectrom.* 253, 256.
- Bush, M.F., Saykally, R.J., Williams, E.R., 2008. *J. Am. Chem. Soc.* 130, 9122.
- Bushnell, J.E., Kemper, P.R., Maitre, P., Bowers, M.T., 1994. *J. Am. Chem. Soc.* 116, 9710.
- Caraiman, D., Bohme, D.K., 2002. *J. Phys. Chem. A* 106, 9705.
- Caraiman, D., Koyanagi, G.K., Bohme, D.K., 2004. *J. Phys. Chem. A* 108, 978.
- Carnegie, P.D., Bandyopadhyay, B., Duncan, M.A., 2011. *J. Chem. Phys.* 134, 014302.
- Carretas, J.M., Marçalo, J., Pires de Matos, A., 2004. *Int. J. Mass Spectrom.* 234, 51.
- Carretas, J.M., Pires de Matos, A., Marçalo, J., Pissavini, M., Decouzon, M., Gèribaldi, S., 1998. *J. Am. Soc. Mass Spectrom.* 9, 1035.
- Castleman Jr., A.W., 2011. *Catal. Lett.* 141, 1243.
- Chandrasekharaiah, M.S., Gingerich, K.A., 1989. Thermodynamic properties of gaseous species. In: Gschneidner Jr., Karl A., LeRoy, E. (Eds.), *Handbook on the Physics and Chemistry of Rare Earths*, vol. 12. Elsevier, Amsterdam, p. 409.
- Chen, Q., Goodings, J.M., 1998. *Int. J. Mass Spectrom.* 176, 1.
- Chen, Q.F., Goodings, J.M., 1999. *Int. J. Mass Spectrom.* 188, 213.
- Chen, Y.M., Clemmer, D.E., Armentrout, P.B., 1994. *J. Phys. Chem.* 98, 11490.
- Cheng, P., Bohme, D.K., 2006. *Inorg. Chem.* 45, 7856.
- Cheng, P., Koyanagi, G.K., Bohme, D.K., 2006a. *J. Phys. Chem. A* 110, 2718.
- Cheng, P., Koyanagi, G.K., Bohme, D.K., 2006b. *J. Phys. Chem. A* 110, 12832.
- Cheng, P., Koyanagi, G.K., Bohme, D.K., 2006c. *ChemPhysChem* 7, 1813.
- Cheng, P., Koyanagi, G.K., Bohme, D.K., 2007. *J. Phys. Chem. A* 111, 8561.
- Cheng, P., Shayesteh, A., Bohme, D.K., 2009. *Inorg. Chem.* 48, 1018.
- Cheng, Z.L., Siu, K.W.M., Guevremont, R., Berman, S.S., 1992. *Org. Mass Spectrom.* 27, 1370.
- Chien, W., Anbalagan, V., Zandler, M., Van Stipdonk, M., Hanna, D., Gresham, G., Groenewold, G., 2004. *J. Am. Soc. Mass Spectrom.* 15, 777.
- Chow, C.C.Y., Goodings, J.M., 1995. *Can. J. Chem.* 73, 2263.
- Clemmer, D.E., Aristov, N., Armentrout, P.B., 1993. *J. Phys. Chem.* 97, 544.
- Clemmer, D.E., Dalleska, N.F., Armentrout, P.B., 1992. *Chem. Phys. Lett.* 190, 259.
- Clemmer, D.E., Elkind, J.L., Aristov, N., Armentrout, P.B., 1991. *J. Chem. Phys.* 95, 3387.

- Clemmer, D.E., Jarrold, M.F., 1997. *J. Mass Spectrom.* 32, 577.
- Clemmer, D.E., Shelimov, K.B., Jarrold, M.F., 1994a. *J. Am. Chem. Soc.* 116, 5971.
- Clemmer, D.E., Shelimov, K.B., Jarrold, M.F., 1994b. *Nature* 367, 718.
- Clemmer, D.E., Sunderlin, L.S., Armentrout, P.B., 1990. *J. Phys. Chem.* 94, 3008.
- Cockett, M.C.R., Dyke, J.M., Ellis, A.M., Feher, M., Morris, A., 1989. *J. Am. Chem. Soc.* 111, 5994.
- Cockett, M.C.R., Dyke, J.M., Ellis, A.M., Feher, M., Wright, T.G., 1990. *J. Electron Spectrosc.* 51, 529.
- Cockett, M.C.R., Dyke, J.M., Ellis, A.M., Wright, T.G., 1991a. *J. Chem. Soc. Faraday Trans.* 87, 19.
- Cockett, M.C.R., Nyulaszi, L., Veszpremi, T., Wright, T.G., Dyke, J.M., 1991b. *J. Electron Spectrosc.* 57, 373.
- Compton, R.N., 1977. *J. Chem. Phys.* 66, 4478.
- Cornehl, H.H., Heinemann, C., Marçalo, J., deMatos, A.P., Schwarz, H., 1996a. *Angew. Chem. Int. Ed.* 35, 891.
- Cornehl, H.H., Heinemann, C., Schröder, D., Schwarz, H., 1995. *Organometallics* 14, 992.
- Cornehl, H.H., Hornung, G., Schwarz, H., 1996b. *J. Am. Chem. Soc.* 118, 9960.
- Cornehl, H.H., Wesendrup, R., Diefenbach, M., Schwarz, H., 1997a. *Chem. Eur. J.* 3, 1083.
- Cornehl, H.H., Wesendrup, R., Harvey, J.N., Schwarz, H., 1997b. *J. Chem. Soc., Perkin Trans.* 2, 2283.
- Cox, D.M., Reichmann, K.C., Kaldor, A., 1988. *J. Chem. Phys.* 88, 1588.
- Cox, D.M., Trevor, D.J., Reichmann, K.C., Kaldor, A., 1986. *J. Am. Chem. Soc.* 108, 2457.
- Crellin, K.C., Beauchamp, J.L., Geribaldi, S., Decouzon, M., 1996. *Organometallics* 15, 5368.
- Crellin, K.C., Beauchamp, J.L., Goddard, W.A., Geribaldi, S., Decouzon, M., 1999. *Int. J. Mass Spectrom.* 182, 121.
- Crellin, K.C., Geribaldi, S., Beauchamp, J.L., 1994. *Organometallics* 13, 3733.
- Crellin, K.C., Geribaldi, S., Widmer, M., Beauchamp, J.L., 1995. *Organometallics* 14, 4366.
- Dai, P., McCullough-Catalano, S., Bolton, M., Jones, A.D., Lebrilla, C.B., 1995. *Int. J. Mass Spectrom. Ion Process.* 144, 67.
- Dance, I., Fisher, K., Willett, G., 1995. *Angew. Chem. Int. Ed. Engl.* 34, 201.
- Dance, I.G., Fisher, K.J., Willett, G.D., 1996. *Inorg. Chem.* 35, 4177.
- Decouzon, M., Gal, J.F., G eribaldi, S., Rouillard, M., Sturla, J.M., Bouchoux, G., 1989. *Rapid Commun. Mass Spectrom.* 3, 298.
- Di Marco, V.B., Bombi, G.G., 2006. *Mass Spectrom. Rev.* 25, 347.
- Ding, X.-L., Wu, X.-N., Zhao, Y.-X., He, S.-G., 2012. *Acc. Chem. Res.* 45, 382.
- Ding, X.L., Wu, X.N., Zhao, Y.X., Ma, J.B., He, S.G., 2011. *ChemPhysChem* 12, 2110.
- Di Santo, E., Santos, M., Michelini, M.C., Marçalo, J., Russo, N., Gibson, J.K., 2011. *J. Am. Chem. Soc.* 133, 1955.
- Donald, W.A., Demireva, M., Leib, R.D., Aiken, M.J., Williams, E.R., 2010. *J. Am. Chem. Soc.* 132, 4633.
- Donald, W.A., Leib, R.D., Demireva, M., O'Brien, J.T., Prell, J.S., Williams, E.R., 2009. *J. Am. Chem. Soc.* 131, 13328.
- Donald, W.A., Williams, E.R., 2011. *Pure Appl. Chem.* 83, 2129.
- Duncan, M.A., 2012. *Rev. Sci. Instrum.*, 83, 041101.
- Dunk, P.W., Kaiser, N.K., Mulet-Gas, M., Rodriguez-Fortea, A., Poblet, J.M., Shinohara, H., Hendrickson, C.L., Marshall, A.G., Kroto, H.W., 2012. *J. Am. Chem. Soc.* 134, 9380.
- Dyke, J.M., Ellis, A.M., Feher, M., Morris, A., 1988. *Chem. Phys. Lett.* 145, 159.
- Elkind, J.L., Armentrout, P.B., 1987. *J. Phys. Chem.* 91, 2037.

- Elkind, J.L., Sunderlin, L.S., Armentrout, P.B., 1989. *J. Phys. Chem.* 93, 3151.
- Eller, K., Schwarz, H., 1991. *Chem. Rev.* 91, 1121.
- Ervin, K.M., 2001. *Chem. Rev.* 101, 391–444.
- Ervin, K.M., Rodgers, M.T., 2013. *J. Phys. Chem. A* 117, 967.
- Fisher, E.R., Elkind, J.L., Clemmer, D.E., Georgiadis, R., Loh, S.K., Aristov, N., Sunderlin, L.S., Armentrout, P.B., 1990. *J. Chem. Phys.* 93, 2676.
- Fisher, K., Dance, I., Willett, G., 1998. *J. Chem. Soc. Dalton Trans.*, 975.
- Fisher, K.J., 2001. *Gas-Phase Coordination Chemistry of Transition Metal Ions. Progress in Inorganic Chemistry.* John Wiley & Sons, Inc, p.343.
- Fite, W.L., Irving, P., 1972. *J. Chem. Phys.* 56, 4227.
- Fite, W.L., Lo, H.H., Irving, P., 1974. *J. Chem. Phys.* 60, 1236.
- Flick, T.G., Donald, W.A., Williams, E.R., 2013. *J. Am. Soc. Mass Spectrom.* 24, 193.
- Flick, T.G., Williams, E.R., 2012. *J. Am. Soc. Mass Spectrom.* 23, 1885.
- Forbes, R.A., Tews, E.C., Freiser, B.S., Wise, M.B., Perone, S.P., 1986a. *Anal. Chem.* 58, 684.
- Forbes, R.A., Tews, E.C., Freiser, B.S., Wise, M.B., Perone, S.P., 1986b. *J. Chem. Inf. Comput. Sci.* 26, 93.
- Forbes, R.A., Tews, E.C., Huang, Y., Freiser, B.S., Perone, S.P., 1987. *Anal. Chem.* 59, 1937.
- Freiser, B.S., 1996. *J. Mass Spectrom.* 31, 703.
- Gagliardi, L., Pyykkö, P., 2004. *Angew. Chem. Int. Ed.* 43, 1573.
- Gapeev, A., Dunbar, R., 2002. *J. Am. Soc. Mass Spectrom.* 13, 477.
- Geribaldi, S., Breton, S., Decouzon, M., Azzaro, M., 1995. *New J. Chem.* 19, 887.
- Geribaldi, S., Breton, S., Decouzon, M., Azzaro, M., 1996. *J. Am. Soc. Mass Spectrom.* 7, 1151.
- Gibson, J.K., 1994a. *J. Phys. Chem.* 98, 6063.
- Gibson, J.K., 1994b. *J. Phys. Chem.* 98, 11321.
- Gibson, J.K., 1995. *J. Appl. Phys.* 78, 1274.
- Gibson, J.K., 1996a. *J. Phys. Chem.* 100, 15688.
- Gibson, J.K., 1996b. *J. Phys. Chem.* 100, 507.
- Gibson, J.K., 1996c. *J. Fluorine Chem.* 78, 65.
- Gibson, J.K., 1997a. *J. Vacuum Sci. Technol. A* 15, 2107.
- Gibson, J.K., 1997b. *Organometallics* 16, 4214.
- Gibson, J.K., 1998a. *J. Phys. Chem. A* 102, 4501.
- Gibson, J.K., 1998b. *Organometallics* 17, 2583.
- Gibson, J.K., 1998c. *J. Alloys Compd.* 275, 759.
- Gibson, J.K., 1998d. *J. Am. Chem. Soc.* 120, 2633.
- Gibson, J.K., 1998e. *J. Alloys Compd.* 271, 359.
- Gibson, J.K., 1999a. *Inorg. Chem.* 38, 165.
- Gibson, J.K., 1999b. *Radiochim. Acta* 84, 135.
- Gibson, J.K., 1999c. *J. Mass Spectrom.* 34, 1166.
- Gibson, J.K., 1999d. *J. Alloys Compd.* 290, 52.
- Gibson, J.K., 2000. *Int. J. Mass Spectrom.* 202, 19.
- Gibson, J.K., 2001. *J. Mass Spectrom.* 36, 284.
- Gibson, J.K., 2002a. *Int. J. Mass Spectrom.* 216, 185.
- Gibson, J.K., 2002b. *Int. J. Mass Spectrom.* 214, 1.
- Gibson, J.K., 2003. *J. Phys. Chem. A* 107, 7891.
- Gibson, J.K., Haire, R.G., 1998. *J. Phys. Chem. A* 102, 10746.
- Gibson, J.K., Haire, R.G., 1999. *Organometallics* 18, 4471.
- Gibson, J.K., Haire, R.G., 2000. *Int. J. Mass Spectrom.* 203, 127.
- Gibson, J.K., Haire, R.G., 2001a. *Radiochim. Acta* 89, 363.

- Gibson, J.K., Haire, R.G., 2001b. *Radiochim. Acta* 89, 709.
- Gibson, J.K., Haire, R.G., 2001c. *J. Alloys Compd.* 322, 143.
- Gibson, J.K., Haire, R.G., 2002. *Inorg. Chem.* 41, 5897.
- Gibson, J.K., Haire, R.G., 2003. *Radiochim. Acta* 91, 441.
- Gibson, J.K., Haire, R.G., 2004. *J. Alloys Compd.* 363, 112.
- Gibson, J.K., Haire, R.G., 2005. *Organometallics* 24, 119.
- Gibson, J.K., Haire, R.G., Marçalo, J., Santos, M., Pires de Matos, A., Mroziak, M.K., Pitzer, R.M., Bursten, B.E., 2007. *Organometallics* 26, 3947.
- Gibson, J.K., Haire, R.G., Santos, M., Marçalo, J., Pires de Matos, A., 2005. *J. Phys. Chem. A* 109, 2768.
- Gibson, J.K., Haire, R.G., Santos, M., Pires de Matos, A., Marçalo, J., 2008. *J. Phys. Chem. A* 112, 11373.
- Gibson, J.K., Marçalo, J., 2006. *Coord. Chem. Rev.* 250, 776.
- Goncharov, V., Heaven, M.C., 2006. *J. Chem. Phys.* 124, 064312/1.
- Goncharov, V., Kaledin, L.A., Heaven, M.C., 2006. *J. Chem. Phys.* 125, 133202/1.
- Gong, Y., Gibson, J.K., 2013. *J. Phys. Chem. A* 117, 783.
- Gong, Y., Hu, H.S., Tian, G., Rao, L., Li, J., Gibson, J.K., 2013. *Angew. Chem. Int. Ed.* 52, 6885.
- Goodings, J.M., Hassanali, C.S., Patterson, P.M., Chow, C., 1994. *Int. J. Mass Spectrom. Ion Process.* 132, 83.
- Goodings, J.M., Tran, Q., Karellas, N.S., 1988. *Can. J. Chem.* 66, 2219.
- Gresham, G.L., Dinescu, A., Benson, M.T., Van Stipdonk, M.J., Groenewold, G.S., 2011. *J. Phys. Chem. A* 115, 3497.
- Gresham, G.L., Gianotto, A.K., Harrington, P.D., Cao, L.B., Scott, J.R., Olson, J.E., Appelhans, A.D., Van Stipdonk, M.J., Groenewold, G.S., 2003. *J. Phys. Chem. A* 107, 8530.
- Grimm, R.L., Mangrum, J.B., Dunbar, R.C., 2004. *J. Phys. Chem. A* 108, 10897.
- Groenewold, G.S., Cossel, K.C., Gresham, G.L., Gianotto, A.K., Appelhans, A.D., Olson, J.E., Van Stipdonk, M.J., Chien, W., 2006a. *J. Am. Chem. Soc.* 128, 3075.
- Groenewold, G.S., de Jong, W.A., Oomens, J., Van Stipdonk, M.J., 2010a. *J. Am. Soc. Mass Spectrom.* 21, 719.
- Groenewold, G.S., Gianotto, A.K., Cossel, K.C., Van Stipdonk, M.J., Moore, D.T., Polfer, N., Oomens, J., de Jong, W.A., Visscher, L., 2006b. *J. Am. Chem. Soc.* 128, 4802.
- Groenewold, G.S., Gianotto, A.K., McIlwain, M.E., Van Stipdonk, M.J., Kullman, M., Moore, D.T., Polfer, N., Oomens, J., Infante, I., Visscher, L., Siboulet, B., De Jong, W.A., 2008a. *J. Phys. Chem. A* 112, 508.
- Groenewold, G.S., Oomens, J., de Jong, W.A., Gresham, G.L., McIlwain, M.E., Van Stipdonk, M.J., 2008b. *Phys. Chem. Chem. Phys.* 10, 1192.
- Groenewold, G.S., Van Stipdonk, M.J., de Jong, W.A., Oomens, J., Gresham, G.L., McIlwain, M.E., Gao, D., Siboulet, B., Visscher, L., Kullman, M., Polfer, N., 2008c. *ChemPhysChem* 9, 1278.
- Groenewold, G.S., Van Stipdonk, M.J., Gresham, G.L., Chien, W., Bulleigh, K., Howard, A., 2004. *J. Mass Spectrom.* 39, 752.
- Groenewold, G.S., van Stipdonk, M.J., Oomens, J., de Jong, W.A., Gresham, G.L., McIlwain, M.E., 2010b. *Int. J. Mass Spectrom.* 297, 67.
- Groenewold, G.S., van Stipdonk, M.J., Oomens, J., de Jong, W.A., McIlwain, M.E., 2011. *Int. J. Mass Spectrom.* 308, 175.
- Gross, M.L., Caprioli, R.M., 2007. In: Gross, M.L., Caprioli, R.M. (Eds.), *The Encyclopedia of Mass Spectrometry. Ionization Methods*, vol. 6. Elsevier, Amsterdam.

- Guo, B.C., Kerns, K.P., Castleman, A.W., 1992a. *Science* 255, 1411.
- Guo, J.Z., Goodings, J.M., 2002a. *Int. J. Mass Spectrom.* 214, 349.
- Guo, J.Z., Goodings, J.M., 2002b. *Int. J. Mass Spectrom.* 214, 339.
- Guo, T., Diener, M.D., Chai, Y., Alford, M.J., Haufler, R.E., McClure, S.M., Ohno, T., Weaver, J.H., Scuseria, G.E., Smalley, R.E., 1992b. *Science* 257, 1661.
- Harvey, J.N., Schröder, D., Koch, W., Danovich, D., Shaik, S., Schwarz, H., 1997. *Chem. Phys. Lett.* 278, 391.
- Heath, J.R., O'Brien, S.C., Zhang, Q., Liu, Y., Curl, R.F., Tittel, F.K., Smalley, R.E., 1985. *J. Am. Chem. Soc.* 107, 7779.
- Heaven, M.C., Gibson, J.K., Marçalo, J., 2010. Molecular spectroscopy and reactions of actinides in the gas phase and cryogenic matrices. In: Morss, L.R., Edelstein, N.M., Fuger, J. (Eds.), *The Chemistry of the Actinide and Transactinide Elements*, vol. 6. Springer, Dordrecht, p. 4079.
- Heinemann, C., Cornehl, H.H., Schröder, D., Dolg, M., Schwarz, H., 1996. *Inorg. Chem.* 35, 2463.
- Heinemann, C., Cornehl, H.H., Schwarz, H., 1995a. *J. Organomet. Chem.* 501, 201.
- Heinemann, C., Goldberg, N., Tornieporthoetting, I.C., Klapotke, T.M., Schwarz, H., 1995b. *Angew. Chem. Int. Ed. Engl.* 34, 213.
- Heinemann, C., Schröder, D., Schwarz, H., 1994. *Chem. Ber.* 127, 1807.
- Heinemann, C., Schwarz, H., 1995. *Chem. Eur. J.* 1, 7.
- Hettich, R.L., Freiser, B.S., 1987. *J. Am. Chem. Soc.* 109, 3543.
- Higashide, H., Kaya, T., Kobayashi, M., Shinohara, H., Sato, H., 1990. *Chem. Phys. Lett.* 171, 297.
- Hildenbrand, D.L., Gurvich, L.V., Yungman, V.S., 1985. *The Chemical Thermodynamics of Actinide Elements and Compounds, Part 13, the Gaseous Actinide Ions*. International Atomic Energy Agency, Vienna.
- Hill, Y.D., Freiser, B.S., Bauschlicher, C.W., 1991. *J. Am. Chem. Soc.* 113, 1507.
- Hill, Y.D., Huang, Y.Q., Ast, T., Freiser, B.S., 1997. *Rapid Commun. Mass Spectrom.* 11, 148.
- Hopwood, F.G., Fisher, K.J., Greenhill, P., Willett, G.D., Zhang, R., 1997. *J. Phys. Chem. B* 101, 10704.
- Huang, H., Chaudhary, S., Van Horn, J.D., 2005. *Inorg. Chem.* 44, 813.
- Huang, Y., Freiser, B.S., 1991. *J. Am. Chem. Soc.* 113, 9418.
- Huang, Y., Hill, Y.D., Freiser, B.S., 1991a. *J. Am. Chem. Soc.* 113, 840.
- Huang, Y., Wise, M.B., Jacobson, D.B., Freiser, B.S., 1987. *Organometallics* 6, 346.
- Huang, Y.Q., Freiser, B.S., 1988a. *J. Am. Chem. Soc.* 110, 4434.
- Huang, Y.Q., Freiser, B.S., 1988b. *J. Am. Chem. Soc.* 110, 387.
- Huang, Y.Q., Hill, Y.D., Sodupe, M., Bauschlicher, C.W., Freiser, B.S., 1991b. *Inorg. Chem.* 30, 3822.
- Huang, Y.Q., Hill, Y.D., Sodupe, M., Bauschlicher, C.W., Freiser, B.S., 1992. *J. Am. Chem. Soc.* 114, 9106.
- Jackson, G.P., Gibson, J.K., Duckworth, D.C., 2002a. *Int. J. Mass Spectrom.* 220, 419.
- Jackson, G.P., Gibson, J.K., Duckworth, D.C., 2004a. *J. Phys. Chem. A* 108, 1042.
- Jackson, G.P., King, F.L., Goeringer, D.E., Duckworth, D.C., 2002b. *Int. J. Mass Spectrom.* 216, 85.
- Jackson, G.P., King, F.L., Goeringer, D.E., Duckworth, D.C., 2002c. *J. Phys. Chem. A* 106, 7788.
- Jackson, G.P., King, F.L., Goeringer, D.E., Duckworth, D.C., 2004b. *J. Phys. Chem. A* 108, 2139.
- Jarvis, M.J., Blagojevic, V., Koyanagi, G.K., Bohme, D.K., 2010. *Phys. Chem. Chem. Phys.* 12, 4852.
- Jarvis, M.J., Blagojevic, V., Koyanagi, G.K., Bohme, D.K., 2013. *J. Phys. Chem. A* 117, 1151.

- Jennings, K.R., Kemp, T.J., Read, P.A., 1989. *Inorg. Chim. Acta* 157, 157.
- Jiao, C.Q., Freiser, B.S., 1993. *J. Am. Chem. Soc.* 115, 6268.
- Johnsen, R., Biondi, M.A., 1972. *J. Chem. Phys.* 57, 1975.
- Johnsen, R., Castell, F.R., Biondi, M.A., 1974. *J. Chem. Phys.* 61, 5404.
- Johnson, G.E., Tyo, E.C., Castleman Jr., A.W., 2008. *Proc. Natl. Acad. Sci. U.S.A.* 105, 18108.
- Kahwa, I.A., Selbin, J., Hsieh, T.C.-Y., Evans, D.W., Pamidimukkala, K.M., Laine, R., 1988a. *Inorg. Chim. Acta* 144, 275.
- Kahwa, I.A., Selbin, J., Hsieh, T.C.Y., Laine, R.A., 1988b. *Inorg. Chim. Acta* 141, 131.
- Kaledin, L.A., Heaven, M.C., Field, R.W., 1999. *J. Mol. Spectrosc.* 193, 285.
- Kan, S.Z., Lee, S.A., Freiser, B.S., 1996. *J. Mass Spectrom.* 31, 62.
- Kazacic, S., Kazacic, S.P., Klasinc, L., Rolman, M., Srzic, D., 2006. *Croat. Chem. Acta* 79, 125.
- Kazacic, S., Kazacic, S.P., Klasinc, L., Rozman, M., Srzic, D., 2005. *Croat. Chem. Acta* 78, 269.
- Kemp, T.J., Jennings, K.R., Read, P.A., 1995a. *J. Chem. Soc. Dalton Trans.*, 885.
- Kemp, T.J., Read, P.A., 1995. *J. Chem. Soc. Dalton Trans.*, 875.
- Kemp, T.J., Read, P.A., 1996. *Inorg. Chim. Acta* 241, 105.
- Kemp, T.J., Read, P.A., Beatty, R.N., 1995b. *Inorg. Chim. Acta* 238, 109.
- Kemper, P.R., Bowers, M.T., 1991. *J. Phys. Chem.* 95, 5134.
- Kickel, B.L., Armentrout, P.B., 1995. *J. Am. Chem. Soc.* 117, 4057.
- Kojima, T., Kudaka, I., Sato, T., Asakawa, T., Akiyama, R., Kawashima, Y., Hiraoka, K., 1999. *Rapid Commun. Mass Spectrom.* 13, 2090.
- Konings, R.J.M., Morss, L.R., Fuger, J., 2006. Thermodynamic properties of actinides and actinide compounds. In: Morss, L.R., Edelstein, N.M., Fuger, J. (Eds.), *The Chemistry of the Actinide and Transactinide Elements*. Springer, Netherlands, p. 2113.
- Koyanagi, G.K., Bohme, D.K., 2001. *J. Phys. Chem. A* 105, 8964.
- Koyanagi, G.K., Bohme, D.K., 2006. *J. Phys. Chem. A* 110, 1232.
- Koyanagi, G.K., Caraiman, D., Blagojevic, V., Bohme, D.K., 2002. *J. Phys. Chem. A* 106, 4581.
- Koyanagi, G.K., Cheng, P., Bohme, D.K., 2010. *J. Phys. Chem. A* 114, 241.
- Koyanagi, G.K., Lavrov, V.V., Baranov, V., Bandura, D., Tanner, S., McLaren, J.W., Bohme, D.K., 2000. *Int. J. Mass Spectrom.* 194, L1.
- Koyanagi, G.K., Zhao, X., Blagojevic, V., Jarvis, M.J.Y., Bohme, D.K., 2005. *Int. J. Mass Spectrom.* 241, 189.
- Kraiem, M., Mayer, K., Gouder, T., Seibert, A., Wiss, T., Thiele, H., Hiernaut, J.P., 2010. *Int. J. Mass Spectrom.* 289, 108.
- Kretschmer, R., Schlangen, M., Schwarz, H., 2012. *Chem. Asian J.* 7, 1214.
- Kretschmar, I., Schröder, D., Schwarz, H., Armentrout, P.B., 2001. The binding in neutral and cationic 3d and 4d transition-metal monoxides and sulfides. In: Duncan, M.A. (Ed.), *Advances in Metal and Semiconductor Clusters. Metal Ion Solvation and Metal-Ligand Interactions*, vol. 5. Elsevier Science, Amsterdam.
- Kretschmar, I., Schröder, D., Schwarz, H., Armentrout, P.B., 2006. *Int. J. Mass Spectrom.* 249–250, 263.
- Kretschmar, I., Schröder, D., Schwarz, H., Rue, C., Armentrout, P.B., 2000. *J. Phys. Chem. A* 104, 5046.
- Kurikawa, T., Negishi, Y., Hayakawa, F., Nagao, S., Miyajima, K., Nakajima, A., Kaya, K., 1998. *J. Am. Chem. Soc.* 120, 11766.
- Kurikawa, T., Negishi, Y., Hayakawa, F., Nagao, S., Miyajima, K., Nakajima, A., Kaya, K., 1999a. *Eur. Phys. J. D.* 9, 283.
- Kurikawa, T., Takeda, H., Hirano, M., Judai, K., Arita, T., Nagao, S., Nakajima, A., Kaya, K., 1999b. *Organometallics* 18, 1430.

- Laatiaoui, M., Backe, H., Habs, D., Kunz, P., Lauth, W., Sewtz, M., 2012. *Eur. Phys. J. D.* 66, 1.
- Lavrov, V.V., Blagojevic, V., Koyanagi, G.K., Orlova, G., Bohme, D.K., 2004. *J. Phys. Chem. A* 108, 5610.
- Leavitt, C.M., Bryantsev, V.S., de Jong, W.A., Diallo, M.S., Goddard, W.A., Groenewold, G.S., Van Stipdonk, M.J., 2009. *J. Phys. Chem. A* 113, 2350.
- Lech, L.M., Freiser, B.S., 1988. *Organometallics* 7, 1948.
- Lech, L.M., Gord, J.R., Freiser, B.S., 1989. *J. Am. Chem. Soc.* 111, 8588.
- Leskiw, B.D., Castleman Jr., A.W., 2002. *C. R. Phys.* 3, 251.
- Li, F., Byers, M.A., Houk, R.S., 2003. *J. Am. Soc. Mass Spectrom.* 14, 671.
- Li, Z.Y., Zhao, Y.X., Wu, X.N., Ding, X.L., He, S.G., 2011. *Chem. Eur. J.* 17, 11728.
- Lias, S.G., Bartmess, J.E., Liebman, J.F., Holmes, J.L., Levin, R.D., Mallard, W.G., 1988. Gas-phase ion and neutral thermochemistry. *J. Phys. Chem. Ref. Data* Vol. 17, Supplement No. 1.
- Linstrom, P.J., Mallard, W.G., 2013. Nist Chemistry Webbook. NIST Standard Reference Database Number 69. National Institute of Standards and Technology, Gaithersburg, MD.
- Lu, W.Y., Huang, R.B., Yang, S.H., 1995. *J. Phys. Chem.* 99, 12099.
- Lu, W.Y., Yang, S.H., 1998. *J. Phys. Chem. A* 102, 1954.
- Lu, X., Akasaka, T., Nagase, S., 2013. *Acc. Chem. Res.* 46, 1627.
- Lu, X., Feng, L., Akasaka, T., Nagase, S., 2012. *Chem. Soc. Rev.* 41, 7723.
- Luo, Y.-R., 2007. *Comprehensive Handbook of Chemical Bond Energies*. CRC Press, Boca Raton, FL.
- Ma, J.-B., Wang, Z.-C., Schlangen, M., He, S.-G., Schwarz, H., 2012. *Angew. Chem. Int. Ed.* 51, 5991.
- Ma, J.B., Wang, Z.C., Schlangen, M., He, S.G., Schwarz, H., 2013. *Angew. Chem. Int. Ed.* 52, 1226.
- Magnera, T.F., David, D.E., Michl, J., 1989. *J. Am. Chem. Soc.* 111, 4100.
- Marçalo, J., Gibson, J.K., 2009. *J. Phys. Chem. A* 113, 12599.
- Marçalo, J., Leal, J.P., Pires de Matos, A., 1996a. *Int. J. Mass Spectrom. Ion Process.* 157, 265.
- Marçalo, J., Leal, J.P., Pires de Matos, A., Marshall, A.G., 1997a. *Organometallics* 16, 4581.
- Marçalo, J., Pires de Matos, A., 2002. *J. Organomet. Chem.* 647, 216.
- Marçalo, J., Pires de Matos, A., Evans, W.J., 1996b. *Organometallics* 15, 345.
- Marçalo, J., Pires de Matos, A., Evans, W.J., 1997b. *Organometallics* 16, 3845.
- Marçalo, J., Santos, M., Gibson, J.K., 2011. *Phys. Chem. Chem. Phys.* 13, 18322.
- Marçalo, J., Santos, M., Pires de Matos, A., Gibson, J.K., 2009. *Inorg. Chem.* 48, 5055.
- Marçalo, J., Santos, M., Pires de Matos, A., Gibson, J.K., Haire, R.G., 2008. *J. Phys. Chem. A* 112, 12647.
- Marchande, N., Breton, S., Géribaldi, S., Carretas, J.M., Pires de Matos, A., Marçalo, J., 2000. *Int. J. Mass Spectrom.* 195, 139.
- Martin, W.C., Zalubas, R., Hagan, L., 1978. *Atomic Energy Levels—The Rare-Earth Elements*. Nat. Stand. Ref. Data Series. Nat. Bur. Stand (U.S.).
- Martinho Simões, J.A., Beauchamp, J.L., 1990. *Chem. Rev.* 90, 629.
- Matsuo, Y., Maeda, H., Takami, M., 1993. *Chem. Phys. Lett.* 201, 341.
- McAskill, N.A., 1975. *Aust. J. Chem.* 28, 1879.
- McCullough-Catalano, S., Lebrilla, C.B., 1993. *J. Am. Chem. Soc.* 115, 1441.
- McElvany, S.W., 1992. *J. Phys. Chem.* 96, 4935.
- McLuckey, S.A., Mentinova, M., 2011. *J. Am. Soc. Mass Spectrom.* 22, 3.
- McLuckey, S.A., Wells, J.M., 2001. *Chem. Rev.* 101, 571.
- McQuinn, K., Hof, F., McIndoe, J.S., 2007. *Chem. Commun.*, 4099.

- Mele, A., Consalvo, D., Stranges, D., Giardini-Guidoni, A., Teghil, R., 1989. *Appl. Surf. Sci.* 43, 398.
- Mele, A., Consalvo, D., Stranges, D., Giardini-Guidoni, A., Teghil, R., 1990. *Int. J. Mass Spectrom. Ion Process.* 95, 359.
- Mercero, J.M., Matxain, J.M., Lopez, X., York, D.M., Largo, A., Eriksson, L.A., Ugalde, J.M., 2005. *Int. J. Mass Spectrom.* 240, 37.
- Merritt, J.M., Han, J., Heaven, M.C., 2008. *J. Chem. Phys.* 128, 084304.
- Michelini, M.D., Marçalo, J., Russo, N., Gibson, J.K., 2010. *Inorg. Chem.* 49, 3836.
- Michiels, E., Gijbels, R., 1984. *Anal. Chem.* 56, 1115.
- Miyajima, K., Kurikawa, T., Hashimoto, M., Nakajima, A., Kaya, K., 1999. *Chem. Phys. Lett.* 306, 256.
- Moore, C.E., 1971a. Atomic Energy Levels as Derived from the Analyses of Optical Spectra. *Nat. Stand. Ref. Data Series. Nat. Bur. Stand. (U.S.)*, vol. I. 1h to 23v. .
- Moore, C.E., 1971b. Atomic Energy Levels as Derived from the Analyses of Optical Spectra. *Nat. Stand. Ref. Data Series. Nat. Bur. Stand. (U.S.)*, vol. II. 24cr to 41nb. .
- Moreland, P.E., Rokop, D.J., Stevens, C.M., 1970. *Int. J. Mass Spectrom. Ion Phys.* 5, 127.
- Moro, L., Ruoff, R.S., Becker, C.H., Lorents, D.C., Malhotra, R., 1993. *J. Phys. Chem.* 97, 6801.
- Morss, L.R., 1994. Comparative thermochemical and oxidation–reduction properties of lanthanides and actinides. In: Gschneidner Jr., K.A., Eyring, L., Choppin, G.R., Lander, G.H. (Eds.), *Handbook on the Physics and Chemistry of Rare Earths*, vol. 18. Elsevier, Amsterdam, p. 239.
- Moulin, C., Amekraz, B., Hubert, S., Moulin, V., 2001. *Anal. Chim. Acta* 441, 269.
- Moulin, C., Charron, N., Planque, G., Virelizier, H., 2000. *Appl. Spectrosc.* 54, 843.
- Murad, E., 1984. *Int. J. Mass Spectrom. Ion Process.* 58, 159.
- Nagao, S., Kurikawa, T., Miyajima, K., Nakajima, A., Kaya, K., 1998. *J. Phys. Chem. A* 102, 4495.
- Nagao, S., Negishi, Y., Kato, A., Nakamura, Y., Nakajima, A., Kaya, K., 1999. *J. Phys. Chem. A* 103, 8909.
- Nakajima, A., Kaya, K., 2000. *J. Phys. Chem. A* 104, 176.
- Nöbfler, M., Mitrić, R., Bonačić-Koutecký, V., Johnson, G.E., Tyo, E.C., Castleman, A.W., 2010. *Angew. Chem. Int. Ed.* 49, 407.
- Oikawa, T., Urabe, T., Kawano, S.-i., Tanaka, M., 2011. *J. Solution Chem.* 40, 1094.
- Olesik, J.W., Jones, D.R., 2006. *J. Anal. At. Spectrom.* 21, 141.
- Operti, L., Rabazzana, R., 2003. *Mass Spectrom. Rev.* 22, 407.
- Operti, L., Rabazzana, R., 2006. *Mass Spectrom. Rev.* 25, 483.
- Pape, J., McQuinn, K., Hof, F., McIndoe, J.S., 2011. *New J. Chem.* 35, 1582.
- Pasilis, S., Somogyi, A., Herrmann, K., Pemberton, J.E., 2006. *J. Am. Soc. Mass Spectrom.* 17, 230.
- Pasilis, S.P., Pemberton, J.E., 2003. *Inorg. Chem.* 42, 6793.
- Patterson, P.M., Goodings, J.M., 1995. *Int. J. Mass Spectrom. Ion Process.* 148, 55.
- Patterson, P.M., Goodings, J.M., 1996. *Int. J. Mass Spectrom. Ion Process.* 152, 43.
- Pereira, C.C.L., Marsden, C.J., Marçalo, J., Gibson, J.K., 2011. *Phys. Chem. Chem. Phys.* 13, 12940.
- Pereira, C.C.L., Maurice, R., Lucena, A.F., Hu, S., Gonçalves, A.P., Marçalo, J., Gibson, J.K., Andrews, L., Gagliardi, L., 2013. *Inorg. Chem.* 52, 10968.
- Pillai, E.D., Molek, K.S., Duncan, M.A., 2005. *Chem. Phys. Lett.* 405, 247.
- Polfer, N.C., 2011. *Chem. Soc. Rev.* 40, 2211.
- Pope, R.M., Buckner, S.W., 1993. *Org. Mass Spectrom.* 28, 1616.

- Pozniak, B.P., Dunbar, R.C., 1997. *J. Am. Chem. Soc.* 119, 10439.
- Prell, J.S., Flick, T.G., Oomens, J., Berden, G., Williams, E.R., 2010. *J. Phys. Chem. A* 114, 854.
- Prell, J.S., O'Brien, J.T., Williams, E.R., 2011. *J. Am. Chem. Soc.* 133, 4810.
- Quemet, A., Vitorge, P., Cimas, A., Li, S.S., Salpin, J.Y., Marsden, C., Tortajada, J., Gagliardi, L., Spezia, R., Gaigeot, M.P., Brennetot, R., 2013. *Int. J. Mass Spectrom.* 334, 27.
- Ranasinghe, Y.A., Freiser, B.S., 1992. *Chem. Phys. Lett.* 200, 135.
- Ranasinghe, Y.A., Macmahon, T.J., Freiser, B.S., 1992. *J. Am. Chem. Soc.* 114, 9112.
- Ranatunga, D.F.A., Hill, Y.D., Freiser, B.S., 1996. *Organometallics* 15, 1242.
- Rannulu, N.S., Amunugama, R., Yang, Z., Rodgers, M.T., 2004. *J. Phys. Chem. A* 108, 6385.
- Reed, Z.D., Duncan, M.A., 2008. *J. Phys. Chem. A* 112, 5354.
- Richardson, D.E., Plattner, D.A., 2007. *Organometallic chemistry in the gas phase*. In: Crabtree, R.H., Mingos, D.M.P. (Eds.), *Comprehensive Organometallic Chemistry III*. Elsevier, Oxford, p. 801.
- Ricks, A.M., Gagliardi, L., Duncan, M.A., 2010. *J. Am. Chem. Soc.* 132, 15905.
- Ricks, A.M., Gagliardi, L., Duncan, M.A., 2011. *J. Phys. Chem. Lett.* 2, 1662.
- Rios, D., Gibson, J.K., 2012. *Eur. J. Inorg. Chem.*, 1054.
- Rios, D., Michelini, M.C., Lucena, A.F., Marçalo, J., Bray, T.H., Gibson, J.K., 2012a. *Inorg. Chem.* 51, 6603.
- Rios, D., Michelini, M.C., Lucena, A.F., Marçalo, J., Gibson, J.K., 2012b. *J. Am. Chem. Soc.* 134, 15488.
- Rios, D., Rutkowski, P.X., Shuh, D.K., Bray, T.H., Gibson, J.K., Van Stipdonk, M.J., 2011a. *J. Mass Spectrom.* 46, 1247.
- Rios, D., Rutkowski, P.X., Van Stipdonk, M.J., Gibson, J.K., 2011b. *Inorg. Chem.* 50, 4781.
- Rios, D., Schoendorff, G., Van Stipdonk, M.J., Gordon, M.S., Windus, T.L., Gibson, J.K., de Jong, W.A., 2012c. *Inorg. Chem.* 51, 12768.
- Rodgers, M.T., Armentrout, P.B., 2000. *Mass Spectrom. Rev.* 19, 215.
- Rodgers, M.T., Armentrout, P.B., 2002. *J. Am. Chem. Soc.* 124, 2678.
- Rodgers, M.T., Stanley, J.R., Amunugama, R., 2000. *J. Am. Chem. Soc.* 122, 10969.
- Roithova, J., 2012. *Chem. Soc. Rev.* 41, 547.
- Roithova, J., Schröder, D., 2007. *Phys. Chem. Chem. Phys.* 9, 2341.
- Roithova, J., Schröder, D., 2010. *Chem. Rev.* 110, 1170.
- Roth, L.M., Freiser, B.S., 1991. *Mass Spectrom. Rev.* 10, 303.
- Rutkowski, P.X., Michelini, M.C., Bray, T.H., Russo, N., Marçalo, J., Gibson, J.K., 2011a. *Theor. Chem. Acc.* 129, 575.
- Rutkowski, P.X., Michelini, M.C., Gibson, J.K., 2012. *Phys. Chem. Chem. Phys.* 14, 1965.
- Rutkowski, P.X., Michelini, M.C., Gibson, J.K., 2013. *J. Phys. Chem. A* 117, 451.
- Rutkowski, P.X., Rios, D., Gibson, J.K., Van Stipdonk, M.J., 2011b. *J. Am. Soc. Mass Spectrom.* 22, 2042.
- Ryan, M.F., Stoeckigt, D., Schwarz, H., 1994. *J. Am. Chem. Soc.* 116, 9565.
- Sansonetti, J.E., Martin, W.C., 2005. *J. Phys. Chem. Ref. Data* 34, 1559.
- Santos, L.S., Knaack, L., Metzger, J.O., 2005. *Int. J. Mass Spectrom.* 246, 84.
- Santos, M., Marçalo, J., Leal, J.P., Pires de Matos, A., Gibson, J.K., Haire, R.G., 2003. *Int. J. Mass Spectrom.* 228, 457.
- Santos, M., Marçalo, J., Pires de Matos, A., Gibson, J.K., Haire, R.G., 2002. *J. Phys. Chem. A* 106, 7190.
- Santos, M., Marçalo, J., Pires de Matos, A., Gibson, J.K., Haire, R.G., 2006a. *Eur. J. Inorg. Chem.*, 3346.

- Santos, M., Pires de Matos, A., Marçalo, J., Gibson, J.K., Haire, R.G., Tyagi, R., Pitzer, R.M., 2006b. *J. Phys. Chem. A* 110, 5751.
- Schilling, J.B., Beauchamp, J.L., 1988. *J. Am. Chem. Soc.* 110, 15.
- Schlangen, M., Schwarz, H., 2009. *Dalton Trans.* 10155.
- Schlangen, M., Schwarz, H., 2012. *Catal. Lett.* 142, 1265.
- Schofield, K., 2006. *J. Phys. Chem. A* 110, 6938.
- Schröder, D., 2012a. *Acc. Chem. Res.* 45, 1521.
- Schröder, D., 2012b. *Phys. Chem. Chem. Phys.* 14, 6382.
- Schröder, D., Diefenbach, M., Klapotke, T.M., Schwarz, H., 1999. *Angew. Chem. Int. Ed.* 38, 137.
- Schröder, D., Schwarz, H., 1993. *Angew. Chem. Int. Ed. Engl.* 32, 1420.
- Schröder, D., Schwarz, H., 1995. *Angew. Chem. Int. Ed. Engl.* 34, 1973.
- Schröder, D., Schwarz, H., 1999. *J. Phys. Chem. A* 103, 7385.
- Schröder, D., Schwarz, H., 2008. *Proc. Natl. Acad. Sci. U.S.A.* 105, 18114.
- Schröder, D., Schwarz, H., Harvey, J.N., 2000a. *J. Phys. Chem. A* 104, 11257.
- Schröder, D., Schwarz, H., Shaik, S., 2000b. Characterization, orbital description, and reactivity patterns of transition-metal oxo species in the gas phase. In: Meunier, B. (Ed.), *Metal-Oxo and Metal-Peroxo Species in Catalytic Oxidations*, vol. 97. Springer, Berlin, Heidelberg, p. 91.
- Schröder, D., Shaik, S., Schwarz, H., 2000c. *Acc. Chem. Res.* 33, 139.
- Schröder, D., Trage, C., Schwarz, H., Danovich, D., Shaik, S., 2000d. *Int. J. Mass Spectrom.* 200, 163.
- Schwarz, H., 2003. *Angew. Chem. Int. Ed.* 42, 4442.
- Schwarz, H., 2011. *Angew. Chem. Int. Ed.* 50, 10096.
- Scott, A.C., Foster, N.R., Grieves, G.A., Duncan, M.A., 2007. *Int. J. Mass Spectrom.* 263, 171.
- Seemeyer, K., Schröder, D., Kempf, M., Lettau, O., Muller, J., Schwarz, H., 1995. *Organometallics* 14, 4465.
- Shayesteh, A., Lavrov, V.V., Koyanagi, G.K., Bohme, D.K., 2009. *J. Phys. Chem. A* 113, 5602.
- Shelimov, K.B., Clemmer, D.E., Jarrold, M.F., 1994. *J. Phys. Chem.* 98, 12819.
- Shelimov, K.B., Clemmer, D.E., Jarrold, M.F., 1995. *J. Phys. Chem.* 99, 11376.
- Shelimov, K.B., Clemmer, D.E., Jarrold, M.F., 1996. *J. Chem. Soc. Dalton Trans.*, 567.
- Shelimov, K.B., Jarrold, M.F., 1996. *J. Am. Chem. Soc.* 118, 1139.
- Shi, T., Hopkinson, A.C., Siu, K.W., 2007a. *Chem. Eur. J.* 13, 1142.
- Shi, T., Siu, C.K., Siu, K.W.M., Hopkinson, A.C., 2008. *Angew. Chem. Int. Ed.* 47, 8288.
- Shi, T., Siu, K.W.M., Hopkinson, A.C., 2007b. *J. Phys. Chem. A* 111, 11562.
- Shinohara, H., Saito, Y., 2011. Metallofullerenes. In: Gschneidner, K.A., Bünzli, J.-C.G., Pecharsky, V.K. (Eds.), *Handbook on the Physics and Chemistry of Rare Earths*, vol. 41. Elsevier, Amsterdam, p. 95.
- Shvartsburg, A.A., 2002a. *Chem. Phys. Lett.* 360, 479.
- Shvartsburg, A.A., 2002b. *J. Am. Chem. Soc.* 124, 12343.
- Shvartsburg, A.A., 2002c. *J. Am. Chem. Soc.* 124, 7910.
- Shvartsburg, A.A., Jones, R.C., 2004. *J. Am. Soc. Mass Spectrom.* 15, 406.
- Sievers, M.R., Armentrout, P.B., 1999. *Inorg. Chem.* 38, 397.
- Sievers, M.R., Chen, Y.-M., Armentrout, P.B., 1996a. *J. Chem. Phys.* 105, 6322.
- Sievers, M.R., Chen, Y.M., Elkind, J.L., Armentrout, P.B., 1996b. *J. Phys. Chem.* 100, 54.
- Sokalska, M., Prussakowska, M., Hoffmann, M., Gierczyk, B., Franski, R., 2010. *J. Am. Soc. Mass Spectrom.* 21, 1789.
- Somogyi, A., Pasilis, S.P., Pemberton, J.E., 2007. *Int. J. Mass Spectrom.* 265, 281.

- Soto-Guerrero, J., Gajdošová, D., Havel, J., 2001. *J. Radioanal. Nucl. Chem.* 249, 139.
- Szric, D., Kazacic, S., Klasinc, L., Budzikiewicz, H., 1997a. *Rapid Commun. Mass Spectrom.* 11, 1131.
- Szric, D., Kazacic, S., Klasinc, L., Gusten, H., McGlynn, S.P., 1997b. *Croat. Chem. Acta* 70, 223.
- Stace, A.J., 2002. *J. Phys. Chem. A* 106, 7993.
- Steppert, M., Walther, C., 2013. *Radiochim. Acta* 101, 307.
- Steppert, M., Walther, C., Fuss, M., Buchner, S., 2012. *Rapid Commun. Mass Spectrom.* 26, 583.
- Stewart, I.I., 1999. *Spectrochim. Acta B* 54, 1649.
- Stewart, I.I., Horlick, G., 1994. *Anal. Chem.* 66, 3983.
- Streit, G.E., Babcock, L.M., 1987. *Int. J. Mass Spectrom. Ion Process.* 75, 221.
- Streit, G.E., Newton, T.W., 1980. *J. Chem. Phys.* 73, 3178.
- Sunderlin, L., Aristov, N., Armentrout, P.B., 1987. *J. Am. Chem. Soc.* 109, 78.
- Sunderlin, L.S., Armentrout, P.B., 1989. *J. Am. Chem. Soc.* 111, 3845.
- Sunderlin, L.S., Armentrout, P.B., 1990. *Organometallics* 9, 1248.
- Tanner, S.D., Baranov, V.I., Bandura, D.R., 2002. *Spectrochim. Acta B* 57, 1361.
- Tench, R.J., Balooch, M., Bernardez, L., Allen, M.J., Siekhaus, W.J., Olander, D.R., Wang, W., 1991. *J. Vac. Sci. Technol. B* 9, 820.
- Tian, L.H., Zhao, Y.X., Wu, X.N., Ding, X.L., He, S.G., Ma, T.M., 2012. *ChemPhysChem* 13, 1282.
- Tolbert, M.A., Beauchamp, J.L., 1984. *J. Am. Chem. Soc.* 106, 8117.
- Tonkyn, R., Ronan, M., Weisshaar, J.C., 1988. *J. Phys. Chem.* 92, 92.
- Tonkyn, R., Weisshaar, J.C., 1986. *J. Phys. Chem.* 90, 2305.
- Tsierkezos, N.G., Roithova, J., Schröder, D., Oncak, M., Slavicek, P., 2009. *Inorg. Chem.* 48, 6287.
- Van Stipdonk, M., Anbalagan, V., Chien, W., Gresham, G., Groenewold, G., Hanna, D., 2003. *J. Am. Soc. Mass Spectrom.* 14, 1205.
- Van Stipdonk, M.J., Chien, W., Anbalagan, V., Bulleigh, K., Hanna, D., Groenewold, G.S., 2004a. *J. Phys. Chem. A* 108, 10448.
- Van Stipdonk, M.J., Chien, W., Anbalagan, V., Gresham, G.L., Groenewold, G.S., 2004b. *Int. J. Mass Spectrom.* 237, 175.
- Van Stipdonk, M.J., Chien, W., Bulleigh, K., Wu, Q., Groenewold, G.S., 2006. *J. Phys. Chem. A* 110, 959.
- Van Stipdonk, M.J., Justes, D.R., English, R.D., Schweikert, E.A., 1999. *J. Mass Spectrom.* 34, 677.
- Verkerk, U.H., Zhao, J.F., Saminathan, I.S., Lau, J.K.C., Oomens, J., Hopkinson, A.C., Siu, K.W. M., 2012. *Inorg. Chem.* 51, 4707.
- Vieira, M.D., Marçalo, J., Pires de Matos, A., 2001. *J. Organomet. Chem.* 632, 126.
- Vukomanovic, D., Stone, J.A., 2000. *Int. J. Mass Spectrom.* 202, 251.
- Walker, N.R., Wright, R.R., Stace, A.J., Woodward, C.A., 1999. *Int. J. Mass Spectrom.* 188, 113.
- Walther, C., Fuss, M., Buchner, S., 2008. *Radiochim. Acta* 96, 411.
- Walther, C., Fuss, M., Buchner, S., Geckeis, H., 2009. *J. Radioanal. Nucl. Chem.* 282, 1003.
- Wang, Z.-C., Dietl, N., Kretschmer, R., Ma, J.-B., Weiske, T., Schlangen, M., Schwarz, H., 2012. *Angew. Chem. Int. Ed.* 51, 3703.
- Watanabe, N., Shiromaru, H., Negishi, Y., Achiba, Y., Kobayashi, N., Kaneko, Y., 1993. *Chem. Phys. Lett.* 207, 493.
- Weiss, F.D., Elkind, J.L., O'Brien, S.C., Curl, R.F., Smalley, R.E., 1988. *J. Am. Chem. Soc.* 110, 4464.
- Weisshaar, J.C., 1993. *Acc. Chem. Res.* 26, 213.

- Wesendrup, R., Schalley, C.A., Schröder, D., Schwarz, H., 1995. *Chem. Eur. J.* 1, 608.
- Wilson, K.L., Buckner, S.W., 1993. *Rapid Commun. Mass Spectrom.* 7, 848.
- Wilson, K.L., Cooper, B.T., Buckner, S.W., 1993. *Rapid Commun. Mass Spectrom.* 7, 844.
- Wu, Q., Cheng, X., Hofstadler, S.A., Smith, R.D., 1996. *J. Mass Spectrom.* 31, 669.
- Wu, X.N., Zhao, Y.X., Xue, W., Wang, Z.C., He, S.G., Ding, X.L., 2010. *Phys. Chem. Chem. Phys.* 12, 3984.
- Xu, B., Zhao, Y.X., Li, X.N., Ding, X.L., He, S.G., 2011. *J. Phys. Chem. A* 115, 10245.
- Xua, B., Zhao, Y.-X., Ding, X.-L., He, S.-G., 2013. *Int. J. Mass Spectrom.* 334, 1.
- Yin, W.W., Marshall, A.G., Marçalo, J., Dematos, A.P., 1994. *J. Am. Chem. Soc.* 116, 8666.
- Zhang, R., Achiba, Y., Fisher, K.J., Gadd, G.E., Hopwood, F.G., Ishigaki, T., Smith, D.R., Suzuki, S., Willett, G.D., 1999. *J. Phys. Chem. B* 103, 9450.
- Zhang, R., Dinca, A., Fisher, K.J., Smith, D.R., Willett, G.D., 2005. *J. Phys. Chem. A* 109, 157.
- Zhao, X., Koyanagi, G.K., Bohme, D.K., 2005. *Can. J. Chem.* 83, 1839.
- Zhao, X., Koyanagi, G.K., Bohme, D.K., 2006. *J. Phys. Chem. A* 110, 10607.
- Zhao, X., Xin, B., Xing, X., Zhang, X., Wang, G., Gao, Z., 2001. *Rapid Commun. Mass Spectrom.* 15, 1317.
- Zhao, Y.X., Wu, X.N., Ma, J.B., He, S.G., Ding, X.L., 2011a. *Phys. Chem. Chem. Phys.* 13, 1925.
- Zhao, Y.X., Yuan, J.Y., Ding, X.L., He, S.G., Zheng, W.J., 2011b. *Phys. Chem. Chem. Phys.* 13, 10084.

Chapter 264

Symbiosis of Intermetallic and Salt: Rare-Earth Metal Cluster Complexes with Endohedral Transition Metal Atoms

Gerd Meyer

Department of Chemistry, Universität zu Köln, Köln, Germany

Department of Chemistry, Iowa State University, Ames, Iowa, USA

Chapter Outline

1 Introduction	111	4.3 Oligomers of Mostly Octahedral Clusters	136
2 Cluster Complexes $\{ZR_n\}X_x$	116	4.4 Cluster Chains and Double Chains: CN(T) of 6 and 7	144
2.1 Rare-Earth Metals R	116	4.5 Cluster Chains or Networks?	153
2.2 Endohedral Atoms Z (=T, E)	117	4.6 Eight-Coordinate Endohedral Atoms	155
2.3 Ligands X	118	4.7 Layers of Edge- and Face-Connected Clusters	162
3 Synthesis	119	5 Electronic Structure	166
3.1 Reduction Routes in General	119	6 Conclusions	172
3.2 The Comproportionation Route	120	Acknowledgments	173
3.3 The Metallothermic Reduction Route	120	References	173
4 Crystal Chemistry	121		
4.1 Compounds and Structures	121		
4.2 Isolated Octahedral Clusters	121		

1 INTRODUCTION

“A metal atom cluster may be defined as a group of two or more metal atoms in which there are substantial and direct bonds between the metal atoms” (Cotton and Wilkinson, 2008). A cluster complex is a cluster surrounded by

Dedicated to the Late Professor John D. Corbett, Pioneer of this Chemistry.

ligands. Prominent cluster complexes are $[\{\text{Rh}_6\}(\text{CO})_{16}]$ and $[\{\text{Mo}_6\}\text{Cl}_{14}]^{2-}$ both with octahedral clusters, $\{\text{Rh}_6\}$ and $\{\text{Mo}_6\}$, respectively. The former is a molecular complex with 16 CO ligands surrounding the $\{\text{Rh}_6\}$ octahedron, in which $d-\pi^*$ back bonding plays an important role. The latter is a complex anion, existent in solution and in salts like $\text{Cs}_2[\{\text{Mo}_6\}\text{Cl}_{14}]$; back donation is impossible. There are $2 + (6 \times 6) - 14 = 24$ electrons available for intracuster bonding. A molecular orbital (MO) scheme shows that the electrons occupy the 12 highest bonding orbitals (see Fig. 1). Clusters built of the electron-poorer niobium atoms, as in $\text{K}_4[\{\text{Nb}_6\}\text{Cl}_{18}]$, have only 16 cluster-based electrons (CBEs). Note that the magic numbers 24 and 16 are often associated with 12 two-center–two-electron ($2c-2e$) and 8 $3c-2e$ bonds, respectively, figuratively occupying the 12 edges and 8 faces of the octahedron $\{\text{M}_6\}$. However, this is a beautiful but oversimplified and physically wrong picture.

Still, the magic numbers persist, even in clusters with the electron-poorer zirconium. These then need an endohedral atom contributing electrons to intracuster bonding. In $\text{Cs}_2\text{Zr}\{\{\text{CZr}_6\}\text{I}_{18}\}$ (Payne and Corbett, 1990), with a single carbon atom in the center of the octahedral zirconium cluster, there are $(2 \times 1) + (1 \times 4) + (1 \times 4) + (6 \times 4) - 18 = 16$ electrons available for bonding within the $\{\text{CZr}_6\}$ cluster. But there are also zirconium cluster complexes that have only 14 or 15 cluster-based electrons (CBEs), for example, $\text{Cs}\{\{\text{CZr}_6\}\text{I}_{14}\}$ (Smith and Corbett, 1985) and $\text{Cs}_4[\{\text{BZr}_6\}\text{Br}_{17}]$ (Qi and Corbett, 1997), respectively. The a_{2u} MO (Fig. 1) appears to be somewhat flexible in energy and, although bonding, it does not affect the total energy too much if it is unoccupied.

Moving on to group 3, Sc, Y, and the lanthanides (La–Lu), that is, the rare-earth elements R, the number of valence electrons available for (polar covalent) bonding drops to three because the 4f electrons present for Ce through Lu (1 through 14) may be well treated as core electrons. Thus, without a few although prominent exceptions like Gd_2Cl_3 (Lokken and Corbett, 1973),

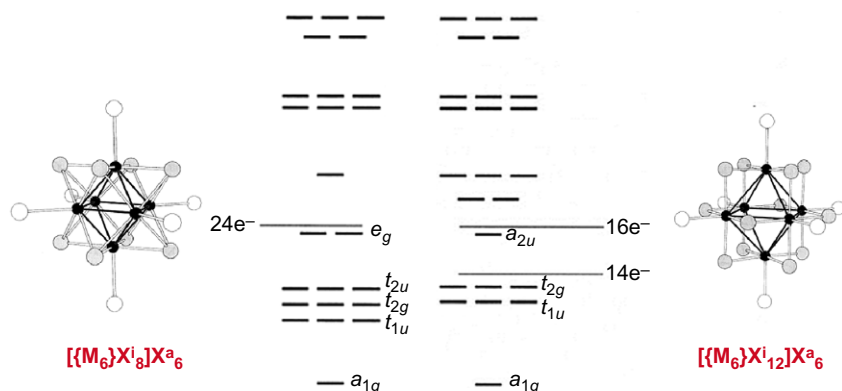


FIGURE 1 Schematic molecular orbital (MO) diagrams for $[\{\text{M}_6\}\text{X}_8^i]\text{X}_6^a_6$ and $[\{\text{M}_6\}\text{X}_{12}^i]\text{X}_6^a_6$ cluster complexes. Adapted from Janiak *et al.* (2012).

rare-earth element clusters always contain an endohedral atom Z (or a small atom group like C₂). The majority of these clusters are octahedral, although tetrahedra, trigonal bipyramids, trigonal prisms, monocapped trigonal prisms, cubes, and square antiprisms have been observed too. Only a few of the cluster complexes are isolated, the most puzzling example being Cs₂Lu[{CLu₆}Cl₁₈] (Artelt et al., 1992), with only nine (!) CBEs (see Fig. 2).

Here and in the following, a cluster is distinguished by waved brackets, for example, {CLu₆}, and the cluster complex by square brackets, [{CLu₆}Cl₁₈]⁵⁻, adopting the nomenclature for Werner-type complexes (Werner, 1893). Cluster complexes are also *anti*-Werner complexes in the sense that the central atom (C) is more electronegative than its first coordination sphere atoms (Lu₆) with halide ligands (Cl₁₈) surrounding the cluster. Hence, the polarities are - + -, in opposition to classical Werner complexes, + - +, as, for example, in solid [PtCl₆]K_{8/2} (Meyer, 2008). The chloride ligands in [{CLu₆}Cl₁₈]⁵⁻ fall in two groups of which 12 cap the octahedral edges and 6 are terminal, residing above the

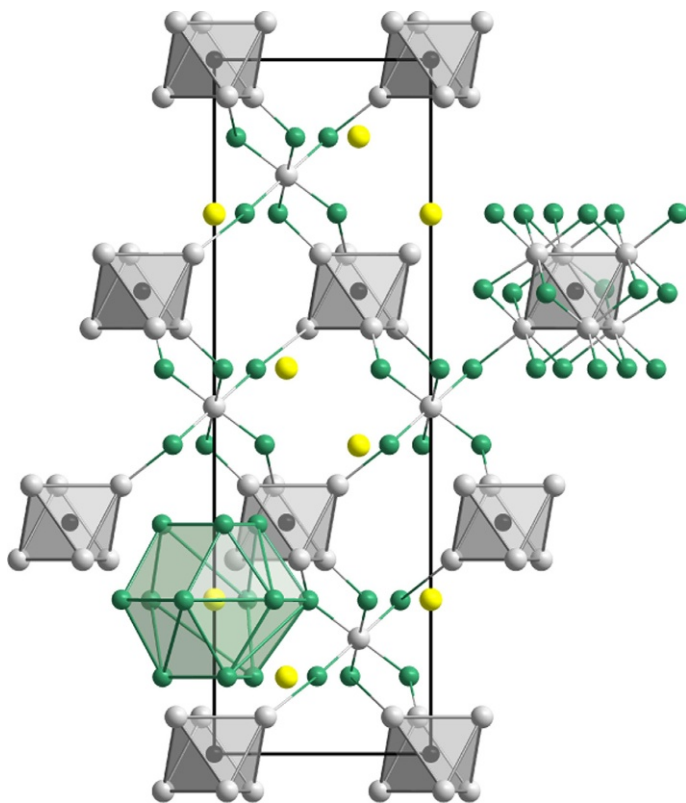


FIGURE 2 Projection of part of the crystal structure of the cluster complex salt [{CLu₆}Cl₁₂Cl₆]⁵⁻ Cs₂Lu, exhibiting {CLu₆} clusters and [{CLu₆}Cl₁₂Cl₆]⁵⁻ cluster complexes and the octahedral and cuboctahedral surroundings of the counter cations Lu³⁺ and Cs⁺, respectively.

corners of the octahedron. The former are called the inner ligands (superscript *i*), while the latter are outer ligands (superscript *a*, from German *äußere Liganden*); hence, we can write $[\{\text{CLU}_6\}\text{Cl}^i_{12}\text{Cl}^a_6]^{5-}$ (Schäfer and Schnering, 1964).

Almost all cluster complexes share common halide ligands. Still, there is a small group of structure types where the clusters are isolated, only surrounded by ligands, but these may belong to two or more clusters. The prolific structure types $\{\text{ZR}_6\}\text{X}_{12}\text{R}$ and $\{\text{ZR}_6\}\text{X}_{10}$ are good examples of which, in 2012, 69 and 35 individuals were known (Rustige et al., 2012) (see Section 4.2). The letter *Z* denotes the endohedral atom that may be a transition metal atom ($Z=\text{T}$) or a main group atom ($Z=\text{E}$); *X* is a halogen atom of the triad chlorine, bromine, and iodine. Formulas with some structural information for the $\{\text{ZR}_6\}\text{X}_{12}\text{R}$ and $\{\text{ZR}_6\}\text{X}_{10}$ structure types are $\{\text{ZR}_6\}\text{X}_{6/1}^i\text{X}_{6/2}^{i-a}\text{X}_{6/2}^{a-i}\text{R}_2$ and $\{\text{ZR}_6\}\text{X}_{2/1}^i\text{X}_{4/2}^{i-i}\text{X}_{6/2}^{i-a}\text{X}_{6/2}^{a-i}$ (see Fig. 3) for a structural representation. $\text{X}_{6/1}^i$ means that six inner ligands belong to one cluster alone; $\text{X}_{6/2}^{i-a}$ means that six ligands inner to one cluster (each capping an edge) are also terminal (*a*) to a neighboring cluster so that they count only half (6/2), according to a nomenclature introduced by Niggli (1916, 1946).

Most of the rare-earth clusters are, however, condensed in a sense that not only the complexes share common halide ligands but also the clusters share common atoms. In the majority of cases, they share common edges (Simon, 1981). Two $\{\text{ZR}_6\}$ octahedra sharing a common edge build a $\{(\text{ZR}_{4/1}\text{R}_{2/2})_2\} = \{\text{Z}_2\text{R}_{10}\}$ dimer, as it appears, for example, in $\text{Cs}\{[(\text{C}_2)_2\text{Er}_{10}]\text{I}_{18}\}$ (see Fig. 4) (Uhrlandt et al., 1994). A small number of further oligomers, trimers through pentamers, are known (see Section 4.3). Further condensation produces linear or corrugated chains, double chains, layers, and a small number of network structures.

Thus, the structural chemistry of reduced rare-earth metal cluster complexes may be described in a way similar to silicates—where $[\text{SiO}_4]$ tetrahedra share common vertices—or like (anti-)Werner complexes that are either monomers, oligomers, or developed into coordination polymers of various dimensionalities.

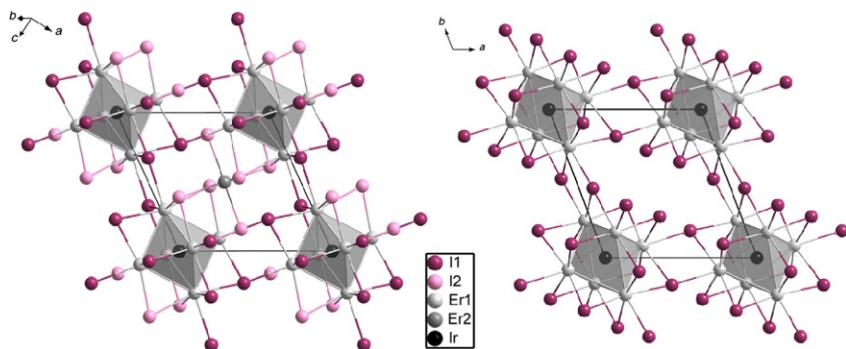


FIGURE 3 A comparison of like projections of the unit cells of $\{\text{IrEr}_6\}\text{I}_{12}\text{Er}$ (left) and $\{\text{IrEr}_6\}\text{I}_{10}$ (right) exhibiting *i*-*a* and *a*-*i* connections of the cluster complexes.

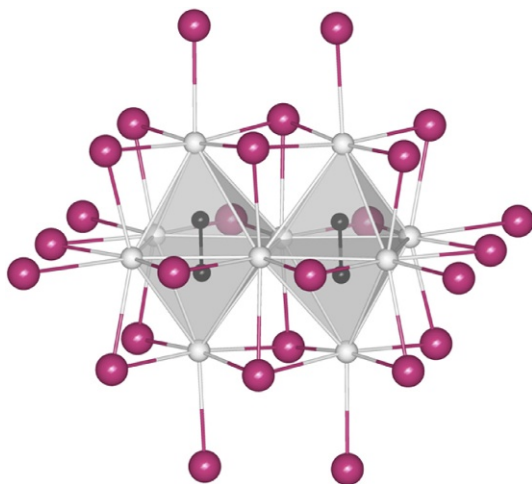


FIGURE 4 The dimer $[(C_2)_2Er_{10}]I_{26}$ as it appears in $Cs[(C_2)_2Er_{10}]I_{18} = Cs[(C_2)_2Er_{10}]I_{10}I_{8/2}^{i-a}I_{8/2}^{a-i}$.

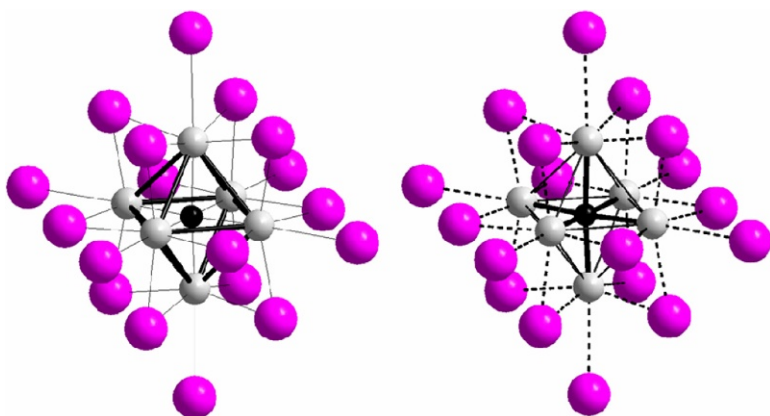


FIGURE 5 Left: A $[(ZR_6)X_{12}X_6]^{n-}$ cluster complex as it is usually depicted highlighting the octahedron. Right: A more realistic description of the bonding situation.

Bonding interactions in these cluster complexes are—as will be pointed out more clearly in [Section 5](#)—predominantly of the heteroatomic Z–R and R–X type with only little to no homoatomic Z–Z (only in polymeric structures possible), R–R, and X–X contributions. Thus, the picture usually shown highlighting the octahedral cluster with an endohedral atom in the center ought to be replaced by a picture emphasizing the polar covalent Z–R interactions (see [Fig. 5](#)).

As we are dealing with extended structures, band structure calculations offer the best insight into the bonding situation (see [Section 5](#)). In any way,

we have to expand Cotton's definition of a cluster as follows: "A metal atom cluster may be defined as a group of two or more metal atoms in which there are substantial and direct bonds between the metal atoms *and/or the endohedral atom (or atom group) centering the cluster.*" These isolated or condensed heteroatomic anti-Werner coordination complexes $\{ZR_r\}$ are, in principle, cutouts of polar intermetallics, $Z=T$. Some of their high negative charge needs to be transferred to the ligands with which they build cluster complexes. Thus, we may well consider them as a symbiotic conglomerate of (polar) intermetallic and salt.

2 CLUSTER COMPLEXES $\{ZR_r\}X_X$

2.1 Rare-Earth Metals R

Rare-earth metals R that may form clusters and encapsulate endohedral atoms (or small atom groups such as $(C_2)^{n-}$) are such that they have 3d (Sc), 4d (Y), or 5d (La, Ce–Lu) states energetically available for Z–R bonding interactions. For the lanthanides, a configuration crossover from a $[Xe]4f^n5d^06s^2$ to a $[Xe]4f^{n-1}5d^16s^2$ must be energetically favorable, which is the case with elements with low third ionization potentials, I_3 (see Fig. 6). One may translate this behavior into standard electrode potentials for the half-cells R^{3+}/R^{2+} , E°

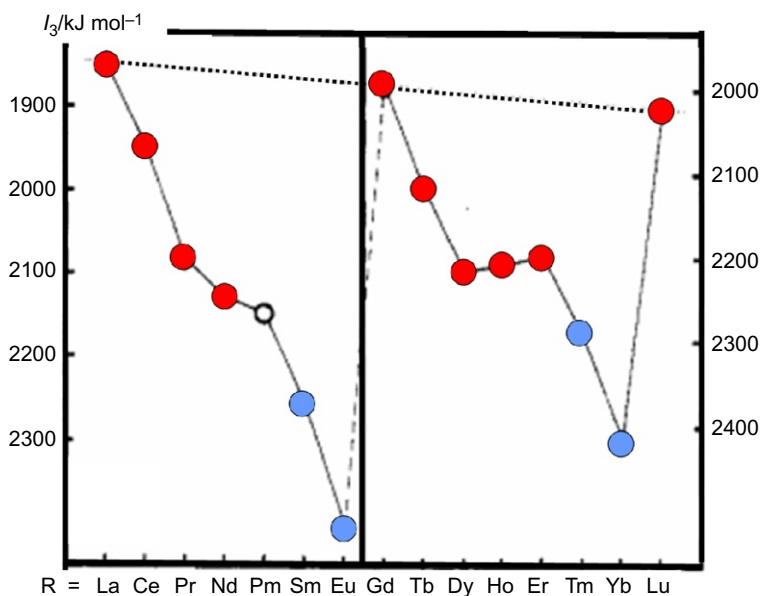


FIGURE 6 Third ionization potential I_3 versus atomic number for the lanthanide series. Elements marked in red form (darker grey) clusters, and elements marked in blue form (lighter grey, Sm, Eu, Tm, Yb) stable divalent compounds with $4f^n5d^0$ electronic configurations.

Sc						
Y						
La	Ce	Pr	Nd	Pm	Sm	Eu
Gd	Tb	Dy	Ho	Er	Tm	Yb
Lu						

FIGURE 7 Periodic table of the lanthanides. “Red” (darker grey) elements form clusters, “blue” (lighter grey) ones do not, and blue + red ones can do both, at different degrees.

(R^{3+}/R^{2+}), because in a Born–Haber-type thermodynamic cycle, the third ionization potential is the only physical property that does not parallel the trend of the lanthanide contraction and hence is periodic (Johnson, 1969, 1982, 2006; Meyer, 1988, 2007; Morss, 1976, 1985). Lanthanides with relatively small $-E^{\text{wo}}(R^{3+}/R^{2+})$ values ($R = \text{Eu, Yb, Sm, Tm}$) form dihalides RX_2 analogous to alkaline-earth metal dihalides (saltlike; see Corbett, 1973), while those with high values form (semi)metallic dihalides and clusters. There is some overlap, however. At least the elements dysprosium and neodymium can do both. This behavior is summarized in a periodic table of the rare-earth elements as shown in Fig. 7.

2.2 Endohedral Atoms Z (=T, E)

The first reduced rare-earth halide whose crystal structure exhibits *trans*-edge-connected chains of $\{R_6\}$ clusters is $\text{Gd}_2\text{Cl}_3 = \{\text{Gd}_{2/1}\text{Gd}_{4/2}\}\text{Cl}_6$ (Lokken and Corbett, 1970, 1973; Mee and Corbett, 1965). This compound was very thoroughly studied and no endohedral atom could ever be detected (Bauhofer and Simon, 1982; Ebbinghaus et al., 1982; Mikheev et al., 1992; Morss et al., 1987; Simon et al., 1979, 1987). It is also a rare example for a cluster complex that is derived from the 6–8 cluster type (ligands capping the faces of the octahedron). Almost all other rare-earth metal clusters are derived from the 6–12 type (ligands cap the edges) and are generally larger because 12 rather than 8 inner ligands cause larger repulsion. Thus, relatively large atoms may be accommodated in the center of the cluster as endohedral atoms (“interstitials”). Around 1980, it was first recognized that light atoms $E = \text{H, C, N, O}$ enter the center of an octahedral rare-earth metal cluster and that, without these ubiquitous atoms (impurities in reactants and containers and atmosphere), almost all reduced rare-earth cluster complexes do not exist (Corbett et al., 1987; Ford et al., 1983; Meyer et al., 1986; Simon, 1985). The encapsulation of transition metal atoms in both zirconium and rare-earth metal clusters was first emphasized in 1986 (Hughbanks and Corbett, 1988; Hughbanks et al., 1986).

Indeed, homoatomic R–R bonding interactions do not play a large role and octahedral clusters are quite flexible in size and symmetry. Therefore, a large variety of atoms with high electron affinities and the possibility to

3 SYNTHESIS

3.1 Reduction Routes in General

The reduction of rare-earth metal trihalides, RX_3 , is in principle possible with all sorts of reducing agents as long as they have standard electrode potentials E° that can overcome that of the respective potentials of $E^\circ(R^{3+}/R^{2+})$ (see [Section 2.1](#)). Therefore, the classical reducing agents, nonmetals like hydrogen or carbon, or like metals (comproportionation route) and unlike metals (metallothermic reduction) are all possible but (may) lead to different products. Cathodic reduction of appropriate melts is also an option.

Metal oxides or halides may be reduced to the respective metal by a number of reductants; hydrogen and carbon are the most easily available and inexpensive for large scales. When pure compounds or even metals are desired, the use of carbon as reductant is disadvantageous because the rare-earth metals form carbide halides and carbides. These are in fact metallic carbides with carbon atoms occupying octahedral or tetrahedral voids in the metal's lattice. Hydrogen is more advantageous although hydrides are also ubiquitous with the rare-earth metals. However, with sufficient care, hydrogen can be pumped off at elevated temperatures and, subsequently, the metals or compounds may be sublimed or distilled, whatever is possible and feasible.

Indeed, hydrogen has been used in the early days as a reductant, for example, for the trichlorides RCl_3 , when the rare-earth metals for comproportionation reactions were either not available or too valuable ([Jantsch and Klemm, 1933](#)). As it is a solid–gas reaction, temperature and surface blocking are always big issues, also time. Only for europium, ytterbium, and samarium, the dichlorides RCl_2 are stable enough and can be produced at reasonably low temperatures. At higher temperatures and with all the other trichlorides, the metals are produced, actually hydrides, the hydrogen content depending upon hydrogen pressure and cooling procedures.

The comproportionation route is straightforward whenever the respective phase diagram is known ([Corbett, 1973](#)). One can also make use of a melt of some kind. If properly carried out, pure products will be obtained. This method can also be used to prepare ternary and quaternary compounds with the proper choice of starting materials. The problem here is that the phase diagrams are in most cases unknown. This approach is, therefore, exploratory and rather serendipitous.

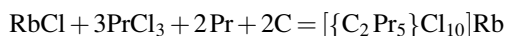
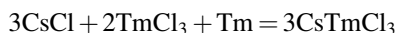
The reduction of rare-earth metal halides with unlike metals, Wöhler's metallothermic reduction ([Wöhler, 1828](#)), has originally been used to produce the rare-earth metals ([Klemm and Bommer, 1937](#)). When used properly, intermediates with oxidation states between +3 and 0 can be obtained.

Cathodic reduction of appropriate halide melts (mostly chlorides) is an important process to produce rare-earth metals. Unless in certain cases, lower-valent halides have not been obtained by this route or did not form during the cooling process ([Masse and Simon, 1981](#)).

In the following, we will discuss only the comproportionation route and the metallothermic reduction route as the two most commonly used synthetic approaches to rare-earth metal/transition metal cluster complexes.

3.2 The Comproportionation Route

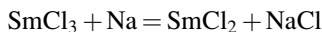
The comproportionation route (Corbett, 1983a, 1991) is widely used and is very efficient when pure phases are desired, especially when the phase relationships are known or can be anticipated. It led to a great variety of “reduced” rare-earth halides, binary, ternary, and higher, simple, and complex salts, and such that incorporate metal clusters interstitially stabilized by a non-metal atom or by a (transition) metal atom, for example,



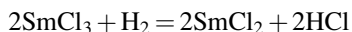
Disadvantages of this route are the often high reaction temperatures and unknown phase equilibriums. Especially when it comes to “higher-component” systems, phase diagrams are not known at all. It was a great thrust for this chemistry when it was discovered that sealed metal ampoules (mostly produced from refractory niobium and tantalum tubing by helium arc welding) were reaction containers sufficiently inert to the corrosive molten salts to allow for pure products (Corbett, 1983b). Still, all constituents of air need to be excluded, which is possible thanks to modern dry box techniques. The unintended incorporation of ubiquitous hydrogen or carbon led to a whole new world of cluster complexes with endohedral atoms, mostly with extended structures (Corbett et al., 1987; Ford et al., 1983; Mattausch et al., 1992; Meyer et al., 1986; Simon, 1985), as in $\{\text{H}_x\text{Lu}\}\text{Cl}$ or in $\{\text{CLu}_2\}\text{Cl}_2$ (Schleid and Meyer, 1987).

3.3 The Metallothermic Reduction Route

The metallothermic reduction of SmCl_3 designed for the preparation of samarium metal with an (apparently) insufficient quantity of sodium resulted in the formation of SmCl_2 (Klemm and Bommer, 1937):



It gave birth to a new approach to “reduced” rare-earth metal halides that were previously synthesized only by the comproportionation route or by reduction with hydrogen, viz.,



In principle, the same experimental techniques as outlined earlier for the comproportionation route may be used for the reduction of rare-earth metal halides with unlike metals, that is, the metallothermic reduction route (Meyer, 2007; Meyer and Schleid, 1987; Wöhler, 1828) with low melting and highly electropositive metals, alkali and alkaline-earth metals in particular. The low melting points of these metals are certainly an advantage, as the reaction temperatures are much lower than for comparable comproportionation reactions. The most obvious disadvantage is that pure products are in most cases (but note the reaction $\text{Cs} + \text{SmCl}_3 = \text{CsSmCl}_3$) not available as one of the driving forces of this route is the production of high-lattice-energy alkali-metal halides.

The separation of the products is not easy, although not impossible. For the exploration of the respective systems and their phase contents, it is, however, often not necessary to obtain pure products because modern, fast X-ray crystallography is an easy means to analyze even multiproduct reactions. Afterward, when the respective compounds are known, care has to be taken to produce the new compounds as pure phase by whatever route is desirable. One major advantage of the metallothermic reduction route is the fairly low reaction temperatures as these allow for the synthesis and crystal growth of compounds that decompose in the solid state, melt incongruently, or even form and decompose in the solid state at fairly low temperatures. Also, low-temperature modifications may be grown as single crystals below the transition temperature.

4 CRYSTAL CHEMISTRY

4.1 Compounds and Structures

In the following, we will focus on rare-earth cluster complexes with endohedral transition metal atoms, $\{\text{T}_t\text{R}_r\}\text{X}_x$, alone. Such with endohedral main group element atoms E have been reviewed in this chapter (Meyer and Wickleder, 2000; Simon and Mattausch, 2013; Simon et al., 1991). Table 1 summarizes the formula types in detail and gives first structural information. It also contains some higher compositions, of which $\{\text{T}_1\text{R}_6\}\text{X}_{12}\text{R}$ is the most prolific. All these compounds are metal-rich halides in a sense that their metal to halide ratio, $t + r/x$, is larger than 0.5. In compounds with isolated clusters, this ratio is between 0.583, $\{\text{TR}_6\}\text{X}_{12}\text{R}$, and 0.824, $\{(\text{TR}_6)_2\}\text{I}_{17}$; for oligomers, it is still below 1.0; for chains and double chains, it is between 0.83 and 1.33; and for layers, it reaches 2.0, $\{\text{TR}\}\text{X}$, and 4.0, $\{\text{T}_2\text{R}_2\}\text{X}$.

4.2 Isolated Octahedral Clusters

Only octahedral clusters $\{\text{TR}_6\}$ ($=\{\text{T}_t\text{R}_r\}$ with $r/t=6.0$) are known as being isolated in a sense that cluster atoms R are not shared with other clusters.

TABLE 1 Compilation of $[(\{T_rR_r\}X_x)(R/A)_z]$ -Type Structures

r/t	x/r	Formula type	Example	Structure	References
CN(T) = 6					
6.5	2.00	$[(\{TR_6\}X_{12})_2RA]$	$[(\{CoEr_6\}I_{12})_2ErCs]$	$0[O-T-6-12]$	Sweet and Hughbanks (2006)
6.1	1.52	$[(\{TR_6\}X_{9.13})R_{0.13}]$	$[(\{MnCe_6\}I_{9.13})Ce_{0.13}]$	$0[O-T-6-12]$	Sweet and Hughbanks (2006)
6.0	2.33	$[(\{TR_6\}X_{14})A_4]$	$[(\{OsLa_6\}I_{14})K_4]$	$0[O-T-6-12]$	Uma et al. (1999)
	2.17	$[(\{TR_6\}X_{13})A_4]$	$[(\{OsPr_6\}I_{13})Cs_4]$	$0[O-T-6-12]$	Lulei and Corbett (1996a)
	2.00	$[(\{TR_6\}X_{12})A_2]$	$[(\{OsLa_6\}I_{12})K_2]$	$0[O-T-6-12]$	Uma and Corbett (1998)
	2.00	$[(\{TR_6\}X_{12})R]$	$[(\{IrEr_6\}I_{12})Er]$	$0[O-T-6-12]$	Rustige et al. (2012)
	2.00	$[(\{TR_6\}X_{12})A]$	$[(\{OsLa_6\}I_{12})Na]$	$0[O-T-6-12]$	Jensen and Corbett (2002)
	1.83	$\{TR_6\}X_{11}$	$\{IrPr_6\}Cl_{11}$	$0[O-T-6-12]$	Herzmann et al. (2010)
	1.83	$\{TR_6\}X_{11}$	$\{CoLa_6\}Cl_{11}$	$0[O-T-6-8/12]$	Zheng et al. (2009a)
	1.71	$[(\{TR_6\}_4)X_{41}]$	$[(\{RuCe_6\}_4)Cl_{41}]$	$0[O-T-6-8/12]$	Steinberg (2013)
	1.69	$[(\{TR_6\}_8)X_{81}]$	$[(\{OsLa_6\}_8)Br_{81}]$	$0[O-T-6-8/12]$	Hong et al. (2000)
	1.67	$[(\{TR_6\}X_{10})A]$	$[(\{MnLa_6\}I_{10})Cs]$	$0[O-T-6-12]$	Lulei and Corbett (1996b)
	1.67	$\{TR_6\}X_{10}$	$\{RuY_6\}I_{10}$	$0[O-T-6-12]$	Hughbanks and Corbett (1989)
	1.67	$\{TR_6\}X_{10}$	$\{FeLa_6\}Br_{10}$	$0[O-T-6-8/12]$	Zheng et al. (2008a)
	1.42	$\{(\{TR_6\}_2)I_{17}\}$	$\{Fe_2Pr_{12}\}I_{17}$	$0[O-T-6-12]$	Park and Corbett (1994)
5.0	1.70	$[(\{T_2R_{10}\}X_{17})A_2]$	$[(\{Os_2Ce_{10}\}I_{17})Cs_2]$	$2 \times 0[O-T-6-12]$	Lulei et al. (1997)
	1.50	$\{T_2R_{10}\}X_{15}$	$\{Os_2La_{10}\}I_{15}$	$2 \times 0[O-T-6-12]$	Lulei et al. (1997)

4.0	2.25	$\{T_4R_{16}X_{36}\}R_4$	$\{Ir_4Y_{16}Br_{36}\}Y_4$	$4 \times 0[O-T-6-12]$	Steinwand and Corbett (1996)
	1.75	$\{T_4R_{16}X_{28}\}R_4$	$\{Mn_4Gd_{16}I_{28}\}Gd_4$	$4 \times 0[O-T-6-12]$	Ebihara et al. (1994)
	1.75	$\{T_4R_{16}X_{28}\}R_3$	$\{Ru_4Sc_{16}Br_{28}\}Sc_3$	$4 \times 0[O-T-6-12]$	Steinwand et al. (1997)
	1.50	$\{T_4R_{16}X_{24}\}$	$\{Ir_4Y_{16}Br_{24}\}$	$4 \times 0[O-T-6-12]$	Steinwand and Corbett (1996)
	1.50	$\{TR_4\}X_6$	$\{MnTb_4\}I_6$	$1[O-T-6-12]$	Rustige (2011)
	1.44	$\{T_4R_{16}X_{23}\}$	$\{Ru_4Gd_{16}Br_{23}\}$	$4 \times 0[O-T-6-12]$	Brühmann (2011)
	1.25	$\{T_4R_{16}X_{20}\}$	$\{Ru_4Y_{16}I_{20}\}$	$4 \times 0[O-T-6-12]$	Payne et al. (1991a)
	1.25	$\{TR_4\}X_5$	$\{RuPr_4\}I_5$	$1[O-T-6-12]$	Payne et al. (1991b)
3.67	1.36	$\{T_3R_{11}X_{15}\}$	$\{Ir_3Gd_{11}Br_{15}\}$	$3 \times 0[O-T-6-12]$	Brühmann and Meyer (2010)
3.0	1.00	$\{TR_3\}X_3$	$\{RuPr_3\}I_3$	$2 \times 1[O-T-6-12]-M1$	Payne et al. (1992)
	1.00	$\{TR_3\}X_3$	$\{RuLa_3\}Br_3$	$1[O-T-6-12]-C2$	Steinberg et al. (2012)
	1.00	$\{TR_3\}X_3$	$\{NiLa_3\}Br_3$	$1[O-T-6-12]-T$	Zheng et al. (2009b)
2.0	0.88	$\{T_4R_8\}X_7$	$\{Ni_4La_8\}Br_7$	$1[TP-T-6-X]$	Zheng et al. (2008b)
1.0	1.00	$\{TR\}X$	$\{Fe_{2+x}Y_2\}Br_2$	$2[O-T-6-12]$	Ruck and Simon (1993)
	0.50	$\{T_2R_2\}X$	$\{Fe_2Gd_2\}I$	$2[O-T-6-12]$	Ruck and Simon (1993)
CN(T)=7					
3.0	1.00	$\{TR_3\}X_3$	$\{RuPr_3\}Cl_3$	$2 \times 1[CTP-T-7-X]-O$	Herzmann et al. (2008)
	1.00	$\{TR_3\}X_3$	$\{RuY_3\}I_3$	$2 \times 1[CTP-T-7-X]-M2$	Payne et al. (1992)
2.8	1.43	$\{T_5R_{14}\}X_{20}$	$\{Ru_5La_{14}Cl_{20}\}$	$5 \times 0[BCHAP-T-14-X]$	Zheng et al. (2012)
	1.39	$\{T_5R_{14}\}_2X_{39}$	$\{Ru_5La_{14}\}_2Br_{39}$	$5 \times 0[BCHAP-T-14-X]$	Steinberg (2013)

Continued

TABLE 1 Compilation of $\{T_rR_r\}X_x\}(R/A)_z$ -Type Structures—Cont'd

r/t	x/r	Formula type	Example	Structure	References
2.5	1.00	$\{T_2R_5\}X_5$	$\{Ir_2Gd_5\}Br_5$	$2 \times 1[CTP-T-7-X]$	Brühmann and Meyer (2012)
CN(T)=8					
4.0	1.33	$\{T_3R_{12}\}X_{16}$	$\{Ir_3Sc_{12}\}Br_{16}$	$1[C+2SAP-T-8-X]$	Zimmermann et al. (2010)
	1.33	$\{[T_3R_{12}]X_{16}\}R$	$\{[Os_3Sc_{12}]Br_{16}\}Sc$	$1[C+2SAP-T-8-X]$	Zimmermann et al. (2010)
	1.20	$\{T_5R_{20}\}X_{24}$	$\{Os_5Lu_{20}\}I_{24}$	$1[C+4SAP-T-8-X]$	Brühmann et al. (2011)
	1.00	$\{TR_4\}X_4$	$\{OsSc_4\}Cl_4$	$1[SAP-T-8-X]-M$	Zimmermann et al. (2010)
	1.00	$\{TR_4\}X_4$	$\{OsTb_4\}I_4$	$1[SAP-T-8-X]-O$	Rustige (2011)
	1.00	$\{TR_4\}X_4$	$\{ReGd_4\}Br_4$	$1[SAP-T-8-X]-T$	Zimmermann et al. (2010)

T, transition metal; A, group I/II element.

Structure: Before [...]: 0 (isolated), 2×0 (dimer), 3×0 (trimer), 4×0 (tetramer), 5×0 (pentamer), 1 (chain), 2×1 (double chain), 2 (layer). Inside [...]: O (octahedron), TP (trigonal prism), CTP (capped trigonal prism), BCHAP (bicapped hexagonal antiprism), C (cube), SAP (square antiprism), T (transition metal as endohedral atom), 6, 7, 8 (number of cluster atoms), 8, 12, X (number of ligands). After [...]: C (cubic), T (tetragonal), O (orthorhombic), M (monoclinic)

The only isolated cluster complex, with no chloride ligands shared, is known for $[\{\text{CLu}_6\}\text{Cl}_{18}]\text{Cs}_2\text{Lu}$ (Fig. 2), with $r/e=6.0$ and $x/r=3.0$, with a single carbon atom as the endohedral atom (Artelt et al., 1992).

With $Z=\text{T}$, there are two formula/structure types that are most prolific $[\{\text{TR}_6\}\text{X}_{12}]\text{R}$ and $\{\text{TR}_6\}\text{X}_{10}$ of course both with $r/t=6.0$ and with $x/r=2.0$ and 1.67, respectively. Hence, the clusters are still surrounded by 12 edge-capping (i) and 6 terminal ligands (a), *in summa* 18, but the cluster complexes share common ligands according to the formulations $\{\text{TR}_6\}\text{X}_{6/1}^i\text{X}_{6/2}^{i-a}\text{X}_{6/2}^{a-i}\text{R}_2$ (for $[\{\text{TR}_6\}\text{X}_{12}]\text{R}$) and $\{\text{TR}_6\}\text{X}_{2/1}^i\text{X}_{4/2}^{i-i}\text{X}_{6/2}^{i-a}\text{X}_{6/2}^{a-i}$ (for $\{\text{TR}_6\}\text{X}_{10}$) (see Fig. 3). From the point of view of the ligands, outer, a ligands have coordination number (CN) 1, i ligands CN=2, shared i-a as well as a-i ligands CN=3, and shared i-i ligands CN=4.

For a comparison of the two structure types, $[\{\text{TR}_6\}\text{X}_{12}]\text{R}$ and $\{\text{TR}_6\}\text{X}_{10}$, one needs to compare the primitive rhombohedral unit cell of $[\{\text{TR}_6\}\text{X}_{12}]\text{R}$ with the triclinic unit cell of $\{\text{TR}_6\}\text{X}_{10}$ (Fig. 3). The difference between the two formulas, $[\{\text{TR}_6\}\text{X}_{12}]\text{R} - \{\text{TR}_6\}\text{X}_{10} = \text{RX}_2$, is the seventh R atom in the former, residing in the octahedral holes of the iodide, which is missing in the latter, and two iodide ligands. Four of the inner iodide ligands in $[\{\text{TR}_6\}\text{X}_{12}]\text{R}$ become two in $\{\text{TR}_6\}\text{X}_{10}$ that is accomplished by a shear process along the shear plane $(2\bar{1}0)$ with respect to the primitive rhombohedral cell of $[\{\text{TR}_6\}\text{X}_{12}]\text{R}$ (Rustige et al., 2012). Figure 9 shows this process; depicted are only the cuboctahedra of inner ligands and the central Z atom.

Tables 2 and 3 show the many examples for both structure types. At present, there are 69 representatives of the $\{\text{ESc}_6\}\text{Cl}_{12}\text{Sc}$ type with $E=\text{B}, \text{N}$ (Hwu and Corbett, 1986); the crystal structures of 42 have been determined from single-crystal X-ray diffraction data, and the remaining 27 were identified by powder X-ray diffraction only. The statistic for the $\{\text{RuY}_6\}\text{I}_{10}$ type (Hughbanks and Corbett, 1989) is 35, 31+4. The majority of halides are iodides (55 and 16), followed by bromides (10 and 17) and chlorides (4 and 2).

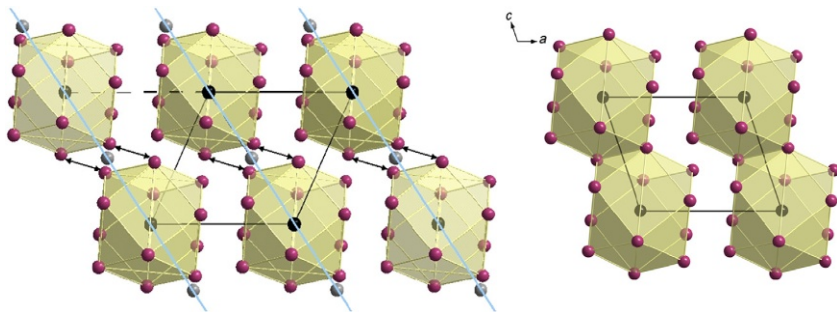


FIGURE 9 The inner iodide cuboctahedra centered by T as they occur in $[\{\text{TR}_6\}\text{X}_{12}]\text{R}$ (left) and $\{\text{TR}_6\}\text{X}_{10}$ (right) as they are connected by a shear process (left) and the i-i connections arising therefrom by double arrows.

TABLE 2 A Compilation of Cluster-Based Electron (CBE) per One Formula Unit and Important Interatomic Distances, in pm, for $\{ZR_6\}X_{12}R$ -Type Compounds^a

Compound	CBE	$\langle d \rangle R-R$	$\langle d \rangle R2-X$	$\langle d \rangle R1-X$	$\langle d \rangle Z-R$	References
$\{CoLa_6\}I_{12}La$	18	399.3	321.4	328.8	282.3	Lukachuk et al. (2008)
$\{OsLa_6\}I_{12}La$	17					Jensen and Corbett (2002)
$\{MnPr_6\}I_{12}Pr$	16					Hughbanks et al. (1986)
$\{FePr_6\}I_{12}Pr$	17	391.3	315.6	324.3	276.7	Palasyuk et al. (2006a)
$\{CoPr_6\}I_{12}Pr$	18	392.2	315.0	323.8	277.3	Palasyuk et al. (2006b)
$\{NiPr_6\}I_{12}Pr$	19					Hughbanks et al. (1986)
$\{CuPr_6\}I_{12}Pr$	20					Payne and Corbett (1990)
$\{RuPr_6\}I_{12}Pr$	17	397.1	314.7	322.3	280.8	Payne and Corbett (1990)
$\{RhPr_6\}I_{12}Pr$	18					Payne and Corbett (1990)
$\{PdPr_6\}I_{12}Pr$	19					Payne and Corbett (1990)
$\{RePr_6\}I_{12}Pr$	16					Payne and Corbett (1990)
$\{OsPr_6\}I_{12}Pr$	17					Payne and Corbett (1990)
$\{IrPr_6\}I_{12}Pr$	18					Payne and Corbett (1990)
$\{PtPr_6\}I_{12}Pr$	19	404.8	315.9	321.6	286.3	Payne and Corbett (1990)
$\{MnGd_6\}Br_{12}Gd$	16	374.1	286.1	296.6	264.6	Rustige et al. (2012)
$\{FeGd_6\}Br_{12}Gd$	17	370.8	283.6	297.9	262.2	Rustige et al. (2012)
$\{BGd_6\}I_{12}Gd$	12					Mattausch et al. (1999)

{MnGd ₆ }I ₁₂ Gd	16					Hughbanks and Corbett (1988)
{FeGd ₆ }I ₁₂ Gd	17					Hughbanks et al. (1986)
{CoGd ₆ }I ₁₂ Gd	18	375.8	305.5	318.7	265.8	Sweet et al. (2006)
{NiGd ₆ }I ₁₂ Gd	19					Payne and Corbett (1990)
{CuGd ₆ }I ₁₂ Gd	20					Payne and Corbett (1990)
{ZnGd ₆ }I ₁₂ Gd	21	396.9	311.6	317.1	280.7	Lukachuk et al. (2008)
{RuGd ₆ }I ₁₂ Gd	17					Payne and Corbett (1990)
{RuGd ₆ }I ₁₂ Gd	17	383.8	308.8	317.7	271.4	Rustige et al. (2012)
{RhGd ₆ }I ₁₂ Gd	18					Payne and Corbett (1990)
{PdGd ₆ }I ₁₂ Gd	19					Payne and Corbett (1990)
{OsGd ₆ }I ₁₂ Gd	17					Payne and Corbett (1990)
{IrGd ₆ }I ₁₂ Gd	18	392.4	305.8	314.8	277.5	Rustige et al. (2012)
{IrGd ₆ }I ₁₂ Gd	18					Payne and Corbett (1990)
{PtGd ₆ }I ₁₂ Gd	19					Payne and Corbett (1990)
{AuGd ₆ }I ₁₂ Gd	20					Payne and Corbett (1990)
{MnTb ₆ }Br ₁₂ Tb	16	361.2	278.7	295.2	255.4	Rustige et al. (2012)
{FeTb ₆ }Br ₁₂ Tb	17	369.3	282.4	297.4	261.2	Rustige et al. (2012)
{RhTb ₆ }Br ₁₂ Tb	18	375.5	285.3	294.8	265.6	Rustige et al. (2012)
{BTb ₆ }I ₁₂ Tb	12					Mattausch et al. (1999)
{MnTb ₆ }I ₁₂ Tb	16	383.3	306.5	314.2	271.0	Rustige et al. (2012)

Continued

TABLE 2 A Compilation of Cluster-Based Electron (CBE) per One Formula Unit and Important Interatomic Distances, in pm, for $\{ZR_6\}X_{12}R$ -Type Compounds—Cont'd

Compound	CBE	$\langle d \rangle R-R$	$\langle d \rangle R2-X$	$\langle d \rangle R1-X$	$\langle d \rangle Z-R$	References
$\{FeTb_6\}I_{12}Tb$	17	376.7	304.7	317.6	266.4	Rustige et al. (2012)
$\{CoTb_6\}I_{12}Tb$	18	374.8	304.8	317.5	265.0	Rustige et al. (2012)
$\{NiTb_6\}I_{12}Tb$	19	377.5	306.2	315.2	266.9	Rustige et al. (2012)
$\{RuTb_6\}I_{12}Tb$	17	383.3	306.2	315.3	271.4	Rustige et al. (2012)
$\{RhTb_6\}I_{12}Tb$	18	381.0	304.8	318.3	269.4	Rustige et al. (2012)
$\{PtTb_6\}I_{12}Tb$	19	386.6	306.9	315.7	273.4	Rustige et al. (2012)
$\{C_2Dy_6\}I_{12}Dy$	15	358.3	313.8	308.6		Rustige et al. (2012)
$\{CoDy_6\}I_{12}Dy$	18	375.1	315.8	316.1	265.2	Rustige et al. (2012)
$\{RuDy_6\}I_{12}Dy$	17	387.8	316.0	317.9	274.18	Rustige et al. (2012)
$\{IrDy_6\}I_{12}Dy$	18					Meyer, (2013)
$\{CoHo_6\}Br_{12}Ho$	18	363.6	281.0	295.7	257.1	Rustige et al. (2012)
$\{NiHo_6\}Br_{12}Ho$	19	367.78	293.9	293.2	260.1	Rustige et al. (2012)
$\{FeHo_6\}I_{12}Ho$	17	368.5	301.1	316.6	260.6	Daub and Meyer (2009)
$\{CoHo_6\}I_{12}Ho$	18	368.4	303.4	316.8	260.5	Rustige et al. (2012)
$\{NiHo_6\}I_{12}Ho$	19	372.6	313.7	315.0	263.5	Rustige et al. (2012)
$\{OsHo_6\}I_{12}Ho$	17	374.0	304.2	316.8	264.4	Rustige et al. (2012)
$\{PtHo_6\}I_{12}Ho$	19	383.3	313.8	315.3	271.0	Rustige et al. (2012)

{FeY ₆ }I ₁₂ Y	17	370.6	302.2	317.8	262.1	Hughbanks and Corbett (1988)
{FeY ₆ }I ₁₂ Y	17	371.8	302.2	318.1	262.9	Rustige et al. (2012)
{CoY ₆ }I ₁₂ Y	18					Hughbanks et al. (1986)
{RuY ₆ }I ₁₂ Y	17					Hughbanks and Corbett (1989)
{FeEr ₆ }I ₁₂ Er	17	367.1	300.5	316.8	259.6	Rustige et al. (2012)
{CoEr ₆ }I ₁₂ Er	18	366.1	302.1	316.3	258.9	Rustige et al. (2012)
{IrEr ₆ }I ₁₂ Er	19	375.7	300.5	316.7	265.7	Rustige et al. (2012)
{BSc ₆ }Cl ₁₂ Sc	12	328.7	254.7	261.2	232.4	Hwu and Corbett (1986)
{NSc ₆ }Cl ₁₂ Sc	12	324.8	255.0	261.0	229.6	Hwu and Corbett (1986)
{CoSc ₆ }Cl ₁₂ Sc	18	336.7	250.3	265.8	238.1	Rustige et al. (2012)
{NiSc ₆ }Cl ₁₂ Sc	19	340.1	258.5	264.1	240.4	Rustige et al. (2012)
{CSc ₆ }Br ₁₂ Sc	13	323.4	270.2	277.0	228.8	Dudis et al. (1986)
{CoSc ₆ }Br ₁₂ Sc	18	341.5	266.5	281.4	241.5	Rustige et al. (2012)
{NiSc ₆ }Br ₁₂ Sc	19	342.3	273.1	279.0	242.0	Rustige et al. (2012)
{BSc ₆ }I ₁₂ Sc	12					Dudis et al. (1986)
{CSc ₆ }I ₁₂ Sc	12	325.6	291.7	302.7	230.4	Dudis et al. (1986)
{CSc ₆ }I ₁₂ Sc	12	325.9	291.8	302.7	230.4	Demir, 2007
{CoSc ₆ }I ₁₂ Sc	18	343.8	287.4	305.7	243.1	Hughbanks and Corbett (1988)
{NiSc ₆ }I ₁₂ Sc	19					Hughbanks et al. (1986)

^aAll compounds crystallize with the {ZSc₆}I₁₂Sc type of structure (trigonal, R $\bar{3}$ or R3). When distances are given, the data are from single-crystal X-ray structure determinations; all other data are from powder X-ray diffraction.

TABLE 3 A Compilation of Cluster-Based Electron (CBE) per One Formula Unit and Important Interatomic Distances, in pm, for {ZR₆}X₁₀-Type Compounds^a

Compound	CBE	$\langle d \rangle_{R-R}$	$\langle d \rangle_{R-X}$	$\langle d \rangle_{Z-R}$	References
{C ₂ La ₆ }I ₁₀	14	389.7	326.1	262.7	Mattausch et al. (2005)
{OsLa ₆ }I ₁₀	16	405.3	328.0	286.5	Mattausch and Simon (2005a,b)
{C ₂ Ce ₆ }I ₁₀	14	385.2	323.3	259.1	Mattausch et al. (2005)
{IrCe ₆ }I ₁₀	17				Larres (2012)
{CoPr ₆ }Br ₁₀	17	387.4	301.7	273.9	Llusar and Corbett (1994)
{RuPr ₆ }Br ₁₀	16	394.4	302.9	278.7	Llusar and Corbett (1994)
{OsPr ₆ }Br ₁₀	16				Llusar and Corbett (1994)
{OsPr ₆ }I ₁₀	16	394.9	302.9	279.1	Payne and Corbett (1990)
{CoGd ₆ }Cl ₁₀	17	371.3	282.0	262.6	Rustige et al. (2012)
{CoGd ₆ }Br ₁₀	17	373.7	295.2	264.3	Lefevre et al. (2005)
{RuGd ₆ }Br ₁₀	16	380.9	296.1	269.4	Rustige et al. (2012)
{RhGd ₆ }Br ₁₀	17	381.8	296.7	270.0	Rustige et al. (2012)
{OsGd ₆ }Br ₁₀	16	382.1	296.1	270.3	Rustige et al. (2012)
{IrGd ₆ }Br ₁₀	17	383.2	296.2	271.0	Rustige et al. (2012)
{OsGd ₆ }I ₁₀	16	388.3	317.2	274.9	Rustige et al. (2012)
{CoTb ₆ }Cl ₁₀	17	368.6	280.4	260.7	Rustige et al. (2012)

{CoTb ₆ }Br ₁₀	17	372.7	294.5	263.6	Rustige et al. (2012)
{NiTb ₆ }Br ₁₀	18	373.2	294.3	263.9	Rustige et al. (2012)
{RuTb ₆ }Br ₁₀	16	379.6	294.9	268.4	Rustige et al. (2012)
{RhTb ₆ }Br ₁₀	17	377.6	294.6	267.1	Rustige et al. (2012)
{IrTb ₆ }Br ₁₀	17	381.7	295.1	270.0	Rustige et al. (2012)
{OsTb ₆ }I ₁₀	16	385.9	316.1	272.9	Rustige et al. (2012)
{IrTb ₆ }I ₁₀	17	385.1	315.5	272.4	Rustige et al. (2012)
{CoY ₆ }Br ₁₀	17	368.7	292.7	260.7	Rustige et al. (2012)
{NiY ₆ }Br ₁₀	18	370.1	293.1	261.7	Rustige et al. (2012)
{PdY ₆ }Br ₁₀	18	370.6	293.1	262.1	Rustige et al. (2012)
{CoY ₆ }I ₁₀	17				Payne and Corbett (1990)
{CoY ₆ }I ₁₀	17	375.9	315.1	265.8	Rustige et al. (2012)
{NiY ₆ }I ₁₀	18				Payne and Corbett (1990)
{NiY ₆ }I ₁₀	18	374.6	264.9	314.3	Steinberg (2013)
{RuY ₆ }I ₁₀	16	381.5	314.9	269.7	Hughbanks and Corbett (1989)
{RhY ₆ }I ₁₀	17				Payne and Corbett (1990)
{OsY ₆ }I ₁₀	16	383.4	315.0	271.1	Payne and Corbett (1990)
{IrY ₆ }I ₁₀	17	382.5	314.9	270.5	Payne and Corbett (1990)

Continued

TABLE 3 A Compilation of Cluster-Based Electron (CBE) per One Formula Unit and Important Interatomic Distances, in pm, for $\{ZR_6\}X_{10}$ -Type Compounds—Cont'd

Compound	CBE	$\langle d \rangle_{R-R}$	$\langle d \rangle_{R-X}$	$\langle d \rangle_{Z-R}$	References
$\{PtY_6\}I_{10}$	18				Payne and Corbett (1990)
$\{PtY_6\}I_{10}$	18	384.3	314.6	271.8	Rustige et al. (2012)
$\{CoEr_6\}Br_{10}$	17	365.8	292.4	258.1	Rustige et al. (2012)
$\{NiEr_6\}I_{10}$	18	370.2	313.4	261.8	Rustige et al. (2012)
$\{IrEr_6\}I_{10}$	17	379.6	313.6	268.5	Rustige et al. (2012)

^aAll compounds crystallize with the $\{RuY_6\}I_{10}$ type of structure (triclinic, $P-1$). When distances are given, the data are from single-crystal X-ray structure determinations; all other data are from powder X-ray diffraction.

7	8	9	10	11	12	13	14	15
						B	C	N
Mn	Fe	Co	Ni	Cu	Zn			
	Ru	Rh	Pd					
Re	Os	Ir	Pt	Au				

FIGURE 10 Endohedral atoms observed for $\{Zr_6\}X_{12}R$ - and $\{Zr_6\}X_{10}$ -type cluster complexes. Red (dark grey) elements occur as endohedral atoms in both structure types, and orange (light grey) elements only in the 7–12 type.

The endohedral atoms that have been observed so far for these two compound types are summarized in Fig. 10. For $\{Zr_6\}X_{10}$ (6–10)-type compounds, endohedral atoms are from groups 8 to 10; single-atom main group elements have not been observed as interstitials, only the C_2 group. For $\{C_2La_6\}I_{10}$, the C–C distance is 145(2) pm (Mattausch et al., 2005), which can be associated with a single bond; thus, there are 14 electrons available for intracluster bonding. In 6–10 compounds with transition metals, there are then 16–18 CBEs.

For $\{Zr_6\}X_{12}R$ (7–12)-type compounds, the variety of endohedral atoms is larger. Main group atoms from groups 13 to 15 may be incorporated, accounting to 12 to 14 electrons for intracluster bonding; with transition metal atoms from groups 7 to 12, there are 16–21 electrons.

Thus, the upper limit for 6–10 and 7–12 intracluster bonding electron counts appears to be 14 with main group and 18–21 with transition metal atoms. As the octahedral clusters $\{Zr_6\}$ can be considered as isolated, MO diagrams may be considered for a first evaluation of the electron count. With main group endohedral atoms, 14 CBEs would be in perfect accord with the MO diagram as shown in Fig. 1 (see also Fig. 11). The incorporation of a T atom into the $\{R_6\}$ cluster (ideal octahedron!) leads to an MO diagram in which nine orbitals are bonding (Fig. 11) and, thus, the ideal electron count would be 18 CBEs. For $\{TR_6\}X_{12}R$ clusters, this number is achieved with group 9 atoms, and for the $\{TR_6\}X_{10}$ type, it would have to be group 10 atoms. As we can see from Fig. 11, there is some flexibility, but only for $\{TR_6\}X_{12}R$ beyond 18 CBEs. This may be explained by a distortion of the octahedron that leads to a breakup of the degeneracy of the t_{1u} orbitals and the occupation of the then lowest-lying MO (Payne and Corbett, 1990).

There are further possibilities for a rich chemistry of halides with isolated clusters that all have 15–18 CBEs. One possibility is to derivatize the R2 position in $\{TR_6\}X_{12}R_2$ by partial or full substitution of this rare-earth metal atom by an alkali-metal or alkaline-earth metal atom (Jensen and

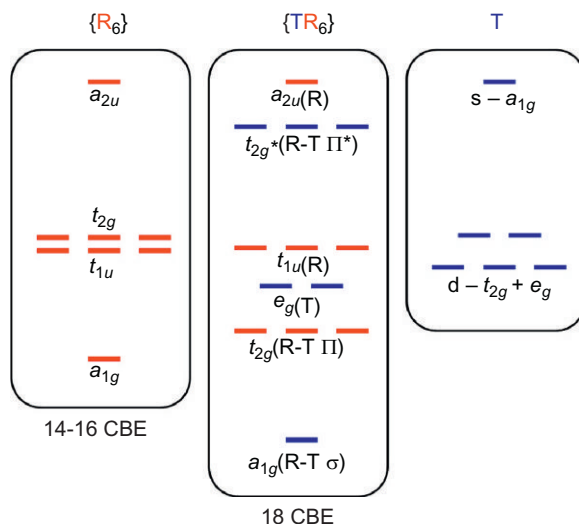


FIGURE 11 Schematic cutouts of molecular orbital diagrams of (left) an $\{R_6\}$ cluster of the $[\{R_6\}X_{12}X^*_6]$ type and its combination with an endohedral T atom (right) to an 18 cluster-based electrons (CBEs) $\{TR_6\}$ cluster (middle).

Corbett, 2002; Sweet and Hughbanks, 2006; Uma and Corbett, 1998) or by the addition of both halide and alkali metals, as in $K_4[\{OsLa_6\}I_{14}]$ (Uma et al., 1999).

Another possibility that nature found is not only to have the 12 edges of the octahedron capped but also to have face capping. Interestingly, a small series of these compounds has now been established, independently in three different laboratories: $\{FeLa_6\}Br_{10}$ (Zheng et al., 2008a), $\{OsLa_6\}_8Br_{81}$ (Hong et al. 2000), $\{RuCe_6\}Cl_{41}$ (Steinberg, 2013), and $\{CoLa_6\}Cl_{11}$ (Zheng et al., 2009a) or, for a better comparison, $\{FeLa_6\}Br_{10}$, $\{OsLa_6\}Br_{10.125}$, $\{RuCe_6\}Br_{10.25}$, and $\{CoLa_6\}Br_{11}$ with 16, 15.875, 15.75, and 16 CBEs. All four crystal structures are represented by large unit cells with a multitude of crystallographically independent clusters. The octahedra are compressed along the pseudofourfold axis, and they are surrounded by a number of ligands that far exceed 18. In the case of $\{RuCe_6\}_4Br_{41}$, the number of ligands (with reasonable R–X distances) is 23 (see Fig. 12). Connections between these cluster complexes are complicated and may be put in the formulation $\{RuCe_6\}_4Cl_{41} = \{RuCe_6\}_4Cl_1^i Cl_{36/4}^{i-i} Cl_{32/3}^{i-a-a} Cl_{20/4}^{f-a} Cl_{12/4}^{a-i} Cl_{16/3}^{a-a-i} Cl_{20/4}^{a-f} Cl_{4/4}^{a-a-a} Cl_{3/3}^{a-a}$ where a and i denote the usual μ_1 - and μ_2 -type ligands capping corners and edges and f denotes μ_3 -type face capping. A coordination number of X of four, that is, X caps a face of one cluster and is an outer ligand for a second one, has also been seen in $\{(C_2)La_5\}Br_9$ where 21 ligands surround a trigonal bipyramid that encapsulates a dicarbon unit (Heuer et al., 1996).

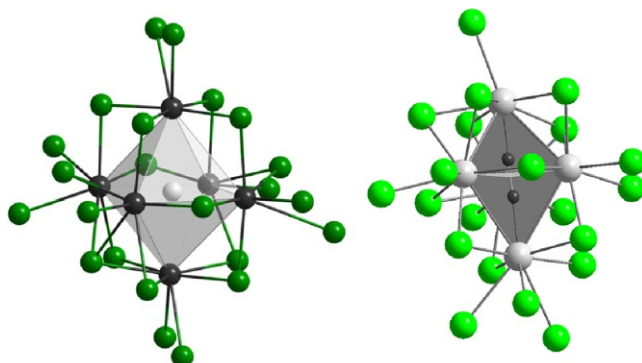


FIGURE 12 Mixed μ_2/μ_3 capping of the compressed $\{\text{RuCe}_6\}$ cluster surrounded by 23 chlorido ligands in the crystal structure of $\{\text{RuCe}_6\}_4\text{Cl}_{41}$ and mixed capping in $\{(\text{C}_2)\text{La}_5\}\text{Br}_9$ with 21 ligands surrounding the trigonal bipyramid.

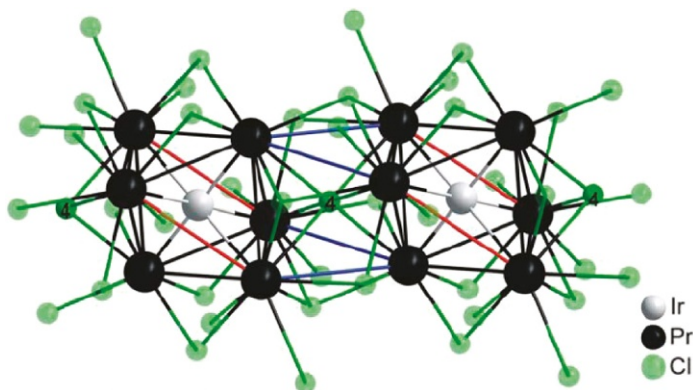


FIGURE 13 A chain of face-sharing $\{\text{Pr}_6\}$ octahedra with endohedral iridium and chloride in $\{\text{IrPr}_6\}\text{Cl}_{11} = \{(\text{Ir},\text{Cl})\text{Pr}_6\}\text{Cl}_{10}$.

Another interesting phenomenon was seen in $\{\text{IrPr}_6\}\text{Cl}_{11}$ (Herzmann et al., 2010). There are also face-capping chlorido ligands, but they now have coordination number six as they cap the faces of two clusters simultaneously (see Fig. 13). Another interpretation of the structure would be that of chains of face-sharing $\{\text{Pr}_6\}$ octahedra with alternating endohedral iridium and chloride, $\{(\text{Ir},\text{Cl})\text{Pr}_6\}\text{Cl}_{10}$.

Face capping has been observed only for the rarer chlorides and bromides. The iodide ligand appears to be too large to cap faces, a phenomenon that is also known from early transition metal cluster complexes. For a rare example, there is $\{\text{Nb}_6\}\text{I}_{11} = \{\text{Nb}_6\}\text{I}_8\text{I}_{6/2}^{\text{a-a}}$ (Simon et al., 1967), a “hypo-electronic” 6–8-type cluster with only 19 CBEs. The electron count may be enhanced by encapsulating an H atom (20 CBEs; Simon, 1967) and adding a cesium

atom in the cuboctahedral hole of the perovskite-type derivative (21 CBEs; Imoto and Corbett, 1980). A rare-earth metal iodide with a fairly high number of CBE (17.5) and with the lowest x/r ratio known so far for noncondensed clusters (see Table 1) is $\{\text{FePr}_6\}_2\text{I}_{17}$ (Park and Corbett, 1994). The low number of ligands results in a high number of i–i connections according to $\{\text{FePr}_6\}\text{I}^{i-i}_{7/2}\text{I}^{i-a}_4\text{I}^{i-a-a}_1 = \{\text{FePr}_6\}\text{I}_{8.5}$, with rather undistorted $\{\text{FePr}_6\}$ clusters, contrary to the chlorides and bromides mentioned earlier with higher x/r ratios.

4.3 Oligomers of Mostly Octahedral Clusters

Cluster condensation begins with two clusters sharing one or more atoms. At present, oligomers with endohedral transition metal atoms are only known with octahedral clusters, $\{\text{TR}_6\}$. Obviously, T atoms are too big to be accommodated in tetrahedra or trigonal bipyramids. On the other hand, oligomers always compete both thermodynamically and electronically with chains; the more cluster atoms are shared, the lesser the electron count has to be, scaled to one endohedral atom.

Octahedra can share corners, edges, and faces. Sharing of corners is only known for $\text{C1-}\{\text{TR}_3\}\text{X}_3$ (see Section 4.5) and face sharing for $\{\text{T}_3\text{R}_{11}\}\text{X}_{15}$ (Section 4.3). Most common is sharing of edges. Table 4 summarizes our present knowledge about oligomers built from rare-earth metal octahedra with endohedral transition metal atoms.

4.3.1 Dimeric Clusters, $\{\text{T}_2\text{R}_{10}\}$

Only one ternary compound, $\{\text{Os}_2\text{La}_{10}\}\text{I}_{15}$, which is composed of edge-sharing lanthanum bioctahedra incorporating endohedral osmium atoms, has been reported, along with a fair number of quaternary iodides, $\text{A}_2[\{\text{T}_2\text{R}_{10}\}\text{I}_{17}]$ with $\text{A} = \text{Rb}, \text{Cs}$; $\text{R} = \text{La}, \text{Ce}, \text{Pr}$; and $\text{T} = \text{Co}, \text{Ni}, \text{Ru}, \text{Os}$ (not all possible combinations; see Table 4) (Lulei et al., 1997). The latter, however, have been characterized mostly from powder X-ray diffraction patterns, whereas the crystal structures of $\{\text{Os}_2\text{La}_{10}\}\text{I}_{15}$ (space group $P-1$, no. 2), $\text{Cs}_2[\{\text{Co}_2\text{La}_{10}\}\text{I}_{17}]$, and $\text{Cs}_2[\{\text{Os}_2\text{Ce}_{10}\}\text{I}_{17}]$ ($C2/m$, no. 12) were determined from single-crystal X-ray diffraction data (Lulei et al., 1996, 1997). Figure 14 shows the structure constituting unit $[\{\text{Os}_2\text{La}_{10}\}\text{I}_{26}]^{11-}$ of $\{\text{Os}_2\text{La}_{10}\}\text{I}_{15}$; thus, the $\{\text{Os}_2\text{La}_{10}\}$ dimers surrounded by 26 iodide ligands are connected according to $\{\text{Os}_2\text{La}_{10}\}\text{I}^{i-i}_4\text{I}^{i-i}_{6/2}\text{I}^{i-a}_{8/2}\text{I}^{a-i}_{8/2}$. In the $\{\text{Os}_2\text{La}_{10}\}$ dimers, Os–La distances range from 276.2 (5) to 300.6(4) pm, with an average of 287.6 pm, and the Os–Os distance is rather long with 440.6(4) pm (see also Table 5 for a comparison with other oligomers).

4.3.2 Trimeric Clusters, $\{\text{T}_3\text{R}_{17}\}$

trans-Edge-connected “open” trimers of octahedral clusters, as, for example, in $\{(\text{C}_2)_3\text{Pr}_{14}\}\text{I}_{20}$ (Wigluszt et al., 2007), are not known with endohedral

TABLE 4 Oligomeric R Cluster Complexes with Endohedral Transition Metal Atoms T

Oligomer	r/t	x/r	Type	Compound	References
Dimer	5.0	1.50	$\{T_2R_{10}\}X_{15}$	$\{Os_2La_{10}\}I_{15}$	Lulei et al. (1997)
	5.0	1.70	$A_2\{T_2R_{10}\}X_{17}$	$Rb_2\{[Co_2La_{10}]I_{17}\}$, $Cs_2\{[T_2La_{10}]I_{17}\}$	Lulei et al. (1997)
				(T=Co, Ni, Ru, Os)	
				$Cs_2\{[Os_2Ce_{10}]I_{17}\}$, $Cs_2\{[T_2Pr_{10}]I_{17}\}$	Lulei et al. (1997)
			(T=Co, Ru, Os)		
Trimer	3.7	1.36	$\{T_3R_{11}\}X_{15}$	$\{Ru_3Gd_{11}\}Cl_{15}$	Wolberg (2014)
				$\{Ir_3Gd_{11}\}Cl_{15}$	Brühmann (2011)
				$\{Ir_3Gd_{11}\}Br_{15}$	Brühmann and Meyer (2010)
Tetramer	4.0	1.25	$TR_4X_5 = \{T_4R_{16}\}X_{20}$	$\{Fe_4Sc_{16}\}Cl_{20}$	Zimmermann (2006)
			Type IIT1	$\{Fe_4Sc_{16}\}Br_{20}$	Steinwand and Corbett (1996), Zimmermann (2006)
				$\{Os_4Sc_{16}\}Br_{20}$	Steinwand and Corbett (1996)
				$\{Ru_4Y_{16}\}Br_{20}$	Steinwand and Corbett (1996), Steinberg (2010)
				$\{Ru_4Y_{16}\}I_{20}$	Payne et al. (1991a,b)
				$\{Ru_4Ho_{16}\}Br_{20}$	Meyer (2013)

Continued

TABLE 4 Oligomeric R Cluster Complexes with Endohedral Transition Metal Atoms T—Cont'd

Oligomer	r/t	x/r	Type	Compound	References
	4.0	1.44	$TR_4X_{5.75} = \{T_4R_{16}\}X_{23}$ Type I	$\{Ru_4Gd_{16}\}Br_{23}$	Brühmann (2011)
	4.0	1.50	$TR_4X_6 = \{T_4R_{16}\}X_{24}$ Type IIO	$\{Ir_4Y_{16}\}Br_{24}$	Steinwand and Corbett (1996)
	5.0	1.40	$TR_5X_7 = \{T_4R_{16}\}X_{20}\{R_4X_8\}$ Type IIC	$\{Mn_4Gd_{16}\}I_{20}\{Gd_4I_8\}$	Ebihara et al. (1994)
				$\{T_4Sc_{16}\}Br_{20}\{Sc_4Br_8\}$ (T = Mn, Fe, Ru, Os)	Mattausch and Simon (1997)
				$\{Ru_4Dy_{16}\}I_{20}\{Dy_4I_8\}$	Meyer (2013)
				$\{Ru_4Ho_{16}\}I_{20}\{Ho_4I_8\}$	Daub (2009)
	5.0	1.80	$TR_5X_9 = \{T_4R_{16}\}X_{24}\{RX_3\}_4$ Type IIT2	$\{Ru_4Sc_{16}\}Cl_{24}\{ScCl_3\}_4$ $\{Os_4Sc_{16}\}Cl_{24}\{ScCl_3\}_4$ $\{Ir_4Sc_{16}\}Cl_{24}\{ScCl_3\}_4$ $\{Ru_4Y_{16}\}Cl_{24}\{YCl_3\}_4$ $\{Co_4Y_{16}\}Cl_{24}\{YCl_3\}_4$ $\{Ir_4Y_{16}\}Cl_{24}\{YCl_3\}_4$ $\{Ru_4Y_{16}\}Br_{24}\{YBr_3\}_4$ $\{Ir_4Y_{16}\}Br_{24}\{YBr_3\}_4$	Zimmermann (2008) Zimmermann (2008) Zimmermann (2008) Steinberg (2013) Steinberg (2013) Steinwand and Corbett (1996) Steinberg (2013) Steinwand and Corbett (1996)

				$\{\text{Ru}_4\text{Gd}_{16}\}\text{Br}_{24}(\text{GdBr}_3)_4$	Wolberg (2014)
				$\{\text{Ir}_4\text{Ho}_{16}\}\text{Br}_{24}(\text{HoBr}_3)_4$	Meyer (2013)
				$\{\text{Ir}_4\text{Tb}_{16}\}\text{Cl}_{24}(\text{TbCl}_3)_4$	Bell (2013)
				$\{\text{Rh}_4\text{Tb}_{16}\}\text{Br}_{24}(\text{TbBr}_3)_4$	Rustige (2011)
				$\{\text{Ir}_4\text{Tb}_{16}\}\text{Br}_{24}(\text{TbBr}_3)_4$	Rustige (2011)
Pentamer	2.8	1.39	$\{\text{T}_5\text{R}_{14}\}\text{X}_{19.5}$	$\{\text{Ru}_5\text{La}_{14}\}_2\text{Br}_{39}$	Steinberg (2013)
		1.43	$\{\text{T}_5\text{R}_{14}\}\text{X}_{20}$	$\{\text{Ru}_5\text{La}_{14}\}\text{Cl}_{20}$	Zheng et al. (2012)
Archetypes are in bold letters.					

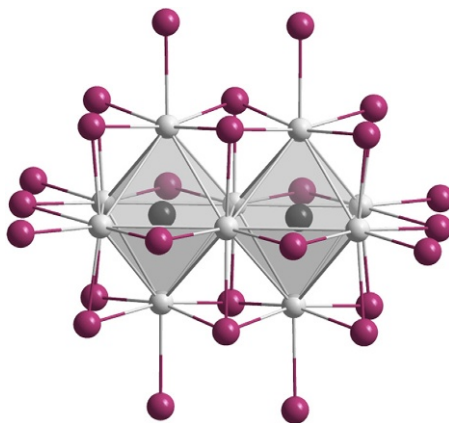


FIGURE 14 The unbridged dimer $[\{\text{Os}_2\text{La}_{10}\}\text{I}_{26}]^{11-}$ as it appears in $\{\text{Os}_2\text{La}_{10}\}\text{I}_{15}$ and in the quaternary iodides $\text{A}_2[\{\text{T}_2\text{R}_{10}\}\text{I}_{17}]$. Os atoms (black) are encapsulated in lanthanum (light gray) biotahedra that are surrounded by 26 iodide ligands (purple, or dark grey in the periphery).

transition metal atoms T. “Closed” trimers are known instead for $\{\text{Ir}_3\text{Gd}_{11}\}\text{X}_{15}$ ($\text{X}=\text{Cl}, \text{Br}$) (Brühmann, 2011; Brühmann and Meyer, 2010) and $\{\text{Ru}_3\text{Gd}_{11}\}\text{Cl}_{15}$ (Wolberg, 2014), all $P6_3/m$, no. 176 (see Fig. 15). These consist of three octahedra sharing common triangular faces, each encapsulating one endohedral T (=Ru, Ir) atom. The $\{\text{T}_3\text{Gd}_{11}\} = \{\text{T}_3\text{Gd}_6^c\text{Gd}_5^f\}$ clusters (f =face sharing) that have the same topology as the cesium suboxide $\{\text{O}_3\text{Cs}_{11}\}$ (Simon and Westerbeck, 1972) are surrounded by 30 halido ligands. These are shared with like cluster complexes to form a three-dimensional structure according to $\{\text{Ir}_3\text{Gd}_{11}\}\text{Cl}^{i-i}{}_{12/2}\text{Cl}^{i-a}{}_{9/2}\text{Cl}^{a-i}{}_{9/2}$.

4.3.3 Tetrameric Clusters, $\{\text{T}_4\text{R}_{16}\}$

The connection of two dimers, $\{\text{T}_2\text{R}_{10}\}$, leads to two types of tetramers, $\{\text{T}_4\text{R}_{16}\}$. In type I, five common edges are shared, $\{\text{T}_4\text{R}_{16}\} = \{\text{T}_4\text{R}_c^c{}_{10}\text{R}_e^e{}_6\}$, whereas six common edges are shared between four octahedra in type II, $\{\text{T}_4\text{R}_{16}\} = \{\text{T}_4\text{R}_c^c{}_{12}\text{R}_e^e{}_4\}$. There is also a third type of tetramer, which has been observed exclusively for R cluster complexes encapsulating main group elements E as endohedral atoms, in $\{(\text{C}_2)_2\text{E}_2\text{R}_{14}\}\text{I}_{24}$ with ($\text{E}=\text{N}, \text{O}$; $\text{R}=\text{Y}, \text{Er}$) (Daub and Meyer, 2010; Mattausch et al., 1995; Steffen and Meyer, 1995). In this tetramer, two tetrahedra (T) and two octahedra (O) are *trans*-connected via three common edges with the sequence OTTO, $\{\text{E}_4\text{R}_{14}\} = \{\text{E}_4\text{R}_c^c{}_8\text{R}_e^e{}_6\}$. An analog with encapsulated transition metal atoms appears impossible because T atoms are too big for tetrahedra.

Type I is only known for two examples, $\{\text{B}_4\text{Tb}_{16}\}\text{Br}_{23}$ (Mattausch et al., 2001a,b) and $\{\text{Ru}_4\text{Gd}_{16}\}\text{Br}_{23}$ (Brühmann, 2011); both crystallize in $C2/m$, no. 12. Two dimers are attached to each other in a way as depicted in Fig. 16. Therefore, the four endohedral atoms Z ($\text{E}=\text{B}$; $\text{T}=\text{Ru}$) form a

TABLE 5 Cluster-Based Electron (CBE) and Mean Distances (in pm) for Oligomeric Cluster Complexes $\{T_nR_r\}X_x$

Compound	CBE	$\langle d \rangle$ (T-T)	$\langle d \rangle$ (T-R)	$\langle d \rangle$ (R-R)	$\langle d \rangle$ (R-X)
$\{Os_2La_{10}\}I_{15}$	15.5	440.6	287.6	408.1	331.3
$\{Ru_3Gd_{11}\}Cl_{15}$	14	297.5	275.2	385.7	289.9
$\{Ir_3Gd_{11}\}Cl_{15}$	15	292.9	278.1	388.5	293.5
$\{Ir_3Gd_{11}\}Br_{15}$	15	295.5	278.9	392.3	310.1
$\{Fe_4Sc_{16}\}Cl_{20}$	15	294.6	253.0	348.7	268.9
$\{Fe_4Sc_{16}\}Br_{20}$	15	304.0	254.3	352.7	285.0
$\{Ru_4Y_{16}\}Br_{20}$	15	335.8	275.7	368.7	300.0
$\{Ru_4Ho_{16}\}Br_{20}$	15	332.2	275.9	366.9	300.8
$\{Ru_4Gd_{16}\}Br_{23}$	14.25	355.0	275.7	380.6	298.5
$\{Ir_4Y_{16}\}Br_{24}$	15	331.5	278.7	372.1	293.7
$\{Ru_4Dy_{16}\}I_{20}\{Dy_4I_8\}$	15 + 1	351.7	276.3	377.1	324.8
$\{Ru_4Ho_{16}\}I_{20}\{Ho_4I_8\}$	15 + 1	345.7	274.9	373.4	320.7
$\{Ru_4Sc_{16}\}Cl_{24}(ScCl_3)_4$	14	296.6	271.6	355.6	263.0
$\{Os_4Sc_{16}\}Cl_{24}(ScCl_3)_4$	14	291.8	272.0	356.4	263.7
$\{Ir_4Sc_{16}\}Cl_{24}(ScCl_3)_4$	15	297.8	272.0	355.7	263.9
$\{Co_4Y_{16}\}Cl_{24}(YCl_3)_4$	15	324.3	272.0	363.8	274.1
$\{Ru_4Y_{16}\}Cl_{24}(YCl_3)_4$	14	320.6	279.7	369.2	274.9
$\{Ir_4Y_{16}\}Cl_{24}(YCl_3)_4$	15	322.2	279.5	368.8	275.6
$\{Ru_4Y_{16}\}Br_{24}(YBr_3)_4$	14	332.9	279.1	373.9	290.0
$\{Ru_4Gd_{16}\}Br_{24}(GdBr_3)_4$	14	343.4	281.7	378.0	296.9
$\{Ir_4Tb_{16}\}Cl_{24}(TbCl_3)_4$	15	324.3	280.9	370.8	276.9
$\{Rh_4Tb_{16}\}Br_{24}(TbBr_3)_4$	15	352.3	278.5	377.1	291.5
$\{Ir_4Tb_{16}\}Br_{24}(TbBr_3)_4$	15	340.1	280.6	375.6	291.4
$\{Ir_4Ho_{16}\}Br_{24}(HoBr_3)_4$	15	330.1	277.7	370.2	293.0
$\{Ru_5La_{14}\}_2Cl_{40}$	12.4	268.7	287.3	417.5	268.7
$\{Ru_5La_{14}\}_2Br_{39}$	12.5	274.2	288.9	409.7	321.0

Only examples for which single-crystal data are available are tabulated. For references, see [Table 4](#).

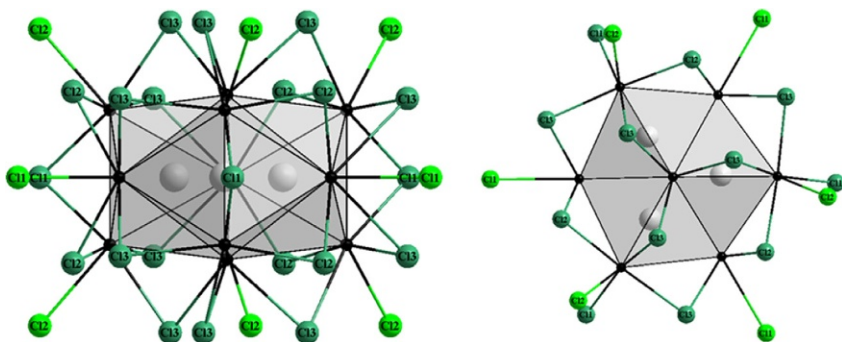


FIGURE 15 Two views of the unbridged trimer $\{T_3Gd_{11}\}X_{30}$ as it appears in $\{T_3Gd_{11}\}X_{15}$.

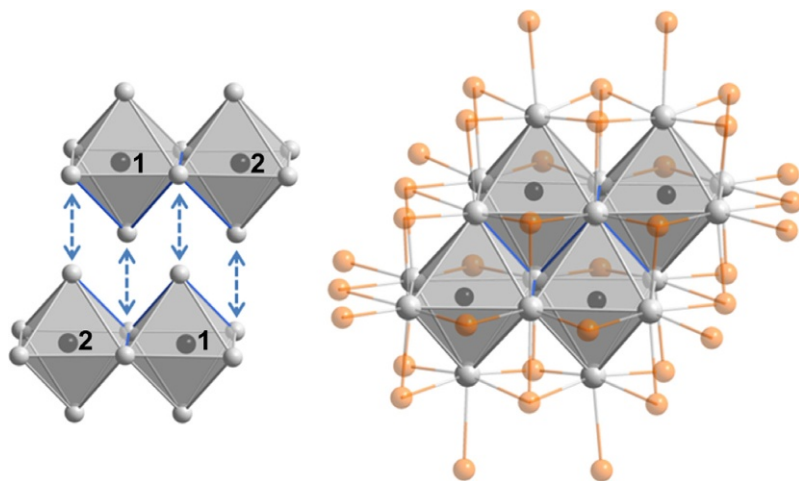


FIGURE 16 In the crystal structure of $\{Ru_4Gd_{16}\}Br_{23}$, two edge-connected $\{Z_2R_{10}\}$ dimers are connected via common edges to a tetrameric cluster $\{Z_4R_{16}\} = \{Z_4R^c_{10}R^e_6\}$ (left), in which the four Z atoms form a rhomboid.

rhomboid in which the Z1–Z1 and Z1–Z2 distances are almost equal and long in $\{B_4Tb_{16}\}Br_{23}$ (413 and 410 pm, respectively) and differ by 30 pm in $\{Ru_4Gd_{16}\}Br_{23}$ (340 and 370 pm). Surprisingly, the Z–Z distances are much shorter in $\{Ru_4Gd_{16}\}Br_{23}$ than in the isostructural boride containing tetramer. The 36 bromido ligands surrounding the clusters are partially shared with like cluster complexes according to $\{Z_4R_{16}\}Br_{12}^i Br_{10/2}^{i-i} Br_{4/2}^{i-a} Br_{4/2}^{a-i} Br_{6/3}^{a-a-a}$.

Type II has, as of today, been observed for 27 distinct compounds that may adopt four different types of structure (see [Tables 4 and 5](#)): the cubic $\{Mn_4Gd_{16}\}I_{20}\{Gd_4I_8\}$ type of structure (IIC, $P-43m$, no. 215; [Ebihara et al., 1994](#)); two independent tetragonal structure types, first observed for $\{Ru_4Y_{16}\}I_{20}$ (IIT1, $P4_2/nmm$, no. 134; [Payne et al., 1991a,b](#)) and $\{Ir_4Y_{16}\}Br_{24}(YBr_3)_4$ (IIT2, $I4_1/a$, no. 88; [Steinwand and Corbett, 1996](#)); and the

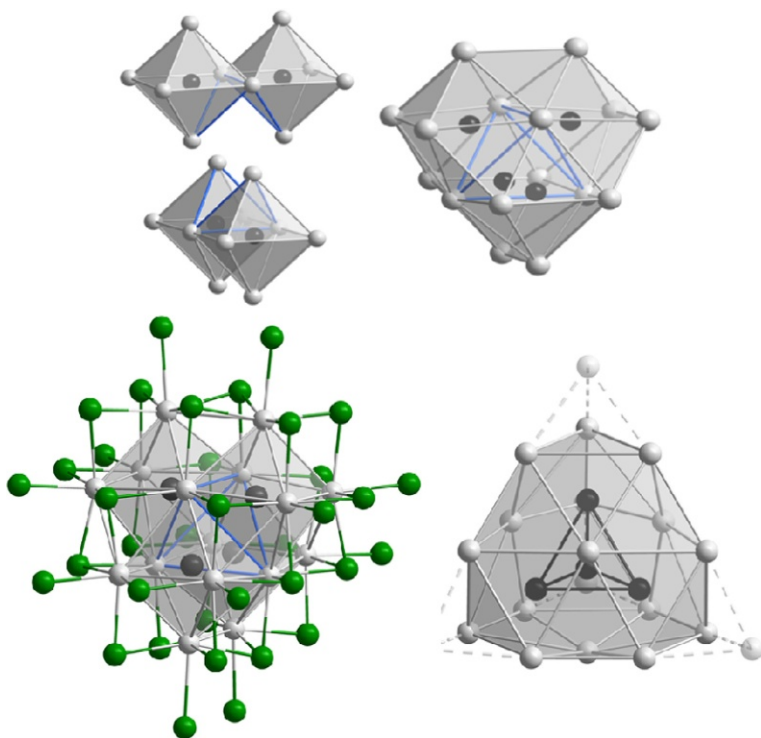


FIGURE 17 Top: Two edge-connected dimers $\{T_2R_{10}\}$ (T black and R light gray) condense to a tetrameric cluster $\{T_4R_{16}\} = \{T_4R^c_{12}R^e_4\}$. Bottom: Each cluster is surrounded by 36 halido ligands (green, or dark grey in the periphery); one tetrameric R_{16} metal skeleton is also a T^3 super-tetrahedron truncated at all four vertices, a *Friauf*-type polyhedron.

orthorhombic $\{Ir_4Y_{16}\}Br_{24}$ type of structure (IIO, *Fddd*, no. 70; [Steinwand and Corbett, 1996](#)). All of these contain type II tetramers, $\{T_4R^c_{12}R^e_4\}$ (see [Fig. 17](#)). In the IIO- $\{Ir_4Y_{16}\}Br_{24}$ type of structure, 24 halido ligands are shared with ten like cluster complexes, whereas 32 halido ligands of one $\{T_4R^c_{12}R^e_4\}$ -type tetramer interconnect to eight neighboring $\{T_4R_{16}\}$ cluster complexes in T1- $\{Ru_4Y_{16}\}I_{20}$. In T2- $\{Ir_4Y_{16}\}Br_{24}(YBr_3)_4$, 16 halido ligands are connected to eight neighboring tetramers; additional noncluster Y atoms reside in octahedral voids of bromido ligands, which are *cis*-edge-connected to two like complexes $[YBr_6]$, thus forming zigzag chains of the composition $(YBr_{6/2}) = (YBr_3)$. In IIC- $\{Mn_4Gd_{16}\}I_{20}\{Gd_4I_8\}$, however, empty tetrahedral clusters $\{\square Gd_4I_8\}$ are surrounded and connected to four $\{Mn_4Gd_{16}\}I_{36}$ tetramers sharing common iodide ligands. The $\{\square Gd_4I_8\}$ cluster complexes are isostructural with those first observed in binary PrI_2 -V ([Meyer and Palasyuk, 2006](#); [Warkentin and Bärnighausen, 1979](#)).

Type II $\{T_4R_{16}\}$ clusters originate from the condensation of two $\{T_2R_{10}\}$ perpendicular to each other such that the endohedral T atoms form a tetrahedron.

The R_{16} polyhedron can be viewed as an all vertices truncated supertetrahedron or, alternatively, as a Friauf-type polyhedron (see Fig. 17). Each $\{T_4R^c_{12}R^e_4\}$ -type tetramer is surrounded by 36 halido ligands. Of these 12 μ_3 -halido ligands cap the faces of each tetramer, whereas 12 halido ligands bridge edges between the R^c atoms in a μ_2 -like fashion. In addition, each R atom bonds to one outer terminal μ_1 -halido ligand that resides in the inner coordination sphere of like tetramers. Averaged T–T, T–R, R–R, and X–R distances (see Table 5) are consistent with data of previously reported compounds (see, e.g., Rustige et al., 2012) and seem to reflect the lanthanide contraction.

4.3.4 Pentameric Clusters, $\{T_5R_{14}\}$

With endohedral transition metal atoms T, pentamers have been observed for only two compounds, $\{Ru_5La_{14}\}Cl_{20}$ ($P-1$, no. 2; Zheng et al., 2012) and $\{Ru_5La_{14}\}_2Br_{39}$ (Cc , no. 9; Steinberg, 2013) (see Tables 4 and 5). The $\{Ru_5La_{14}\}$ cluster may be regarded as a compressed bicapped hexagonal anti-prism $\{La_{14}\}$ that includes a Ru_5 pentagon (see Fig. 18). The relatively short Ru–Ru distances inside the Ru_5 pentagon (see Table 5) indicate strong Ru–Ru bonding interactions, which is confirmed by extended Hückel MO calculations (Zheng et al., 2012). In $\{Ru_5La_{14}\}_2Br_{39}$, the pentamers are encapsulated by 39 bromido ligands that are face capping and edge capping and terminal and all belong to two clusters, according to $[\{Ru_5La_{14}\}Br_{17/2}^I Br_{7/2}^e Br_{15/2}^I]_2$. Stacks of clusters build up a hexagonal packing of rods (see Fig. 18).

The electron count for all oligomers, divided by the number of T atoms per formula unit, is more or less 15 CBEs (see Table 5) with the exception of the two pentamers that account to little more than 12 CBEs. This goes hand in hand with a very small r/t ratio, of only 2.8, and with the shortest T–T and the largest R–R distances, rationalizing strong Ru–Ru and “normal” Ru–La with minor La–La bonding.

4.4 Cluster Chains and Double Chains: CN(T) of 6 and 7

The alternative to oligomers is chains. Connecting octahedra through common *trans*-edges leads from the monomer $\{TR_6\}$ to the dimer $\{T_2R_{10}\}$ and would go on to the trimer $\{T_3R_{14}\}$, to tetramer $\{T_4R_{18}\}$, and hence to oligomers (finite chains) of the general formula $\{T_nR_{4n+2}\}$. The open trimer and tetramer are not known, but there are the closed trimer $\{T_3R_{11}\}$ and tetramer $\{T_4R_{16}\}$ where T–T bonding may play a more pronounced role. Connecting an infinite number of octahedra, $n = \infty$, leads to the cluster chain composition $\{TR_4\} = \{TR_{2/1}R_{4/2}\}$. There are five structure types known with that T–R ratio: four of the composition $\{TR_4\}X_6$ (abbreviated: 146) and one for $\{TR_4\}X_5$ (145).

In 146-O1 (*Pbam*), established first for $\{ESc_4\}Cl_6$, E = B, N (Hwu and Corbett, 1986) and then observed for $\{SiR_4\}Br_6$, R = Gd (Mattausch and Simon, 2005a,b), Tb (Mattausch et al., 2003), the chains are just as described and the most symmetrical (see Fig. 19). Distortions arise through the incorporation of (C_2) units that may be arranged roughly parallel to one of the three

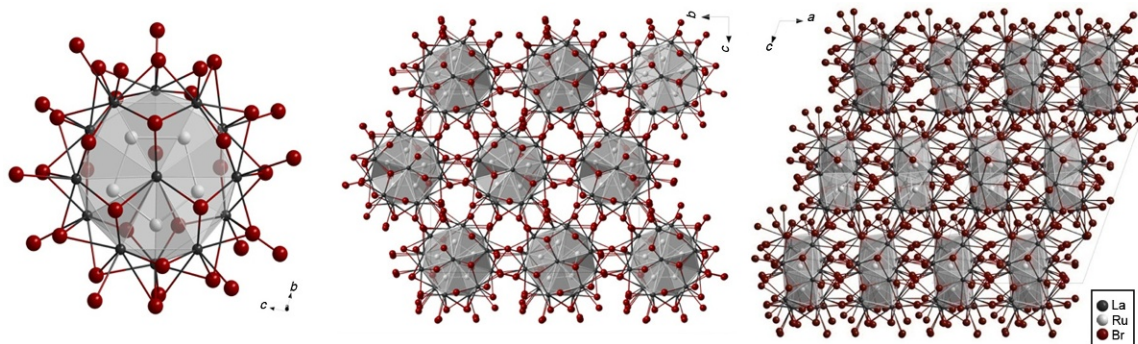


FIGURE 18 Side and top view of the pentameric $\{\text{Ru}_5\text{La}_{14}\}$ cluster surrounded by 36 bromido ligands and the hexagonal close packing of stacks of these cluster complexes.

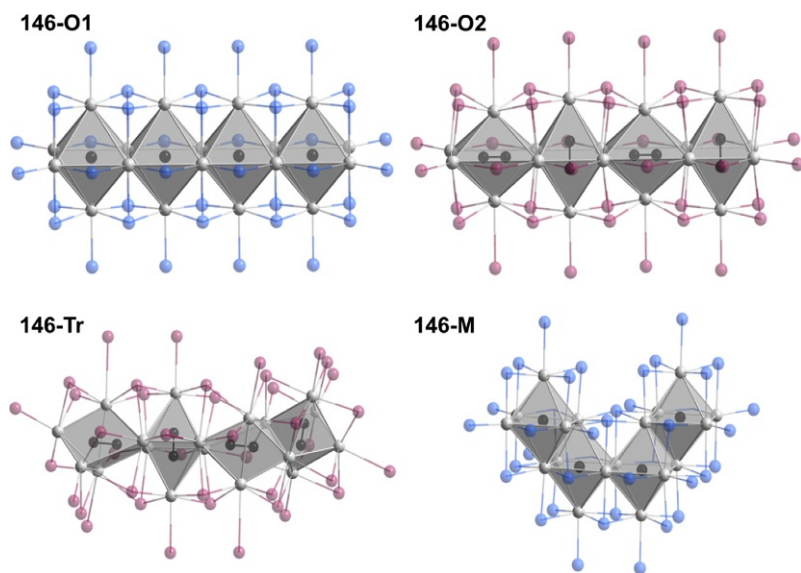


FIGURE 19 A variety of (distorted) octahedral chains in $\{TR_4\}X_6$ with their surrounding by halido ligands; only four of the infinite number of “octahedra” are shown.

fourfold axes of the $\{R_6\}$ octahedron. The distortions are more pronounced with the smaller scandium octahedron in $\{C_2Sc_4\}I_6$ (Dudis and Corbett, 1987), 146-Tr ($P-1$), than with larger R atoms in $\{(C_2)R_4\}I_6$, R=Dy (Mattausch et al., 2007), Er (Daub, 2009), 146-O2 ($Pnmm$). The chains are already not linear in 146-Tr, and therefore, it is not a big step to mixed *cis-trans* chains as in $\{BR_4\}Br_6$, R=Y (Mattausch and Simon, 1997), Tb (Mattausch et al., 2000), and $\{GeGd_4\}I_6$ (Lukachuk et al., 2006) as well as in $\{MnTb_4\}I_6$ (Rustige, 2011), the only member of the $\{TR_4\}X_6$ family with an endohedral transition metal atom (146-M; $C2/c$) (see Fig. 19).

Electron counts for these chain cluster complexes are low, 9–10 CBEs with nonmetal interstitials and only 13 with manganese in $\{MnTb_4\}I_6$. This appears to be the lower limit when judging from the chain-like compounds to come, $\{TR_3\}I_3$, where there is also only one manganese compound known with this electron count, $\{MnGd_3\}I_3$ (see Table 6).

One may also cut down on the number of ligands through further sharing of ligands surrounding the $\{TR_4\}$ chains leading to the composition $\{ZR_4\}X_5$ (Fig. 20). The corresponding structure was first observed for $\{CY_4\}I_5$ (Kauzlarich et al., 1988) and for $\{SiGd_4\}I_5$ (Nagaki et al., 1989), both with 11 CBEs. It has then been observed for a number of iodides with endohedral transition metal atoms, $\{RuLa_4\}I_5$ and $\{TPr_4\}I_5$ with T=Co, Ni, Ru, Os (Park et al., 1997; Payne et al., 1991b), with 15–17 CBEs, a rather acceptable number for somewhat more condensed clusters.

TABLE 6 {TR₃}X₃ Cluster Halides, Structure Types, Cluster-Based Electron (CBE), and Mean Distances (in pm)

Compound	Type	CBE	$\langle d \rangle$ T-T	$\langle d \rangle$ T-R	$\langle d \rangle$ R-R	References
{GaLa ₃ }Br ₃	C1	9	607.5	303.8	429.6	Zheng et al. (2002)
{GaLa ₃ }I ₃	C2	9	447.8	302.2	405.9	Zheng et al. (2001)
{GaCe ₃ }Br ₃	C1	9	600.43	300.22	424.57	Zheng et al. (2005)
{NiLa ₃ }Br ₃	T	16	425.4	286.2	415.2	Zheng et al. (2009b)
{RuLa ₃ }Br ₃	C2	14	428.7	286.5	408.6	Steinberg et al. (2012)
{RhLa ₃ }Br ₃	C2	15				Steinberg et al. (2012)
{IrLa ₃ }Br ₃	C2	15	287.9	430.4	410.5	Steinberg et al. (2012)
{PtLa ₃ }Br ₃	C2	16				Steinberg et al. (2012)
{RuLa ₃ }I ₃	M1	14				Payne et al. (1992)
	M1	14	429.5	287.0	401.2	Köckerling and Martin (2001)
{OsLa ₃ }I ₃	C2	14				Dorhout et al. (1991)
{IrLa ₃ }I ₃	C2	15				Dorhout et al. (1991)
{PtLa ₃ }I ₃	C2	16				Dorhout et al. (1991)
{AuLa ₃ }I ₃	C2	17	447.6	299.63	398.4	Mattausch et al. (2004)
{IrCe ₃ }Cl ₃	O	15				Larres (2012)
{RuCe ₃ }Br ₃	C2	14	404.9	284.0	377.5	Herzmann (2009)
{RuCe ₃ }I ₃	M1	14	426.1	283.8	405.5	Steinberg (2013)

Continued

TABLE 6 {TR₃}X₃ Cluster Halides, Structure Types, Cluster-Based Electron (CBE), and Mean Distances (in pm)—Cont'd

Compound	Type	CBE	$\langle d \rangle$ T-T	$\langle d \rangle$ T-R	$\langle d \rangle$ R-R	References
{IrCe ₃ }I ₃	C2	15	440.2	288.3	412.6	Steinberg et al. (2013)
{RuPr ₃ }Cl ₃	O	14	357.1	303.8	372.4	Herzmann et al. (2008)
{RuPr ₃ }Br ₃	M1	14				Llusar and Corbett (1994)
	M1	14	416.6	297.7	401.9	Hassel (2013)
	C2	14	421.1	282.1	402.2	Hassel (2013)
{OsPr ₃ }Br ₃	C2	14				Llusar and Corbett (1994)
{CoPr ₃ }Br ₃	C2	15				Llusar and Corbett (1994)
{RhPr ₃ }Br ₃	C2	15				Llusar and Corbett (1994)
{IrPr ₃ }Br ₃	C2	15				Llusar and Corbett (1994)
	C2	15	422.4	283.0	403.5	Klein (2013)
{PtPr ₃ }Br ₃	C2	16				Llusar and Corbett (1994)
{RuPr ₃ }I ₃	M1	14	422.9	281.7	407.0	Payne et al. (1992)
{OsPr ₃ }I ₃	C2	14				Dorhout et al. (1991)
	M1	14	422.3	282.5	379.2	Park et al. (1997)
	C2	14	437.7	286.2	369.0	Herzmann (2009)
{PtPr ₃ }I ₃	C2	16	438.9	288.5	374.5	Dorhout et al. (1991)
{IrNd ₃ }I ₃	C2	15				Herzmann (2009)

$\{\text{RuGd}_3\}\text{Br}_3$	M2	14	317.1	278.2	367.1	Wolberg (2014)
$\{\text{MnGd}_3\}\text{I}_3$	M2	13	266.5	299.7	392.1	Ebihara et al. (1994)
$\{\text{RuGd}_3\}\text{I}_3$	M2	14				Payne et al. (1992)
$\{\text{IrGd}_3\}\text{I}_3$	M2	15				Payne et al. (1992)
$\{\text{RuY}_3\}\text{I}_3$	M2	14	315.9	287.5	376.2	Payne et al. (1992)
$\{\text{IrY}_3\}\text{I}_3$	M2	15	314.3	287.4	399.6	Payne et al. (1992)
$\{\text{RuTb}_3\}\text{Br}_3$	M2	14	314.1	277.1	374.2	Rustige (2011)
$\{\text{RuTb}_3\}\text{I}_3$	M2	14				Rustige (2011)
$\{\text{IrTb}_3\}\text{I}_3$	M2	15				Rustige (2011)
$\{\text{RuHo}_3\}\text{I}_3$	M2	14	321.1	289.8	379.1	Meyer (2013)
$\{\text{IrHo}_3\}\text{I}_3$	M2	15	313.0	287.4	362.5	Daub (2009)
$\{\text{RuEr}_3\}\text{I}_3$	M2	14	309.8	341.2	373.0	Rustige (2011)
$\{\text{IrEr}_3\}\text{I}_3$	M2	15	309.0	330.1	374.1	Rustige (2011)

When distances are given, the data are from single-crystal X-ray structure determinations; all other data are from powder X-ray diffraction.

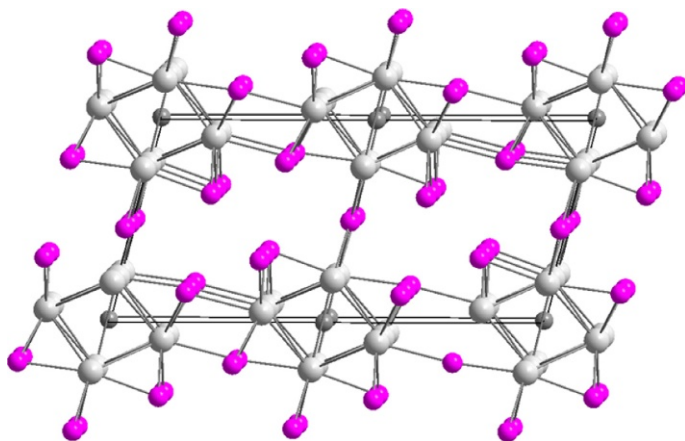


FIGURE 20 A view down the $\{TR_4\}$ chains sharing further halido ligands leading to the composition $\{ZR_4\}X_5$, for example, in $\{RuPr_4\}I_5$.

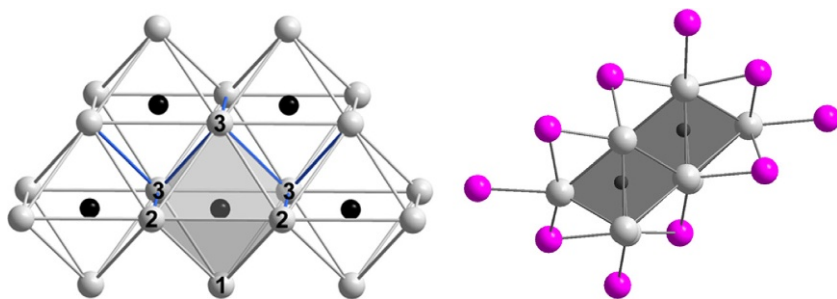


FIGURE 21 Part of a double chain in $\{Z_2R_6\}X_7$, for example, in $\{(C_2)Er_6\}I_7$, with shared edges of the two individual chains in blue (lines between atoms numbered “3”), and a view down the double chains with surrounding ligands.

The condensation of two double octahedra $\{Z_2R_{10}\}$ produces the type I tetramers $\{Z_4R_{16}\}X_{23} = ZR_4X_{5.75}$ for which only two examples are known, $\{B_4Tb_{16}\}Br_{23}$ (Mattausch et al., 2001a,b) and $\{Ru_4Gd_{16}\}Br_{23}$ (Brühmann, 2011) (see Section 4.3). This condensation is carried further to an infinite double chain, $\{Z_2R_6\}$ (see Fig. 21). Such a structure was first seen for $\{Tb_6\}Br_7$ and $\{Er_6\}I_7$ with $R = Tb, Er$; additional electron density in the cluster center was recognized that amounts to a carbon atom (Berroth, 1980; Berroth et al., 1980). Further examples are $\{C_2Y_6\}I_7$ (Kauzlarich et al., 1988) and $\{C_2Gd_6\}X_7$ ($X = Br, I$) (Schwanitz-Schüller, 1984; Simon et al., 1991). Very recently, $\{C_2Er_6\}I_7$ was obtained that indeed confirms the original “ $\{Er_6\}I_7$ ” with a single carbon atom centering the $\{Er_6\}$ clusters (Rustige, 2011).

The same double chains are also found for $\{RuPr_3\}I_3$ (Payne et al., 1992). The smaller halide content as compared with $\{C_2Er_6\}I_7 = \{CER_3\}I_{3.5}$ is again achieved by additional i–i connections of halido ligands, according to

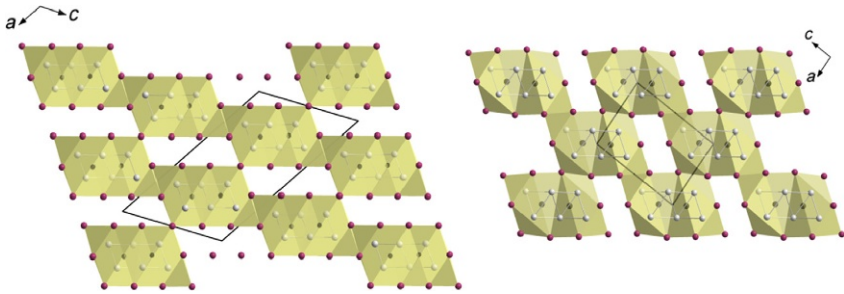


FIGURE 22 A shear process transforms the structural topologies of $\{(C)_2Er_6\}I_7 = \{CEr_3\}_2I_{4/1}^i I_{2/2}^{i-1} I_{2/2}^{i-a} I_{2/2}^{a-i}$ into $\{RuPr_3\}I_3 = \{RuPr_3\}I_{2/1}^i I_{4/2}^{i-1} I_{2/2}^{i-a} I_{2/2}^{a-i}$.

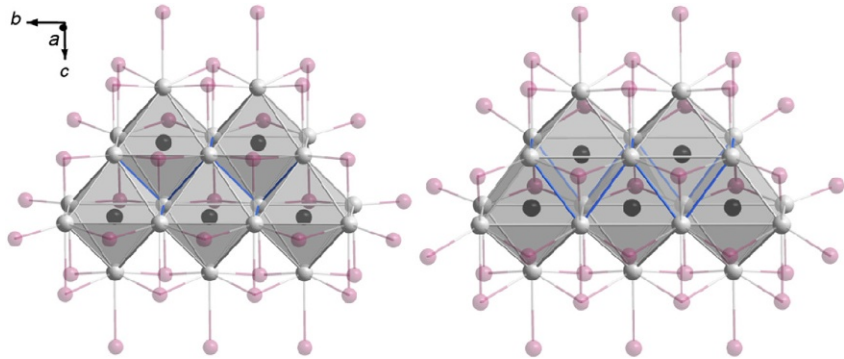


FIGURE 23 Parts of the chains in the structures of $\{RuPr_3\}I_3$ (left) and $\{RuY_3\}I_3$ (right) exhibiting the distortion of a double chain of edge-connected octahedra to a single chain of face-sharing monocapped trigonal prisms.

$\{CEr_3\}_2I_{4/1}^i I_{2/2}^{i-1} I_{2/2}^{i-a} I_{2/2}^{a-i} \rightarrow \{RuPr_3\}I_{2/1}^i I_{4/2}^{i-1} I_{2/2}^{i-a} I_{2/2}^{a-i}$, which may mechanically be understood as a shear process (Fig. 22) similar to that connecting the structure of $\{ZR_6\}X_{12}R$ figuratively to $\{ZR_6\}X_{10}$ (see Fig. 10).

The monoclinic structure of $\{RuPr_3\}I_3$ is adopted by many combinations of $T = Mn, Ru, Os, Ir$; $R = La, Ce, Pr, Gd, Y, Tb, Ho, Er$; and $X = Br$ (see Table 6) for individuals that have been observed so far. With the larger $R = La, Ce, Pr$, the $\{TR_6\}$ octahedra are fairly undistorted. For example, in $\{RuPr_3\}I_3$, the $Ru-Pr$ distances range from 257 to 288 pm with an average of 282 pm; the next distance is then 480 pm. This next distance comes much closer in $\{RuY_3\}I_3$, 350 pm, with the other six $Ru-Y$ distances ranging from 272 to 287 pm with an average of 277 pm, in accordance with the lanthanide contraction. Thus, for the smaller $R = Gd, Y, Tb, Ho, Er$, there is a considerable distortion tending towards a monocapped trigonal prism, hence a coordination number of T of 7. These prisms then share common rectangular faces, and the chain may also be understood as a single zigzag chain of face-sharing monocapped trigonal prisms rather than a double chain of octahedra (see Fig. 23). As this is a gradual process,

there is some arbitrariness in this description. Nevertheless, the distortion has a dramatic effect on the T–T distances within the T zigzag chain, from $\{\text{RuPr}_3\}\text{I}_3$ to $\{\text{RuY}_3\}\text{I}_3$ from 423 to 316 pm! In Table 6, the structures of $\{\text{RuPr}_3\}\text{I}_3$ and of $\{\text{RuY}_3\}\text{I}_3$ are, although formally isotopic, distinguished as M1 and M2.

Not only smaller rare-earth metal atoms cause a severe distortion of the $\{\text{TR}_6\}$ octahedron, but also the smaller chlorido ligands do the same. As of now, there are only two chlorides known, $\{\text{RuPr}_3\}\text{Cl}_3$ (Herzmann et al., 2008) and $\{\text{IrCe}_3\}\text{Cl}_3$ (Larres, 2012), where the distortion is even more pronounced. In $\{\text{RuPr}_3\}\text{Cl}_3$, if the surrounding of the central Ru atom would be viewed as a monocapped trigonal prism, Ru–Pr1 and Ru–Pr3 distances of the square just above the Ru atom (referring to Fig. 24) are 277.2(1) and 274.4(1) pm, respectively, and thus approximately the same as the mean Y–I distance in $\{\text{RuY}_3\}\text{I}_3$. The distances Ru–Pr1 and Ru–Pr3 to the edge completing the trigonal prism are, however, 325.9(1) and 351.4(1) pm, and $d(\text{Ru–Pr}2)$ is 337.7(2) pm long. This seems to be the best compromise allowing the ruthenium atoms getting as close as 307.8(1) pm causing considerable Ru–Ru bonding interactions (Gupta et al., 2010; Herzmann et al., 2008).

Two of the chains as in $\{\text{RuPr}_3\}\text{Cl}_3$ may be connected via common edges to a double chain, $\{\text{TR}_3\}_2 = \{\text{T}_2\text{R}_6\}$, having common R atoms yielding the composition $\{\text{T}_2\text{R}_5\}$ (Fig. 25), as was observed for $\{\text{Ir}_2\text{Gd}_5\}\text{Br}_5$ (Brühmann and Meyer, 2012). Ir–Ir distances in the zigzag chain are as short as 301.8(1) pm; Ir–Gd distances in the two crystallographically independent monocapped trigonal prisms are less scattered compared to $\{\text{RuPr}_3\}\text{Cl}_3$, 293 and 295 pm on the average.

A different way to put chains of monocapped trigonal prisms together is observed in $\{\text{Ni}_4\text{La}_8\}\text{Br}_7$ (Zheng et al., 2008a,b). The nonequality of the seven T–R distances in the monocapped trigonal prisms of $\{\text{Ni}_4\text{La}_8\}\text{Br}_7$ is very similar to that in $\{\text{RuPr}_3\}\text{Cl}_3$ (four Ni1–La distances around 280 pm and three around 335 pm). The connection of two of these chains produces, in this case, rather regular trigonal prisms surrounding Ni2 with distances

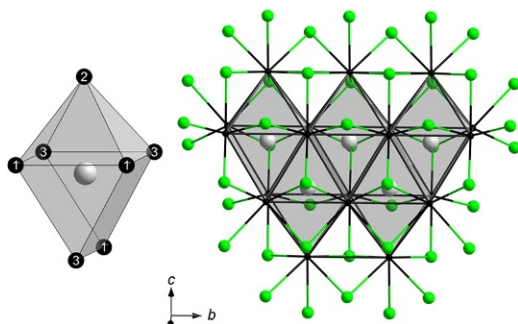


FIGURE 24 The distorted monocapped trigonal prism surrounding the central ruthenium atom in $\{\text{RuPr}_3\}\text{Cl}_3$ and part of the zigzag chain of face-sharing monocapped trigonal prisms with their surrounding of chlorido ligands.

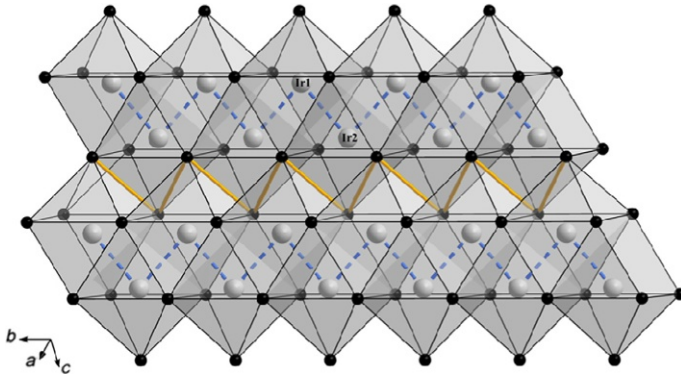


FIGURE 25 Mon capped trigonal prisms $\{\text{IrGd}_7\}$ connected via common faces and edges to a double chain as observed in $\{\text{Ir}_2\text{Gd}_5\}\text{Br}_5$.

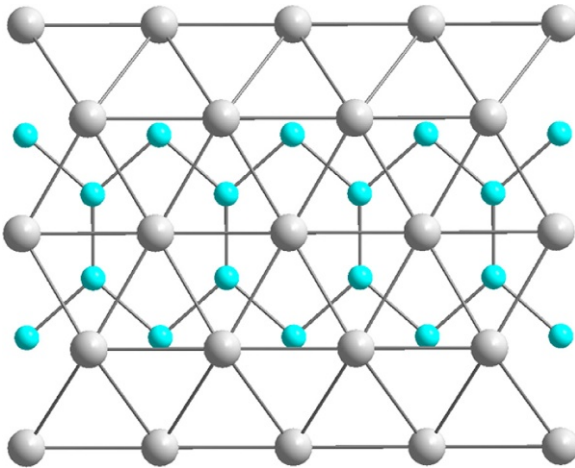


FIGURE 26 Mon capped trigonal prisms $\{\text{NiLa}_7\}$ and trigonal prisms $\{\text{NiLa}_6\}$ connected via common faces and edges in $\{\text{Ni}_4\text{La}_8\}\text{Br}_7$ producing nickel hexagons sharing edges to ribbons.

between 282.6(2) and 301.6(1) pm (average: 294 pm). The striking feature of the crystal structure of $\{\text{Ni}_4\text{La}_8\}\text{Br}_7$ is, however, edge-sharing hexagons of nickel atoms (“ribbons”) running parallel to the monoclinic b -axis (see Fig. 26). The nickel hexagons are distorted with very short Ni–Ni distances of 269 and 253 pm, comparing quite well to the average $d(\text{Ru}–\text{Ru})$ of 274 pm in the isolated pentagons of $\{\text{Ru}_5\text{La}_{14}\}_2\text{Br}_{39}$ (Steinberg, 2013).

4.5 Cluster Chains or Networks?

As Table 6 summarizes, the smaller rare-earth metals, $\text{R} = \text{Gd}, \text{Tb}, \text{Y}, \text{Ho}, \text{Er}$, adopt the distorted 133-M2 structure in $\{\text{TR}_3\}\text{X}_3$ compounds, with a few

bromides as exceptions, otherwise only iodides. With the larger R metals (R=La, Ce, Pr, Nd), a variety of structures are adopted, of which 133-M1 is closely related, formally isotypic, as we have just seen. Another variant of distorted octahedra tending to monocapped trigonal prisms is seen in the orthorhombic 113-O type, adapted, so far, only by the chlorides $\{\text{RuPr}_3\}\text{Cl}_3$ and $\{\text{IrCe}_3\}\text{Cl}_3$. All the others, bromides and iodides as well, crystallize in a cubic structure, 113-C2, first determined, with an endohedral transition metal, for $\{\text{PtPr}_3\}\text{I}_3$ (Dorhout et al., 1991). The structure has been known before for Ca_3PI_3 (Hamon et al., 1974) and for $\{\text{CGd}_3\}\text{Cl}_3$ (Warkentin and Simon, 1983).

The valence compound Ca_3PI_3 and its homologue Ca_3PCl_3 (Hadenfeldt and Herdejürgen, 1982) may both be understood as defect variants of the NaCl-type structure. The latter has a primitive cubic unit cell ($Pm\bar{3}m$) and relates to NaCl as follows, $\text{Na}_4\text{Cl}_4 \rightarrow (\square\text{Ca}_3)(\text{PCl}_3)$, leaving the corners of the cubic unit cell void (see Fig. 27). As in the perovskite (CaTiO_3) type of structure, where the corners are occupied by Ca and the edges are vacant, the octahedra $[\text{PCl}_{6/2}]$ and $[\text{TiO}_{6/2}]$, respectively, share all six vertices to form a three-dimensional network structure. $\{\text{ZR}_3\}\text{X}_3$ -type compounds ($=\{\text{PCl}_3\}\text{Ca}_3$) have not been observed with an endohedral transition metal atom, but with gallium, $\{\text{GaR}_3\}\text{Br}_3$ (Zheng et al., 2002, 2005).

The ordering of the vacancies in Ca_3PI_3 is more complicated such that the unit cell edge is doubled with respect to Ca_3PCl_3 . The ordered vacancies in the $2 \times 2 \times 2$ supercell lead to a symmetry reduction from $Fm\bar{3}m$ via $F432$ and $P4_232$ to, finally, $I4_132$ (no. 214). The $\{\text{TR}_6\}$ octahedra in $\text{C}2\text{-}\{\text{TR}_3\}\text{X}_3$ share common edges and wind along the 4_1 screw axes such that they

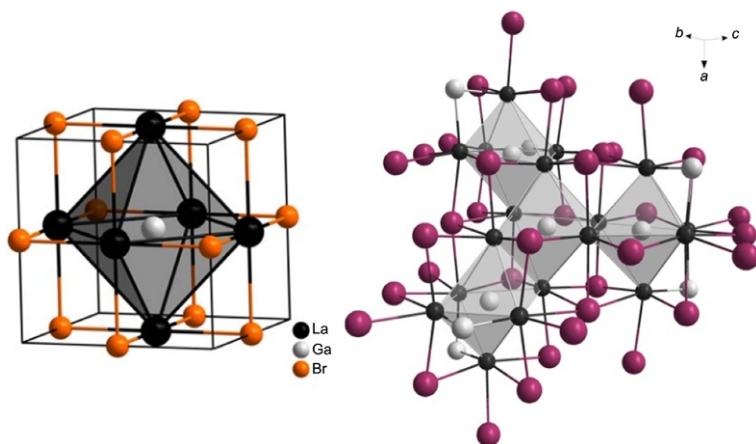


FIGURE 27 The primitive cubic unit cell of $\{\text{GaLa}_3\}\text{Br}_3$ ($=\{\text{PCl}_3\}\text{Ca}_3$) (left) and part of the crystal structure of $\{\text{PtPr}_3\}\text{I}_3$ ($=\{\text{PI}_3\}\text{Ca}_3$) showing $\{\text{PtPr}_{6/2}\}$ octahedral clusters sharing three common edges (right).

interpenetrate to build a three-dimensional network structure. Unlike in 113-C1 where the octahedra $\{\text{TR}_6\}$ share six common vertices, in 113-C2, the octahedra share three common edges (see Fig. 27). The 113-C2 structure is also adopted by $\{\text{CGd}_3\}\text{I}_3$ (Mattausch et al., 1993), as is the 113-C1 structure by $\{\text{CGd}_3\}\text{Cl}_3$. Although there are many examples for the cubic 113-C2 structure, certain endohedral atoms may cause variations, as the examples of $\{\text{NiLa}_3\}\text{Br}_3$ (Zheng et al., 2009b) and $\{\text{C}_2\}\text{La}_3\text{Br}_3$ (Zheng et al., 2001) show. The cubic symmetry of 113-C2 ($I4_132$) is reduced to tetragonal ($I4_122$) for the nickel compound and further to orthorhombic ($C222_1$) with the incorporation of a C_2 unit into the lanthanum octahedron. In $\{\text{NiLa}_3\}\text{Br}_3$, the a -axis is almost the same as in $\{\text{PtLa}_3\}\text{Br}_3$, 1217.58(9) versus 1216.3(1)pm, but the c -axis is shorter, 1174.4(2)pm. The distortion is explained through a Jahn–Teller compression of the $\{\text{NiLa}_6\}$ octahedron with equatorial versus apical distances of 293 and 272 pm, respectively.

4.6 Eight-Coordinate Endohedral Atoms

A rare-earth metal octahedron appears to be by far the best choice to accommodate a transition metal atom from groups 7 to 12 (most prolific of groups 8 to 10) as an endohedral atom to form a centered heteroatomic cluster $\{\text{TR}_6\}$. As we have seen in the previous sections, these octahedra may be isolated or connected to each other via common edges or, in extremely rare cases, via vertices and faces to build oligomers, chains, double chains, layers (see text later), or even networks. Quite frequently, the cluster symmetry is not $O_h = 4/m\bar{3}2/m$, and we talk about a distorted octahedron. It may be elongated or compressed, or twisted from a trigonal antiprism to a trigonal prism, or even tending to two tetrahedra sharing a common edge, or, in condensed clusters, distortions may tend to monocapped trigonal prisms. Distortions may have all kinds of reasons. They may originate from the size of the endohedral atom relative to the size of the cluster cavity or from the electronic structure of the cluster, from its electron count, or from the size of ligands and their electronegativity that surround the (condensed) clusters and, furthermore, of the connection to a three-dimensional structure through these ligands that may be terminal (a) or bridging (a–a, a–i, i–a, i–i, or higher).

Beyond the predominant coordination number of the endohedral atom of six (and to a much lesser degree seven), there is a growing number of clusters with coordination number eight. The coordination polyhedra are cubes and, preferred, square antiprisms, and the paramount formula type is $\{\text{TR}_4\}\text{X}_4$. In all structures, the eight-coordinate polyhedra share common opposite faces producing a chain, $\{\text{TR}_{8/2}\}$ (Fig. 28). R atoms of the clusters are from the second half of the lanthanides, R=Gd, Tb, Dy, Ho, Er, Lu, Sc, including Y that somehow proves that the cluster atoms are chosen for their size. Endohedral atoms are 4d and 5d metal atoms from groups 7 to 9 with a strong preference of T=Os that produces 16 CBE clusters. Halido ligands are mostly chloride

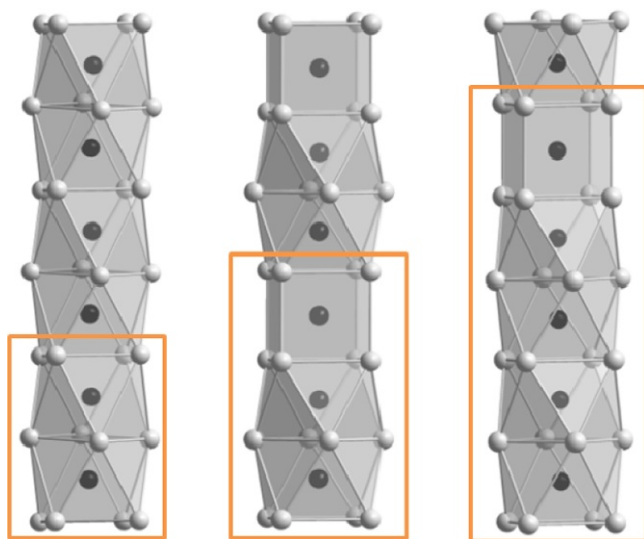


FIGURE 28 Columns of face-sharing square antiprisms and cubes with their repeat units as they appear in $\{\text{TR}_4\}\text{X}_4$, $\{\text{Ir}_3\text{Sc}_{12}\}\text{Br}_{16}$, and $\{\text{Os}_5\text{Lu}_{20}\}\text{I}_{24}$ (from left to right).

and bromide with some iodides that cause immense crystallographic problems. All compounds crystallize in extremely thin needles, the morphology reflecting their structures. Bridging connections between the cluster chains surrounded by halido ligands through the halido ligands are sparse or nonexistent (see text later). Surprisingly, there is a quantitatively small but diverse chemistry with the smallest rare-earth metals, lutetium and scandium. Present knowledge is summarized in [Table 7](#).

The first of these compounds was recognized for yttrium and erbium, $\{\text{OsR}_4\}\text{Br}_4$ ($\text{R}=\text{Y}, \text{Er}$), hence all with osmium as the endohedral atom and therefore 16 CBEs ([Dorhout and Corbett, 1992](#)). Topologically, the same columns of face-shared square antiprisms were also seen in the isoelectronic $\{\text{SiTa}_4\}\text{Te}_4$ ([Badding and DiSalvo, 1990](#)). In both the monoclinic $\{\text{OsY}_4\}\text{Br}_4$ and the orthorhombic $\{\text{SiTa}_4\}\text{Te}_4$, the columns are packed in a tetragonally close-packed manner (see [Fig. 29](#)). The electronegative ligands X (Cl, Br, I, Te) are situated above the edges and faces, which depends upon the actual sizes of rare-earth atoms and, maybe more, on the size of the ligand. For $\{\text{OsEr}_4\}\text{Br}_4$, for example, the connection scheme might be written as $\{\text{OsEr}_4^f\}\text{Br}_4^{i-a}$. However, interchain connections are weak, mostly of the van der Waals type. Closest ligand contacts are larger than 340 pm in $\{\text{OsEr}_4\}\text{Cl}_4$, 352 pm in $\{\text{OsEr}_4\}\text{Br}_4$, 370 pm in $\{\text{OsEr}_4\}\text{I}_4$, and 380 pm in $\{\text{SiTa}_4\}\text{Te}_4$, which appears to be pretty much a size effect.

Crystallographic problems arise mostly through the uneven distribution of ligands along the columns (see [Fig. 30](#)) and the tetragonal pseudosymmetry ($P4/nnc$) of the monoclinic unit cell ($C2/c$) that has been addressed to most

TABLE 7 {TR₄}X₄ Cluster Halides and Derivatives, Structure Types, Cluster-Based Electron (CBE), and (Mean) Distances (in pm)

Compound	Type	CBE	$\langle d \rangle$ T-T	$\langle d \rangle$ T-R	$\langle T-T \rangle$	References
{ReGd ₄ }Br ₄	T	15	329.3	294.4	180	Zimmermann et al. (2010)
{OsGd ₄ }Cl ₄	M	16	326.4	293.2	180	Wolberg (2014)
{OsGd ₄ }Br ₄	M	16	327.9	293.8	180	Brühmann (2011)
{OsGd ₄ }I ₄	O	16	317	293	177	Brühmann (2011)
{OsY ₄ }Cl ₄	M/T	16				Steinberg (2013)
{OsY ₄ }Br ₄	M	16	328.7	290.4	175.1	Dorhout and Corbett (1992)
{OsTb ₄ }Br ₄	M	16	327.8	292	178.3	Rustige (2011)
{OsTb ₄ }I ₄	O	16	315	290	176.3	Rustige (2011)
{IrDy ₄ }Br ₄	M	17	325.3	288.4		Meyer (2013)
{OsHo ₄ }Cl ₄	M	16	321.9	286.8		Meyer (2013)
{OsHo ₄ }Br ₄	M	16	326.2	289.3		Meyer (2013)
{OsHo ₄ }I ₄	O	16	314.0	288.3		Meyer (2013)
{ReEr ₄ }I ₄	O	15	310	288	174.6	Rustige (2011)
{OsEr ₄ }Cl ₄	M	16	321.1	286.1	177.4	Rustige (2011)
{OsEr ₄ }Br ₄	M	16				Dorhout and Corbett (1992)
			324.7	287	177.0	Rustige (2011)
{OsEr ₄ }I ₄	O	16	309	286	175.3	Rustige (2011)

Continued

TABLE 7 {TR₄}X₄ Cluster Halides and Derivatives, Structure Types, Cluster-Based Electron (CBE), and (Mean) Distances (in pm)—Cont'd

Compound	Type	CBE	$\langle d \rangle$ T-T	$\langle d \rangle$ T-R	$\langle T-T-T \rangle$	References
{OsLu ₄ }Br ₄	M	16	322.9	284.1	176.2	Brühmann (2011)
{OsSc ₄ }Cl ₄	M	16	307.4	272.4	173.1	Zimmermann et al. (2010)
{Ir ₃ Sc ₁₂ }Br ₁₆		15.67	283.3	275.4	179.5	Zimmermann et al. (2010)
			302.7		180.0	
{Os ₃ Sc ₁₂ }Br ₁₆ Sc		15.67	290.2	271.9	180.0	Zimmermann et al. (2010)
			302.7			
{Ru ₅ Lu ₂₀ }I ₂₄		15.2				Brühmann (2011)
{Os ₅ Lu ₂₀ }I ₂₄		15.2	298.8	281.5		Brühmann et al. (2011)
			302.9	281.9		
			325.0	293.2		

When distances are given, the data are from single-crystal X-ray structure determinations; all other data are from powder X-ray diffraction.

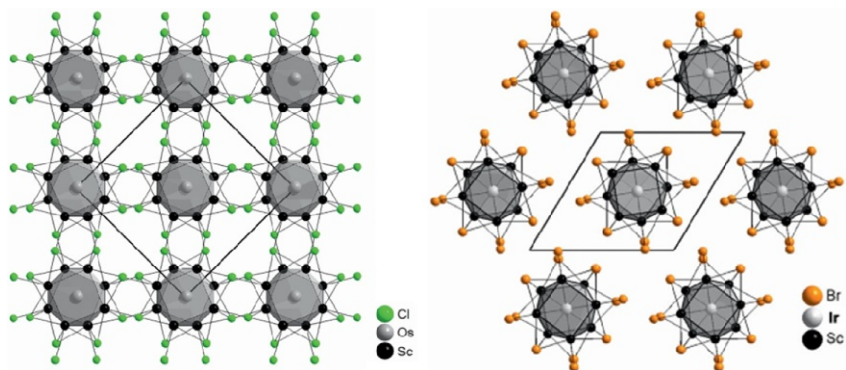


FIGURE 29 Tetragonal and hexagonal packing of $\{\text{TR}_{8/2}\}$ columns, surrounded by halido ligands, as in $\{\text{TR}_4\}\text{X}_4$ ($\text{X}=\text{Cl}, \text{Br}$) and in $\{\text{Ir}_3\text{Sc}_{12}\}\text{Br}_{16}$.

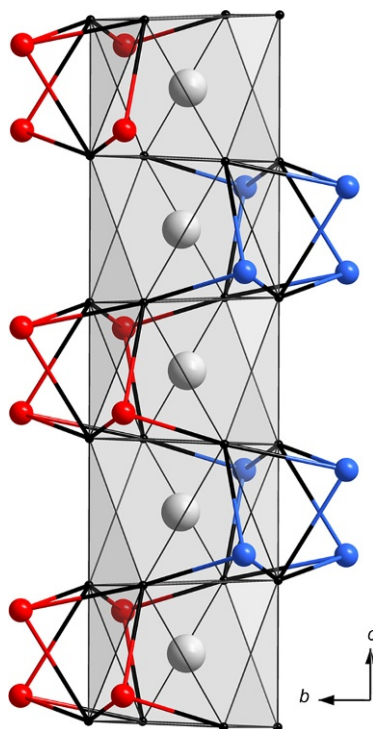


FIGURE 30 The coordination of $\{\text{TR}_{8/2}\}$ columns with ligands X in monoclinic $\text{M}-\{\text{TR}_4\}\text{X}_4$ ($\text{X}=\text{Cl}, \text{Br}$).

of the $\{\text{TR}_4\}\text{X}_4$ ($\text{X} = \text{Cl}, \text{Br}$)-type compounds. For example, the lattice constants for the neighbors $\{\text{ReGd}_4\}\text{Br}_4$ and $\{\text{OsGd}_4\}\text{Br}_4$ are $a = 1269.6(1)/1270.9(2)$, $b = 1269.6(1)/1269.2(3)$, $c = 658.59(6)/655.8(1)$ pm, and $\beta = 90/90.05^\circ$, respectively (Brühmann, 2011). The structure of $\{\text{ReGd}_4\}\text{Br}_4$ has indeed been solved in the tetragonal space group $P4/nnc$ (Zimmermann et al., 2010), and there is some doubt whether $\{\text{OsY}_4\}\text{Cl}_4$ is tetragonal or monoclinic (Steinberg, 2013). In any case, the uneven distribution of ligands along the columns may lead to twinning because the columns may be rotated along the twofold axis running in this direction.

The crystallographic difficulties become even more pronounced when iodides $\{\text{OsR}_4\}\text{I}_4$ ($\text{R} = \text{Gd}, \text{Tb}, \text{Ho}, \text{Er}$) and $\{\text{ReEr}_4\}\text{I}_4$ come into view (Brühmann, 2011; Meyer, 2013; Rustige, 2011). Still, square antiprisms $\{\text{TR}_8\}$ share common opposite faces to form chains/columns $\{\text{TR}_{8/2}\}$ that are surrounded by iodido ligands. These seem to be too large to be accommodated in the same way as in the chlorides and bromides, $\{\text{TR}_4\}\text{X}_4$ ($\text{X} = \text{Cl}, \text{Br}$). Instead, a modulation of the columns is observed where identity in the chain propagation is only reached after nine antiprisms (see Fig. 31). This causes large unit cells, for example, for $\{\text{OsGd}_4\}\text{I}_4$, $a = 2046.0(2)$, $b = 2528.1(2)$, and $c = 3903.3(3)$ pm, orthorhombic, $Fddd$. The columns propagate in the $[010]$ direction; the b -axis compares with the c -axis of $\{\text{OsGd}_4\}\text{Br}_4$, $655.8(1) \times 4 = 2623.2$ pm, such that the b -axis in the iodide is shortened, despite the larger iodide ligands, subject to the undulating columns. The columns are not all in phase in the $[010]$ direction as Fig. 31 shows. On the sides where the columns are stretched, thermal ellipsoids are unreasonably large. It is also obvious that

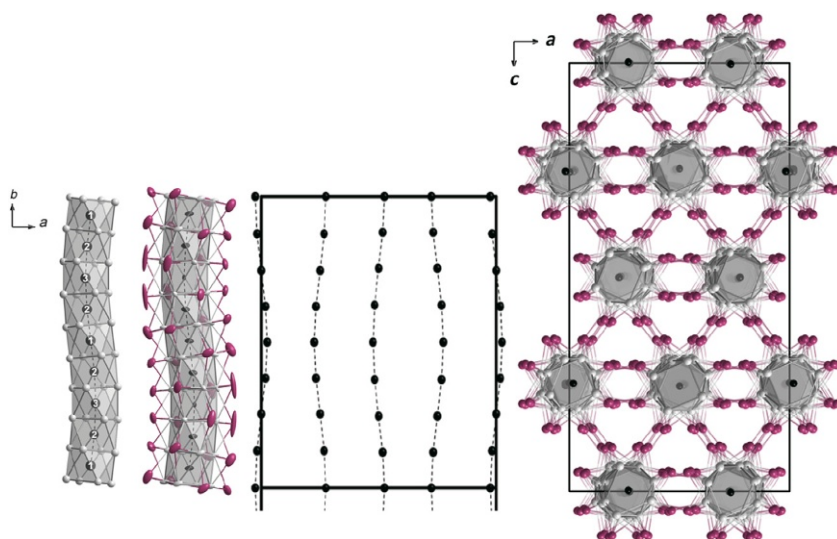


FIGURE 31 The undulating columns $\{\text{TR}_{8/2}\}$ in the iodides $\{\text{TR}_4\}\text{I}_4$. From left to right: The column $\{\text{TR}_{8/2}\}$ alone, the column with ligands, the T atoms alone, all in $[001]$ projection; far right a view down $[100]$ showing the hexagonal packing of the columns.

all kinds of disorder and incommensurate arrangements of the columns may occur and obviously occur as the crystallographic refinements so far have shown (Brühmann, 2011; Meyer, 2013; Rustige, 2011). Refinements in *Fddd* were always the best, and reduction in symmetry did not help.

Some diversity in the crystal chemistry of eight-coordinate endohedral atoms in rare-earth metal clusters is seen with the smallest rare-earth elements, lutetium and scandium. In $\{\text{Ir}_3\text{Sc}_{12}\}\text{Br}_{16}$, square antiprisms and cubes, in a 2:1 ratio, define the identity period of the $\{\text{Ir}_3\text{Sc}_{12}\}$ columns (see Fig. 32) (Zimmermann et al., 2010). The Ir–Ir chain is no longer equidistant, although linear. Distances of 283 and 303 could suggest a Peierls distortion due to Ir–Ir bonding. Indeed, if two electrons are reserved from the overall 47 CBEs, these could form an Ir–Ir bond, and there were 15 CBEs for each $\{\text{IrSc}_8\}$ cluster available, much the same as in the other compounds discussed in this section. Although this is a rather primitive picture, the electron count for this type of columns must have some meaning as the isoelectronic compounds $\{\text{Os}_3\text{Sc}_{12}\}\text{Br}_{16}\text{Sc}$ —the three electrons that are missing because of the substitution of Ir for Os are compensated by an additional Sc atom that resides in octahedral holes in the structure—and $\{\text{Os}_3\text{Sc}_{12}\}\text{Te}_8\text{Sc}_{2-x}$ (with $x = 1$) show (Chen and Corbett, 2003; Zimmermann et al., 2010).

Furthermore, the mere existence of $\{\text{Os}_5\text{Lu}_{20}\}\text{I}_{24}$ demonstrates that there might be more to come. Here, square antiprisms and cubes are face-connected

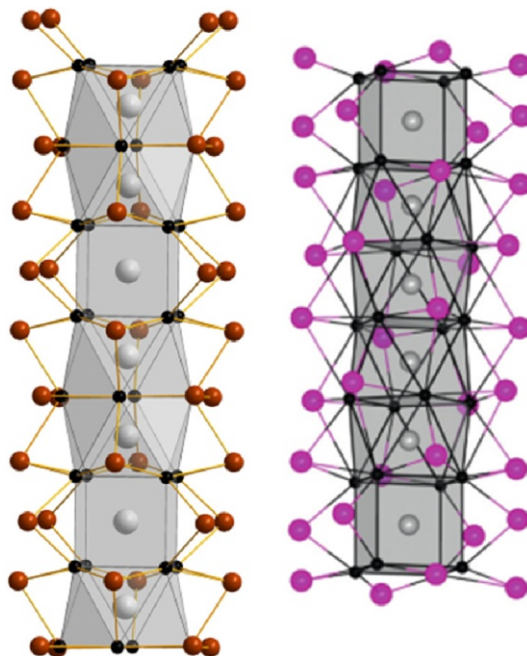


FIGURE 32 The 2:1 and 4:1 square antiprism/cube chains in the crystal structures of $\{\text{Ir}_3\text{Sc}_{12}\}\text{Br}_{16}$ and $\{\text{Os}_5\text{Lu}_{20}\}\text{I}_{24}$.

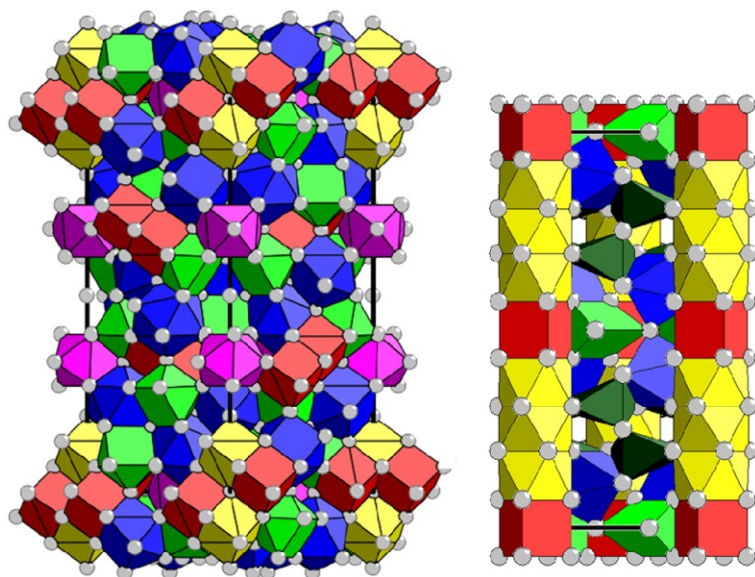


FIGURE 33 Square antiprisms and cubes among other polyhedra in the crystal structures of $\{\text{Ru}_{11}\text{Lu}_{20}\}$ and $\{\text{Rh}_2\text{Er}_3\}$.

to columns in a 4:1 ratio (see Fig. 32) (Brühmann et al., 2011). Although the composition seems complicated, the surrounding of the columns with iodido ligands is rather straightforward, $\{\text{Os}_5\text{Lu}_{20}\}\text{I}_4^{\text{i(e)}}\text{I}_{20}^{\text{i(f)}}$, and there are little interchain interactions other than van der Waals bonding. So far, the only other compound of that type is the isoelectronic $\{\text{Ru}_5\text{Lu}_{20}\}\text{I}_{24}$ (Brühmann 2011), with 15.2 CBEs per $\{\text{TR}_{8/2}\}$ cluster.

Coordination numbers of eight and higher are not common in polar intermetallics. In all CsCl-type intermetallics, the coordination number is eight, as in $\{\text{RuLu}\}$ with a Ru–Lu distance of 334 pm (Iandelli and Palenzona, 1976). Interestingly, the structurally hitherto unknown $\{\text{Ru}_{11}\text{Lu}_{20}\}$, which is perhaps the Ru_3Lu_5 phase for which no data are reported in the phase diagram (Okamoto, 1990), contains ruthenium atoms with coordination numbers of 8–10, with 13.45 CBEs per $\{\text{RuLu}_7\}$ cluster (Zimmermann et al., 2012). This is reasonable because it is a three-dimensional intermetallic phase (see Fig. 33). Ru–Lu distances in $\{\text{Ru}_{11}\text{Lu}_{20}\}$ are, on the average, 285, 297, and 308 pm for CN=8, 9, and 10, respectively. Even more importantly, in $\{\text{Rh}_2\text{Er}_3\}$, there are columns of square antiprisms and cubes in a 3:1 ratio (Bell, 2013), a structural feature that we have not yet seen for condensed cluster complexes (see Fig. 33).

4.7 Layers of Edge- and Face-Connected Clusters

The monohalides ZrX ($\text{X}=\text{Cl}, \text{Br}$; Adolphson and Corbett, 1976; Daake and Corbett, 1977; Izmailovich et al., 1974) have structures in which four

two-dimensionally closest-packed layers of Zr and X form $XZrZrX$ slabs (AbcA or AcbA) that are further stacked in the third dimension as AbcA BcaB CabC, ZrCl, or AcbA BacB CbaC, ZrBr, both in space group $R\bar{3}m$. The double-metal layers may be understood as two metal layers hexagonally closest packed.

After the pitfalls of ubiquitous hydrogen or other light main group element atoms (as C, N, and O) having occupied interstices between rare-earth metal double-metal layers, for example, in GdCl (Simon et al., 1976) or ScCl (Poepfelmeier and Corbett, 1977), unnoticed at first by single-crystal structure determination in low-yield reactions, a rich chemistry of reduced rare-earth metal cluster halides with endohedral atoms emerged. Historically, this was the beginning of the ever-growing chemistry as described in previous sections of this chapter for transition metal endohedral atoms. The inclusion of hydrogen, boron, and carbon has already been amply reviewed (Simon and Mattausch, 2013; Simon et al., 1991).

Two formula types are particularly important, $\{ZR_2\}X_2$ and $\{ZR_2\}X$. Focusing on carbon-containing halides (carbide halides) alone at first, the $\{ZR_2\}X_2$ type represents four-layer slabs of the ZrX type with carbon atoms (or dicarbon units) occupying octahedral holes between the double-metal layers. Two structure types were recognized, often in the same reaction, 1T- and 3R- $\{ZR_2\}X_2$ where 1 and 3 stands for one or three slabs stacked to identity and T and R for trigonal and rhombohedral, respectively; space groups are $P\bar{3}m1$ and $R\bar{3}m$. Compounds of that type were independently discovered in three laboratories, 3R- $\{CGd_2\}Br_2$ and $\{(C_2)Gd_2\}Br_2$ (Schwanitz-Schüller and Simon, 1985); $\{CSc_2\}Cl_2$, both 1T and 3R (Hwu and Corbett, 1986); and $\{CLu_2\}Cl_2$, both 1T and 3R (Schleid and Meyer, 1987).

Quite obviously, one of the two halide layers may be relinquished as the example of $\{CGd_2\}X$ ($X=Cl, Br, I$) (Bauhofer et al., 1990; Mattausch et al., 1987) clearly exhibits. The structure of $\{CGd_2\}Cl$ can be related to the α -NaFeO₂ type (Goldsztaub, 1935), which is as such an ordered derivative of NaCl, and that of $\{CGd_2\}X$ ($X=Br, I$) is topologically related to β -RbScO₂ (Hoppe and Sabrowsky, 1965; Wiench et al., 1977) or LiNbO₂ (Meyer and Hoppe, 1974, 1976). In both structures, the carbon atoms occupy octahedral interstices between the double-metal layers, but the halide ions are in octahedral voids within the GdXGd sequence ($\{CGd_2\}Cl$) and occupy trigonal prismatic voids in $\{CGd_2\}X$ ($X=Br, I$).

An alternative to this structure represents the $\{Fe_2Gd_2\}I$ type of structure (Ruck and Simon, 1993) in which the gadolinium atoms are stacked in a primitive way, then leaving trigonal prismatic voids for the iron atoms. These occupy all possible voids and in itself form a graphite-like layer of condensed hexagons. Between these three-layer slabs, one closest-packed layer of iodide ions is “intercalated,” and iodide occupies octahedral holes between Gd–Gd layers. This appears to be a rather prolific structure type, as Table 8 shows, the structure type denominated as 2H (space group $P6_3/mmc$) (see Fig. 34). $\{Ni_2La_2\}I$ and $\{Cu_2La_2\}I$ were found in a structure with a slightly different

TABLE 8 Layered $\{T_2R_2\}X$ - and $\{ZR_2\}X_2$ -Type Halides, Structure Types, Cluster-Based Electron (CBE), and (Mean) Distances (in pm)

Compound	Type	CBE	$\langle d \rangle$ (T-T)	$\langle d \rangle$ (T-R)	$\langle d \rangle$ (R-R)	References
$\{Fe_2La_2\}I$	2H	10.5	236.9	307.7	392.8	Park et al. (1997) , Mattausch et al. (2002a,b)
$\{Co_2La_2\}I$	2H	11				Park et al. (1997) , Mattausch et al. (2002a,b)
$\{Ru_2La_2\}I$	2H	10.5				Park et al. (1997) , Mattausch et al. (2002a,b)
$\{Rh_2La_2\}I$	2H	11				Park et al. (1997) , Mattausch et al. (2002a,b)
$\{Os_2La_2\}I$	2H	10.5				Park et al. (1997) , Mattausch et al. (2002a,b)
$\{Ni_2La_2\}I$	1H	11.5	239.0	303.5	374.4	Hong et al. (1998)
$\{Cu_2La_2\}I$	1H	12				Hong et al. (1998)
$\{Al_2La_2\}I$	2 H	5.5	253.3	329.1	437.9	Mattausch et al. (2001a)
$\{TeLa_2\}_2$	3R	10	449.8	314.5	446.5	Ryazanov et al. (2006)
$\{Co_2Pr_2\}I$	2H	11	233.3	297.6	375.5	Palasyuk et al. (2006a,b) Lefevre et al. (2008)
$\{Ni_2Pr_2\}I$	2H	11.5				Park et al. (1997)
$\{Co_2Nd_2\}I$	2H	11				Lefevre et al. (2008)
$\{Fe_2Gd_2\}Br$	2H	10.5				Reisser et al. (1995)
$\{Fe_2Gd_2\}I$	2H	10.5	232.7	297.3	372.5 408.4	Ruck and Simon (1993)
$\{Co_2Gd_2\}I$	2H	11				Ruck (1991)
$\{GeGd_2\}Br_2$	1T	8	416.7	290.4	412.7	Lukachuk et al. (2007)

$\{\text{GeGd}_2\}\text{I}_2$	3R	8				Lukachuk et al. (2007)
$\{\text{Co}_2\text{Tb}_2\}\text{I}$	2H	11.5	229.5 341.2	291.7	392.0	Lefevre et al. (2008)
$\{\text{Co}_2\text{Dy}_2\}\text{I}$	2H	11.5				Lefevre et al. (2008)
$\{\text{Co}_2\text{Ho}_2\}\text{I}$	2H	11.5				Lefevre et al. (2008)
$\{\text{Co}_2\text{Y}_2\}\text{I}$	2H	11.5				Lefevre et al. (2008)
$\{\text{Fe}_{2+x}\text{Y}_2\}\text{Br}_2$	3R	11	226.9	298.4	390.6	Ruck and Simon (1993)
$\{\text{GeY}_2\}\text{I}_2$	3R	8	421.4	289.5	397.2	Lukachuk et al. (2007)

When distances are given, the data are from single-crystal X-ray structure determinations; all other data are from powder X-ray diffraction.

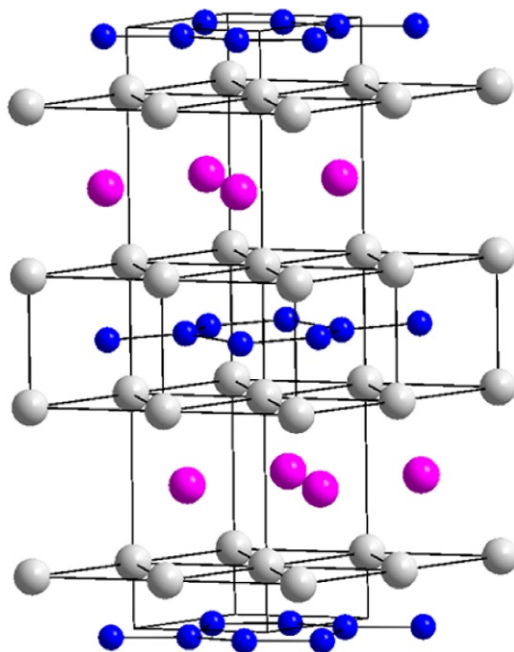


FIGURE 34 Crystal structure of $2H\text{-}\{TR_2\}I$ (for the example of $\{CoPr_2\}I$ showing face-sharing trigonal prisms of R atoms with endohedral T atoms that form graphite-like layers).

stacking sequence as $2H\text{-}\{Fe_2La_2\}I$, for example, thus with a doubled c -axis, now named $1H$. The relation between $1H$ - and $2H\text{-}\{T_2R_2\}X$ is similar as that between $1T$ - and $3R\text{-}\{ZR_2\}X_2$ (see text earlier). Interestingly, the former two structures with the endohedral atoms in octahedral voids are almost exclusively observed with main group element endohedral atoms (see the examples $\{GeGd_2\}X_2$ and $\{TeLaGd_2\}I_2$ in Table 8), whereas the latter two with their trigonal prismatic voids are exclusively seen with transition metal endohedral atoms and with only one halide layer between the three metal layers. One may address this to a transition from a salt to an intermetallic phase. Indeed, $\{T_2R_2\}X$ are the most (heterometallic) metal-rich phases in the chemistry discussed in this chapter.

5 ELECTRONIC STRUCTURE

For a compound like LaI_2 , it is easy to address oxidation states (numbers). It would be $+2$ for lanthanum and -1 for iodine, applying Pauling's definition in that the oxidation number is the "number which represents the electrical charge which the atom would have if the electrons in a compound were assigned to the atoms" (Pauling, 1947). The electronic configuration for La^{2+} could be $[Xe]4f^15d^06s^0$ or $[Xe]4f^05d^16s^0$. The properties of LaI_2 ,

a two-dimensional 5d metal, are only compatible with the latter configuration; the 5d orbitals delocalize into a two-dimensional conduction band. LaI_2 was also addressed as $(\text{La}^{3+})(\text{e}^-)(\text{I}^-)_2$ (see Corbett, 1973), with lanthanum effectively trivalent, that is, the localized electronic configuration of lanthanum is just that of xenon.

The assignment of oxidation numbers to atoms in compounds like $\{\text{IrGd}_6\}\text{Br}_{10}$ is easy for the cluster atoms and ligands with their low and high electron affinities (Gd: +3, Br: -1) that would, applying Pauling's definition, leave an oxidation number for the endohedral iridium atom of -8. In the light of the relatively high electron affinity of iridium, there is certainly truth in the negative sign, but the absolute value makes no sense. Thus, we will not assign formal oxidation numbers.

The electron count is another and better way to deal with the electronic structure of these metal-rich compounds. Here, we count the number of electrons that are available for bonding interactions within the cluster $\{\text{TR}_r\}$, that is, CBE. For $\{\text{IrGd}_6\}\text{Br}_{10}$, this number is $(+9) + (6 \times 3) - (10 \times 1) = 17$. Note that the sum of the oxidation number of -8 (see text earlier) and the number of valence electrons of Ir (-9) is -17. Thus, CBEs are just a number without a sign and are equivalent to electron counting rules like the octet or 18-electron rules in main group molecular or transition metal coordination chemistry. As most of the rare-earth metal cluster complexes are not isolated but share common cluster atoms, CBEs are always divided by the number of endohedral atoms (see preceding sections). For example, for $\{\text{Ir}_3\text{Sc}_{12}\}\text{Br}_{16}$, the number of CBEs is $[(3 \times 9) + (12 \times 3) - (16 \times 1)]/3 = 15.667$.

Whenever clusters are isolated, one may depict their electronic structure in the same way as is done for isolated clusters of the early transition metals, especially of niobium or molybdenum. The encapsulation of an endohedral atom in the cluster alters the MO diagram in a way that Fig. 11 shows schematically. For $\{\text{TR}_6\}$ clusters, an 18 CBE rule may be deduced from that scheme. As we have seen, many of the isolated clusters of the $\{\text{TR}_6\}\text{X}_{12}\text{R}$ and $\{\text{TR}_6\}\text{X}_{10}$ families have electron counts of 16–21 CBEs. Figure 35 shows part of the MO scheme, as it may be obtained by extended Hückel molecular orbital calculations (Hoffmann, 1963; Hoffmann and Lipscomb, 1962), for an isolated cluster complex $[\{\text{IrY}_6\}\text{I}_{18}]^{8-}$, extracted from $\{\text{IrY}_6\}\text{I}_{10}$, with representations of the three highest occupied MOs (Rustige et al., 2012). As $\{\text{IrY}_6\}\text{I}_{10}$ has 17 CBEs, the HOMO is singly occupied. The three degenerate t_{1u} orbitals as in Fig. 11 are now split because the symmetry of the cluster is far from O_h in the triclinic crystal structure of $\{\text{IrY}_6\}\text{I}_{10}$; a Jahn–Teller distortion would be expected anyway due to the odd number of electrons.

Cluster complexes in compounds of the general formula $\{\text{T}_r\text{R}_r\}\text{X}_x$ are never really isolated. They are connected via either common ligands or common cluster atoms to extended (crystal) structures. Thus, a much better approach to their electronic structure is density functional theory-based electronic structure calculations, making use of the tight-binding linear

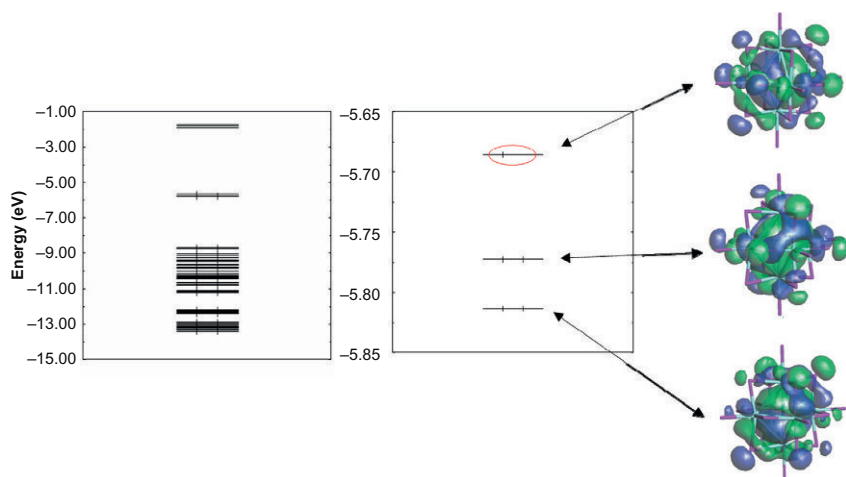


FIGURE 35 Results of extended Hückel molecular orbital (EHMO) calculations for the isolated $[\{\text{IrY}_6\}\text{I}_{18}]^{8-}$ cluster complex in $\{\text{IrY}_6\}\text{I}_{10}$ and representation of the three highest occupied molecular orbitals.

muffin-tin orbital method in the local density and atomic sphere approximations (Andersen, 1975; Andersen and Jepsen, 1984). Crystal orbital Hamilton population (COHP) may be derived therefrom by a band structure energy partitioning scheme (Dronskowski, 2005; Dronskowski and Blöchl, 1993). COHP diagrams indicate bonding, nonbonding, and antibonding energy regions for specific atom pairs. Figure 36 shows, as an example, the COHP diagram for $\{\text{IrY}_6\}\text{I}_{10}$ (Rustige et al., 2012). Bonding is dominated by heteroatomic Ir–Y and Y–I interactions (to the left) with little contributions of homoatomic Y–Y bonding. Antibonding Y–Y and Y–I (close to the Fermi level, EF) are also clearly seen.

The integration of COHPs for atom pairs yields individual –ICOHP values. Averaging for crystallographically independent atom sites and multiplying by the number of “bonds” (i.e., the number of distances up to a certain limit) give cumulative –ICOHPs (–CICOHP), which may be expressed as percentage contributions to chemical bonding. See Table 9 for the example of cubic $\{\text{RuLa}_3\}\text{Br}_3\text{-C2}$. Table 10 gives homo- and heteroatomic bonding contributions for a variety of compounds, in a yet not truly systematic way.

Although the picture certainly needs to gain a better resolution, a number of conclusions may already be drawn from Table 10. Considering $\{\text{TR}_3\}\text{X}_3$ compounds first, bonding interactions of an endohedral 3d-T atom (Mn) with the surrounding $\{\text{R}_6\}$ cluster are much less pronounced than 4d/5d-T–R interactions. Exchange of the halide ligand X appears to have little influence on R–X contributions. In the case of $\{\text{MnGd}_3\}\text{I}_3$, the relatively small Mn–Gd contributions are superseded by relatively high Mn–Mn and Gd–Gd contributions. T–T interactions are also more pronounced in $\{\text{RuPr}_3\}\text{Cl}_3$ (13%) than in

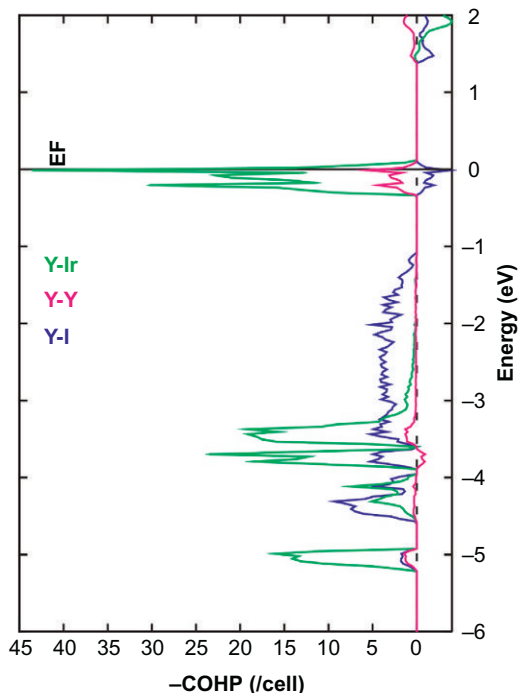


FIGURE 36 Crystal orbital Hamiltonian population (COHP) diagram for homoatomic (Y–Y) and heteroatomic (Ir–Y and Y–I) bonding (left) and antibonding (right) interactions in $\{\text{IrY}_6\}\text{I}_{10}$.

the other 4d/5d-T- $\{\text{TR}_3\}\text{X}_3$ -type compounds, usually less than 1%. R–R contributions must be higher because the number of “bonds” is higher than the number of T–T contacts, 84 versus 12 in $\{\text{RuLa}_3\}\text{Br}_3$, for example. The structure type has also an important influence: for 133-C2, the R–R contributions are between 3% and 5.5%, whereas for 133-M2, the same contributions reach almost 10%. In the chain structure of $\{\text{OsEr}_4\}\text{Cl}_4$, the picture is practically the same.

In the much halide-richer compounds with $\{\text{T}_4\text{R}_{16}\}$ tetramers, $\{\text{Ru}_4\text{Y}_{16}\}\text{Br}_{20}$, $\{\text{Ru}_4\text{Gd}_{16}\}\text{Br}_{23}$, $\{\text{Rh}_4\text{Tb}_{16}\}\text{Br}_{24}(\text{TbBr}_3)_4$, and $\{\text{Ir}_4\text{Tb}_{16}\}\text{Cl}_{24}(\text{TbCl}_3)_4$ with x/r ratios of 1.25, 1.44, and 2.25 ($2x$), R–X contributions jump to almost 45% (the first two) and 60% (the latter two) going hand in hand with a drop of T–R contributions to around 50% and 35%, respectively. Although still minor, T–T contributions double from $\{\text{Rh}_4\text{Tb}_{16}\}\text{Br}_{24}(\text{TbBr}_3)_4$ to $\{\text{Ir}_4\text{Tb}_{16}\}\text{Cl}_{24}(\text{TbCl}_3)_4$.

One polar intermetallic compound, $\{\text{Rh}_2\text{Er}_3\}$, is also listed in Table 10. Its crystal structure features chains of face-sharing square antiprisms and cubes in a 3:1 ratio (see Fig. 33; Bell, 2013). $\{\text{RhEr}_{8/2}\}$ chains are connected via additional Rh and Er atoms according to $\{\text{RhEr}_4\}_{16}(\text{Rh}_2\text{Er})_{20}$ (see Fig. 37). Rh–Er contributions by far outnumber (83.6%) homoatomic Rh–Rh (6.8%) and

TABLE 9 Contributions to Hetero- and Homoatomic Bonding in {RuLa₃}Br₃-C2

	<i>d</i> (pm)	-ICOHP (per Bond)	No. Bonds (per Cell)	⟨-ICOHP⟩ (eV/Bond)	-CICOHP (per Cell)	Contribution (%)
Ru-La	286.47(1)	1.9092	48	1.9092	91.640	65.061
Ru-Ru	428.67(4)	0.0037	12	0.0037	0.044	0.031
La-La1	380.10(3)	0.1725	12			
La-La2	405.86(2)	0.0603	24	0.0702	5.901	4.189
La-La3	417.07(9)	0.0496	48			
La-Br1	314.43(2)	0.4864	48	0.4507	43.268	30.719
La-Br2	321.55(1)	0.4150	48			

Distances, -ICOHP per bond, number of interactions ("bonds"), average -ICOHP, ⟨-ICOHP⟩, cumulative -ICOHP per cell (-CICOHP), and percentage contribution to bonding interactions. Values taken from [Steinberg et al. \(2012\)](#).

TABLE 10 Percentage Contributions to Hetero- (T–R and R–X) and Homoatomic (T–T and R–R) Bonding Interactions in Some Oligomeric and Chain Cluster Complexes $\{T_rR_r\}X_x$

	ST	T–R	T–T	R–R	R–X	References
$\{MnGd_3\}I_3$	M2	39.4	16.0	10.5	34.1	Gupta et al. (2010)
$\{RuPr_3\}Cl_3$	O	52.5	13.2	4.3	30.0	Gupta et al. (2010)
$\{RuLa_3\}Br_3$	C2	65.1	0.0	4.2	30.7	Steinberg et al. (2012)
$\{RuPr_3\}Br_3$	M1	63.9	0.1	9.1	26.9	Hassel (2013)
$\{RuPr_3\}Br_3$	C2	64.5	0.1	4.9	30.5	Hassel (2013)
$\{RuLa_3\}I_3$	M1	60.9	0.0	9.9	29.2	Steinberg et al. (2012)
$\{RuPr_3\}I_3$	M1	62.7	0.3	8.7	28.4	Gupta et al. (2010)
$\{Ru_4Gd_{16}\}Br_{23}$	I	47.3	2.1	5.0	45.5	Steinberg (2013)
$\{Ru_4Y_{16}\}Br_{20}$	IIT1	48.8	2.9	5.2	43.2	Steinberg (2013)
$\{RhLa_3\}Br_3$	C2	60.6	0.0	5.3	34.0	Steinberg (2013)
$\{Rh_4Tb_{16}\}Br_{24}(TbBr_3)_4$	IIT2	33.9	1.9	3.5	59.3	Bell (2013)
$\{Ir_4Tb_{16}\}Cl_{24}(TbCl_3)_4$	IIT2	37.3	3.8	3.6	55.2	Bell (2013)
$\{IrLa_3\}Br_3$	C2	67.2	0.0	3.7	29.1	Steinberg et al. (2012)
$\{IrPr_3\}Br_3$	C2	67.4	0.1	3.0	29.5	Klein (2013)
$\{IrLa_3\}I_3$	C2	65.0	0.1	4.1	30.8	Steinberg (2013)
$\{OsEr_4\}Cl_4$	M	58.8	4.5	10.5	28.0	Bell (2013)
Rh_2Er_3		83.6	6.8	9.6	–	Bell (2013)

ST: structure type; see for $\{TR_3\}X_3$ [Table 6](#), and for tetramers, [Table 4](#) and text.

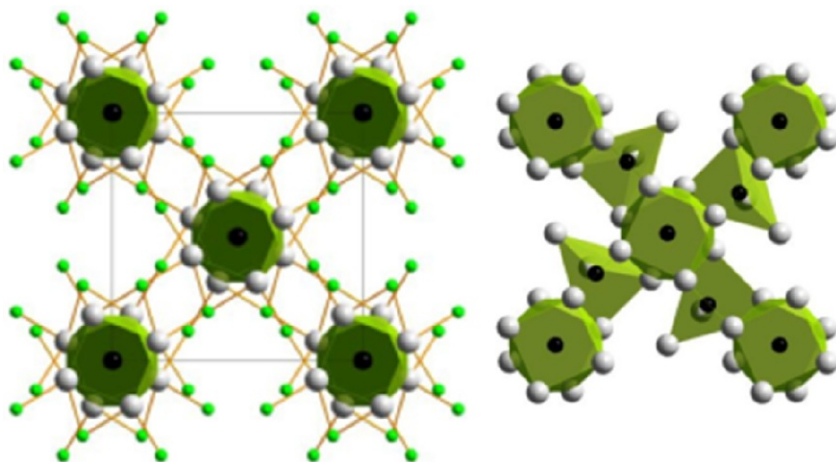


FIGURE 37 Comparison of similar parts of the crystal structures of $\{\text{OsEr}_4\}\text{Cl}_4$ and $\{\text{Rh}_2\text{Er}_3\} = \{\text{RhEr}_4\}(\text{Rh}_{2.5}\text{Er}_{1.25})$.

Er–Er (9.6%) contributions to the bonding in this intermetallic compound. However, a closer look at the $-\text{ICOHP}$ values per bond shows that Rh–Rh bonding is effective (0.24 eV/bond), although less than polar Rh–Er bonding (0.76 eV/bond); Er–Er bonding is indeed negligible (0.09 eV/bond). The exceptionally high Rh–Er contributions originate from far more bonds per cell (504), in comparison with Rh–Rh contacts (132).

There can only be one type of heteroatomic contacts (Rh–Er) in binary $\{\text{Rh}_2\text{Er}_3\}$ amounting to a bonding contribution of 83.6%. The sum of the two types of heteroatomic contributions, Os–Er and Os–Er, in $\{\text{OsEr}_4\}\text{Cl}_4$, with a similar structure (see Fig. 37) amounts to $(58.8 + 28.0) = 86.8$, essentially the same number. Thus, the symbiosis of intermetallic Os–Er and salt-like Er–Cl bonding interactions plays a similar role in $\{\text{OsEr}_4\}\text{Cl}_4$ as the purely polar Rh–Er interactions in $\{\text{Rh}_2\text{Er}_3\}$.

6 CONCLUSIONS

The rare-earth elements, R, may form clusters of six to eight R atoms encapsulating an endohedral transition metal atom T to compensate for the low number of valence electrons of the R atoms (only three). These heteroatomic clusters, $\{\text{TR}_r\}$, are surrounded by halide ligands, X, to build cluster complexes, $\{\text{TR}_r\}\text{X}_x$. Cluster complexes may be isolated (extremely rare), connected via common ligands (more frequent), or connected (most frequent) by common edges, faces, or vertices (with steeply decreasing frequency) to assemble oligomers, chains, layers, or networks of clusters. The heterometallic clusters alone may be understood as polar intermetallics of (usually) low dimensionality. Together with halide ligands, they form metal-rich halides. Thus, these solids are excellent

examples for a symbiosis of intermetallic and salt. Bonding is mainly heteroatomic, T–R and R–X, as well as R–X–R, with minor homoatomic contributions, T–T and R–R, and van der Waals X–X attractions.

Future work is expected to focus, besides hunting for new compounds and structures, on the relationships between T–R intermetallics and (extended) T–R–X cluster complexes and on the production of pure samples of both large(r) crystals and powders to allow for a deeper understanding of their physical properties. Serious attempts should also be made to secure cluster complexes with endohedral atoms in solution with the exchange of halide by organic ligands. This would bring a now well-developed organometallic chemistry of lower-valent rare-earth elements and the solid state chemistry of reduced rare-earth elements together. The exploration of the chemical properties of rare-earth element clusters would then become possible.

ACKNOWLEDGMENTS

Little less than three decades ago, the late John D. Corbett published a communication, coauthored by Tim Hughbanks and Guy Rosenthal (Hughbanks et al., 1986), on “Alloy Clusters: The Encapsulation of Transition Metals (Mn, Fe, Co, Ni) within Cluster Halides of Zirconium and the Rare-Earth Metals.” This was the beginning of the chemistry outlined in this chapter. We were drawn into this field originating from interest in reduced scandium and praseodymium chemistry to which two postdoctoral associates, Liesbet Jongen and Andriy Palasyuk, have contributed so much. Sina Zimmermann, Nina Herzmann, Kathrin Daub, Matthias Brühmann, Christian Rustige, Simon Steinberg, and Eva Meyer have devoted their Dr. rer. nat. theses (2008–2013) to various aspects of rare-earth cluster complexes with endohedral transition metal atoms, and Marike Wolberg and Thomas Bell followed their footsteps. I am most grateful to Anja-Verena Mudring and Ingo Pantenburg for the many discussions and for her guidance in understanding electronic structures and for his aid in getting the graphics right, respectively. Financial support came from the University of Cologne, the Deutsche Forschungsgemeinschaft (SFB 608), and the Fonds der Chemischen Industrie. Last but by no means least, writing this chapter would not have been possible without the spirit of Iowa State University and my wonderful friend John D. Corbett who taught us “. . .the wonder and excitement of finding the unprecedented and unimaginable that makes research enjoyable, even exhilarating, and worthwhile” (Corbett, 2000).

REFERENCES

- Adolphson, D.G., Corbett, J.D., 1976. *Inorg. Chem.* 15, 1820.
 Andersen, O.K., 1975. *Phys. Rev. B* 12, 3060.
 Andersen, O.K., Jepsen, O., 1984. *Phys. Rev. Lett.* 53, 2571.
 Artelt, H.M., Schleid, Th., Meyer, G., 1992. *Z. Anorg. Allg. Chem.* 618, 18.
 Badding, M.E., DiSalvo, F.J., 1990. *Inorg. Chem.* 29, 3952.
 Bauhofer, W., Simon, A., 1982. *Z. Naturforsch.* 37a, 568.
 Bauhofer, C., Mattausch, H.J., Miller, G.J., Bauhofer, W., Cockcroft, J.K., Kremer, R.K., Simon, A., 1990. *J. Less Common Met.* 167, 65.

- Bell, T., 2013. Unpublished work.
- Bertho, K., 1980. Dr. rer. nat. Thesis, University of Stuttgart.
- Bertho, K., Mattausch, H., Simon, A., 1980. *Z. Naturforsch.* 35b, 626.
- Brühmann, M., 2011. Dr. rer. nat. Thesis, University of Cologne.
- Brühmann, M., Meyer, G., 2010. *Eur. J. Inorg. Chem.* 2609.
- Brühmann, M., Meyer, G., 2012. *Z. Anorg. Allg. Chem.* 638, 1257.
- Brühmann, M., Mudring, A.-V., Valldor, M., Meyer, G., 2011. *Eur. J. Inorg. Chem.* 4083.
- Chen, L., Corbett, J.D., 2003. *J. Am. Chem. Soc.* 125, 1170.
- Cockcroft, J.K., Mattausch, H., Raju, N.P., Kremer, R.K., Simon, A., 1992. *J. Alloys Comp.* 183, 241.
- Corbett, J.D., 1973. *Rev. Chim. Minér.* 10, 239.
- Corbett, J.D., 1983a. *Inorg. Synth.* 22, 15.
- Corbett, J.D., 1983b. *Inorg. Synth.* 22, 31.
- Corbett, J.D., 1991. In: Meyer, G., Morss, L.R. (Eds.), *Synthesis of Lanthanide and Actinide Compounds*. Kluwer Academic Publishers, Dordrecht, NL, p. 159.
- Corbett, J.D., 2000. *Inorg. Chem.* 39, 5178.
- Corbett, J.D., Dudis, D.S., Ford, J.E., Hwu, S.-J., Meyer, G., Wijeyesekera, S., 1987. *J. Less Common Met.* 127, 1.
- Cotton, F.A., Wilkinson, G., 2008. *Advanced Inorganic Chemistry*, fifth ed. Wiley-Interscience, New York, 1053 (Chapter 23).
- Daake, R.L., Corbett, J.D., 1977. *Inorg. Chem.* 16, 2029.
- Daub, K., 2009. Dr. rer. nat. Thesis, University of Cologne.
- Daub, K., Meyer, G., 2009. *Acta Crystallogr.* E65, i9.
- Daub, K., Meyer, G., 2010. *Z. Anorg. Allg. Chem.* 636, 1716.
- Demir, S., 2007. Diploma Thesis, University of Cologne.
- Dorhout, P.K., Corbett, J.D., 1992. *J. Am. Chem. Soc.* 114, 1697.
- Dorhout, P.K., Payne, M.W., Corbett, J.D., 1991. *Inorg. Chem.* 30, 4960.
- Dronskowski, R., 2005. *Computational Chemistry of Solid State Materials*. Wiley-VCH, Weinheim, Germany.
- Dronskowski, R., Blöchl, P.E., 1993. *J. Phys. Chem.* 97, 8617.
- Dudis, D., Corbett, J.D., 1987. *Inorg. Chem.* 26, 1933.
- Dudis, D.S., Corbett, J.D., Hwu, S.-J., 1986. *Inorg. Chem.* 25, 3434.
- Ebbinghaus, G., Simon, A., Griffith, A., 1982. *Z. Naturforsch.* 37a, 564.
- Ebihara, M., Martin, J.D., Corbett, J.D., 1994. *Inorg. Chem.* 33, 2079.
- Ford, J.E., Corbett, J.D., Hwu, S.-J., 1983. *Inorg. Chem.* 22, 2789.
- Gerlitzki, N., Hammerich, S., Pantenburg, I., Meyer, G., 2006. *Z. Anorg. Allg. Chem.* 632, 2024.
- Goldsztaub, M.S., 1935. *Bull. Soc. Chim. Fr.* 58, 6.
- Gupta, S., Meyer, G., Corbett, J.D., 2010. *Inorg. Chem.* 49, 9949.
- Hadenfeldt, C., Herdejürgen, H., 1982. *J. Less Common Met.* 124, 93.
- Hamon, C., Marchand, R., Laurent, Y., Lang, J., 1974. *Bull. Soc. Fr. Miner.* 97, 6.
- Hassel, J., 2013. B.Sc. Thesis, University of Cologne.
- Herzmann, N., 2009. Dr. rer. nat. Thesis, University of Cologne.
- Herzmann, N., Mudring, A.-V., Meyer, G., 2008. *Inorg. Chem.* 47, 7954.
- Herzmann, N., Brühmann, M., Mudring, A.-V., Meyer, G., 2010. *Inorg. Chem.* 49, 5347.
- Heuer, T., Steffen, F., Meyer, G., 1996. *Eur. J. Solid State Inorg. Chem.* 33, 265.
- Hoffmann, R., 1963. *J. Chem. Phys.* 39, 1397.
- Hoffmann, R., Lipscomb, W.N., 1962. *J. Chem. Phys.* 36, 2179.
- Hong, S.-T., Martin, J.D., Corbett, J.D., 1998. *Inorg. Chem.* 37, 3385.

- Hong, S.-T., Hoistad, L.M., Corbett, J.D., 2000. *Inorg. Chem.* 39, 98.
- Hoppe, R., Sabrowsky, H., 1965. *Z. Anorg. Allg. Chem.* 339, 144.
- Hughbanks, T., Corbett, J.D., 1988. *Inorg. Chem.* 27, 2022.
- Hughbanks, T., Corbett, J.D., 1989. *Inorg. Chem.* 28, 631.
- Hughbanks, T., Rosenthal, G., Corbett, J.D., 1986. *J. Am. Chem. Soc.* 108, 8289.
- Hwu, S.-J., Corbett, J.D., 1986. *J. Solid State Chem.* 64, 331.
- Iandelli, A., Palenzona, A., 1976. *Rev. Chim. Miner.* 13, 55.
- Imoto, H., Corbett, J.D., 1980. *Inorg. Chem.* 19, 1241.
- Izmailovich, A.S., Trayanov, S.I., Tsirelnikov, V.I., 1974. *Russ. J. Inorg. Chem.* 19, 1597.
- Janiak, C., Meyer, H.-J., Gudat, D., Alsfasser, R., 2012. In: Meyer, H.-J. (Ed.), *Riedel Moderne Anorganische Chemie*, fourth ed. De Gruyter, Berlin.
- Jantsch, G., Klemm, W., 1933. *Z. Anorg. Allg. Chem.* 216, 80.
- Jensen, E.A., Corbett, J.D., 2002. *Inorg. Chem.* 41, 6199.
- Johnson, D.A., 1969. *J. Chem. Soc. A*, 1525, 1529, 2578.
- Johnson, D.A., 1982. *Some Thermodynamic Aspects of Inorganic Chemistry*, second ed. Cambridge University Press, Cambridge, England.
- Johnson, D.A., 2006. In: Meyer, G., Naumann, D., Wesemann, L. (Eds.), *Inorganic Chemistry in Focus*. Wiley-VCH, Weinheim, pp. 1–13. (Chapter 3).
- Kauzlarich, S.M., Hughbanks, T., Corbett, J.D., Klavins, P., Shelton, R.N., 1988. *Inorg. Chem.* 27, 1791.
- Klein, N., 2013. M.Ed. Thesis, University of Cologne.
- Klemm, W., Bommer, H., 1937. *Z. Anorg. Allg. Chem.* 231, 138.
- Köckerling, M., Martin, J.D., 2001. *Inorg. Chem.* 40, 389.
- Kremer, R.K., Cockcroft, J.K., Mattausch, H., Raju, N.P., Simon, A., 1992. *J. Magn. Magn. Mater.* 104–107, 959.
- Larres, M., 2012. Dr. rer. nat. Thesis, University of Cologne and unpublished work.
- Lefevre, C., Hoch, C., Eger, R., Simon, A., 2005. *Z. Kristallogr. New Cryst. Struct.* 220, 3.
- Lefevre, C., Hoch, C., Kremer, R.K., Simon, A., 2008. *Solid State Sci.* 10, 1625.
- Llusar, R., Corbett, J.D., 1994. *Inorg. Chem.* 33, 849.
- Lokken, D.A., Corbett, J.D., 1970. *J. Am. Chem. Soc.* 92, 1799.
- Lokken, D.A., Corbett, J.D., 1973. *Inorg. Chem.* 12, 556.
- Lukachuk, M., Mattausch, H., Simon, A., 2006. *Z. Kristallogr. New Cryst. Struct.* 221, 3.
- Lukachuk, M., Kremer, R.K., Mattausch, H., Simon, A., 2007. *Inorg. Chem.* 46, 3231.
- Lukachuk, M., Kienle, L., Zheng, C., Mattausch, H., Simon, A., 2008. *Inorg. Chem.* 47, 4656.
- Lulei, M., Corbett, J.D., 1996a. *Inorg. Chem.* 35, 4084.
- Lulei, M., Corbett, J.D., 1996b. *Z. Anorg. Allg. Chem.* 622, 1677.
- Lulei, M., Maggard, P.A., Corbett, J.D., 1996. *Angew. Chem.* 108, 1798.
- Lulei, M., Martin, J.D., Hoistad, L.M., Corbett, J.D., 1997. *J. Am. Chem. Soc.* 119, 513.
- Masse, R., Simon, A., 1981. *Mater. Res. Bull.* 16, 1007.
- Mattausch, H., Simon, A., 1997. *Z. Kristallogr. New Cryst. Struct.* 212, 99.
- Mattausch, H., Simon, A., 2005a. *Z. Kristallogr. New Cryst. Struct.* 220, 121.
- Mattausch, H., Simon, A., 2005b. *Z. Kristallogr. New Cryst. Struct.* 220, 313.
- Mattausch, H., Schwarz, C., Simon, A., 1987. *Z. Krist.* 178, 156.
- Mattausch, H., Eger, R., Simon, A., 1991. *Z. Anorg. Allg. Chem.* 597, 155.
- Mattausch, H., Eger, R., Corbett, J.D., Simon, A., 1992. *Z. Anorg. Allg. Chem.* 616, 157.
- Mattausch, H., Kremer, R.K., Simon, A., Bauhofer, W., 1993. *Z. Anorg. Allg. Chem.* 619, 741.
- Mattausch, H., Borrmann, H., Eger, R., Kremer, R.K., Simon, A., 1995. *Z. Naturforsch.* 50b, 931.
- Mattausch, H., Oeckler, O., Simon, A., 1999. *Inorg. Chim. Acta* 289, 174.

- Mattausch, HJ, Oeckler, O., Simon, A., 2000. *Z. Kristallogr. New Cryst. Struct.* 215, 199.
- Mattausch, H.J., Oeckler, O., Zheng, C., Simon, A., 2001a. *Z. Anorg. Allg. Chem.* 627, 1523.
- Mattausch, HJ, Vajenine, G.V., Oeckler, O., Kremer, R.K., Simon, A., 2001b. *Z. Anorg. Allg. Chem.* 627, 2542.
- Mattausch, HJ, Oeckler, O., Zheng, C., Simon, A., 2002a. *Z. Anorg. Allg. Chem.* 627, 1523.
- Mattausch, HJ, Oeckler, O., Simon, A., 2002b. *Z. Kristallogr. New Cryst. Struct.* 217, 323.
- Mattausch, HJ, Oeckler, O., Simon, A., 2003. *Z. Kristallogr. New Cryst. Struct.* 218, 282.
- Mattausch, H.J., Zheng, C., Kienle, L., Simon, A., 2004. *Z. Anorg. Allg. Chem.* 630, 2367.
- Mattausch, HJ, Hoch, C., Simon, A., 2005. *Z. Anorg. Allg. Chem.* 631, 1423.
- Mattausch, HJ, Hoch, C., Simon, A., 2007. *Z. Naturforsch.* 62b, 148.
- Mattausch, H., Hoch, C., Simon, A., 2008. *Z. Anorg. Allg. Chem.* 634, 641.
- Mee, J.D., Corbett, J.D., 1965. *Inorg. Chem.* 4, 88.
- Meyer, G., 1988. *Chem. Rev.* 88, 93.
- Meyer, G., 2007. *Z. Anorg. Allg. Chem.* 633, 2537.
- Meyer, G., 2008. *Z. Anorg. Allg. Chem.* 634, 2729.
- Meyer, G., 2012. In: Atwood, D. (Ed.), *The Rare Earth Elements: Fundamentals and Applications*. John Wiley & Sons, Chichester, UK, pp. 415–436.
- Meyer, E., 2013. *Dr. rer. nat. Thesis*, University of Cologne.
- Meyer, G., Hoppe, R., 1974. *Angew. Chem. Int. Ed. Engl.* 13, 744.
- Meyer, G., Hoppe, R., 1976. *J. Less Common Met.* 46, 55.
- Meyer, G., Palasyuk, A., 2006. In: Meyer, G., Naumann, D., Wesemann, L. (Eds.), *Inorganic Chemistry in Focus III*. Wiley-VCH, Weinheim, pp. 45–60.
- Meyer, G., Schleid, Th., 1987. *Inorg. Chem.* 26, 217.
- Meyer, G., Uhrlandt, S., 1993. *Angew. Chem. Int. Ed. Engl.* 32, 1318.
- Meyer, G., Wickleder, M.S., 2000. In: Gschneidner Jr., K.A., Eyring, L. (Eds.), *Handbook on the Physics and Chemistry of Rare Earths*, vol. 28. Elsevier Science, Amsterdam, pp. 53–129 (Chapter 177).
- Meyer, G., Hwu, S.-J., Wijeyesekera, S., Corbett, J.D., 1986. *Inorg. Chem.* 25, 4811.
- Mikheev, N.B., Kamenskaya, A.N., Rumer, I.A., Novitschenko, I.A., Simon, A., Mattausch, HJ, 1992. *Z. Naturforsch.* 47b, 992.
- Morss, L.R., 1976. *Chem. Rev.* 76, 827.
- Morss, L.R., 1985. In: Bard, A.J., Parsons, R., Jordan, J. (Eds.), *Standard Potentials in Aqueous Solution*. Marcel Dekker, New York, p. 587.
- Morss, L.R., Mattausch, HJ, Kremer, R., Simon, A., Corbett, J.D., 1987. *Inorg. Chim. Acta* 140, 107.
- Nagaki, D., Simon, A., Borrmann, H., 1989. *J. Less Common Met.* 156, 193.
- Niggli, P., 1916. *Z. Anorg. Allg. Chem.* 94, 207.
- Niggli, P., 1946. *Grundlagen der Stereochemie*. Birkhäuser, Basel.
- Okamoto, H., 1990. In: Massalski, T.B. (Ed.), second ed. *Binary Alloy Phase Diagrams*, vol. 3. 2497.
- Palasyuk, A., Pantenburg, I., Meyer, G., 2006a. *Acta Crystallogr.* E62, i61.
- Palasyuk, A., Pantenburg, I., Meyer, G., 2006b. *Z. Anorg. Allg. Chem.* 632, 1969.
- Park, Y.-B., Corbett, J.D., 1994. *Inorg. Chem.* 33, 1705.
- Park, Y., Martin, J.D., Corbett, J.D., 1997. *J. Solid State Chem.* 129, 277.
- Pauling, L., 1947. *General Chemistry*. Freeman, San Francisco (Chapter 8).
- Payne, M.W., Corbett, J.D., 1990. *Inorg. Chem.* 29, 2246.
- Payne, M.W., Ebihara, M., Corbett, J.D., 1991a. *Angew. Chem. Int. Ed. Engl.* 30, 856.
- Payne, M.W., Dorhout, P.K., Corbett, J.D., 1991b. *Inorg. Chem.* 30, 1467.

- Payne, M.W., Dorhout, P.K., Kim, S.-J., Hughbanks, T.R., Corbett, J.D., 1992. *Inorg. Chem.* 31, 1389.
- Poepfelmeier, K.R., Corbett, J.D., 1977. *Inorg. Chem.* 16, 294.
- Qi, R.-Y., Corbett, J.D., 1997. *Inorg. Chem.* 36, 6039.
- Reisser, R., Kremer, R.K., Simon, A., 1995. *Physica B* 204, 265.
- Ruck, M., 1991. Dr. rer. nat. Thesis, University of Stuttgart.
- Ruck, M., Simon, A., 1993. *Z. Anorg. Allg. Chem.* 619, 327.
- Rustige, C., 2011. Dr. rer. nat. Thesis, University of Cologne.
- Rustige, C., Brühmann, M., Steinberg, S., Meyer, E., Daub, K., Zimmermann, S., Wolberg, M., Mudring, A.-V., Meyer, G., 2012. *Z. Anorg. Allg. Chem.* 638, 1922.
- Ryazanov, M., Simon, A., Mattausch, H., 2006. *Inorg. Chem.* 45, 10728.
- Schäfer, H., Schnering, H.G., 1964. *Angew. Chem.* 76, 833.
- Schleid, Th., Meyer, G., 1987. *Z. Anorg. Allg. Chem.* 552, 90.
- Schwanitz-Schüller, U., 1984. Dr. rer. nat. Thesis, University of Stuttgart.
- Schwanitz-Schüller, U., Simon, A., 1985. *Z. Naturforsch.* 40b, 710.
- Simon, A., 1967. *Z. Anorg. Allg. Chem.* 355, 311.
- Simon, A., 1981. *Angew. Chem. Int. Ed. Engl.* 20, 1.
- Simon, A., 1985. *J. Solid State Chem.* 57, 2.
- Simon, A., Westerbeck, E., 1972. *Angew. Chem. Int. Ed. Engl.* 11, 1105.
- Simon, A., von Schnering, H.G., Schäfer, H., 1967. *Z. Anorg. Allg. Chem.* 355, 295.
- Simon, A., Mattausch, H., Holzer, N., 1976. *Angew. Chem. Int. Ed. Engl.* 15, 624.
- Simon, A., Holzer, N., Mattausch, H., 1979. *Z. Anorg. Allg. Chem.* 456, 207.
- Simon, A., Mattausch, H., Mikheev, N.B., 1987. *Z. Naturforsch.* 42b, 666.
- Simon, A., Mattausch, H.J., Miller, G.J., Bauhofer, W., Kremer, R.K., 1991. Metal-rich halides. In: Gschneidner Jr., K.A., Eyring, L. (Eds.), *Handbook on the Physics and Chemistry of Rare Earths*, vol. 15. Elsevier Science, Amsterdam, pp. 191–285 (Chapter 100).
- Simon, A., Mattausch, H., 2013. Low-valence compounds of the lanthanoids. In: Reedijk, J., Poepfelmeier, K. (Eds.), *Comprehensive Inorganic Chemistry*, vol. II. Elsevier Science, Amsterdam, pp. 535–581 (Chapter 2.20).
- Smith, J.D., Corbett, J.D., 1985. *J. Am. Chem. Soc.* 107, 5704.
- Steffen, F., Meyer, G., 1995. *Z. Naturforsch.* 50b, 1570.
- Steinberg, S., 2010. Diploma Thesis, University of Cologne.
- Steinberg, S., 2013. Dr. rer. nat. Thesis, University of Cologne and unpublished work.
- Steinberg, S., Brgoch, J., Miller, G.J., Meyer, G., 2012. *Inorg. Chem.* 51, 11356.
- Steinberg, S., Valldor, M., Meyer, G., 2013. *J. Solid State Chem.* 206, 176.
- Steinwand, S.J., Corbett, J.D., 1996. *Inorg. Chem.* 35, 7056.
- Steinwand, S.J., Martin, J.D., Corbett, J.D., 1997. *Inorg. Chem.* 36, 6413.
- Sweet, L.E., Hughbanks, T., 2006. *Inorg. Chem.* 45, 9696.
- Sweet, L.E., Roy, L.E., Meng, F., Hughbanks, T., 2006. *J. Am. Chem. Soc.* 128, 10193.
- Uhrlandt, S., Meyer, G., 1994. *Z. Anorg. Allg. Chem.* 620, 1872.
- Uhrlandt, S., Meyer, G., 1995. *Z. Anorg. Allg. Chem.* 621, 1466.
- Uhrlandt, S., Artelt, H.M., Meyer, G., 1994. *Z. Anorg. Allg. Chem.* 620, 1532.
- Uhrlandt, S., Heuer, T., Meyer, G., 1995. *Z. Anorg. Allg. Chem.* 621, 1299.
- Uma, S., Corbett, J.D., 1998. *Inorg. Chem.* 37, 1944.
- Uma, S., Martin, J.D., Corbett, J.D., 1999. *Inorg. Chem.* 38, 3825.
- Warkentin, E., Bärnighausen, H., 1979. *Z. Anorg. Allg. Chem.* 459, 187.
- Warkentin, E., Simon, A., 1983. *Rev. Chim. Miner.* 20, 488.
- Werner, A., 1893. *Z. Anorg. Chem.* 3, 267.

- Wiench, H., Brachtel, G., Hoppe, R., 1977. *Z. Anorg. Allg. Chem.* 437, 169.
- Wiglusz, R., Pantenburg, I., Meyer, G., 2007. *Z. Kristallogr. New Cryst. Struct.* 222, 9.
- Wöhler, F., 1828. *Poggendorf's Ann.* 12, 577.
- Wolberg, M., 2014. Dr. rer. nat. Thesis, University of Cologne.
- Zheng, C., Oeckler, O., Mattausch, H.J., Simon, A., 2001. *Z. Anorg. Allg. Chem.* 627, 2151.
- Zheng, C., Simon, A., Mattausch, H., 2002. *J. Alloys Compd.* 338, 165.
- Zheng, C., Mattausch, H., Simon, A., 2005. *Z. Kristallogr. New Cryst. Struct.* 220, 314.
- Zheng, C., Mattausch, H.J., Hoch, C., Simon, A., 2008a. *Inorg. Chem.* 47, 2356.
- Zheng, C., Mattausch, H.J., Hoch, C., Simon, A., 2008b. *Inorg. Chem.* 47, 10753.
- Zheng, C., Mattausch, H.J., Hoch, C., Simon, A., 2009a. *J. Solid State Chem.* 182, 2307.
- Zheng, C., Mattausch, H.J., Hoch, C., Simon, A., 2009b. *Z. Anorg. Allg. Chem.* 635, 2429.
- Zheng, C., Köhler, J., Mattausch, H.J., Hoch, C., Simon, A., 2012. *J. Am. Chem. Soc.* 134, 5026.
- Zimmermann, S., 2006. Diploma Thesis, University of Cologne.
- Zimmermann, S., 2008. Dr. rer. nat. Thesis, University of Cologne.
- Zimmermann, S., Brühmann, M., Casper, F., Heyer, O., Lorenz, T., Felser, C., Mudring, A.-V., Meyer, G., 2010. *Eur. J. Inorg. Chem.* 2613.
- Zimmermann, S., Pantenburg, I., Meyer, G., 2012. *Crystals* 2, 704.

Chapter 265

Solid-State Optical Refrigeration

Markus P. Hehlen^{*}, Mansoor Sheik-Bahae[†] and Richard I. Epstein^{†,‡}

^{*}*Materials Science & Technology Division, Los Alamos National Laboratory, Los Alamos, New Mexico, USA*

[†]*Department of Physics & Astronomy, University of New Mexico, Albuquerque, New Mexico, USA*

[‡]*ThermoDynamic Films, LLC, Santa Fe, New Mexico, USA*

Chapter Outline

1 Introduction	179	3.2 Role of Impurities	204
1.1 Motivation for Cooling Solids with Light	179	3.3 Homogeneous and Inhomogeneous Broadening	208
1.2 Definition of Solid-State Optical Refrigeration	182	4 Experimental Techniques	210
1.3 History of Optical Refrigeration	183	4.1 Reciprocity of Absorption and Luminescence	210
2 Principles of Solid-State Optical Refrigeration	191	4.2 Thermometry Techniques	212
2.1 Electronic States of Lanthanide Ions	191	4.3 Measurement of Minimum Achievable Temperature	224
2.2 Anti-Stokes Fluorescence and Thermal Equilibrium	194	5 Lanthanide-Doped Laser-Cooling Materials	225
2.3 The Four-Level Model and the Laser-Cooling Efficiency	197	5.1 Yb ³⁺ -Doped Materials	225
2.4 Thermodynamic Considerations	199	5.2 Tm ³⁺ -Doped Materials	237
3 Material Considerations	201	5.3 Er ³⁺ -Doped Materials	240
3.1 Energy Levels and Nonradiative Decay	201	5.4 Other Lanthanides	244
		6 Toward Laser-Cooling Devices	245
		6.1 Optical Cavities	245
		6.2 Thermal Management	249
		7 Conclusions and Outlook	252
		References	253

1 INTRODUCTION

1.1 Motivation for Cooling Solids with Light

Refrigeration dates back thousands of years in man's quest to store food for extended periods of time. As early as 400 BC, the Persians gathered ice from mountains during winter and stored it in thermally insulated structures

(yakhchals), providing refrigeration of foodstuffs during the hot desert summer months (Mahdavinejad and Javanrudi, 2012). Ice and snow harvesting was also practiced by the Chinese, Hebrews, Greeks, and Romans. By the nineteenth century, the harvesting, storage, and transportation of ice had been perfected and became a big business. Other historic refrigeration techniques include cooling of water during the night, evaporation of water during the day, and dissolving salts in water. All these early methods were noncyclic, that is, they required a steady resupply of the refrigerant. The discovery of cyclic refrigeration systems was a major breakthrough. They allowed a working fluid (refrigerant) to absorb and reject heat in a closed system as external work was applied to the refrigerator to drive a thermodynamic cycle. One of the first such systems was a vapor-compression refrigerator described by Oliver Evans in 1805. In 1851, John Gorrie was granted the first US patent on the “improved process for the artificial production of ice” (Gorrie, 1851).

Today, vapor-compression, vapor-absorption, and gas-cycle refrigerators meet the vast majority of everyday refrigeration needs, and they are critical enablers for a significant portion of the global economy. In the late nineteenth century, Carl von Linde used the Joule–Thomson effect in a first foray into the cryogenic regime (< 123 K) to achieve the liquefaction of air. The ensuing rapid development of cryogenic refrigeration techniques ushered in a new era in physics and condensed matter science that led to many fundamental discoveries such as superconductivity by Heike Kamerlingh Onnes in 1908 (van Delft and Kes, 2010), superfluidity independently by Kapista and by Allen and Meisener in 1937 (Chodos 2006), and Bose–Einstein condensation (Anderson et al., 1995; Cornell and Wieman, 1995).

Cryogenic technologies have enabled a wide range of new applications. Detectors based on semiconductors are one important class of devices that benefit from refrigeration. For example, HgCdTe and InSb are used in detectors for long-wave (8–12 μm) and midwave (3–5 μm) infrared (IR) light (Rogalski, 2011), while high-purity germanium (HPGe) is used for high-resolution gamma-ray spectroscopy (Knoll, 2000). In these materials, the incident radiation excites electrons from the valence band to the conduction band and thereby induces an electric current that can be measured as a signal. However, electrons also can be promoted to the conduction band by random thermal excitations, creating an undesired “dark” current that masks the signal and ultimately limits the performance of the detector. The magnitude of the respective thermal noise is proportional to the square root of the dark current, that is, $\exp(-E_g/2kT)$, where T is the temperature in Kelvin, k is the Boltzmann constant, and $E_g = E_c - E_v$ is the bandgap energy of the semiconductor defined as the energy difference between the bottom of the conduction band (E_c) and the top of the valence band (E_v). To operate as IR detectors, such materials must have relatively small bandgaps (0.15 eV for HgCdTe, 0.23 eV for InSb, and 0.73 eV for Ge) and, as a result, thermal excitation of electrons to the conduction band is a likely process at ambient temperatures (note that

$kT = 0.0259 \text{ eV}$ at 300 K). Such detectors therefore have to be cooled, often to cryogenic temperatures, to sufficiently reduce the thermal noise and correspondingly increase the detector sensitivity (Rogalski, 2005).

Cryogenic refrigeration of semiconductor devices can be particularly challenging in applications that have tight constraints for size, weight, and power, such as in portable, airborne, and space-based detector systems. Liquid helium has been used as a refrigerant on spacecraft because it has a total enthalpy per mass ratio that is only surpassed by hydrogen, which is usually avoided because of its flammability (Green, 2003). Subliming solid cryogenics such as methane, ethylene, carbon dioxide, or ammonia can provide cooling to the 60–150 K range. The main drawbacks of such stored cryogen systems however are their complexity and weight, the finite supply of refrigerant, and the associated limited useful lifetime that rarely exceeds one year in space applications (Nast et al., 1976).

Thermoelectric coolers (TECs) overcome the lifetime constraints of stored cryogenics. They are based on the Peltier effect in which a temperature change is achieved when an electric current flows through a junction of two different materials. However, the lowest temperatures even of advanced multistage TECs are limited to $\sim 175 \text{ K}$, which is still well above the desired operating temperature for many semiconductor detectors. This currently leaves mechanical coolers as the only available long-duration cryogenic technology, with the most common types being Stirling, Brayton, Gifford–McMahon, Joule–Thomson, and pulse tube refrigerators. They allow for cooling to $< 10 \text{ K}$, can have multiyear reliability, and offer multiwatt cooling power (Zagarola et al., 2009). The main disadvantages arise from the moving parts that are present in all these mechanical devices. They impose inherent reliability limitations and are the source of vibrations that impart microphonic noise to the detector and the associated electronics. These vibrations cause capacitive changes in the electric connections between the HPGe and the preamplifier that degrade the signal resolution in gamma-ray spectrometers (Gilmore and Hemingway, 1998). In optical cameras, mechanical vibrations can cause the image to blur and limit the resolution (Veprik et al., 2009). Significant advances in enhancing reliability (Zagarola et al., 2009), reducing vibrations (Veprik et al., 2009), and digital signal filtering (Schultz et al., 2007) have been achieved over the past decades. Nevertheless, microphonic noise remains the major factor limiting the resolution of detectors in many applications.

In 1995, Epstein et al. observed the cooling of a solid by a laser for the first time (Epstein et al., 1995). The effect was based on the principle of anti-Stokes fluorescence and produced a mere 0.3 K/W temperature drop of the glass sample near room temperature. Since then, the fundamental aspects of this phenomenon have been studied extensively, and both laser-cooling materials and optical cryocooler devices have been developed. In 2010, optical refrigeration into the cryogenic regime using an ytterbium-doped fluoride crystal ($\text{YLiF}_4:\text{Yb}^{3+}$)

(Seletskiy et al., 2010b) was first achieved, and a temperature of 114 K was reached starting from 300 K (Melgaard et al., 2013a). The most recent report is on cooling to 93 K of a 10 mol% Yb^{3+} -doped YLiF_4 crystal (Melgaard et al., 2014). Optical refrigeration to liquid-nitrogen temperatures (<77 K) appears within reach in the near future as both the materials and the device architecture are being optimized. Anti-Stokes fluorescence cooling is a solid-state, all-optical process that does not involve any moving parts and is therefore inherently free of mechanical vibrations. This property makes it a highly attractive method for the refrigeration of materials and devices that are susceptible to microphonic noise and/or require high reliability. In this chapter, we will review the principles of solid-state optical refrigeration (Section 2), the associated experimental techniques (Section 3), the relevant material properties (Section 4), the materials studied to date (Section 5), and the engineering aspects of optical cryocoolers (Section 5). We will conclude with an outlook on the remaining challenges and on the application potential of this new cooling technology (Section 6).

1.2 Definition of Solid-State Optical Refrigeration

The term “laser cooling” is used for several distinct phenomena. It is therefore worthwhile to define it precisely for the context of this chapter. In general, “laser cooling” describes the cooling of a physical system upon interaction with laser light. The role of the laser light is to reduce the amount of energy contained in a particular degree of freedom. In gases at low temperatures (<10 K), for example, the energy is primarily contained in translational degrees of freedom. Such a system can be laser-cooled by the Doppler effect (Cohen-Tannoudji and Phillips, 1990; Hänsch and Schawlow, 1975). When a laser is tuned to the low-frequency side of an atomic absorption, the atoms in the gas will more strongly absorb when they move toward the light source than when they move away from it. Each time an atom absorbs a photon moving toward it, it loses momentum equal to that of the photon. When the excited atom subsequently relaxes by spontaneous emission, the photon is emitted in a random direction and, on the average, does not change the atom’s momentum. Arranging two counterpropagating laser beams and performing many such absorption–emission cycles reduces the momentum in the direction of the laser propagation axis. Three orthogonal sets of counterpropagating laser beams create an optical molasses that cools the ensemble of atoms in the gas, in the best case, down to the Doppler-cooling limit. Chu, Cohen-Tannoudji, and Phillips were awarded the 1997 Nobel Prize in Physics for developing the methods to cool and trap atoms with laser light.

While Doppler cooling and related techniques can cool and trap small numbers of atoms in dilute gases to low temperatures, they are not suited to cool the bulk quantities of material that are needed for the refrigeration of macroscopic objects. To do so, one has to turn to the vibrational degrees of

freedom. Translational motion is largely absent in solids, and their thermal energy is primarily contained in vibrations, that is, the oscillations of atoms about fixed equilibrium positions. The elastic excitations of vibrations in a solid are referred to as phonons that are further classified as acoustic phonons and, in crystals consisting of more than one type of atom, optical phonons. Acoustic phonons are wavelike collective motions of atoms along the same direction (e.g., sound waves), while optical phonons encompass localized motions of different atoms in opposing directions. The opposing motion of cations and anions associated with optical phonon modes can induce electric dipoles that can then interact with the electric component of the incident electromagnetic wave, hence the name “optical” phonon. The resulting electron–phonon coupling allows laser light to interact with the vibrational degrees of freedom in a solid (Kim and Kaviani, 2009), making laser cooling of solids possible in certain cases as we shall see in the following. In the present context, the term “laser cooling” shall describe the laser-induced reduction of energy contained in the *vibrational* degrees of freedom of a solid.

1.3 History of Optical Refrigeration

For the vast majority of luminescent materials, the emission spectrum is shifted to *lower* energy with respect to the absorption spectrum of the corresponding electronic transition. The associated energy difference is referred to as the Stokes shift, named after the Irish physicist Sir George G. Stokes (1819–1903). This energy difference between the excitation source and the fluorescence is converted into vibrational and/or translational energy within the medium, causing the well-known heating of solids and gases upon excitation with light. In the 1920s, it was observed, however, that some phosphors doped with transition metals emitted light of *higher* energy than the excitation source, an effect that was termed “anti-Stokes fluorescence.” Lenard, Schmidt, and Tomascheck proposed in 1928 that anti-Stokes fluorescence had to be accompanied by the emission of longer-wavelength light such as not to produce a quantum efficiency greater than unity and not to violate the second law of thermodynamics (Lenard et al., 1928). This argument was challenged by Peter Pringsheim in 1929, who was working at the Physical Institute of the University of Berlin at the time (Pringsheim, 1929). He described a Gedankenexperiment in which he used a filtered sodium vapor lamp as a spectrally narrow light source to excite sodium vapor in Dewar 1 to the $^2P_{1/2}$ electronic excited state (see Fig. 1). Inelastic collisions in the gas cause some excited Na atoms to be further excited to the $^2P_{3/2}$ excited state, which is only 17.3 cm^{-1} ($0.08 kT$ at 300 K) above $^2P_{1/2}$. Both excited states then relax radiatively to the ground state by resonant ($^2P_{1/2} \rightarrow ^2S_{1/2}$) and anti-Stokes ($^2P_{3/2} \rightarrow ^2S_{1/2}$) fluorescence. As a result, the Na gas in Dewar 1 cools because its mean emission wavelength is slightly shorter than the excitation wavelength, with the energy difference corresponding to the energy that has been transferred from the translational degrees of freedom

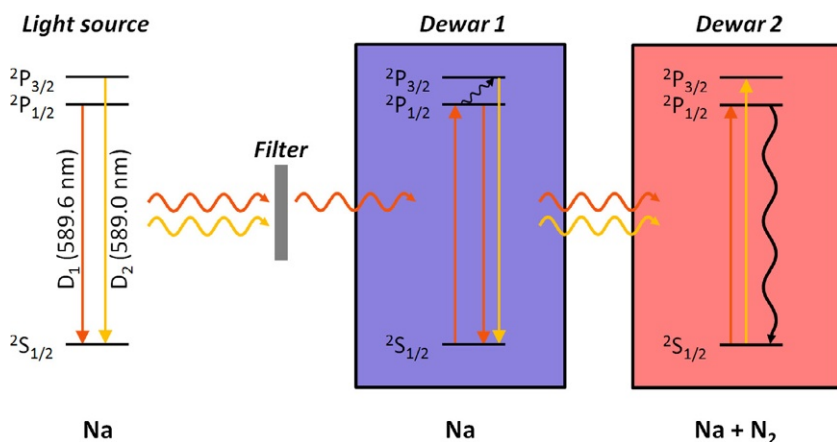


FIGURE 1 Gedankenexperiment described by Pringsheim in 1929 (Pringsheim, 1929). A filtered sodium vapor lamp is used as a spectrally narrow light source to excite the $2S_{1/2} \rightarrow 2P_{1/2}$ electronic transition of sodium atoms in Dewar 1. Inelastic collisions in the gas promote some sodium atoms from the $2P_{1/2}$ to the $2P_{3/2}$ excited state (wiggly arrow), causing both resonant ($2P_{1/2} \rightarrow 2S_{1/2}$) and anti-Stokes ($2P_{3/2} \rightarrow 2S_{1/2}$) fluorescence. Dewar 1 cools as a result of the transfer of translational energy of the gas to electromagnetic energy. The fluorescence emitted by Dewar 1 is absorbed by sodium vapor in Dewar 2, in which nitrogen has been added to quench the $2P$ fluorescence. Dewar 2 heats up as a result of the transfer of electromagnetic to translational energy of the gas.

to electromagnetic radiation. The emission from Dewar 1 is then absorbed by sodium gas in Dewar 2, in which the $2P$ emission has been completely quenched by the addition of nitrogen. As a result, Dewar 2 heats up because of the transfer of electromagnetic energy to the translational degrees of freedom of the gas. Pringsheim pointed out that, while Dewar 1 by itself may violate the second law of thermodynamics, the system as a whole did not. His argument was the first to postulate that one part of a physical system could be cooled by light. However, it was not fully accepted until 1946, when Landau presented a consistent description that included the entropy of the radiation field based on Bose–Einstein statistics applied to a “photon gas” (Landau, 1946; Ruan et al., 2007). He showed that the entropy of the radiation field is a function of both the solid angle of the propagating light and the frequency bandwidth of the light. Hence, a laser with high directionality and narrow spectral bandwidth represents a low-entropy radiation field. In contrast, luminescence isotropically emitted by a sample and comprising a range of emission frequencies represents a higher-entropy radiation field. The process of optical refrigeration therefore converts low-entropy laser light into higher-entropy anti-Stokes fluorescence, in agreement with the second law of thermodynamics.

It was realized early that a high quantum efficiency was a prerequisite for realizing cooling of a system by laser light. For example, Dewar 1 in Fig. 1 can only achieve net cooling if the two excited states $2P_{1/2}$ and $2P_{3/2}$ predominantly decay by radiative relaxation (resonant and anti-Stokes fluorescence)

rather than by nonradiative decay (like in Dewar 2). Nonradiative relaxation transfers the entire excitation energy into the translational/vibrational degrees of freedom and thus causes significant heating. This is particularly detrimental because the energy of the excited state is typically much larger than the energy gained by anti-Stokes fluorescence (on the order of kT). In 1981, Djeu et al. achieved the first net cooling by anti-Stokes luminescence in CO_2 gas at 250–300 °C (Djeu and Whitney, 1981). They pumped the $(100) \rightarrow (001)$ excited-state absorption (ESA) with a CO_2 laser at 10.6 μm to produce anti-Stokes luminescence from the $(001) \rightarrow (000)$ transition at 4.3 μm . Net laser-induced cooling or heating was observed as negative or positive changes in the total gas pressure. The inferred temperature drop was ~ 1 K.

Kastler pointed out in 1950 that lanthanide ions doped into transparent solids could be effective fluorescent coolers because they possess excited states with high quantum efficiencies (Kastler, 1950). A first experimental attempt to achieve laser cooling of a solid was undertaken by Kushida and Geusic of Bell Telephone Laboratories in 1968 (Kushida and Geusic, 1968). They used the 1064 nm light of a Nd^{3+} -doped $\text{Y}_3\text{Al}_5\text{O}_{12}$ (YAG:Nd) laser to excite another Nd^{3+} -doped YAG crystal that was placed inside the laser cavity. Laser excitation of Nd^{3+} at 1064 nm produced some anti-Stokes luminescence at 946 nm. As shown in Fig. 2, they measured the sample temperature

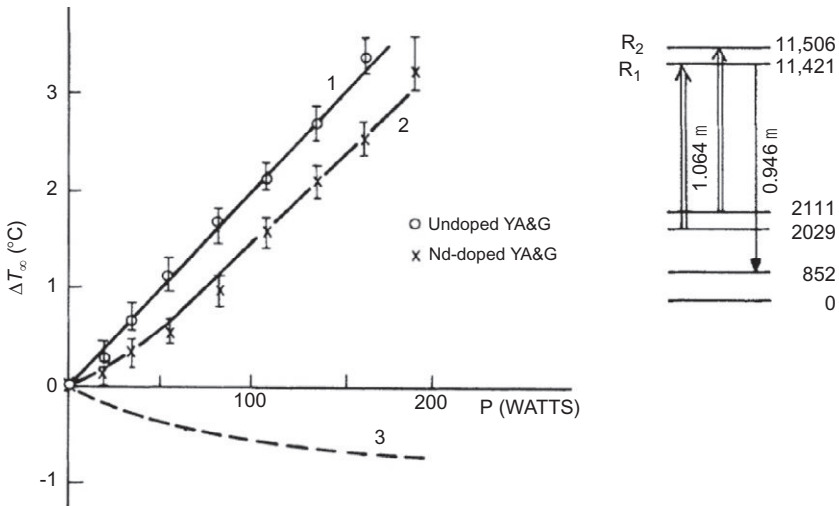


FIGURE 2 Observation of laser-induced cooling in a Nd^{3+} -doped $\text{Y}_3\text{Al}_5\text{O}_{12}$ (YAG) crystal (Kushida and Geusic, 1968). The sample was excited by a YAG:Nd laser at 1064 nm and produced anti-Stokes luminescence at 946 nm. A YAG crystal doped with Nd^{3+} (crosses) showed less heating than an undoped YAG crystal (open circles). While no net cooling of the bulk was achieved, the difference of the two measurements (dashed line) provided first experimental evidence for the presence of laser cooling in a solid. Reprinted with permission from Kushida and Geusic (1968). Copyright (2014) by the American Physical Society.

as a function of laser power first for an *undoped* YAG reference crystal. They observed a linear increase in temperature with increasing laser power even though the undoped YAG crystal should have had no absorption at 1064 nm. They concluded that their crystals contained impurities (suspected to be mostly Dy^{3+}) that were excited by the 1064 nm laser and that decayed nonradiatively, causing internal heating. In comparison, however, the Nd^{3+} -doped YAG crystal exhibited *less* heating than the undoped crystal, which provided direct evidence for the presence of additional laser-induced cooling by anti-Stokes luminescence from Nd^{3+} . The difference of the two experiments (dashed line in Fig. 2) indicates a laser-induced cooling effect of up to ~ 0.7 K at a pump power of 200 W. While no net cooling of the bulk crystal was achieved in this experiment, this early work correctly recognized and explicitly stressed the importance of high sample purity for achieving a net refrigeration effect.

The year 1995 marked a milestone in solid-state optical refrigeration when Epstein et al. at Los Alamos National Laboratory (LANL) were able to observe net laser cooling of a bulk Yb^{3+} -doped fluoride glass for the first time (Epstein et al., 1995). At that time, fluoride glasses such as ZBLANP (an acronym for the glass composition $\text{ZrF}_4\text{-BaF}_2\text{-LaF}_3\text{-AlF}_3\text{-NaF-PbF}_2$) were being developed for use in long-haul fiber-optic telecommunications. Fluoride glasses have low optical attenuation in the near-IR spectral region and thus offered the possibility of repeater-less transoceanic fiber-optic telecom links. Low-loss fluoride fiber preforms of high purity were produced commercially for subsequent drawing into optical fibers. The sample used by Epstein et al. was a fiber preform of ZBLANP doped with 1 wt% Yb^{3+} . It was cut to $2.5 \times 2.5 \times 6.9$ mm³ size and prepared with optical-quality surfaces. They used two identical samples placed next to each other. One of the samples was excited in the 870–1050 nm wavelength range of the ${}^2\text{F}_{7/2} \rightarrow {}^2\text{F}_{5/2}$ absorption of Yb^{3+} using a tunable titanium-sapphire laser. The temperature difference between the pumped and unpumped samples was measured using a calibrated InSb thermal camera that detected thermal emission in the 3–5 μm range. As shown in Fig. 3, the pumped ZBLANP: Yb^{3+} glass showed net bulk cooling of up to 0.3 K per Watt of optical pump power when the laser wavelength was greater than the mean fluorescence wavelength ($\tilde{\lambda}_F$), that is, when the regime of net anti-Stokes fluorescence was realized.

The Epstein team at LANL focused their early efforts on Yb^{3+} -doped ZBLANP glass, and they developed the various experimental techniques along with higher-power lasers and pumping geometries. By 1999, LANL researchers had cooled a fiber sample of ZBLANP: Yb by 65 K to a final temperature of 236 K (Gosnell, 1999), fueling the promise of optical refrigeration of solids to cryogenic temperatures (see Fig. 4). The potential for higher cooling efficiencies in Tm^{3+} compared to Yb^{3+} set the theme for the 2000–2005 time period during which Tm^{3+} -doped ZBLANP glass and BaY_2F_8 crystals

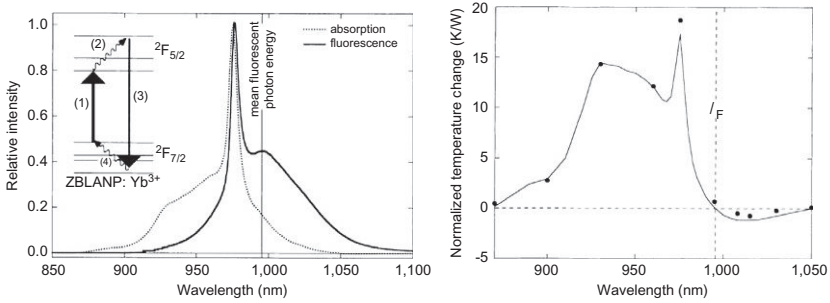


FIGURE 3 Left: Absorption (dotted line) and fluorescence (solid line) spectrum of the $2F_{7/2} \leftrightarrow 2F_{5/2}$ transition (inset) of Yb^{3+} in the fluoride glass ZBLANP at room temperature. The vertical line indicates the mean fluorescence wavelength ($\tilde{\lambda}_F$) at ~ 995 nm. Right: Temperature change (normalized to laser power) of ZBLANP: Yb^{3+} at different pump laser wavelengths. Net bulk cooling of up to 0.3 K/W was observed when the pump wavelength exceeded $\tilde{\lambda}_F$. Reprinted with permission from Macmillan Publishers Ltd: *Epstein et al. (1995)*. Copyright 1995.

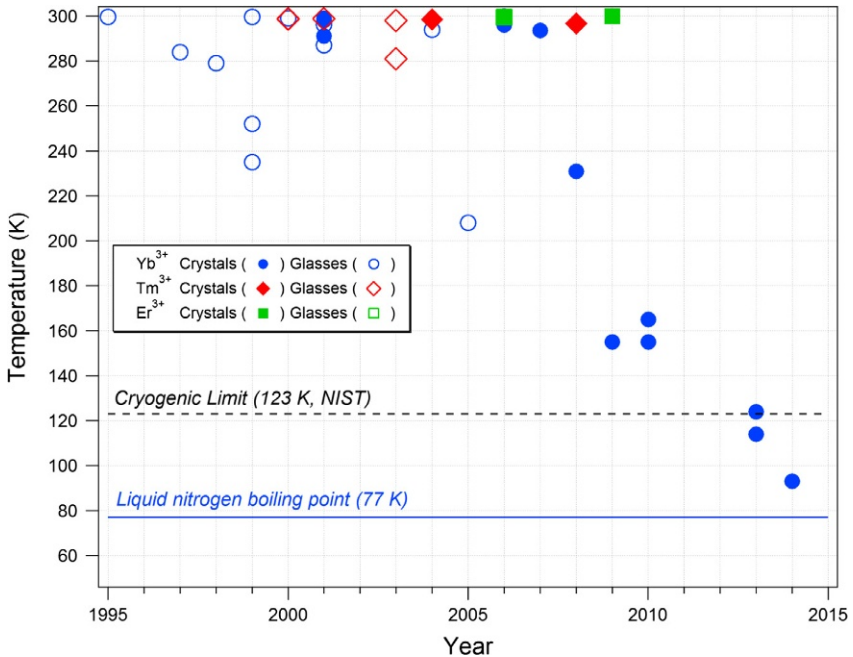


FIGURE 4 History of solid-state optical refrigeration. The experimental results shown here are taken from studies that observed net laser-induced bulk cooling in glasses (open symbols) or crystals (solid symbols) doped with lanthanide ions. To date, net laser cooling has been achieved in solids doped with Yb^{3+} (circles), Tm^{3+} (diamonds), and Er^{3+} (squares). Also indicated is the cryogenic limit of 123 K as defined by the National Institute of Standards and Technology (NIST; dashed line) and the boiling point of liquid nitrogen at 77 K (solid line).

were studied. By 2003, ZBLANP:Tm³⁺ had been cooled by 19 K to a final temperature of 281 K (Hoyt et al., 2003). While a higher intrinsic cooling efficiency in Tm³⁺ was experimentally confirmed, the net cooling did not surpass earlier results achieved with Yb³⁺ primarily because the experimenters did not have high-power laser sources near the 2 μm pump wavelength. Research on Yb³⁺-doped glasses continued in parallel and culminated in cooling of a ZBLANP:Yb³⁺ glass to 208 K in 2005 (Thiede et al., 2005). This result remains the lowest temperature achieved to date using a glass host. By this time, the preparation of sample surfaces and the design of the cooling chamber had been greatly improved, and high-power lasers (up to 11 W) at the optimum pump wavelength of 1026 nm for ZBLANP:Yb³⁺ had been developed. It was believed that the cooling performance was primarily limited by impurities in the ZBLANP glass. Impurities such as transition-metal ions can absorb laser light, and rather than emitting anti-Stokes fluorescence and contributing to cooling, they decay nonradiatively and cause parasitic heating within the sample. Various efforts were undertaken to reduce transition-metal impurities in fluoride glasses, including electrochemical purification of the ZBLANP melt (Bao et al., 1995; Fajardo et al., 1997) and chelate-assisted solvent-extraction purification of precursor materials (Patterson et al., 2011). However, they did not provide a significant improvement of the net cooling performance, and the cryogenic regime remained elusive.

These early results also sparked an interest in using optical refrigeration to counteract heat generation in lasers. Bowman et al. proposed that net heat generation could be eliminated in a solid-state laser by balancing the radiated power from stimulated and spontaneous emission and the absorbed power (Bowman and Mungan, 2000; Bowman et al., 2002, 2010). Such radiation-balanced lasers would reduce thermal gradients that cause strains in the laser material and distortion of optical waves and thus enable higher average output powers than currently possible.

A profound change in focus began in 2005 when Bigotta et al. observed laser cooling in a BaY₂F₈ fluoride crystal doped with 2.5% Yb³⁺ and measured a 4 K temperature drop upon exciting the crystal with 3 W at 1025 nm in a single-pass configuration (Bigotta et al., 2006a). While Yb³⁺-doped YAG and Y₂SiO₅ crystals (Epstein et al., 2001) and a Tm³⁺-doped BaY₂F₈ crystal (Patterson et al., 2004) had been studied before with similar results, Yb³⁺-doped fluoride crystals would prove to open the way for laser cooling to the cryogenic regime. Bigotta et al. presented a subsequent study of Yb³⁺-doped BaY₂F₈ and YLiF₄ (YLF) crystals that slightly improved on their earlier cooling results and provided detailed spectroscopic information (Bigotta et al., 2007). Their results were soon followed by a series of record-breaking laser-cooling results obtained by Sheik-Bahae's group at the University of New Mexico using Yb³⁺-doped YLF crystals (Melgaard et al., 2013a,b; Seletskiy et al., 2008, 2009, 2010b,c). In 2013, Melgaard et al. placed a 10 mol% Yb³⁺-doped YLF crystal in a multipass cavity (see Section 6.1 for details)

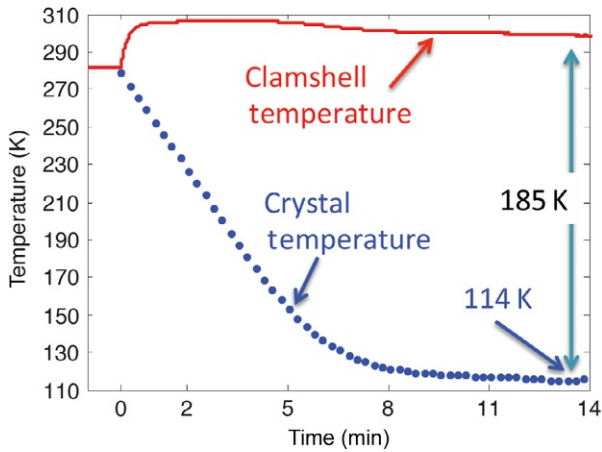


FIGURE 5 Cooling of a 10 mol% Yb^{3+} -doped YLF crystal. The 45 W pump laser operating at 1020 nm was turned on at $t=0$. Reprinted from *Melgaard et al. (2013a)* with permission from SPIE.

contained in a tightly fitting low-thermal-emissivity cavity and pumped the crystal with 45 W at 1020 nm. They achieved laser cooling to 114 K (see Fig. 5) (Melgaard et al., 2013a), surpassing the performance of all earlier studies with glassy samples and advancing the field into the cryogenic regime (<123 K). The latest report by this group has shown cooling of YLF:10% Yb^{3+} to 93 K starting from 271 K, advancing the field into the sub-100 K range for the first time (Melgaard et al., 2014).

Interestingly, the purity of these record-breaking YLF: Yb^{3+} samples did not significantly improve over that of earlier ZBLAN-based fluoride glasses. Rather, the primary advance was enabled by the much lower magnitude of inhomogeneous broadening of crystal-field transitions in the crystal hosts. In a glass, the absence of long-range structural order leads to a distribution of coordination geometries and thus crystal-field strengths around the Yb^{3+} ions. This causes an associated spread in the spectral width of the electronic transitions. In contrast, the highly ordered structure of crystals minimizes this broadening and concentrates the absorption cross section of the ensemble of Yb^{3+} ions into a much narrower spectral range. This is illustrated in Fig. 6, where the long-wavelength side of the ${}^2\text{F}_{7/2} \rightarrow {}^2\text{F}_{5/2}$ absorption is shown for Yb^{3+} in ZBLAN glass (red bottom traces) and YLF crystal (blue top traces) at three different temperatures. The lower inhomogeneous broadening of the crystal-field transitions in the crystal results in a significantly greater peak absorption cross section at 1020 nm, particularly at low temperatures. The higher peak absorption cross section in crystals allows for correspondingly more efficient absorption of the pump light by Yb^{3+} ions and thus cooling to lower temperatures compared to glasses. The following sections provide a detailed review of the principles of solid-state laser cooling, the basic material choices and trade-offs, the experimental techniques,

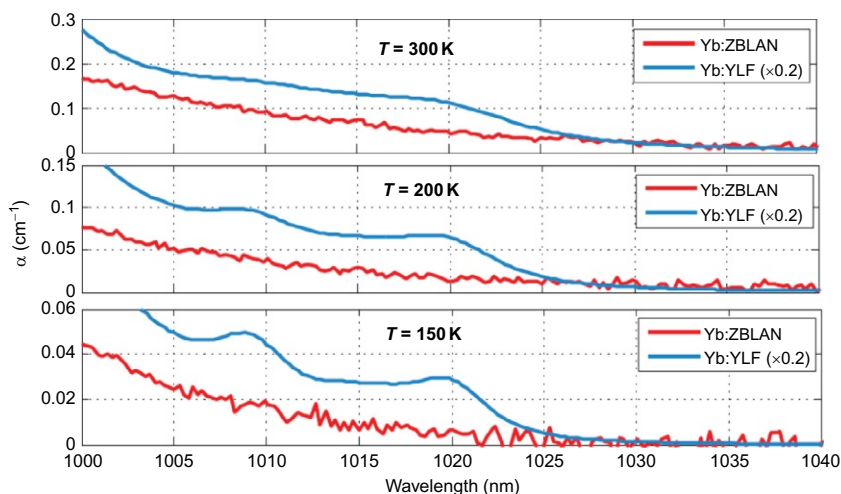


FIGURE 6 Comparison of the long-wavelength side of the ${}^2F_{7/2} \rightarrow {}^2F_{5/2}$ absorption in Yb^{3+} doped into ZBLAN glass (red bottom traces) and YLiF_4 crystal (YLF, blue top traces) at different temperatures normalized to 1 mol% Yb^{3+} doping (Melgaard, 2013). The peak absorption coefficient at the 1020 nm pump wavelength is significantly greater in the crystal compared to the glass, most importantly at low temperatures. Reprinted with permission from the University of New Mexico.

the achievements with various laser-cooling materials, and the device design considerations.

Semiconductors are another class of materials with potential for optical refrigeration. Over the past 18 years, numerous theoretical and experimental studies have been published. Materials such as III–V GaAs heterostructures and AlGaAs quantum wells grown by metal-organic chemical vapor deposition and molecular beam epitaxy have been studied extensively. Laser cooling of semiconductors however has proven to be quite elusive. Challenges include the stringent purity requirements for achieving low background absorption, surface recombination effects, a quantum efficiency that depends on carrier density, and inefficient extraction of the luminescence from the high refractive index semiconductor substrates. In 2013, Zhang et al. reported the first net cooling of a semiconductor (Li et al., 2013; Zhang et al., 2013). They used chemical vapor deposition to fabricate CdS nanobelts with thicknesses ranging from 40 to 240 nm and lengths of tens of μm . The CdS nanobelts were then suspended across inverted square pyramid-shaped holes etched into a SiO_2/Si substrate and excited with different lines of an argon ion laser. They achieved 40 K of net cooling of a 110 nm thick CdS nanobelt starting from 290 K when pumping at 514 nm. Semiconductor laser cooling shall be excluded from this chapter, and the reader is referred to recent reviews on this topic (Epstein and Sheik-Bahae, 2009; Sheik-Bahae and Epstein, 2007).

2 PRINCIPLES OF SOLID-STATE OPTICAL REFRIGERATION

2.1 Electronic States of Lanthanide Ions

The most successful solid-state optical refrigeration results to date have been achieved using solids doped with tripositive lanthanide (Ln^{3+}) ions. The 4f shell is only partially filled along the series from Ce^{3+} to Yb^{3+} , giving rise to electron configurations ranging from $[\text{Xe}]4f^1$ to $[\text{Xe}]4f^{13}$, respectively. Electrostatic (Coulomb) interactions between the 4f electrons and spin-orbit interactions are of comparable magnitude (10^3 – 10^4 cm^{-1}) and are dominant in the lanthanides. They produce a set of electronic states (multiplets) that are characteristic for each $[\text{Xe}]4f^n$ electron configuration (Dieke and Crosswhite, 1963; Hehlen et al., 2013). The multiplets are designated with $^{2S+1}L_J$ term symbols, where S , L , and J are the total spin angular momentum, total orbital angular momentum, and total angular momentum, respectively. In a Ln^{3+} -doped insulator, the coordination of anions around the Ln^{3+} cation produces an electrostatic field having a symmetry lower than spherical. As a result, the $(2J+1)$ -fold degeneracy of the $^{2S+1}L_J$ multiplets in the “free ion” case is partially or completely lifted, causing the multiplets to split into crystal-field levels. The magnitude of this crystal-field interaction is much smaller (10^1 – 10^2 cm^{-1}) than Coulomb and spin-orbit interactions because the 4f electrons are shielded quite effectively from the surroundings by the outer 5s and 5p orbitals. As a result, Ln^{3+} ions maintain much of their “free ion” character even when they are placed into a solid. A now famous energy-level diagram of $^{2S+1}L_J$ multiplets up to $40,000 \text{ cm}^{-1}$ was first presented by Dieke and Crosswhite in 1963 (Dieke and Crosswhite, 1963), and a full calculation of all $^{2S+1}L_J$ energy levels was recently reported by Peijzel et al. (2005). Figure 7 shows the $^{2S+1}L_J$ multiplets up to $20,000 \text{ cm}^{-1}$ for select Ln^{3+} ions that are relevant for solid-state laser cooling.

Consider a metal cation (M) coordinated by anions (X) in a solid. Viewed in isolation, this $[\text{MX}_n]^{m+}$ coordination in the solid has $3(n+1) - 6$ fundamental vibrations (normal modes), each with its characteristic vibrational energy and phonon occupation number at the given temperature. Exciting the metal ion by a parity-allowed electronic transition typically causes a change in the equilibrium M–X bond length between the ground state (d_g) and the excited state (d_e) (Fig. 8, left). As a consequence of the high ratio of nuclear to electron masses, this change in bond length (nuclear motion) occurs *after* the electronic excitation has taken place, resulting in the conversion of some of the electronic excitation energy to vibrational energy (wiggly arrows). In most cases, the M–X bond is weakened by the electronic excitation so that $d_e > d_g$. This leads to the “Stokes shift” of the luminescence relative to its corresponding absorption (i.e., $E_L < E_A$) and causes the well-known heating of materials upon excitation. The situation is different for the Ln^{3+} ions. Electronic excitations within the 4f electron configuration, that is, transitions between the $^{2S+1}L_J$ multiplets shown in Fig. 7, are parity-forbidden.

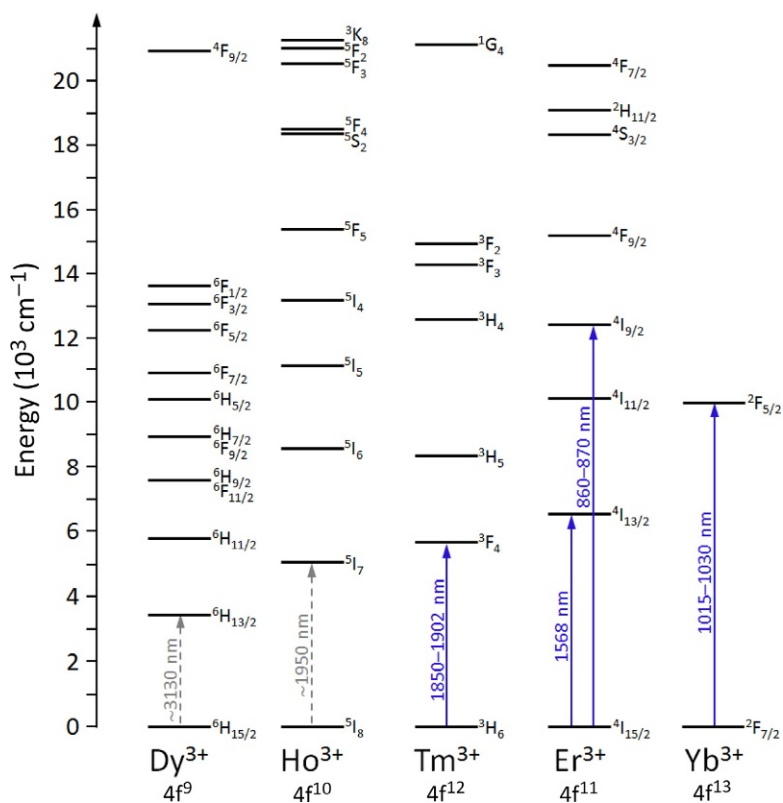


FIGURE 7 Partial energy-level diagram for the $2S+1L_J$ multiplets of select Ln^{3+} ions relevant for solid-state laser cooling. The ions are ordered with increasing energy of the first excited state. The solid blue arrows for Tm^{3+} , Er^{3+} , and Yb^{3+} indicate the pump wavelengths of transitions that have been used successfully for net laser cooling. The dashed gray arrows for Dy^{3+} and Ho^{3+} give approximate pump wavelengths for future experiments.

In addition, the 4f electrons are shielded by the outer 5s and 5p orbitals, and the M–X chemical bond is only minimally affected by a 4f electronic excitation. Consequently, equilibrium bond lengths in the ground and excited states are similar as illustrated in Fig. 8 (right). Excitation and relaxation of Ln^{3+} ions can therefore be dominated by electronic transitions with only minimal involvement of vibrational modes ($E_L \approx E_A$, no Stokes shift), thereby eliminating much of the internal heating that is inherent to Stokes-shifted parity-allowed transitions. This key feature makes Ln^{3+} ions particularly attractive for solid-state laser cooling because it allows anti-Stokes fluorescence to dominate in some special cases.

While the crystal-field interactions are relatively weak in lanthanides, they are an essential ingredient for solid-state optical refrigeration. Each $2S+1L_J$ multiplet has a $(2J+1)$ -fold degeneracy in the total angular momentum that

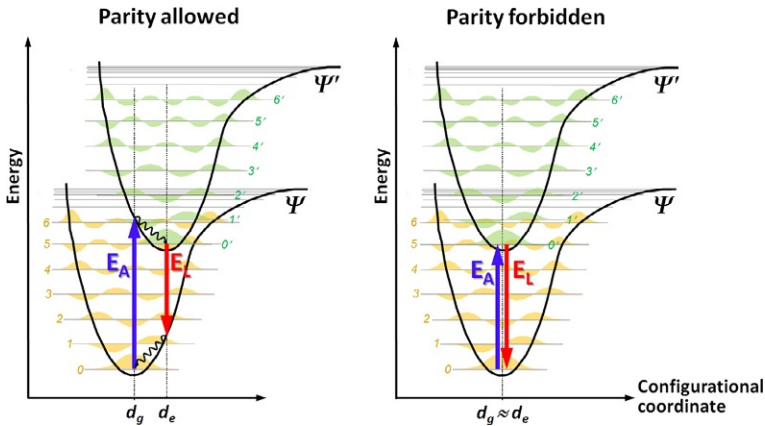


FIGURE 8 Illustration of excitation (at energy E_A) and relaxation (at energy E_L) for a parity-allowed (left) and a parity-forbidden (right) electronic transition between a ground (Ψ) state and an excited (Ψ') state. Nonradiative relaxation processes are indicated as wiggly arrows. The potential energy of the electronic states (solid black lines) is shown as a function of a configurational coordinate (i.e., one of the normal modes). The vibrational wavefunctions are illustrated along with the respective vibrational quantum numbers. d_g and d_e denote the equilibrium bond distance in the ground and excited states, respectively.

is lifted into M_J components under the influence of the nonspherical electrostatic field created by the neighboring ions in a solid. The number of resulting $2S+1L_J(M_J)$ crystal-field levels depends on the point symmetry of the crystal field at the location of the lanthanide ion. A complete lifting of the $(2J+1)$ -fold degeneracy is achieved in sufficiently low symmetry (note however that the crystal-field levels of Ln^{3+} ions with an odd number of 4f electrons always maintain at least a twofold Kramers degeneracy that can only be lifted in a magnetic field). The magnitude of the overall crystal-field splitting of a $2S+1L_J$ multiplet is typically a few hundred wavenumbers, that is, it is comparable to kT at room temperature ($kT = 209 \text{ cm}^{-1}$ at 300 K).

Figure 9 (left) illustrates the energy-level diagram of Yb^{3+} . The $[\text{Xe}]4f^{13}$ electron configuration produces only one 2F manifold that splits into a $^2F_{7/2}$ ground-state and $^2F_{5/2}$ excited-state multiplet under the influence of the spin-orbit interaction. The two multiplets further split into 4 and 3 twofold (Kramers) degenerate crystal-field levels, respectively, if the point symmetry of Yb^{3+} is sufficiently low (less than cubic). Note that Fig. 9 is not to scale: The $^2F_{5/2}$ - $^2F_{7/2}$ splitting is $\sim 10,000 \text{ cm}^{-1}$, while the $^2F_{7/2}$ crystal-field splitting is about 300–600 cm^{-1} , depending on the material (Hehlen, 2010). Further note that the energy-level diagram in Fig. 9 implies zero Stokes shift, for example, the $E_4 \rightarrow E_5$ absorption occurs at essentially the same energy as the corresponding $E_5 \rightarrow E_4$ luminescence. With the assumption of no Stokes shift, the electronic energy levels can be represented by horizontal lines rather than the full potential curves as shown in Fig. 8 (right).

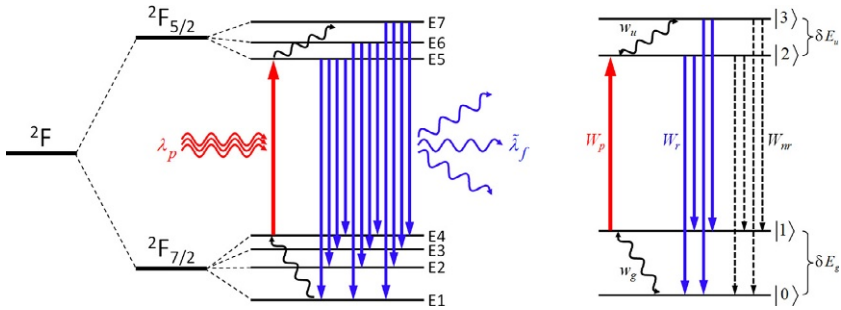


FIGURE 9 Left: Energy-level diagram of Yb^{3+} (not to scale) illustrating the removal of thermal energy from and thus cooling of a solid by anti-Stokes fluorescence (average emission wavelength $\bar{\lambda}_f$ shorter than the pump laser wavelength λ_p). Right: Simplified four-level model of Yb^{3+} used for the derivation of the laser-cooling efficiency (see Section 2.3).

2.2 Anti-Stokes Fluorescence and Thermal Equilibrium

The lattice strains associated with vibrations in the solid modulate the crystal field. This influences the 4f spins via the spin–orbit interaction and thereby induces electron–phonon transitions between the Ln^{3+} crystal-field levels. Such transitions represent an exchange of energy between the vibrational and electronic systems of the solid. A coupling of the lattice vibrations to the spins of a Ln^{3+} ion of this type is referred to as van Vleck mechanism (Poole, 2004). The probability P_{pq} for a lattice-induced transition between two crystal-field levels $p \rightarrow q$ is related to that for the reverse transition by $P_{pq} = P_{qp} \exp[(E_p - E_q)/kT]$, where E_i is the energy of the crystal-field level i (Gill, 1975). Here, it is assumed that there is no “phonon bottleneck” (Auzel and Pellé, 1997), that is, that phonons with energy $E_p - E_q$ can be created or annihilated as needed. In thermal equilibrium, the respective transition rates are equal over the ensemble of Ln^{3+} ions, and the relative population of crystal-field level i at temperature T is given by

$$n_i(T) = g_i \exp[-(E_i - E_0)/kT] / Z(T), \quad (1)$$

where $Z(T)$ is the partition function $Z(T) = \sum_{k=0}^{N-1} g_k \exp(-E_k/kT)$ taken over the

N crystal-field levels of the system and g_i is the degeneracy factor of crystal-field level i . For Yb^{3+} in the ground state, for example, $Z(T)$ has to be taken over all $N=7$ crystal-field levels. Since the ${}^2\text{F}_{5/2}$ crystal-field levels are at much greater energy than those of the ${}^2\text{F}_{7/2}$ ground state, their respective terms in $Z(T)$ are essentially zero for common temperatures, and taking $Z(T)$ over the four crystal-field levels of the ${}^2\text{F}_{7/2}$ ground state provides an adequate description.

The phonon absorption and emission processes that establish the thermal equilibrium in Eq. (1) take place on ns to ps timescales for temperatures

>50 K (Kohmoto et al., 2000), that is, much faster than the μs to ms lifetimes typical of many Ln^{3+} excited states. For Yb^{3+} , for example, these disparate timescales are the reason why a ${}^2\text{F}_{7/2} \rightarrow {}^2\text{F}_{5/2}$ excitation is first followed by the thermalization of the population among the ${}^2\text{F}_{5/2}$ crystal-field levels, and the subsequent ${}^2\text{F}_{5/2} \rightarrow {}^2\text{F}_{7/2}$ radiative decay takes place from this quasi-equilibrium population. This is the fundamental origin of anti-Stokes fluorescence and is illustrated in Fig. 9 (left). Tuning a laser to the $\text{E4} \rightarrow \text{E5}$ crystal-field transition at energy $h\nu_p$ (red up arrow) excites Yb^{3+} ions exclusively to the ${}^2\text{F}_{5/2}(\text{E5})$ level. For temperatures greater than absolute zero, however, exclusive population of E5 in the ${}^2\text{F}_{5/2}$ excited state does not correspond to thermal equilibrium, which therefore is rapidly established by the net absorption of vibrational energy (wiggly arrow). Subsequently, the ensemble of excited thermalized Yb^{3+} ions can decay radiatively to the ${}^2\text{F}_{7/2}$ ground state via any one of the 12 possible crystal-field transitions (blue down arrows). The mean energy of these fluorescence transitions, $h\tilde{\nu}_f$, is given by

$$h\tilde{\nu}_f = \frac{\int \Phi(\nu) h\nu d\nu}{\int \Phi(\nu) d\nu} \quad (2)$$

which corresponds to a mean fluorescence wavelength of

$$\tilde{\lambda}_f = \frac{\int S(\lambda) \lambda d\lambda}{\int S(\lambda) d\lambda}, \quad (3)$$

where $\Phi(\nu)$ is the mean photon flux density and $S(\lambda)$ is the power spectral density. Energy conservation requires $\Phi(\nu)h\nu d\nu = S(\lambda)d\lambda$ and thus

$$\tilde{\lambda}_f = \frac{\int S(\lambda) \lambda d\lambda}{\int S(\lambda) d\lambda} = \frac{hc \int \Phi(\nu) d\nu}{h \int \Phi(\nu) \nu d\nu} = \frac{c}{\tilde{\nu}_f}. \quad (4)$$

Since $h\tilde{\nu}_f$ is greater than $h\nu_p$, the thermalization processes lead to anti-Stokes fluorescence that carries vibrational energy (heat) away from the solid in the form of light, cooling the solid in the process. In a final step, thermal equilibrium is reestablished in the ground-state multiplet, thereby repopulating the E4 initial state and completing the “laser-cooling cycle.” Laser-induced cooling can, therefore, occur if $h\tilde{\nu}_f > h\nu_p$, that is, as long as anti-Stokes fluorescence on average predominates over resonant and Stokes fluorescence (Mungan, 2005). This is illustrated in Fig. 10 for a 5% Yb^{3+} -doped YLiF_4 (YLF) crystal. A mean fluorescence wavelength of $\tilde{\lambda}_f \approx 999\text{nm}$ is obtained from the luminescence spectrum at 300 K and Eq. (2). Laser excitation into

the “cooling tail” of the absorption spectrum at $\lambda_p > \tilde{\lambda}_f$ (red shaded area) produces a net anti-Stokes luminescence by the ensemble of Yb^{3+} ions and should, in the ideal case, lead to cooling. Figure 10B shows that the measured cooling efficiency (see Section 2.3) indeed crosses from $\eta_c < 0$ (laser-induced heating) to $\eta_c > 0$ (laser-induced cooling) as the pump laser wavelength is tuned from $\lambda_p < \tilde{\lambda}_f$ to $\lambda_p > \tilde{\lambda}_f$ into the “cooling tail.” The ratio of the amount of heat extracted per cycle, $Q = h\tilde{\nu}_f - hv_p$, to the excitation energy can be viewed as an idealized cooling efficiency, that is, as (Sheik-Bahae and Epstein, 2009)

$$\eta_c = \frac{h\tilde{\nu}_f - hv_p}{hv_p}, \quad (5)$$

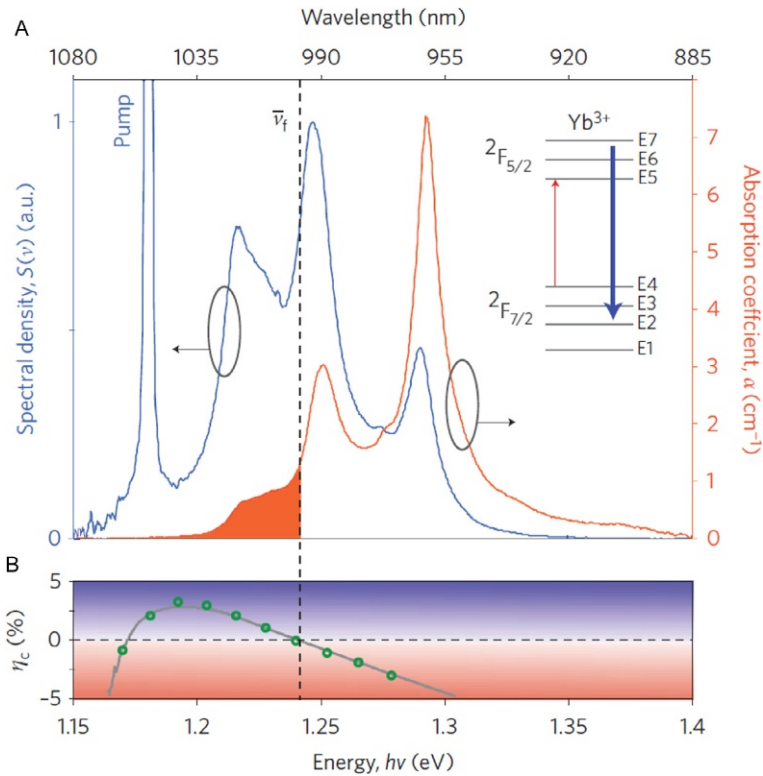


FIGURE 10 Optical absorption, emission, and cooling efficiency spectra of a 5% Yb^{3+} -doped YLiF_4 (YLF) crystal (Seletskiy et al., 2010b). (A) Absorption (right axis) and luminescence (left axis) spectra, for a laser excitation at 1055 nm polarized along the crystal c -axis. The cooling tail corresponding to the absorption spectrum for photon energies below the mean fluorescence energy ($h\tilde{\nu}_f$) is shaded in red. (B) Experimental (open circles) cooling efficiency at 300 K.

where positive and negative values of η_c indicate laser-induced cooling and heating, respectively. The next section will show a more detailed description, and it will show that this idealized cooling efficiency has to be modified by both the external quantum efficiency and the competition with absorption by impurities.

2.3 The Four-Level Model and the Laser-Cooling Efficiency

The simplified four-level scheme shown in Fig. 9 (right) reveals the essential features of solid-state laser cooling with lanthanide ions (Petrushkin and Samartsev, 2009). Following the derivation given in Sheik-Bahae and Epstein (2009), we define a system consisting of a ground state with two levels $|0\rangle$ and $|1\rangle$ separated by δE_g and an excited state with two levels $|2\rangle$ and $|3\rangle$ separated by δE_u . The ensemble of ions is excited by a laser tuned to the $|1\rangle \rightarrow |2\rangle$ transition (red up arrow), and the associated pumping rate is given by $W_p = (I\sigma_{12}/h\nu_{12})N_1$, where N_1 is the population of level $|1\rangle$, I is the incident laser irradiance, and σ_{12} and ν_{12} are the cross section and frequency of the $|1\rangle \rightarrow |2\rangle$ transition, respectively. The excited levels $|2\rangle$ and $|3\rangle$ can decay to the ground-state levels by radiative relaxation (blue down arrows) with rate constant W_r , assumed here to be identical for each of the four radiative transitions. Alternatively, the excited levels can decay by nonradiative relaxation (dashed arrows) with rate constant W_{nr} , likewise assumed identical for each of the four nonradiative transitions. Thermal equilibrium in the ground and excited states is established by spin–lattice interactions, and the respective rate constants w_g and w_u are assumed to be equal ($w = w_g = w_u$) in this model. The population of the four levels is then given by

$$\frac{dN_1}{dt} = -\frac{I\sigma_{12}}{h\nu_{12}}\left(N_1 - \frac{g_1}{g_2}N_2\right) + \frac{R}{2}(N_2 + N_3) - w_g\left(N_1 - \frac{g_1}{g_2}N_0e^{-\delta E_g/kT}\right), \quad (6)$$

$$\frac{dN_2}{dt} = \frac{I\sigma_{12}}{h\nu_{12}}\left(N_1 - \frac{g_1}{g_2}N_2\right) - RN_2 + w_u\left(N_3 - \frac{g_3}{g_2}N_2e^{-\delta E_u/kT}\right), \quad (7)$$

$$\frac{dN_3}{dt} = -RN_3 + w_u\left(N_3 - \frac{g_3}{g_2}N_2e^{-\delta E_u/kT}\right), \quad (8)$$

$$N_t = N_0 + N_1 + N_2 + N_3, \quad (9)$$

where N_t is the total number of Ln^{3+} ions in the ensemble, and $R=2$ (W_r+W_{nr}) is the total upper-state decay rate constant. The latter definition assumes that spin–lattice processes are much faster than the excited-state radiative decay and nonradiative decay, that is, $w \gg R$. The degeneracy factor of level i is denoted by g_i , which in the following we assume to be equal for all levels. The total power density deposited in the system, P_{net} , corresponds to the difference of the absorbed (P_{abs}) and emitted (P_{rad}) contributions, that is,

$$P_{net} = P_{abs} - P_{rad} = [\alpha(I) + \alpha_b]I - W_r[N_2(E_{20} + E_{21}) + N_3(E_{30} + E_{31})], \quad (10)$$

where $E_{ij} = E_i - E_j$, and the resonant absorption coefficient $\alpha(I) = \sigma_{12}(N_1 - N_2)$. Equation (10) also introduces the background absorption coefficient α_b . It allows for the possibility that some of the incident laser light is absorbed by “impurity” species other than the four-level system and that this absorbed fraction decays nonradiatively, that is, is not reemitted but rather converted to heat. The system cools if $P_{net} < 0$, that is, when the radiated power density exceeds the absorbed one. In steady state ($dN_i/dt = 0$) and assuming the system to be far from saturation ($N_0 + N_1 \gg N_2 + N_3$), the net power density is then obtained as

$$P_{net} = \alpha I \left(1 - \eta_e \frac{h\tilde{\nu}_f}{h\nu_p} \right) + \alpha_b I, \quad (11)$$

where $\eta_e = (1 + W_{nr}/\eta_{ext}W_r)^{-1}$ is the external quantum efficiency with η_{ext} being the extraction efficiency for the fluorescence. In Eq. (11),

$$\alpha = \frac{\sigma_{12}N_t}{1 + \exp(\delta E_g/kT)} \quad (12)$$

is the absorption coefficient of $|1\rangle \rightarrow |2\rangle$ (resonant absorption). The derivation also yields the mean fluorescence energy of the four-level system as (Sheik-Bahae and Epstein, 2009)

$$h\tilde{\nu}_f = h\nu_p + \frac{\delta E_g}{2} + \frac{\delta E_u}{1 + (1 + R/w_u)e^{\delta E_u/kT}}. \quad (13)$$

The cooling efficiency can now be defined as the net deposited power density relative to the total absorbed power density, that is,

$$\eta_c = -\frac{P_{net}}{P_{abs}} = \eta_e \eta_{abs} \frac{h\tilde{\nu}_f}{h\nu_p} - 1, \quad (14)$$

where the absorption efficiency

$$\eta_{abs} = \frac{\alpha}{(\alpha + \alpha_b)} \quad (15)$$

has been introduced. It represents the fraction of the *total* absorbed power that has been used to excite the four-level system rather than an impurity species. The definition in Eq. (14) is such that a positive η_c corresponds to laser-induced cooling.

This derivation highlights several key features of solid-state laser refrigeration. First, Eq. (12) shows that the pump absorption coefficient diminishes exponentially as the temperature is lowered, which is a result of the thermal depletion of the initial state $|1\rangle$. This reduces the net power density that can be extracted from the solid (Eq. 11) and ultimately sets a lower limit for the temperature that can be reached by laser cooling. Finding materials with a small ground-state crystal-field splitting (δE_g) is advantageous in this respect.

Second, the $|1\rangle \rightarrow |2\rangle$ transition competes with absorption by impurities (α_b). As evident from Eq. (15), this can be particularly detrimental if the impurity absorption does not change much with temperature while the resonant absorption α decreases exponentially as the temperature is lowered (Eq. 12). The presence of impurities becomes increasingly detrimental as the temperature decreases and an ever larger fraction of the absorbed power is used to excite impurities that cause parasitic heating. Third, Eq. (13) describes how the mean fluorescence energy decreases (redshifts) at low temperatures which, as seen in Eq. (14), reduces the cooling efficiency. Overall, as the temperature is lowered, the redshift of the mean fluorescence wavelength combined with the reduction of the resonant absorption reduces the cooling efficiency. Cooling stops at a temperature where $\eta_c = 0$. This minimum temperature can be lowered by reducing the amount of background absorption (i.e., reducing the level of impurities), increasing the quantum efficiency, and enhancing the resonant absorption (e.g., by choosing crystalline hosts and materials with a small ground-state crystal-field splitting).

2.4 Thermodynamic Considerations

The question whether anti-Stokes fluorescent refrigeration is consistent with the laws of thermodynamics was controversial early on, and it was already considered in the first publication in this field by Pringsheim (1929). Landau resolved the issue formally in 1946 (Landau, 1946). Several authors have since reviewed the thermodynamics of solid-state laser cooling (Edwards et al., 1998; Mungan, 2005; Nemova and Kashyap, 2010; Rayner et al., 2003; Ruan and Kaviany, 2006; Ruan et al., 2007). The second law of thermodynamics states that the entropy of an isolated system never decreases, and it sets a maximum for the efficiency of an optical refrigerator. A key insight is that light itself has entropy. The rate at which entropy is carried by a steady, unpolarized beam of light in vacuum across a surface A is given by (Mungan, 2005)

$$\dot{S} = \frac{2k}{c^2} \int_A \int_{\Omega} \int_{\Delta\nu} [(1+n) \ln(1+n) - n \ln n] v^2 dv \cos \theta d\Omega dA, \quad (16)$$

where k is the Boltzmann constant, c is the speed of light, and θ and ϕ are the polar and azimuthal angles, respectively, at which the light is propagating into solid angle element $d\Omega = \sin \theta d\theta d\phi$ relative to the normal to an element dA of the surface. Furthermore, the radiation is distributed among a set of optical modes with mean occupation number n and frequency ν . Note that Eq. (16) is valid for thermal radiation, laser radiation, and the nonequilibrium photon distribution of fluorescence from an excited state (such as shown in Fig. 9). From Eq. (16), it is evident that a monochromatic ($\Delta\nu \rightarrow 0$) light source with low divergence ($d\Omega \rightarrow 0$) such as a laser carries with it a lower entropy than a broadband ($\Delta\nu \gg 0$) isotropic ($\int \cos \theta d\Omega = 4\pi$) light source

such as a fluorescent ion. The flux temperature of a light source can then be defined as $T = \dot{E}/\dot{S}$, where \dot{E} and \dot{S} are the energy and entropy flux rates, respectively.

A complete description of an optical refrigerator has to include the energy and entropy fluxes of the heat load and those of the pump and fluorescent radiation. As illustrated in Fig. 11 (Edwards et al., 1998), energy and entropy are removed from the pump laser radiation at rates \dot{E}_p and \dot{S}_p , respectively. They are added to the fluorescent radiation field at rates \dot{E}_f and \dot{S}_f , respectively. The cooled reservoir loses thermal energy at a rate of \dot{Q}_c and thus loses entropy at a rate of $\dot{S}_c = \dot{Q}_c/T_c$. In steady state, the conservation of energy requires that $\dot{E}_p + \dot{Q}_c = \dot{E}_f$, and the second law of thermodynamics requires that the total entropy does not decrease, that is, $\dot{S}_f - \dot{S}_p - (\dot{Q}_c/T_c) \geq 0$. Using the flux temperatures T_p and T_f for the pump and fluorescent lights, respectively, one thus finds that the cooling efficiency for converting light to heat lift is

$$\eta_c = \frac{\dot{Q}_c}{\dot{E}_p} \leq \frac{1 - (T_f/T_p)}{(T_f/T_c) - 1}. \quad (17)$$

For the conditions of an optical refrigerator, one has $T_p \gg T_f > T_c$, which simplifies Eq. (17) to

$$\eta \leq \frac{T_c}{T_f - T_c}, \quad (18)$$

an expression that is similar to the Carnot efficiency, except that the temperature of the hot thermal reservoir has been replaced by the fluorescence flux temperature T_f .

For an optical refrigerator, the photon occupation number n in the entropy flux rate (Eq. 16) has contributions from both the fluorescent photons of the refrigerator, $n_f(\nu)$, and the ambient thermal photons, $n_a(\nu)$. The latter is given

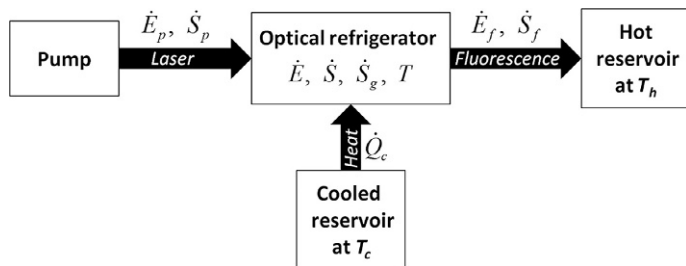


FIGURE 11 Energy and entropy fluxes for an optical refrigerator.

by $n_a(v) = 1/[\exp(hv/kT_a) - 1]$, with T_a being the ambient temperature. Therefore, the entropy flux rate due to fluorescence is given by

$$\dot{S}_f = \frac{2k}{c^2} \int_A \int_{\Omega} \int_{\Delta v} \{[(1+n) \ln(1+n) - n \ln n] - [(1+n_a) \ln(1+n_a) - n_a \ln n_a]\} v^2 dv \cos \theta d\Omega dA \quad (19)$$

and the energy flux rate due to fluorescence is given by

$$\dot{E}_f = \frac{2k}{c^2} \int_A \int_{\Omega} \int_{\Delta v} hv_f n_f v^2 dv \cos \theta d\Omega dA, \quad (20)$$

yielding a fluorescent temperature of $T_f = \dot{E}_f / \dot{S}_f$. In Eqs. (19) and (20), fluorescent contributions typically dominate over ambient contributions. Edwards et al. estimated the thermodynamic properties of an optical refrigerator based on Yb^{3+} -doped ZBLANP fluoride glass that is pumped by a 40 W laser and produces a heat lift of 500 mW (Edwards et al., 1998). After correcting a numerical error, their analysis finds that $T_f \sim 1700$ K, which implies that the refrigerator efficiency is limited by thermodynamics to $\sim 5\%$ at 77 K.

3 MATERIAL CONSIDERATIONS

3.1 Energy Levels and Nonradiative Decay

The detailed analysis of the four-level system in Section 2.3 has shown that the laser-cooling efficiency is inversely proportional to the pump laser energy $h\nu_p$ (Eq. 14). This favors the use of lanthanide ions with a low energy of the first excited state. Most of the work to date has been performed on Yb^{3+} -doped materials. Here, the ${}^2F_{5/2} - {}^2F_{7/2}$ energy separation of $\sim 9800 \text{ cm}^{-1}$ is large compared to kT , limiting the cooling efficiency to $\sim 2.2\%$ at 300 K (Eq. 5). The possibility of three times greater cooling efficiencies by going to a cooling ion such as Dy^{3+} (see Fig. 7) is tantalizing, but it is met with formidable challenges. This is because a Ln^{3+} excited state can, besides radiative decay, also relax to a lower-energy state via the emission of vibrational energy into the solid. Such a nonradiative (multiphonon) process is obviously detrimental to laser cooling as it converts electronic excitation energy to heat. It is therefore necessary to find materials in which the competition between the radiative (W_r) and the nonradiative (W_{nr}) decay rates is strongly in favor of radiative decay, that is, $W_r \gg W_{nr}$, such that the internal quantum efficiency $\eta_q = (1 + W_{nr}/W_r)^{-1}$ approaches unity. Electronic transitions between 4f energy levels have oscillator strengths on the order of $10^{-5} - 10^{-6}$, and the radiative relaxation rate of the first excited state is on the order of $W_r = 10^2 - 10^3 \text{ s}^{-1}$ for a wide variety of materials. In contrast, the type and magnitude of the nonradiative relaxation depend on the material. Nonradiative processes primarily include the multiphonon relaxation of the excited state, but they can also encompass two-ion processes such as cross relaxation and energy-transfer

upconversion that can be active in Ln^{3+} ions with many excited states (e.g., Tm^{3+} and Er^{3+} ; see Fig. 7). We shall focus on multiphonon relaxation in the following.

A nonradiative relaxation between an excited electronic state Ψ' and a lower-energy electronic state Ψ separated by ΔE involves both an electronic $\Psi' \rightarrow \Psi$ transition and a vibrational transition that causes the emission of one or multiple vibrational quanta with a combined energy equaling ΔE . The rate of this nonradiative relaxation is proportional to the product of the probabilities of the electronic and vibrational processes, $W_{nr} \propto p_{el} p_{vib}$. At zero Kelvin, p_{vib} is proportional to the overlap integral of the lowest-energy ($n=0$) vibrational wavefunction of the excited state, $\Psi'(0)$, and the resonant vibrational wavefunction of the ground state, $\Psi(m)$. Here, $m = \Delta E/\hbar\omega$, where $\hbar\omega$ is the energy of the accepting vibrational mode, and we have assumed for simplicity that there is only one accepting mode, m is integer, and the Stokes shift is nominally zero. For the hypothetical example shown in Fig. 8 (right), the overlap of the vibrational wavefunctions $\Psi'(0)$ and $\Psi(5)$ would be dominant. In the approximation of a diatomic quantum harmonic oscillator with the atomic mass M , the vibrational wavefunctions are given by $\Psi_m(y) = (\alpha/\pi)^{1/4} (2^m m!)^{-1/2} H_m(y) \exp(-y^2/2)$ with $y = \sqrt{\alpha}x$ and $\alpha = M\omega/\hbar$, where $H_m(y)$ are the Hermite polynomials and x is the internuclear separation. It can be shown that the vibrational overlap integrals $|\langle \Psi'_0 | \Psi_m \rangle|^2$, also known as the Franck–Condon factors, decrease biexponentially with increasing n (and approximately exponentially for $n > 4$). This is the fundamental origin of the energy-gap law (Riseberg and Moos, 1968)

$$W_{mp} = \beta e^{-\alpha m}, \quad (21)$$

which describes the multiphonon relaxation rate W_{mp} as a function of the number of emitted vibrational quanta, m , and vibrational (α) and electronic (β) parameters that are material-specific. Modified versions of the energy-gap law have been introduced as well, and they take into account both promoting and accepting modes (see Auzel and Pellé, 1997 for a detailed discussion). One common modified energy-gap law yields $W_{mp} = W_0 \exp[-\alpha'(\Delta E - 2.6\hbar\omega_{\max})]$, where the energy gap has been reduced by $2.6\hbar\omega_{\max}$ to take into account the promoting mode, and W_0 and α' are material-specific parameters describing the electronic and vibrational processes, respectively (Auzel and Pellé, 1997). The energy-gap law has two important implications. First, W_{mp} decreases exponentially with an increasing number of phonons created in the process. Second, in a real system with a large number of vibrational modes, the vibration with the highest energy ($\hbar\omega_{\max}$) will have the lowest m and thus be the most likely accepting mode creating the highest multiphonon relaxation rate. The vibration with $\hbar\omega_{\max}$ is typically an optical phonon that corresponds to a local vibration of the anions that coordinate the Ln^{3+} ion, such as the totally symmetrical stretching vibration of the $[\text{YbF}_8]$ unit in an Yb^{3+} -doped YLiF_4 crystal with an energy of $\sim 450 \text{ cm}^{-1}$ (Orlovskii et al., 2002).

The energy-gap law provides quantitative guidance on the maximum phonon energy a material can have to still enable laser cooling of a transition with energy ΔE (Nemova and Kashyap, 2010). Assuming $W_r = 10^3 \text{ s}^{-1}$, requiring $\eta_q > 0.99$, and using typical values for α and β yield the criterion of $\hbar\omega_{\max} < \Delta E/8$, which is illustrated in Fig. 12 (Hehlen, 2009). It shows the $\hbar\omega_{\max} < \Delta E/8$ criterion in relation to the energy of the first excited state of select Ln^{3+} ions (Fig. 7), ΔE , and the highest optical phonon energy, $\hbar\omega_{\max}$. W_{nr} should be sufficiently suppressed (relative to W_r) for materials that fall below the $\Delta E/8$ criterion indicated by the solid black line. This is indeed found in practice, as illustrated by the open circles in Fig. 12, which indicates Ln^{3+} -doped solids for which laser cooling has been observed. Yb^{3+} is advantageous for solid-state optical refrigeration because its large ${}^2\text{F}_{5/2} - {}^2\text{F}_{7/2}$ energy gap of $\sim 9800 \text{ cm}^{-1}$ (Fig. 7) ensures inefficient ${}^2\text{F}_{5/2}$ multiphonon relaxation and thus a high quantum efficiency for materials with phonon energies up to $\sim 1200 \text{ cm}^{-1}$. This large energy gap makes Yb^{3+} a viable laser-cooling ion in all halide (fluorides, chlorides, bromides, and iodides) crystals and glasses; some oxide crystals such as Y_2SiO_5 , $\text{KGd}(\text{WO}_4)_2$, and YAG; and possibly even a few non-silica oxide glasses (Hehlen, 2009). In contrast, Er^{3+} , Tm^{3+} , Ho^{3+} , and Dy^{3+} have first excited states with much lower energies, that is, ~ 6100 , ~ 5200 , 4700 , and $\sim 3150 \text{ cm}^{-1}$, respectively. While the smaller gap and thus lower laser pump energy, in principle, allow for a higher

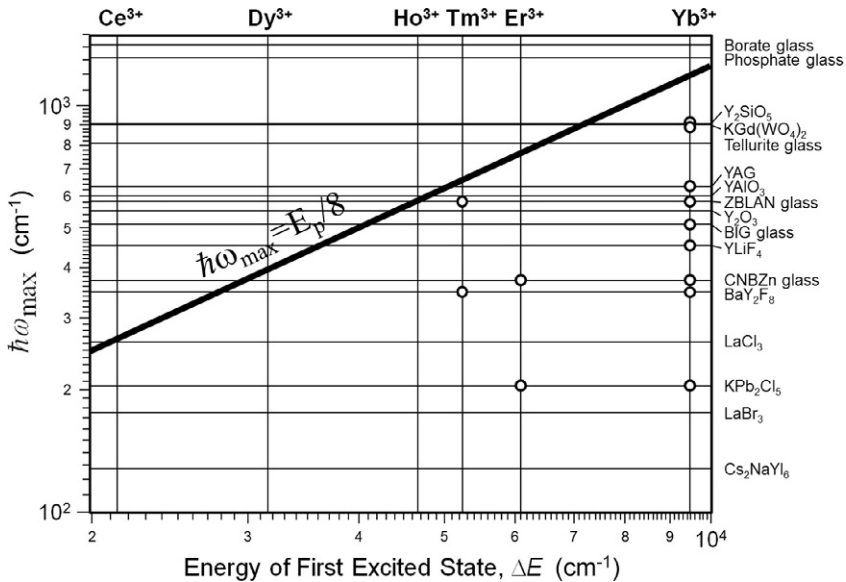


FIGURE 12 Combinations of Ln^{3+} ions and host materials. Combinations for which $\hbar\omega_{\max} < \Delta E/8$ are expected to be candidates for optical refrigeration. The open circles indicate materials for which optical refrigeration has been observed to date. Hehlen (2009).

cooling efficiency (see Eq. 14), finding viable host materials to realize this potential is more challenging. Oxides become marginal for laser cooling with Tm^{3+} for which a halide material such as a fluoride is required. No laser cooling has yet been demonstrated for a Dy^{3+} -doped material for which a host material with $\hbar\omega_{\text{max}} < 400\text{cm}^{-1}$ is needed. This is only realized in sulfides and the heavy halides (chlorides, bromides, and iodides). These materials are generally very hygroscopic and mechanically weak, posing formidable challenges during synthesis and sample preparation.

3.2 Role of Impurities

Section 3.1 considered multiphonon relaxation in which the accepting vibrations were modes of the host material itself. As illustrated in Fig. 13, however, multiphonon relaxation can also be introduced by impurities that are present in the material. One possibility is multiphonon relaxation caused by molecular species that are incorporated inadvertently in the host material. Depending on the preparation conditions, hydroxyl (OH^-), ammonium (NH_4^+), sulfate (SO_4^{2-}), phosphate (PO_4^{3-}), and carbon dioxide (CO_2) species can be present as impurities. Such molecular species are more easily incorporated into the three-dimensional amorphous network of glasses than into crystals. For example, CO_2 , CO , and O_2 gases can dissolve into or react with ZBLAN glass melts (Parker, 1989). Molecular species usually have vibrational modes with much higher energies than the optical phonon modes of the host material. They therefore become likely acceptor modes in multiphonon relaxation and reduce the quantum efficiency of the Ln^{3+} excited state, as shown in Fig. 13A.

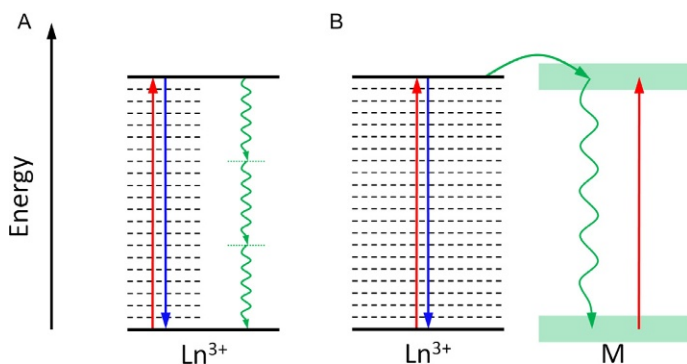


FIGURE 13 Nonradiative decay mechanisms of the excited state of a laser-cooling ion caused by impurities. Multiphonon relaxation can be induced by (A) molecular impurities with high-energy vibrational modes (wiggly arrows) and (B) energy transfer to an impurity ion having low quantum efficiency. The dashed horizontal lines indicate the low-energy optical phonon modes of the host material. The red up and blue down arrows represent the pump and fluorescence transition, respectively, of the laser-cooling cycle.

Another possibility is the presence of metal ions (M) with absorptions near the laser-cooling wavelength. As shown in Fig. 13B, energy can be transferred from the excited Ln^{3+} to a nearby M ion, which then decays via multiphonon relaxation, thereby reducing the quantum efficiency of the Ln^{3+} excited state. The $\text{Ln}^{3+} \rightarrow \text{M}$ energy transfer can occur nonradiatively due to electric-multipole interactions, and its rate is particularly high if the donor and acceptor levels are in resonance (Dexter, 1953). Furthermore, the rate increases with an increasing product of the oscillator strengths of the Ln^{3+} emission (donor) and the M absorption (acceptor) transitions. The latter becomes especially large if the transition on the M ion is allowed. Many transition-metal ions such as Fe^{2+} , Cu^{2+} , Co^{2+} , Ni^{2+} , Cr^{3+} , V^{3+} , and Ti^{3+} have transitions with high cross sections in the near-IR spectral region (France et al., 1986) where many of the laser-cooling transitions are located (Fig. 7), and they are thus detrimental to laser cooling. Two additional effects further exacerbate the problem. First, recall that high Ln^{3+} ion concentrations are desired in order to increase the absorption efficiency (Eq. 15). In this regime, however, energy migration among the Ln^{3+} ions is efficient, and the M impurities become accessible to a large number of Ln^{3+} ions. The M ions then act as efficient traps for excitation energy and further reduce the quantum efficiency. Second, the often large cross section of the M ions causes a background absorption (α_b) and thus reduces the absorption efficiency (Eq. 15), that is, a portion of the incident pump laser light is absorbed directly by the M ions followed by conversion to heat. Hehlen et al. had estimated an upper limit of 10–100 ppb (parts per billion) for transition-metal impurities in Yb^{3+} -doped ZBLAN glass for efficient laser cooling (Hehlen et al., 2007). The upper limit for other Ln^{3+} impurities (such as Er^{3+} , Tm^{3+} , and Ho^{3+} ions in Yb^{3+} -based laser-cooling materials) appears to be much higher than for transition metals. This is because the product of donor and acceptor oscillator strengths is smaller as it involves two forbidden 4f transitions. Furthermore, Ln^{3+} excited states have generally higher quantum efficiencies so that Ln^{3+} impurities tend to primarily decay via radiative relaxation without adding excessive heat load. Goldner et al. studied the effect of Er^{3+} and Tm^{3+} impurities on the laser-cooling performance of a ZBLAN glass doped with 2.9 mol% YbF_3 ($5 \times 10^{20} \text{Yb}^{3+}/\text{cm}^3$) (Goldner and Mortier, 2001). They found that Er^{3+} had a negligible effect up to 10^{17} – $10^{18} \text{Er}^{3+}/\text{cm}^3$, that is, a concentration of 6–60 ppm (parts per million). The presence of Tm^{3+} was even less problematic, with concentrations up to $10^{19} \text{Tm}^{3+}/\text{cm}^3$ (~ 600 ppm) having negligible effect on laser cooling.

The aforementioned considerations were recently corroborated by Melgaard et al. who had performed a detailed analysis of metal impurities in a series of YLF crystals doped with 1%, 5%, 7%, and 10% Yb^{3+} (Melgaard, 2013; Melgaard et al., 2013a, 2014). For this purpose, they managed to dissolve the chemically very stable YLiF_4 by boiling finely crushed crystal powder in a 1:1 volume mixture of 15 N nitric acid and 6 N hydrochloric acid (*aqua regia*)

for several hours. The reactants were contained in a lidded Teflon container that was previously leached in acid to minimize recontamination from the container. The dissolved YLF:Yb³⁺ was then analyzed by a quadrupole mass spectrometer to measure the concentrations of a large number of different trace metals. In addition, they performed optical measurements of α_b for each of the original YLF:Yb³⁺ crystals. They found that the iron concentration showed a statistically significant correlation with α_b and was the main source of background absorption. The authors further discovered that α_b decreased with increasing YbF₃ added to YLiF₄. Their 10% Yb³⁺-doped YLF crystal had a record-low background absorption coefficient of $\alpha_b = 2.0 \times 10^{-4} \text{ cm}^{-1}$ and in turn produced the lowest temperature of $114 \pm 1 \text{ K}$ of the samples analyzed. This study provided quantitative information on the role of different impurities and serves as valuable guidance for future material purification efforts.

It was observed early on that samples of nominally the same composition and pedigree often differed substantially in their laser-cooling performance. This was considered to be a result of both surface contamination and impurities in the bulk material (Mungan et al., 1997b). Reducing the amount of transition-metal impurities was therefore of high priority. Zhou et al. proposed an electrochemical approach to purifying ZBLAN melts (Zhou et al., 1992), a method that was further studied by Macfarlane et al. (1999, 2004). Their goal was to lower the amount of reduced zirconium species and transition-metal ions to obtain fluoride glasses suited for the fabrication of ultralow-loss optical fibers. They contained the ZBLAN melt in a glassy carbon crucible at 600 °C in nitrogen atmosphere and inserted a three-electrode system into the melt consisting of a 10 mm × 10 mm Pt plate as working electrode, a Pt wire as reference electrode, and the crucible itself as the counter electrode. The electrochemical window of the glass extended from +400 mV, a potential at which fluorine is generated at the anode, to -1300 mV, a potential at which Zr⁴⁺ and Al³⁺ are reduced at the cathode. They showed that within this window, transition-metal ions could be removed from the melt by depositing them at the cathode at -220, -400, -400, and -650 mV for Cu, Ni, Co, and Fe, respectively (Zhou et al., 1992, 1993a,b). The electrochemical treatment also lowered the amount of reduced Zr species. Fajardo et al. explored this approach for preparing high-purity fluoride glasses for laser cooling (Fajardo et al., 1997). During the preparation of ZBLANP:Yb³⁺, they exposed the melt to a voltage for a period of 1, 6, 12, and 24 h at 600 °C. Their main focus was the removal of iron impurities, and the voltage was therefore slowly increased to above the cathodic deposition potential for Fe. Using photothermal deflection spectroscopy to probe internal cooling, they found that glasses made from melts that were electrochemically treated for <6 h (or not at all) exhibited no laser cooling while glasses that were treated for >6 h did. The magnitude of the improvement however was less than expected, and their result indicated that some level of impurities remained. Murtagh et al. used

resonant laser ablation combined with mass spectrometry to obtain a semi-quantitative analysis of trace transition metals in fluoride glasses fabricated with and without electrochemical purification (Murtagh et al., 1999b). They found that exposing a ZBLANP:Yb³⁺ melt to a voltage for 18 h at 600 °C reduced Fe, Cr, and Cu impurities by factors of 4.2, 5.5, and 18.0 respectively, compared to the untreated glass. The removal of Cu was more efficient than of Fe due to the smaller cathodic plate-out potential of Cu (−220 mV) compared to Fe (−650 mV). This sample showed internal cooling by 0.33 K as measured by photothermal deflection spectroscopy. Another glass (BIG: Yb³⁺) showed a much smaller improvement upon electrochemical purification, likely because the electrochemical window of BIG glass was not known and the treatment potential may have been chosen incorrectly.

Patterson et al. pursued a different purification method (Patterson et al., 2011). Instead of purification at the melt stage, they developed a procedure for purifying each of the starting materials of Yb³⁺-doped ZBLANI (ZrF₄–BaF₂–LaF₃–AlF₃–NaF–InF₃) glass prior to glass melting. The chemical inertness and relatively high melting temperatures of metal fluorides make them unsuited for many standard purification techniques such as recrystallization, zone refining, sublimation, and distillation. Therefore, Patterson et al. started from high-purity commercial precursors that were not fluorides, that is, ZrCl₂·8H₂O, BaCO₃, La₂O₃, AlCl₃·6H₂O, Na₂CO₃, La₂O₃, In metal, and Yb₂O₃. These precursors were dissolved in ultrahigh-purity water or acids, filtered through 0.2 μm pore size filters, and then subjected to a three-step solvent-extraction process. It first involved the addition of ammonium pyrrolidine dithiocarbamate (APDC) to the aqueous metal ion solution followed by the addition of methyl isobutyl ketone (MIBK), an organic solvent that is immiscible with water, thus forming a two-phase system. APDC had a strong affinity for transition-metal ions, and the respective APDC–metal coordination complexes were extracted to the MIBK phase because they were more soluble in the organic than in the aqueous phase. Hydrofluoric acid was added in a final step to precipitate the high-purity metal fluoride that was subsequently dried in hot HF gas before being used in ZBLANI:Yb³⁺ glass fabrication. They tracked the evolution of trace metals in the Zr solution as it was purified by solvent extraction, and they found that the total transition-metal concentration (Cu, Fe, Co, Ni, V, Cr, Mn, and Zn) was reduced from 72,540 to 115 ppb after the third solvent-extraction step, a 650-fold purification. Of these, Fe was the dominant impurity and was reduced 882-fold from 51,600 to 58.5 ppb. A sample of ZBLANI:Yb³⁺ fabricated by this process showed internal laser cooling to a temperature of 238 K (Patterson et al., 2010a), a result that was on par with the best cooling results achieved with ZBLAN-based materials. However, the many components of ZBLAN-based glasses make such a purification method extremely laborious and also prone to recontamination during the numerous processing steps. Chelate-assisted solvent extraction is therefore more attractive for the purification of crystalline systems that typically have a small number of precursors.

The previously mentioned melt and solvent purification methods were developed for fluoride glasses, and they are expected to be adaptable to crystalline systems. We also note that the process of growing a crystal is in itself a purification method; the growth of a highly ordered crystal lattice tends to include or exclude trace impurities based on both their ionic radius and their charge. This area of research has not received much attention yet, and studies analyzing impurity concentrations in starting materials and laser-cooling crystals grown from those are expected to yield valuable insights.

3.3 Homogeneous and Inhomogeneous Broadening

The quasi-zero Stokes shift associated with electronic transitions within the 4f shell produces spectral profiles in absorption and emission that are relatively narrow compared to allowed Stokes-shifted transitions (see Fig. 8). In a Ln^{3+} -doped solid, the spectral width of electronic transitions is determined by both homogeneous and inhomogeneous effects. Homogeneous broadening equally affects all Ln^{3+} ions in the solid and includes the broadening induced by (1) the modulation of the crystal field via the thermal motions of the coordinating atoms and (2) the decay (lifetime) of the transition final state. The magnitude of both contributions is temperature-dependent, and the homogeneous width of the Lorentzian spectral profile increases with increasing temperature with a T^k dependence. $k \approx 2$ above the Debye temperature, but lower values of $k = 1 \dots 2$ are often observed at $T < 50 \text{ K}$ (Lei et al., 1998). In contrast, inhomogeneous broadening is a result of different local coordination geometries of the Ln^{3+} ions. The distribution of different local crystal fields leads to a distribution of transition energies for the ensemble of Ln^{3+} ions in the solid, independent of temperature. Inhomogeneous broadening is generally well described by a Gaussian distribution of crystal fields and thus transition energies. It is absent in a perfect crystal in which all Ln^{3+} ions are subjected to an identical crystal field and thus produce the same transition energies (assuming that there is only one site for the Ln^{3+} ion in crystal lattice). In contrast, the structural disorder in glassy materials offers a range of different coordination environments for Ln^{3+} ions and can correspondingly lead to substantial inhomogeneous broadening. In this case, the Lorentzian homogeneous lineshape profile $g_L(\nu)$ with width $\Delta\nu_L$ is convoluted with the inhomogeneous Gaussian distribution of transition energies $g_G(\nu)$ with width $\Delta\nu_G$. The resulting spectral shape is described by the Voigt profile $g_V(\nu, T) = \int_{-\infty}^{\infty} g_G(\nu') g_L(\nu - \nu', T) d\nu'$ (Di Bartolo, 2010; Schreier, 1992), which includes the dependence of the homogeneous linewidth on temperature.

Lei et al. had performed a detailed study of the magnitude of homogeneous and inhomogeneous broadening as a function of temperature in a 1% Yb^{3+} -doped ZBLANP glass (Lei et al., 1998). They deconvoluted the Voigt profiles measured for the ${}^2\text{F}_{7/2} \rightarrow {}^2\text{F}_{5/2}$ absorption and ${}^2\text{F}_{5/2} \rightarrow {}^2\text{F}_{7/2}$ emission and determined an inhomogeneous linewidth of $990 \pm 40 \text{ GHz}$, a value that

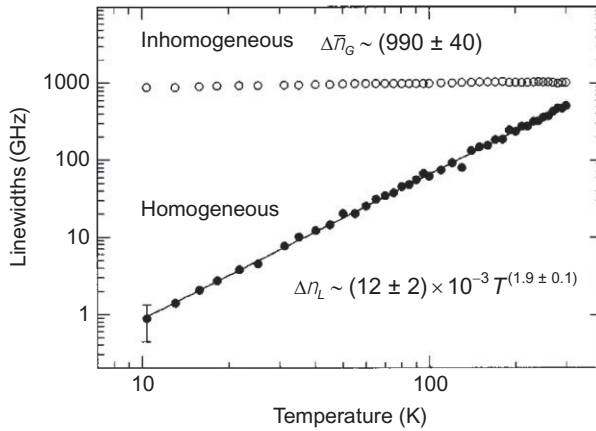


FIGURE 14 Homogeneous and inhomogeneous linewidths of the ${}^2F_{5/2}(E5) \rightarrow {}^2F_{7/2}(E1)$ transition of Yb^{3+} (see Fig. 9, left) in ZBLANP fluoride glass (Lei et al., 1998). Reproduced with permission from the American Physical Society. Copyright (2014).

was found to be essentially independent of temperature (see Fig. 14). The homogeneous linewidth increased with a nearly T^2 dependence in the 10–300 K temperature range, as expected. It is important to note that inhomogeneous broadening dominated homogeneous broadening for all temperatures in this range.

The absorption coefficient of a crystal-field transition is given by $\alpha(\nu, T) = \sigma(\nu, T)N(E_i, T)$. The cross section is given by $\sigma(\nu, T) = (1/8\pi)(g_2/g_1)\lambda^2 A_{21} \cdot g_V(\nu, T)$, where A_{21} is the Einstein coefficient for spontaneous emission; g_1 and g_2 are the degeneracy factors of the ground and excited states, respectively; λ is the transition wavelength; and $g_V(\nu, T)$ is the spectral lineshape function. $N(E_i, T)$ is the thermal population density of the initial state at energy E_i at T , and it is proportional to $\exp(-E_i/kT)$. Therefore, $\alpha(\nu, T)$ is proportional to $g_V(\nu, T)\exp(-E_i/kT)$. In a glassy material such as ZBLAN where inhomogeneous broadening dominates, therefore, $g_V(\nu, T) \approx \text{constant}$, and the peak absorption coefficient decreases exponentially with temperature. For a crystal, in contrast, inhomogeneous broadening is negligible, and the homogeneous lineshape is given by the area-normalized Lorentzian profile

$$g_V(\nu, T) = g_L(\nu, T) = \frac{2}{W\pi} \frac{1}{1 + \frac{4(\nu - \nu_0)^2}{W^2}}, \quad (22)$$

where ν_0 is the mean transition frequency and W is the full width at half maximum. Assuming that the homogeneous linewidth scales as $W \propto T^2$, one finds that the peak value of the lineshape ($\nu = \nu_0$) is proportional to T^{-2} ; thus, the peak absorption coefficient is proportional to $T^{-2} \exp(-E/kT)$. That is, as

temperature decreases, the decrease in thermal population is partially offset by the reduction in homogeneous linewidth and the corresponding increase in peak cross section. As a result, an electronic transition maintains a higher *peak* absorption coefficient, α , with decreasing temperature in a crystal than in a glass. Using the linewidths shown in Fig. 14, one predicts that at 150 K, the peak value of α is $6.4 \times$ greater in a crystal than in ZBLAN glass. This is indeed found for the E4 \rightarrow E5 transition in ZBLAN:Yb³⁺, as was shown earlier in Fig. 6. The α advantage of crystals over glasses is predicted to grow to ≈ 23 -fold at 80 K, and it directly translates into an increased absorption efficiency (Eq. 15) and thus cooling power (Eq. 10). This is one reason why crystals have generally shown better laser-cooling performance than glasses. Conversely, the higher peak absorption coefficient of crystals enables them to tolerate a higher background absorption for the same absorption efficiency, thus relaxing the purity requirements to reach a given laser-cooling performance.

4 EXPERIMENTAL TECHNIQUES

4.1 Reciprocity of Absorption and Luminescence

Equation (12) has highlighted the need for measuring the absorption spectrum as a function of temperature, in particular the absorption coefficient at the pump wavelength, $\alpha(T)$. Laser excitation is usually performed in the long-wavelength tail of the absorption spectrum (see Fig. 10) to maximize the cooling efficiency (see Eq. 14). However, the absorption coefficients are typically small in this regime because of the low thermal population of the initial state, and they decrease rapidly with decreasing temperatures. This poses experimental challenges that make it difficult to determine $\alpha(T)$ directly from absorption spectroscopy. Absorption spectra are therefore often calculated from luminescence via reciprocity. McCumber had shown in 1964 (McCumber, 1964) that the absorption and luminescence spectra of a given transition $i \leftrightarrow j$ are related because the Einstein coefficients of absorption, spontaneous emission, and stimulated emission are governed by the same matrix elements ($\sigma_{ij} = \sigma_{ji}$) and because of the principle of detailed balance (Siegman, 1986). Quimby et al. had explored the applicability of the McCumber theory and shown that it is only strictly valid if the linewidth of all crystal-field transitions is $\ll kT$ (Quimby, 2002). Following their derivation and notation, we consider luminescence transitions between the crystal-field transitions of an excited state (i) and of the ground state (j). Assuming thermal equilibrium among the crystal-field levels, the emission cross section is given by an average over initial states and a sum over final states, that is,

$$\sigma_e(h\nu) = \sum_i \sum_j \frac{\sigma_{ij}(h\nu) e^{-\Delta_i/kT}}{Z_2}, \quad (23)$$

where the partition function $Z_2 \equiv \sum_i \exp(-\Delta_i/kT)$ and Δ_i is the energy of the initial state with respect to the lowest crystal-field level of the excited state. In analogy, the absorption cross section is given by

$$\sigma_a(h\nu) = \sum_j \sum_i \frac{\sigma_{ji}(h\nu) e^{-\Delta_j/kT}}{Z_1}, \quad (24)$$

where the partition function $Z_1 \equiv \sum_j \exp(-\Delta_j/kT)$ and Δ_j is the energy of the initial state with respect to the lowest crystal-field level of the ground state. Note that $\Delta_i + E_0 = \Delta_j + E_{ij}$, where E_0 is the energy difference between the lowest crystal-field levels of the excited-state and ground-state multiplets and E_{ij} is the transition energy. This yields the exact relation

$$Z_2 \sigma_e(h\nu) = \sum_i \sum_j \sigma_{ij}(h\nu) e^{-\Delta_i/kT} e^{-(E_{ij}-h\nu)/kT} e^{-(E_0-h\nu)/kT}. \quad (25)$$

Assuming that the linewidth δE_{ij} is much less than kT yields $E_{ij} - h\nu/kT \ll 1$. Using the relation $\sigma_{ij}(h\nu) = \sigma_{ji}(h\nu)$ and introducing an effective energy, ε , according to $e^{\varepsilon/kT} \equiv (Z_1/Z_2) e^{E_0/kT}$ simplifies Eq. (25) to the usual McCumber equation

$$\sigma_e(h\nu) = \sigma_a(h\nu) e^{(\varepsilon-h\nu)/kT}. \quad (26)$$

The assumption $\delta E_{ij} \ll kT$ is quite good for homogeneously broadened 4f crystal-field transitions in the 0–300 K temperature range. At 300 K, homogeneous linewidths are in the 20–80 cm^{-1} range, which is small compared to $kT \approx 210 \text{cm}^{-1}$. Equation (26) can therefore be used to relate emission and absorption spectra of crystalline systems for $T \leq 300 \text{K}$, which encompasses many situations in solid-state laser-cooling studies.

The presence of substantial inhomogeneous broadening in glasses adds complication. Quimby et al. had studied this case in detail (Quimby, 2002). Starting from the homogeneous case discussed in the preceding paragraph, they introduced inhomogeneous broadening by defining a “site” variable, Q , that followed a Gaussian distribution $f(Q) = (1/\sqrt{\pi}) \exp(-Q^2)$. They assumed an $f(Q)$ distribution of energies for each crystal-field level and a linear dependence of the cross section on Q . They found that there is no simple relationship between absorption and emission profiles in the presence of inhomogeneous broadening. As seen in Section 3.3, the presence of both homogeneous broadening and inhomogeneous broadening leads to Voigt profiles that arise from the convolution of the respective Lorentzian and Gaussian line-shapes. Quimby et al. showed that the McCumber equation for the inhomogeneous case

$$\sigma_e^{\text{inh}}(h\nu) = \sigma_a^{\text{inh}}(h\nu) e^{(\varepsilon-h\nu)/kT} \quad (27)$$

is still valid as long as the width of the Voigt profile, δE_V , is less than kT . This implies that both the homogeneous and the inhomogeneous widths must be

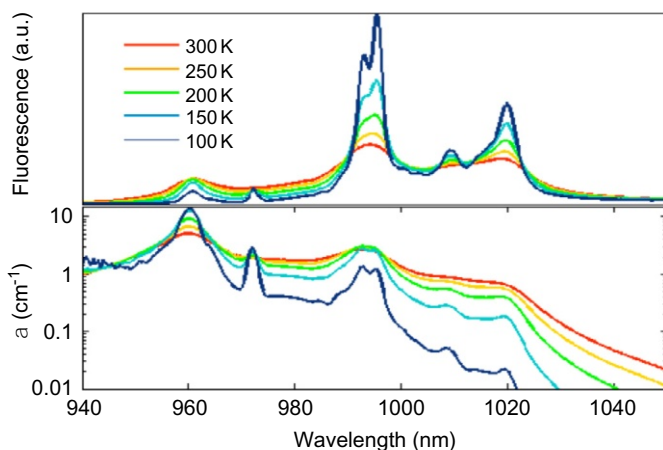


FIGURE 15 Determination of the absorption spectrum of a YLF:Yb³⁺ crystal via reciprocity from luminescence spectra (Melgaard et al., 2010). Note the rapid decrease in the absorption coefficient at the E4 → E5 pump transition around 1020 nm with decreasing temperature.

$\ll kT$. Subsequent studies by Martin et al. of Nd³⁺-doped fluorozirconate glass and Nd³⁺-doped silicate glass found that the McCumber theory deviated significantly from observations for $kT < 1.8\Delta v_{\text{inh}}$ (Martin and Quimby, 2006, 2007). Referring back to Fig. 14, the homogeneous and inhomogeneous linewidths in ZBLANP:Yb³⁺ at 300 K were ~ 20 and ~ 33 cm⁻¹, respectively, which are small compared to $kT \approx 210$ cm⁻¹ and justify the use of the McCumber equation. The lower limit of validity is expected at ~ 85 K below which $kT < 1.8\Delta v_{\text{inh}}$.

McCumber and Martin had shown that the error in absorption cross sections derived from emission spectra within the validity range of the McCumber equation is on the order of 3–5%. Despite such errors, reciprocity is a particularly valuable tool for the characterization of laser-cooling materials. Direct absorption measurements become impractical for absorption coefficients < 0.03 cm⁻¹, a regime in which background subtraction errors dominate the measured absorption signal (Epstein et al., 2001). An example of a reciprocity analysis for Yb³⁺-doped YLF is shown in Fig. 15 (Melgaard et al., 2010). The absorption coefficient of the pumped E4 → E5 crystal-field transition around 1020 nm in the long wavelength of the spectrum rapidly drops into the $10^{-2} - 10^{-3}$ cm⁻¹ range with decreasing temperature. Reciprocity is therefore preferred over direct absorption measurements to quantify the small pump absorption coefficients at low temperatures.

4.2 Thermometry Techniques

The measurement of the sample temperature is clearly one of the key experiments in solid-state optical refrigerator research, and a great amount of work

has been dedicated to developing a variety of techniques. Typical experiments include the measurement of the local temperature at the laser focal area inside a sample, the measurement of the bulk sample temperature, and the measurement of the temperature of a payload attached to the laser-cooling material. IR cameras, thermocouples, laser deflection, Mach–Zehnder interferometers, and luminescence thermometry have all been employed in a variety of configurations for this purpose. Each method has a set of advantages and disadvantages and an inherent temperature range in which sufficient sensitivity is achieved. The main distinction is between contact and noncontact techniques, with the latter having prevailed in recent times. A review published in 2003 by Rayner et al. discussed the earlier thermometry techniques including photothermal deflection spectroscopy, fluorescence thermometry, and microthermocouples (Rayner et al., 2003). These are described later in the text along with more recent advances in optical thermometry.

4.2.1 Thermocouples

The most obvious and deceptively simple method is to attach a thermocouple or diode to the laser-cooling medium and measure the temperature via the electric response of the sensor. As early as 1968, Kushida et al. used a thermocouple attached to the Nd^{3+} -doped YAG crystal in their first observation of reduced heating in a solid upon optical pumping (Kushida and Geusic, 1968). Edwards et al. used both T - and K -type thermocouples glued to ZBLAN: Yb^{3+} glass (Edwards et al., 1999). They recognized that conduction of heat through the thermocouple wires and absorption of sample fluorescence by and associated heating of the thermocouple distorted the measurements. Some improvement was achieved by reducing the diameter of the thermocouple wires from 1 to 0.5 mil (12.7 μm). Thiede et al. used a similar setup in their record-cooling result with ZBLANP: Yb^{3+} to 208 K (Thiede et al., 2005). They epoxied a 0.5 mil diameter K -type thermocouple to the backside of the cooling element, accompanied by thermocouples on the sample chamber and the chamber base. As shown in Fig. 16, the chamber and cooling element temperature rose quickly when the laser was turned on (at $t=0$ h), and both showed a drop when the laser was turned off (at $t=3.1$ h). This effect was attributed to fluorescent heating of the chamber and the cooling element thermocouple when the pump laser was on. Rayner et al. had pointed out correctly that such fine-gauge thermocouples are mechanically quite fragile and difficult to mount to the cooling element (Rayner et al., 2003). They used an E -type (Ni:Cr–Ni:Cu) unsheathed fine-gauge thermocouple with a sensitivity of 0.05 mV/K in the -20 – 70 °C temperature range (Rayner et al., 2001b). They first pumped the 250 μm diameter ZBLAN: Yb^{3+} fiber (cooling medium) for 3 min to induce steady-state optical cooling, and then they blocked the laser, brought the thermocouple in contact with the sample, and measured its signal as it equilibrated with the sample temperature over the

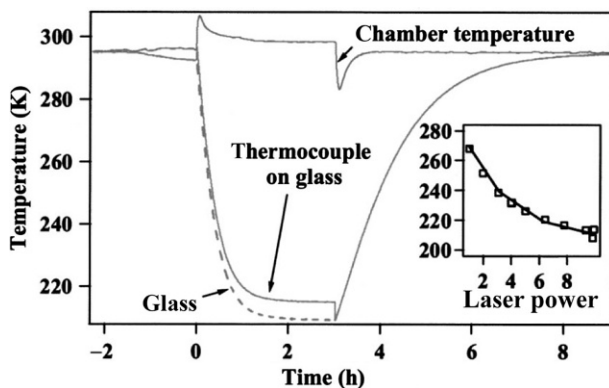


FIGURE 16 Measurement of optical refrigeration in ZBLANP:Yb³⁺ glass using thermocouples (TCs) (Thiede et al., 2005). The lower solid curve corresponds to the TC readings from the cooling element, and the upper solid curve corresponds to the TC readings attached to the sample chamber. The pump laser ($\lambda=1026$ nm, $P_0=9.6$ W) is turned on at $t=0$ h and off at $t=3.1$ h. The inset shows the lowest temperatures achieved for different pump powers ($\lambda=1026$ nm).

course of about 2 min. Condon et al. used a fine-wire (1 mil diameter) *T*-type (copper/constantan) thermocouple in contact with their KPb₂Cl₅:Er³⁺ sample and its complementary junction in contact with an isothermal block (Condon et al., 2009, 2010). A second identical thermocouple was placed near the sample as a reference. As in the previously mentioned experiment by Rayner et al. they avoided the undesired heating of the thermocouple by sample fluorescence and stray pump light by first exciting the sample for ~ 6 min, then turning off the laser, and recording the thermocouple signal at 5 Hz for 200 s. Depending on the final temperature of the crystal, the thermocouple would either cool or heat in an exponential fashion as it reequilibrated back toward ambient temperature. This procedure was repeated for different pump wavelengths, and they were able to quantify the transition from laser-induced cooling to laser-induced heating as the pump wavelength was tuned from 1567.6 to 1527.0 nm. Murtagh et al. used a calibrated silicon diode, rather than a thermocouple, in their laser-cooling evaluation of various Yb³⁺-doped fluorozirconate glasses (ZBLANP and BiGaZyBTZr); however, they did not provide detailed information on the diode type and arrangement (Murtagh et al., 1999a).

Such contact measurements of temperature are appealing because they provide a direct measure of the bulk-cooling element temperature. Furthermore, the extraction of heat from an attached sensor is in itself a demonstration of cooling a thermal load. However, the use of thermocouples becomes difficult because of fluorescent heating and heat conduction through the wires. These drawbacks can be avoided with some of the noncontact thermometry methods reviewed in the following.

4.2.2 Thermal Cameras

The first report of optical refrigeration in ZBLANP:Yb³⁺ used a liquid-nitrogen-cooled InSb IR camera for the noncontact measurement of temperature (Epstein et al., 1995). InSb is sensitive in the 3–5 μm spectral range while being insensitive to the pump laser light and Yb³⁺ fluorescence around 1 μm . However, ZBLANP glass like all fluorides has a low emissivity in the 3–5 μm spectral range. Therefore, a 1 mm² gold foil was attached to the ZBLANP:Yb³⁺ sample and painted black on the outside in order to enhance the emissivity. The assumption was that the outer black surface of the foil would be a good measure of the sample temperature while the inner shiny surface would reflect >90% of the fluorescence light and therefore not experience substantial fluorescent heating. This method was susceptible to drifts of the ambient temperature, and a reference sample was therefore placed next to the pumped sample in the field of view of the camera. The authors were able to resolve temperature differences of 0.02 K between the two samples. Hoyt et al. used a pyroelectric camera to measure the temperature of a Tm³⁺-doped ZBLANP sample (Hoyt et al., 2000; Sheik-Bahae et al., 2000, 2001). The thermal images in Fig. 17 (inset) clearly show the sample (middle right in chamber) changing from cooling to heating as the pump laser

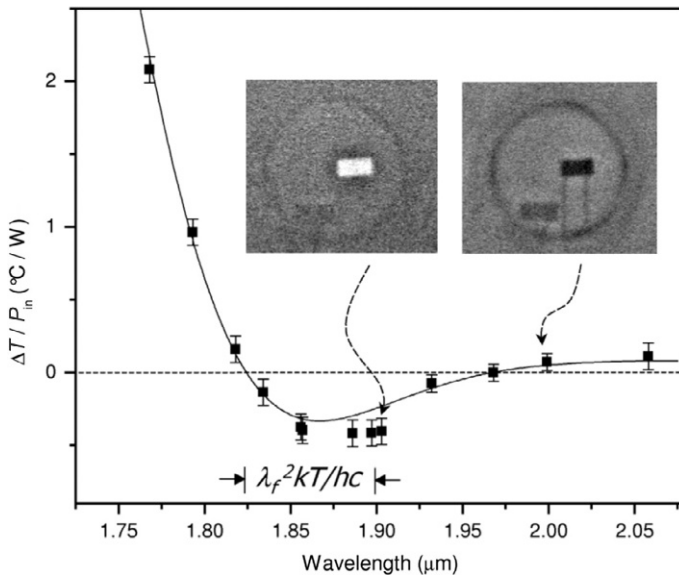


FIGURE 17 Temperature measurement of a Tm³⁺-doped ZBLANP sample using a pyroelectric infrared camera (inset) (Hoyt et al., 2000). The pumped sample (middle right in chamber) is compared to an unpumped reference sample (bottom left in chamber) to determine the net temperature change. The sample changes from cooling to heating as the pump laser wavelength is tuned from 1.90 to 2.00 μm (main graph).

wavelength is tuned from 1.90 (maximum cooling) to 2.00 μm (heating due to background absorption). The unpumped reference sample is seen faintly at the bottom left in the chamber, and it allowed the determination of the net temperature change induced by optical refrigeration. In this study, the sample was imaged directly, that is, without the application of a black foil. Similar IR camera-based temperature measurements were reported by Epstein et al. for Yb^{3+} -doped YAG and Y_2SiO_5 (Epstein et al., 2001), Patterson et al. for $\text{BaY}_2\text{F}_8:\text{Tm}^{3+}$ (Patterson et al., 2004, 2008), Bigotta et al. for $\text{BaY}_2\text{F}_8:\text{Tm}^{3+}$ (Bigotta et al., 2006a,b), Guiheen et al. for Yb^{3+} - and Tm^{3+} -doped ABCYS glasses (Guiheen et al., 2006), Bigotta et al. for $\text{BaY}_2\text{F}_8:\text{Yb}^{3+}$ (Bigotta et al., 2007), and Seletskiy et al. for ZBLAN: Yb^{3+} (Seletskiy et al., 2010a). Hoyt et al. found that pyroelectric- or microbolometer-based thermal cameras have an absolute resolution of ~ 0.2 K in the $\Delta T = \pm 10$ K range from room temperature (Hoyt et al., 2003), which limits their use to the study of cooling performance around room temperature. However, thermal cameras are relatively easy to use and therefore attractive for sample screening purposes.

4.2.3 Photothermal Deflection Spectroscopy

Photothermal deflection spectroscopy (PTDS) is another noncontact thermometry technique that has found widespread use in the field. It measures the local temperature near the pumped volume within a sample. It was first described in detail by Boccara et al. who used this technique for measuring ultralow absorption coefficients (10^{-5} cm^{-1}) in highly transparent solids (Boccara et al., 1980). The technique is based on the thermo-optic coefficient, that is, the change of refractive index with temperature, which is typically negative. When a laser beam is incident on an absorbing medium, a local radial temperature gradient is established that in turn induces a local radial refractive index gradient via the thermo-optic effect. This index gradient causes a probe laser beam propagating parallel or antiparallel to the pump laser to deflect. If the pump laser heats the sample, a divergent lens is formed and the probe beam is deflected away from the pump beam. Conversely, if the pump laser cools the sample, a convergent lens is formed and the probe beam is deflected toward the pump laser (Rayner et al., 2003). This 180° phase reversal can be used to detect the presence of laser-induced heating and cooling. The thermo-optic effect can be assumed linear for small temperature changes, and the deflection magnitude is therefore proportional to the heating or cooling power induced by the pump laser (Rayner et al., 2003). This makes PTDS a useful technique for analyzing small temperature changes and for screening laser-cooling samples.

Epstein et al. used PTDS in their first demonstration of solid-state laser cooling of ZBLANP: Yb^{3+} glass (Epstein et al., 1995). They pumped the sample with a titanium-sapphire laser that was mechanically chopped with a period of 1.8 s. A helium-neon laser probe beam propagating in the opposite

direction was colligned with and slightly displaced from the pump beam. The ZBLANP sample was transparent at the 632.8 nm wavelength of the probe beam, which thus did not introduce any temperature change itself. The angular deflections of the probe beam, caused by thermally induced refractive index gradients, were then measured using a position-sensitive detector. As shown in Fig. 18A, the PTDS waveform reversed sign as the pump wavelength was changed from 980 to 1010 nm, that is, from laser-induced heating to laser-induced cooling. The results of the full investigation are shown in Fig. 18B and clearly demonstrate the 180° phase difference between pumping at wavelengths less than (heating) or greater than (cooling) the mean fluorescence wavelength. Fajardo, Murtagh, and coworkers used PTDS for testing ZBLANP:Yb³⁺ samples fabricated under different electrochemical purification conditions (see Section 3.2) (Fajardo et al., 1997; Murtagh et al., 1999b). A similar setup was used by Mungan et al. who displaced the probe beam laterally from the pump beam by 50 μm in order to sensitively probe the pump-induced thermal gradient (Mungan et al., 1997a). The lateral displacement of the probe beam had to be chosen carefully. Rapid artificial transients due to the finite time required for the chopper blade to cross the 2 mm pump beam were observed if the probe beam was closer than 50 μm to the pump beam. Bowman et al. measured photothermal deflections in Yb³⁺-doped YAG, YLF, KGd(WO₄)₂, and ZBLANP samples by placing a large-area dual-cathode silicon diode several meters away from the sample, and they were able to resolve angular probe beam deflections as small as 0.01 μrad , taking care to minimize vibrations and air turbulence (Bowman and Mungan, 2000). They also used temperature control and optical isolation of the helium–neon laser to minimize pointing fluctuations. PTDS

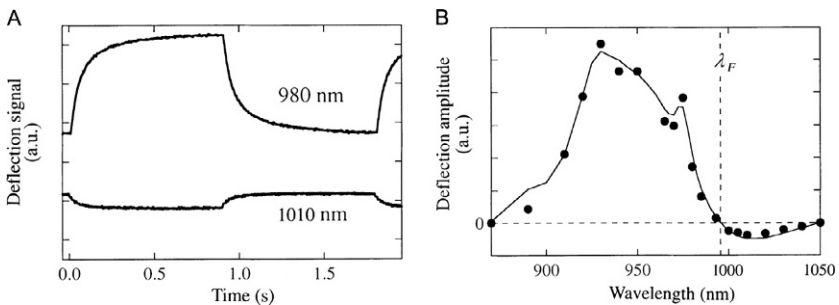


FIGURE 18 Photothermal deflection waveforms of ZBLANP:Yb³⁺ glass. (A) Deflection waveforms for two pump wavelengths showing the 180° phase difference between pumping at 980 nm (heating) and pumping at 1010 nm (cooling); (B) deflection amplitude as a function of wavelength showing sign reversal as wavelength is tuned from the heating ($\lambda_p < \tilde{\lambda}_f$) to the cooling ($\lambda_p > \tilde{\lambda}_f$) regime. Reprinted with permission from Macmillan Publishers Ltd: Epstein et al. (1995). Copyright 1995.

techniques were also used by Rayner et al. for characterizing a 250 μm diameter ZBLAN:Yb³⁺ fiber (Rayner et al., 2001a) and a ZBLAN:Yb³⁺ bulk sample (Rayner et al., 2001a); Fernandez et al. for Yb³⁺-doped CNBZn and BIG glasses (Fernández et al., 2000, 2001a,b, 2002, 2012); Mendioroz, Fernandez, and coworkers for KPb₂Cl₅:Yb³⁺ (Fernandez et al., 2002, 2012; Mendioroz et al., 2002); García-Adeva et al. for KPb₂Cl₅:Er³⁺ (Fernandez et al., 2006, 2012; Garcia-Adeva, 2008; Garcia-Adeva et al., 2007, 2009); García-Adeva et al. for KPb₂Br₅:Er³⁺ (Garcia-Adeva, 2008; Garcia-Adeva et al., 2009); and Fernandez et al. for Er³⁺-doped CNBZn glass (Fernandez et al., 2006, 2012).

Following the derivation presented by Fernandez et al. (2001a) and using the notation of Section 2, assume a quasi two-level system such as that shown for Yb³⁺ in Fig. 9 pumped at $h\nu_p$ with amplitude modulation frequency ω_m and emitting at the mean luminescence energy $h\tilde{\nu}_f$. The heat the sample exchanges per unit time and unit volume is then given by

$$H = N_2 [W_{nr}h\nu_p + W_r h(\nu_p - \tilde{\nu}_f)], \quad (28)$$

where N_2 is the population density in the excited state and W_r and W_{nr} are the radiative and nonradiative relaxation rates of the excited state, respectively. Here, N_2 is given by $dN_2/dt = N_1(\sigma_a I/h\nu_p) - (N_2/\tau)$, where $\tau = 1/(W_r + W_{nr})$ is the excited-state lifetime and σ_a is the absorption cross section. Assuming a low pump laser amplitude modulation frequency ($\tau\omega_m \ll 1$), Eq. (28) simplifies to

$$H = N_1 \sigma_a I_0 \left[1 - \eta_q \frac{\tilde{\nu}_f}{\nu_p} \right], \quad (29)$$

where $\eta_q = W_r/(W_r + W_{nr})$ is the internal quantum efficiency of the excited state. Salazar et al. have shown that in the collinear geometry of a PTDS experiment, the angular deviation of the probe beam is proportional to the amount of heat the sample exchanges (Salazar et al., 1993). With this assumption, the photothermal deflection signal (PDS) can be related to the spectroscopic parameters of the active ion according to

$$\frac{\text{PDS}}{\alpha(\lambda_p, T) I_0} = C \left[1 - \eta_q \frac{\lambda_p}{\tilde{\lambda}_f} \right] + \frac{\alpha_b}{\alpha(\lambda_p, T)}, \quad (30)$$

where C is a constant, I_0 is the incident pump intensity, and $\alpha(\lambda_p, T)$ is the resonant absorption coefficient. Here, we have included the heating caused by background absorption (α_b) (Mungan and Gosnell, 1999). From Eq. (30), one therefore expects a nearly linear dependence of the normalized photothermal deflection signal as a function of pump wavelength. This linear relationship has been found experimentally for a number of materials such as Yb³⁺-doped ZBLAN, KGW, YLF, and YAG (Bowman and Mungan, 2000). The quantum efficiency can then be deduced from the slope and intercept of a linear fit to

the experimental PDS data (Bowman and Mungan, 2000; Epstein et al., 1995, 2001; Fernández et al., 2001a).

PTDS has several significant drawbacks. First, it depends on careful alignment of the pump and probe laser beams and is therefore only used for single-pass pump geometries. This limits its use to the screening of laser-cooling materials, and PTDS is not a useful thermometry method for multipass power-cooling experiments. Second, the refractive index depends not only on temperature through the thermo-optic effect (thermal lensing) but also on the density of excited activator ions (population lensing) (Anashkina and Antipov, 2010; Antipov et al., 2006; Messias et al., 2007; Passilly et al., 2006; Seletskiy et al., 2011). While the thermo-optic effect usually dominates and is an indication of temperature, population lensing distorts the thermal signal and can become important. This is another reason why the probe beam has to be laterally displaced from the pump beam, as described earlier in the text. The lateral displacement reduces the effect of activator excitation, which is local, while maintaining sufficient sensitivity for thermo-optic effects since heat diffuses in a radial direction with respect to the pump beam. This makes the optimum alignment of pump and probe lasers even more challenging and can even lead to erroneous results (Seletskiy et al., 2011).

Silva et al. had presented an alternate photothermal experiment in which pump and probe beams are collinear and the sample temperature is determined from probe beam phase shifts rather than probe beam deflection (Silva et al., 2013a,b). Their experimental arrangement used a continuous-wave Gaussian (TEM₀₀ with radius w_e) pump beam and a weak collinear (i.e., zero lateral displacement) He–Ne laser probe beam (TEM₀₀ with radius w_p), and they tested Yb³⁺-doped fluorozirconate (ZBLAN) and low-silica calcium aluminosilicate (LSCAS) glass. They measured the intensity of the central portion of the probe beam in the far field (pinhole/photodiode assembly) as a function of time, which is expected to follow

$$I(t) = I(0) \left| \int_0^\infty \exp[-(1 + iV)g - i\Phi(g, t)] dg \right|^2. \quad (31)$$

Here, $I(0)$ is the signal at $t=0$, $g = (r/w_p)^2$, and $V = Z_1/Z_c$, where r is the radial coordinate, Z_c is the confocal distance of the probe beam, and Z_1 is the distance from the probe beam waist to the sample. Besides these geometric factors, the intensity $I(t)$ is governed by the total phase shift, $\Phi = \Phi_{th} + \Phi_{PL}$, the probe beam experiences as it propagates through the pumped volume and acquires contributions from both thermal (th) and population effects (PL). Both Φ_{th} and Φ_{PL} depend on a number of material parameters such as the thermal diffusivity, thermal conductivity, excited-state lifetime, activator ion density, refractive index, and absorption and emission cross sections. Fits of Eq. (31) to measured transients yielded material parameters that were in good agreement with published results. The average

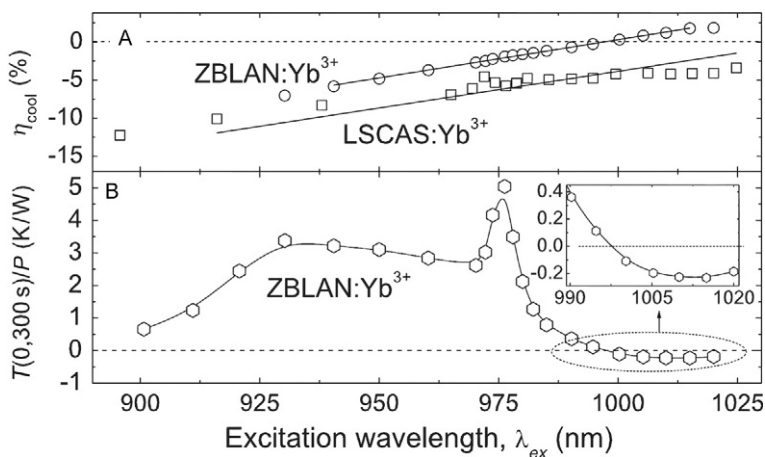


FIGURE 19 (A) Cooling efficiency and (B) normalized temperature change determined from collinear photothermal transients recorded for Yb³⁺-doped ZBLAN and LSCAS glass pumped at different wavelengths. Reproduced with permission from *Silva et al. (2013a)*. Copyright 2013, AIP Publishing LLC.

temperature change of the pumped volume could then be found from the transients because the probe beam phase shift is directly proportional to the temperature change. Furthermore, the amplitude of the thermal effect was expected to be proportional to the net power density (Eq. 11) and thus allowed measurement of the cooling efficiency. The temperature and cooling efficiency results are shown in Fig. 19 and were in good agreement with previously published results obtained by photothermal deflection. This time-resolved collinear method eliminates the difficulties in finding an optimum lateral displacement of the probe beam relative to the pump beam; its quantitative use however necessitates exact knowledge of several optical and material parameters.

4.2.4 Mach–Zehnder Interferometry

Mach–Zehnder (MZ) interferometry is another technique that has been used for noncontact thermometry. The technique is based on the fact that the optical path length in the sample changes linearly over a wide temperature range (Jewell et al., 1991; Lima et al., 2000). Figure 20 (left) shows the MZ interferometer used by Hoyt et al. to measure the laser-induced temperature change in Tm³⁺-doped ZBLAN glass (Hoyt et al., 2003). One advantage of this technique over PTDS is that it can be applied to both single-pass and multipass pump geometries and yields a measure of the bulk sample temperature. The difference in optical path length between the two interferometer arms is given by $\mathcal{L} = nL - L$, where L is the sample length and n is the sample refractive index. As a function of temperature, one then obtains (Hoyt et al., 2003)

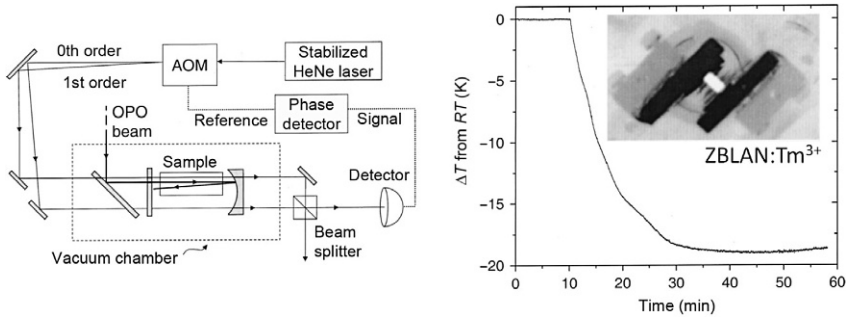


FIGURE 20 Left: Experimental setup for noncontact thermometry using a calibrated Mach-Zehnder (MZ) heterodyne interferometer (AOM=acoustooptic modulator; OPO=optical parametric oscillator) (Hoyt et al., 2003). Right: Temperature change from room temperature (RT) of a 1 wt% Tm^{3+} -doped ZBLAN glass (pumped at $1.9\ \mu\text{m}$ with $\sim 3.5\ \text{W}$ starting at $t=10\ \text{min}$) deduced from MZ measurements. The inset shows an infrared image of the cold sample (white rectangle in center) and the hot mirror mounts (black rectangles).

$$\frac{d\mathcal{L}}{dT} = L \left[\frac{dn}{dT} + \beta(n-1) \right], \quad (32)$$

where $\beta=(1/L)(dL/dT)$ is the coefficient of thermal expansion, for which values of $-5.8 \times 10^{-6} \pm 0.4\ \text{K}^{-1}$ (Lima et al., 2000) and $-5.9 \times 10^{-6}\ \text{K}^{-1}$ (Jewell et al., 1991) have been reported. They placed the ZBLAN: Tm^{3+} in a cryostat and calibrated Eq. (32) by determining the quantity in brackets. The interferometer measurements were found to agree to within 1 K when compared to thermal camera images. The resolution of this technique was found to be $\pm 3\ \text{K}$ and was limited by background phase drifts that occurred over timescales of 1 h. Figure 20 (right) shows the temperature change deduced from MZ measurements for a Tm^{3+} -doped ZBLAN glass sample pumped at $1.9\ \mu\text{m}$ with $\sim 3.5\ \text{W}$ from an optical parametric oscillator (OPO). Cooling by 19 K starting at room temperature was observed after pumping for $\sim 30\ \text{min}$. Thermometry with a MZ interferometer was also used by Gainov et al. who measured the temperature in the core of a strongly pumped Yb^{3+} -doped fiber under lasing conditions (Gainov et al., 2010).

4.2.5 Luminescence Thermometry

Luminescence thermometry has become the most common noncontact technique in recent years. As shown in Section 2.2, the crystal-field levels of the excited state rapidly thermalize after an excitation and, as a result, the luminescence spectrum varies as a function of temperature. Furthermore, thermal equilibrium is rapidly established regardless of the crystal-field transition that has been used for the excitation, causing the luminescence spectral profile to become independent of the pump wavelength (DeLoach et al., 1993). Absolute, differential, and ratios of luminescence intensities have been used as

thermometers. Mungan et al. were the first to use a basic implementation of this technique for the measurement of laser-induced temperature changes in 1 wt% Yb^{3+} -doped ZBLANP fiber (Mungan et al., 1997b). They first performed a calibration by placing the sample in a He-filled chamber, measuring the chamber temperature with a thermocouple, weakly exciting the sample at the mean fluorescence wavelength such as to induce neither cooling nor heating, and measuring the luminescence spectrum. This was repeated for different temperatures in the 280–303 K range, and the difference spectra between the high-temperature (303 K) and lower-temperature luminescence spectra were calculated. They found that the integral of the difference spectra was proportional to ΔT within this narrow temperature range. This differential luminescence thermometry method allowed them to resolve temperature changes down to at least 1 K and measure a 16 K local temperature drop in the sample when pumped at 1015 nm with 770 mW. The same technique was used by Luo to measure a 21 K temperature drop in a ZBLAN:Yb³⁺ fiber (Luo et al., 1998). Gosnell used a similar approach but could not rely on a linear dependence of the magnitude of the difference spectra on temperature because of the larger 65 K temperature drop observed in his experiment (Gosnell, 1999). Rather, he recorded reference spectra in 1 K intervals from 140 K to room temperature and subsequently deduced the temperature by a least-squares comparison of the sample spectrum and the reference spectra. Similar experiments using differences of the full luminescence spectra have been reported recently in Seletskiy et al. (2009, 2010b) and Melgaard et al. (2013a). The technique was also used to perform thermometry of a semiconductor payload that was attached to a laser-cooling crystal. Seletskiy et al. conducted an experiment in which a GaAs/InGaP double heterostructure attached to a YLF:Yb³⁺ crystal was cooled to 165 K in order to demonstrate the ability to cool a device by means of solid-state optical refrigeration (Seletskiy et al., 2010c). Probe light from a GaAs laser diode (25 mW at 650 nm) was launched through a Y-split optical fiber to excite the GaAs/InGaP payload, and its fluorescence was collected through the other fiber arm for detection by a spectrometer. The shift of the GaAs bandgap with temperature is well known and causes the GaAs luminescence spectrum to blue shift from ~ 850 nm at 265 K to ~ 839 nm at 165 K. This large change enabled thermometry to within ± 2 K at low temperatures, the limiting factor being the wavelength resolution of the spectrometer.

A variation of the full-spectrum techniques takes the difference in the luminescence intensity of only two spectral bands, an approach that was used by Patterson et al. (2010a,b, 2011). They collected the luminescence from ZBLAN:Yb³⁺ with a multimode optical fiber and divided the sample light into two beams using a nonpolarizing beam splitter. The first beam was passed through an interference filter having high transmittance in the $935 < \lambda < 965$ nm spectral range (band A), while the second beam was passed through a filter with a $995 < \lambda < 1010$ nm transmission range (band B).

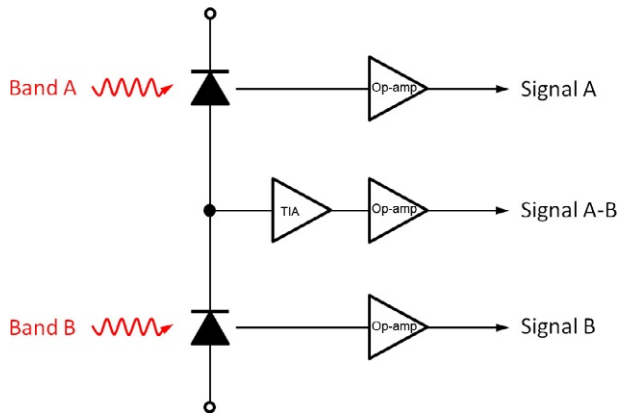


FIGURE 21 Functional block diagram of a detector using a pair of balanced photodiodes, a transimpedance amplifier (TIA), and operational amplifiers (op-amp's). This circuit is implemented in commercial balanced detectors such as PDB450C from Thorlabs.

The two beams were then detected by a pair of photodiodes having well-matched responsivities and being arranged according to the functional diagram shown in Fig. 21. The balanced detector provided signals that were proportional to the optical powers in each band. In addition, an ultralow-noise high-speed transimpedance amplifier (TIA) provided a signal whose magnitude was proportional to the difference signal A–B of the two luminescence intensities. The difference signal A–B was then used as a sensitive noncontact thermometer. The advantages of using a balanced detector include rejection of common-mode noise (e.g., noise in the luminescence signal due to fluctuation in the pump laser intensity) and corresponding improvement of the signal-to-noise ratio, possibility of high electric gain of the detected signal, and fast response time (>100 kHz bandwidth sampling rates). Seletskiy et al. used a similar balanced detection approach but improved on the light collection efficiency by coupling the light into a multimode fiber that was circular (600 μm diameter) on the input side and elongated (200 μm \times 5000 μm) on the output side, which served as the input to a monochromator (Seletskiy et al., 2008, 2011, 2013). A bicell-balanced detector was placed at the monochromator exit to detect the intensity of two spectral bands as described in the preceding text. Compared to Patterson et al.'s color filter approach, the use of a monochromator provided additional experimental flexibility for thermometry of Yb^{3+} and semiconductor (e.g., GaAs) payloads that fluoresce around 800–900 nm (Melgaard et al., 2010).

Rayner et al. used the strong temperature dependence of the luminescence from ZBLAN: Yb^{3+} at 950 nm directly as a thermometer rather than using reference or difference spectra (Rayner et al., 2001b, 2003). They performed a calibration by mounting the ZBLAN: Yb^{3+} fiber in good thermal contact with a Peltier device, exciting it with ~ 200 mW of laser light at 1015 nm, and

recording the luminescence intensity at 950 nm as a function of temperature as measured with a thermistor. Their calibration found an essentially linear intensity decrease of $\sim 20\%$ upon lowering the sample temperature from 298 to 268 K, corresponding to a sensitivity of 0.67%/K. Heeg et al. used the ratio of the ZBLAN:Yb³⁺ luminescence intensities at 950 and 973 nm as a thermometer (Heeg et al., 2004). The former is on the short-wavelength tail of the 973 nm luminescence peak of Yb³⁺, and the ratio is therefore sensitive to the decrease in homogeneous linewidth with decreasing temperature. They measured the ratio at 20 K intervals between 100 and 300 K with the sample in a liquid-nitrogen cryostat. An essentially linear dependence on temperature with a sensitivity of $\sim 0.45\%/K$ and a root-mean-square temperature variance of ~ 0.5 K were found. This allowed them to sensitively measure a 6 K temperature drop from room temperature by pumping the sample at 1027 nm with an absorbed power of 1.25 W. Sui et al. utilized the ratio of ${}^2H_{11/2} \rightarrow {}^4I_{15/2}$ (at 524 nm) and ${}^4S_{3/2} \rightarrow {}^4I_{15/2}$ (at 547 nm) luminescence from Er³⁺ as a thermometer, transitions that have been used extensively for thermometry before (Sui et al., 2013). The authors explored the possibility of using the closely spaced ${}^4S_{3/2}$ and ${}^2H_{11/2}$ multiplets for solid-state laser cooling in Er³⁺-doped telluride and germanate glasses. The ~ 800 cm⁻¹ ${}^4S_{3/2} \sim {}^2H_{11/2}$ multiplet spacing makes this a useful thermometer for higher temperatures, and they achieved a sensitivity of 0.65–0.85%/K around 550–600 K in different glasses. The sensitivity, conversely, is much lower at temperatures well below 300 K where $kT \ll 800$ cm⁻¹, likely limiting the usefulness of this technique to room-temperature material screening studies.

4.3 Measurement of Minimum Achievable Temperature

We have shown in Section 2.3 (Eq. 14) that the cooling efficiency, η_c , depends on the external quantum efficiency, η_e , and the background absorption coefficient, α_b . Furthermore, η_c depends on temperature via the temperature dependence of both the mean fluorescence wavelength, $\tilde{\lambda}_f$, and the pump absorption coefficient, α . Thus, for a given material pumped at λ_p , there will be a temperature—referred to as the minimum achievable temperature (MAT) (Seletskiy et al., 2008)—for which $\eta_c = 0$. The sample will show laser-induced cooling for $T > \text{MAT}$, while it will show laser-induced heating for $T < \text{MAT}$. Separate measurements of η_e , α_b , $\alpha(\lambda, T)$, and $\tilde{\lambda}_f(T)$ can serve as input for the calculation of the cooling efficiency as a function of both T and λ_p . An example of such a calculation is shown in Fig. 22C for a 5 mol% Yb³⁺-doped YLF crystal where the areas above (blue) and below (red) the white dividing line indicate regions of laser-induced heating and cooling, respectively, and the white dividing line indicates the MAT (Seletskiy et al., 2008, 2013). While there is a MAT for a given pump wavelength, there is also one global MAT that indicates the lowest possible temperature the material can be cooled to. In this case, the global MAT corresponds to exciting the E4 \rightarrow E5 crystal-field transition around

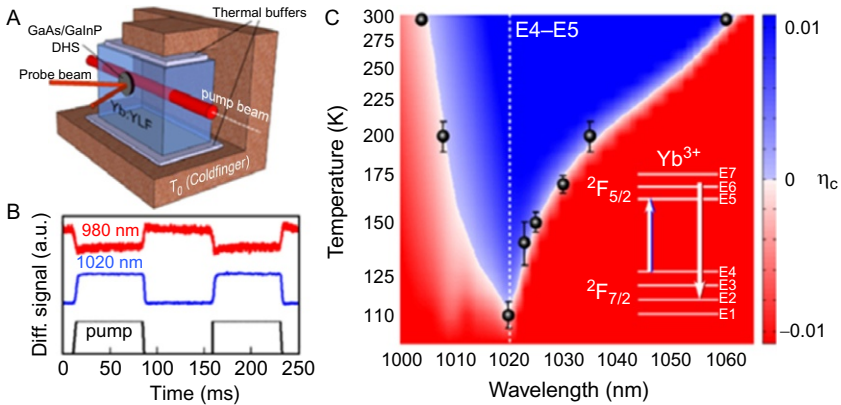


FIGURE 22 Measurement of the minimum achievable temperature (MAT) in an Yb^{3+} -doped YLF crystal (Seletskiy et al., 2011). (A) Experimental arrangement showing the YLF:Yb crystal mounted on a cold finger (temperature T_0) and being pumped by a tunable Ti:sapphire laser. Also shown is a small GaAs/GaInP double heterostructure (DHS) attached to the side of the crystal and being used for luminescence thermometry. (B) Examples of luminescence thermometry traces (at 300 K) for heating ($\lambda_p = 980$ nm) and cooling ($\lambda_p = 1020$ nm) as the pump laser is cycled on and off. (C) Calculated cooling efficiency (η_c) as a function of temperature and pump wavelength with the red area (above the white dividing line) and the blue area (below the white dividing line) indicating regions of laser-induced heating and cooling, respectively, and the white dividing line indicating the MAT.

1020 nm (see Fig. 9 and insert in Fig. 22C). Seletskiy et al. performed luminescence thermometry experiments in order to experimentally verify the calculated MAT. They mounted the YLF:Yb $^{3+}$ crystal on a cold finger in a liquid-nitrogen cryostat that allowed them to hold the sample at different temperatures T_0 (see Fig. 22C). As described in Section 2.2, they attached a GaAs/GaInP double heterostructure to the side of the laser-cooling crystal, excited it with a weak GaAs laser diode, and observed the differential luminescence using a balanced photodiode. They achieved ~ 250 μK temperature resolution on a submillisecond timescale with this technique, allowing them to follow the rapid local temperature change as the pump laser was turned on. As shown in Fig. 22B, the signs of the signals obtained from cooling and heating conditions are reversed. They fixed the pump wavelength and then measured the differential luminescence signal at various sample temperatures T_0 in order to find the MAT at which crossover from cooling to heating occurred. The results are shown as black circles in Fig. 22C, and they provided excellent confirmation of the theoretical predictions from Eq. (14).

5 LANTHANIDE-DOPED LASER-COOLING MATERIALS

5.1 Yb^{3+} -Doped Materials

Glasses and crystals doped with Yb^{3+} represent the majority of laser-cooling materials studied to date. Table 1 summarizes the systems in which net laser-induced bulk cooling has been observed experimentally. The dominance of

TABLE 1 Yb³⁺-Doped Materials for Which a Net Laser-Induced Bulk-Cooling Effect Has Been Reported

Host	Yb	ΔT (K)	Final T (K)	P_{pump} (W)	λ_{pump} (nm)	Notes	References
YLiF ₄ (YLF)	10%	178.5	93	54	1020	Brewster cut, $\vec{E} \parallel \vec{c}$, $\alpha_b = 2.0 \times 10^{-4} \text{ cm}^{-1}$, $\eta_e = 0.996$, nonresonant cavity, external mirrors	Melgaard et al. (2014)
YLiF ₄ (YLF)	10%	185	114	50	1020	Brewster cut, $L = 12 \text{ mm}$, $\vec{E} \parallel \vec{c}$, $\alpha_b = 2.0 \times 10^{-4} \text{ cm}^{-1}$, $\eta_e = 0.996$, nonresonant cavity, external mirrors	Melgaard et al. (2013a)
YLiF ₄ (YLF)	5%	162	123	40	1020	Brewster cut, $L = 12 \text{ mm}$, $\vec{E} \parallel \vec{c}$, $\alpha_b = 4.6 \times 10^{-4} \text{ cm}^{-1}$, $\eta_e = 0.995$, nonresonant cavity, external mirrors	Melgaard et al. (2013a)
YLiF ₄ (YLF)	5%	176	124	45	1020	Brewster cut, $3 \times 3 \times 12 \text{ mm}^3$, $\vec{E} \parallel \vec{c}$, nonresonant cavity, external mirrors, 50 mW heat lift	Melgaard et al. (2013b)
YLiF ₄ (YLF)	7%	155	130	12	1020	Brewster cut, $2 \times 2 \times 2 \text{ mm}^3$, $\vec{E} \parallel \vec{c}$, intracavity VECSEL, 150 mW heat lift	Ghasemkhani et al. (2014)
YLiF ₄ (YLF)	5%	145	155	9	1023	Brewster cut, $3 \times 3 \times 11 \text{ mm}^3$, $\vec{E} \parallel \vec{c}$, nonresonant cavity, external mirrors, 90 mW heat lift	Seletskiy et al. (2010b)
YLiF ₄ (YLF)	5%	143	164	15.5	1022	Brewster cut, $L = 11 \text{ mm}$, $\vec{E} \parallel \vec{c}$, resonant cavity, 110 mW heat lift	Seletskiy et al. (2009)
YLiF ₄ (YLF)	5%	135	165	9	1023	Brewster cut, $\vec{E} \parallel \vec{c}$, nonresonant cavity, external mirrors, attached GaAs/GaN load ($2 \mu\text{m}$ thick, $800 \mu\text{m}$ diameter)	Seletskiy et al. (2010c)

ZBLANP glass	2 wt%		208	10	1026	8 mm diameter, $L=8$ mm, nonresonant cavity, dielectric mirrors on sample, 29 mW heat lift	Thiede et al. (2005)
YLiF ₄ (YLF)	5%	69		45	1030	Piezoelectrically controlled Fabry-Pérot cavity	Seletskiy et al. (2008)
ZBLANP glass	1 wt%	65		2.2	1015	Multimode fiber, 175 μ m diameter core, $L=7$ mm, double pass	Gosnell (1999)
ZBLAN glass		48		1.6	1030	Fiber preform, 12 mm diameter, $L=10$ mm, nonresonant cavity, dielectric mirrors on sample	Edwards et al. (1999)
ZBLANP glass	1 wt%	21		1.36	1015	Multimode fiber, 175 μ m diameter core, $L=10$ mm, single pass	Luo et al. (1998)
ZBLANP glass	1 wt%	16		0.77	1015	Multimode fiber, 250 μ m diameter core, $L=10$ mm, single pass	Mungan et al. (1997b)
ZBLAN glass	1 wt%	13		0.85	1015	Multimode fiber, 250 μ m diameter, 175 μ m diameter core, $L=40$ mm, single pass	Rayner et al. (2001a)
Y ₃ Al ₅ O ₁₂ (YAG)	2.3	8.9		1.8	1030	Nonresonant cavity, external mirrors	Epstein et al. (2001)
YLiF ₄ (YLF)	5	6.3		3	1025	$4 \times 4 \times 12$ mm ³ , single pass	Bigotta et al. (2007)
ZBLAN glass	2	6		6	1027	$2 \times 2 \times 3$ mm ³ , intracavity with KYW:Yb laser	Heeg et al. (2004)
BaY ₂ F ₈ (BYF)	2.5	4		3	1025	$3 \times 4 \times 10$ mm ³ , single pass	Bigotta et al. (2006a,b, 2007)

Continued

TABLE 1 Yb³⁺-Doped Materials for Which a Net Laser-Induced Bulk-Cooling Effect Has Been Reported—Cont'd

Host	Yb	ΔT (K)	Final T (K)	P_{pump} (W)	λ_{pump} (nm)	Notes	References
ZBLAN glass	1 wt%	3.7		1	1013	250 μm diameter, 175 μm diameter core, single pass	Rayner et al. (2001b)
Y ₃ Al ₅ O ₁₂ (YAG)	1 wt%	1.9		2.2	1030	Double pass	Sheik-Bahae et al. (2001)
Y ₂ SiO ₅ (YSO)	5%	1		0.75	1050	Single pass	Epstein et al. (2001)
ZBLANP glass	1 wt%	0.3			1015	2.5 \times 2.5 \times 6.9 mm ³ , single pass	Epstein et al. (1995)
ABCYS glass	2 wt%	0.13			1030		Guiheen et al. (2006)

Yb^{3+} is because of both fundamental and practical reasons. First, the simple energy-level structure of Yb^{3+} is advantageous since it most closely resembles the ideal case of a four-level laser-cooling cycle (see Fig. 9). The absence of any other excited states eliminates competing processes such as ESA and upconversion that are possible with ions such as Tm^{3+} (see Section 5.2) and Er^{3+} (see Section 5.3) and that can introduce nonradiative processes and associated internal heating. Second, the ${}^2\text{F}_{7/2} \leftrightarrow {}^2\text{F}_{5/2}$ transitions of Yb^{3+} have significantly larger cross sections than many 4f transitions of other lanthanides because of relatively strong electron–phonon coupling (Bigotta et al., 2006b), an effect that is more pronounced at the beginning and end of the lanthanide series (Buchanan et al., 1967; Lupei et al., 1999; Malta, 1995; Yen et al., 1964). This facilitates absorption of the pump laser light and relaxes the purity requirements (see Eq. 15). Third, the energy gap between the ${}^2\text{F}_{5/2}$ excited-state and the ${}^2\text{F}_{7/2}$ ground-state multiplet is $\sim 10,000 \text{ cm}^{-1}$, an energy that is large compared to the highest-energy optical phonons of many oxide and halide glasses and crystals (see Section 3.3). As a result, ${}^2\text{F}_{5/2}$ multiphonon relaxation rates are small compared to ${}^2\text{F}_{5/2}$ radiative relaxation, that is, the Yb^{3+} luminescence can have the high quantum efficiency that is desired for maximizing the laser-cooling efficiency (see Eq. 14). Fourth, high-power pump lasers in the $\sim 1 \mu\text{m}$ pump wavelength range of Yb^{3+} are available from commercial vendors. This facilitates initial laboratory-based studies and is also attractive for the development of deployable devices. High-power compact diode lasers with high efficiency and excellent reliability can, in principle, be manufactured at a desired Yb^{3+} pump wavelength. In contrast, high-power lasers operating around $1.9 \mu\text{m}$ (Tm^{3+}) or $3.1 \mu\text{m}$ (Dy^{3+}) are less mature.

5.1.1 Glasses

5.1.1.1 ZBLAN

Optical fibers made from fluoride glasses were a major focus of research and development in the 1980s and early 1990s (Tran et al., 1984). Fluoride glasses have an intrinsically low propagation loss in the near-IR spectral region ($1.5\text{--}4 \mu\text{m}$) where the sum of multiphonon absorption (increases toward longer wavelengths) and Rayleigh scattering (increases toward shorter wavelengths) is at a minimum (Gan, 1995). The theoretical propagation loss of $0.001\text{--}0.01 \text{ dB/km}$ held the promise of enabling long-haul fiber-optic telecommunication links with minimal need for expensive optical amplifiers and optoelectronic repeaters. Various fluoride glass compositions were developed commercially in very high purity and fabricated into fiber preforms from which optical fibers were then drawn. Despite intensive efforts, the goal of ultralow propagation loss was not reached in part because of issues with mechanical strength, scattering by noble metal and oxide inclusions, glass stability and crystallization, and chemical durability that are inherent to fluoride

glasses (Takahashi, 1992). The competing technology of using mechanically rugged and chemically stable silica-based fibers with higher propagation loss (~ 0.2 dB/km) in conjunction with erbium-doped fiber amplifiers penetrated the telecom market in the late 1990s, and research on fluoride glasses diminished considerably as a result. Besides scattering and multiphonon absorption losses intrinsic to fluoride glass, absorption by trace-metal impurities was another factor contributing to the overall propagation loss of a fluoride fiber. Common transition metals such as Fe^{3+} , Fe^{2+} , Cu^{2+} , Ni^{2+} , Co^{2+} , V^{2+} , Ti^{3+} , and Cr^{3+} have optical absorptions in the visible and near-IR spectral range (France et al., 1986) that had to be minimized in order to approach the intrinsic propagation loss. By the mid-1990s, therefore, tremendous progress had been made in the fabrication of high-purity fluoride glasses, and glass preforms with trace-metal concentrations in the 1–200 ppb range were available (Takahashi, 1992).

This advanced fluoride glass technology enabled the first observation of net solid-state laser cooling by Epstein in 1995 as described in Section 1.3 (Epstein et al., 1995). They used a preform of the fluoride glass ZBLANP doped with Yb^{3+} . The acronym stands for the constituents ZrF_4 – BaF_2 – LaF_3 – AlF_3 – NaF – PbF_2 , a glass composition that is part of the family of heavy-metal fluoride glasses. Such glasses were first discovered around 1974 by Lucas, Poulain, and coworkers who used ZrF_4 as the primary glass former, BaF_2 as the main network modifier, and other fluorides such as ThF_4 , LaF_3 , and alkali fluorides as glass stabilizers (Tran et al., 1984). An important property of a glass is its stability against crystallization (devitrification), which typically increases with increasing difference $T_x - T_g$ between the glass transition (T_g) and the crystallization (T_x) temperature. Fluoride glasses are generally more prone to devitrification than oxide glasses, making their fabrication significantly more challenging. Fluorozirconate glasses with at least four constituents have $T_x - T_g$ in the range of 100–150 K and are among the most stable fluoride glasses, with ZBLAN consisting of 53% ZrF_4 –20% BaF_2 –4% LaF_3 –3% AlF_3 –20% NaF (mol%) being a common composition. Besides limited glass stability, the synthesis of fluoride glasses poses several additional challenges. Fluoride melts have low viscosity and readily react with oxygen and water present in the ambient atmosphere or crucible materials. Moreover, Zr^{4+} has a tendency to undergo reduction to Zr^{3+} or even lower oxidation states in the melt, causing the formation of black residue and associated absorption and scattering loss in the final glass. A typical fabrication begins with the thorough fluorination of the starting materials in order to reduce oxide contaminations. This is most effectively achieved by treatment of the metal oxides or nominal metal fluorides in hydrogen fluoride (HF) gas at elevated temperatures. All subsequent steps have to be carried out under inert atmosphere in glove boxes. The mix of starting fluorides is then melted under either inert (Ar, N_2 , or He) or reactive (CCl_4 , SF_6 , HF, CF_4 ,

or BF_4) atmosphere. The latter is often used to convert zirconium to the desired Zr^{4+} oxidation state without having to introduce an oxygen-based oxidizer. Melting is performed in nonreactive crucible materials such as glassy carbon, platinum, or gold (Tran et al., 1984), and it is followed by casting of the melt into preheated molds for solidification, controlled cooling, and finally annealing of the glass.

A typical glass composition used for many of the early laser-cooling studies was 53% ZrF_4 –18% BaF_2 –3% LaF_3 –3% AlF_3 –20% NaF –2% PbF_2 –1% YbF_3 (ZBLANP: Yb^{3+}) (Murtagh et al., 1999b). They were custom fabricated by commercial vendors from ultrahigh-purity starting materials in a process that typically involved melting at 950 °C in glassy carbon crucibles for 1 h in inert atmosphere, reactive atmosphere processing (SF_6 gas) at 775 °C for 1 h to lower the amounts of residual oxygen impurities and reduce zirconium species, and finally casting. The samples were produced as cylindrical preforms consisting of an Yb^{3+} -doped core comprising $\sim 70\%$ of the total diameter and an undoped ZBLAN cladding having a refractive index that was $\sim 1\%$ lower than the 1.52 index of the core (often by addition of HfF_4 to the composition), creating a structure with a numerical aperture of 0.2 (Mungan et al., 1997b). Some studies used the preforms as is (Edwards et al., 1999; Thiede et al., 2005). They polished the endfaces to high optical quality and applied a dielectric coating to create a nonresonant cavity. The pump light was launched into the cavity through a small (< 1 mm diameter) pinhole in one of the mirrors at an off-normal angle to achieve multipass excitation of the Yb^{3+} -doped core. Edwards et al. achieved 48 K of cooling from room temperature with such a geometry by pumping a ZBLAN: Yb^{3+} sample with 1.6 W at 1030 nm (Edwards et al., 1999). The largest net laser cooling in this geometry was achieved by Thiede et al. who cooled a 2% Yb^{3+} -doped ZBLANP glass to 208 K from room temperature using ~ 10 W of pump light from a diode-pumped YAG: Yb laser operating at 1026 nm (Thiede et al., 2005). This result is the lowest temperature achieved to date using an Yb^{3+} -doped glass host. Other studies drew the preform into a multimode fiber to improve the confinement of the pump light to the Yb^{3+} -doped core (Gosnell, 1999; Luo et al., 1998; Mungan et al., 1997b; Rayner et al., 2001a,b). They launched pump light into the fiber core (typically 175 μm diameter) in a single-pass geometry or, by addition of a retroreflector at the output, a double-pass geometry. The largest net cooling of a ZBLAN multimode fiber was achieved by Gosnell using a 1 wt% Yb^{3+} -doped sample in a double-pass geometry producing cooling by 65 K from room temperature when pumped with 2.2 W at 1015 nm (Gosnell, 1999). Besides using higher power than previous experiments, Gosnell et al. also implemented a multimode silica fiber to achieve transverse-mode scrambling of the pump laser prior to launch into the ZBLAN: Yb^{3+} fiber. This reduced optical saturation and thus increased the absorbed power and cooling power compared to pumping with a single-mode beam.

5.1.1.2 Other Glasses

As discussed earlier in the text, the standard composition of ZBLAN glass contains 4 mol% of LnF_3 . Increasing the LnF_3 content to above ~ 6 mol% causes the glass to become increasingly unstable. This is a drawback for laser cooling because higher Yb^{3+} concentrations are generally desired as they afford a greater resonant absorption coefficient α and may enable a greater net cooling power density (see Eq. 11). This is one of the reasons why some glass compositions other than ZBLAN have been considered. The family of fluoride glasses of general composition $\text{BaF}_2\text{-InF}_3\text{-GaF}_3\text{-ZnF}_2\text{-LuF}_3\text{-GdF}_3$ (BIG) is stable for higher lanthanide fluoride concentrations than ZBLAN. For example, the composition 30% BaF_2 -18% InF_3 -12% GaF_3 -20% ZnF_2 -10% YbF_3 -6% ThF_4 -4% ZrF_4 (mol%) (BIGaZYbTZr) contains 10 mol% Yb^{3+} and has been considered for laser cooling (Murtagh et al., 1999b). Another family of glasses is fluorochlorides such as the composition $\text{CdF}_2\text{-ClCl}_2\text{-NaF-BaF}_2\text{-BaCl}_2\text{-ZnF}_2$ (CNBZn). The admixture of heavier chloride ions to a fluoride glass lowers the average phonon energy and will tend to reduce multiphonon relaxation rates. This may be of particular value for laser cooling with Ln^{3+} ions having a low energy of the first excited state such as Tm^{3+} , Ho^{3+} , or Dy^{3+} (see Fig. 7). Fernandez et al. had studied optical refrigeration in BIG (Fernández et al., 2000, 2001a) and CNBZn (Fernández et al., 2000, 2001a,b, 2012) glasses doped with 1 mol% Yb^{3+} . Photothermal deflection measurement showed that CNBZn: Yb^{3+} had an estimated cooling efficiency of 2.0% at 300 K when pumped at 1010 nm, while the cooling efficiency of the BIG: Yb^{3+} glass was estimated to be only $\sim 0.6\%$.

5.1.2 Crystals

5.1.2.1 Oxide Crystals

The need for nonhygroscopic materials with high hardness and high thermal conductivity has made oxide crystals attractive soon after the first experimental demonstration of laser cooling in Yb^{3+} -doped fluoride glasses that do not possess these properties. Furthermore, it was recognized early that the higher peak absorption cross sections in crystals compared to glasses would be advantageous for laser cooling to low temperatures (Bowman and Mungan, 2000). Bowman and Mungan were the first to demonstrate laser cooling in a crystal (Bowman and Mungan, 2000). They used the photothermal deflection technique to look for signs of cooling in Yb^{3+} -doped $\text{KGd}(\text{WO}_4)_2$ (KGW), YLiF_4 (YLF), and $\text{Y}_3\text{Al}_5\text{O}_{12}$ (YAG) crystals. While no net bulk cooling was achieved, they observed local internal cooling in 3.5 at% Yb^{3+} -doped $\text{KGd}(\text{WO}_4)_2$ when the pump laser was tuned to wavelengths > 1009 nm, that is, to wavelengths longer than the mean emission wavelength of 993 nm.

The first crystal host to show net laser-induced bulk cooling was Yb^{3+} -doped YAG (Epstein et al., 2001). The authors pumped a 1 wt% Yb -doped YAG crystal with 2.2 W of laser power at 1030 nm in a double-pass

geometry and observed a temperature drop of 1.9 K from room temperature. YAG is particularly attractive because its thermal conductivity is $14\times$ greater than that of ZBLAN glass (13 vs. 0.9 W/m K), and it is mechanically rugged and chemically stable. The main drawback is its higher refractive index (1.93) compared to ZBLAN (1.5), which enhances undesired trapping and reabsorption of the fluorescence within the crystal and thus reduces the external quantum efficiency. YAG also has a higher phonon energy ($\sim 630\text{ cm}^{-1}$) which, however, should still allow for near-unity quantum yield of the Yb^{3+} excited state. Epstein et al. performed detailed spectroscopic studies on a commercial YAG: Yb^{3+} crystal. They found an internal quantum efficiency of 98.8% and a background absorption coefficient of $2.2 \times 10^{-4}\text{ cm}^{-1}$. The crystal showed internal cooling down to 252 K in a photothermal deflection setup. The crystal was then placed onto the edges of glass cover slides in a vacuum chamber (10^{-6} Torr) to minimize conductive and convective heat loads. The crystal temperature was measured with a thermal camera through a NaCl window as the crystal was excited at 1030 nm with 750 mW from a Ti:sapphire laser of which only $\sim 10\%$ was absorbed. They observed a temperature drop of 0.36 K from room temperature. In a subsequent experiment, a nonresonant external cavity was created around the YAG:2.3% Yb^{3+} crystal, and a temperature drop of 8.9 K was measured in this multipass pump geometry. Epstein et al. also showed 1 K of bulk cooling in a $\text{Y}_2\text{SiO}_5:\text{Yb}^{3+}$ crystal pumped at 1050 nm (Epstein et al., 2001).

5.1.2.2 KPb_2Cl_5 (KPC)

KPC has a very low maximum phonon energy of $\sim 203\text{ cm}^{-1}$ (Nostrand et al., 2001) and may therefore enable high quantum efficiencies even in laser-cooling ions that have a small energy gap (Er^{3+} , Tm^{3+} , Ho^{3+} , and Dy^{3+}). Most strikingly, KPC is one of only two chloride hosts known to be only slightly hygroscopic (see Section 5.3). Mendioroz et al. studied laser cooling of a KPC crystal doped with $\sim 5 \times 10^{19}\text{ Yb}^{3+}\text{ cm}^{-3}$ (Mendioroz et al., 2002). KPC is monoclinic and crystallizes in the space group $P2_1/c$ with a unit cell volume of 876.3 \AA^3 ($Z=4$) (Merkulov et al., 2005), suggesting that their doping level corresponded to $\sim 0.55\text{ mol}\%$ Yb^{3+} with respect to Pb^{2+} . The KPC: Yb^{3+} single crystal was grown in a two-zone Bridgman furnace under a chloride atmosphere at a growth rate of 1 mm/h. A $4.6 \times 4 \times 3.3\text{ mm}^3$ sample was cut from the boule and polished. They measured a mean fluorescence wavelength of $\tilde{\lambda}_f = 986\text{ nm}$ at 300 K and observed internal laser cooling for pump wavelengths $>986.5\text{ nm}$ using a photothermal deflection technique. A cooling efficiency of 0.2% at room temperature was deduced from the measurement, a value that was low because of the relatively low Yb^{3+} concentration.

5.1.2.3 BaY_2F_8 (BYF)

The group of Tonelli and Di Lieto at the University of Pisa (Italy), have performed extensive studies on Yb^{3+} -doped fluoride crystals. Before their work,

solid-state laser cooling focused primarily on Yb^{3+} -doped fluoride glasses such as ZBLAN. Work on Yb^{3+} -doped crystals had been minimal with small net bulk cooling observed in YAG (Sheik-Bahae et al., 2001) and $\text{Y}_2\text{Si}_2\text{O}_5$ (Epstein et al., 2001) and internal laser cooling detected in KPb_2Cl_5 (Mendioroz et al., 2002) and $\text{KGd}(\text{WO}_4)_2$ (Epstein et al., 2001) by using the photothermal deflection technique. In 2006, Bigotta et al. reported laser cooling in an Yb^{3+} -doped BaY_2F_8 (BYF) single crystal (Bigotta et al., 2006a). BYF has a monoclinic crystal structure ($C2/m$) with two BYF formula units per unit cell (Izotova and Aleksandrov, 1970). This crystal has a number of attractive properties. The low phonon energy of $\sim 350\text{ cm}^{-1}$ (Toncelli et al., 1999) is expected to completely suppress multiphonon relaxation of the $^2\text{F}_{5/2}$ excited state, enabling a high internal quantum efficiency. The crystal has high transparency in the IR up to $12\text{ }\mu\text{m}$, making it less susceptible to radiative heat loading than materials with narrower transparency ranges (such as fluoride glasses and oxide crystals). The thermal conductivity of BYF is $\sim 7\times$ greater than that of ZBLAN glass (Bigotta et al., 2006b), facilitating the extraction of heat in an optical refrigerator. Finally, in contrast to fluoride glasses such as ZBLAN, fluoride crystals such as BYF are not moisture-sensitive, facilitating the preparation of high-quality samples and guaranteeing long-term durability.

Bigotta et al. grew a BYF crystal doped with 2.5 mol% Yb^{3+} (with respect to the Y^{3+} site) using a Czochralski crystal growth furnace and performed an extensive study of the spectroscopic and laser-cooling properties of this sample (Bigotta et al., 2006b, 2007). The starting material was BaY_2F_8 to which BaF_2 and YbF_3 powders were added to achieve the desired doping level. The powders were treated in hot HF gas by AC Materials (Tarpon Springs, FL, the United States) in order to reduce oxygen impurities such as water and OH^- , and they had an estimated purity of 99.999%. The starting materials were baked out in vacuum (10^{-5} Pa), and the subsequent crystal growth was carried out in an atmosphere of high-purity argon and CF_4 . The latter had to be added to prevent the reduction of Yb^{3+} to Yb^{2+} . The Czochralski crystal growth was performed with resistive heating at $995\text{ }^\circ\text{C}$, a pulling rate of 0.5 mm/h , and the crystal rotating at 5 rpm . The system had an automatic optical diameter control and yielded a sample of high optical quality and free of cracks or micro-bubbles. The crystal was oriented by the X-ray Laue technique, and an $\sim 3\times 4\times 10\text{ mm}^3$ sample was cut and polished such that the a - and b -axes were oriented parallel to the shorter sides of the sample. Careful absorption and emission spectroscopy at 10 K allowed the identification of purely electronic transitions, yielding the crystal-field level energies of 0 , 215 , 447 , and 546 cm^{-1} for the $^2\text{F}_{7/2}$ ground-state multiplet and $10,306$, $10,425$, and $10,770\text{ cm}^{-1}$ for the $^2\text{F}_{5/2}$ excited-state multiplet. Importantly, Bigotta et al. pointed out that the absorption spectrum offered peaks that were spectrally narrower and therefore had higher peak cross section (e.g., the $\text{E3}\rightarrow\text{E5}$ transition around 1015 nm ; see Fig. 23, left) than corresponding transitions in

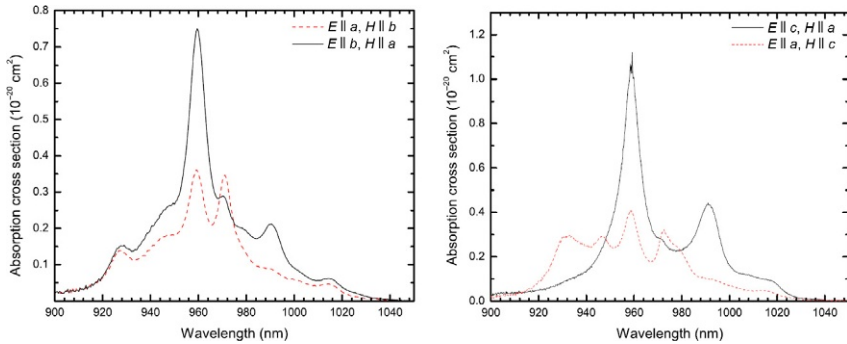


FIGURE 23 Polarized absorption spectra of $\text{BaY}_2\text{F}_8:2.5\%\text{Yb}^{3+}$ (left) and $\text{YLiF}_4:5\%\text{Yb}^{3+}$ (right) at room temperature. Reproduced with permission from *Bigotta et al. (2007)*.

ZBLAN glass. This is a result of the much reduced inhomogeneous broadening in the crystal compared to the glass and allows more efficient excitation of Yb^{3+} . A ${}^2\text{F}_{5/2}$ lifetime of 2.0 ms and a mean fluorescence wavelength $\tilde{\lambda}_f = 995$ nm were measured at 300 K. They used a pair of diode lasers mounted with their junctions oriented perpendicularly, operating at 1024 nm (~ 2 nm bandwidth) and providing ~ 3 W of pump power. The crystal was mounted in a $10 \times 10 \times 10$ cm³ steel vacuum chamber (< 0.1 Pa) by suspending it on two crossed microscope cover slips in order to minimize the convective and conductive heat loads from the environment. The crystal temperature was measured by a thermal camera (calibrated against a thermocouple) that imaged the crystal through a BaF_2 window. The crystal showed a temperature drop of 4 K (starting from 293 K) in ~ 30 min when pumped in a single-pass configuration. From these measurements, a cooling power of 2.4 mW and a cooling efficiency of $\sim 3\%$ were estimated. The laser diodes had limited tunability and prevented excitation of the sample at the predicted optimum wavelength of 1015 nm.

5.1.2.4 YLiF_4 (YLF)

Bigotta et al. presented a first laser-cooling study of Yb^{3+} -doped YLiF_4 (YLF) in 2007 (*Bigotta et al., 2007*). YLF is one of the most common laser materials. It has a scheelite structure and crystallizes in the $I4_1/a$ space group (*Bensalah et al., 2004*). The thermal conductivity is 6.3 W/m K (*Bigotta et al., 2007*), similar to that of BYF. The highest phonon energy in YLF is ~ 450 cm⁻¹ (*Orlovskii et al., 2002*), which is higher than that of BYF (~ 350 cm⁻¹) but still sufficiently low to suppress multiphonon relaxation of the ${}^2\text{F}_{5/2}$ excited state. Bensalah et al. performed a detailed study of $\text{YLF}:\text{Yb}^{3+}$ and reported the crystal-field level energies of 0, 218, 248, and 485 cm⁻¹ for the ${}^2\text{F}_{7/2}$ ground-state multiplet and 10,293, 10,416, and 10,554 cm⁻¹ for the ${}^2\text{F}_{5/2}$ excited-state multiplet. Note that the total crystal-field splitting of the ground state in

YLF:Yb³⁺ is smaller ($\delta E_g = 485 \text{ cm}^{-1}$) than in BYF:Yb³⁺ ($\delta E_g = 546 \text{ cm}^{-1}$), which may, in principle, allow YLF:Yb³⁺ to reach lower temperatures (see Section 2.3).

Bigotta et al. used a Czochralski furnace to grow a 5 mol% Yb³⁺-doped YLF crystal at a pulling rate of 1 mm/h at 845 °C (Bigotta et al., 2007). The starting materials and growth conditions were otherwise identical to the BYF crystal growth described in Section 5.1.2.3. The crystal was oriented by the X-ray Laue technique, and an $\sim 4 \times 4 \times 12 \text{ mm}^3$ sample was cut and polished such that the *a*- and *c*-axes were oriented parallel to the shorter sides of the sample. The sample had a mean fluorescence wavelength of $\tilde{\lambda}_f = 1002 \text{ nm}$ at 300 K. As shown in Fig. 23, the Yb³⁺ absorption cross section was found to be greater in YLF than in BYF, which compensated for its longer mean fluorescence wavelength. They pumped the crystal in single-pass configuration with 2.6 W at 1026 nm in the vacuum chamber geometry described in Section 5.1.2.3 and observed a temperature drop of 6.3 K with an estimated cooling efficiency of $\sim 2\%$.

Since 2008, the focus has been on using Czochralski-grown YLF crystals doped with varying amounts (1–10%) of Yb³⁺ for the development of optical refrigerators that can reach temperatures in the cryogenic regime. Research and further progress on Yb³⁺-doped glasses had essentially ceased since Thiede et al. cooled ZBLANP:Yb³⁺ glass to 208 K in 2005 (Thiede et al., 2005). Significant effort was now devoted to developing the optical, thermal, and mechanical aspects of the pump cavities the crystals were placed in. Seletskiy et al. in collaboration with Bigotta and Tonelli built on recent success with YLF:Yb³⁺ and introduced a cavity-enhanced resonant absorption scheme (Seletskiy et al., 2008). They placed a YLF:5%Yb³⁺ crystal inside an actively stabilized Fabry–Pérot cavity that allowed them to achieve $\sim 89\%$ absorption of the incident pump light (see Section 6.1). The $\sim 45 \text{ W}$ output of a YAG:Yb disk laser operating at 1030 nm was used to pump the crystal, inducing a temperature drop of 69 K from room temperature. Additional measurements showed that this particular crystal had a MAT of $170 \pm 10 \text{ K}$, that is, its cooling potential was not fully realized in this experiment.

Shortly thereafter, the same team demonstrated a temperature drop of 143 K with a YLF:Yb³⁺ crystal placed in a similar actively stabilized cavity (Seletskiy et al., 2009). The sample was a Czochralski-grown YLF crystal doped with 5% Yb³⁺, Brewster-cut (see Section 6.1 for details) to a length of 1.1 cm, and oriented such that its crystal *c*-axis was parallel to the polarization of the laser. A 15.5 W pump laser operating at 1022 nm near the E4 → E5 absorption at 1020 nm was used (see Fig. 23, right), producing a heat lift of $\sim 110 \text{ mW}$ at the lowest crystal temperature. A careful spectroscopic analysis of this crystal allowed them to use Eq. (14) with $\alpha_b = 4 \times 10^{-4} \text{ cm}^{-1}$ and measured fluorescence spectra to calculate the wavelength dependence of the cooling efficiency at different temperatures (Fig. 24). These data showed

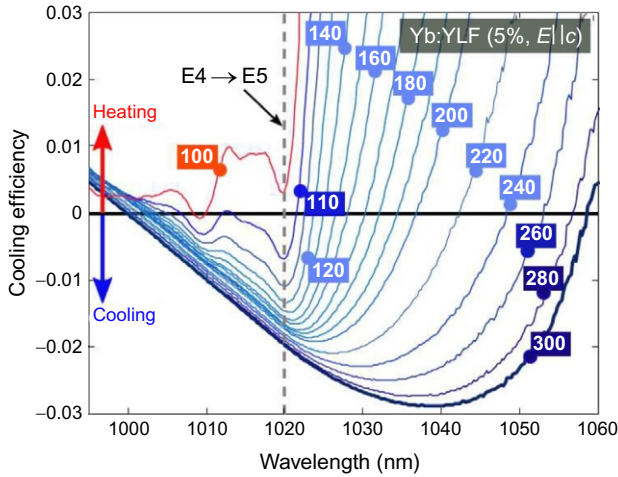


FIGURE 24 Measurement of cooling efficiency as a function of wavelength at different temperatures (in Kelvin, boxed values) in a 5% Yb^{3+} -doped YLF crystal excited with laser light-polarized parallel to the crystal c -axis (Seletskiy et al., 2009). Given the level of background absorption in this crystal, a minimum achievable temperature (MAT) of ~ 105 K is predicted for pumping the $E4 \rightarrow E5$ transition at 1020 nm.

that a minimum temperature of ~ 105 K could be possible with this sample for resonant excitation of $E4 \rightarrow E5$ at 1020 nm and indicated that cryogenic temperatures would be within reach. This result of net cooling by 143 to ~ 164 K with a 110 mW heat lift not only set a new laser-cooling record but also surpassed the lowest temperatures of ~ 180 K that can practically be reached with thermoelectric refrigerators (Mills et al., 2002). Some subsequent improvements allowed this crystal to cool to 155 ± 1 K with a heat lift of 90 mW (Seletskiy et al., 2010b).

5% Yb^{3+} -doped YLF crystals were also used in experiments that cooled a GaAs/InGaP semiconductor load attached to the cooling crystal to 165 K (Seletskiy et al., 2010c). This crystal composition was also used for recent experiments that demonstrated laser cooling to 124 K (Melgaard et al., 2013b). The latest record-cooling results were achieved with 10% Yb^{3+} -doped crystals, which enabled cooling to 114 K (Melgaard et al., 2013a) and 93 K (Melgaard et al., 2014).

5.2 Tm^{3+} -Doped Materials

The first excited state of Tm^{3+} (3F_4) is at approximately half the energy of the first excited state of Yb^{3+} ($^2F_{5/2}$; see Fig. 7). Therefore, the cooling efficiency of Tm^{3+} -doped materials can potentially be about twice as high than for Yb^{3+} -doped materials (see Eq. 14), making Tm^{3+} attractive for optical refrigeration. Multiphonon relaxation of the 3F_4 excited-state to the 3H_6

ground-state multiplet is insignificant in fluorides (maximum phonon energy 350–600 cm^{-1} ; see Fig. 12) given the $\sim 5000 \text{ cm}^{-1}$ energy gap, enabling the required high quantum efficiency of the emitting state. Note that there is inconsistency in the literature regarding the notation of the first excited state of Tm^{3+} . Some studies refer to it as ${}^3\text{H}_4$, which originates from the somewhat confusing albeit correct labeling of the ${}^3\text{H}$ and ${}^3\text{F}$ manifold levels in the original paper by Dieke and Crosswhite (1963). The correct notation of the first excited state of Tm^{3+} is ${}^3\text{F}_4$ as shown in Fig. 7 (Hehlen et al., 2013).

Tm^{3+} -doped ZBLANP glass was the first non- Yb^{3+} -based solid to be cooled (Hoyt, 2003; Hoyt et al., 2000). Hoyt et al. demonstrated that the cooling efficiency scales inversely with the energy gap as expected from Eq. (5). Several studies of net bulk laser cooling in Tm^{3+} -doped materials have been reported in the 2000–2008 time period, and the respective results are summarized in Table 2. Compared to Yb^{3+} , however, Tm^{3+} has received considerably less attention. There are no fundamental obstacles for laser cooling to cryogenic temperatures with Tm^{3+} , and the reasons for the limited number of efforts seem to have more practical origins. For example, all laser-cooling studies with Tm^{3+} reported to date (Table 2) used rather complex Nd:YAG laser-pumped OPOs. Turn-key thulium-fiber lasers with $>100 \text{ W}$ output power have only recently become available at the $\sim 1900 \text{ nm}$ pump wavelength of the ${}^3\text{H}_6 \rightarrow {}^3\text{F}_4$ transition. Such lasers are much less commonly found in laboratories than the widespread commercial tunable Ti:sapphire or semiconductor diode lasers, which may have biased research toward Yb^{3+} materials. Furthermore, the recent advances in the thermal and optical design of laser-cooling cavities achieved with YLF:Yb $^{3+}$ (see Section 6) have not yet been applied to Tm^{3+} -doped crystals for which they promise to allow for equally dramatic improvements of laser-cooling performance. A revival of laser-cooling research on Tm^{3+} -doped materials may therefore be called for and result in high-efficiency cryogenic optical refrigerators in the not too distant future.

5.2.1 Glasses

The only glass in which net cooling with Tm^{3+} has been reported is ZBLANP:Tm $^{3+}$. Sheik-Bahae et al. first observed laser cooling by 1.25 K in ZBLANP:Tm $^{3+}$ in 2000 (Sheik-Bahae et al., 2000). Follow-up studies by Hoyt et al. reported laser cooling in a ZBLANP glass sample doped with 1 wt% Tm^{3+} cut from a high-purity fiber preform (Hoyt et al., 2000; Sheik-Bahae et al., 2001). The sample was pumped by a Nd:YAG pumped OPO having an average output power of 6.2 W and tunability across the 1750–2050 nm wavelength range. The sample was placed on thin glass supports in a vacuum chamber and showed 1.2 K of cooling from room temperature when pumped at 1900 nm in single-pass configuration with 40 mW of absorbed power. The result is presented in Fig. 17 where the normalized temperature change is shown for different pump wavelengths. The sample showed

TABLE 2 Tm³⁺-Doped Materials for Which a Net Laser-Induced Bulk-Cooling Effect Has Been Reported

Host	Tm	ΔT (K)	P_{pump} (W)	λ_{pump} (nm)	Notes	References
ZBLANP glass	1 wt%	19	3.5	1900	$4 \times 4 \times 8 \text{ mm}^3$, nonresonant cavity, external mirrors	Hoyt et al. (2003)
ZBLANP glass	1 wt%	8		1850	Internal reflections (monolithic optical maze)	Sheik-Bahae et al. (2001)
BaY ₂ F ₈ (BYF)	1.2%	3.2	4.4	1855	single pass	Patterson et al. (2008)
ZBLANP glass	2 wt%	2	2.72	1900	$3 \times 3 \times 10 \text{ mm}^3$, single pass	Hoyt et al. (2003)
BaY ₂ F ₈ (BYF)	2 wt%	1.5	6	1902	$7 \times 4.5 \times 4.5 \text{ mm}^3$, single pass	Patterson et al. (2004)
ZBLANP glass	1 wt%	1.25	3	1857	$5 \times 5 \times 9 \text{ mm}^3$	Sheik-Bahae et al. (2000)
ZBLANP glass	1 wt%	1.2	3	1900	$5 \times 5 \times 9 \text{ mm}^3$, single pass	Hoyt et al. (2000)

bulk cooling as the laser wavelength exceeded the mean fluorescence wavelength of 1820 nm, showed maximum cooling around 1900 nm, and heated at pump wavelengths >1965 nm due to background absorption by impurities. These first studies were followed by cooling of a ZBLANP:1 wt% Tm^{3+} sample in multipass pump geometry (Hoyt et al., 2003). A temperature drop of 19 K from room temperature was achieved (see Fig. 20, right), a result that still represents the current laser cooling record with Tm^{3+} . The authors also conducted measurements of the cooling efficiency and were able to experimentally confirm the expected factor of ~ 2 greater cooling efficiency in ZBLANP: Tm^{3+} compared to Yb^{3+} -doped systems.

5.2.2 Crystals

The only Tm^{3+} -doped crystal system studied so far has been $\text{BaY}_2\text{F}_8:\text{Tm}^{3+}$. In 2004, Patterson et al. reported laser cooling of a Tm^{3+} -doped crystal for the first time (Patterson et al., 2004). They used a $\text{BaY}_2\text{F}_8:\text{Tm}^{3+}$ crystal grown by the Czochralski method and pumped it in single-pass geometry using a high-power OPO with 4–6 W output power in the 1700–2100 nm tuning range to achieve cooling by ~ 1.5 K when pumping at 1902 nm. A second study by Patterson et al. used a high-purity BaY_2F_8 crystal doped with 1.2% Tm^{3+} pumped in single-pass geometry (Patterson et al., 2008). They measured a mean fluorescence wavelength of 1793 nm at room temperature and pointed out the advantageous higher peak absorption cross sections afforded by the crystalline host compared to the amorphous ZBLAN samples studied earlier. The measurement of normalized temperature drop for different pump wavelengths is shown in Fig. 25 and indicates maximum cooling at 1855 nm, where a net temperature drop of 3.2 K was obtained with 4.4 W of pump power. The solid curve shown in Fig. 25 is a fit to the experimental data and yielded a quantum efficiency of $\eta=0.98$ and a background absorption coefficient of $2 \times 10^{-4} \text{ cm}^{-1}$. The cooling efficiency was highest with 3.4% at a pump wavelength of 1934 nm.

5.3 Er^{3+} -Doped Materials

Several laser-cooling studies of Er^{3+} -doped materials have been reported, and the respective results are summarized in Table 3. Unlike Yb^{3+} , the $[\text{Xe}]4f^{11}$ electron configuration of Er^{3+} produces a large number of $^{2S+1}L_J$ electronic states (see Fig. 7). While any excited state can—in principle—be chosen for performing a laser-cooling cycle such as shown in Fig. 9, interference from other excited states has to be considered. Absorption from the excited state to even higher excited states (ESA) or multiphonon relaxation to a lower state may be possible. Two-ion processes such as energy-transfer upconversion, cross relaxation, or energy migration to defects may become active at higher Er^{3+} ion densities. While the other excited states may have a high quantum efficiency in low-energy phonon hosts, such side processes are in most cases

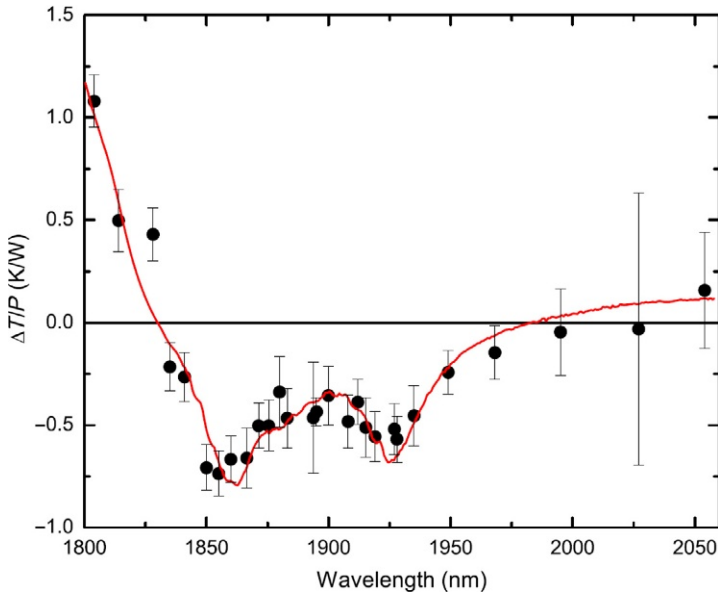


FIGURE 25 Normalized temperature change in 1.2% Tm^{3+} -doped BaY_2F_8 for $E||b$ pump polarization (Patterson et al., 2008). Data below the horizontal line indicate net cooling.

accompanied by some degree of exothermic nonradiative relaxation (heating) and are generally expected to be detrimental to laser cooling. This possible drawback, however, is offset by the possibility of implementing a cooling cycle with lower pump energy and thus potentially higher efficiency compared to Yb^{3+} . As seen in Fig. 7, the first excited state of Er^{3+} ($^4\text{I}_{13/2}$) is at an energy of $\sim 6400 \text{ cm}^{-1}$, that is, only about two-thirds of the energy of the $\text{Yb}^{3+} \text{ } ^2\text{F}_{5/2}$ excited state. Everything else being equal, this may allow for an $\sim 50\%$ higher cooling efficiency compared to Yb^{3+} .

5.3.1 KPb_2Cl_5 (KPC)

KPb_2Cl_5 (Nostrand et al., 2001) and $\text{Cs}_3\text{Tl}_2\text{Cl}_9$ (Kamber et al., 1998) are the only heavy-halide hosts known to be only slightly hygroscopic. While $\text{Cs}_3\text{Tl}_2\text{Cl}_9$ is attractive because it offers a crystallographic site for a M^{3+} ion and is therefore suited for doping with high concentrations of Ln^{3+} ions, the high toxicity of thallium poses challenges for sample preparation and handling. KPb_2Cl_5 is friendlier in this respect, but its Pb^{2+} site requires charge compensation when doping with Ln^{3+} ions. Jenkins et al. presented a spectroscopic study of Er^{3+} -doped KPC and concluded that Er^{3+} replaced Pb^{2+} accompanied by the formation of K^+ vacancies (Jenkins et al., 2003). The need for charge compensation and thus distortion of the crystal lattice limits the maximum doping level to $\sim 3\%$ (Condon et al., 2006). KPC is attractive for its very low maximum phonon energy of $\sim 203 \text{ cm}^{-1}$ (Nostrand et al.,

TABLE 3 Er³⁺-Doped Materials for Which a Net Laser-Induced Bulk-Cooling Effect Has Been Reported

Host	Er	ΔT (K)	P_{pump} (W)	λ_{pump} (nm)	Notes	References
KPb ₂ Cl ₅ (KPC)	0.5%	0.7	1.9	870	4.5 × 6.5 × 2.7 mm ³	Fernandez et al. (2006, 2012)
CNBZn glass	0.5%	0.5	1.9	860	10.7 × 10.7 × 2.2 mm ³	Fernandez et al. (2006, 2012)
KPb ₂ Cl ₅ (KPC)	3.6 × 10 ¹⁹ cm ⁻³	0.0136	0.0053	1567.6	3 mm diameter, L = 13.6 mm	Condon et al. (2009)

2001) that effectively suppresses multiphonon relaxation for most Er^{3+} excited states and thus enables high quantum efficiencies.

KPC crystals however have poor mechanical properties and are rather difficult to grow (Voda et al., 2004). Fernandez et al. grew a 0.5 mol% Er^{3+} -doped KPC single crystal in a sealed silica ampoule by the Bridgman technique (Fernandez et al., 2006). The KCl and PbCl_2 starting materials were first dried under vacuum at 220 °C in quartz vessels. The samples were then cooled, an atmosphere of high-purity argon and CCl_4 was introduced, and the temperature was raised from room temperature to 50 K above the melting point of the respective compound. Quantitative removal of oxygen and water traces was indicated when the meniscus of the melt in the vessel changed from concave to convex, that is, the melt became nonwetting (Voda et al., 2004). This was followed by zone refining with 5–10 passes in a horizontal furnace. The resulting starting materials were then mixed stoichiometrically because KPC melts congruently at 434 °C (Gabriel and Pelton, 1985). The mixture was again dried under vacuum, treated with Ar/CCl_4 , and finally sealed under chlorine atmosphere. The subsequent crystal growth was performed in a two-zone vertical and transparent Bridgman furnace at a growth rate of 1–2 mm/h and under tight temperature control to within 0.1 K at the location of crystallization. The resulting crystal boules were 12–16 mm in diameter and 20–40 mm long, from which a $4.5 \times 6.5 \times 2.7 \text{ mm}^3$ sized sample was cut. Photothermal deflection measurements were performed with the sample in a vacuum chamber ($\sim 10^{-2}$ mbar) and pumped by a 1.5 W tunable laser operating in the 835–875 nm range to excite the ${}^4\text{I}_{15/2} \rightarrow {}^4\text{I}_{9/2}$ transition, that is, the third excited state of Er^{3+} (see Fig. 7). Internal local laser cooling was observed when the pump wavelength exceeded ~ 852.5 nm. A subsequent bulk-cooling experiment utilized a thermal camera and found a temperature drop of ~ 0.7 K over the course of 1500 s when pumping at 870 nm with 1.9 W.

This work was followed in 2009 by Condon et al. who pumped the ${}^4\text{I}_{15/2} \rightarrow {}^4\text{I}_{13/2}$ transition at 1568 nm to excite Er^{3+} to its first rather than its third excited state (Condon et al., 2009). They grew a KPC crystal with a concentration of $3.6 \times 10^{19} \text{ Er}^{3+}/\text{cm}^3$ (i.e., ~ 0.39 mol% with respect to Pb^{2+}). They used a modified Bridgman technique with zone-refined KPC starting materials and an extended cooldown routine (Condon et al., 2006). A crystallographically oriented rod 3 mm in diameter and 13.6 mm long was cut from the boule, polished, and placed on the edges of glass cover slips inside a vacuum chamber. A fine-wire (0.001") thermocouple was put in contact with the surface in the middle of the crystal to allow for a direct temperature measurement. A mean fluorescence wavelength of $\tilde{\lambda}_f = 1539.8 \text{ nm}$ was measured at room temperature. Several low-power laser diodes were then used to provide pumping at different wavelengths. Bulk heating was observed for pumping at 1527.0 and 1533.3 nm ($\lambda < \tilde{\lambda}_f$), almost no temperature change was found for pumping at 1557.7 nm, and bulk cooling by 0.0072 and

0.0136 K was found for pumping at 1564.2 and 1567.6 nm, respectively. Note that the wavelength for crossover from heating to cooling occurred at a significantly longer wavelength (1557.7 nm) than $\tilde{\lambda}_f$ even though the quantum efficiency of the ${}^4I_{13/2}$ excited state was expected to be $\sim 100\%$. The authors attributed this to an additional heat load that was created by excited states other than ${}^4I_{13/2}$ participating in the excitation and relaxation processes.

5.3.2 CNBZn Glass

CNBZn designates a fluorochloride glass having the composition $\text{CdF}_2\text{--CdCl}_2\text{--NaF--BaF}_2\text{--BaCl}_2\text{--ZnF}_2$. Fernandez et al. procured a 0.5 mol% ErF_3 -doped CNBZn sample from the Laboratoire de Verres et Céramiques of the University of Rennes (Fernandez et al., 2006). A $10.7 \times 10.7 \times 2.2 \text{ mm}^3$ sized sample was prepared and characterized following their procedures described earlier in the text for KPC:Er^{3+} . The photothermal deflection experiments showed local internal laser cooling for pump wavelengths $> 843 \text{ nm}$. A subsequent bulk-cooling experiment found a temperature drop of $\sim 0.5 \text{ K}$ over the course of 1200 s when pumping at 860 nm with 1.9 W.

5.4 Other Lanthanides

Yb^{3+} , Tm^{3+} , and Er^{3+} are the only lanthanide ions that have shown net laser-induced bulk cooling to date. As shown in Fig. 7, Ho^{3+} and Dy^{3+} have even lower-energy first excited states and may therefore enable even higher cooling efficiencies. The energy of the first excited state of Ho^{3+} (5I_7) is similar to that of Tm^{3+} (3F_4) and is therefore expected to have minimal multiphonon relaxation in fluoride hosts. The $\text{Ho}^{3+} {}^5I_8 \leftrightarrow {}^5I_7$ transition is at slightly longer wavelength than the $\text{Tm}^{3+} {}^3H_6 \leftrightarrow {}^3F_4$ transition, making it somewhat better suited for pumping with modern Tm-doped fiber lasers that can have 10–50 W (air cooled) or 50–200 W (water cooled) output power in the 1900–2050 nm wavelength range (e.g., IPG Photonics). Another advantage may be the higher absorption cross section of Ho^{3+} compared to Tm^{3+} in the long-wavelength (cooling) tail of the respective absorption spectra (Scholle et al., 2010). As shown in Fig. 26, the features of the ${}^5I_8 \rightarrow {}^5I_7$ absorption in YLF:Ho^{3+} in the 2000–2080 nm range have peak absorption cross sections of up to $5 \times 10^{-21} \text{ cm}^2$ (π -polarization), which is almost $10 \times$ greater than the absorption cross sections of YLF:Tm^{3+} in the 1820–1970 nm range (Walsh et al., 1998) and may allow for a higher cooling efficiency in Ho^{3+} . A comparative study of Tm^{3+} and Ho^{3+} in various fluoride crystalline materials would provide the detailed spectroscopic information needed to assess the trade-offs relevant for laser cooling.

Another interesting candidate for solid-state laser refrigeration is the ${}^6H_{15/2} \leftrightarrow {}^6H_{13/2}$ transition of Dy^{3+} , which may offer a $3 \times$ greater cooling efficiency than Yb^{3+} (see Fig. 7). The low energy of the ${}^6H_{13/2}$ excited state of

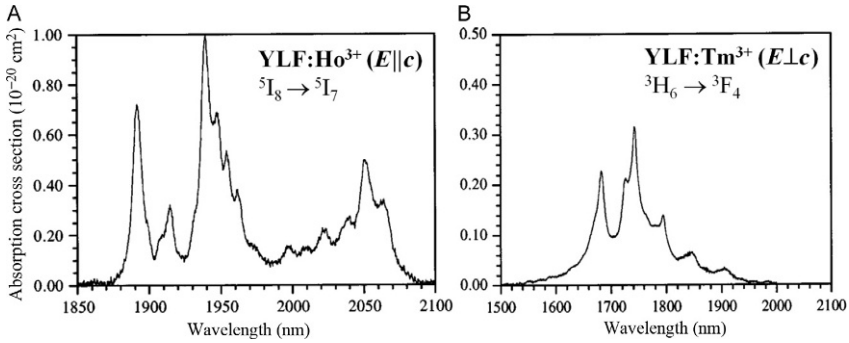


FIGURE 26 Polarized absorption cross sections of (A) Ho^{3+} - and (B) Tm^{3+} -doped YLF at room temperature. Reproduced with permission from *Walsh et al. (1998)*. Copyright 1998, AIP Publishing LLC.

$\sim 3500 \text{ cm}^{-1}$ however makes multiphonon relaxation competitive with radiative relaxation in most oxide and fluoride materials. The high quantum efficiencies needed for efficient laser cooling can likely only be achieved by doping Dy^{3+} into a chloride or bromide host material. KPb_2Cl_5 may be a candidate host as its highest-energy optical phonon energy is only $\sim 203 \text{ cm}^{-1}$ (Nostrand et al., 2001), and it is substantially less hygroscopic than other heavy-halide materials (see Section 5.3).

6 TOWARD LASER-COOLING DEVICES

6.1 Optical Cavities

Practical solid-state optical refrigerators aim at cooling a payload such as an optical or radiation sensor. The specifics of an application will require a trade-off between the refrigerator temperature and the heat lift within the constraints of the laser-cooling material and available pump laser power. A real-world macroscopic payload is likely to represent a significant heat source and will require hundreds of mW or more of heat lift. As shown in Section 2.3, the total power density deposited in the laser-cooling element is given by $P_{net} = -\eta_c P_{abs}$ (see Eq. 14), with $P_{net} < 0$ denoting cooling. The refrigerator therefore has to be designed to maximize the absorption efficiency (see Eq. 15), that is, maximize αL , where α and L are the resonant absorption coefficient and the path length, respectively. The rapid decrease of α with decreasing temperature (see Fig. 15) therefore necessitates a pump geometry that allows for long path lengths of the pump light in the cooling material. Useful path lengths will typically exceed the physical size of the cooling material by a large factor and thus require some sort of cavity in order to create a geometry in which the pump laser makes more than one round trip through the cooling element. A variety of nonresonant and resonant cavities have been suggested and implemented over the years.

6.1.1 Nonresonant Pump Cavities

In nonresonant cavities, the pump light traverses the cooling element multiple times at an angle slightly off-normal to the mirrors (Hoyt, 2003). Edwards et al. were the first to directly deposit high-reflectivity dielectric mirrors onto opposing faces of a cylindrical ZBLAN:Yb³⁺ sample to form a monolithic nonresonant cavity for the pump light (Edwards et al., 1998, 1999). They created a 150 μm diameter hole in one of the mirrors to admit the pump laser beam that was then trapped between the two mirrors. This geometry is shown in Fig. 27A. Thiede et al. used the same geometry with a <1 mm hole in their record-cooling result of ZBLANP:Yb³⁺ to 208 K (Thiede et al., 2005). Depositing the mirrors directly onto the cooling element is attractive because it allows for a potentially large number of passes. However, Epstein et al. found that YAG:Yb³⁺ crystals did not cool when dielectric mirrors were deposited directly onto the crystal to form a monolithic cavity, whereas the same samples cooled in a single-pass pump geometry (Epstein et al., 2001). A similar observation was made by Hoyt et al. for ZBLANP:Tm³⁺ (Hoyt et al., 2003). They attributed this effect to absorption by and thus heating of the mirrors by the pump light. This is particularly detrimental because the mirrors are in contact with the cooling element and directly degrade the cooling performance. Mirror heating effectively represents another contribution to background absorption. Furthermore, trapping of the fluorescence in the

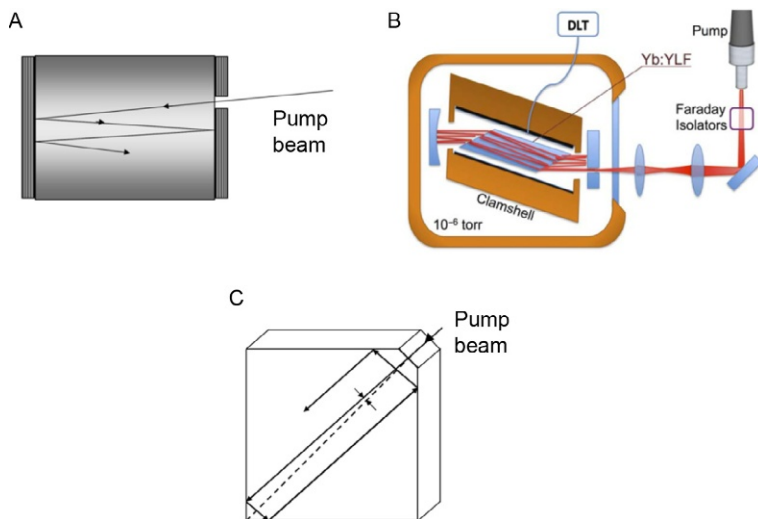


FIGURE 27 Nonresonant pump cavities used in solid-state optical refrigeration (Hoyt, 2003; Melgaard et al., 2013b). (A) Monolithic cavity with dielectric mirrors deposited directly onto the cooling element and a small hole in the mirror to admit the pump light; (B) nonresonant cavity with an external curved back mirror and an external planar mirror with a hole to admit the pump light; (C) monolithic optical maze using multiple total internal reflections to trap the pump light that is injected through a small facet.

crystal is increased because the mirrors are also reflective at the nearby fluorescence wavelengths. These drawbacks have steered subsequent efforts toward nonresonant cavities with external mirrors placed some distance away from the cooling element (see Fig. 27B). Such a geometry eliminates the conduction of heat generated in the mirror to the cooling element and significantly reduces the solid angle for fluorescence trapping. A nonresonant cavity with external mirrors having $\sim 99.9\%$ reflectance was first reported by Hoyt et al. in their work on laser cooling of ZBLANP:Tm³⁺ (Hoyt et al., 2003). Their cavity was formed by a planar dielectric mirror with an ~ 0.4 mm diameter hole to admit the pump beam and a second dielectric mirror with a 1 m radius of curvature. A similar geometry was used in recent record-cooling experiments by Seletskiy and Melgaard et al. using YLF:Yb³⁺ (Melgaard et al., 2013b; Seletskiy et al., 2010b,c). They prepared the facets of the YLF:Yb³⁺ crystal to form the Brewster angle with the laser propagation direction in order to minimize reflection losses. A lens pair was used to mode-match the laser to the nonresonant cavity that consisted of a flat mirror with a 1 mm diameter hole and a concave back mirror ($R=25$ cm) separated by ~ 3.5 cm. Care was taken to avoid saturation of the resonant absorption by optimizing the lens pair separation and focusing spot size at the flat mirror. They achieved five to eight roundtrip passes of the pump laser through the crystal for an effective pump path length of 10–20 cm through the crystal. With a resonant absorption coefficient of ~ 0.03 cm⁻¹ (at 1020 nm, $E \parallel \vec{c}$) for YLF:Yb³⁺ at cryogenic temperatures (see Fig. 6), this corresponds to absorption of 50–75% of the incident pump power. This was confirmed by Melgaard et al. who estimated ~ 18 W of absorbed power for an incident pump power of 45 W with five roundtrip passes through a 1.2 cm long YLF:Yb³⁺ crystal (Melgaard et al., 2013b).

Sheik-Bahae et al. and Hoyt proposed the use of a monolithic optical maze (MOM) for trapping pump light by multiple total internal reflections (Hoyt, 2003; Sheik-Bahae et al., 2001). As shown in Fig. 27C, the laser-cooling element can be shaped into a cuboid with a small triangular facet on one corner or a small rectangular facet on one edge of the slab. The pump beam is then coupled through this facet into the slab at a shallow angle with respect to the cuboid diagonal and undergoes multiple total internal reflections to create an extended path length for the pump beam. The authors were able to demonstrate 7.5 K of cooling from room temperature in ZBLANP:Tm³⁺ pumped with 2.8 W at 1880 nm in such a MOM geometry. This constituted a sixfold increase of the pump absorption compared to a single-pass geometry using a 10 mm long sample of identical composition.

6.1.2 Resonant Pump Cavities

Hoyt, Hasselbeck, and Sheik-Bahae pointed out in 2003 that—in principle—complete absorption of the incident pump light by the cooling element can

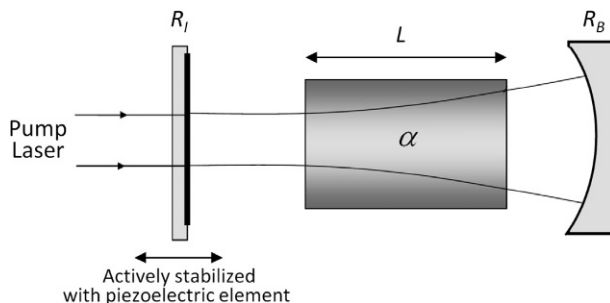


FIGURE 28 Resonant cavity consisting of a partially reflective planar mirror and a highly reflective concave back mirror. As the sample cools, the resonance condition changes and the cavity length must be actively stabilized. Hoyt (2003).

be achieved in a resonant cavity where the pump light interferometrically couples to cavity modes. As shown in Fig. 28, the resonant cavity consists of an input-coupling mirror with reflectivity R_I and a back mirror with high reflectivity R_B . The absorption of the pump light by the cooling element in the cavity is given by (Seletskiy et al., 2010a)

$$A = 1 - \left(\frac{\sqrt{R_I} - e^{-\alpha L}}{1 - e^{-\alpha L} \sqrt{R_I}} \right)^2, \quad (33)$$

where L is the length and α is the absorption coefficient of the crystal. Maximum absorption occurs if $R_I = R_B \exp(-2\alpha L)$. Note that the absorption can reach $A = 1$ if $R_B = 1$. In practice, R_I and R_B are fixed, and the cavity length is actively tuned via piezo control of the input-coupling mirror. Further note that the cavity length has to be adjusted as α changes with changing temperature. Using such a setup, Seletskiy et al. achieved an absorption of 0.89 ± 0.02 with 5% Yb^{3+} -doped YLF (Seletskiy et al., 2008, 2009) and 0.89 ± 0.03 with 2% Yb^{3+} -doped ZBLAN (Seletskiy et al., 2010a). This absorption is on par with the best nonresonant light-trapping schemes (Thiede et al., 2005). A resonant cavity geometry is attractive for a number of reasons including the elimination of losses associated with the pinhole in nonresonant cavities, insensitivity to mirror heating, absence of pump light leakage, and scalability by matching the cavity mode volume to the size of the cooling element (Seletskiy et al., 2010a). The primary drawback of this approach is the complexity associated with the active piezoelectric stabilization of the cavity.

Another variation of pumping the cooling element in a resonant cavity is to place the sample inside a laser cavity. This approach was used in the 1968 experiment by Kushida et al. who placed the YAG:Nd^{3+} cooling element inside the YAG:Nd^{3+} laser cavity and observed less-than-expected heating (Kushida and Geusic, 1968). In 2004, Heeg et al. achieved bulk cooling of a 2% Yb^{3+} -doped ZBLAN glass using intracavity pumping (Heeg et al., 2004). The pump laser consisted of a 10% Yb^{3+} -doped $\text{KY}(\text{WO}_4)_2$ crystal

pumped longitudinally by two counterpropagating 4 W stripe diode lasers operating at 981.2 nm, and it was tunable from ~ 1020 to 1040 nm by means of a Brewster prism (maximum power of 1.2 W at 1032 nm). The Brewster-cut ZBLAN:Yb³⁺ sample was mounted inside a vacuum cell that was then inserted into the laser cavity. They achieved a 6 K temperature drop from room temperature. A more recent intracavity pumping approach uses a vertical-external-cavity surface-emitting laser (VECSEL) (Ghasemkhani et al., 2014). Ghasemkhani et al. designed a VECSEL cavity that consisted of a distributed Bragg reflector made from 24 pairs of GaAs/AlAs layers, followed by a GaAs barrier, 12 InGaAs quantum wells that formed the active region, and a capping layer. This structure was deposited onto a diamond heat spreader and attached to a heat sink. A curved output coupler formed the other side of the cavity. The active structure was optically pumped by a 75 W diode laser operating at 808 nm, and the VECSEL produced ~ 20 W of output power at 1020 nm with tunability from 1003 to 1030 nm by means of a birefringent filter. A 7% Yb³⁺-doped YLF crystal was placed inside the cavity and showed cooling by 155 K (to 130 K from room temperature) with a heat lift of 150 mW for an absorbed power of 12 W. Such a cavity design is particularly amenable to scaling to high pump powers.

6.2 Thermal Management

The performance of a solid-state optical refrigerator is determined by the competition between the cooling power, P_{cool} , and the heat load on the cooling element, P_{load} . The change in temperature of the cooling element is given by (Edwards et al., 1999; Melgaard, 2013)

$$C(T) \frac{dT}{dt} = -P_{cool} + P_{load}, \quad (34)$$

where $C(T) = c_v(T) \rho V_s$ is the heat capacity, which depends on the specific heat, $c_v(T)$, the density, ρ , and the sample volume, V_s . In thermal equilibrium ($dT/dt = 0$), one has $P_{cool} = P_{load}$. The heat load power has contributions from convective, conductive, and radiative heat transfers from the environment to the cooling element, $P_{load} = P_{conv} + P_{cond} + P_{rad}$. Including these in Eq. (34) yields (Melgaard, 2013)

$$C(T) \frac{dT}{dt} = \eta_c P_{abs} + A_s \kappa_h (T_c - T_s) + \frac{N \kappa_L(T) A_L}{d_L} (T_c - T_s) + \frac{\epsilon_s A_s \sigma}{1 + \chi} (T_c^4 - T_s^4). \quad (35)$$

In Eq. (35), the subscripts s and c denote the sample and the surrounding chamber, respectively. The first term on the right-hand side is the cooling power derived earlier (Eq. 14); the second term is the convective heat load, P_{conv} , given by the sample area, A_s , and the convective heat transfer coefficient, κ_h ; the third term is the conductive heat load, P_{cond} , given by the

number of contact points, N , with area A_L , length d_L , and thermal conductivity κ_L ; and the fourth term is the radiative (black body) heat load, P_{rad} , given by the areas A and thermal emissivities ε , where $\chi = (1 - \varepsilon_c)(\varepsilon_s A_s / \varepsilon_c A_c)$ and σ is the Stefan–Boltzmann constant having a value of $5.67 \times 10^{-8} \text{ W/m}^2/\text{K}^4$.

The convective heat load can be minimized by placing the cooling element inside a chamber under vacuum. The convective heat transfer coefficient at a pressure p below standard pressure can be approximated by $\kappa_h = \kappa_h^0 [pd / (pd + CT)]$, where κ_h^0 is the coefficient at standard pressure, T is the sample temperature, d is the distance between the sample and the chamber, and $C = 7.6 \times 10^{-5} \text{ N/mK}$ is a constant (Electric, 1982). Lowering the pressure to 10^{-5} Torr with the sample at 300 K therefore reduces the convective heat transfer coefficient by a factor of $\sim 17,200 \times$. Assuming a sample surface area of $A_s = 100 \text{ mm}^2$ and a convective heat transfer coefficient for air at 300 K of $5\text{--}25 \text{ W/m}^2 \text{ K}$ thus gives a convective heat load of $\sim 2 \times 10^{-7} \text{ W/K}$ (Melgaard, 2013). The conductive heat load is reduced by mounting the sample in a way that minimizes the contact area with the warm chamber. Glass slides and glass fibers have been used for this purpose. Melgaard had used six 500 μm diameter glass fibers ($\kappa \approx 1.0 \text{ W/mK}$) to support a YLF:Yb³⁺ crystal at a distance of 1 mm from the surrounding chamber walls and estimated an upper limit for the conductive heat load of $\sim 1.2 \times 10^{-5} \text{ W/K}$ (Melgaard, 2013). This conductive contribution is a factor of ~ 60 greater than the convective contribution (at 10^{-5} Torr) and therefore requires careful attention in the device design. The radiative heat load from the surrounding chamber is by far the greatest contribution. By assuming small temperature changes, the heat load can be approximated as $P_{rad} = 4\varepsilon_s \sigma A T_c^3 \Delta T / (1 + \chi)$. Seletskiy et al. had studied the warming dynamics of a sample after turning off the pump laser at low temperatures (Seletskiy et al., 2010c). The sample had a surface area of 150 mm^2 and was held in a chamber having inside walls with a low-thermal-emissivity coating. They found $\chi = 2.1$ and $\varepsilon_s \approx 0.8$ from which Melgaard estimated a radiative heat load of $\sim 2.4 \times 10^{-4} \text{ W/K}$ with the chamber at 300 K (Melgaard, 2013). This illustrates that the radiative load dominates the convective and conductive contributions by factors of 1200 and 20, respectively. The key parameter χ is maximized by creating a chamber that fits tightly around the laser-cooling element ($A_s/A_c \rightarrow 1$) and by coating the chamber with low-thermal-emissivity material ($\varepsilon_c \ll \varepsilon_s$) such as Maxorb[®], which is a treated nickel surface having a high solar-spectrum absorptivity of 0.97 and a low IR emissivity of $\varepsilon_c = 0.08$ (Judkoff and Sokol, 1981; Mason and Brendel, 1982). The radiative heat load can also be reduced by lowering the temperature of the chamber. For example, P_{rad} is reduced by a factor of 4 if the chamber is cooled from 300 to $\sim 190 \text{ K}$, a temperature that could be reached by using a thermoelectric cooler. This was experimentally verified by Melgaard, who cooled the sample chamber to 208 K and achieved laser cooling of a YLF:5%Yb³⁺ sample to the MAT of 118.7 K (Melgaard, 2013).

The discussion so far has focused on the laser-cooling material itself. However, practical applications require the cooling of an actual payload. Recall that the quantum efficiency of laser-cooling materials is close to unity, and nearly all of the absorbed laser power is reemitted as fluorescence. Therefore, simply attaching the payload directly to the laser-cooling material is not feasible because it would be exposed to (and absorb) the large fluorescence photon flux and consequently heat up. A “thermal link” therefore has to be provided that prevents most of the fluorescence from reaching the payload while offering good thermal conductivity between the laser-cooling material and the payload. Parker et al. had presented a detailed theoretical and experimental study of four thermal link designs that included a cascaded mirror design, a kinked waveguide, a hemispherical design, and a tapered waveguide, with the latter showing the best overall performance (Parker et al., 2009). Melgaard et al. had performed an experimental analysis of a kinked waveguide thermal link as shown in Fig. 29 (Melgaard et al., 2014). They fabricated the kinked waveguide from sapphire, which has an excellent thermal conductivity of 46 W/m K at 273 K and ~ 1000 W/m K at 75 K (Dobrovinskaya et al., 2009). The sapphire was attached to YLF crystal only by means of van der Waals interactions, that is, atomic-scale adhesion by the intimate contact of two planar surfaces. This method eliminated any chemical adhesives that could have been the source of parasitic heating. As shown in Fig. 29B, there was no measurable temperature gradient between the YLF crystal (cooling element) and the payload side of the thermal link. The optical rejection of this design was measured to 92.9%. A dielectric or metal coating at the payload side of the link could further reduce the amount of fluorescence and residual pump light reaching the payload. Also note that the thermal link, like the laser-cooling element, has to be cooled to the operating temperature and is thus subject to thermal loads from the environment. It is therefore necessary to integrate it into the tightly fitting vacuum chamber structure along with the laser-cooling element.

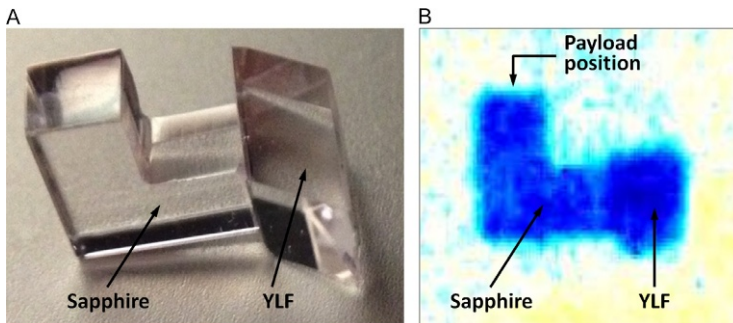


FIGURE 29 Experimental analysis of a thermal link constructed from sapphire. (A) Kinked sapphire waveguide van der Waals-bonded to a YLF crystal; (B) temperature distribution across the YLF crystal and the sapphire thermal link. Adapted from Melgaard et al. (2014).

7 CONCLUSIONS AND OUTLOOK

The performance of optical refrigeration has dramatically improved over the last several years. Lanthanide-based optical refrigeration now shows cooling from room temperature to the neighborhood of 100 K with a cooling efficiency such that the cooling power is about 1% of the input power. Optical refrigeration has become the only solid-state technology that can cool to cryogenic temperatures. The recent discovery of optical refrigeration in CdS semiconductors shows that there are several families of materials that have good prospects for cryogenic optical refrigeration. In contrast, thermoelectric cooling (based on the Peltier effect) is the currently dominant solid-state cooling technology, and it can cool from room temperature to only about 170 K.

As discussed in this chapter, there are well-defined paths forward for lowering the operating temperatures and increasing the cooling efficiencies of lanthanide-based optical refrigerators. Both experiments and calculations indicate that improving the purity of YLF:Yb³⁺ crystals will lead to optical refrigeration to temperatures below the boiling point of liquid nitrogen, 77 K. The needed purity level should be achievable by removing impurities in the starting materials. To further increase the cooling efficiency, one can dope the cooling crystal with a lanthanide ion that has a low-energy first excited state. Doping ions such as Tm³⁺ and Ho³⁺ will provide nearly double the cooling efficiency, and using Dy³⁺ ions should nearly triple the cooling efficiency compared to Yb³⁺. Additionally, “by photovoltaic recycling of” the waste fluorescence, the cooling efficiency may be increased by about another factor of 2 (Sheik-Bahae and Epstein, 2007, 2009).

Even with the demonstrated operating temperatures and efficiencies, the current generation of lanthanide-based optical cooling materials has significant potentials in a number of important areas. For some cooling applications, the elimination of vibrations is so important that optical refrigeration is extremely attractive. High-performance IR cameras and night-vision systems require cooling but are sensitive to vibrations that blur images. This is especially true for satellite-borne systems where even slight vibrations can cause severe image degradation. Another potential early application of optical refrigeration is gamma-ray spectroscopy. High energy resolution is needed to identify nuclear isotopes for medical and national security applications. HPGe gamma-ray spectrometers can provide the required energy resolution when the germanium crystals are cooled to near 100 K. However, even minor vibrations generate variable capacitance and electronic noise that significantly blurs the spectral resolution (Upp et al., 2005). There are niche application areas where the complete lack of vibrations of optical refrigerators may be critical. For example, ultrastable optical cavities for metrology need cooling to 124 K but cannot tolerate vibrations (Kessler et al., 2012). Another example is electron microscopy for studying cryogenically cooled samples (Shirazi et al., 2012).

While there are important applications for optical refrigerators using the current generations of lanthanide-doped materials, the potential uses of optical refrigeration expand greatly as the operating temperatures are lowered and the cooling efficiency grows. Furthermore, with large-scale deployment, the cost of optical refrigerators should drop, since there is nothing inherently costly about any of their components.

REFERENCES

- Anashkina, E., Antipov, O., 2010. Electronic (population) lensing versus thermal lensing in Yb:YAG and Nd:YAG laser rods and disks. *J. Opt. Soc. Am. B* 27 (3), 363–369.
- Anderson, M.H., Ensher, J.R., Matthews, M.R., Wieman, C.E., Cornell, E.A., 1995. Observation of Bose-Einstein condensation in a dilute atomic vapor. *Science* 269 (5221), 198–201.
- Antipov, O.L., Bredikhin, D.V., Eremykin, O.N., Savikin, A.P., Ivakin, E.V., Sukhadolau, A.V., 2006. Electronic mechanism for refractive-index changes in intensively pumped Yb:YAG laser crystals. *Opt. Lett.* 31 (6), 763–765.
- Auzel, F., Pellé, F., 1997. Bottleneck in multiphonon nonradiative transitions. *Phys. Rev. B* 55 (17), 11006–11009.
- Bao, S., Newman, P.J., Voelkel, A., Zhou, Z., MacFarlane, D.R., 1995. Electrochemical purification and GFAAS analysis of heavy metal fluoride glass. *J. Non-Cryst. Solids* 184, 194–199.
- Bensalah, A., Guyot, Y., Ito, M., Brenier, A., Sato, H., Fukuda, T., Boulon, G., 2004. Growth of Yb³⁺-doped YLiF₄ laser crystal by the Czochralski method. Attempt of Yb³⁺ energy level assignment and estimation of the laser potentiality. *Opt. Mater.* 26 (4), 375–383.
- Bigotta, S., Parisi, D., Bonelli, L., Toncelli, A., Lieto, A.D., Tonelli, M., 2006a. Laser cooling of Yb³⁺-doped BaY₂F₈ single crystal. *Opt. Mater.* 28 (11), 1321–1324.
- Bigotta, S., Parisi, D., Bonelli, L., Toncelli, A., Tonelli, M., Di Lieto, A., 2006b. Spectroscopic and laser cooling results on Yb³⁺-doped BaY₂F₈ single crystal. *J. Appl. Phys.* 100 (1), 013109.
- Bigotta, S., Di Lieto, A., Parisi, D., Toncelli, A., Tonelli, M., 2007. Single fluoride crystals as materials for laser cooling applications. *Proc. SPIE* 6461, 64610E–64611E.
- Boccaro, A.C., Jackson, W., Amer, N.M., Fournier, D., 1980. Sensitive photothermal deflection technique for measuring absorption in optically thin media. *Opt. Lett.* 5 (9), 377–379.
- Bowman, S.R., Mungan, C.E., 2000. New materials for optical cooling. *Appl. Phys. B* 71 (6), 807–811.
- Bowman, S.R., Jenking, N.W., O'Connor, S.R., Feldman, B.J., 2002. Sensitivity and stability of a radiation-balanced laser system. *Quantum Electron. IEEE J.* 38 (10), 1339–1348.
- Bowman, S.R., O'Connor, S.P., Biswal, S., Condon, N.J., Rosenberg, A., 2010. Minimizing heat generation in solid-state lasers. *Quantum Electron. IEEE J.* 46 (7), 1076–1085.
- Buchanan, R.A., Wickersheim, K.A., Pearson, J.J., Herrmann, G.F., 1967. Energy levels of Yb³⁺ in gallium and aluminum garnets. I. *Spectra. Phys. Rev.* 159 (2), 245–251.
- Chodos, A., 2006. This month in physics history—January 1938: discovery of superfluidity. *APS News* 15, 2.
- Cohen-Tannoudji, C.N., Phillips, W.D., 1990. New mechanisms for laser cooling. *Phys. Today*, 33–40.
- Condon, N.J., O'Connor, S., Bowman, S.R., 2006. Growth and characterization of single-crystal Er³⁺:KPB₂Cl₅ as a mid-infrared laser material. *J. Cryst. Growth* 291 (2), 472–478.

- Condon, N.J., Bowman, S.R., O'Connor, S.P., Quimby, R.S., Mungan, C.E., 2009. Optical cooling in $\text{Er}^{3+}:\text{KPb}_2\text{Cl}_5$. *Opt. Express* 17 (7), 5466–5472.
- Condon, N.J., Bowman, S.R., O'Connor, S.P., Myers, M.J., 2010. Heat loads in erbium-doped laser materials. *Opt. Mater.* 32 (9), 1050–1054.
- DeLoach, L.D., Payne, S.A., Chase, L.L., Smith, L.K., Kway, W.L., Krupke, W.F., 1993. Evaluation of absorption and emission properties of Yb^{3+} doped crystals for laser applications. *Quantum Electron. IEEE J.* 29 (4), 1179–1191.
- Dexter, D.L., 1953. A theory of sensitized luminescence in solids. *J. Chem. Phys.* 21 (5), 836–850.
- Di Bartolo, B., 2010. *Optical Interactions in Solids*. World Scientific Publishing Co. Pvt. Ltd, Hackensack, NJ.
- Dieke, G.H., Crosswhite, H.M., 1963. The spectra of the doubly and triply ionized rare earths. *Appl. Opt.* 2 (7), 675–686.
- Djeu, N., Whitney, W.T., 1981. Laser cooling by spontaneous anti-Stokes scattering. *Phys. Rev. Lett.* 46 (4), 236–239.
- Dobrovinskaya, E.R., Lytvynov, L.A., Pishchik, V., 2009. *Sapphire: Material, Manufacturing, Applications*. Springer, New York.
- Edwards, B.C., Buchwald, M.I., Epstein, R.I., 1998. Development of the Los Alamos solid-state optical refrigerator. *Rev. Sci. Instrum.* 69 (5), 2050–2055.
- Edwards, B.C., Anderson, J.E., Epstein, R.I., Mills, G.L., Mord, A.J., 1999. Demonstration of a solid-state optical cooler: an approach to cryogenic refrigeration. *J. Appl. Phys.* 86 (11), 6489–6493.
- Epstein, R.I., Sheik-Bahae, M., 2009. *Optical Refrigeration in Solids: Fundamentals and Overview*. Wiley-VCH, Weinheim, pp. 1–32, *Optical Refrigeration*.
- Epstein, R.I., Buchwald, M.I., Edwards, B.C., Gosnell, T.R., Mungan, C.E., 1995. Observation of laser-induced fluorescent cooling of a solid. *Nature* 377 (6549), 500–503.
- Epstein, R.I., Brown, J.J., Edwards, B.C., Gibbs, A., 2001. Measurements of optical refrigeration in ytterbium-doped crystals. *J. Appl. Phys.* 90 (9), 4815–4819.
- Fajardo, J.C., Sigel Jr., G.H., Edwards, B.C., Epstein, R.I., Gosnell, T.R., Mungan, C.E., 1997. Electrochemical purification of heavy metal fluoride glasses for laser-induced fluorescent cooling applications. *J. Non-Cryst. Solids* 213–214, 95–100.
- Fernández, J., Mendioroz, A., García, A.J., Balda, R., Adam, J.L., 2000. Anti-Stokes laser-induced internal cooling of Yb^{3+} -doped glasses. *Phys. Rev. B* 62 (5), 3213–3217.
- Fernández, J., Mendioroz, A., García, A.J., Balda, R., Adam, J.L., 2001a. Laser-induced internal cooling of Yb^{3+} -doped fluoride-based glasses. *J. Alloys Compd.* 323–324, 239–244.
- Fernández, J., Mendioroz, A., García, A.J., Balda, R., Adam, J.L., Arriandiaga, M.A., 2001b. On the origin of anti-Stokes laser-induced cooling of Yb^{3+} -doped glass. *Opt. Mater.* 16 (1–2), 173–179.
- Fernandez, J.R., Mendioroz, A., Balda, R., Voda, M., Al-Saleh, M., Garcia-Adeva, A.J., Adam, J.-L., Lucas, J., 2002. Origin of laser-induced internal cooling of Yb^{3+} -doped systems. *Proc. SPIE* 4645, 135.
- Fernandez, J., Garcia-Adeva, A.J., Balda, R., 2006. Anti-Stokes laser cooling in bulk erbium-doped materials. *Phys. Rev. Lett.* 97 (3), 033001.
- Fernández, J., García-Adeva, A.J., Balda, R., 2012. Anti-Stokes laser-induced cooling in rare-earth doped low phonon materials. *Opt. Mater.* 34 (3), 579–590.
- France, P.W., Carter, S.F., Parker, J.M., 1986. Oxidation states of 3d transition metals in ZrF_4 glasses. *Phys. Chem. Glasses* 27, 32.

- Gabriel, A., Pelton, A.D., 1985. Phase diagram measurements and thermodynamic analysis of the $\text{PbCl}_2\text{-NaCl}$, $\text{PbCl}_2\text{-KCl}$, and $\text{PbCl}_2\text{-KCl-NaCl}$ systems. *Can. J. Chem.* 63 (11), 3276–3282.
- Gainov, V.V., Shaidullin, R.I., Ryabushkin, O.A., 2010. Temperature measurements in the core of active optical fibers under lasing conditions. *Instrum. Exp. Tech.* 53 (6), 853–859.
- Gan, F., 1995. Optical properties of fluoride glasses: a review. *J. Non-Cryst. Solids* 184, 9–20.
- Garcia-Adeva, A.J., 2008. Spectroscopy, upconversion dynamics, and applications of -doped low-phonon materials. *J. Lumin.* 128 (5–6), 697–702.
- Garcia-Adeva, A.J., Balda, R., Fernández, J., 2007. Recent advances in laser-induced cooling in rare-earth doped low phonon materials. *Proc. SPIE* 6469, 64690F–64691F.
- Garcia-Adeva, A.J., Balda, R., Fernandez, J., 2009. Laser cooling of Er^{3+} -doped low-phonon materials: current status and outlook. *Opt. Mater.* 31 (7), 1075–1081.
- General Electric, 1982. Fluid Flow Data Book, Section 410.2. Genium Publishing, Schenectady, New York.
- Ghasemkhani, M., Albrecht, A.R., Melgaard, S.D., Seletskiy, D.V., Cederberg, J., Sheik-Bahae, M., 2014. Intracavity optical refrigeration to 130K using high-power vertical external-cavity surface-emitting lasers (VECSELs). In: *Laser Refrigeration of Solids VII, OPTO Photonics West*, San Francisco, CA: Paper 9000-4.
- Gill, J.C., 1975. The establishment of thermal equilibrium in paramagnetic crystals. *Rep. Prog. Phys.* 38 (1), 91.
- Gilmore, G., Hemingway, J.D., 1998. *Practical Gamma-Ray Spectrometry*. John Wiley & Sons Inc, New York.
- Goldner, P., Mortier, M., 2001. Effect of rare earth impurities on fluorescent cooling in ZBLAN glass. *J. Non-Cryst. Solids* 284 (1–3), 249–254.
- Gorrie, J., 1851. Improved process for the artificial production of ice. U.S. Patent # 8080A.
- Gosnell, T.R., 1999. Laser cooling of a solid by 65 K starting from room temperature. *Opt. Lett.* 24 (15), 1041–1043.
- Green, M.A., 2003. The integration of liquid cryogen cooling and cryocoolers with superconducting electronic systems. Lawrence Berkeley National Laboratory, Report #LBNL-53068.
- Guiheen, J.V., Haines, C.D., Sigel, G.H., Epstein, R.I., Thiede, J., Patterson, W.M., 2006. Yb^{3+} and Tm^{3+} -doped fluoroaluminate glasses for anti-Stokes cooling. *Phys. Chem. Glasses Eur. J. Glass Sci. Technol. B* 47 (2), 167–176.
- Hänsch, T.W., Schawlow, A.L., 1975. Cooling of gases by laser radiation. *Opt. Commun.* 13 (1), 68–69.
- Heeg, B., Stone, M.D., Khizhnyak, A., Rumbles, G., Mills, G., DeBarber, P.A., 2004. Experimental demonstration of intracavity solid-state laser cooling of $\text{Yb}^{3+}:\text{ZrF}_4\text{-BaF}_2\text{-LaF}_3\text{-AlF}_3\text{-NaF}$ glass. *Phys. Rev. A* 70 (2), 021401.
- Hehlen, M.P., 2009. Design and fabrication of rare-earth-doped laser cooling materials. In: Epstein, R.I., Sheik-Bahae, M. (Eds.), *Optical Refrigeration: Science and Applications of Laser Cooling of Solids*. Wiley, Weinheim, Germany, pp. 37–74.
- Hehlen, M.P., 2010. Crystal-field effects in fluoride crystals for optical refrigeration. *Proc. SPIE* 7614, 761404.
- Hehlen, M.P., Epstein, R.I., Inoue, H., 2007. Model of laser cooling in the Yb^{3+} -doped fluorozirconate glass ZBLAN. *Phys. Rev. B* 75 (14), 144302.
- Hehlen, M.P., Brik, M.G., Krämer, K.W., 2013. 50th anniversary of the Judd–Ofelt theory: an experimentalist’s view of the formalism and its application. *J. Lumin.* 136, 221–239.
- Hoyt, C.W., 2003. Laser cooling in thulium-doped solids. Ph.D The University of New Mexico.
- Hoyt, C.W., Sheik-Bahae, M., Epstein, R.I., Edwards, B.C., Anderson, J.E., 2000. Observation of anti-Stokes fluorescence cooling in thulium-doped glass. *Phys. Rev. Lett.* 85 (17), 3600–3603.

- Hoyt, C.W., Hasselbeck, M.P., Sheik-Bahae, M., Epstein, R.I., Greenfield, S., Thiede, J., Distel, J., Valencia, J., 2003. Advances in laser cooling of thulium-doped glass. *J. Opt. Soc. Am. B Opt. Phys.* 20 (5), 1066–1074.
- Izotova, O.Y., Aleksandrov, V.B., 1970. Crystal structure of BaTm₂F₈. *Dokl. Akad. Nauk SSSR* 192 (5), 1037–1039.
- Jenkins, N.W., Bowman, S.R., O'Connor, S., Searles, S.K., Ganem, J., 2003. Spectroscopic characterization of Er-doped KPb₂Cl₅ laser crystals. *Opt. Mater.* 22 (4), 311–320.
- Jewell, J.M., Askins, C., Aggarwal, I.D., 1991. Interferometric method for concurrent measurement of thermo-optic and thermal expansion coefficients. *Appl. Opt.* 30 (25), 3656–3660.
- Judkoff, R., Sokol, F., 1981. Performance of a selective-surface Trombe wall in a small commercial building. Report #TP-721-1158. Solar Energy Research Institute, Boulder, CO.
- Kamber, L., Egger, P., Trusch, B., Giovanoli, R., Hulliger, J., 1998. High temperature phase segregation of a new host for Er³⁺ upconversion: Cs₃Tl₂Cl₉. *J. Mater. Chem.* 8 (5), 1259–1262.
- Kastler, A., 1950. Quelques suggestions concernant la production optique et la detection optique d'une inegalite de population des niveaux de quantification spatiale des atomes. Application a l'experience de Stern et Gerlach et a la resonance magnetique. *J. Phys. Radium* 11, 255–265.
- Kessler, T., Hagemann, C., Grebing, C., Legero, T., Sterr, U., Riehle, F., Martin, M.J., Chen, L., Ye, J., 2012. A sub-40-mHz-linewidth laser based on a silicon single-crystal optical cavity. *Nat. Photonics* 6 (10), 687–692.
- Kim, J., Kaviani, M., 2009. Ab initio calculations of f-orbital electron-phonon interaction in laser cooling. *Phys. Rev. B* 79 (5), 054103.
- Knoll, G.F., 2000. Radiation Detection and Measurement. John Wiley & Sons Inc, New York.
- Kohmoto, T., Fukuda, Y., Kunitomo, M., Isoda, K., 2000. Observation of ultrafast spin-lattice relaxation in Tm²⁺-doped CaF₂ and SrF₂ crystals by optical means. *Phys. Rev. B* 62 (1), 579–583.
- Kushida, T., Geusic, J.E., 1968. Optical refrigeration in Nd-doped yttrium aluminum garnet. *Phys. Rev. Lett.* 21 (16), 1172–1175.
- Landau, L., 1946. On the thermodynamics of photoluminescence. *J. Phys. (Moscow)* 10, 503–506.
- Lei, G., Anderson, J.E., Buchwald, M.I., Edwards, B.C., Epstein, R.I., 1998. Determination of spectral linewidths by Voigt profiles in Yb³⁺-doped fluorozirconate glasses. *Phys. Rev. B* 57 (13), 7673–7678.
- Lenard, P., Schmidt, F., Tomascheck, R., 1928. Handbuch der Experimentalphysik, 1. Teil. Akademische Verlagsgesellschaft, Leipzig.
- Li, D., Zhang, J., Xiong, Q., 2013. Laser cooling of CdS nanobelts: thickness matters. *Opt. Express* 21 (16), 19302–19310.
- Lima, S.M., Sampaio, J.A., Catunda, T., Bento, A.C., Miranda, L.C.M., Baesso, M.L., 2000. Mode-mismatched thermal lens spectrometry for thermo-optical properties measurement in optical glasses: a review. *J. Non-Cryst. Solids* 273 (1–3), 215–227.
- Luo, X., Eisaman, M.D., Gosnell, T.R., 1998. Laser cooling of a solid by 21 K starting from room temperature. *Opt. Lett.* 23 (8), 639–641.
- Lupei, A., Lupei, V., Presura, C., Enaki, V.N., Petraru, A., 1999. Electron-phonon coupling effects on Yb³⁺ spectra in several laser crystals. *J. Phys. Condens. Matter* 11 (18), 3769.
- MacFarlane, D.R., Javorniczky, J., Newman, P.J., 1999. Electrochemical studies of rare earths in fluoride melts. *J. Non-Cryst. Solids* 256, 36–41.
- MacFarlane, D.R., Zhou, Z., Newman, P.J., 2004. Differential pulse voltammetry studies of heavy metal fluoride melts. *J. Appl. Electrochem.* 34 (2), 197–204.
- Mahdavinejad, M., Javanrudi, K., 2012. Assessment of ancient fridges: a sustainable method to storage ice in hot-arid climates. *Asian Cult. Hist.* 4 (2), 133–139.

- Malta, O.L., 1995. The theory of vibronic transitions in rare earth compounds. *J. Phys. Chem. Solids* 56 (8), 1053–1062.
- Martin, R.M., Quimby, R.S., 2006. Experimental evidence of the validity of the McCumber theory relating emission and absorption for rare-earth glasses. *J. Opt. Soc. Am. B* 23 (9), 1770–1775.
- Martin, R.M., Quimby, R.S., 2007. Deviations from the reciprocity theory of McCumber at low temperature in Nd³⁺-doped glasses. *Appl. Phys. Lett.* 90 (22), 221104.
- Mason, J.J., Brendel, T.A., 1982. Maxorb—a new selective surface on nickel. *Proc. SPIE* 324, 139.
- McCumber, D.E., 1964. Einstein relations connecting broadband emission and absorption spectra. *Phys. Rev.* 136 (4A), A954–A957.
- Melgaard, S.D., 2013. Cryogenic optical refrigeration: laser cooling of solids below 123 K. Ph.D. University of New Mexico, Albuquerque, New Mexico.
- Melgaard, S., Seletskiy, D., Sheik-Bahae, M., Bigotta, S., Di Lieto, A., Tonelli, M., Epstein, R., 2010. Spectroscopy of Yb-doped YLF crystals for laser cooling. *Proc. SPIE* 7614, 761407.
- Melgaard, S.D., Seletskiy, D.V., Di Lieto, A., Tonelli, M., Sheik-Bahae, M., 2013a. Optical refrigeration progress: cooling below NIST cryogenic temperature of 123K. *Proc. SPIE* 8638, 863804-1.
- Melgaard, S.D., Seletskiy, D.V., Di Lieto, A., Tonelli, M., Sheik-Bahae, M., 2013b. Optical refrigeration to 119 K, below National Institute of Standards and Technology cryogenic temperature. *Opt. Lett.* 38 (9), 1588–1590.
- Melgaard, S.D., Seletskiy, D.V., Sills, D., Epstein, R.I., Sheik-Bahae, M., 2014. Device applications for cryogenic optical refrigeration. In: *Laser Refrigeration of Solids VII, OPTO Photonics West*, San Francisco, CA, Paper 9000-1.
- Melgaard, S., Seletskiy, D., Polyak, V., Asmerom, Y., Sheik-Bahae, M., 2014. Identification of parasitic losses in Yb:YLF and prospects for optical refrigeration down to 80K. *Optics Express* 22 (7), 7756–7764.
- Mendioroz, A., Fernández, J., Voda, M., Al-Saleh, M., Balda, R., García-Adeva, A.J., 2002. Anti-Stokes laser cooling in Yb³⁺-doped KPb₂Cl₅ crystal. *Opt. Lett.* 27 (17), 1525–1527.
- Merkulov, A.A., Isaenko, L.I., Pashkov, V.M., Mazur, V.G., Virovets, A.V., Naumov, D.Y., 2005. Crystal structure of KPb₂Cl₅ and KPb₂Br₅. *J. Struct. Chem.* 46 (1), 103–108.
- Messias, D.N., Catunda, T., Myers, J.D., Myers, M.J., 2007. Nonlinear electronic line shape determination in Yb³⁺-doped phosphate glass. *Opt. Lett.* 32 (6), 665–667.
- Mills, G.L., Mord, A.J., Slaymaker, P.A., 2002. Design and predicted performance of an optical cryocooler for a focal plane application. In: Ross Jr., R.G. (Ed.), *Cryocoolers 11*. Kluwer Academic/Plenum Publishers, Dordrecht, The Netherlands, pp. 613–620.
- Mungan, C.E., 2005. Radiation thermodynamics with applications to lasing and fluorescent cooling. *Am. J. Phys.* 73 (4), 315–322.
- Mungan, C.E., Gosnell, T.R., 1999. Laser cooling of solids. In: Benjamin, B., Herbert, W. (Eds.), *Advances in Atomic, Molecular, and Optical Physics*, vol. 40. Academic Press, Philadelphia PA, pp. 161–228.
- Mungan, C.E., Buchwald, M.I., Edwards, B.C., Epstein, R.I., Gosnell, T.R., 1997a. Internal laser cooling of Yb³⁺-doped glass measured between 100 and 300 K. *Appl. Phys. Lett.* 71 (11), 1458–1460.
- Mungan, C.E., Buchwald, M.I., Edwards, B.C., Epstein, R.I., Gosnell, T.R., 1997b. Laser cooling of a solid by 16 K starting from room temperature. *Phys. Rev. Lett.* 78 (6), 1030–1033.
- Murtagh, M.T., Sigel Jr., G.H., Fajardo, J.C., Edwards, B.C., Epstein, R.I., 1999a. Compositional investigation of Yb³⁺-doped heavy metal fluoride glasses for laser-induced fluorescent cooling applications. *J. Non-Cryst. Solids* 256–257, 207–211.

- Murtagh, M.T., Sigel Jr., G.H., Fajardo, J.C., Edwards, B.C., Epstein, R.I., 1999b. Laser-induced fluorescent cooling of rare-earth-doped fluoride glasses. *J. Non-Cryst. Solids* 253 (1–3), 50–57.
- Nast, T., Barnes, C., Wedel, R., 1976. Development and orbital operation of a two-stage solid cryogen cooler for infrared detector cooling. In: 11th Thermophysics Conference. American Institute of Aeronautics and Astronautics, New York.
- Nemova, G., Kashyap, R., 2010. Laser cooling of solids. *Rep. Prog. Phys.* 73 (8), 086501.
- Nostrand, M.C., Page, R.H., Payne, S.A., Isaenko, L.I., Yelisseyev, A.P., 2001. Optical properties of Dy³⁺- and Nd³⁺-doped KPb₂Cl₅. *J. Opt. Soc. Am. B* 18 (3), 264–276.
- Orlovskii, Y.V., Basiev, T.T., Vorob'ev, I.N., Orlovskaya, E.O., Barnes, N.P., Mirov, S.B., 2002. Temperature dependencies of excited states lifetimes and relaxation rates of 3–5 phonon (4–6 μm) transitions in the YAG, LuAG and YLF crystals doped with trivalent holmium, thulium, and erbium. *Opt. Mater.* 18 (4), 355–365.
- Parker, J.M., 1989. Fluoride glasses. *Annu. Rev. Mater. Sci.* 19 (1), 21–41.
- Parker, J., Mar, D., Von der Porten, S., Hankinson, J., Byram, K., Lee, C., Mayeda, M.K., Haskell, R., Yang, Q., Greenfield, S., Epstein, R., 2009. Thermal links for the implementation of an optical refrigerator. *J. Appl. Phys.* 105 (1), 013116.
- Passilly, N., Haouas, E., Ménard, V., Moncorgé, R., Ai't-Ameur, K., 2006. Population lensing effect in Cr:LiSAF probed by Z-scan technique. *Opt. Commun.* 260 (2), 703–707.
- Patterson, W., Hasselbeck, M.P., Sheik-Bahae, M., Bigotta, S., Parisi, D., Toncelli, A., Tonelli, M., Epstein, R.I., Thiede, J., 2004. Observation of optical refrigeration in Tm³⁺:BaY₂F₈. In: Conference on Lasers and Electro-Optics (CLEO).
- Patterson, W., Bigotta, S., Sheik-Bahae, M., Parisi, D., Tonelli, M., Epstein, R., 2008. Anti-Stokes luminescence cooling of Tm³⁺ doped BaY₂F₈. *Opt. Express* 16 (3), 1704–1710.
- Patterson, W.M., Seletskiy, D.V., Sheik-Bahae, M., Epstein, R.I., Hehlen, M.P., 2010a. Measurement of solid-state optical refrigeration by two-band differential luminescence thermometry. *J. Opt. Soc. Am. B* 27 (3), 611–618.
- Patterson, W.M., Sheik-Bahae, M., Epstein, R.I., Hehlen, M.P., 2010b. Model of laser-induced temperature changes in solid-state optical refrigerators. *J. Appl. Phys.* 107 (6), 063108–063109.
- Patterson, W.M., Stark, P.C., Yoshida, T.M., Sheik-Bahae, M., Hehlen, M.P., 2011. Preparation and characterization of high-purity metal fluorides for photonic applications. *J. Am. Ceram. Soc.* 94 (9), 2896–2901.
- Peijzel, P.S., Meijerink, A., Wegh, R.T., Reid, M.F., Burdick, G.W., 2005. A complete 4fⁿ energy level diagram for all trivalent lanthanide ions. *J. Solid State Chem.* 178, 448–453.
- Petrushkin, S.V., Samartsev, V.V., 2009. *Laser Cooling of Solids*. Cambridge International Science Publishing Ltd, Cambridge, UK.
- Poole, Charles P., 2004. *Encyclopedic Dictionary of Condensed Matter Physics*. Elsevier, San Diego, CA.
- Pringsheim, P., 1929. Zwei Bemerkungen über den Unterschied von Lumineszenz- und Temperaturstrahlung. *Z. Phys.* 57, 739–746.
- Quimby, R.S., 2002. Range of validity of McCumber theory in relating absorption and emission cross sections. *J. Appl. Phys.* 92 (1), 180–187.
- Rayner, A., Friese, M.E.J., Truscott, A.G., Heckenberg, N.R., Rubinsztein-dunlop, H., 2001a. Laser cooling of a solid from ambient temperature. *J. Mod. Opt.* 48 (1), 103–114.
- Rayner, A., Hirsch, M., Heckenberg, N.R., Rubinsztein-Dunlop, H., 2001b. Distributed laser refrigeration. *Appl. Opt.* 40 (30), 5423–5429.

- Rayner, A., Heckenberg, N.R., Rubinsztein-Dunlop, H., 2003. Condensed-phase optical refrigeration. *J. Opt. Soc. Am. B Opt. Phys.* 20 (5), 1037–1053.
- Riseberg, L.A., Moos, H.W., 1968. Multiphonon orbit-lattice relaxation of excited states of rare-earth ions in crystals. *Phys. Rev.* 174 (2), 429–438.
- Rogalski, A., 2005. HgCdTe infrared detector material: history, status and outlook. *Rep. Prog. Phys.* 68 (10), 2267.
- Rogalski, A., 2011. *Infrared Detectors*. CRC Press, Boca Raton.
- Ruan, X.L., Kaviany, M., 2006. Advances in laser cooling of solids. *J. Heat Transf.* 129 (1), 3–10.
- Ruan, X.L., Rand, S.C., Kaviany, M., 2007. Entropy and efficiency in laser cooling of solids. *Phys. Rev. B* 75 (21), 214304.
- Salazar, A., Sánchez-Lavega, A., Fernández, J., 1993. Thermal diffusivity measurements on solids using collinear mirage detection. *J. Appl. Phys.* 74 (3), 1539–1547.
- Scholle, K., Lamrini, S., Koopmann, P., Fuhrberg, P., 2010. 2 μm laser sources and their possible applications. In: Pal, Bishnu (Ed.), *Frontiers in Guided Wave Optics and Optoelectronics*. InTech, Rijeka, Croatia.
- Schreier, F., 1992. The Voigt and complex error function: a comparison of computational methods. *J. Quant. Spectrosc. Radiat. Transf.* 48 (5–6), 743–762.
- Schultz, M.K., Keyser, R.M., Trammell, R.C., Upp, D.L., 2007. Improvement of spectral resolution in the presence of periodic noise and microphonics for hyper-pure germanium detector gamma-ray spectrometry using a new digital filter. *J. Radioanal. Nucl. Chem.* 271 (1), 101–106.
- Seletskiy, D., Hasselbeck, M.P., Sheik-Bahae, M., Epstein, R.I., Bigotta, S., Tonelli, M., 2008. Cooling of Yb:YLF using cavity enhanced resonant absorption. *Proc. SPIE* 6907, 69070B.
- Seletskiy, D.V., Melgaard, S.D., Bigotta, S., Di Lieto, A., Tonelli, M., Epstein, R.I., Sheik-Bahae, M., 2009. Demonstration of an optical cryocooler. In: *Conference on Lasers and Electro-Optics and Conference on Quantum Electronics and Laser Science (CLEO/QELS)*.
- Seletskiy, D.V., Hasselbeck, M.P., Sheik-Bahae, M., 2010a. Resonant cavity-enhanced absorption for optical refrigeration. *Appl. Phys. Lett.* 96(18), 181106–181103.
- Seletskiy, D.V., Melgaard, S.D., Bigotta, S., Di Lieto, A., Tonelli, M., Sheik-Bahae, M., 2010b. Laser cooling of solids to cryogenic temperatures. *Nat. Photonics* 4 (3), 161–164.
- Seletskiy, D.V., Melgaard, S.D., Di Lieto, A., Tonelli, M., Sheik-Bahae, M., 2010c. Laser cooling of a semiconductor load to 165 K. *Opt. Express* 18 (17), 18061–18066.
- Seletskiy, D.V., Melgaard, S.D., Epstein, R.I., Di Lieto, A., Tonelli, M., Sheik-Bahae, M., 2011. Local laser cooling of Yb:YLF to 110 K. *Opt. Express* 19 (19), 18229–18236.
- Seletskiy, D.V., Melgaard, S.D., Epstein, R.I., Di Lieto, A., Tonelli, M., Sheik-Bahae, M., 2013. Precise determination of minimum achievable temperature for solid-state optical refrigeration. *J. Lumin.* 133, 5–9.
- Sheik-Bahae, M., Epstein, R.I., 2007. Optical refrigeration. *Nat. Photonics* 1 (12), 693–699.
- Sheik-Bahae, M., Epstein, R.I., 2009. Laser cooling of solids. *Laser Photonics Rev.* 3 (1–2), 67–84.
- Sheik-Bahae, M., Hoyt, C.W., Ebrahimzadeh, M., Epstein, R.I., Edwards, B.C., 2000. High power optical parametric oscillators for optical refrigeration in solids. In: *Nonlinear Optics: Materials, Fundamentals, and Applications, Technical Digest*.
- Sheik-Bahae, M., Hoyt, C.W., Imangholi, B., Epstein, R.I., Edwards, B.C., Gibbs, A., Anderson, J.E., 2001. Advances in laser cooling of solids. In: *Quantum Electronics and Laser Science Conference (QELS '01), Technical Digest*.
- Shirazi, R., Kopylov, O., Kovacs, A., Kardynał, B.E., 2012. Temperature dependent recombination dynamics in InP/ZnS colloidal nanocrystals. *Appl. Phys. Lett.* 101 (9).
- Siegman, A.E., 1986. *Lasers*. University Science Books, Mill Valley, CA.

- Silva, J.R., Andrade, L.H.C., Lima, S.M., Hehlen, M.P., Guyot, Y., Medina, A.N., Malacarne, L.C., Baesso, M.L., Astrath, N.G.C., 2013a. Laser-induced lensing effects in solid-state optical refrigerators. *Appl. Phys. Lett.* 102 (14), 141910–141914.
- Silva, J.R., Malacarne, L.C., Baesso, M.L., Lima, S.M., Andrade, L.H.C., Jacinto, C., Hehlen, M.P., Astrath, N.G.C., 2013b. Modeling the population lens effect in thermal lens spectrometry. *Opt. Lett.* 38 (4), 422–424.
- Sui, G.Z., Li, X.P., Cheng, L.H., Zhang, J.S., Sun, J.S., Zhong, H.Y., Tian, Y., Fu, S.B., Chen, B.J., 2013. Laser cooling with optical temperature sensing in Er^{3+} -doped tellurite-germanate glasses. *Appl. Phys. B* 110 (4), 471–476.
- Takahashi, S., 1992. Prospects for ultra-low loss using fluoride glass optical fiber: a review. *J. Non-Cryst. Solids* 140, 172–178.
- Thiede, J., Distel, J., Greenfield, S.R., Epstein, R.I., 2005. Cooling to 208 K by optical refrigeration. *Appl. Phys. Lett.* 86 (15), 154107.
- Toncelli, A., Tonelli, M., Cassanho, A., Jenssen, H.P., 1999. Spectroscopy and dynamic measurements of a Tm, Dy:BaY2F8 crystal. *J. Lumin.* 82 (4), 291–298.
- Tran, D., Sigel, G., Bendow, B., 1984. Heavy metal fluoride glasses and fibers: a review. *J. Lightw. Technol.* 2 (5), 566–586.
- Upp, D.L., Keyser, R.M., Twomey, T.R., 2005. New cooling methods for HPGE detectors and associated electronics. *J. Radioanal. Nucl. Chem.* 264 (1), 121–126.
- van Delft, D., Kes, P., 2010. The discovery of superconductivity. *Phys. Today* (September), 38–43.
- Veprik, A.M., Babitsky, V.I., Pundak, N., Riabzev, S.V., 2009. Suppression of cryocooler-induced microphonics in infrared imagers. *Cryogenics* 49 (8), 449–454.
- Voda, M., Al-Saleh, M., Lobera, G., Balda, R., Fernández, J., 2004. Crystal growth of rare-earth-doped ternary potassium lead chloride single crystals by the Bridgman method. *Opt. Mater.* 26 (4), 359–363.
- Walsh, B.M., Barnes, N.P., Di Bartolo, B., 1998. Branching ratios, cross sections, and radiative lifetimes of rare earth ions in solids: application to Tm^{3+} and Ho^{3+} ions in LiYF_4 . *J. Appl. Phys.* 83 (5), 2772–2787.
- Yen, W.M., Scott, W.C., Schawlow, A.L., 1964. Phonon-induced relaxation in excited optical states of trivalent praseodymium in LaF_3 . *Phys. Rev.* 136 (1A), A271–A283.
- Zagarola, M.V., Breedlove, J.J., Kirkconnell, C.S., Russo, J.T., Chiang, T., 2009. Demonstration of a two-stage turbo-brayton cryocooler for space applications. In: *Cryocoolers 15*, Boulder, CO, International Cryocooler Conference.
- Zhang, J., Li, D., Chen, R., Xiong, Q., 2013. Laser cooling of a semiconductor by 40 kelvin. *Nature* 493 (7433), 504–508.
- Zhou, Z., Newman, P.J., Wong, D.K.Y., MacFarlane, D.R., 1992. Electrochemical purification of fluoride melts. *J. Non-Cryst. Solids* 140, 297–300.
- Zhou, Z., Newman, P.J., MacFarlane, D.R., 1993a. Electroanalytical methods for transition metal analysis in heavy metal fluoride melts. *J. Non-Cryst. Solids* 161, 36–40.
- Zhou, Z., Newman, P.J., MacFarlane, D.R., 1993b. Electrochemistry at a rotating disc electrode in heavy metal fluoride melts. *J. Non-Cryst. Solids* 161, 27–31.

Chapter 266

Rare Earth Arene-Bridged Complexes Obtained by Reduction of Organometallic Precursors

Wenliang Huang and Paula L. Diaconescu

Department of Chemistry & Biochemistry, University of California, Los Angeles, California, USA

Chapter Outline

1 Introduction	262	4 Synthesis of Rare Earth Fused-Arene Complexes and Their Reactivity Toward P₄ Activation	290
1.1 General Remarks About the Organometallic Chemistry of Rare Earths	262	4.1 Scandium Fused-Arene Complexes: Synthesis, Characterization, and Reactivity	290
1.2 Reduction Chemistry of Organometallic Rare Earth Complexes	271	4.2 P ₄ Activation by Scandium Arene Complexes	295
2 Previous Studies of Arene-Bridged Rare Earth Complexes	275	4.3 Yttrium, Lanthanum, and Lutetium Naphthalene Complexes: Synthesis, Characterization, and Reactivity Toward P ₄ Activation	298
3 Previous Studies of Metal Complexes Supported By Ferrocene-Based Diamide Ligands and Development of New Rare Earth Starting Materials	282	4.4 Tautomerization of M ₃ P ₇ Studied by Variable-Temperature NMR Spectroscopy	303
3.1 Advantages of 1,1'-Ferrocenediyl Diamide Ligands	282	4.5 Synthesis of Organic P-Containing Compounds from P ₄	304
3.2 (NN ^{TBS})M(THF) ₂ (M = Sc, Y, La, and Lu) as Precursors for Reduction Chemistry	286		
3.3 Reaction Conditions for Reduction Chemistry	288		

5 Synthesis and Characterization of Rare Earth Biphenyl Complexes: 6C, 10 π -Electron Aromatic Systems	305	6 Group 3 Metal Stilbene Complexes	316
		7 Conclusions and Outlook References	320 321

1 INTRODUCTION

1.1 General Remarks About the Organometallic Chemistry of Rare Earths

This chapter summarizes recent advances in rare earth arene chemistry with an emphasis on complexes obtained by reduction and supported by non-cyclopentadienyl ancillary ligands. In order to discuss this area in context, a brief historical view of rare earth organometallic chemistry, in general, is included in the first section, and a brief historical view of bridging arene complexes, in particular, is included in the second section. The other sections describe chemistry from our group and include previously reported examples that are relevant to a particular section.

Bochkarev wrote a comprehensive review on rare earth arene complexes in 2002 (Bochkarev, 2002) and Nief provided a complete summary of molecular low-valent rare earth complexes in 2010 (Nief, 2010). However, in the past several years, significant advances in these two intrinsically related fields, arene complexes and molecular low-valent complexes, have been accomplished by some laboratories including ours. In addition, with the ever-growing power of computational tools and characterization methods, chemists are now able to understand the electronic structures of fascinating molecular structures better than it was possible even a decade ago.

In the periodic table, the rare earths are placed between alkaline earth metals and group 4 metals. As a consequence, four of them, scandium, yttrium, lanthanum, and lutetium, are also classified as group 3 metals. Unlike transition metals, which usually have multiple common oxidation states, most rare earths only have one common oxidation state, +3. Another significant difference between rare earths and transition metals is that the valence electrons of the former are f electrons, which are barely affected by the ligand field, while the ligand field has a major influence on the d electrons of the latter. Rare earths also differ from main group metals, such as group 13 elements, in part because of their empty d orbitals available for ligand coordination. Therefore, rare earth metal chemistry provides unique opportunities for synthetic chemists.

Organometallic rare earth chemistry witnessed major advances in the decades after the discovery of ferrocene (Kealy and Pauson, 1951; Miller et al., 1952), once π ligands were found to bind rare earth ions strongly (Bombieri and Paolucci, 1998). The most popular π ligands are cyclopentadienyl ($(\eta^5\text{-C}_5\text{H}_5)^-$, commonly referred to as Cp) and its derivatives. Rare earths are highly electropositive elements and prefer ionic bonding similar to alkali and alkaline earth metals. As a consequence, rare earth metal-carbon bonds are highly polarized with a significant amount of negative charge built up on

carbon. Because Cp is a 5-carbon, 6π -electron aromatic system, it can readily diffuse the negative charge through resonance. Therefore, cyclopentadienyls bind tightly to rare earth metals and usually serve as good ancillary ligands, facilitating many reactivity studies of organometallic rare earth chemistry (Chart 1; Arndt and Okuda, 2002; Ephritikhine, 1997; Evans and Davis, 2002). Binary rare earth cyclopentadienyl complexes, Cp_3M ($\text{M}=\text{Sc}$, Y , La , Ce , Pr , Nd , Sm , and Gd), were first synthesized by Wilkinson (Wilkinson and Birmingham, 1954), followed by the metallocenes Cp_2MCl ($\text{M}=\text{Sm}$, Gd , Dy , Ho , Er , Yb , and Lu) and $(\text{Me-Cp})_2\text{MCl}$ ($\text{M}=\text{Gd}$, Er , and Yb ; Maginn et al., 1963) and half-sandwich CpMCl_2 ($\text{M}=\text{Sm}$, Eu , Gd , Dy , Ho , Er , Yb , and Lu ; Manastyrskij et al., 1963) complexes. Substituted cyclopentadienyls were developed next in order to adjust their electronic and steric properties. The most important substituted-Cp ligand is pentamethylcyclopentadienyl ($(\eta^5\text{-C}_5\text{Me}_5)^-$, commonly referred to as Cp^*), which is more electron-donating and more sterically demanding than the unsubstituted cyclopentadienyl. Brintzinger and Bercaw pioneered the Cp^* chemistry for group 3 and 4 metals (Bercaw et al., 1972; Manriquez and Bercaw, 1974; Manriquez et al., 1976; Piers et al., 1990; Roddick et al., 1985; Wolczanski

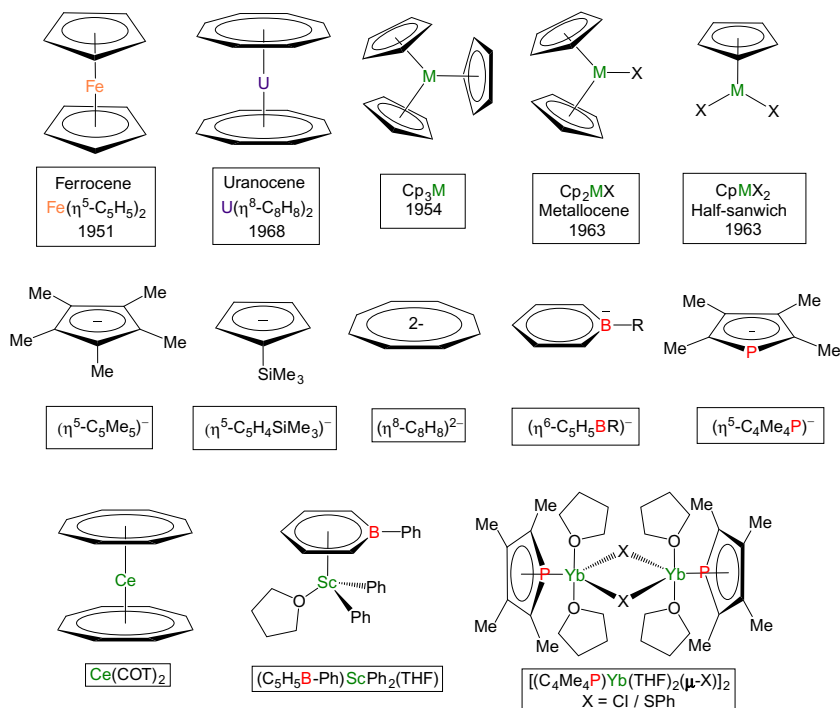


CHART 1 Important organometallic complexes, selected π ligands for organometallic rare earth complexes, and selected examples of rare earth complexes supported by certain π ligands (abbreviations are the same as in text).

and Bercaw, 1980; Wolczanski et al., 1979). Among the first heteroleptic pentamethylcyclopentadienyl complexes synthesized with various lanthanides were Cp^*_2NdCl (Wayda and Evans, 1980), $\text{Li}[\text{Cp}^*\text{MX}_3]$, and $[\text{Cp}^*_2\text{MX}_2]$, $\text{M} = \text{Yb, Lu, X} = \text{Cl, I}$ (Watson et al., 1981), as well as $[\text{M}'(\text{solvent})][\text{Cp}^*_2\text{MCl}_2]$, $\text{M}' = \text{Li, Na, M} = \text{Nd, Sm, Yb}$; $\text{Cp}^*_2\text{NdCl}(\text{THF})$, $\text{Cp}^*_2\text{Nd}(\text{N}[\text{SiMe}_3]_2)$, $\text{Cp}^*_2\text{YbCl}(\text{THF})$; $[\text{Na}(\text{OEt}_2)_2][\text{Cp}^*\text{NdCl}_3]$, and $\text{Cp}^*\text{Nd}(\text{N}[\text{SiMe}_3]_2)_2$ (Tilley and Andersen, 1981).

The coordination chemistry of other π ligands has also been explored (Chart 1; Bombieri and Paolucci, 1998; Edelman et al., 2002). The cyclooctatetraene dianion, $(\eta^8\text{-C}_8\text{H}_8)^{2-}$, commonly referred to as COT, also famous for the isolation of uranocene (Avdeef et al., 1972; Streitwieser and Mueller-Westerhoff, 1968), is known to stabilize lanthanides in all three oxidation states (+2, +3, and +4). In fact, the first COT lanthanide complexes to be prepared were solvated $\text{Ln}(\text{COT})$ species with $\text{Ln} = \text{Eu, Yb}$ (Hayes and Thomas, 1969). Most rare earth COT complexes, which feature both mono- and bis-COT, are, however, of the trivalent lanthanides (Bombieri and Paolucci, 1998). Cerocene, $\text{Ce}(\text{COT})_2$, merits a special mention since its electronic structure is still being actively investigated (Ferraro et al., 2012; Kerridge, 2013; Kumari et al., 2013; Walter et al., 2009).

Aromatic heterocycles that mimic cyclopentadienyl by functioning as multidentate ligands, such as boratabenzene $(\eta^6\text{-C}_5\text{H}_5\text{BR})^-$ (first reported rare earth examples: $(\text{C}_5\text{H}_5\text{B-Ph})\text{ScPh}_2(\text{THF})$ and $(\text{C}_5\text{H}_5\text{B-Ph})_2\text{ScPh}(\text{THF})$) (Putzer et al., 1999), tetramethylphospholyl $(\eta^5\text{-C}_4\text{Me}_4\text{P})^-$ (first reported rare earth examples: $[\text{Yb}(\mu\text{-Cl})(\eta^5\text{-C}_4\text{Me}_4\text{P})(\text{THF})_2]_2$ and $[\text{Yb}(\mu\text{-SPh})(\eta^5\text{-C}_4\text{Me}_4\text{P})(\text{THF})_2]_2$) (Nief and Ricard, 1994), and other heterocyclopentadienyl ligands (Nief, 2001) form rare earth complexes that are far less numerous than those of cyclopentadienyl derivatives because of their relative inaccessibility and difficult modification.

In the last two decades, well-defined ancillary ligands other than the aforementioned π ligands have been developed by various groups (Chart 2). They are usually electron-rich and sterically demanding, in order to tackle the high Lewis acidity and large ionic radii of rare earth ions. Some examples will be mentioned here with relevant compounds described later in the chapter, but the list is not meant to be exhaustive since several reviews cover the area of non-cyclopentadienyl rare earth chemistry (Arnold and Casely, 2009; Diaconescu, 2008; Edelman, 2009; Edelman et al., 2002; Konkol and Okuda, 2008; Li et al., 2010; Piers and Emslie, 2002; Reznichenko and Hultsch, 2010; Trifonov, 2010; Zeimentz et al., 2006). Fryzuk and coworkers pioneered the use of multidentate amidophosphine ligands, which combine soft phosphine and hard amide donors, and incorporated such motifs into the coordination sphere of group 3 metals, including the tridentate $[\text{N}(\text{SiMe}_2\text{CH}_2\text{P}^i\text{Pr}_2)_2]^-$ (P_2N) in $(\text{P}_2\text{N})\text{ScR}_2$ ($\text{R} = \text{Me, Et, CH}_2\text{SiMe}_3$; Fryzuk et al., 1996), tetradentate $(\text{PhP}[\text{CH}_2(\text{SiMe}_2)\text{N}(\text{SiMe}_2)\text{CH}_2]_2\text{PPh})^{2-}$ (P_2N_2) in

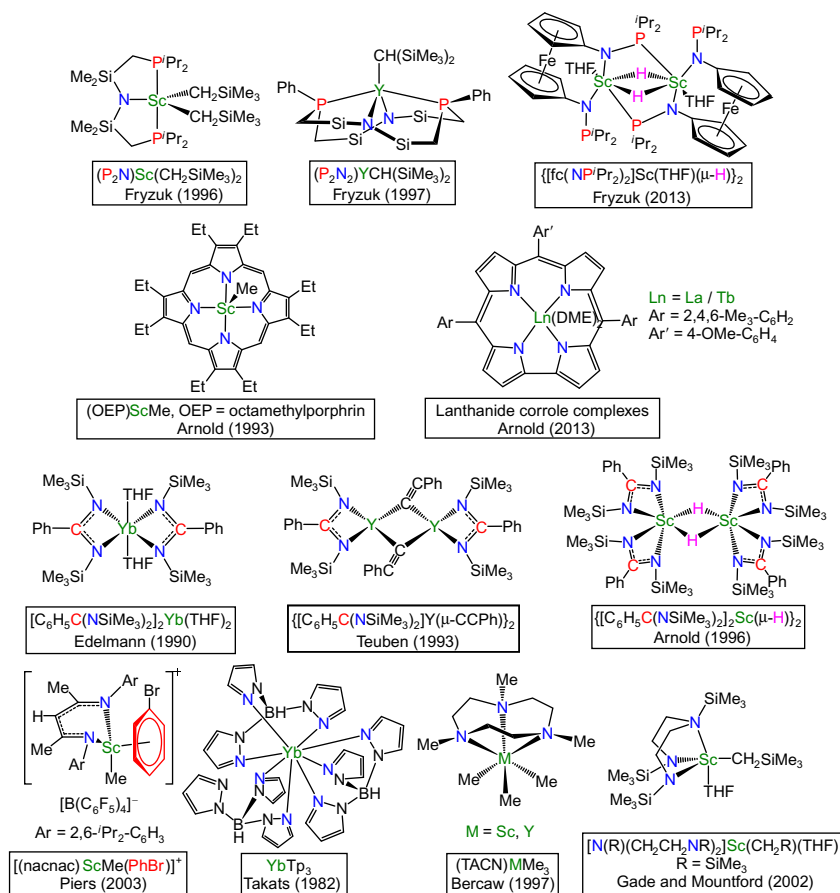


CHART 2 Non-cyclopentadienyl rare earth complexes reported by various groups (abbreviations are the same as in text).

$(P_2N_2)Y[CH(SiMe_3)_2]$ (Fryzuk et al., 1997), and, recently, the tetradentate $fc(NP^iPr_2)_2$ in $\{[fc(NP^iPr_2)_2]Sc(THF)(\mu-H)\}_2$ (Halcovitch and Fryzuk, 2013). J. Arnold popularized porphyrins as supporting ligands for scandium organometallic complexes (Arnold and Hoffman, 1990; Arnold et al., 1993) and, recently, synthesized lanthanum and terbium corrole complexes (Buckley et al., 2013). Several groups reported on the use of mono- and bis-amidinate rare earth complexes as analogs of Cp^*_2M (Duchateau et al., 1993; Hagadorn and Arnold, 1996; Wedler et al., 1990). Piers used bulky β -diketiminato ligands (nacnac) to obtain scandium dialkyl (Hayes et al., 2001) and cationic monoalkyl species (Hayes et al., 2002) and developed a salicylaldiminato ligand to afford group 3 metal hydrides upon hydrogenation by H_2 (Emslie et al., 2002). Takats worked extensively with sterically

demanding pyrazolylborate ligands (scorpionate) (Marques et al., 2002; Stainer and Takats, 1982), with early reports on alkyl and hydride divalent lanthanide complexes (Ferrence et al., 1999; Hasinoff et al., 1994). Scott achieved the synthesis of triamidoamine complexes of rare earths using $N(\text{CH}_2\text{CH}_2\text{NSiMe}_3)_3$ (Roussel et al., 1998). Bercaw introduced the neutral 1,4,7-trimethyl-1,4,7-triazacyclononane (TACN) on group 3 metals (Hajela et al., 1997) that was later modified by Mountford with a monoanionic pendant arm as an anchor (Bylikin et al., 2001). Gade and Mountford also developed a series of diamidopyridine and diamidoamine ligands with flexible backbones for the synthesis of scandium alkyl or aryl complexes (Ward et al., 2002).

New, non-cyclopentadienyl ligands made possible the synthesis of bonding motifs that seemed elusive a decade ago (Chart 3). Mindiola (Scott and Mindiola, 2009) incorporated a pincer-type, rigid tridentate PNP ligand, $N(2\text{-}i\text{-Pr}_2\text{-4-methylphenyl})_2$, on scandium and isolated rare scandium methylenide and oxo complexes (Scott et al., 2008) and, later, a scandium phosphinidene (Wicker et al., 2010). Y. Chen developed a series of tridentate monoanionic (Xu et al., 2010) or dianionic (Lu et al., 2011) β -diketiminato ligands and was able to characterize an unsupported scandium terminal imide (Lu et al., 2010) and studied its reactivity (Chu et al., 2011, 2012a; Lu et al., 2012). Other examples of transient (Scott and Mindiola, 2009; Wicker et al., 2011) or isolated (Chu et al., 2012b; Rong et al., 2013) scandium terminal imide complexes have also been reported. A recent development in this field

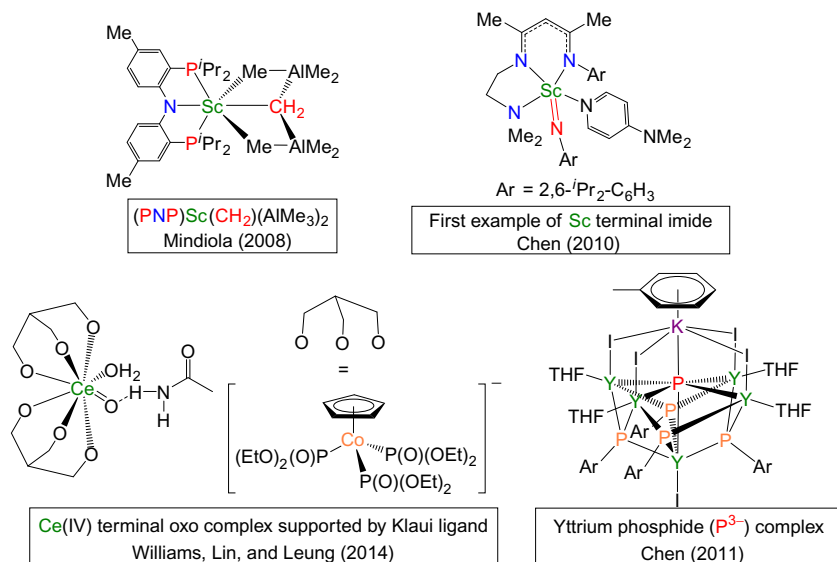


CHART 3 Examples of rare earth-element multiple bonds and phosphide reported by various groups (abbreviations are the same as in text).

is the synthesis of a terminal cerium(IV) oxide supported by the sterically encumbering Kläui tripodal ligand $[\text{CoCp}(\text{P}(\text{O})(\text{OEt})_2)_3]$ and stabilized by hydrogen bonding with a molecule of acetamide (So et al., 2014). These developments, as well as the report of transient (Thomson et al., 2010) and isolated (King et al., 2012) uranium nitride complexes, bide well for the discovery of other interesting bonding motifs with f elements. Recently, a P^{3-} -containing rare earth complex, $[\text{K}(\text{toluene})](\mu\text{-I})_4[\text{Y}_4(\text{THF})_4(\mu\text{-PAr})_4\text{YI}](\mu\text{-P})$ ($\text{Ar}=2,6\text{-di-}i\text{-iso-Pr-C}_6\text{H}_3$), was isolated from $\text{YI}_2(\text{THF})_3[\text{P}(\text{SiMe}_3)]$ [Ar] (Chart 3; Lv et al., 2011).

The list of rare earth-element multiple bonds is still missing terminal metal carbenes. However, Cavell (Aparna et al., 2000), Le Floch (Cantat et al., 2005), and Liddle (Mills et al., 2010; Chart 4) synthesized formal rare earth carbene complexes by incorporating the carbene in the framework of a chelating bis(iminophosphorano)methylene (N_2C^{2-}) or bis(diphenylthiophosphinoyl)methylene (S_2C^{2-}) ligand. Also, P. Arnold reported numerous examples of interesting reactivity of f-block complexes supported by *N*-heterocyclic carbenes (NHCs; Chart 4; Arnold and Casely, 2009; Liddle and Arnold, 2005).

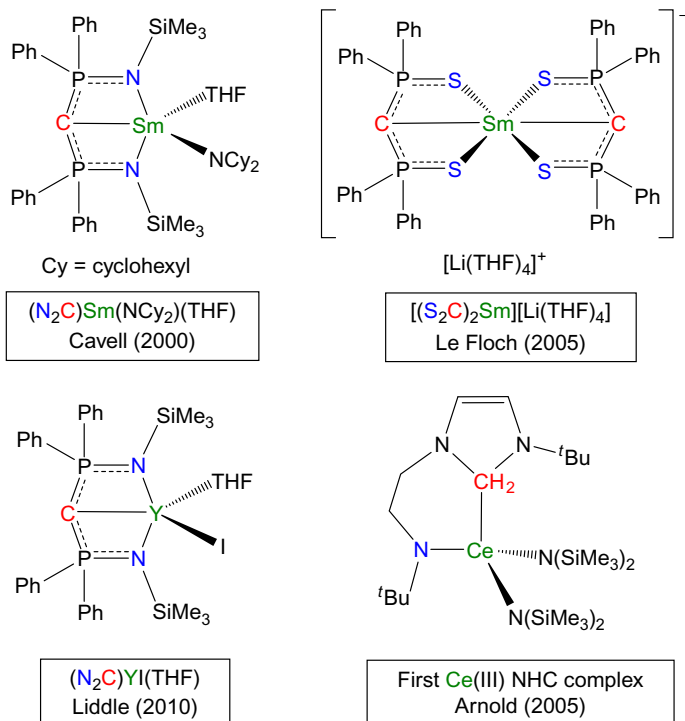


CHART 4 Examples of rare earth carbene complexes reported by various groups (abbreviations are the same as in text).

Another chapter of interesting bonding motifs is that of heterometallic complexes between the rare earths and transition metals with unsupported metal–metal bonds. Although the first structurally characterized lanthanide–transition metal bonds were reported in the early 1990s, $([(\text{MeCN})_3\text{YbFe}(\text{CO})_4]_2 \cdot \text{MeCN})_\infty$ (Deng and Shore, 1991) and $\text{Cp}_2\text{Lu}(\text{THF})\text{-RuCp}(\text{CO})_2$ (Beletskaya et al., 1993), the field started developing at a fast pace only in the last decade (Arnold et al., 2009; Butovskii et al., 2010; Liddle and Mills, 2009; Minasian et al., 2009; Oelkers et al., 2012), spurred by Kempe's report of $[\text{O}(\text{SiMe}_2\text{N-2-C}_5\text{H}_3\text{N-4-Me})_2]_2\text{NdRh}(\eta^2\text{-C}_2\text{H}_4)$ and $[\text{O}(\text{SiMe}_2\text{N-2-C}_5\text{H}_3\text{N-4-Me})_2]_2\text{Nd}(\text{THF})\text{PdMe}$ in 1998 (Chart 5; Spannenberg et al., 1998). Probably the most thought-provoking molecule reported in this area is $\text{Sm}(\text{ReCp}_2)_3$, also by Kempe, which does not feature any traditional supporting ligands for samarium and, instead, is bound solely by transition metals (Chart 5; Butovskii et al., 2010).

Although most rare earth organometallic complexes are discrete mono- or binuclear species, the chemistry of small nuclearity clusters shows that new

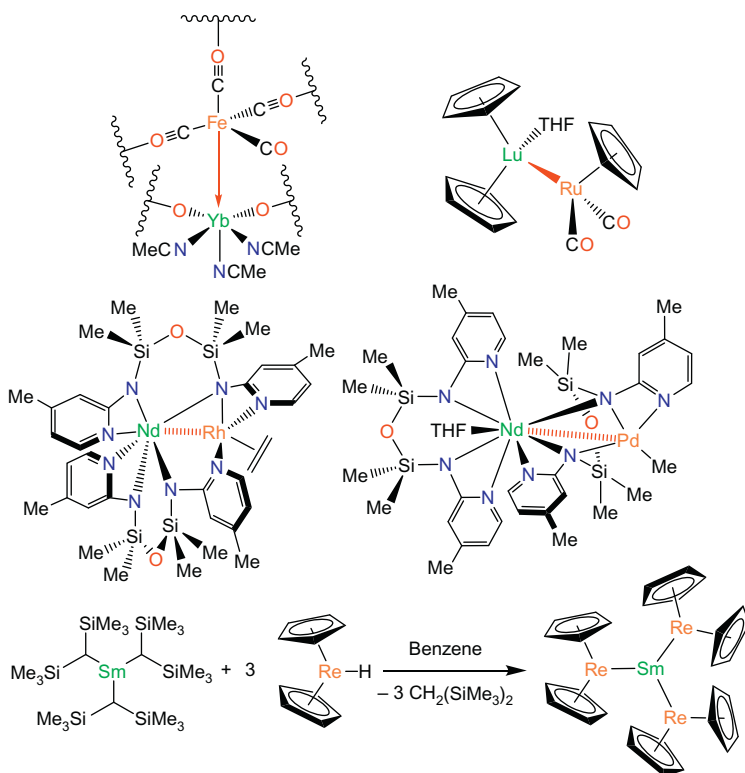


CHART 5 Top and middle: Initial examples of rare earth–transition metal unsupported bonds. Bottom: Synthesis of $\text{Sm}(\text{ReCp}_2)_3$ reported by Kempe's group (Butovskii et al., 2010).

reactivity can be discovered in the area of inert molecule activation when several rare earths act in concert (Chart 6; Hou et al., 2007). In 2003, Hou et al. reported the synthesis and structural characterization of polyhydrido lanthanide cluster complexes, $[(C_5Me_4SiMe_3)Ln(\mu-H)]_4(THF)_n$ ($Ln = Lu, Y, n = 0-2$; Tardif et al., 2003), which represented the first examples of structurally well-defined, salt-free lanthanide polyhydrido clusters (Hou et al., 2001). These clusters and their derivatives could break strong bonds such as the C–O bond in CO (Shima and Hou, 2006) and CO₂ (Tardif et al., 2004) and showed interesting polymerization activity (Li et al., 2006). A related trinuclear titanium polyhydride was found to be able to induce dinitrogen cleavage followed by partial hydrogenation in the presence of dihydrogen (Shima et al., 2013).

Somewhat related to the small nuclearity clusters described in the preceding text are organoaluminum rare earth heterometallic complexes (Chart 7) studied as models of Ziegler-type catalysts used in diene polymerization. Efforts in this area were initiated by Pearce and Lappert, who reported $Cp_2M(\mu-Me)_2AlR_2$ ($R = Me$ and $M = Sc, Gd, Dy, Ho, Er, Tm,$ or Yb ; $R = Et$ and $M = Sc$ or Y) (Ballard and Pearce, 1975; Holton et al., 1976), and were continued by Anwander (Fischbach and Anwander, 2006), who developed homoleptic tetraalkylaluminate rare earth complexes (Dietrich et al., 2011; Occhipinti et al., 2011) and bridging methylidenes (Dietrich et al., 2006b) and methylidyne (Dietrich et al., 2006a) as part of rare earth aluminum small clusters. Interestingly, the crystal structures of isostructural bridging hexacoordinate carbides, $[(TMTAC)M][M_2(\mu-CH_3)][(\mu_6-C)[Al(\mu-CH_3)_2(CH_3)]_3]$ ($(\mu_3-CH_2)(\mu-CH_3)Al(CH_3)_2)_2$] (TMTAC = 1,3,5-trimethyl-1,3,5-triazacyclohexane, $M = Y, Sm$), were also reported (Venugopal et al., 2009).

Our group previously synthesized group 3 metal monoalkyl complexes supported by ferrocene diamide ligands (Chart 8; Diaconescu, 2010a,b) and studied their reactivity toward various organic substrates, including aromatic *N*-heterocycles (Carver and Diaconescu, 2008; Miller et al., 2009) and other

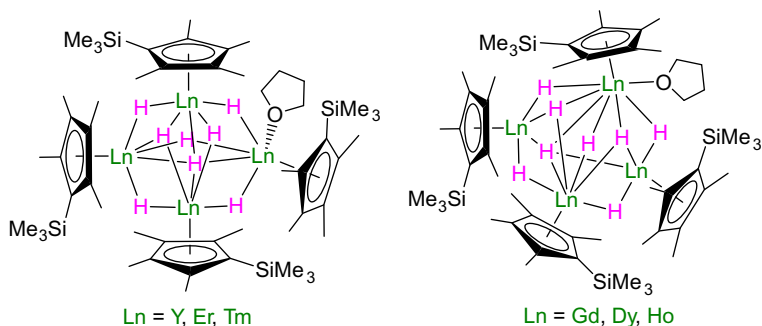


CHART 6 Selected examples of small nuclearity rare earth polyhydride clusters reported by Hou's group.

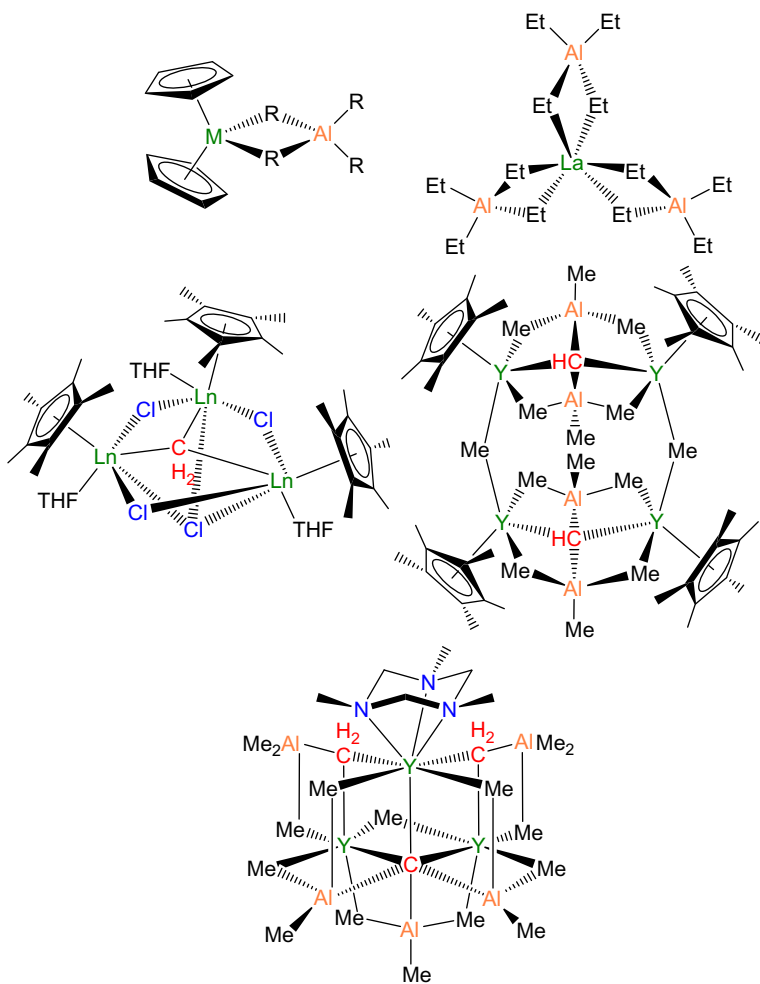


CHART 7 Selected examples of rare earth organoaluminum heterometallic complexes.

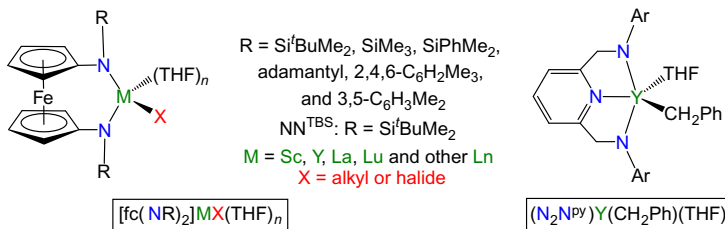


CHART 8 Examples of rare earth complexes supported by chelating diamide ligands reported by Diaconescu's group.

unsaturated substrates (Carver and Diaconescu, 2009). The 1,1'-ferrocenediyl (fc) diamide ligands have the general formula $\text{fc}(\text{NR})_2$; the system studied the most by us has $\text{R} = \text{Si}^t\text{BuMe}_2$ (Carver et al., 2008), while other versions, such as $\text{R} = \text{SiMe}_3$ (Monreal et al., 2007), SiPhMe_2 (Duhović and Diaconescu, 2013), adamantyl (Wong et al., 2010), 2,4,6-trimethylphenyl, and 3,5-dimethylphenyl (Lee et al., 2011), have been explored only briefly. Group 3 metal alkyl complexes supported by a pincer-type pyridine diamide ligand, 2,6-bis(2,6-di-*iso*-propylanilidomethyl)pyridine ($\text{N}_2\text{N}^{\text{PY}}$; Guerin et al., 1995), were also synthesized for a reactivity comparison study (Chart 8; Jie and Diaconescu, 2010).

The continuous development of ancillary ligands has focused recently on nitrogen donors in the field of organometallic rare earth chemistry, as shown in the special issue "Recent Advances in f-Element Organometallic Chemistry" that appeared in *Organometallics* in 2013 (Marks, 2013). Although the non-cyclopentadienyl organometallic chemistry of rare earths has been relatively underdeveloped, more than two-thirds of the research articles in that issue used ancillary ligands other than cyclopentadienyl and its derivatives.

1.2 Reduction Chemistry of Organometallic Rare Earth Complexes

As mentioned previously, rare earth chemistry differs mainly from transition metal chemistry in that most rare earth ions are redox inactive under ordinary conditions. However, a few lanthanides can support the +2 or +4 oxidation state. Lanthanide chemistry in the +4 oxidation state is mostly limited to cerium(IV) compounds (Nair et al., 2003). On the other hand, low-valent chemistry is more nuanced than its high-valent counterpart (Nief, 2010). Table 1 lists the ionic radii for M^{3+} (Shannon, 1976) and the spectroscopically estimated values for $E^0(\text{M}^{3+}/\text{M}^{2+})$ (Nugent et al., 1973).

An interesting study, relevant to organometallic rare earth chemistry, found that most LnI_2 could be synthesized using solid-state techniques with two different types of structures: those with a $[\text{Xe}]d^{0f^n}$ configuration and those with a $[\text{Xe}]d^{1f^{n-1}}$ configuration (Meyer et al., 2004). The former (including NdI_2 , SmI_2 , EuI_2 , DyI_2 , TmI_2 , and YbI_2) are genuine $[\text{M}^{2+}][\text{I}^-]_2$ salts, while the latter (the rest of LnI_2) should be viewed as $[\text{M}^{3+}][\text{I}^-]_2[\text{e}^-]$ due to their metallic character (the valence d electron is not localized on the metal but is found in the conduction band). This phenomenon is well correlated to the spectroscopically estimated values of $\text{M}^{3+/2+}$: the salt-like LnI_2 are those of rare earths having smaller values for the $\text{M}^{3+/2+}$ reduction potential, while the metallic LnI_2 are those with a $\text{M}^{3+/2+}$ reduction potential close to or lower than -3.0 V (the alkali metals have $\text{M}^{1+/0}$ reduction potentials around -3.0 V). These characteristics are also reflected in the organometallic chemistry of these elements: Eu(II) is so stable that it is just as common as

TABLE 1 Ionic Radii for M^{3+} (Effective Ionic Radii Are Listed) and Spectroscopically Estimated Values for $M^{3+/2+}$

Element	r (Å)	$E^0(M^{3+}/M^{2+})$ (V)
Sc	0.74	NA
Y	0.90	NA
La	1.03	-3.1
Ce	1.02	-3.2
Pr	0.99	-2.7
Nd	0.98	-2.6
Pm	0.97	-2.6
Sm	0.96	-1.6 (-1.55)
Eu	0.95	-0.3 (-0.35)
Gd	0.94	-3.9
Tb	0.92	-3.7
Dy	0.91	-2.6
Ho	0.90	-2.9
Er	0.89	-3.1
Tm	0.88	-2.3 (-2.2)
Yb	0.87	-1.1 (-1.1)
Lu	0.86	NA

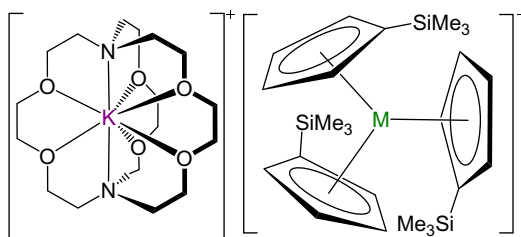
All values referenced to the normal hydrogen electrode; values in brackets are experimentally determined; NA=not applicable.

Values were adapted from [Shannon \(1976\)](#) and [Nugent et al. \(1973\)](#).

Eu(III) in organometallic rare earth chemistry ([Bombieri and Paolucci, 1998](#); [Zimmermann and Anwander, 2010](#)). Indeed, no homoleptic Eu(III) alkyl complexes have been reported yet ([Zimmermann and Anwander, 2010](#)), likely because the alkyl group is readily oxidized by Eu(III). Yb(II) is also common ([Bombieri and Paolucci, 1998](#); [Zimmermann and Anwander, 2010](#)). A major breakthrough in this field was the isolation of organosamarium(II) complexes. Divalent samarium complexes, such as Cp^*_2Sm , are strong reductants. For example, Cp^*_2Sm could reduce N_2 to form the first dinitrogen complex of an f element, $(Cp^*_2Sm)_2(\mu-\eta^2:\eta^2-N_2)$ ([Chart 9](#); [Evans et al., 1988](#)). The synthesis of molecular thulium, dysprosium, and even neodymium(II) complexes could be achieved from the corresponding metal diiodides with the appropriate ligands ([Nief, 2010](#)). Cyclopentadienyls with bulky substituents like

compounds (Nief, 2010). Perhaps the most famous system is LnZ_3/KC_8 developed by Evans, where Z may be various monoanionic ligands, including amides, aryloxides, and cyclopentadienyls, and Ln may be any rare earth (Chart 9). This combination can reduce dinitrogen to form $(\text{N}_2)^{2-}$ (Evans, 2007; Evans et al., 2005). Recently, lanthanide complexes of the radical trianion $(\text{N}_2)^{3-}$ have been isolated and characterized crystallographically (Evans et al., 2009; Fang et al., 2011; Farnaby et al., 2012; Fieser et al., 2013). It is important to note that some lanthanide $(\text{N}_2)^{3-}$ complexes behave as single molecule magnets due to the spin exchange between the lanthanide ions and $(\text{N}_2)^{3-}$ (Rinehart et al., 2011a), and one of them, $[\text{K}(18\text{-crown-6})(\text{THF})_2][\{[(\text{Me}_3\text{Si})_2\text{N}]_2(\text{THF})\text{Tb}\}_2(\mu\text{-}\eta^2\text{:}\eta^2\text{-N}_2)]$ (Chart 9), has one of the highest blocking temperatures (14 K) for a single molecule magnet (Rinehart et al., 2011b).

In 2008, Lappert isolated the first compound in a series of metal complexes with an ambiguous electronic structure: $[\text{K}(18\text{-crown-6})(\text{Et}_2\text{O})][1,3\text{-}(\text{Me}_3\text{Si})_2\text{C}_5\text{H}_3\text{La}]$ (Hitchcock et al., 2008). The authors proposed that it contains a lanthanum(II) ion. Recently, Evans extended this chemistry to almost all the lanthanides (Chart 10; MacDonald et al., 2011, 2012, 2013a). The charge balance requires the lanthanide ion to be in +2 oxidation state. However, intriguingly, the density functional theory (DFT) calculations reported by the authors suggest that all lanthanides have a $[\text{Xe}]4f^m5d^16s^0$ configuration, which is the same as that of solid-state LnI_2 salts. As mentioned earlier, the latter are considered to be $(\text{Ln}^{3+})(\text{I}^-)_2(\text{e}^-)$ (Meyer, 2014; Meyer et al., 2004). Despite the ambiguity in their electronic structure, the isolation of these complexes is nonetheless a remarkable achievement in the reduction chemistry of rare earth metals. Moreover, the advantage of using the $[\eta^5\text{-C}_5\text{H}_4\text{SiMe}_3]_3\text{M}$ platform has proved to be useful beyond supporting lanthanides: it was employed in the first structurally characterized molecular uranium(II) complex, also reported by Evans's group (MacDonald et al., 2013b).



$[\text{K}(2.2.2\text{-cryptand})][(\eta^5\text{-C}_5\text{H}_4\text{SiMe}_3)_3\text{M}]$
 M = Y, La, Ce, Pr, Gd, Tb, Ho, Er, Lu

CHART 10 Examples of reduced tris-cyclopentadienyl rare earth complexes reported by Lappert's and Evans's groups.

Overall, the reduction chemistry of organometallic rare earth compounds is a fast developing field with a lot of recent exciting discoveries (Evans, 2007). Although cyclopentadienyls feature prominently, non-cyclopentadienyl ligands have not been explored in detail (Nief, 2010) and may hold the key to unlock new bonding motifs and reactivity.

2 PREVIOUS STUDIES OF ARENE-BRIDGED RARE EARTH COMPLEXES

Arenes have outstanding stability due to their aromaticity; however, the accessibility of both their π and π^* orbitals allows them to serve as multielectron neutral or anionic ligands. Rare earths ions, because of their large ionic radii and high positive charge, can have high coordination numbers without sacrificing the strength of interactions with a ligand. Therefore, neutral and anionic arenes serve as excellent ligands for rare earth ions (Bochkarev, 2002).

Rare earth metal arene complexes were reviewed extensively by Bochkarev (2002). The first authentic arene-lanthanide complex was reported in 1986 and contained a neutral C_6Me_6 ligand (Cotton and Schwotzer, 1986). Rare earth complexes of reduced arenes have been targeted for a long time due to their fundamental importance as well as their potential use as multi-electron sources for reduction reactions (Bochkarev, 2002). Among them, inverted sandwiches of naphthalene are the most studied and have been synthesized and characterized for almost all rare earths (Bochkarev, 2002). In compounds with anionic arene ligands, the metal is usually found in the +3 oxidation state, while the additional electrons rest in the π^* orbitals of the arene ligand. Because of the relatively high energy of these orbitals, such complexes can serve as strong reductants.

The prototypical example in the class of arene-bridged complexes is the reduced benzene ligand. Lappert and coworkers isolated two types of bridged, reduced benzene complexes (Chart 11): $[K([18]-crown-6)][Ln(C_5H_3(SiMe_3)_2-1,3)_2(C_6H_6)]$ ($Ln=La, Ce, Pr, Nd$) and $[K([18]-crown-6)(C_6H_6)_2][Ln(C_5H_3(tBu)_2-1,3)_2(C_6H_6)]$ (Cassani et al., 1996, 1998, 1999, 2002). The two classes differ by the substituent of the cyclopentadienyl ligand (SiMe₃ vs. *tert*-butyl);

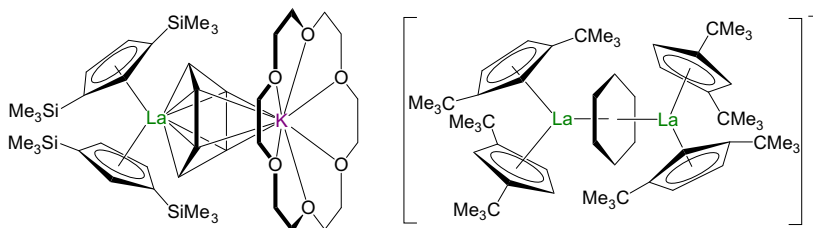


CHART 11 Inverse sandwiches of anionic benzene rare earth complexes as a 1,4-hexadiene-2,5-diyl (left) and as a benzene radical anion (right) ligand reported by Lappert's group.

the latter is more sterically demanding due to the shorter C–C than Si–C distance) and the nature of the benzene anion. Based on X-ray crystallography studies, it was proposed that the first class contains a 1,4-hexadiene-2,5-diyl ligand, while the latter contains a benzenide anion (monoanionic benzene). These differences are reflected in the color of these compounds: while the former are dark red, the latter are dark green. The dark-green toluene radical anion was later isolated as a potassium salt from potassium metal, 18-crown-6, and toluene in a THF solution. The corresponding benzene radical anion could not be obtained probably due to its high reactivity, but instead, the radical-coupled dimer $[\text{K}(18\text{-crown-6})]_2(\mu\text{-}\eta^5\text{:}\eta^5\text{-C}_6\text{H}_6\text{-C}_6\text{H}_6)$ was isolated. It was suggested that the dimer readily dissociated to $\text{C}_6\text{H}_6^{\bullet-}$ in solution (Hitchcock et al., 2001). Although the CCC angles of the benzene anion are similar for the potassium and lanthanum species, the C–C distances differ, with an average of 1.40 and 1.44 Å, respectively. It is interesting to note that the average C–C distance in the 1,4-hexadiene-2,5-diyl lanthanum complex is intermediate between those two values, 1.42 Å.

Biphenyl-bridged rare earth complexes are the least numerous in the class of polyaromatic complexes. As shown later in our chemistry, they can differ greatly from their corresponding fused arene (naphthalene or anthracene) counterparts. The examples from Fryzuk's group (Fig. 1) also show divergent chemistry: biphenyl-bridged complexes of yttrium and lutetium supported by the macrocyclic P_2N_2 ligand were obtained through C–C bond formation of proposed phenyl intermediates (Chart 12; Fryzuk et al., 1997). Depending on the biphenyl ligand, two types of compounds were isolated: from phenyl, the resulting compound featured yttrium ions coordinated to different rings, while from *meta*- and *para*-tolyl, complexes with both yttrium ions coordinated to the same ring were identified. Variable-temperature NMR spectroscopy indicated that the dimethylbiphenyl complexes show fluxional behavior in solution. It was proposed that both types of biphenyl complexes would show such behavior (Fryzuk et al., 1997).

Rare earth complexes in which the naphthalene is reduced and bridges two metal ions are rather numerous and all examples previous to our work were

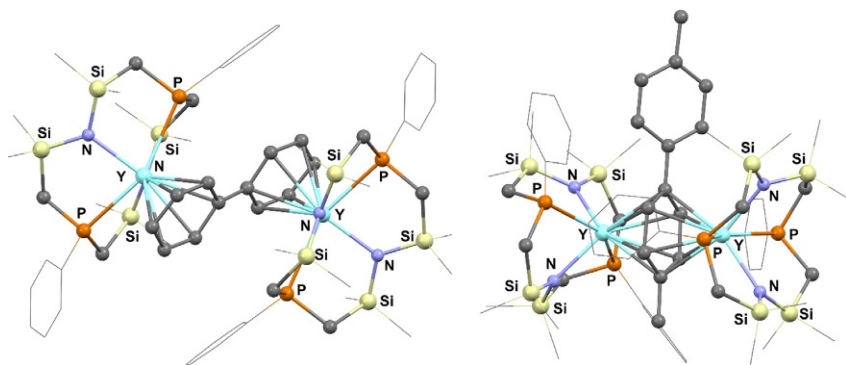


FIGURE 1 Molecular structures of inverse sandwiches of dianionic biphenyl yttrium complexes reported by Fryzuk's group. Figures were redrawn after Fryzuk et al. (1997).

reviewed by Bochkarev (2002). In order to be consistent, those compounds will also be described here since it will allow us to have a perspective view of the field.

Bochkarev's group pioneered the synthesis of bridging, reduced naphthalene complexes (Chart 13) by isolating and structurally characterizing $[\text{LaI}_2(\text{THF})_3]_2(\mu\text{-}\eta^4\text{:}\eta^4\text{-C}_{10}\text{H}_8)$ and $[\text{Eu}(\text{DME})_2]_2(\mu\text{-}\eta^4\text{:}\eta^4\text{-C}_{10}\text{H}_8)$ (Fedushkin et al., 1995). Shortly after, the series of lanthanide(III) diiodides

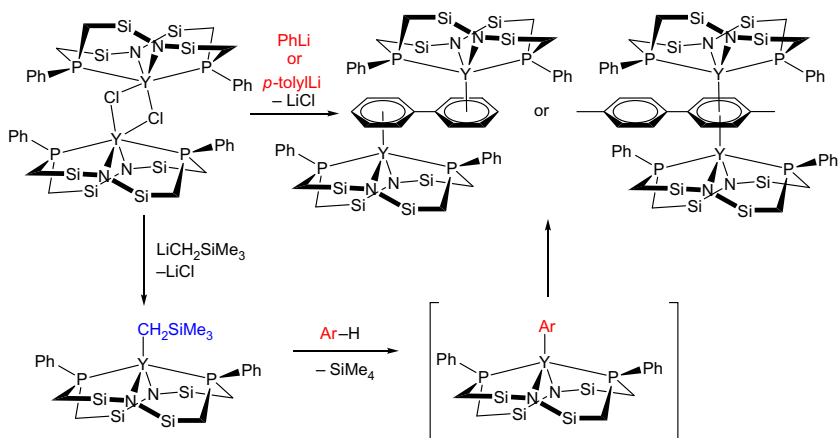


CHART 12 Inverse sandwiches of dianionic biphenyl yttrium complexes reported by Fryzuk's group.

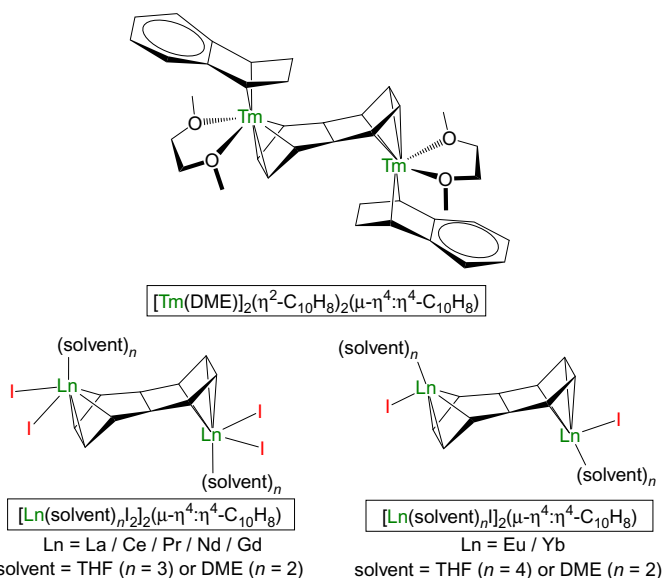


CHART 13 Inverse sandwiches of dianionic naphthalene lanthanide complexes reported by Bochkarev's group.

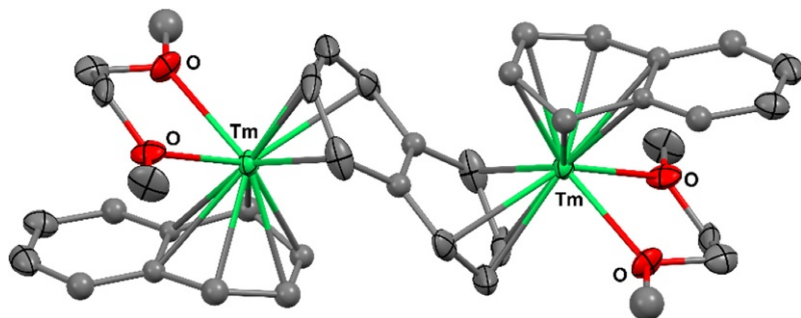


FIGURE 2 Molecular structure of $[\text{Tm}(\text{DME})]_2(\eta^2\text{-C}_{10}\text{H}_8)_2(\mu\text{-}\eta^4\text{:}\eta^4\text{-C}_{10}\text{H}_8)$ reported by Bochkarev's group. Figure was adapted from Bochkarev et al. (1997).

and an additional ytterbium(II) complex were reported (Bochkarev et al., 1996). A triple-decker binary thulium(III) naphthalene complex $[\text{Tm}(\text{DME})]_2(\eta^2\text{-C}_{10}\text{H}_8)_2(\mu\text{-}\eta^4\text{:}\eta^4\text{-C}_{10}\text{H}_8)$ (Fig. 2) was also isolated from the reaction of TmI_2 and lithium naphthalenide in 1,2-dimethoxyethane (DME) solution (Bochkarev et al., 1997). In all these complexes, the bridging naphthalene ligand is dianionic and coordinates in a $\mu\text{-}\eta^4\text{:}\eta^4$ mode. Samarium and ytterbium dinuclear complexes supported by cyclopentadienyl were also synthesized and reported to adopt the same coordination mode for the bridging naphthalene based on infrared (IR) spectroscopic data, but an X-ray structural analysis was not included (Protchenko et al., 1996).

A similar bridging mode was observed by Fryzuk's group, who synthesized naphthalene-bridged complexes of yttrium and lutetium supported by the macrocyclic P_2N_2 ligand $([\text{P}_2\text{N}_2]\text{Ln})_2(\mu\text{-}\eta^4\text{:}\eta^4\text{-C}_{10}\text{H}_8)$, $\text{Ln} = \text{Y}, \text{Lu}$; Fig. 3) from the reduction with KC_8 of the corresponding chloride-bridged bimetallic starting materials (Chart 14; Fryzuk et al., 2000). Similar to what was found for the dianionic, bridging biphenyl rare earth complexes supported by the same ligand, fluxional behavior was observed for the naphthalene complexes.

Probably the most interesting anionic naphthalene complex from the point of view of the naphthalene coordination mode is $([\text{Cp}^*\text{Lu}]_3(\text{C}_{10}\text{H}_8)(\text{C}_{10}\text{H}_7)(\text{H}))[\text{Na}(\text{THF})_3]_2[\text{C}_{10}\text{H}_8]$, which was isolated from the reaction of $[\text{Cp}^*\text{LuCl}_2]\text{NaCl}$ with $\text{C}_{10}\text{H}_8\text{Na}$ (Chart 15; Protchenko et al., 1997). X-ray analysis indicated that there is an interstitial dianionic naphthalene, which does not coordinate any cation but balances the charge for the two trinuclear lutetium clusters. In addition, one of the bridging naphthalenes is a dianion (indicated in Chart 15 by an η^6 coordination to Lu_2), while the other is a trianion that coordinates η^4 to Lu_3 and η^1 to Lu_2 . Since the cluster is diamagnetic, charge balance requires the presence of a hydride ligand. This proposal has not been verified directly, but was supported by the isolation of neodymium and dysprosium naphthalene complexes from hydride-containing starting materials (Burin et al., 2011).

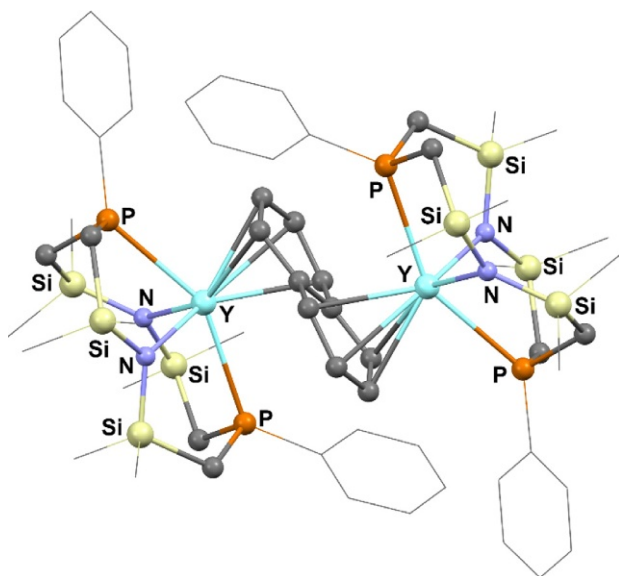


FIGURE 3 Molecular structure of $[(P_2N_2)Y]_2(\mu-\eta^4:\eta^4-C_{10}H_8)$ reported by Fryzuk's group. Figure adapted from Fryzuk *et al.* (2000).

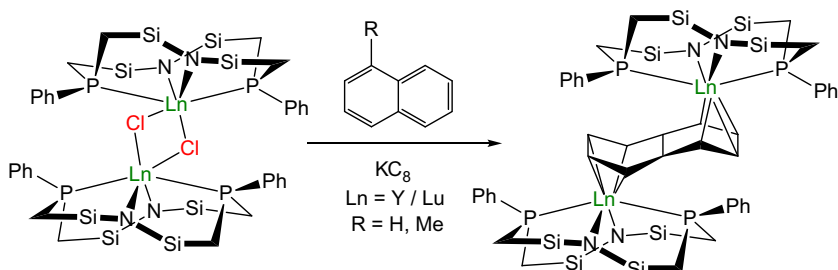


CHART 14 Inverse sandwiches of anionic naphthalene yttrium and lutetium complexes reported by Fryzuk's group.

Crystallographically characterized bridging, reduced anthracene complexes are less numerous than their naphthalene counterparts. For anthracene, there is the possibility that the two metal ions bind symmetrically involving both terminal rings or to a terminal and the middle ring (Chart 16). In the first case, a $\mu-\eta^3:\eta^3$ coordination mode was observed for $(Cp^*_2Ln)_2(C_{14}H_{10})$ ($Ln = Sm, La$) (Evans *et al.*, 1994; Thiele *et al.*, 1996), in which the two lanthanides bind symmetrically to a terminal and the middle ring, while a $\mu-\eta^4:\eta^4$ coordination mode was observed for $[(P_2N_2)Ln]_2(\mu-\eta^4:\eta^4-C_{14}H_{10})$ ($Ln = Y, Lu$) (Fryzuk *et al.*, 2000), akin to that of naphthalene in the analogous complexes. The solid-state molecular structures of $[(P_2N_2)Ln]_2$

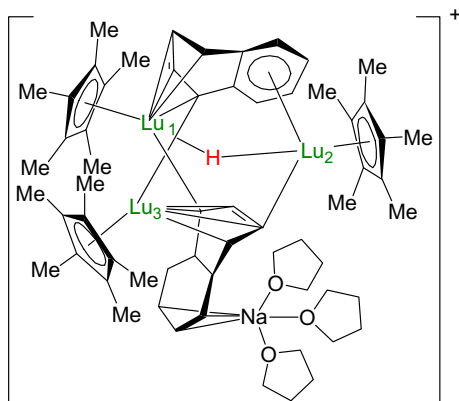


CHART 15 Proposed structure of a bridging naphthalene hydride tritlutetium complex reported by Bochkarev's group (Protchenko et al., 1997).

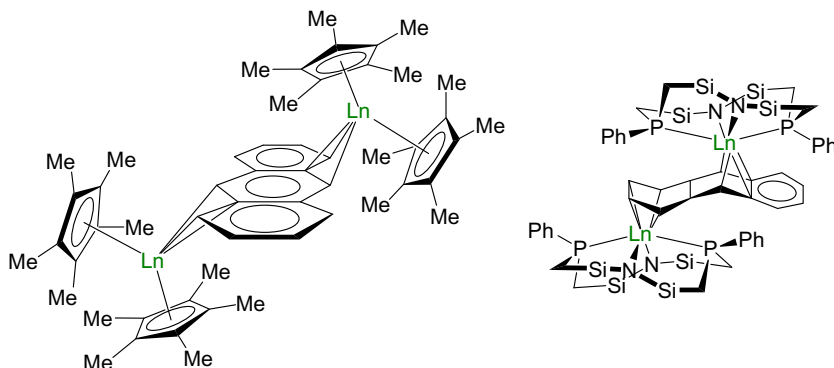


CHART 16 Bridging dianionic anthracene rare earth complexes.

$(\mu\text{-}\eta^4\text{:}\eta^4\text{-C}_{14}\text{H}_{10})$ (Fig. 4) indicate an unsymmetrical bonding of the two lanthanides; however, variable-temperature NMR spectroscopy pointed to a fluxional behavior and a symmetrical solution structure.

Complexes of bridging, reduced polycyclic arenes with more than three fused phenyl rings were also reported and various coordination modes identified (Chart 17). These range from $(\text{Cp}^*\text{Sm})_2(\mu\text{-}\eta^3\text{:}\eta^3\text{-C}_{16}\text{H}_{10})$ (Evans et al., 1994) to $[(\text{Cp}^*\text{La})_3(\mu\text{-Cl})_3(\text{THF})(\mu\text{-}\eta^2\text{:}\eta^6\text{:}\eta^6\text{-C}_{16}\text{H}_{10})]$ (Thiele et al., 1998) in pyrene compounds and $(\text{Cp}^*\text{Sm})_2(\mu\text{-}\eta^3\text{:}\eta^3\text{-C}_{18}\text{H}_{12})$ (Evans et al., 1994) in a 2,3-benzanthracene complex.

Overall, the molecules mentioned in this section show that a bridging anionic aromatic ligand can adopt a variety of coordination modes in the corresponding rare earth complexes. A feature worth noticing is that, when

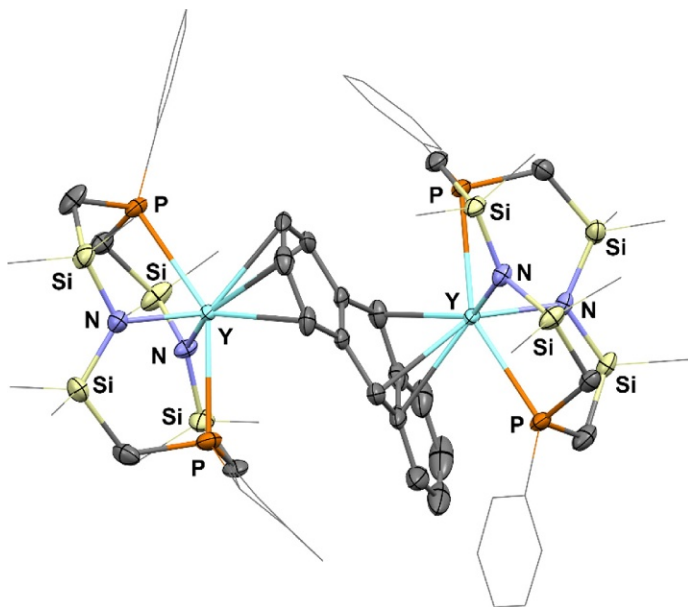


FIGURE 4 Molecular structure of $[(P_2N_2)Y]_2(\mu-\eta^4:\eta^4-C_{14}H_{10})$ reported by Fryzuk's group. Figure was adapted from Fryzuk *et al.* (2000).

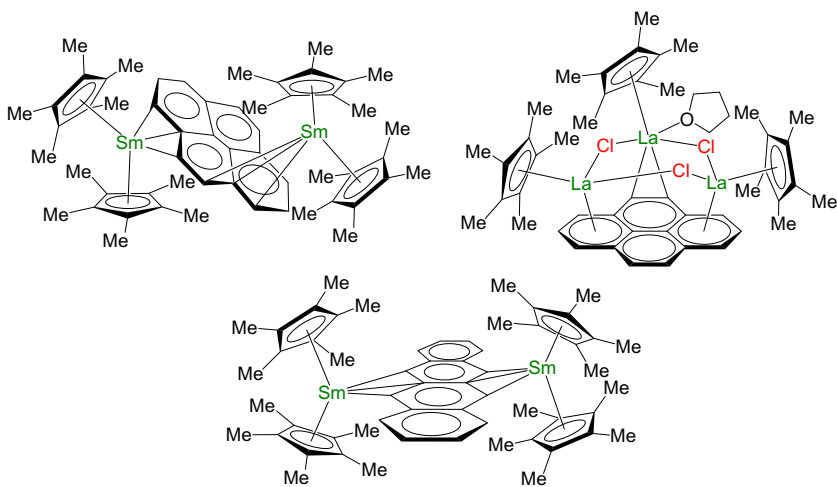


CHART 17 Bridging, dianionic pyrene and 2,3-benzanthracene rare earth complexes.

studied, all these compounds showed fluxional behavior and it is likely that most of them would do so in solution. This is explained, in part, by the ionic nature of the interaction between the lanthanide ions and the bridging anionic arenes.

3 PREVIOUS STUDIES OF METAL COMPLEXES SUPPORTED BY FERROCENE-BASED DIAMIDE LIGANDS AND DEVELOPMENT OF NEW RARE EARTH STARTING MATERIALS

3.1 Advantages of 1,1'-Ferrocenediyl Diamide Ligands

In 2000, J. Arnold reported a reliable synthesis of 1,1'-diaminoferrrocene (Shafir et al., 2000) and introduced the trimethylsilyl version $\text{fc}(\text{NHSiMe}_3)_2$ ($\text{H}_2(\text{NN}^{\text{TMS}})$) to group 4 metals, titanium and zirconium, to afford metal dimethyl and dibenzyl complexes $(\text{NN}^{\text{TMS}})\text{TiMe}_2$ and $(\text{NN}^{\text{TMS}})\text{ZrBn}_2$ ($\text{Bn}=\text{CH}_2\text{Ph}$) (Chart 18; Shafir et al., 2001). $[(\text{NN}^{\text{TMS}})\text{ZrBn}][(\mu\text{-Bn})\text{B}(\text{C}_6\text{F}_5)_3]$ could be obtained by treating $(\text{NN}^{\text{TMS}})\text{ZrBn}_2$ with one equivalent of $\text{B}(\text{C}_6\text{F}_5)_3$ and its reactivity toward olefin polymerization was studied (Shafir and Arnold, 2003). Our group introduced the 1,1'-ferrocenediyl diamide ligands to uranium and reported the synthesis and characterization of $(\text{NN}^{\text{TBS}})_2\text{U}$ ($\text{NN}^{\text{TBS}}=1,1'\text{-fc}(\text{NHSi}^t\text{BuMe}_2)_2$) and its one-electron oxidation product $[(\text{NN}^{\text{TBS}})_2\text{U}][\text{BPh}_4]$ in 2007 (Chart 18). The redox process was studied in detail, and it was found that the electronic communication between the two iron centers was mediated by uranium in the mixed-valent (Fe(II) and Fe(III)) complex, $[(\text{NN}^{\text{TBS}})_2\text{U}][\text{BPh}_4]$ (Monreal et al., 2007). At the time, it was also observed that the *tert*-butyldimethylsilyl version, $1,1'\text{-fc}(\text{NHSi}^t\text{BuMe}_2)_2$ ($\text{H}_2(\text{NN}^{\text{TBS}})$), was easier to handle because of its improved solubility, which allowed many compounds to crystallize easily. As a consequence, later efforts focused on this particular ligand platform. Group 3 metal monoalkyl complexes with the general formula $(\text{NN}^{\text{TBS}})\text{M}(\text{CH}_2\text{Ar})(\text{THF})$ ($\text{M}=\text{Sc}$ (Carver et al., 2008) and Lu (Carver et al., 2009), $\text{Ar}=3,5\text{-C}_6\text{H}_3\text{Me}_2$; $\text{M}=\text{Y}$ (Carver and Diaconescu, 2008) and La (Miller et al., 2009), $\text{Ar}=\text{C}_6\text{H}_5$) and the uranium dialkyl complex $(\text{NN}^{\text{TBS}})\text{UBn}_2$ (Monreal and Diaconescu, 2008) were successfully synthesized (Chart 18 and Fig. 5). The electron-donating 1,1'-ferrocenediyl group (Sauro and Workentin, 2002) makes the amide donor bind strongly to the highly electropositive group 3 metals and uranium(IV) ion. By using NN^{TBS} as the ancillary ligand for d^{0f^n} metal alkyl complexes, the C–H bond activation of aromatic heterocycles (Williams et al., 2011), successive C–C bond coupling (Carver et al., 2009, 2010; Monreal and Diaconescu, 2010; Williams et al., 2010), dearomatization of aromatic heterocycles (Miller et al., 2009), and the unprecedented ring-opening of 1-methylimidazole (Carver and Diaconescu, 2008; Monreal et al., 2009), 1-methylbenzimidazole (Miller et al., 2010), or other aromatic heterocycles (Duhović et al., 2010) were observed and studied (Diaconescu, 2010a,b).

It is likely that the ferrocene backbone has a specific role in facilitating the unique reactivity observed by our group. Our hypothesis is that when the electron-rich iron center of ferrocene and the electropositive metal ion are brought into close proximity, a donor–acceptor interaction takes place between the iron and the metal (Bauer et al., 2012). This type of Lewis acid–Lewis base interaction was observed previously with both electrophilic

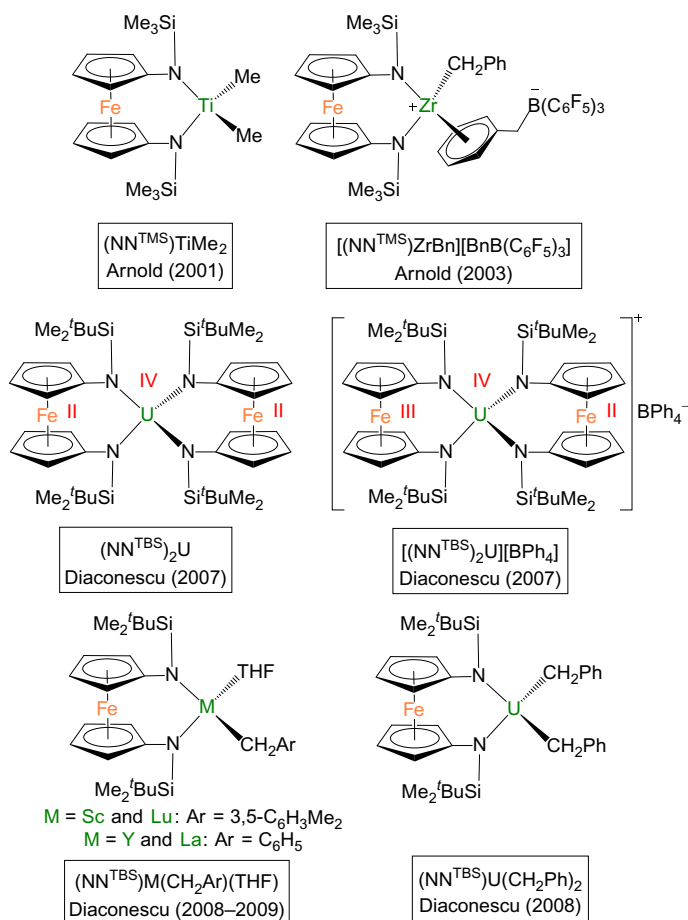


CHART 18 Group 4, uranium, and group 3 metal complexes supported by 1,1'-ferrocenediyl diamide ligands.

early and late transition metals (Chart 19): Seyferth suggested a weak, dative Fe–Pd bond in $[\text{Fe}(\eta^5\text{-C}_5\text{H}_4\text{S})_2]\text{Pd}(\text{PPh}_3)$ (Seyferth et al., 1983); Akabori later provided a comprehensive study based on $[\text{M}(\eta^5\text{-C}_5\text{H}_4\text{O})_2]\text{M}'(\text{PPh}_3)$ ($\text{M} = \text{Fe}$ or Ru , $\text{M}' = \text{Pd}$ or Ni) that supported a dative $\text{M}–\text{M}'$ interaction (Akabori et al., 1987); Nataro recently reported on the electronic structure of palladium(II) and platinum(II) compounds of 1,1'-bis(phosphino)metallocenes (Gramigna et al., 2013). In the area of early transition metals, J. Arnold suggested a dative Fe–Ti bond based on the short Fe–Ti distance in $[(\text{NN}^{\text{TMS}})\text{-Ti}(\mu\text{-Cl})_2][\text{B}(\text{C}_6\text{F}_5)_4]_2$ (Shafir and Arnold, 2001), and Stephan showed the importance of a ferrocenyl-titanium or zirconium interaction in stabilizing reactive cations (Ramos et al., 2009). More interestingly, J. Arnold observed

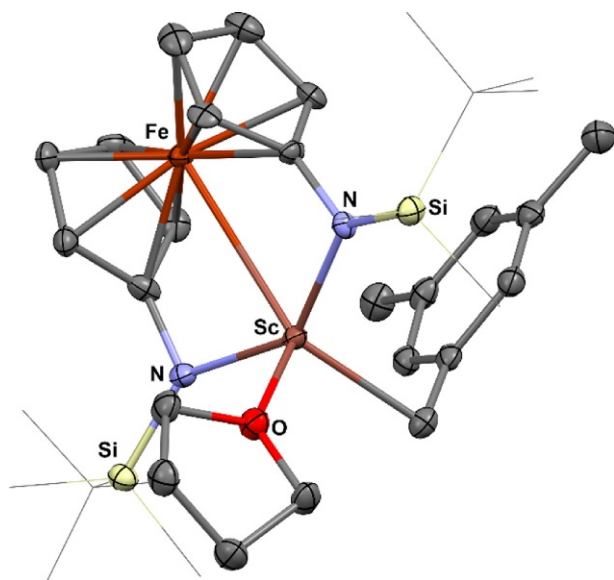


FIGURE 5 Molecular structure of $(\text{NN}^{\text{TBS}})\text{Sc}(\text{CH}_2\text{Ar})(\text{THF})$ ($\text{Ar} = 3,5\text{-C}_6\text{H}_3\text{Me}_2$). Figure was adapted from Carver *et al.* (2008).

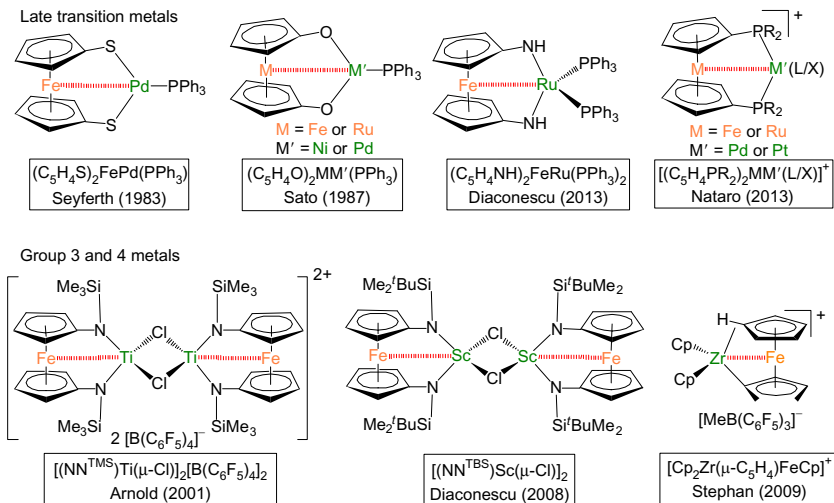


CHART 19 Metallocene complexes containing dative iron–metal bonds (indicated as red (dark gray in print) dashed lines).

that the Fe–Ti distance in a series of compounds with the NN^{TMS} ligand varied according to the electrophilicity of the titanium center: Fe–Ti distance is 3.32 Å in the neutral dialkyl complex $(\text{NN}^{\text{TMS}})\text{TiMe}_2$, but it shortens to 3.07 Å in the Lewis acid adduct $[(\text{NN}^{\text{TMS}})\text{TiMe}][(\mu\text{-Me})\text{B}(\text{C}_6\text{F}_5)_3]$ and

reaches the shortest value, 2.49 Å, in the chloride-bridged dicationic complex $[(\text{NN}^{\text{TMS}}\text{Ti}(\mu\text{-Cl}))_2][\text{B}(\text{C}_6\text{F}_5)_4]_2$. Our group observed a similar trend for group 3 metal complexes supported by the NN^{TBS} ligand: the Fe–Sc distance is 3.16 and 2.80 Å in $(\text{NN}^{\text{TBS}}\text{Sc}(\text{CH}_2\text{C}_6\text{H}_3\text{Me}_2\text{-3,5})(\text{THF}))$ (Fig. 5) and $[(\text{NN}^{\text{TBS}}\text{Sc}(\mu\text{-Cl}))_2]$ (Fig. 6), respectively (Carver et al., 2008). Recently, our group also reported a dative Fe–Ru interaction in $[\text{Fe}(\eta^5\text{-C}_5\text{H}_4\text{NH})_2]\text{Ru}(\text{PPh}_3)_2$ and characterized it by spectroscopic methods and DFT calculations (Green et al., 2013).

Besides the weak Fe–M interaction, ferrocene-based ligands inherit the redox-active nature of ferrocene. The ferrocenium–ferrocene redox couple is usually reversible (Connelly and Geiger, 1996). Therefore, the ferrocene unit can serve as a redox switch providing an indirect control of active sites for polymerization or other chemical transformations (Gregson et al., 2006; Yoon et al., 2010). Recently, our group reported a redox-switchable catalyst used for ring-opening polymerization and the synthesis of biodegradable materials (Broderick et al., 2011). This result highlighted the potential of the redox-active ferrocene backbone in tuning the reactivity of the metal center found in the vicinity of ferrocene. On the other hand, the possibility to reduce ferrocene was evidenced by the reversible redox event observed for ferrocene in 1,2-dimethoxyethane at -3.45 V (referenced to ferrocene⁺⁰) (Ito et al., 1983).

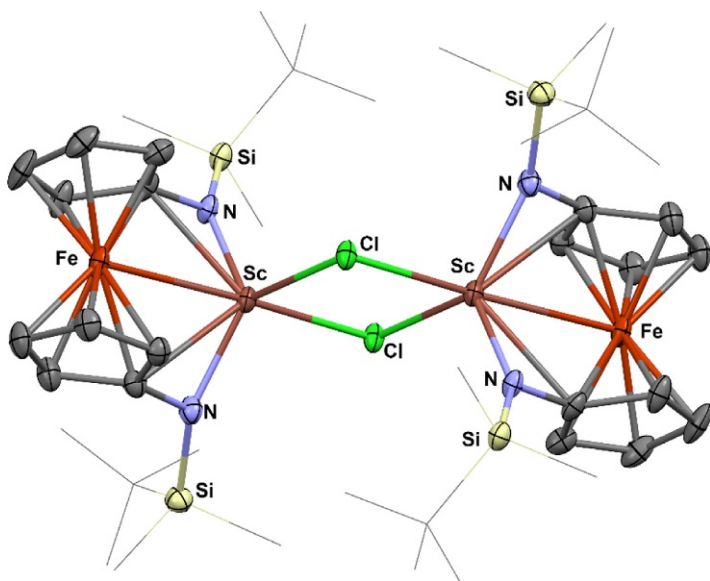


FIGURE 6 Molecular structure of $[(\text{NN}^{\text{TBS}}\text{Sc}(\mu\text{-Cl}))_2]$. Figure was adapted from Carver et al. (2008).

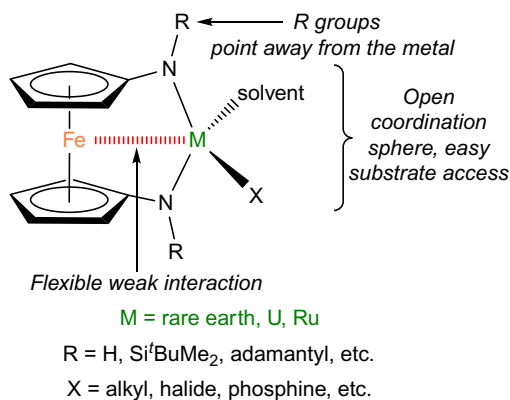


FIGURE 7 Advantages/features of 1,1'-ferrocenediyl diamide ligands to support electrophilic d^0f^n metals.

Based on experimental observations and computational studies on the organometallic compounds supported by the 1,1'-ferrocenediyl diamide ligands, the following advantages/features were attributed to this type of ligands (Fig. 7): (1) The weak, dative iron–metal interaction stabilizes complexes of the Lewis-acidic metal center, and probably more importantly, this interaction is flexible since the barrier for the ferrocene unit to move toward or away from the metal center is low (nearly free rotation of $C_{\text{ipso}}\text{--N}$ bonds); and (2) the 1,1'-ferrocenediyl diamide blocks one side of the metal leaving the other side widely open for substrate coordination. This is particularly important when comparing it to substituted cyclopentadienyls. From our point of view, substituted cyclopentadienyls are usually sterically demanding, which facilitates the isolation of unstable compounds but hinders their reactivity (Evans and Davis, 2002).

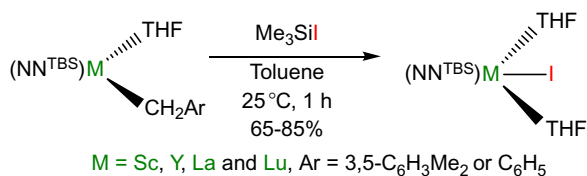
3.2 $(\text{NN}^{\text{TBS}})\text{MI}(\text{THF})_2$ ($M = \text{Sc, Y, La, and Lu}$) as Precursors for Reduction Chemistry

In rare earth reduction chemistry, the metal precursor complex is crucial. For example, Evans and coworkers synthesized the first scandium dinitrogen complex by using a specific Sc(III) cationic species, $[(\text{C}_5\text{Me}_4\text{H})_2\text{Sc}][(\mu\text{-Ph})\text{BPh}_3]$, as the precursor (Demir et al., 2010). Similarly, in our chemistry, initial attempts using $[(\text{NN}^{\text{TBS}})\text{Sc}(\mu\text{-Cl})_2(\text{Carver et al., 2008})]$ and potassium graphite (KC_8) in common organic solvents such as hexanes, toluene, diethyl ether (Et_2O), and tetrahydrofuran (THF) did not result in any products that could be identified. However, the iodide analog proved to be a good starting material.

$(\text{NN}^{\text{TBS}})\text{ScI}(\text{THF})_2$ could be readily prepared from $(\text{NN}^{\text{TBS}})\text{Sc}(\text{CH}_2\text{C}_6\text{H}_3\text{Me}_2\text{-3,5})(\text{THF})$ on a gram scale. Clean conversion to $(\text{NN}^{\text{TBS}})\text{MI}(\text{THF})_2$ ($M = \text{Sc, Y, La, and Lu}$) was achieved by stirring two equivalents of

Me_3SiI and $(\text{NN}^{\text{TBS}})\text{M}(\text{CH}_2\text{Ar})(\text{THF})$ in toluene at 25°C for one hour (Scheme 1). Compounds $(\text{NN}^{\text{TBS}})\text{MI}(\text{THF})_2$ are barely soluble in saturated hydrocarbons but readily soluble in aromatic solvents and ethers. Except for $(\text{NN}^{\text{TBS}})\text{ScI}(\text{THF})_2$, which crystallized in the space group $\text{C}2/c$, all other $(\text{NN}^{\text{TBS}})\text{MI}(\text{THF})_2$ crystallized in the same space group, $P-1$, and differed only slightly in their structural parameters (Fig. 8). In all $(\text{NN}^{\text{TBS}})\text{MI}(\text{THF})_2$ structures, the rare earth ion is coordinated by two nitrogen donors, two oxygen donors, and one iodide ligand, while the ferrocene backbone sits oppositely to iodide. If iron coordination is taken into account, the metal center has a pseudo-octahedral geometry. However, the Fe–M interaction is in the “off” mode (indicated by long Fe–M distances) in the presence of two coordinating THF molecules, which supply enough electron density to the metal center.

A molecular orbital analysis by using DFT calculations was performed for $(\text{NN}^{\text{TBS}})\text{MI}(\text{THF})_2$ (Fig. 9). From the point of view of reduction chemistry, the LUMO of $(\text{NN}^{\text{TBS}})\text{MI}(\text{THF})_2$ is of particular interest because it may indicate whether the ferrocene backbone is involved in the reduction process. Somewhat surprisingly, the LUMO of various metal iodides was not the same,



SCHEME 1 Synthesis of $(\text{NN}^{\text{TBS}})\text{MI}(\text{THF})_2$ ($M = \text{Sc, Y, La, and Lu}$).

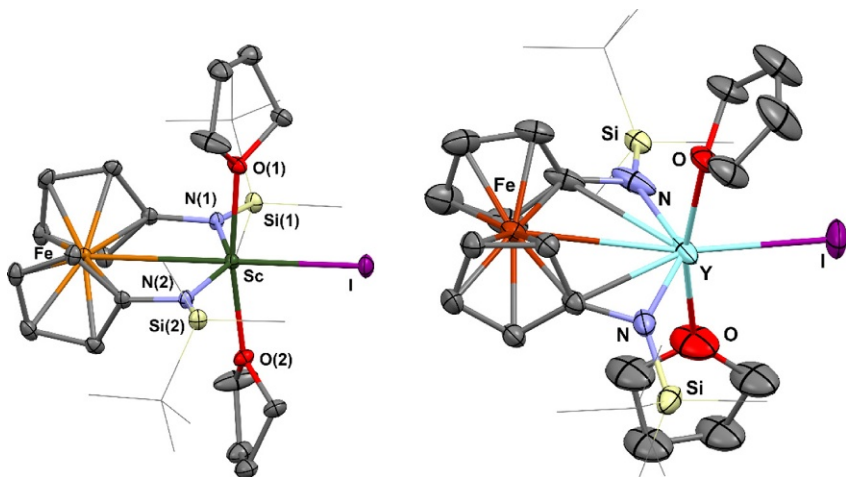


FIGURE 8 Molecular structure of $(\text{NN}^{\text{TBS}})\text{ScI}(\text{THF})_2$ (left) and $(\text{NN}^{\text{TBS}})\text{YI}(\text{THF})_2$ (right). Figures were adapted from [Huang et al. \(2011\)](#) and [Huang and Diaconescu \(2012\)](#).

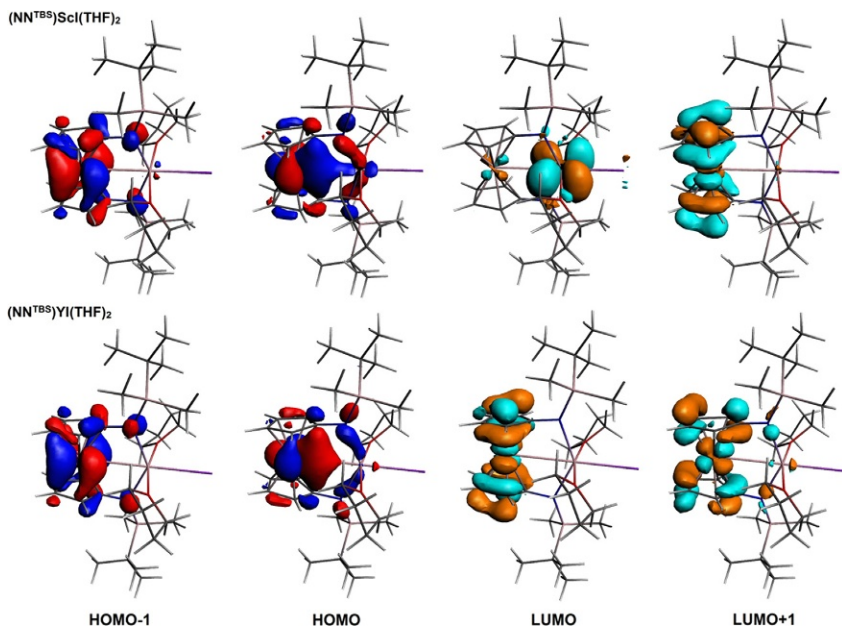


FIGURE 9 Selected molecular orbitals for $(\text{NN}^{\text{TBS}})\text{ScI}(\text{THF})_2$ and $(\text{NN}^{\text{TBS}})\text{YI}(\text{THF})_2$. Top, $(\text{NN}^{\text{TBS}})\text{ScI}(\text{THF})_2$; bottom, $(\text{NN}^{\text{TBS}})\text{YI}(\text{THF})_2$. Hydrogen atoms were omitted for clarity.

although HOMO and HOMO-1 were always the 3d orbitals of iron. For $(\text{NN}^{\text{TBS}})\text{ScI}(\text{THF})_2$, the LUMO was localized on the 3d orbital of scandium, while the LUMO + 1 was the π^* orbital of the ferrocene backbone; however, for $(\text{NN}^{\text{TBS}})\text{YI}(\text{THF})_2$, both the LUMO and LUMO + 1 were the π^* orbitals of the ferrocene backbone. Since the reduction usually involves population of the LUMO from an external electron source, this difference suggests that the ferrocene backbone might serve as an electron shuttle in addition to a direct reduction pathway of the rare earth halide that is operative in other rare earth halides.

3.3 Reaction Conditions for Reduction Chemistry

It is well documented that reaction conditions are crucial to the outcome of reduction chemistry. As a typical heterogeneous reductant, KC_8 forms a suspension in common organic solvents such as *n*-pentane, Et_2O , and THF (Bergbreiter and Killough, 1978). However, the reaction of KC_8 with acidic protons (water, methanol, and other alcohols) in different solvents resulted in a different amount of evolved hydrogen gas. It was suggested that this difference in reactivity was caused by the fact that the suspensions formed by

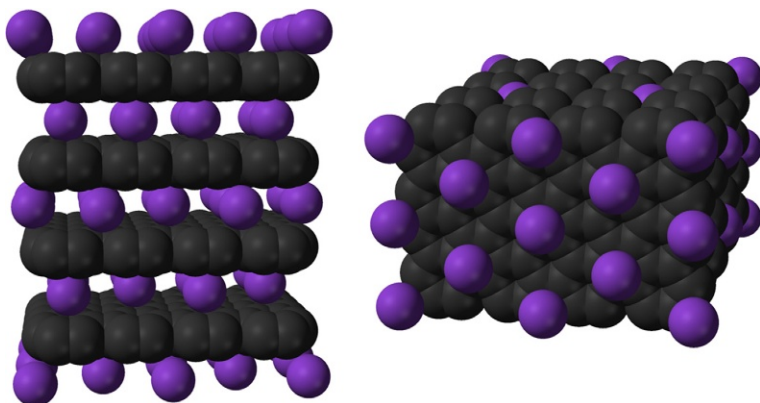


FIGURE 10 Space-filling model of KC₈: left, side view; right, top view. Use granted by Ben Mills from the Wikimedia Commons.

KC₈ in *n*-pentane and Et₂O are not as well dispersed as those formed in THF (Bergbreiter and Killough, 1978).

Potassium graphite (commonly referred to as KC₈) is the most potassium-rich form of a series of graphite intercalation compounds with potassium (Rüdrorf and Schulze, 1954). A space-filling model of KC₈ is shown in Fig. 10. KC₈ is probably the most widely used reductant in organometallic rare earth chemistry (Nief, 2010). The system composed of trivalent lanthanide precursors LnZ₃ (Z represents a monoanionic ligand) and KC₈ developed by Evans proved successful in reducing dinitrogen to form stable lanthanide dinitrogen complexes with the general formula (Z₂Ln)₂(μ-η²:η²-N₂) (Evans et al., 2005). In addition, KC₈ was used in obtaining a series of divalent lanthanide complexes [K(2.2.2-cryptand)][(C₅H₄SiMe₃)₃Ln] (Chart 10; MacDonald et al., 2013a). The strategy of using KC₈ as a reductant was also employed in main group chemistry to obtain structurally fascinating and fundamentally important molecules such as LB(H)=B(H)L (Wang et al., 2007) and LSi=SiL (Wang et al., 2008) (L = :C[N(2,6-ⁱPr₂C₆H₃)CH]₂), containing a B=B bond and a Si=Si bond, respectively, although similar molecules, L:B(Br)=B(Br):L and L:B≡B:L, could also be prepared using sodium naphthalenide as a reductant by another group (Braunschweig et al., 2012). The use of KC₈ as a reductant in organic synthesis has also been explored (Bergbreiter and Killough, 1978). It was concluded that, as a reducing agent, it behaved similarly or poorly compared to its homogeneous analog sodium naphthalenide but it had the advantage that it did not form any soluble by-products. This advantage is particularly important in organometallic chemistry (Jensen et al., 1965; Schwindt et al., 1990; Ungurenasu and Palie, 1975).

4 SYNTHESIS OF RARE EARTH FUSED-ARENE COMPLEXES AND THEIR REACTIVITY TOWARD P₄ ACTIVATION

4.1 Scandium Fused-Arene Complexes: Synthesis, Characterization, and Reactivity

Prior to our work, rare earth reduced naphthalene complexes were missing examples of scandium compounds. Similarly, no scandium complex with another fused arene, such as anthracene, was known, although reduced anthracene complexes with other rare earths are common (Bochkarev, 2002). The synthesis of scandium arene complexes had been limited to the co-condensation of scandium metal vapors and benzene derivatives with bulky substituents (1,3,5-*t*Bu₃C₆H₃) (Cloke et al., 1991) or heteroaromatic hydrocarbons (2,4,6-*t*Bu₃C₅H₂N and 2,4,6-*t*Bu₃C₃P₃) to give sandwich, formally zero-valent and subvalent scandium arene complexes (Chart 20; Arnold et al., 1996, 1998; Cloke, 1993). The gas-phase reaction of scandium ion with benzene and its derivatives led to products that could only be characterized by mass spectrometry (Huang et al., 1987). Neutral arene scandium(III) complexes supported by β -diketiminato ligands were isolated and structurally characterized by Piers's group (Chart 21; Hayes et al., 2003, 2007). The reports from Piers's group highlighted the strong Lewis acidity of scandium(III).

The observed lack of scandium reduced arene complexes may be related to the unique characteristics of scandium. Scandium(III) is the smallest among

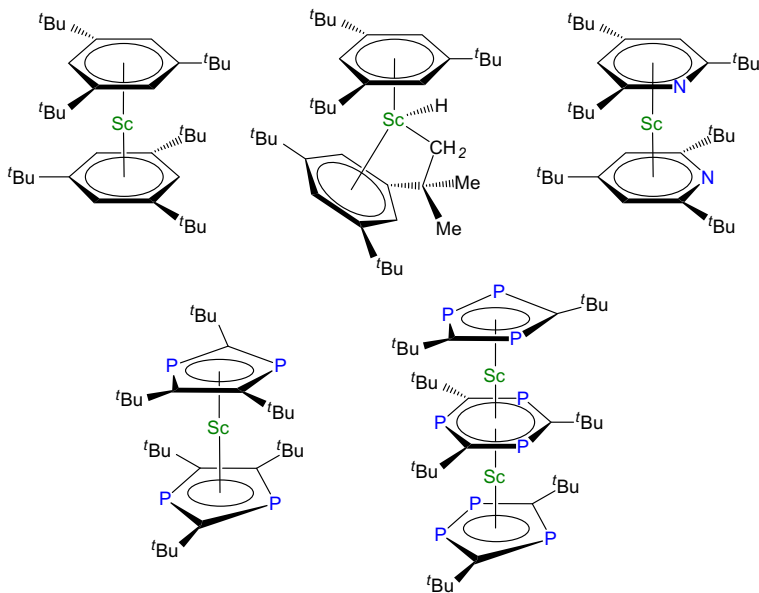


CHART 20 Formally zero-valent and subvalent scandium arene complexes.

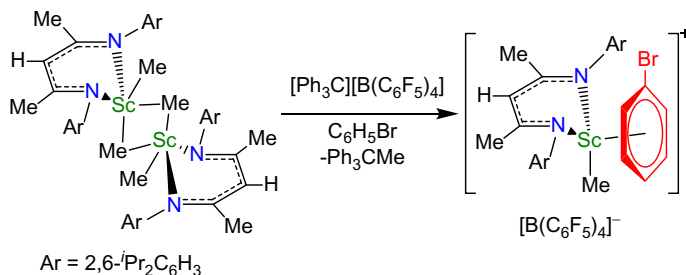


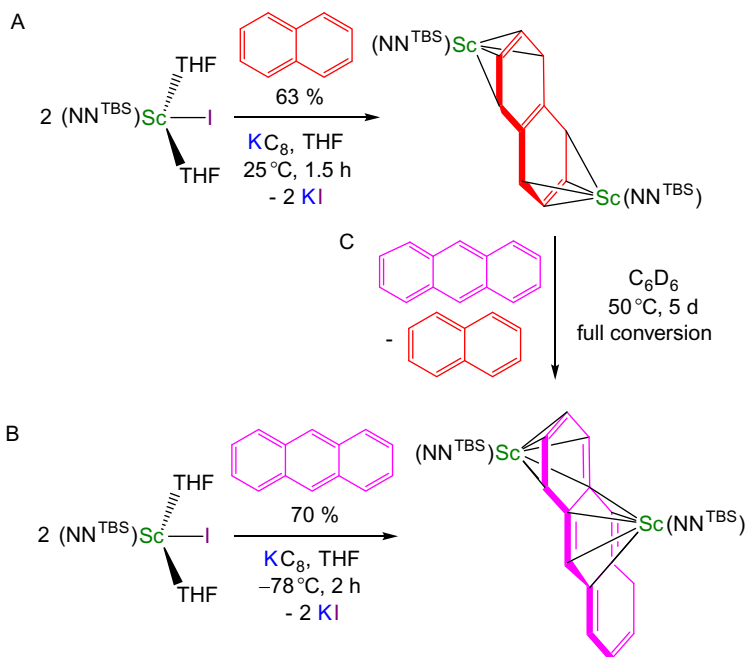
CHART 21 Coordination of neutral arene to cationic scandium(III) species reported by Piers's group.

rare earths: its ionic radius of 0.74 Å is 0.12 Å smaller than that of lutetium(III) (Shannon, 1976). The large difference in ionic radius between scandium and other rare earths leads to special properties and reactivity of scandium complexes (Moeller et al., 1965; Zimmermann and Anwender, 2010). This is best illustrated by the product from the co-condensation of scandium metal and 1,3,5-*t*Bu₃C₆H₃ (Cloke et al., 1991). While other rare earths gave the formally zero-valent sandwich complexes (1,3,5-*t*Bu₃C₆H₃) Ln (Ln = Y, La, Pr, Nd, Sm, Gd, Tb, Dy, Ho, Er, and Lu) (Anderson et al., 1989), in the case of scandium, a second product arising from the insertion of scandium into the C–H bond of the *tert*-butyl groups was also observed (Cloke et al., 1991).

The NN^{TBS} ligand proved to be the right choice for supporting inverse sandwiches of reduced arene scandium complexes: the reaction between (NN^{TBS})ScI(THF)₂ (NN^{TBS} = 1,1'-*fc*(NHSi^{*t*}BuMe₂)₂) and 0.5 equivalents of naphthalene (Scheme 2A) led to the first scandium naphthalene complex, [(NN^{TBS})Sc]₂(μ-η⁴:η⁴-C₁₀H₈) (**Sc₂-naph**) (Fig. 11; Huang et al., 2011). The analogous anthracene complex, [(NN^{TBS})Sc]₂(μ-η⁶:η⁶-C₁₄H₁₀) (**Sc₂-anth**), could be obtained by following a similar protocol (Scheme 2B) and was also crystallographically characterized (Fig. 11).

The molecular structure of **Sc₂-naph** (Fig. 11) was reminiscent of previously reported yttrium naphthalene complexes (Fryzuk et al., 2000). The naphthalene is distorted from planarity with C2/C3 and C2A/C3A bending in opposite directions from the plane composed of the other six carbon atoms (ca. 20° torsion angle). The C–C bonds within the naphthalene are best described as two isolated double bonds (C2=C3 and C2A=C3A), with short distances averaging 1.37 Å, and a 6C, 8π-electron system for the six coplanar center carbon atoms. Each scandium ion binds η⁴ to C1 through C4 (or C1A through C4A) with similar distances averaging 2.51 Å. These features are also reminiscent of those of the lithium naphthalene dianion [Li(TMEDA)]₂(μ-η⁴:η⁴-C₁₀H₈) (TMEDA = tetramethylethylenediamine) (Melero et al., 2009).

Besides common structural parameters with previously reported rare earth or alkali metal naphthalene dianion complexes, **Sc₂-naph** featured a short



SCHEME 2 (A) Synthesis of **Sc₂-naph**; (B) synthesis of **Sc₂-anth**; (C) conversion of **Sc₂-naph** to **Sc₂-anth**. Adapted with permission from Huang *et al.* (2011). Copyright © 2011, American Chemical Society.

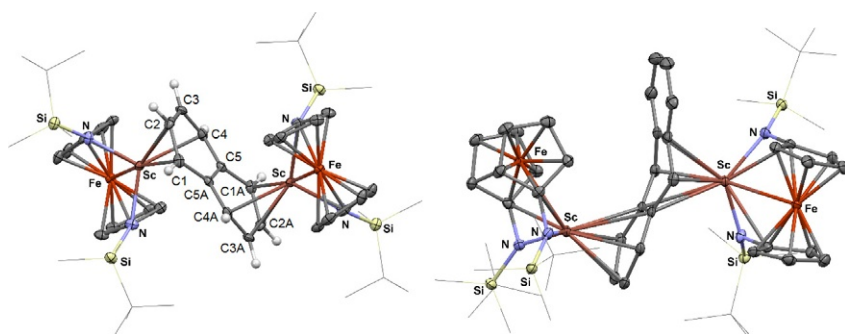


FIGURE 11 Molecular structures of **Sc₂-naph** (left) and **Sc₂-anth** (right). Thermal ellipsoids are drawn at the 50% probability level. Adapted from Huang *et al.* (2011).

Fe–Sc distance of 2.83 Å, which was significantly shorter than that of (NN^{TBS})ScI(THF)₂ (3.12 Å) and among the shortest Fe–Sc distances observed by our group with the NN^{TBS} ligand (Diaconescu, 2010b; Huang *et al.*, 2010), indicative of a relatively strong interaction between scandium and iron; this interaction is likely essential to the stability of **Sc₂-naph**. Geometrically, with

the short Fe–Sc distance, the scandium ion is sterically protected because it is shielded by the ferrocene backbone. An even shorter Fe–Sc distance of 2.74 Å was observed in **Sc₂-anth**. When using a non-ferrocene-based amide complex, [(Me₃Si)₂N]₂ScI(THF), instead of (NN^{TBS})ScI(THF)₂, no formation of a scandium naphthalene complex was observed. This result highlighted the advantages of the NN^{TBS} ligand in stabilizing highly electrophilic scandium(III) complexes.

The solid-state molecular structure of **Sc₂-anth** (Fig. 11) was similar to that of ((P₂N₂)₂Y)₂(μ-C₁₄H₁₀) (Fig. 4; Fryzuk et al., 2000), featuring an unsymmetrical coordination mode of the two metals. The two scandium ions are bound to opposite sides of the middle and an outer ring. ¹H NMR spectroscopy, however, indicated that the solution structure of **Sc₂-anth** was symmetrical at 25 °C in C₆D₆. A variable-temperature NMR experiment conducted with a toluene-*d*₈ solution of **Sc₂-anth** indicated that coalescence took place at –15 °C and further cooling led to the appearance of new, sharp peaks, which were correlated with the unsymmetrical molecular structure obtained by X-ray crystallography (Fig. 12). As previously mentioned, a similar fluxional behavior was reported for ((P₂N₂)₂Y)₂(μ-C₁₄H₁₀) (Fryzuk et al., 2000).

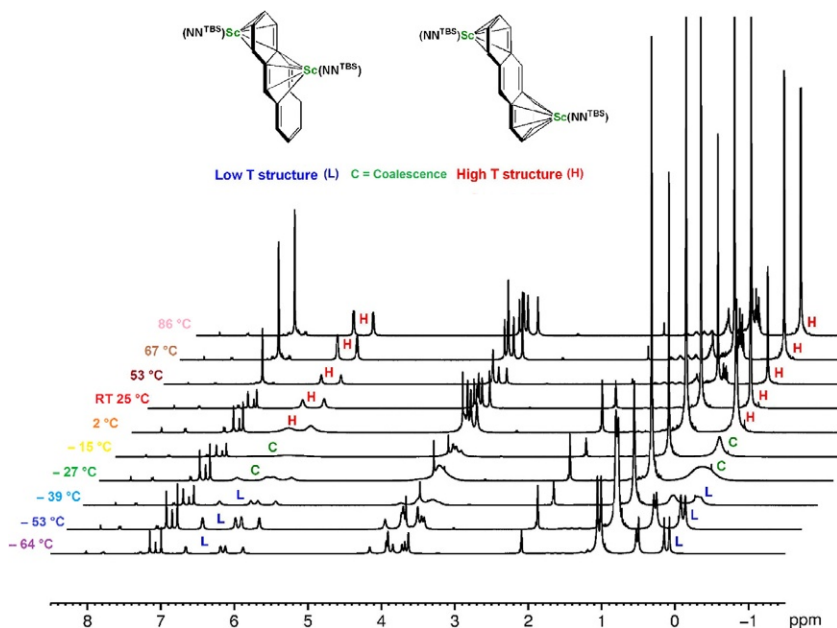


FIGURE 12 Variable-temperature ¹H NMR spectra of **Sc₂-anth** in aromatic solvents (209–298 K in C₇D₈; 326–359 K in C₆D₆). NN^{fc}=NN^{TBS}. Peaks corresponding to low-T and high-T structures are labeled and highlighted with L and H. The coalescence peaks were labeled and highlighted with C. Adapted with permission from Huang et al. (2011). Copyright © 2011, American Chemical Society.

DFT calculations carried out on the full molecule of **Sc₂-naph** indicated that the naphthalene dianion has an electronic structure similar to that found in other rare earth naphthalene complexes. It was found that the HOMO was composed mostly of naphthalene orbitals, consistent with its dianionic nature (Fig. 13), and that the negative charge was mainly localized on C1 and C4 (average -0.30), while C5 had the least (-0.07), and C2 and C3 were in the middle (average -0.14), confirming the η^4 coordination mode observed in the solid state. The nearly degenerate HOMO-1 and HOMO-2 (HOMO-5 for **Sc₂-anth**; Fig. 13) showed some orbital mixing between the 3d orbitals of iron and scandium together with the 2p orbitals of nitrogen and carbon of the NN^{TBS} ligand supporting the presence of the iron–scandium interaction. That interaction was also supported by the Mayer bond order of 0.41, and Mulliken charges, calculated to be $+1.02$ for scandium and -0.04 for iron, which indicated that the interaction between scandium and iron was mainly electrostatic, with iron serving as a donor and scandium being the acceptor. Similar results were obtained from DFT calculations carried out on **Sc₂-anth**.

Although few examples of converting a bridging, reduced arene rare earth complex into another have been reported (Bochkarev, 2002), these studies are important in understanding and supporting bonding considerations. Conversion of **Sc₂-naph** to **Sc₂-anth** could be achieved by heating a 1:1 mixture of **Sc₂-naph** and anthracene at 50 °C in C₆D₆ for five days (Scheme 2C), indicating that the naphthalene ligand in **Sc₂-naph** is more reducing than the anthracene ligand in **Sc₂-anth**.

Rare earth arene complexes are good precursors for difficult-to-synthesize rare earth compounds (Bochkarev, 2002) and the same was true for the scandium arene complexes supported by NN^{TBS}. Hessen previously showed that a scandium complex of the 2,2'-bipyridyl radical anion could be readily accessed from a reduced 1,3-diene scandium complex (Beetstra et al., 2003). Similarly, the addition of 2,2'-bipyridine to a C₆D₆ solution of **Sc₂-naph** (Scheme 3A) led to the formation of the previously reported radical anionic bipyridyl complex (NN^{TBS})Sc(2,2'-bipyridine) (Williams et al., 2010).

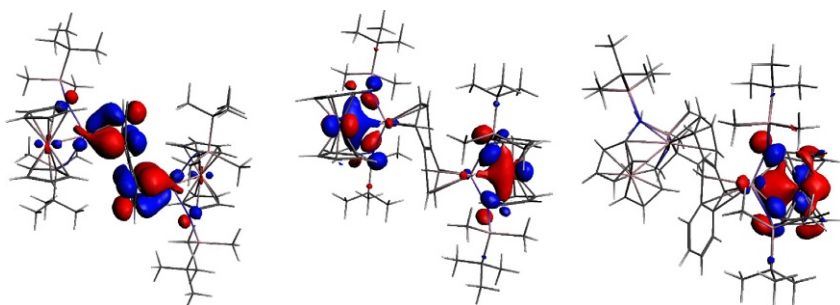
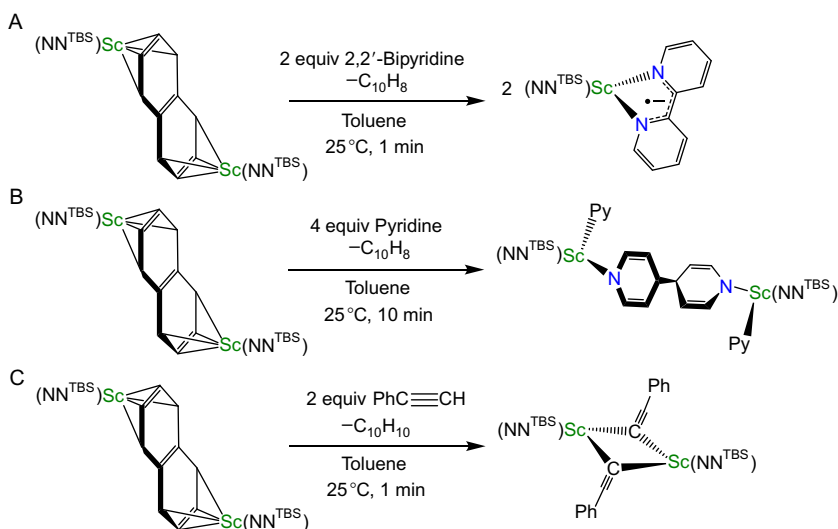


FIGURE 13 Top: Selected molecular orbitals of **Sc₂-naph**: HOMO (left); HOMO-1 (right). Bottom: HOMO-5 of **Sc₂-anth**. Reproduced with permission from Huang et al. (2011). Copyright © 2011, American Chemical Society.



SCHEME 3 (A) Reaction of **Sc₂-naph** with 2,2'-bipyridine to form $(\text{NN}^{\text{TBS}}\text{Sc})(2,2'\text{-bipyridine})$ with the elimination of free naphthalene; (B) reaction of **Sc₂-naph** with pyridine to form $[(\text{NN}^{\text{TBS}}\text{Sc})(\text{NC}_5\text{H}_5)]_2[\mu\text{-(NC}_5\text{H}_5\text{-C}_5\text{H}_5\text{N})]$ with the elimination of free naphthalene; (C) reaction of **Sc₂-naph** with phenylacetylene to form $[(\text{NN}^{\text{TBS}}\text{Sc})(\mu\text{-CCPh})]_2$ with the elimination of dihydronaphthalene. Reproduced with permission from Huang et al. (2011). Copyright © 2011, American Chemical Society.

The reaction of **Sc₂-naph** with excess pyridine (Scheme 3B) led to the isolation of a rare, reductively 4,4'-C-C-coupled diamide linker that bridges the two scandium ions in the complex $[(\text{NN}^{\text{TBS}}\text{Sc})(\text{NC}_5\text{H}_5)]_2[\mu\text{-(NC}_5\text{H}_5\text{-C}_5\text{H}_5\text{N})]$. A similar reduction was reported in the reactions of divalent thulium complexes (Fedushkin et al., 2003; Jaroschik et al., 2007b) and, recently, samarium(II) (Labouille et al., 2012) with pyridine; however, the reaction of a rare earth arene complex with pyridine had not been reported previously.

A common substrate used with rare earth arene complexes is phenylacetylene (Bochkarev, 2002). The reaction of **Sc₂-naph** with two equivalents of phenylacetylene led to the immediate formation of $[(\text{NN}^{\text{TBS}}\text{Sc})(\mu\text{-CCPh})]_2$ (Scheme 3C) presumably from protonation of the naphthalene dianion since a mixture of dihydronaphthalene isomers was also observed as by-products. X-ray crystallography confirmed the isolation of the phenylacetylide bridging dimer with a short Fe-Sc (2.89 Å) distance.

4.2 P₄ Activation by Scandium Arene Complexes

White phosphorous (P₄) activation has been long targeted by synthetic chemists (Caporali et al., 2010; Cossairt et al., 2010b; Scheer et al., 2010). Unlike main group elements and late transition metals (Caporali et al., 2010;

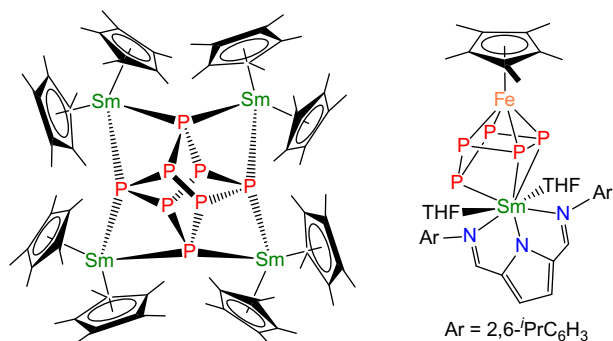
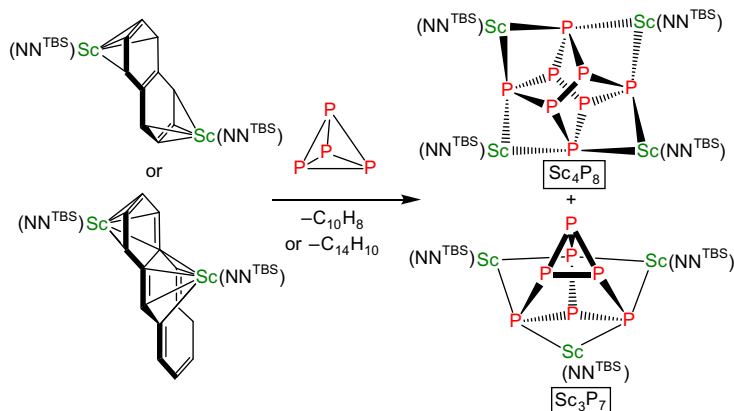


CHART 22 Examples of rare earth P_n -containing complexes reported by Roesky's group.

Scheer et al., 2010), the number of P_n -containing early transition metal complexes formed from direct P_4 activation is much smaller (Chirik et al., 2002; Cossairt et al., 2010b; Hey et al., 1987; Scherer et al., 1988; Seidel et al., 2009). Among early transition metals, rare earths are more Lewis-acidic, leading to a more pronounced mismatch in bonding between their ions and phosphorous anions (Cui et al., 2008; Lv et al., 2011; Masuda et al., 2008). All known examples of lanthanide (Chart 22; Konchenko et al., 2009; Li et al., 2011)-mediated and actinide (Scherer et al., 1991; Stephens, 2004)-mediated P_4 activation had involved low-valent metal complexes prior to our reports. For example, $(Cp^*_2Sm)P_8$ was obtained by vapor transfer of P_4 to a toluene solution of Cp^*_2Sm over the course of a week in a low yield (ca. 10%). The heterometallic Sm–Fe P_5 complex was obtained by reacting $Cp^*Fe(\eta^5-P_5)$ with samarium reagents. It is worth noting that late transition metal arene complexes have also been used for P_4 activation recently (Schnöckelborg et al., 2011).

Because the scandium naphthalene complex **Sc₂-naph** was found to be an excellent two-electron reductant toward a variety of substrates, its reactivity toward P_4 was investigated. The reaction took place smoothly at ambient conditions and was accompanied by the generation of free naphthalene (Scheme 4). The formation of $[(NN^{TBS})Sc]_4(\mu_4-\eta^2:\eta^2:\eta^2:\eta^2-P_8)$ (**Sc₄P₈**) was supported by X-ray crystallography (Huang and Diaconescu, 2012). **Sc₄P₈** was also characterized by 1H , ^{13}C , and ^{31}P NMR spectroscopy. Although the solid-state molecular structure had only C_2 symmetry, the 1H spectrum of **Sc₄P₈** indicated that all four $[(NN^{TBS})Sc]$ fragments were equivalent in solution on the NMR timescale. The ^{31}P NMR spectrum featured an AA'A''A'''MM'M''M''' spin system.

The molecular structure of **Sc₄P₈** (Fig. 14) has a realgar-type P_8 unit in the center and four $[(NN^{TBS})Sc]$ fragments at the corners, each bonding to two anionic phosphorus atoms. A short Fe–Sc distance of 2.80 Å was observed again and it was proposed to play a role in stabilizing the structural motif of



SCHEME 4 Reactions of $\text{Sc}_2\text{-naph}$ and $\text{Sc}_2\text{-anth}$ with P_4 to form $(\text{NN}^{\text{TBS}})\text{Sc}_4(\mu_4\text{-}\eta^2\text{-}\eta^2\text{-}\eta^2\text{-}\eta^2\text{-P}_8)$ (Sc_4P_8) and $(\text{NN}^{\text{TBS}})\text{Sc}_3(\mu_3\text{-}\eta^2\text{-}\eta^2\text{-}\eta^2\text{-P}_7)$ (Sc_3P_7) with the elimination of free naphthalene or anthracene. Adapted with permission from *The Royal Society of Chemistry* from [Huang and Diaconescu \(2012\)](#).

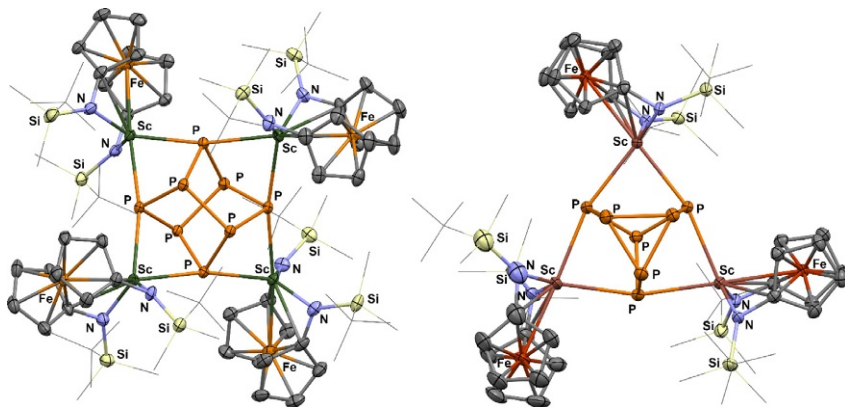


FIGURE 14 Molecular structures of $(\text{NN}^{\text{TBS}})\text{Sc}_4(\mu_4\text{-}\eta^2\text{-}\eta^2\text{-}\eta^2\text{-}\eta^2\text{-P}_8)$ (left) and $(\text{NN}^{\text{TBS}})\text{Sc}_3(\mu_3\text{-}\eta^2\text{-}\eta^2\text{-}\eta^2\text{-P}_7)$ (right). Thermal ellipsoids are drawn at the 50% probability level. Hydrogen atoms are omitted for clarity. Redrawn after [Huang and Diaconescu \(2012\)](#).

Sc_4P_8 . The P_8 unit showed local C_{2v} symmetry, with two distinct types of P atoms: P_{inner} (three neighboring P atoms) and P_{corner} (two neighboring P atoms). The average $\text{P}_{\text{inner}}\text{-P}_{\text{inner}}$ distance is 2.31 Å, 0.11 Å longer than that of $\text{P}_{\text{inner}}\text{-P}_{\text{corner}}$. The average $\text{P}_{\text{inner}}\text{-P}_{\text{corner}}$ distance of 2.20 Å is close to the P-P interatomic distance in P_4 (2.21 Å) ([Corbridge and Lowe, 1952](#)) or a recent updated gas-phase value 2.1994(3) Å ([Cossairt et al., 2010a](#)). The structure of the P_8 unit resembled that of $(\text{Cp}^*\text{2Sm})_4\text{P}_8$ ([Konchenko et al., 2009](#)). The P_8 unit had been previously observed in some late transition metal complexes, which were obtained from the photolysis reaction of P_4 with

cyclopentadienyl iron or iridium carbonyl species (Barr et al., 1991; Scheer et al., 1996), and in the tricyclic [3.3.0.0^{3,7}]octaphosphane (Butts et al., 2008).

A second product was also obtained from the reaction of **Sc₂-naph** and P₄ and was isolated based on its solubility properties, different from those of **Sc₄P₈**. X-ray crystallography indicated it to be the first early transition metal P₇ compound, [(NN^{TBS})Sc]₃(μ₃-η²:η²:η²-P₇) (**Sc₃P₇**) (Fig. 14). It was also found that the product distribution could be tuned by either changing the stoichiometry of P₄ or using a different scandium arene starting material: employing one equivalent of or a substoichiometric amount of P₄ favored the formation of **Sc₄P₈**, while using excess P₄ or the less reactive but more labile **Sc₂-anth** (as indicated by its fluxional behavior in solution) favored the formation of **Sc₃P₇**.

Sc₃P₇ was the first example of a Zintl-type P₇³⁻ compound formed directly from P₄ activation without using an alkali metal or its equivalent as reducing agents (Baudler and Faber, 1980; Charles et al., 1996; Fritz et al., 1990; Scheer et al., 2010; Schnöckelborg et al., 2011). Three types of phosphorous atoms were found to be present in **Sc₃P₇**: P_{apex}, P_{edge}, and P_{bottom}. The difference in P–P distances was smaller than that observed in **Sc₄P₈**, with almost identical P_{apex}–P_{edge} and P_{edge}–P_{bottom} distances of 2.20 Å and a slightly longer P_{bottom}–P_{bottom} distance of 2.23 Å. The P₇³⁻ unit in **Sc₃P₇** resembles that of the solid-state structure of Li₃P₇, although in the latter case, the difference in P–P distances is larger. Similar to **Sc₄P₈**, **Sc₃P₇** also bears a short Fe–Sc distance of 2.80 Å. The ³¹P NMR spectrum showed three sets of peaks, at δ = +23.1, –118.9, and –131.4 ppm, in a 3:1:3 ratio, featuring an AA'A''MM'M''X spin system similar to the previously reported Li₃P₇, Fe₃P₇, and P₇R₃ (R = silyl or alkyl) cases (Ahlrichs et al., 1996; Fritz and Härer, 1983).

DFT calculations on model molecules of **Sc₄P₈** and **Sc₃P₇** indicated that the two polyphosphide complexes exhibit mostly ionic interactions between the metal and the polyphosphide anion as described for (Cp*₂Sm)₄P₈ (Konchenko et al., 2009). The examination of bonding orbitals with the same symmetry, HOMO-15 for **Sc₄P₈** and HOMO-18 for **Sc₃P₇** (Fig. 15), revealed some overlapping between the 3d orbitals of scandium and the 3p orbitals of phosphorous. In addition, the calculated Mayer bond order for Sc–P was found to be 0.53 and 0.51 for **Sc₄P₈** and **Sc₃P₇**, respectively. DFT calculations also supported the existence of an iron–scandium interaction: Mayer bond orders of Fe–Sc interaction were found to be 0.44 and 0.42 for **Sc₄P₈** and **Sc₃P₇**, respectively.

4.3 Yttrium, Lanthanum, and Lutetium Naphthalene Complexes: Synthesis, Characterization, and Reactivity Toward P₄ Activation

The success of direct P₄ activation by scandium arene complexes was mirrored when other rare earths, such as yttrium, lanthanum, and lutetium, were employed. The yttrium, lanthanum, and lutetium naphthalene complexes were prepared by a similar protocol to that of **Sc₂-naph** (Scheme 5). Different from

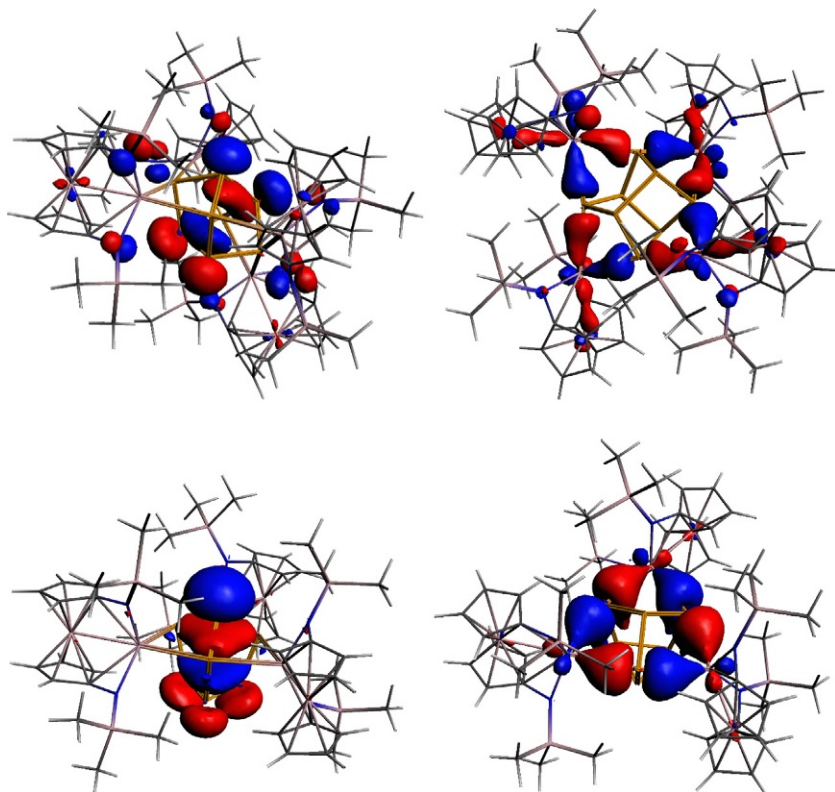
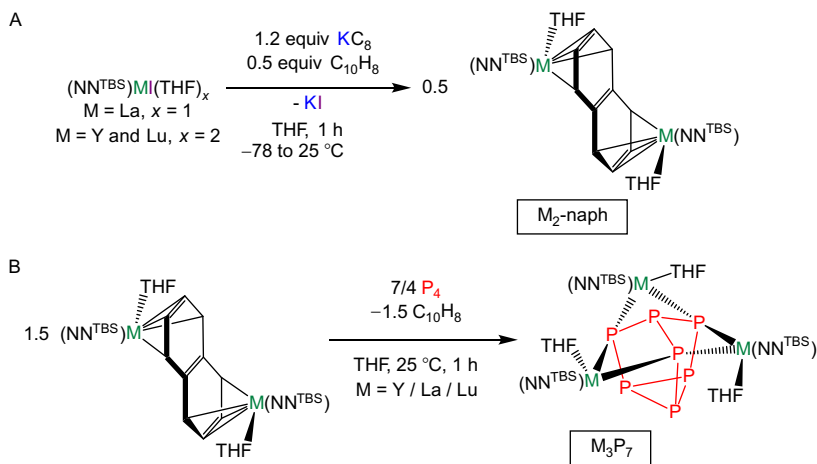


FIGURE 15 Selected molecular orbitals of Sc_4P_8 and Sc_3P_7 . Top: HOMO-12 (left) and HOMO-15 (right) for Sc_4P_8 . Bottom: HOMO-17 (left) and HOMO-18 (right) for Sc_3P_7 . Reproduced with permission from *The Royal Society of Chemistry* from [Huang and Diaconescu \(2012\)](#).

Sc₂-naph, which did not coordinate THF, the other rare earth naphthalene complexes were synthesized with the general formula of $[(\text{NN}^{\text{TBS}})\text{M}(\text{THF})_2(\mu\text{-}\eta^4\text{:}\eta^4\text{-C}_{10}\text{H}_8)]$ (**M₂-naph**, M=Y, La, and Lu) ([Huang and Diaconescu, 2012, 2013](#)), containing one THF per metal center. With the complete series of diamagnetic rare earth naphthalene complexes supported by the NN^{TBS} ligand, it was possible to compare their physical properties. **Sc₂-naph** is a black solid barely soluble in hexanes but soluble in aromatic solvents. However, **Y₂-naph** is a dark-red solid barely soluble in hexanes, aromatic solvents, and diethyl ether but only soluble in THF. While **Lu₂-naph** has similar physical properties to **Y₂-naph**, **La₂-naph**, with the largest ionic radius of all rare earths and same molecular formula as **Y₂-naph** and **Lu₂-naph**, has physical properties similar to **Sc₂-naph**: it is a black solid soluble in aromatic solvents and even slightly soluble in hexanes. These counterintuitive observations show that, in the present case, the properties of rare earth complexes do not follow the trend of their metal ion size.

All **M₂-naph** were characterized by ¹H and ¹³C NMR spectroscopy, X-ray crystallography, and elemental analysis. While the proton chemical shifts of the scandium, yttrium, and lutetium naphthalene complexes were close to each other, the proton chemical shifts of the naphthalene fragment in **La₂-naph** were shifted significantly upfield compared with the other three complexes (Table 2). However, it was found that the ¹³C chemical shifts for **La₂-naph** were similar to those of other rare earth naphthalene complexes (Huang and Diaconescu, 2013).



SCHEME 5 (A) Synthesis of **M₂-naph** (M = Y, La, and Lu); (B) exclusive formation of $[(\text{NN}^{\text{TBS}}\text{M})(\text{THF})]_3(\mu_3-\eta^2-\eta^2-\text{P}_7)$ (**M₃P₇**) from P_4 activation by employing **M₂-naph**. Adapted with permission from Huang and Diaconescu (2013). Copyright © 2013 WILEY-VCH Verlag GmbH & Co. KGaA, Weinheim.

TABLE 2 Summary of ¹H and ¹³C NMR Chemical Shifts (Unit in ppm) of $(\text{C}_{10}\text{H}_8)^{2-}$ Unit and Structural Parameters (Distance in Å) for **M₂-naph** (M = Sc, Y, La, and Lu)

	Sc ₂ -naph	Y ₂ -naph	La ₂ -naph	Lu ₂ -naph
α -CH and β -CH	5.06, 4.02	5.09, 3.94	4.28, 2.73	5.17, 4.23
<i>ipso</i> -C, α -C, β -C	158, 120, 95	158, 118, 94	157, 122, 100	155, 118, 95
C $_{\alpha}$ -C $_{\beta}$	1.428(7)	1.441(6)	1.433(4)	1.444(6)
C $_{\beta}$ -C $_{\beta}$	1.368(7)	1.376(7)	1.374(4)	1.374(6)
C $_{ipso}$ -C $_{\alpha}$	1.421(6)	1.423(6)	1.418(3)	1.424(6)
C $_{ipso}$ -C $_{ipso}$	1.445(9)	1.450(6)	1.451(5)	1.452(6)

Although **M₂-naph** (M=Y, La, and Lu) crystallized in different space groups, they were shown to have similar structural parameters (Huang and Diaconescu, 2013). The molecular structure of **Y₂-naph** is shown in Fig. 16 as a representative for **M₂-naph**. Despite differences in the strength of the iron–metal interaction, as determined by the ratio of the sum of the covalent radii of the two metals and the observed distance, compounds **M₂-naph** were found to contain the usual $\mu\text{-}\eta^4,\eta^4$ coordination motif of the bridging naphthalene ligand.

The reactivity of **M₂-naph** (M=Y, La, and Lu) toward P₄ was also tested. Regardless of the stoichiometry of P₄ versus **M₂-naph**, a single product was formed with the general formula of [(NN^{TBS})M(THF)]₃($\mu_3\text{-}\eta^2:\eta^2:\eta^2\text{-P}_7$) (**M₃P₇**) (Huang and Diaconescu, 2012, 2013). The exclusive formation of **M₃P₇** from **M₂-naph** raises an interesting question about the mechanism of P₄ activation by rare earth arene complexes. It seems plausible that there are two competing reaction pathways: The first leads to the formation of **M₄P₈** and the second leads to the formation of **M₃P₇**. For scandium, the two pathways have similar activation barriers since both products **Sc₄P₈** and **Sc₃P₇** are observed; for other rare earths, the pathway to form **M₃P₇** is more favorable, so **M₃P₇** forms exclusively in the reaction.

Compounds **M₃P₇** (M=Y, La, and Lu) were isolated in good yield after crystallization from various organic solvents. It was found that **La₃P₇** was more soluble than **Y₃P₇** and **Lu₃P₇** in common organic solvents: **La₃P₇** was soluble in hexanes and aromatic solvents, while **Y₃P₇** and **Lu₃P₇** were barely soluble in hexanes and slightly soluble in aromatic solvents. While the solubility of **Lu₃P₇** was similar to that of the previously reported **Y₃P₇**, the solubility of **La₃P₇** was different but similar to that of the THF free compound **Sc₃P₇**. The unexpected solubility properties of **M₃P₇** (M=Sc, Y, La, and Lu) echoed the different solubilities of **M₂-naph** described earlier.

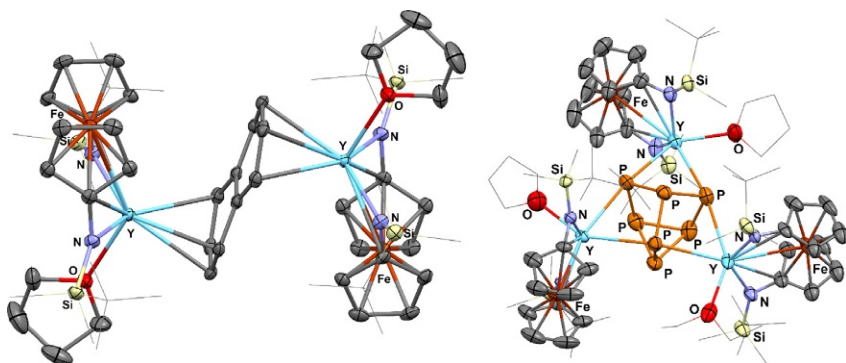


FIGURE 16 Molecular structure of **Y₂-naph** (left) and **Y₃P₇** (right). Thermal ellipsoids are drawn at the 50% probability level. Hydrogen atoms are omitted for clarity. Adapted from Huang and Diaconescu (2012).

The molecular structure of Y_3P_7 is shown in Fig. 16 as a representative for M_3P_7 . While Lu_3P_7 is isostructural to Y_3P_7 , La_3P_7 crystallized in a different space group, and two out of the three lanthanum ions were coordinated by diethyl ether instead of THF. It was found that different batches of La_3P_7 showed different ratios between THF and diethyl ether as a coordinating solvent. Similar to La_3P_7 , some batches of $\text{La}_2\text{-naph}$ also had diethyl ether replacing THF. This lack of selectivity for the coordinating solvent was attributed to the weaker Lewis acidity of lanthanum(III) compared to that of yttrium(III) and lutetium(III) (Tsuruta et al., 1999).

All M_3P_7 structures feature a central Zintl-type polyphosphide P_7^{3-} anion surrounded by three $[(\text{NN}^{\text{TBS}})\text{M}(\text{solvent})]$ fragments (Huang and Diaconescu, 2013). Except for Sc_3P_7 , which does not coordinate any THF, all the other M_3P_7 adopt a similar coordination environment. Despite this difference in the coordination environment, P–P distances (listed in Table 3) followed a trend consistent with the size of the metal ion: the larger the rare earth ion, the shorter the $\text{P}_{\text{edge}}\text{-P}_{\text{bottom}}$ distance. In alkaline earth metal-stabilized P_7^{3-} compounds, the three distinguishable P–P bonds also have different distances, with the shortest being the $\text{P}_{\text{edge}}\text{-P}_{\text{bottom}}$ and the longest being the $\text{P}_{\text{bottom}}\text{-P}_{\text{bottom}}$ distance (Baudler and Glinka, 1993). For instance, in Sr_3P_{14} , $\text{P}_{\text{apex}}\text{-P}_{\text{edge}}$, $\text{P}_{\text{edge}}\text{-P}_{\text{bottom}}$, and $\text{P}_{\text{bottom}}\text{-P}_{\text{bottom}}$ are 2.21, 2.17, and 2.25 Å, respectively (Dahlmann and Schnering, 1972). For La_3P_7 , the difference among the P–P distances is comparable to those of alkali earth metal P_7^{3-} binary complexes; for Sc_3P_7 , the difference among the P–P distances is at the minimum and is close to that observed for silyl-substituted P_7R_3 compounds. For instance, in $\text{P}_7(\text{SiMe}_3)_3$, $\text{P}_{\text{apex}}\text{-P}_{\text{edge}}$, $\text{P}_{\text{edge}}\text{-P}_{\text{bottom}}$, and $\text{P}_{\text{bottom}}\text{-P}_{\text{bottom}}$ distances are 2.180(4), 2.192(4), and 2.214(4) Å (Hönle and Schnering, 1978). As a consequence, the P–P distances were taken as an indication of the bonding character of the M–P interaction: For covalent Si–P bonds, the difference among the three types of P–P bonds is the smallest; for highly ionic Sr–P interactions, the difference among the three types of P–P bonds is the largest. Those considerations indicated that the larger the rare earth ion, the more ionic is the bond character.

TABLE 3 P–P Distances of M_3P_7

M_3P_7	$\text{P}_{\text{apex}}\text{-P}_{\text{edge}}$	$\text{P}_{\text{edge}}\text{-P}_{\text{bottom}}$	$\text{P}_{\text{bottom}}\text{-P}_{\text{bottom}}$
$\text{Sc}_3\text{P}_7^{\text{a}}$	2.201(2)	2.197(2)	2.229(2)
Lu_3P_7	2.183(2)	2.181(2)	2.233(2)
Y_3P_7	2.188(2)	2.176(3)	2.238(2)
La_3P_7	2.191(2)	2.161(2)	2.258(2)

Unit: Å, error in brackets, all are average values.

^aUnlike other M_3P_7 , Sc_3P_7 has no solvent molecule coordinated to scandium.

4.4 Tautomerization of M_3P_7 Studied by Variable-Temperature NMR Spectroscopy

P_7^{3-} is the major product of P_4 activation by strong reductants or nucleophiles as well as the “dead end” of the decompositions of other polyphosphide species (Baudler and Glinka, 1993; Scheer et al., 2010). Intense experimental and theoretical studies have been performed on its alkali and alkaline earth metal complexes. For example, Li_3P_7 was studied by variable-temperature spectroscopy and 2D ^{31}P NMR spectroscopy (Baudler and Hahn, 1990; Baudler et al., 1979, 1980), and it was found that the ^{31}P NMR spectrum of Li_3P_7 in THF- d_8 is temperature-dependent: At low temperature ($-60^\circ C$), three distinguishable signals were observed for the three different types of phosphorus atoms in P_7^{3-} ; however, upon warming, coalescence took place and, eventually, at high temperature ($50^\circ C$), only one peak was observed. That phenomenon was attributed to a fluxional behavior of P_7^{3-} (Baudler and Glinka, 1993). The free P_7^{3-} anion can tautomerize to essentially the same tautomer (there are 1680 of them) (Baudler et al., 1979) by simultaneously breaking one $P_{\text{bottom}}-P_{\text{bottom}}$ bond and forming a new P–P bond between two P_{edge} atoms right next to the two P_{bottom} atoms of the P–P bond that breaks. This tautomerization mechanism, which is analogous to bullvalene tautomerization (Schröder et al., 1965), was calculated to have a low-energy barrier (Böhm and Gleiter, 1981) and was further supported by a topology study (Radic et al., 1986). Apparently, the tautomerization only takes place in highly ionic compounds such as Li_3P_7 and Cs_3P_7 (Kraus et al., 2003); no tautomerization was observed for silyl-substituted P_7R_3 compounds (Baudler and Glinka, 1993).

The ^{31}P NMR spectra of Sc_3P_7 , Y_3P_7 , and Lu_3P_7 , at $25^\circ C$ in benzene- d_6 or toluene- d_8 , were similar and showed three well-resolved peaks that integrated to a 3:1:3 ratio, indicating that the tautomerization process of the P_7^{3-} anion was frozen (Huang and Diaconescu, 2013). However, the ^{31}P NMR spectrum ($25^\circ C$, benzene- d_6) of La_3P_7 showed only one, broad signal centered at -75 ppm, similar to Li_3P_7 in THF- d_8 . ^{31}P NMR spectra (Fig. 17 left) collected from -75 to $107^\circ C$ showed the fluxional behavior of P_7^{3-} in La_3P_7 and a coalescence temperature comparable to that of Li_3P_7 .

The fluxional behavior took place in nonpolar solvents (benzene- d_6 or toluene- d_8) for La_3P_7 , while for Li_3P_7 , it was only observed in polar and strongly coordinating solvents such as THF, DME (1,2-dimethoxyethane), and TMEDA (tetramethylethylenediamine); without a strongly coordinating solvent, Li_3P_7 decomposed. This difference was explained by the migration of the $(NN^{\text{TBS}})La(\text{THF})$ fragment from one phosphorous atom to another, allowing the valence tautomerization to occur (Huang and Diaconescu, 2013). This mechanism for P_7^{3-} tautomerization in La_3P_7 requires the simultaneous breaking and formation of four La–P bonds (Fig. 17 right). The tautomerization involves one of the five-member rings of P_7^{3-} :

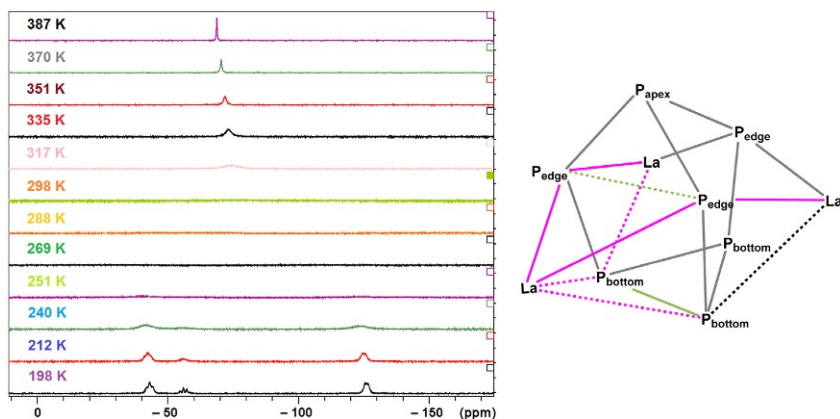
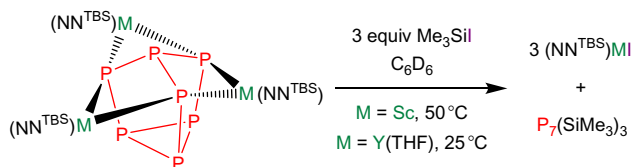


FIGURE 17 Left: Overlay of ^{31}P NMR spectra (toluene- d_8) of La_3P_7 at different temperatures. Right: Proposed mechanism for valence tautomerization of P_7^{3-} in La_3P_7 . NN^{TBS} ligands and solvent molecules were omitted for clarity. The pink solid line represents the La–P bond to break. The pink dashed line represents the La–P bond to form. The green solid line represents the P–P bond to break. The green dashed line represents the P–P bond to form. The gray solid lines represent La–P and P–P bonds not affected by this particular tautomerization process. Adapted with permission from Huang and Diaconescu (2013). Copyright © 2013 WILEY-VCH Verlag GmbH & Co. KGaA, Weinheim.

A $\text{P}_{\text{bottom}}\text{--P}_{\text{bottom}}$ bond breaks, while a $\text{P}_{\text{edge}}\text{--P}_{\text{edge}}$ bond forms; at the same time, the lanthanum fragment coordinated to that face migrates from two P_{edge} atoms to two P_{bottom} atoms. The other two lanthanum ions only break and form one La–P bond each. Such a process, together with the necessary breaking and formation of P–P bonds, is made possible by the coordination of lanthanum to two neighboring P_{edge} atoms and two neighboring P_{bottom} atoms. To support this hypothesis, the average La– P_{edge} distance is 3.10 Å, while the average La– P_{bottom} distance is 3.54 Å. The 0.44 Å difference is smaller than the corresponding distance difference in the other M_3P_7 ($\text{M} = \text{Sc}$: 0.67 Å, Lu : 0.57 Å, and Y : 0.53 Å). If it is assumed that the metal–P distances vary linearly with the strength of the metal–P interaction, then it will be easier to form new metal–P bonds for La_3P_7 than for $\text{Y}_3\text{P}_7 > \text{Lu}_3\text{P}_7 > \text{Sc}_3\text{P}_7$. Consequently, it was found that the tautomerization also took place in Y_3P_7 but at a high temperature (coalescence temperature higher than 75 °C). Unfortunately, the low solubility of Y_3P_7 in aromatic solvents and the high coalescence temperature prevented a detailed variable-temperature ^{31}P NMR spectroscopy study for this complex (Huang and Diaconescu, 2013).

4.5 Synthesis of Organic P-Containing Compounds from P_4

Transferring the activated polyphosphide is essential to generate organophosphorus compounds (Cossairt et al., 2010b). The reaction of Sc_3P_7 or Y_3P_7



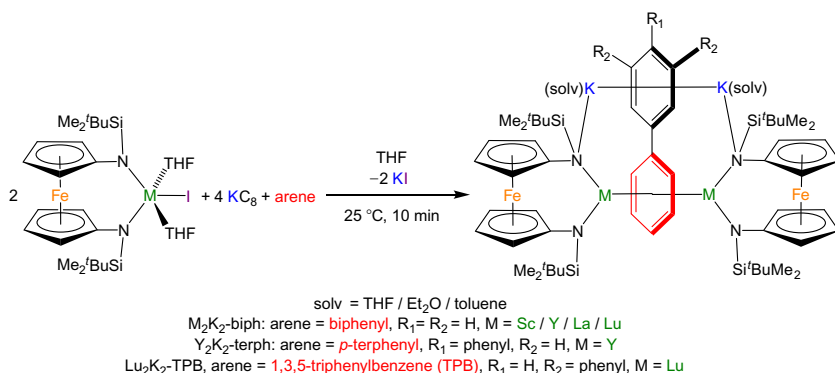
SCHEME 6 Reaction of M_3P_7 with Me_3SiI . Adapted with permission from *The Royal Society of Chemistry* from Huang and Diaconescu (2012).

(Scheme 6) with three equivalents of Me_3SiI led to the formation of the corresponding rare earth iodide and $\text{P}_7(\text{SiMe}_3)_3$ (Huang and Diaconescu, 2012), as confirmed by ^{31}P NMR spectroscopy (Fritz and Härer, 1983).

5 SYNTHESIS AND CHARACTERIZATION OF RARE EARTH BIPHENYL COMPLEXES: 6C , 10π -ELECTRON AROMATIC SYSTEMS

A DFT study predicted in 2005 that the barium complex of the benzene tetraanion would be stable as an inverse sandwich, $\text{Ba}_2(\text{C}_6\text{H}_6)$, with D_{6h} symmetry (Diefenbach and Schwarz, 2005). The C–C distance was calculated to be 1.466 Å. Calculated charge and molecular orbitals suggested that the benzene moiety is reduced by four electrons as a 10π -electron system. The calculated nuclear-independent chemical shift (NICS) confirmed the $(\text{C}_6\text{H}_6)^{4-}$ formulation. The report suggested some suitable metal centers, such as thorium, to stabilize the highly electron-rich $(\text{C}_6\text{H}_6)^{4-}$. This suggestion, based on the Lewis acid character of thorium, is in line with what is described in Section 2, where several benzene/arene polyanions stabilized by coordination to lanthanides are presented. For actinides, several groups reported that benzene or its derivatives can serve as a bridging ligand between two uranium ions (Arnold et al., 2012; Diaconescu and Cummins, 2012; Diaconescu et al., 2000; Evans et al., 2004; Monreal et al., 2011; Patel et al., 2011). Magnetic susceptibility measurements, X-ray absorption near-edge structure (XANES) spectroscopy, and DFT studies showed that most of these complexes can be described as having a benzene (or a substituted benzene) dianion bridging two U(III) centers (Diaconescu and Cummins, 2012; Evans et al., 2004). Liddle and coworkers suggested a [toluene] $^{4-}$ ligand in $[\text{U}(\text{Ts}^{\text{Xy}})]_2(\mu\text{-}\eta^6\text{:}\eta^6\text{-C}_6\text{H}_5\text{Me})$ ($\text{Ts}^{\text{Xy}} = \text{HC}(\text{SiMe}_2\text{-NAr})_3$; Ar = 3,5-Me $_2$ C $_6$ H $_3$) (Patel et al., 2011, 2013); however, XANES spectroscopy studies have not been reported for this or the other uranium examples, $[\text{U}(\text{OSi}(\text{O}^t\text{Bu})_3)_3]_2(\mu\text{-}\eta^6\text{:}\eta^6\text{-C}_7\text{H}_8)$, $\text{K}[\text{U}(\text{OSi}(\text{O}^t\text{Bu})_3)_3]_2(\mu\text{-}\eta^6\text{:}\eta^6\text{-C}_7\text{H}_8)$, and $\text{K}_2[\text{U}(\text{OSi}(\text{O}^t\text{Bu})_3)_3]_2(\mu\text{-}\eta^6\text{:}\eta^6\text{-C}_7\text{H}_8)$ (Camp et al., 2013), containing proposed [toluene] $^{4-}$ ligand.

Compound $[(\text{NN}^{\text{TBS}}\text{Y})_2[\text{K}(\text{toluene})]_2(\mu\text{-biphenyl})]$ ($\text{Y}_2\text{K}_2\text{-biph}$) was obtained by addition of potassium graphite to a premixed tetrahydrofuran (THF) solution of $(\text{NN}^{\text{TBS}}\text{Y})\text{I}(\text{THF})_2$ and biphenyl (Scheme 7) and was crystallographically characterized (Fig. 18; Huang et al., 2013). The two yttrium ions coordinate to opposite sides of the same phenyl ring in an η^6 fashion, while the two potassium ions coordinate to the other biphenyl ring in an η^6 fashion as well. Based on charge balance, by assuming that yttrium is Y(III) and potassium is K(I), a -4 charge was assigned to the biphenyl ligand. XANES spectroscopy studies agreed with this formulation for $\text{Y}_2\text{K}_2\text{-biph}$.



SCHEME 7 Synthesis of quadruply reduced substituted benzene complexes $\text{M}_2\text{K}_2\text{-biph}$ ($\text{M} = \text{Sc}, \text{Y}, \text{La},$ and Lu), $\text{Y}_2\text{K}_2\text{-terph}$, and $\text{Lu}_2\text{K}_2\text{-TPB}$. Adapted from Huang et al. (2013). Copyright © 2013, Rights Managed by Nature Publishing Group.

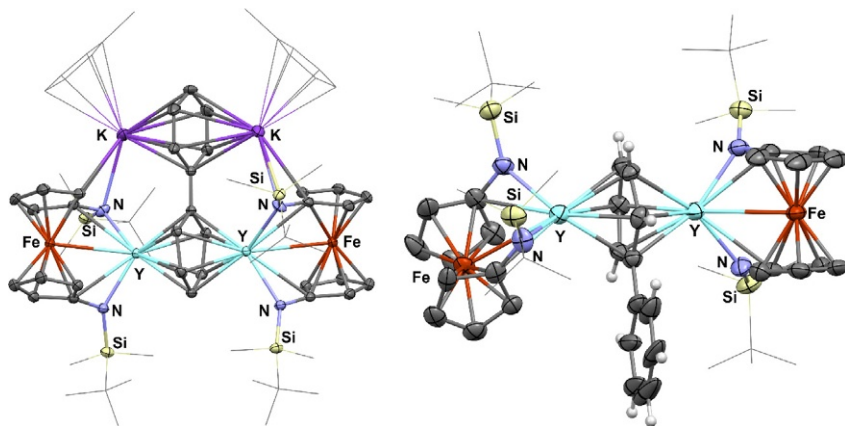


FIGURE 18 Thermal-ellipsoid (50% probability) representation of $\text{Y}_2\text{K}_2\text{-biph}$ (left) and the anion of $[\text{K}(\text{18-crown-6})(\text{THF})_{1.5}]_2[(\text{NN}^{\text{TBS}}\text{Y})_2(\mu\text{-biphenyl})]$ ($\text{Y}_2\text{-biph-K}_2\text{-crown}_2$) (right). Details of structural parameters are presented in Fig. 20 and Table 6. Redrawn after Huang et al. (2013).

It was shown that the unusual binding mode of biphenyl in $\mathbf{Y}_2\mathbf{K}_2\text{-biph}$ with yttrium and potassium coordinating to different rings was maintained in solution. The ^1H NMR spectra of $\mathbf{Y}_2\mathbf{K}_2\text{-biph}$ at 25, -45 , or -89 °C in THF- d_8 all showed two distinct sets of signals for the phenyl rings. The ^1H NMR pattern for the ring coordinated to the yttrium centers is shifted upfield, while that for the other ring appeared in the expected aromatic region (complete assignment of ^1H and ^{13}C chemical shifts is summarized in Table 4). In addition, $^{13}\text{C}\{^1\text{H}\}$ NMR spectroscopy showed that the signals for the *ortho*- and *meta*-carbon atoms of the ring coordinating to yttrium were triplets due to coupling to ^{89}Y ; the *para*- and *ipso*-carbon atoms, being the farthest from the yttrium ions, were not coupled to them and appeared as singlets.

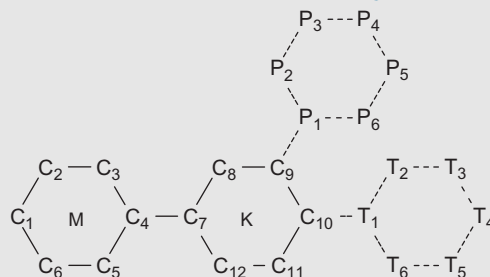
As mentioned previously (Fryzuk et al., 1997), reported lanthanide complexes of reduced biphenyl exhibited fluxional behavior in solution even when their solid-state structures indicated that the two metal centers coordinated in an unsymmetrical fashion. In the case of $\mathbf{Y}_2\mathbf{K}_2\text{-biph}$, no fluxional behavior was observed in solution. In addition, the isolation of the 18-crown-6 version of $\mathbf{Y}_2\mathbf{K}_2\text{-biph}$, $[\text{K}(18\text{-crown-6})(\text{THF})_{1.5}]_2\{[(\text{NN}^{\text{TBS}})\text{Y}]_2(\mu\text{-biphenyl})\}$ ($\mathbf{Y}_2\text{-biph-K}_2\text{-crown}_2$, Fig. 18), indicated that the coordination of potassium ions to the biphenyl ligand was not required to maintain the rigid structure.

The stability imparted by the aromatic character of the bridged tetraanionic biphenyl ligand was also manifested when attempts to isolate the corresponding dianionic species failed (Scheme 8). For example, $\mathbf{Y}_2\mathbf{K}_2\text{-biph}$ was formed exclusively even when substoichiometric amounts of KC_8 were used and the comproportionation reaction between $(\text{NN}^{\text{TBS}})\text{Y}(\text{THF})_2$ and $\mathbf{Y}_2\mathbf{K}_2\text{-biph}$ did not occur. Selective oxidation of the quadruply reduced arene to the doubly reduced species also failed (Scheme 8).

The structural motif of $\mathbf{Y}_2\mathbf{K}_2\text{-biph}$ was not restricted to yttrium and/or biphenyl: other group 3 metals, namely, scandium, lanthanum, and lutetium, formed $\mathbf{Sc}_2\mathbf{K}_2\text{-biph}$, $\mathbf{La}_2\mathbf{K}_2\text{-biph}$, and $\mathbf{Lu}_2\mathbf{K}_2\text{-biph}$, respectively, following a synthetic protocol analogous to that for $\mathbf{Y}_2\mathbf{K}_2\text{-biph}$ (Fig. 18). These compounds show ^1H and ^{13}C NMR spectra and solid-state molecular structures similar to $\mathbf{Y}_2\mathbf{K}_2\text{-biph}$. Other nonfused arenes (Scheme 7) such as *p*-terphenyl or 1,3,5-triphenylbenzene (TPB) led to $[(\text{NN}^{\text{TBS}})\text{Y}]_2[\text{K}(\text{THF})_2]_2[\mu\text{-}(p\text{-terphenyl})]$ ($\mathbf{Y}_2\mathbf{K}_2\text{-terph}$) and $[(\text{NN}^{\text{TBS}})\text{Lu}]_2[\text{K}(\text{THF})_2]_2[\mu\text{-}1,3,5\text{-C}_6\text{H}_3\text{Ph}_3]$ ($\mathbf{Lu}_2\mathbf{K}_2\text{-TPB}$, Ph = C_6H_5), respectively (Fig. 19; Huang et al., 2013). Table 4 summarizes the ^1H and ^{13}C NMR chemical shifts of the related substituted bridging benzene complexes. Table 5 compares the ^1H and ^{13}C NMR chemical shifts with literature values for anionic biphenyl species. Table 6 summarizes the representative structural parameters for $\mathbf{M}_2\mathbf{K}_2\text{-arene}$ complexes; while Table 7 compares those values with literature examples of anionic biphenyl or benzene species.

Density functional theory calculations showed that the optimized structures for the model dianion 2-Y^{2-} (Si^iBuMe_2 was replaced by SiMe_3 ; potassium counteranions were omitted) of $\mathbf{Y}_2\mathbf{K}_2\text{-biph}$ or $\mathbf{Y}_2\text{-biph-K}_2\text{-crown}_2$

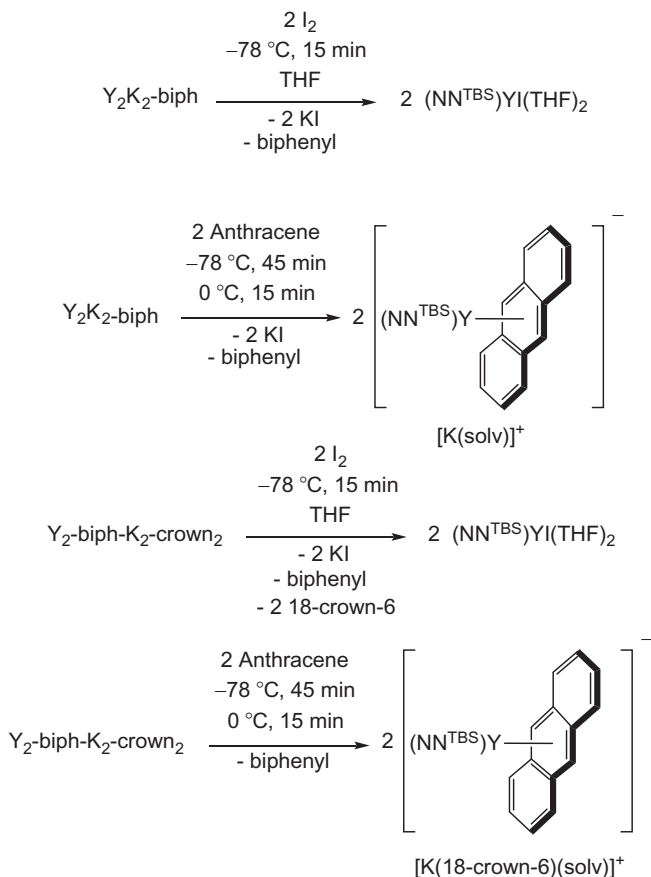
TABLE 4 Summary of ^1H and ^{13}C NMR Chemical Shifts (in ppm) for $\text{M}_2\text{K}_2\text{-biph}$ ($\text{M}=\text{Sc}$, Y , La , and Lu) and $\text{Y}_2\text{K}_2\text{-terph}$, $\text{Lu}_2\text{K}_2\text{-TPB}$, and $\text{Y}_2\text{-biph-K}_2\text{-crown}_2$ (all measured at -40 to -50 °C) (Huang et al., 2013)^a



	$\text{Y}_2\text{K}_2\text{-biph}$	$\text{Sc}_2\text{K}_2\text{-biph}$	$\text{La}_2\text{K}_2\text{-biph}$	$\text{Lu}_2\text{K}_2\text{-biph}$	$\text{Y}_2\text{-biph-K}_2\text{-crown}_2$	$\text{Y}_2\text{K}_2\text{-terph}$	$\text{Lu}_2\text{K}_2\text{-TPB}$
H1	4.02	4.23	4.20	3.76	3.83	4.13	3.77
H2	3.85	4.17	3.89	3.59	3.76	3.82	3.77
H3	2.92	3.69	2.87	2.92	3.03	2.85	3.00
H8	6.06	6.53	5.81	6.03	6.27	5.96	6.24
H9	6.17	6.43	5.91	6.21	6.16	6.52	NA
H10	5.03	5.52	4.73	5.03	5.22	NA	5.60
H(T2, P2)	NA	NA	NA	NA	NA	7.00	7.26
H(T3, P3)	NA	NA	NA	NA	NA	6.86	7.59
H(T4, P4)	NA	NA	NA	NA	NA	6.42	7.15

C1	84.9	88.1	88.1	86.1	78.8	91.9	87.9
C2	68.4	78.1	73.7	72.3	67.4	70.4	73.1
C3	52.1	63.9	61.5	56.9	54.0	52.4	58.4
C4	76.0	79.8	82.0	78.2	74.7	85.3	81.4
C7	138.8	142.3	135.6	137.2	142.4	131.4	136.7
C8	114.3	116.7	113.8	114.2	115.8	115.1	112.2
C9	128.6	128.4	128.5	128.3	127.2	124.0	140.8
C10	103.2	108.5	100.0	102.1	106.5	110.1	94.5
T1(P1)	NA	NA	NA	NA	NA	140.6	144.2
T2(P2)	NA	NA	NA	NA	NA	119.6	126.0
T3(P3)	NA	NA	NA	NA	NA	128.5	128.5
T4(P4)	NA	NA	NA	NA	NA	118.4	126.4

^aT1–T6 for p-terphenyl and P1–P6 for 1,3,5-triphenylbenzene (the other equivalent ring was omitted for clarity). The proton was labeled the same as the carbon attached to it (e.g., H1 on C1). The values in italic for proton and in bold for carbon are on the phenyl ring coordinated to group 3 metals.



SCHEME 8 Oxidation attempts involving $\text{Y}_2\text{K}_2\text{-biph}$ and $\text{Y}_2\text{-biph-K}_2\text{-crown}_2$. Adapted from Huang *et al.* (2013). Copyright © 2013, Rights Managed by Nature Publishing Group.

were in excellent agreement with the experimental findings, with average C–C distances of 1.472–1.479 Å for the coordinated phenyl ring (Huang *et al.*, 2013). The ground state was found to be a singlet, with no unpaired electrons on the yttrium ions and an iron(II) electronic configuration, in agreement with the oxidation states derived from XANES measurements. Kohn–Sham frontier molecular orbitals (Fig. 21) also confirmed the presence of a benzene unit reduced by four electrons and that the highest occupied molecular orbital (HOMO) and HOMO-1 clearly resulted from the population of the two e_{2u} vacant orbitals (π_4 and π_5) of the benzene motif. In addition, the calculated natural bond orbital (NBO) charges for the coordinated benzene ring (−1.90 to −1.95) and the uncoordinated phenyl group (−0.26 to −0.27) were significantly different. The putative complex in which each yttrium ion is coordinated to a different phenyl ring could also be investigated

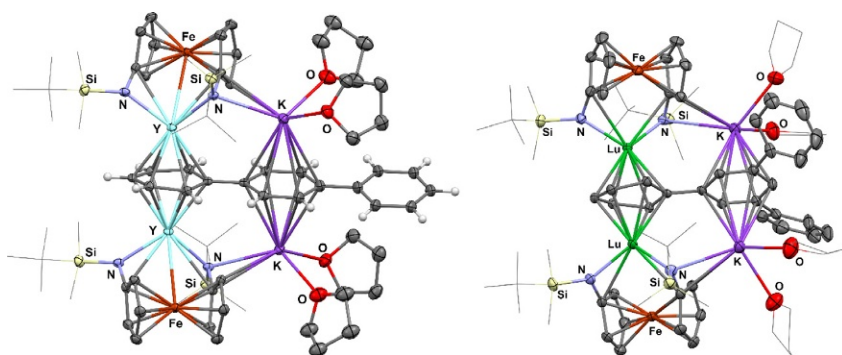


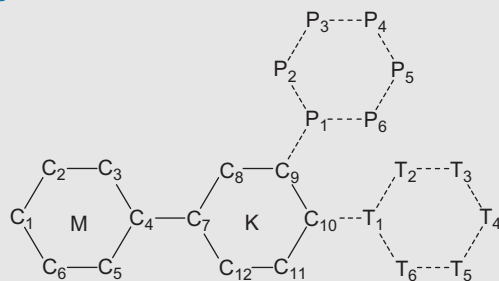
FIGURE 19 Thermal-ellipsoid (50% probability) representation of Y_2K_2 -terph (left) and Lu_2K_2 -TPB (right). Hydrogen and solvent atoms are omitted for clarity. Details of structural parameters are presented in Table 6. Adapted from Huang et al. (2013).

TABLE 5 Comparison of 1H and ^{13}C Chemical Shifts (in ppm) for the Coordinated Biphenyl Ring of M_2K_2 -biph ($M=Y, Sc, La,$ and Lu) and Literature Values Reported on Biphenyl Dianion Species (Using the Same Numbering Scheme as Table 4) (Huang et al., 2013)^a

	Average for M_2K_2 -biph	(Biphenyl) ²⁻	Y_2 -biph	Y-biph-Y
H1	4.05	2.96	NA	4.2
H2	3.88	5.28	4.2	5.1
H3	3.10	3.96	4.2	4.5
H8	6.11	3.96	4.2	4.5
H9	6.18	5.28	4.2	5.1
H10	5.08	2.96		4.2
C1	86.8	74.2		
C2	73.1	128.5	110.5	
C3	58.6	104.6	104.0	
C4	79.0	102.3	136.8	
C7	138.5	102.3	136.8	
C8	114.8	104.6	104.0	
C9	128.5	128.5	110.5	
C10	103.5	74.2		

^a(Biphenyl)²⁻ values are from Huber et al. (1981); Y_2 -biph and Y-biph-Y values were adopted from Fryzuk et al. (1997), in which Y_2 -biph had two yttrium ions coordinated to the same ring of the 4,4'-dimethylbiphenyl dianion and Y-biph-Y had two yttrium ions on different rings of the biphenyl dianion.

TABLE 6 X-Ray Structural Data for Y_2K_2 -biph, Sc_2K_2 -biph, Lu_2K_2 -biph, Y_2 -biph- K_2 -crown₂, Y_2K_2 -terph, and Lu_2K_2 -TPB (Distances in Å and Angles in °) (Huang et al., 2013)



	Y_2K_2 -biph	Sc_2K_2 -biph	Lu_2K_2 -biph	Y_2 -biph- K_2 -biph	Y_2K_2 -terph	Lu_2K_2 -TPB
C1–C2	1.422	1.436	1.413	1.441	1.420	1.436
C2–C3	1.477	1.474	1.474	1.496	1.476	1.493
C3–C4	1.486	1.481	1.498	1.489	1.484	1.492
C4–C7	1.414	1.418	1.416	1.477	1.411	1.420
C7–C8	1.448	1.444	1.438	1.405	1.444	1.439
C8–C9	1.391	1.390	1.390	1.405	1.372	1.391
C9–C10	1.402	1.405	1.399	1.329 ^a	1.423	1.420
M–C1	2.547	2.367	2.512	2.536	2.569	2.511
M–C2	2.606	2.448	2.599	2.604	2.613	2.599
M–C3	2.487	2.319	2.395	2.453	2.502	2.403

M–C4	2.565	2.516	2.535	2.522	2.568	2.553
K–C(7–12)	3.066–3.189	3.064–3.344	3.079–3.205	NA	3.099–3.231	3.156–3.279
C10–T1(P1)	NA	NA	NA	NA	1.465	1.493
T1(P1)–T2(P2)	NA	NA	NA	NA	1.412	1.382
T2(P2)–T3(P3)	NA	NA	NA	NA	1.381	1.394
T3(P3)–T4(P4)	NA	NA	NA	NA	1.376	1.379
C8–C7–C12	115	114	115	117	113	115
C3–C4–C7–C8	–5	–8	3	1	4	–5

^aThis value contains large errors due to the disorder of C9 and C10 atoms in **Y₂-biph-K₂-crown₂**.

TABLE 7 Comparison of C–C distances with reported examples (Unit in Å)^a

	Average	Y-biph-Y	Y ₂ -biph	Cp ₂ La(C ₆ H ₆)K	(Cp ₂ Ln) ₂ (C ₆ H ₆)K	U ₂ -biph	U ₂ -tol	Calcd. C ₆ H ₆ ⁴⁻	Calcd. Ba ₂ (C ₆ H ₆)	C ₆ H ₆
C1–C2	1.429	1.415	1.404	1.459	1.45–1.47	1.422	Av. 1.440	1.507	1.46	1.39
C2–C3	1.482	1.378	1.508	1.348	1.35–1.36	1.433				
C3–C4	1.489	1.453	1.416	1.468	1.44–1.46	1.467				
C4–C7	1.417	1.393	1.481	NA	NA	NA	NA	NA		NA
C7–C8	1.447		Av. 1.384			1.404				
C8–C9	1.388					1.400				
C9–C10	1.428					1.358				
Angle in C ₁₋₆ ring	118–122	NA	NA	110–124	112–124	NA	NA	120	120	120

^aAverage is for **Y₂K₂-biph**, **Sc₂K₂-biph**, **Lu₂K₂-biph**, **Y₂K₂-terph**, and **Lu₂K₂-TPB**. **Y-biph-Y** and **Y₂-biph** are from *Fryzuk et al. (1997)*. **Cp₂La(C₆H₆)K** is [(Cp^{fl}₂La)₂(μ-η⁶,η⁶-C₆H₆)]⁻ (*Cassani et al., 1998*); **(Cp₂Ln)₂(C₆H₆)K** represents [K(18-crown-6)][(Cp^{fl}₂Ln)(C₆H₆)] (Ln = La, Ce, and Nd) (*Cassani et al., 1999*). **U₂-biph** is from *Diaconescu and Cummins (2012)*. **U₂-tol** is from *Evans et al. (2004)*. Calcd. C₆H₆⁴⁻ value is from *Li et al. (1993)*. Calcd. Ba₂(C₆H₆) value is from *Diefenbach and Schwarz (2005)*.

compounds containing different groups, including halide, alkyl, and the aromatic anion $\text{Cp}-(\text{NN}^{\text{TBS}})\text{Y}(\text{THF})_2$ (**Y-I**), $(\text{NN}^{\text{TBS}})\text{Y}(\text{CH}_2\text{C}_6\text{H}_5)(\text{THF})_2$ (**Y-Bn**), and $(\text{NN}^{\text{TBS}})\text{Y}(\text{Cp})(\text{THF})$ (**Y-Cp**)—together with **Y₂K₂-biph** and **Y₂K₂-terph** were investigated. It was found that the value (in ppm) of the ⁸⁹Y chemical shift decreased in the series: **Y-Bn** (+436), **Y-I** (+370), **Y₂K₂-terph** (+213), **Y₂K₂-biph** (+189), and **Y-Cp** (+69). These results confirmed the presence of a significant aromatic ring current in the phenyl ring coordinating to yttrium in **Y₂K₂-biph** and **Y₂K₂-terph** since ⁸⁹Y chemical shifts in **Y₂K₂-biph** and **Y₂K₂-terph** were different from **Y-Bn** and **Y-I** but closer to **Y-Cp**, which contains the aromatic ligand Cp. The values obtained experimentally were matched by the corresponding calculated values as well.

The isolation of tetraanionic, substituted benzenes was possible because of their coordination to rare earth ions. In addition to the group 3 metals, the phenyl substituents of the reduced benzene ring also have a stabilizing influence on the four-electron reduction state of the arene ligands (Huang et al., 2013).

6 GROUP 3 METAL STILBENE COMPLEXES

As described earlier, the metal naphthalene complexes with the general formula $[(\text{NN}^{\text{TBS}})\text{M}(\text{THF})_x](\mu-\eta^4:\eta^4-\text{C}_{10}\text{H}_8)$ (**M₂-naph**, M = Sc, x = 0; M = Y, La, Lu, x = 1) contain a naphthalene dianion bridging the two metal centers through different phenyl rings. On the other hand, the metal biphenyl complexes with the general formula $[(\text{NN}^{\text{TBS}})\text{M}](\mu-\eta^6:\eta^6-\text{C}_6\text{H}_5\text{Ph})[\text{K}(\text{solvent})]_2$ (**M₂K₂-biph**, M = Sc, Y, La, Lu, solvent = toluene, tetrahydrofuran, diethyl ether, or 18-crown-6) contain a biphenyl tetraanion bridging the two rare earth centers through the same phenyl ring. While the negative charges in **M₂-naph** are equally distributed over the entire naphthalene fragment, as observed with previously reported complexes, the four-electron reduction is mainly localized on the coordinating phenyl ring in **M₂K₂-biph** and results in a 6C, 10π-electron aromatic system. DFT calculations on the naphthalene and biphenyl complexes showed π overlap for the former and δ overlap for the latter between the metal orbitals and arene π* orbitals.

The divergence in bonding modes observed for the bridged arene group 3 metal complexes supported by NN^{TBS} is unlike the situation described for diuranium inverse-sandwiched arene complexes of biphenyl, *p*-terphenyl, naphthalene, and (*E*)-stilbene supported by a ketimide ligand (Diaconescu and Cummins, 2012). In the case of uranium, all reduced arene complexes had an analogous electronic structure, featuring δ overlap between LUMOs of one phenyl ring and the two uranium centers. Other related diuranium inverse-sandwiched benzene or toluene complexes that were synthesized with different supporting ligands adhere to similar bonding considerations (Arnold et al., 2012; Diaconescu et al., 2000; Evans et al., 2004; Monreal et al., 2011; Mougél et al., 2012; Patel et al., 2011).

Stilbene is an unusual arene as a ligand in that it offers the possibility of coordination to an arene ring or to the double bond. In spite of the abundance of rare earth naphthalene complexes in literature (Bochkarev, 2002; Bochkarev et al., 1997; Fryzuk et al., 2000), (*E*)-stilbene complexes are rare. Evans et al. reported the synthesis of $[(C_5Me_5)_2Sm]_2((E)\text{-stilbene})$ from the direct reaction of $(C_5Me_5)_2Sm$ and (*E*)-stilbene (Chart 23; Evans et al., 1990). Due to the poor quality of the crystal, the structure of the molecule could not be unambiguously determined but the authors suggested an unsymmetrical coordination mode based on connectivity. The analogous samarium styrene and butadiene complexes (styrene complex shown in Chart 23) showed two-electron reduction of the C=C bond and concomitant oxidation of Sm(II) to Sm(III) (Evans et al., 2001). Related yttrium and lutetium complexes of the readily available tetraphenylethylene dianion have been reported with similar structural features (Chart 23; Roitershtein et al., 1998, 2004).

Compound $[(NN^{TBS})Y(THF)]_2(\mu\text{-}\eta^3\text{:}\eta^3\text{-}(E)\text{-stilbene})$ (**Y₂-stilbene**) was obtained by KC_8 reduction of $(NN^{TBS})YI(THF)_2$ in the presence of 0.5 equivalents of (*E*)-stilbene (Scheme 9) and its structure (Fig. 22) determined by single-crystal X-ray diffraction (Huang et al., 2014). The analogous lanthanum complex was synthesized following the same protocol and structurally characterized. A heterobimetallic complex, $[(NN^{TBS})Y(THF)]((E)\text{-stilbene})[K(THF)]$ (**Y-stilbene-K**), was obtained in the presence of excess KC_8 (Scheme 9). The ion-separated pair $[(NN^{TBS})Y(THF)]((E)\text{-stilbene})[K(18\text{-crown-6})]$ (**Y-stilbene-K-crown**) could also be structurally characterized (Fig. 22).

In both molecular structures of **M₂-stilbene** (M = Y, La), the central C–C bond was flipped and disordered over two symmetrical positions (Huang

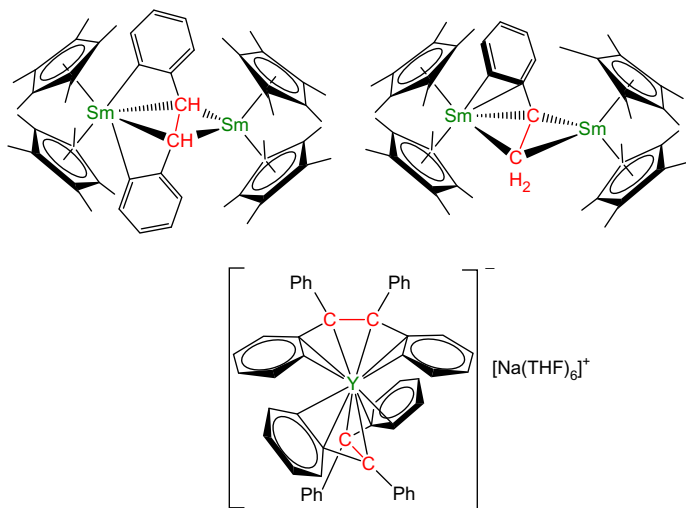
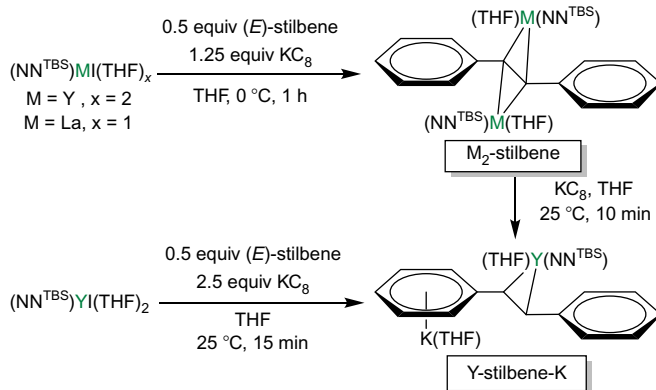


CHART 23 Rare earth alkene complexes reported by Evans's group.



SCHEME 9 Synthesis of **M₂-stilbene**, **Y-stilbene-K**, and transformation of **Y₂-stilbene** to **Y-stilbene-K**. Adapted with permission from The Royal Society of Chemistry from [Huang et al. \(2014\)](#).

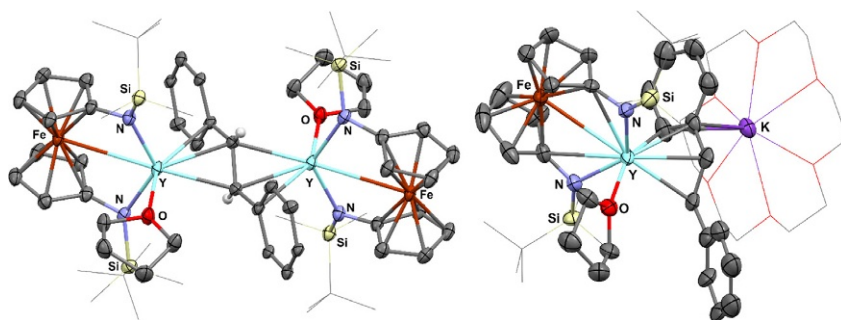
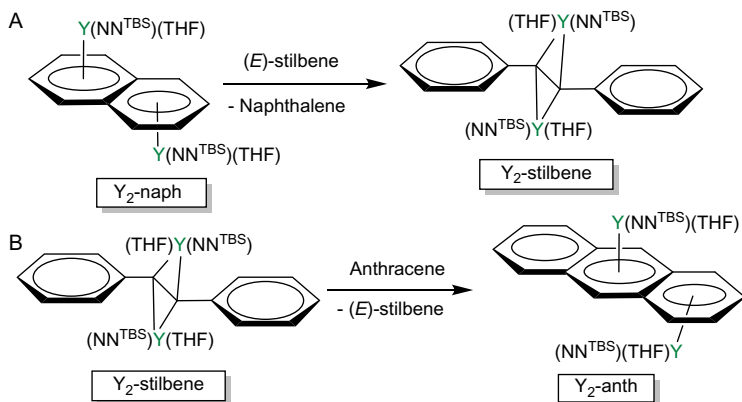


FIGURE 22 Molecular structure of **Y₂-stilbene** (left) and **Y-stilbene-K-crown** (right). Adapted from [Huang et al. \(2014\)](#).

[et al., 2014](#)). The bridging (*E*)-stilbene ligand is coordinated equally to the two yttrium centers in an η^3 fashion through the central C–C bond and one *ipso*-carbon, with Y–C distances of 2.60, 2.58, and 2.74 Å, respectively. This symmetrical coordination mode is different from the unsymmetrical coordination mode suggested for $[(C_5Me_5)_2Sm]_2((E)\text{-stilbene})$ ([Evans et al., 1990](#)). The C–C distance corresponding to the original double bond was found to be 1.52 Å, consistent with single bond character.

Arene exchange experiments ([Scheme 10](#)) were employed to compare the reducing power of **Y₂-stilbene** with that of its dianionic arene analogs ([Huang et al., 2014](#)). It was found that **Y₂-naph** is the strongest reducing agent, while **Y₂-anth** is the weakest, with **Y₂-stilbene** being in the middle of the series. This series parallels the reduction potential of the bridging arenes in the free form ([Abdul-Rahim et al., 2013](#); [Connelly and Geiger, 1996](#)). Consequently, the reaction of **Y₂-stilbene** and 2,2'-bipyridine (bipy) or phenylacetylene



SCHEME 10 Relative reducing strength of Y_2 -stilbene. Adapted with permission from The Royal Society of Chemistry from Huang *et al.* (2014).

(PhCCH) resembled the reactivity of Sc_2 -naph and yielded $(NN^{TBS})Y(THF)$ (bipy) and $[(NN^{TBS})Y(THF)][(NN^{TBS})Y](CCPh)_2$ with the concomitant formation of (E) -stilbene and bibenzyl, respectively; however, the addition of excess pyridine did not yield the corresponding C–C coupled complex.

As remarked in this section, group 3 metals prefer bonding to the central C–C bond rather than an aromatic ring as observed for uranium (Diaconescu and Cummins, 2012). This difference in the bonding mode was also probed by DFT calculations for the stilbene complexes described here (Huang *et al.*, 2014). The HOMOs of M_2 -stilbene were found to be composed of the π^* orbitals of the central C–C bond and are stabilized by a π interaction with the metal ions and delocalization to adjacent phenyl rings (Fig. 23). This contrasts the case of uranium and substantiates different bonding preferences for rare earths that are similar to those of transition metals and not actinides with respect to arene bonding.

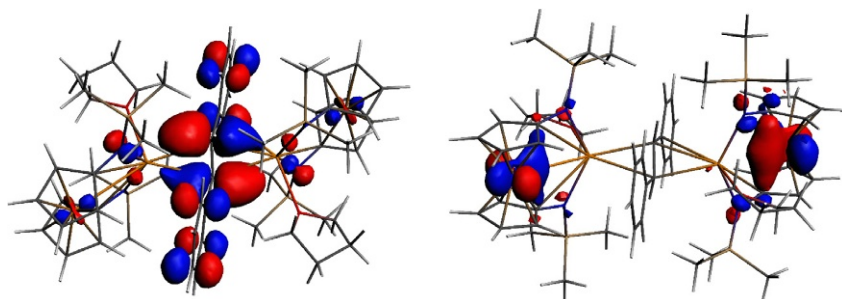


FIGURE 23 HOMO (left) and HOMO-1 (right) for Y_2 -stilbene. Reproduced with permission from The Royal Society of Chemistry from Huang *et al.* (2014).

7 CONCLUSIONS AND OUTLOOK

Rare earth organometallic chemistry enjoyed a rapid growth after the introduction of cyclopentadienyl and its derivatives as ancillary ligands in the 1970s. Metallocene (Cp_2MX) and half-sandwich complexes (CpMX_2) constituted the main body of this area for a long time. Recently, supporting ligands other than cyclopentadienyls have been developed and introduced, resulting in uncovering chemistry that has not been previously observed with metallocene or half-sandwich complexes.

This chapter summarized recent advances in the reduction chemistry of rare earth metals and described our own efforts in synthesizing inverse sandwiches of rare earth arene complexes using ferrocene-based diamide ligands. Unprecedented molecules were synthesized and their unusual electronic structures were studied. Highlights included the synthesis of the first scandium naphthalene complex and its reactivity toward P_4 activation and the isolation and characterization of a 6-carbon, 10π -electron aromatic system stabilized by coordination to rare earth metals. The reactivity of those complexes was also discussed.

New developments in the chemistry of reduced arene rare earth complexes show that although this is a relatively mature field, there are still plenty of surprising results at the horizon. Aside from the synthesis of unusual or long-sought molecules, the reduction chemistry of rare earths has the advantage of combining the high Lewis acidity of the metal with storing electrons on a reactive ligand in order to obtain unusual reactivity. Although most of these complexes are air- and water-sensitive, they can still teach the scientific community important lessons about what is necessary in order to achieve "extreme" reactivity and advance our fundamental knowledge of structure and bonding.

It is likely that the future will see the isolation of other interesting bonding motifs, some predicted and others maybe not even imagined. Their characterization will benefit greatly from theoretical calculations and advanced spectroscopy techniques, as is becoming more and more the case in the present. And although lanthanides are considered to form mostly ionic compounds, a detailed and subtle understanding of covalent contributions to bonding will likely emerge as new molecules are reported.

ACRONYMS AND ABBREVIATIONS

18-crown-6	1,4,7,10,13,16-hexaoxacyclooctadecane
2.2.2-cryptand	4,7,13,16,21,24-hexaoxa-1,10-diazabicyclo[8.8.8] hexacosane
anth	anthracene
biph	biphenyl
bipy	2,2'-bipyridine

Bn	benzyl
COT²⁻	cyclooctatetraene dianion, ($\eta^8\text{-C}_8\text{H}_8$) ²⁻
Cp⁻	cyclopentadienyl anion, ($\eta^5\text{-C}_5\text{H}_5$) ⁻
Cp*⁻	pentamethylcyclopentadienyl anion, ($\eta^5\text{-C}_5\text{Me}_5$) ⁻
DFT	density functional theory
DME	1,2-dimethoxyethane
Et₂O	diethyl ether
fc	1,1'-ferrocenediyl
HOMO	highest occupied molecular orbital
ⁱPr	<i>iso</i> -propyl
IR	infrared
KC₈	potassium graphite
LUMO	lowest unoccupied molecular orbital
N₂N^{py}	2,6-bis(2,6-di- <i>iso</i> -propylanilidomethyl)pyridine
nacnac	β -diketiminato
naph	naphthalene
NBO	natural bond orbital
NHC	<i>N</i> -heterocyclic carbene
NICS	nuclear-independent chemical shift
NMR	nuclear magnetic resonance (spectroscopy)
NN^{fc}	see NN ^{TBS}
NN^{TBS}	[fc(NSi ^{<i>i</i>} BuMe ₂) ₂] ²⁻
NN^{TMS}	[fc(NSiMe ₃) ₂] ²⁻
OEP	octamethylporphyrin
TACN	1,4,7-triazacyclononane
^tBu	<i>tert</i> -butyl
terph	<i>p</i> -terphenyl
THF	tetrahydrofuran
TMTAC	1,3,5-trimethyl-1,3,5-triazacyclohexane
TPB	1,3,5-triphenylbenzene
XANES	X-ray absorption near-edge structure

REFERENCES

- Abdul-Rahim, O., Simonov, A.N., Rütther, T., Boas, J.F., Torriero, A.A.J., Collins, D.J., Perlmutter, P., Bond, A.M., 2013. *Anal. Chem.* 85, 6113–6120.
- Ahlich, R., Fenske, D., Fromm, K., Krautscheid, H., Krautscheid, U., Treutler, O., 1996. *Chem. Eur. J.* 2, 238–244.
- Akabori, S., Kumagai, T., Shirahige, T., Sato, S., Kawazoe, K., Tamura, C., Sato, M., 1987. *Organometallics* 6, 2105–2109.
- Anderson, D.M., Cloke, F.G.N., Cox, P.A., Edelstein, N., Green, J.C., Pang, T., Sameh, A.A., Shalimoff, G., 1989. *J. Chem. Soc. Chem. Commun.* 53–55.
- Aparna, K., Ferguson, M., Cavell, R.G., 2000. *J. Am. Chem. Soc.* 122, 726–727.
- Arndt, S., Okuda, J., 2002. *Chem. Rev.* 102, 1953–1976.
- Arnold, P.L., Casely, I.J., 2009. *Chem. Rev.* 109, 3599–3611.

- Arnold, J., Hoffman, C.G., 1990. *J. Am. Chem. Soc.* 112, 8620–8621.
- Arnold, J., Hoffman, C.G., Dawson, D.Y., Hollander, F.J., 1993. *Organometallics* 12, 3645–3654.
- Arnold, P.L., Cloke, F.G.N., Hitchcock, P.B., Nixon, J.F., 1996. *J. Am. Chem. Soc.* 118, 7630–7631.
- Arnold, P.L., Cloke, F.G.N., Nixon, J.F., 1998. *Chem. Commun.* 797–798.
- Arnold, P.L., McMaster, J., Liddle, S.T., 2009. *Chem. Commun.* 818–820.
- Arnold, P.L., Mansell, S.M., Maron, L., McKay, D., 2012. *Nat. Chem.* 4, 668–674.
- Avdeef, A., Raymond, K.N., Hodgson, K.O., Zalkin, A., 1972. *Inorg. Chem.* 11, 1083–1088.
- Ballard, D.G.H., Pearce, R., 1975. *J. Chem. Soc. Chem. Commun.* 621a.
- Barr, M.E., Adams, B.R., Weller, R.R., Dahl, L.F., 1991. *J. Am. Chem. Soc.* 113, 3052–3060.
- Baudler, M., Faber, W., 1980. *Chem. Ber.* 113, 3394–3395.
- Baudler, M., Glinka, K., 1993. *Chem. Rev.* 93, 1623–1667.
- Baudler, M., Hahn, J., 1990. *Z. Naturforsch.* 45b, 1279.
- Baudler, M., Temberger, H., Faber, W., Hahn, J., 1979. *Z. Naturforsch.* 34b, 1690.
- Baudler, M., Pontzen, T., Hahn, J., Temberger, H., Faber, W., 1980. *Z. Naturforsch.* 35b, 517.
- Bauer, J., Braunschweig, H., Dewhurst, R.D., 2012. *Chem. Rev.* 112, 4329–4346.
- Beetstra, D.J., Meetsma, A., Hessen, B., Teuben, J.H., 2003. *Organometallics* 22, 4372–4374.
- Beletskaya, I.P., Voskoboinikov, A.Z., Chuklanova, E.B., Kirillova, N.I., Shestakova, A.K., Parshina, I.N., Gusev, A.I., Magomedov, G.K.I., 1993. *J. Am. Chem. Soc.* 115, 3156–3166.
- Bercaw, J.E., Marvich, R.H., Bell, L.G., Brintzinger, H.H., 1972. *J. Am. Chem. Soc.* 94, 1219–1238.
- Bergbreiter, D.E., Killough, J.M., 1978. *J. Am. Chem. Soc.* 100, 2126–2134.
- Bochkarev, M.N., 2002. *Chem. Rev.* 102, 2089–2118.
- Bochkarev, M.N., Fedushkin, I.L., Larichev, R.B., 1996. *Russ. Chem. Bull.* 45, 2443–2444.
- Bochkarev, M.N., Fedushkin, I.L., Fagin, A.A., Schumann, H., Demtschuk, J., 1997. *Chem. Commun.* 1783–1784.
- Böhm, M.C., Gleiter, R., 1981. *Z. Naturforsch.* 36b, 498.
- Bombieri, G., Paolucci, G., 1998. Organometallic π complexes of the f-elements. In: Gschneidner Jr., Karl A., LeRoy, E. (Eds.), *Handbook on the Physics and Chemistry of Rare Earths*. Elsevier, Amsterdam: The Netherlands, Chapter 168.
- Braunschweig, H., Dewhurst, R.D., Hammond, K., Mies, J., Radacki, K., Vargas, A., 2012. *Science* 336, 1420–1422.
- Broderick, E.M., Guo, N., Vogel, C.S., Xu, C., Sutter, J., Miller, J.T., Meyer, K., Mehrkhodavandi, P., Diaconescu, P.L., 2011. *J. Am. Chem. Soc.* 133, 9278–9281.
- Buckley, H.L., Anstey, M.R., Gryko, D.T., Arnold, J., 2013. *Chem. Commun.* 49, 3104–3106.
- Burin, M.E., Logunov, A.A., Faerman, V.I., Bochkarev, M.N., 2011. *Russ. Chem. Bull.* 60, 1591–1594.
- Butovskii, M.V., Döring, C., Bezugly, V., Wagner, F.R., Grin, Y., Kempe, R., 2010. *Nat. Chem.* 2, 741–744.
- Butts, C.P., Green, M., Hooper, T.N., Kilby, R.J., McGrady, J.E., Pantazis, D.A., Russell, C.A., 2008. *Chem. Commun.* 856–858.
- Bylikin, S.Y., Robson, D.A., Male, N.A.H., Rees, L.H., Mountford, P., Schroder, M., 2001. *J. Chem. Soc. Dalton Trans.* 170–180.
- Camp, C., Mougél, V., Pécaut, J., Maron, L., Mazzanti, M., 2013. *Chem. Eur. J.* 19, 17528–17540.
- Cantat, T., Jaroschik, F., Nief, F., Ricard, L., Mezailles, N., Le Floch, P., 2005. *Chem. Commun.* 5178–5180.
- Caporali, M., Gonsalvi, L., Rossini, A., Peruzzini, M., 2010. *Chem. Rev.* 110, 4178–4235.
- Carver, C.T., Diaconescu, P.L., 2008. *J. Am. Chem. Soc.* 130, 7558–7559.

- Carver, C.T., Diaconescu, P.L., 2009. *J. Alloys Compd.* 488, 518–523.
- Carver, C.T., Monreal, M.J., Diaconescu, P.L., 2008. *Organometallics* 27, 363–370.
- Carver, C.T., Benitez, D., Miller, K.L., Williams, B.N., Tkatchouk, E., Goddard, W.A., Diaconescu, P.L., 2009. *J. Am. Chem. Soc.* 131, 10269–10278.
- Carver, C.T., Williams, B.N., Ogilby, K.R., Diaconescu, P.L., 2010. *Organometallics* 29, 835–846.
- Cassani, M.C., Gun'ko, Y.K., Hitchcock, P.B., Lappert, M.F., 1996. *Chem. Commun.* 1987–1988.
- Cassani, M.C., Duncalf, D.J., Lappert, M.F., 1998. *J. Am. Chem. Soc.* 120, 12958–12959.
- Cassani, M.C., Gun'ko, Y.K., Hitchcock, P.B., Lappert, M.F., Laschi, F., 1999. *Organometallics* 18, 5539–5547.
- Cassani, C.M., Gun'ko, Y.K., Hitchcock, P.B., Hulkes, A.G., Khvostov, A.V., Lappert, M.F., Protchenko, A.V., 2002. *J. Organomet. Chem.* 647, 71–83.
- Charles, S., Fettinger, J.C., Bott, S.G., Eichhorn, B.W., 1996. *J. Am. Chem. Soc.* 118, 4713–4714.
- Chirik, P.J., Pool, J.A., Lobkovsky, E., 2002. *Angew. Chem. Int. Ed.* 41, 3463–3465.
- Chu, J., Lu, E., Liu, Z., Chen, Y., Leng, X., Song, H., 2011. *Angew. Chem. Int. Ed.* 50, 7677–7680.
- Chu, J., Lu, E., Chen, Y., Leng, X., 2012a. *Organometallics* 32, 1137–1140.
- Chu, T., Piers, W.E., Dutton, J.L., Parvez, M., 2012b. *Organometallics* 32, 1159–1165.
- Cloke, F.G.N., 1993. *Chem. Soc. Rev.* 22, 17–24.
- Cloke, F.G.N., Khan, K., Perutz, R.N., 1991. *J. Chem. Soc. Chem. Commun.* 1372–1373.
- Connelly, N.G., Geiger, W.E., 1996. *Chem. Rev.* 96, 877–910.
- Corbridge, D.E.C., Lowe, E.J., 1952. *Nature* 170, 629.
- Cossairt, B.M., Cummins, C.C., Head, A.R., Lichtenberger, D.L., Berger, R.J.F., Hayes, S.A., Mitzel, N.W., Wu, G., 2010a. *J. Am. Chem. Soc.* 132, 8459–8465.
- Cossairt, B.M., Piro, N.A., Cummins, C.C., 2010b. *Chem. Rev.* 110, 4164–4177.
- Cotton, F.A., Schwotzer, W., 1986. *J. Am. Chem. Soc.* 108, 4657–4658.
- Cui, P., Chen, Y., Xu, X., Sun, J., 2008. *Chem. Commun.* 5547–5549.
- Dahlmann, W., Schnering, H.G., 1972. *Naturwissenschaften* 59, 420.
- Demir, S., Lorenz, S.E., Fang, M., Furche, F., Meyer, G., Ziller, J.W., Evans, W.J., 2010. *J. Am. Chem. Soc.* 132, 11151–11158.
- Deng, H., Shore, S.G., 1991. *J. Am. Chem. Soc.* 113, 8538–8540.
- Diaconescu, P.L., 2008. *Curr. Org. Chem.* 12, 1388–1405.
- Diaconescu, P.L., 2010a. *Comments Inorg. Chem.* 31, 196–241.
- Diaconescu, P.L., 2010b. *Acc. Chem. Res.* 43, 1352–1363.
- Diaconescu, P.L., Cummins, C.C., 2012. *Inorg. Chem.* 51, 2902–2916.
- Diaconescu, P.L., Arnold, P.L., Baker, T.A., Mindiola, D.J., Cummins, C.C., 2000. *J. Am. Chem. Soc.* 122, 6108–6109.
- Diefenbach, M., Schwarz, H., 2005. *Chem. Eur. J.* 11, 3058–3063.
- Dietrich, H.M., Grove, H., Törnroos, K.W., Anwander, R., 2006a. *J. Am. Chem. Soc.* 128, 1458–1459.
- Dietrich, H.M., Törnroos, K.W., Anwander, R., 2006b. *J. Am. Chem. Soc.* 128, 9298–9299.
- Dietrich, H.M., Törnroos, K.W., Anwander, R., 2011. *Angew. Chem. Int. Ed.* 50, 12089–12093.
- Duchateau, R., Van Wee, C.T., Meetsma, A., Teuben, J.H., 1993. *J. Am. Chem. Soc.* 115, 4931–4932.
- Duhović, S., Diaconescu, P.L., 2013. *Polyhedron* 52, 377–388.
- Duhović, S., Monreal, M.J., Diaconescu, P.L., 2010. *Inorg. Chem.* 49, 7165–7169.
- Edelmann, F.T., 2009. *Chem. Soc. Rev.* 38, 2253–2268.
- Edelmann, F.T., Freckmann, D.M.M., Schumann, H., 2002. *Chem. Rev.* 102, 1851–1896.

- Emslie, D.J.H., Piers, W.E., Macdonald, R., 2002. *J. Chem. Soc. Dalton Trans.* 293–294.
- Ephritikhine, M., 1997. *Chem. Rev.* 97, 2193–2242.
- Evans, W.J., 2007. *Inorg. Chem.* 46, 3435–3449.
- Evans, W.J., Davis, B.L., 2002. *Chem. Rev.* 102, 2119–2136.
- Evans, W.J., Ulibarri, T.A., Ziller, J.W., 1988. *J. Am. Chem. Soc.* 110, 6877–6879.
- Evans, W.J., Ulibarri, T.A., Ziller, J.W., 1990. *J. Am. Chem. Soc.* 112, 219–223.
- Evans, W.J., Gonzales, S.L., Ziller, J.W., 1994. *J. Am. Chem. Soc.* 116, 2600–2608.
- Evans, W.J., Giarikos, D.G., Robledo, C.B., Leong, V.S., Ziller, J.W., 2001. *Organometallics* 20, 5648–5652.
- Evans, W.J., Allen, N.T., Ziller, J.W., 2002. *Angew. Chem. Int. Ed.* 41, 359–361.
- Evans, W.J., Kozimor, S.A., Ziller, J.W., Kaltsoyannis, N., 2004. *J. Am. Chem. Soc.* 126, 14533–14547.
- Evans, W.J., Lee, D.S., Johnston, M.A., Ziller, J.W., 2005. *Organometallics* 24, 6393–6397.
- Evans, W.J., Fang, M., Zucchi, G.L., Furche, F., Ziller, J.W., Hoekstra, R.M., Zink, J.I., 2009. *J. Am. Chem. Soc.* 131, 11195–11202.
- Fang, M., Lee, D.S., Ziller, J.W., Doedens, R.J., Bates, J.E., Furche, F., Evans, W.J., 2011. *J. Am. Chem. Soc.* 133, 3784–3787.
- Farnaby, J.H., Fang, M., Ziller, J.W., Evans, W.J., 2012. *Inorg. Chem.* 51, 11168–11176.
- Fedushkin, I.L., Bochkarev, M.N., Schumann, H., Esser, L., 1995. *J. Organomet. Chem.* 489, 145–151.
- Fedushkin, I.L., Nevodchikov, V.I., Bochkarev, M.N., Dechert, S., Schumann, H., 2003. *Russ. Chem. Bull.* 52, 154.
- Ferraro, F., Barboza, C.A., Arratia-Pérez, R., 2012. *J. Phys. Chem. A* 116, 4170–4175.
- Ferrence, G.M., McDonald, R., Takats, J., 1999. *Angew. Chem. Int. Ed.* 38, 2233–2237.
- Fieser, M.E., Bates, J.E., Ziller, J.W., Furche, F., Evans, W.J., 2013. *J. Am. Chem. Soc.* 135, 3804–3807.
- Fischbach, A., Anwander, R., 2006. Rare-earth metals and aluminum getting close in Ziegler-type organometallics. In: (Ed.), *Neodymium Based Ziegler Catalysts—Fundamental Chemistry*. Springer, Berlin.
- Fritz, G., Härer, J., 1983. *Z. Anorg. Allg. Chem.* 500, 14–22.
- Fritz, G., Schneider, H.W., Hoenle, W., Von Schnering, H.G., 1990. *Z. Anorg. Allg. Chem.* 585, 51.
- Fryzuk, M.D., Giesbrecht, G., Rettig, S.J., 1996. *Organometallics* 15, 3329–3336.
- Fryzuk, M.D., Love, J.B., Rettig, S.J., 1997. *J. Am. Chem. Soc.* 119, 9071–9072.
- Fryzuk, M.D., Jafarpour, L., Kerton, F.M., Love, J.B., Rettig, S.J., 2000. *Angew. Chem. Int. Ed.* 39, 767–770.
- Gramigna, K.M., Oria, J.V., Mandell, C.L., Tiedemann, M.A., Dougherty, W.G., Piro, N.A., Kassel, W.S., Chan, B.C., Diaconescu, P.L., Nataro, C., 2013. *Organometallics* 32, 5966–5979.
- Green, A.G., Kiesz, M.D., Oria, J.V., Elliott, A.G., Buechler, A.K., Hohenberger, J., Meyer, K., Zink, J.I., Diaconescu, P.L., 2013. *Inorg. Chem.* 52, 5603–5610.
- Gregson, C.K.A., Gibson, V.C., Long, N.J., Marshall, E.L., Oxford, P.J., White, A.J.P., 2006. *J. Am. Chem. Soc.* 128, 7410–7411.
- Guerin, F., Mcconville, D.H., Vittal, J.J., 1995. *Organometallics* 14, 3154–3156.
- Hagadorn, J.R., Arnold, J., 1996. *Organometallics* 15, 984–991.
- Hajela, S., Schaefer, W.P., Bercaw, J.E., 1997. *J. Organomet. Chem.* 532, 45–53.
- Halcovitch, N.R., Fryzuk, M.D., 2013. *Organometallics* 32, 5705–5708.
- Hasinoff, L., Takats, J., Zhang, X.W., Bond, A.H., Rogers, R.D., 1994. *J. Am. Chem. Soc.* 116, 8833–8834.

- Hayes, R.G., Thomas, J.L., 1969. *J. Am. Chem. Soc.* 91, 6876.
- Hayes, P.G., Piers, W.E., Lee, L.W.M., Knight, L.K., Parvez, M., Elsegood, M.R.J., Clegg, W., 2001. *Organometallics* 20, 2533–2544.
- Hayes, P.G., Piers, W.E., McDonald, R., 2002. *J. Am. Chem. Soc.* 124, 2132–2133.
- Hayes, P.G., Piers, W.E., Parvez, M., 2003. *J. Am. Chem. Soc.* 125, 5622–5623.
- Hayes, P.G., Piers, W.E., Parvez, M., 2007. *Chem. Eur. J.* 13, 2632–2640.
- Hey, E., Lappert, M.F., Atwood, J.L., Bott, S.G., 1987. *J. Chem. Soc. Chem. Commun.* 597–598.
- Hitchcock, P.B., Lappert, M.F., Protchenko, A.V., 2001. *J. Am. Chem. Soc.* 123, 189–190.
- Hitchcock, P.B., Lappert, M.F., Maron, L., Protchenko, A.V., 2008. *Angew. Chem. Int. Ed.* 47, 1488–1491.
- Holton, J., Lappert, M.F., Scollary, G.R., Ballard, D.G.H., Pearce, R., Atwood, J.L., Hunter, W.E., 1976. *J. Chem. Soc. Chem. Commun.* 425–426.
- Hönle, W., Schnering, P.D.H.G.V., 1978. *Z. Anorg. Allg. Chem.* 440, 171–182.
- Hou, Z., Zhang, Y., Tardif, O., Wakatsuki, Y., 2001. *J. Am. Chem. Soc.* 123, 9216–9217.
- Hou, Z., Nishiura, M., Shima, T., 2007. *Eur. J. Inorg. Chem.* 2007, 2535–2545.
- Huang, W., Diaconescu, P.L., 2012. *Chem. Commun.* 48, 2216–2218.
- Huang, W., Diaconescu, P.L., 2013. *Eur. J. Inorg. Chem.* 2013, 4090–4096.
- Huang, Y., Wise, M.B., Jacobson, D.B., Freiser, B.S., 1987. *Organometallics* 6, 346–354.
- Huang, W., Carver, C.T., Diaconescu, P.L., 2010. *Inorg. Chem.* 50, 978–984.
- Huang, W., Khan, S.I., Diaconescu, P.L., 2011. *J. Am. Chem. Soc.* 133, 10410–10413.
- Huang, W., Dulong, F., Wu, T., Khan, S.I., Miller, J.T., Cantat, T., Diaconescu, P.L., 2013. *Nat. Commun.* 4, 1448.
- Huang, W., Abukhalil, P.M., Khan, S.I., Diaconescu, P.L., 2014. *Chem. Commun.* <http://dx.doi.org/10.1039/C3CC47505K>.
- Huber, W., May, A., Müllen, K., 1981. *Chem. Ber.* 114, 1318.
- Ito, N., Saji, T., Aoyagui, S., 1983. *J. Organomet. Chem.* 247, 301–305.
- Jaroschik, F., Nief, F., Le Goff, X.-F., Ricard, L., 2007a. *Organometallics* 26, 1123–1125.
- Jaroschik, F., Nief, F., Le Goff, X.-F., Ricard, L., 2007b. *Organometallics* 26, 3552–3558.
- Jaroschik, F., Momin, A., Nief, F., Le Goff, X.-F., Deacon, G.B., Junk, P.C., 2009. *Angew. Chem. Int. Ed.* 48, 1117–1121.
- Jensen, K.A., Nygaard, B., Elisson, G., Nielsen, P.H., 1965. *Acta Chem. Scand.* 19, 768–770.
- Jie, S., Diaconescu, P.L., 2010. *Organometallics* 29, 1222–1230.
- Kealy, T.J., Pauson, P.L., 1951. *Nature* 168, 1039–1040.
- Kerridge, A., 2013. *Dalton Trans.* 42, 16428–16436.
- King, D.M., Tuna, F., McInnes, E.J.L., McMaster, J., Lewis, W., Blake, A.J., Liddle, S.T., 2012. *Science* 337, 717–720.
- Konchenko, S.N., Pushkarevsky, N.A., Gamer, M.T., Köppe, R., Schnöckel, H., Roesky, P.W., 2009. *J. Am. Chem. Soc.* 131, 5740–5741.
- Konkol, M., Okuda, J., 2008. *Coord. Chem. Rev.* 252, 1577–1591.
- Kraus, F., Aschenbrenner, J.C., Korber, N., 2003. *Angew. Chem. Int. Ed.* 42, 4030–4033.
- Kumari, S., Roudjane, M., Hewage, D., Liu, Y., Yang, D.-S., 2013. *J. Chem. Phys.* 138.
- Labouille, S., Nief, F., Le Goff, X.-F., Maron, L., Kindra, D.R., Houghton, H.L., Ziller, J.W., Evans, W.J., 2012. *Organometallics* 31, 5196–5203.
- Lee, J.A., Williams, B.N., Ogilby, K.R., Miller, K.L., Diaconescu, P.L., 2011. *J. Organomet. Chem.* 696, 4090–4094.
- Li, J., Liu, C.-W., Lu, J.-X., 1993. *J. Mol. Struct.* 280, 223–231.
- Li, X., Baldamus, J., Nishiura, M., Tardif, O., Hou, Z., 2006. *Angew. Chem. Int. Ed.* 45, 8184–8188.

- Li, T., Jenter, J., Roesky, P., 2010. Rare-earth metal postmetallocene catalysts with chelating amido ligands. In: Roesky, P.W. (Ed.), *Molecular Catalysis of Rare-Earth Elements*. Springer, Berlin.
- Li, T., Wiecko, J., Pushkarevsky, N.A., Gamer, M.T., Köppe, R., Konchenko, S.N., Scheer, M., Roesky, P.W., 2011. *Angew. Chem. Int. Ed.* 50, 9491–9495.
- Liddle, S.T., Arnold, P.L., 2005. *Organometallics* 24, 2597–2605.
- Liddle, S.T., Mills, D.P., 2009. *Dalton Trans.* 5592–5605.
- Lu, E., Li, Y., Chen, Y., 2010. *Chem. Commun.* 46, 4469–4471.
- Lu, E., Gan, W., Chen, Y., 2011. *Dalton Trans.* 40, 2366–2374.
- Lu, E., Zhou, Q., Li, Y., Chu, J., Chen, Y., Leng, X., Sun, J., 2012. *Chem. Commun.* 48, 3403–3405.
- Lv, Y., Xu, X., Chen, Y., Leng, X., Borzov, M.V., 2011. *Angew. Chem. Int. Ed.* 50, 11227–11229.
- Macdonald, M.R., Ziller, J.W., Evans, W.J., 2011. *J. Am. Chem. Soc.* 133, 15914–15917.
- Macdonald, M.R., Bates, J.E., Fieser, M.E., Ziller, J.W., Furche, F., Evans, W.J., 2012. *J. Am. Chem. Soc.* 134, 8420–8423.
- Macdonald, M.R., Bates, J.E., Ziller, J.W., Furche, F., Evans, W.J., 2013a. *J. Am. Chem. Soc.* 135, 9857–9868.
- Macdonald, M.R., Fieser, M.E., Bates, J.E., Ziller, J.W., Furche, F., Evans, W.J., 2013b. *J. Am. Chem. Soc.* 135, 13310–13313.
- Maginn, R.E., Manastyrskyj, S., Dubeck, M., 1963. *J. Am. Chem. Soc.* 85, 672–676.
- Manastyrskyj, S., Maginn, R.E., Dubeck, M., 1963. *Inorg. Chem.* 2, 904–905.
- Manriquez, J.M., Bercaw, J.E., 1974. *J. Am. Chem. Soc.* 96, 6229–6230.
- Manriquez, J.M., Mcalister, D.R., Sanner, R.D., Bercaw, J.E., 1976. *J. Am. Chem. Soc.* 98, 6733–6735.
- Marks, T.J., 2013. *Organometallics* 32, 1133–1136.
- Marques, N., Sella, A., Takats, J., 2002. *Chem. Rev.* 102, 2137–2160.
- Masuda, J.D., Jantunen, K.C., Ozerov, O.V., Noonan, K.J.T., Gates, D.P., Scott, B.L., Kiplinger, J.L., 2008. *J. Am. Chem. Soc.* 130, 2408–2409.
- Melero, C., Guijarro, A., Yus, M., 2009. *Dalton Trans.* 1286–1289.
- Meyer, G., 2014. *Angew. Chem. Int. Ed.*
- Meyer, G., Gerlitzki, N., Hammerich, S., 2004. *J. Alloys Compd.* 380, 71–78.
- Miller, S.A., Tebboth, J.A., Tremaine, J.F., 1952. *J. Chem. Soc.* 632–635.
- Miller, K.L., Williams, B.N., Benitez, D., Carver, C.T., Ogilby, K.R., Tkatchouk, E., Goddard, W.A., Diaconescu, P.L., 2009. *J. Am. Chem. Soc.* 132, 342–355.
- Miller, K.L., Carver, C.T., Williams, B.N., Diaconescu, P.L., 2010. *Organometallics* 29, 2272–2281.
- Mills, D.P., Soutar, L., Lewis, W., Blake, A.J., Liddle, S.T., 2010. *J. Am. Chem. Soc.* 132, 14379–14381.
- Minasian, S.G., Krinsky, J.L., Rinehart, J.D., Copping, R., Tylliszczak, T., Janousch, M., Shuh, D.K., Arnold, J., 2009. *J. Am. Chem. Soc.* 131, 13767–13783.
- Moeller, T., Martin, D.F., Thompson, L.C., Ferrús, R., Feistel, G.R., Randall, W.J., 1965. *Chem. Rev.* 65, 1–50.
- Monreal, M.J., Diaconescu, P.L., 2008. *Organometallics* 27, 1702–1706.
- Monreal, M.J., Diaconescu, P.L., 2010. *J. Am. Chem. Soc.* 132, 7676–7683.
- Monreal, M.J., Carver, C.T., Diaconescu, P.L., 2007. *Inorg. Chem.* 46, 7226–7228.
- Monreal, M.J., Khan, S., Diaconescu, P.L., 2009. *Angew. Chem. Int. Ed.* 48, 8352–8355.

- Monreal, M.J., Khan, S.I., Kiplinger, J.L., Diaconescu, P.L., 2011. *Chem. Commun.* 47, 9119–9121.
- Mougel, V., Camp, C., Pécaut, J., Copéret, C., Maron, L., Kefalidis, C.E., Mazzanti, M., 2012. *Angew. Chem. Int. Ed.* 51, 12280–12284.
- Nair, V., Balagopal, L., Rajan, R., Mathew, J., 2003. *Acc. Chem. Res.* 37, 21–30.
- Nief, F., 2001. *Eur. J. Inorg. Chem.* 2001, 891–904.
- Nief, F., 2010. Molecular chemistry of the rare-earth elements in uncommon low-valent states. In: Gschneidner Jr., K.A., Bünzli, J.C.G., Vitalij, K.P. (Eds.), *Handbook on the Physics and Chemistry of Rare Earths*. Elsevier, Amsterdam: The Netherlands (Chapter 246).
- Nief, F., Ricard, L., 1994. *J. Chem. Soc. Chem. Commun.* 2723–2724.
- Nugent, L.J., Baybarz, R.D., Burnett, J.L., Ryan, J.L., 1973. *J. Phys. Chem.* 77, 1528–1539.
- Ochchipintî, G., Meermann, C., Dietrich, H.M., Litlabø, R., Auras, F., Törnroos, K.W., Maichle-Mössmer, C., Jensen, V.R., Anwander, R., 2011. *J. Am. Chem. Soc.* 133, 6323–6337.
- Oelkers, B., Butovskii, M.V., Kempe, R., 2012. *Chem. Eur. J.* 18, 13566–13579.
- Patel, D., Moro, F., McMaster, J., Lewis, W., Blake, A.J., Liddle, S.T., 2011. *Angew. Chem. Int. Ed.* 50, 10388–10392.
- Patel, D., Tuna, F., McInnes, E.J.L., McMaster, J., Lewis, W., Blake, A.J., Liddle, S.T., 2013. *Dalton Trans.* 42, 5224–5227.
- Piers, W.E., Emslie, D.J.H., 2002. *Coord. Chem. Rev.* 233–234, 131–155.
- Piers, W., Shapiro, P., Bunel, E., Bercaw, J., 1990. *Synlett* 74–84.
- Protchenko, A.V., Zakharov, L.N., Fukin, G.K., Struchkov, V.T., Bochkareva, M.N., 1996. *Russ. Chem. Bull.* 45, 950–953.
- Protchenko, A.V., Almazova, O.G., Zakharov, L.N., Fukin, G.K., Struchkov, Y.T., Bochkarev, M.N., 1997. *J. Organomet. Chem.* 536–537, 457–463.
- Putzer, M.A., Rogers, J.S., Bazan, G.C., 1999. *J. Am. Chem. Soc.* 121, 8112–8113.
- Ramos, A., Otten, E., Stephan, D.W., 2009. *J. Am. Chem. Soc.* 131, 15610–15611.
- Randic, M., Oakland, D.O., Klein, D.J., 1986. *J. Comput. Chem.* 7, 35.
- Reznichenko, A., Hultzsck, K., 2010. Catalytic σ -bond metathesis. In: Roesky, P.W. (Ed.), *Molecular Catalysis of Rare-Earth Elements*. Springer, Berlin.
- Rinehart, J.D., Fang, M., Evans, W.J., Long, J.R., 2011a. *Nat. Chem.* 3, 538–542.
- Rinehart, J.D., Fang, M., Evans, W.J., Long, J.R., 2011b. *J. Am. Chem. Soc.* 133, 14236–14239.
- Roddick, D.M., Fryzuk, M.D., Seidler, P.F., Hillhouse, G.L., Bercaw, J.E., 1985. *Organometallics* 4, 97–104.
- Roitershtein, D.M., Ziller, J.W., Evans, W.J., 1998. *J. Am. Chem. Soc.* 120, 11342–11346.
- Roitershtein, D.M., Minyaev, M.E., Lyssenko, K.A., Belyakov, P.A., Antipin, M.Y., 2004. *Russ. Chem. Bull. Int. Ed.* 53, 2152–2161.
- Rong, W., Cheng, J., Mou, Z., Xie, H., Cui, D., 2013. *Organometallics*.
- Roussel, P., Alcock, N.W., Scott, P., 1998. *Chem. Commun.* 801–802.
- Rüdruff, W., Schulze, E., 1954. *Z. Anorg. Allg. Chem.* 277, 156–171.
- Sauro, V.A., Workentin, M.S., 2002. *Can. J. Chem.* 80, 250–262.
- Scheer, M., Becker, U., Matern, E., 1996. *Chem. Ber.* 129, 721–724.
- Scheer, M., Balázs, G., Seitz, A., 2010. *Chem. Rev.* 110, 4236–4256.
- Scherer, O.J., Swarowsky, M., Swarowsky, H., Wolmershäuser, G., 1988. *Angew. Chem. Int. Ed.* 27, 694–695.
- Scherer, O.J., Werner, B., Heckmann, G., Wolmershäuser, G., 1991. *Angew. Chem. Int. Ed.* 30, 553–555.

- Schnöckelborg, E.-M., Weigand, J.J., Wolf, R., 2011. *Angew. Chem. Int. Ed.* 50, 6657–6660.
- Schröder, G., Oth, J.F.M., Merényi, R., 1965. *Angew. Chem. Int. Ed.* 4, 752–761.
- Schwindt, M.A., Lejon, T., Hegedus, L.S., 1990. *Organometallics* 9, 2814–2819.
- Scott, J., Mendiola, D.J., 2009. *Dalton Trans.* 8463–8472.
- Scott, J., Fan, H., Wicker, B.F., Fout, A.R., Baik, M.-H., Mendiola, D.J., 2008. *J. Am. Chem. Soc.* 130, 14438–14439.
- Seidel, W.W., Summerscales, O.T., Patrick, B.O., Fryzuk, M.D., 2009. *Angew. Chem. Int. Ed.* 48, 115–117.
- Seyferth, D., Hames, B.W., Rucker, T.G., Cowie, M., Dickson, R.S., 1983. *Organometallics* 2, 472–474.
- Shafir, A., Arnold, J., 2001. *J. Am. Chem. Soc.* 123, 9212–9213.
- Shafir, A., Arnold, J., 2003. *Organometallics* 22, 567–575.
- Shafir, A., Power, M.P., Whitener, G.D., Arnold, J., 2000. *Organometallics* 19, 3978–3982.
- Shafir, A., Power, M.P., Whitener, G.D., Arnold, J., 2001. *Organometallics* 20, 1365–1369.
- Shannon, R., 1976. *Acta Crystallogr. A32*, 751–767.
- Shima, T., Hou, Z., 2006. *J. Am. Chem. Soc.* 128, 8124–8125.
- Shima, T., Hu, S., Luo, G., Kang, X., Luo, Y., Hou, Z., 2013. *Science* 340, 1549–1552.
- So, Y.-M., Wang, G.-C., Li, Y., Sung, H.H.Y., Williams, I.D., Lin, Z., Leung, W.-H., 2014. *Angew. Chem. Int. Ed.* 53, 1626–1629.
- Spannenberg, A., Oberthür, M., Noss, H., Tillack, A., Arndt, P., Kempe, R., 1998. *Angew. Chem. Int. Ed.* 37, 2079–2082.
- Stainer, M.V.R., Takats, J., 1982. *Inorg. Chem.* 21, 4050–4053.
- Stephens, F.H., 2004. Activation of white phosphorus by molybdenum- and uranium tris-amides. Ph.D Massachusetts Institute of Technology.
- Streitwieser, A., Mueller-Westerhoff, U., 1968. *J. Am. Chem. Soc.* 90, 7364.
- Tardif, O., Nishiura, M., Hou, Z., 2003. *Organometallics* 22, 1171–1173.
- Tardif, O., Hashizume, D., Hou, Z., 2004. *J. Am. Chem. Soc.* 126, 8080–8081.
- Thiele, K.-H., Bambirra, S., Schumann, H., Hemling, H., 1996. *J. Organomet. Chem.* 517, 161–163.
- Thiele, K.-H., Bambirra, S., Sieler, J., Yelonek, S., 1998. *Angew. Chem.* 110, 3016–3018.
- Thomson, R.K., Cantat, T., Scott, B.L., Morris, D.E., Batista, E.R., Kiplinger, J.L., 2010. *Nat. Chem.* 2, 723–729.
- Tilley, T.D., Andersen, R.A., 1981. *Inorg. Chem.* 20, 3267–3270.
- Trifonov, A.A., 2010. *Coord. Chem. Rev.* 254, 1327–1347.
- Tsuruta, H., Imamoto, T., Yamaguchi, K., 1999. *Chem. Commun.* 1703–1704.
- Ungurenasu, C., Palie, M., 1975. *J. Chem. Soc. Chem. Commun.* 388a.
- Venugopal, A., Kamps, I., Bojer, D., Berger, R.J.F., Mix, A., Willner, A., Neumann, B., Stammer, H.-G., Mitzel, N.W., 2009. *Dalton Trans.* 5755–5765.
- Walter, M.D., Booth, C.H., Lukens, W.W., Andersen, R.A., 2009. *Organometallics* 28, 698–707.
- Wang, Y., Quillian, B., Wei, P., Wannere, C.S., Xie, Y., King, R.B., Schaefer, H.F., Schleyer, P.V.R., Robinson, G.H., 2007. *J. Am. Chem. Soc.* 129, 12412–12413.
- Wang, Y., Xie, Y., Wei, P., King, R.B., Schaefer, H.F., Schleyer, P.V.R., Robinson, G.H., 2008. *Science* 321, 1069–1071.
- Ward, B.D., Dubberley, S.R., Maise-Francois, A., Gade, L.H., Mountford, P., 2002. *J. Chem. Soc. Dalton Trans.* 4649–4657.
- Watson, P.L., Whitney, J.F., Harlow, R.L., 1981. *Inorg. Chem.* 20, 3271–3278.
- Wayda, A.L., Evans, W.J., 1980. *Inorg. Chem.* 19, 2190–2191.

- Wedler, M., Noltemeyer, M., Pieper, U., Schmidt, H.-G., Stalke, D., Edelmarin, F.T., 1990. *Angew. Chem. Int. Ed. Engl.* 29, 894–896.
- Wicker, B.F., Scott, J., Andino, J.G., Gao, X., Park, H., Pink, M., Mindiola, D.J., 2010. *J. Am. Chem. Soc.* 132, 3691–3693.
- Wicker, B.F., Scott, J., Fout, A.R., Pink, M., Mindiola, D.J., 2011. *Organometallics* 30, 2453–2456.
- Wilkinson, G., Birmingham, J.M., 1954. *J. Am. Chem. Soc.* 76, 6210.
- Williams, B.N., Huang, W., Miller, K.L., Diaconescu, P.L., 2010. *Inorg. Chem.* 49, 11493–11498.
- Williams, B.N., Benitez, D., Miller, K.L., Tkatchouk, E., Goddard, W.A., Diaconescu, P.L., 2011. *J. Am. Chem. Soc.* 133, 4680–4683.
- Wolczanski, P.T., Bercaw, J.E., 1980. *Acc. Chem. Res.* 13, 121–127.
- Wolczanski, P.T., Threlkel, R.S., Bercaw, J.E., 1979. *J. Am. Chem. Soc.* 101, 218–220.
- Wong, A.W., Miller, K.L., Diaconescu, P.L., 2010. *Dalton Trans.* 39, 6726–6731.
- Xu, X., Chen, Y., Zou, G., Sun, J., 2010. *Dalton Trans.* 39, 3952–3958.
- Yoon, H.J., Kuwabara, J., Kim, J.-H., Mirkin, C.A., 2010. *Science* 330, 66–69.
- Zeimentz, P.M., Arndt, S., Elvidge, B.R., Okuda, J., 2006. *Chem. Rev.* 106, 2404–2433.
- Zimmermann, M., Anwander, R., 2010. *Chem. Rev.* 110, 6194–6259.

This page intentionally left blank

Index

Note: Page numbers followed by “*f*” indicate figures, “*t*” indicate tables, and “*np*” indicate foot notes.

A

ABCYS glasses, 215–216
Absorption coefficient, 190*f*, 197–199,
209–211, 212, 212*f*, 216, 218–219, 224–225,
232, 245, 246–248
Absorption cross section, 189–190, 210–211,
212, 218–219, 236, 240, 244, 245*f*
Absorption efficiency, 198, 205, 209–210, 245
Ac, 45–46, 234–235
Actinyl, 30–35, 37–38, 63, 66–67, 85–86
Activation of white phosphorus, 295–296
Actively-stabilized cavity, 236–237, 248*f*
Alkoxides, 84–85
Am, 27–30, 35–36, 37, 87
Ancillary ligands, 262–266, 271, 282, 320
Anti-Stokes fluorescence, 181–182, 183–185,
186–188, 191–192, 194–197, 194*f*, 199–200
Anti-Werner complex, 113–114, 115–116
Arene-bridged, 275–281
Atomic sphere approximations (LDA, ASA),
167–168

B

Background absorption, 189–190, 198–199,
205–206, 209–210, 215–216, 218–219,
232–233, 237*f*, 238–240, 246–247
Balanced detector, 222–223, 223*f*
BaY₂F₈ (BYF), 186–189, 215–216, 233–236,
240, 241*f*
BDE. *See* Bond dissociation energies (BDE)
BIG glass, 206–207, 216–218
Biphenyl Complexes, 276, 276*f*, 277*f*, 278,
305–316
BIRD. *See* Blackbody infrared radiative
dissociation (BIRD)
Bk, 9*t*, 77
Blackbody infrared radiative dissociation
(BIRD), 60–61
Bond activation, 13–14, 15, 41, 42, 43–44,
45–49, 50–51, 57, 72–73, 83, 94–95, 282
Bond dissociation energies (BDE), 1–2, 15–16,
27–30, 71–72, 79–80, 87, 88–92, 90*t*, 91*f*,
93–95

Bond energies, 15–16, 17–22, 25, 36, 38,
88–92, 91*f*
Bonding interactions, 17–22, 86–87, 115,
116–118, 144, 152, 167, 168–169, 171*t*
Brewster-cut, 236–237, 248–249
Brewster’s angle, 246–247
Bridgman furnace, 233, 243
Bulk cooling, 186, 187*f*, 206–207, 214,
225–229, 226*t*, 232–234, 238–240, 239*t*,
242*t*, 243–244, 248–249
BYF. *See* BaY₂F₈ (BYF)

C

Carbides, 14, 15–16, 74–75, 77, 119, 163, 269
6-Carbon, 10- π electron aromatic system, 316,
320
Carbonyl, 54, 60, 77–79, 81–83, 82*f*, 88–89,
296–298
Carnot efficiency, 200
Cavity-enhanced resonant absorption, 236
CBE. *See* Cluster-based electrons (CBE)
Centered heteroatomic cluster {TR₆}, 9*t*, 77, 155
Chelate-assisted solvent-extraction
purification, 186–188, 207, 252
Chemi-ionization, 14, 79, 86
CID. *See* Collision-induced dissociation (CID)
Cluster-based electrons (CBE), 112, 134*f*
Cluster chains, 144–156, 171*t*
Cluster complexes, 111–112, 113–114, 113*f*,
114*f*, 115–116, 117, 118, 118*f*, 120,
121–125, 133*f*, 134, 135–142, 137*t*, 145*f*,
146, 167–168, 172–173, 268–269
Cluster condensation, 136, 143–144
Cm, 9*t*, 48–49, 77, 89–92, 93*t*, 94*t*
CNBZn glass, 216–218, 232, 242*t*, 244
COHP. *See* Crystal orbital Hamilton
populations (COHP)
COHP diagrams, 167–168, 169*f*
Collision-induced dissociation (CID), 3–4,
16–17, 23, 41, 50, 51–52, 59–60, 62, 65,
66–68, 69–70, 71, 72, 73–75, 76, 77–79,
81–82, 83–85, 88–89

- Comproportionation route, 119, 120–121
 Condensed clusters, 146, 155
 Conductive heat loads, 234–235, 249–250
 Configurational coordinate, 193*f*
 Convective heat loads, 232–233, 249–250
 Convective heat transfer coefficient, 249–250
 Cooling efficiency, 185–188, 194*f*, 195–199, 196*f*, 200, 201–202, 203–204, 220*f*, 224–229, 225*f*, 226*t*, 232, 233, 234–235, 236–241, 237*f*, 239*t*, 242*t*, 244–245, 252, 253
 COS, 23, 24, 35–36
 COT. *See* Cyclooctatetraene (COT)
 Cross-relaxation, 201–202, 240–241
 Cross section, 15–16, 37, 40*f*, 56, 75, 189–190, 197–198, 205, 209–212, 218–220, 225–229, 232, 234–235, 240, 244, 245*f*
 Cryogenic regime, 180, 181–182, 186–189, 236
 Crystal-field levels, 191, 192–193, 194–195, 210–212, 221–222, 234–236
 Crystal-field transitions, 189–190, 194–195, 210–211
 Crystal orbital Hamilton populations (COHP), 167–168, 169*f*
 CS₂, 23, 24, 35–36
 Cyclooctatetraene (COT), 56–57, 75–76, 264
 Cyclopentadienyl, 262–264, 271–274, 275–276, 277–278, 286, 296–298, 320
 Czochralski crystal growth, 234–235, 236, 240
- D**
- Dehydrogenation, 24–25, 37, 40, 42–44, 46–47, 48–49, 50, 52, 56–57, 74–75, 81
 Density functional theory (DFT), 13, 37–38, 46–47, 58–59, 62–63, 64*f*, 65*f*, 67–68, 70–71, 71*f*, 72–73, 74–75, 77, 167–168, 274, 287–288, 294, 298, 305, 307–315, 316, 319
 Devitrification, 230–231
 DFT. *See* Density functional theory (DFT)
 Dielectric mirrors, 226*t*, 246–247, 246*f*
 Differential luminescence thermometry, 221–222, 224–225
 Dimeric clusters, {T₂R₁₀}, 136, 143–144, 143*f*
 Dioxide, 15–17, 26–27, 50, 82–83, 89–92, 93*f*, 93*t*, 181, 204
 Donor–acceptor interaction, 205, 282–285, 294
 Dy³⁺-doped materials, 203–204
- E**
- Edge- and face-connected clusters, 162–166
 Eight-coordinate endohedral atoms, 155–162
 Einstein coefficient, 209–211
 Electrochemical purification, 186–188, 206–207, 216–218
 Electronic configurations, 5, 6*t*, 13, 42–43, 44–45, 49–50, 57–58, 80–81, 88–89, 116*f*, 166–167, 307–315
 Electronic structure, 1–2, 13–14, 62, 69, 155, 166–172, 274, 282–285, 294, 316
 Electron-phonon coupling, 182–183, 225–229
 Electron transfer, 5–13, 17–22, 30–35, 36–37, 42–43, 47, 54–56, 83, 85–86, 92–93
 Electrospray ionization (ESI), 4–5, 14, 24–25, 59–61, 62–63, 65, 66–68, 69–71, 71*f*, 79, 95–96
 Emission cross section, 2, 210–211
 Emissivity, 188–189, 215–216, 250
 Endohedral atom, 112–113, 114, 115, 116–118, 118*f*, 120, 121–125, 131–133, 133*f*, 136, 140–142, 154–162, 163–166, 167, 173
 Energy flux rate, 200–201
 Energy-gap law, 202, 203–204
 Energy migration, 205, 240–241
 Energy transfer, 204*f*, 205
 Energy-transfer upconversion, 201–202, 240–241
 Entropy flux rate, 199–201
 Entropy of the radiation, 183–184
 Er³⁺-doped materials, 240–244, 242*t*
 Es, 2–3, 9*t*, 13, 36
 ESA. *See* Excited-state absorption (ESA)
 ESI. *See* Electrospray ionization (ESI)
 (E)-stilbene, 316, 317–319
 Excited-state absorption (ESA), 184–185, 225–229, 240–241
 Extended Hückel molecular orbital (EHMO) calculations, 167, 168*f*
 External quantum efficiency, 195–197, 224–225
 Extraction efficiency, 197–198
- F**
- Fabry–Pérot cavity, 226*t*, 236
 5*f* electrons, 5, 13–14, 45–46, 48–49, 94–95
 Ferrocene, 77–79, 81, 262–264, 269–271, 282–285, 286–288, 286*f*, 291–293, 320
 1,1'-Ferrocenediyl diamide, 282, 283*f*, 286, 286*f*
 Fluoride, 36–37, 87, 118, 181–182, 186, 188–189, 203–204, 207, 215–216, 229–231, 232, 233–234, 237–238, 244–245
 Fluoride glasses, 186–188, 187*f*, 189–190, 200–201, 206–207, 208, 209*f*; 229–231, 232, 233–234

Fluorozirconate glasses, 211–212, 230–231
Flux temperature, 199–200
Fm, 94–95
Fourier transform ion cyclotron resonance (FTICR), 3–4, 16–17, 78f
Four-level scheme, 197–198
Franck–Condon factors, 202
FTICR. *See* Fourier transform ion cyclotron resonance (FTICR)
Fullerenes, 73–75
Fused arenes, 276, 290–305

G

GIB. *See* Guided ion beam (GIB)
Guided ion beam (GIB), 3–4, 15–16, 23, 25, 26, 40

H

Harmonic oscillator, 202
Heat lift, 200–201, 236–237, 245, 248–249
Heavy-metal fluoride (HMF) glasses, 230–231
Heterometallic, 163–166, 172–173, 268, 269, 270f, 295–296, 317
Highest-energy optical phonons, 203–204, 225–229, 244–245
HMF glasses. *See* Heavy-metal fluoride (HMF) glasses
Ho³⁺-doped materials, 205
Homoatomic R–R bonding, 117–118, 171t, 172–173
Homogeneous broadening, 208–210, 211–212
Host materials, 203–204, 203f, 204f, 244–245
Hydration, 14, 59–68
Hydrides, 13, 25, 26, 42–43, 47, 88–89, 91f, 119, 264–266, 268–269, 269f, 278, 280f
Hydrolysis, 59–68, 70–71, 95–96

I

ICP. *See* Inductively coupled plasma (ICP)
IE. *See* Ionization energies (IE)
Inductively coupled plasma (ICP), 24–25, 79–80, 87, 240
Infrared camera, 215f
Infrared multiphoton dissociation (IRMPD), 59–60, 68f, 69
Infrared (IR) spectra, 67–68, 69
Inhomogeneous broadening, 189–190, 208–210, 211–212, 234–235
Internal quantum efficiency, 201–202, 218–219, 232–234
Interstitial, 117, 120, 131–133, 146, 278
Intra-cavity pumping, 248–249

Intra-cluster bonding, 111–112, 131–133
Ionization energies (IE), 1–2, 5–13, 17–22, 30–35, 41–42, 47–48, 53, 59–61, 67, 69, 86–87, 89, 92–93, 94
Ion mobility, 2, 75, 80–81, 87
Ion spectroscopy, 2, 14
IRMPD. *See* Infrared multiphoton dissociation (IRMPD)
Isolated octahedral clusters, 121–136

K

KGd(WO₄)₂, 203–204, 216–218, 232, 233–234
KPB₂Cl₅ (KPC), 213–214, 218–219, 233–234, 241–245

L

LA. *See* Laser ablation (LA)
LAPRD. *See* Laser ablation with prompt reaction and detection (LAPRD)
Laser ablation (LA), 3–4, 14, 27, 50, 52, 71–73, 74–75, 76, 77, 79–80, 81
Laser ablation with prompt reaction and detection (LAPRD), 3–4, 25, 40–41, 50–51, 52, 54–56
Laser cooling cycle, 195–197, 204f, 225–229, 240–241
Laser desorption/ionization (LDI), 76
Laser-induced cooling, 184–186, 185f, 195–197, 198, 213–214, 216–218, 224–225
Laser-induced heating, 195–197, 213–214, 216–218, 224–225, 225f
LDI. *See* Laser desorption/ionization (LDI)
Lifetime, 181, 194–195, 208, 218–220, 234–235
 π Ligands, 262–266, 263f
Low thermal emissivity coating, 250
Low-valent, 119, 243–244, 262, 271, 273–274
Lr, 9t, 13, 94–95
Luminescence thermometry, 212–213, 221–225, 225f

M

Mach–Zehnder interferometry, 212–213, 220–221
Mass spectrometry (MS), 1–2, 3–5, 13, 14, 15, 17, 24–25, 60–61, 61f, 62, 67–68, 69, 70, 72–76, 77, 79–80, 87, 88, 89, 205–207, 290
MAT. *See* Minimum achievable temperature (MAT)
Maximum phonon energy, 233, 237–238, 241–243
McCumber equation, 211–212
Md, 9t, 13, 94–95

- Mean fluorescence wavelength, 186, 187*f*,
194–197, 198–199, 204*f*; 221–222, 224–225,
233, 236, 240, 243–244
- Mean photon flux density, 194–195
- Metallocene, 54–56, 81–82, 262–264, 284*f*, 320
- Metallofullerenes, 14, 73–75
- Metallothermic reduction route, 119, 120–121
- Metal-rich compounds, 121, 167
- Microphonic noise, 181–182
- Minimum achievable temperature (MAT),
224–225, 236, 237*f*, 250
- Molecular orbital (MO) diagram, 112*f*, 133,
134*f*, 167
- MOM. *See* Monolithic optical maze (MOM)
- Monolithic optical maze (MOM), 239*t*, 246*f*,
247
- Monoxide, 16–17, 22–23, 23*f*, 31*t*, 48–49, 50,
51–52, 54–56, 82–83, 89–92, 93*t*
- MS. *See* Mass spectrometry (MS)
- Multiphonon relaxation, 201–202, 203–204,
204*f*, 205, 225–229, 232, 233–234, 235–236,
237–238, 240–243, 244–245
- ## N
- Naphthalene complexes, 277–278, 290,
291–293, 294, 296, 298–302, 316, 317, 320
- Nd, 6*t*, 16–17, 50, 59–60, 70–71, 73–76,
77–79, 92*f*, 117–118, 153–154, 262–264,
272*t*, 275–276, 290–291, 314*np*
- Neptunyl, 37–38, 63, 66–67, 68
- Net power density, 197–199, 219–220
- No, 9*t*, 13, 24–25, 59–60, 94–95, 203–204
- Non-cyclopentadienyl ancillary ligands, 262
- Nonradiative decay, 184–185, 197–198,
201–204, 204*f*
- Nonradiative relaxation, 184–185, 193*f*,
197–198, 201–202, 218–219, 240–241
- Nonresonant cavity, 231, 246–248, 246*f*
- Nonresonant pump cavities, 246–247
- Np, 2–3, 27–30, 37, 48–49, 63, 77
- Oxidation reactions, 14, 15–16, 27–30, 74
- Oxide crystals, 203–204, 232–234
- Oxides, 13, 14, 16–17, 26, 27–35, 42, 48–49,
50, 54, 57, 58–60, 66–67, 71–73, 74–75, 76,
77, 79–80, 85, 87, 88–94, 119, 203–204,
225–231, 244–245, 266–267
- Oxo-exchange, 63, 64*f*
- ## P
- Pa, 2–3, 9*t*, 27–30, 36, 48–49, 93*t*, 94*t*,
234–235
- Parasitic heating, 186–188, 198–199, 251
- Payload, 212–213, 221–223, 245, 251
- P-containing compounds, 304–305
- PE. *See* Promotion energy (PE)
- Peak absorption coefficient, 190*f*, 209–210
- Peak absorption cross sections, 189–190, 232,
240, 244
- Pentameric clusters, {T₅R₁₄}, 144
- Peptides, 14, 69, 70
- Photodissociation, 60–61, 62, 71–72, 73–74,
75–76, 82*f*, 83, 89
- Photothermal deflection spectroscopy (PTDS),
206–207, 212–213, 216–221
- Piezoelectric stabilization, 247–248
- Plutonyl, 37–38, 63, 65, 66–67, 68, 85–86
- Pm, 2–3, 6*t*, 71*f*, 126*t*, 141*t*, 147*t*, 157*t*, 164*t*,
170*t*, 272*t*
- Polar intermetallics, 115–116, 118, 162, 169–173
- Polyphosphide, 298, 302, 303, 304–305
- Population lensing, 219
- Potassium graphite, 289, 306
- Power spectral density, 194–195
- Promotion energy (PE), 5, 12*f*, 22*f*, 25, 42*f*,
45–48, 53*f*, 58, 88–89, 91*f*, 92*f*
- PTDS. *See* Photothermal deflection
spectroscopy (PTDS)
- Pu, 9*t*, 27–30, 35–36, 37, 63, 72, 77, 93*t*, 94*t*
- Pump absorption coefficient, 198–199, 212,
224–225
- ## Q
- QIT. *See* Quadrupole ion trap (QIT)
- Quadrupole ion trap (QIT), 3–4, 62, 70–71, 89
- Quantum efficiency, 184–186, 190, 195–199,
201–202, 204, 204*f*, 205, 218–219, 224–229,
232–234, 237–238, 240–243, 251
- ## R
- Radiation-balanced lasers, 188
- Radiative (black body) heat load, 205,
233–234, 249–250

- Radiative relaxation, 184–185, 197–198, 205, 225–229
- Rate constants, 4, 16–17, 21*np*, 26–27, 30*np*, 33*np*, 34*np*, 45*np*, 45, 74–75, 197–198
- Reaction efficiencies, 4, 17, 21*np*, 22*f*, 24, 25, 27–30, 30*np*, 33*np*, 34*np*, 44*f*, 45, 45*t*, 48*f*, 53, 56–57, 77–79, 87
- Reciprocity, 210–212
- Reduced rare-earth halide, 117, 120–121, 163
- Reduction chemistry, 271–275, 286–289, 320
- Reduction routes, 119–121
- Refractive index, 216–218, 219–220, 231, 232–233
- Resonant absorption coefficient, 197–198, 232, 245, 246–247
- Resonant pump cavities, 246–249
- S**
- Scandium fused-arene complexes, 290–295
- Selected-ion flow tube (SIFT), 3–4, 17, 24–25, 38
- Semiconductors, 180–181, 190, 222–223, 237
- SIFT. *See* Selected-ion flow tube (SIFT)
- Silicon diode, 213–214, 216–218
- Sm, 6*t*, 56, 59–60, 69, 70–71, 73–76, 92*f*, 116–117, 262–264, 269, 272*t*, 290–291
- Solid-state optical refrigerators, 181–183, 186, 187*f*, 191–201, 203–204, 212–213, 221–222, 245, 246*f*, 249
- Solvation, 14, 59–68, 95–96
- Solvent extraction, 186–188, 207, 252
- Speciation, 4–5, 65, 66–67
- Spectral lineshape function, 209–210
- Stilbene complexes, 316–319
- Stokes shift, 183–184, 191–192, 193, 202, 208
- Stored cryogenics, 181
- Sulfides, 23, 24, 35–36, 74–75, 88–89, 203–204
- T**
- TECs. *See* Thermoelectric coolers (TECs)
- Tetrameric clusters, {T₄R₁₆}, 140–144
- Th, 2–3, 9*t*, 13, 48–49, 77, 81–83, 89–92, 93*t*, 94*t*, 219–220
- Thermal conductivity, 219–220, 232–234, 235–236, 249–250, 251
- Thermal equilibrium, 194–198, 210–211, 249
- Thermal lensing, 219
- Thermal link, 251, 251*f*
- Thermal noise, 180–181
- Thermal population density, 209–210
- Thermoelectric coolers (TECs), 181, 250, 252
- Thermometry techniques, 212–224
- Thermooptic coefficient, 216
- Thiols, 57–58
- Third ionization potential *I*₃, 116–117, 116*f*
- Tight-binding linear muffin-tin orbital (TB-LMTO) method, 167–168
- Time of flight (TOF), 62
- Tm³⁺-doped materials, 186–189, 215–216, 215*f*, 220–221, 221*f*, 237–240, 241*f*, 244, 245*f*
- TOF. *See* Time of flight (TOF)
- Total internal reflections, 246*f*, 247
- Trace metal impurities, 229–230
- Transition metal ions, 5, 15–16, 25, 81, 88–89, 91*f*, 186–188, 205, 206–207
- Translational degrees of freedom, 182, 183–184
- Trimeric clusters, {T₃R₁₁}, 136–140
- {TR₄}X₅, 122*t*, 137*t*, 144
- {TR₄}X₆, 122*t*, 144–146, 146*f*
- {TR₂}X and {ZR₂}X₂ type halides, 164*t*
- {TR₃}X₃ cluster halides, 147*t*
- {TR₄}X₄ cluster halides, 157*t*
- [(T_iR_j)X_k](R/A)_z type structures, 122*t*
- U**
- U, 2–3, 9*t*, 13, 26, 27–30, 37, 48–49, 76, 77, 81–83, 86–87, 89–92, 93*t*, 94*t*
- Upconversion, 225–229
- Uranyl, 14, 30–35, 37–38, 57, 58–59, 62–63, 65, 66–68, 70, 76, 81, 83–85
- V**
- Van Vleck mechanism, 194
- Vertical external cavity surface emitting, 226*t*, 248–249
- Vibrational degrees of freedom, 56–57, 182–183, 184–185
- Vibrational overlap integrals, 202
- W**
- Werner-type complex, 113–114
- Y**
- YAG, 185–186, 185*f*, 188–189, 203–204, 213–214, 215–219, 231, 232–234, 236, 238, 246–247, 248–249
- Y₃Al₅O₁₂, 185–186, 185*f*, 226*t*, 232
- Yb³⁺-doped materials, 201–202, 225–237

YLiF₄ (YLF), 181–182, 188–190, 189*f*, 190*f*,
195–197, 196*f*, 202, 205–206, 212, 212*f*,
216–219, 221–222, 224–225, 225*f*, 226*t*,
232, 235–237, 235*f*, 238, 244, 245*f*,
246–249, 250, 251, 251*f*, 252
Y₂SiO₅ (YSO), 188–189, 203–204, 215–216,
226*t*, 232–233

Z

ZBLAN, 189–190, 190*f*, 204, 205, 206–207,
209–210, 213–214, 215–219, 220–224,
229–231, 232–235, 240, 246–249

ZBLANP, 186–188, 187*f*, 200–201,
206–207, 211–212, 213–214, 214*f*,
215–218, 221–222, 230–231, 236,
238–240, 246–247

ZBLANP glass, 186–188, 187*f*,
208–209, 215–216, 226*t*, 230–231,
238–240, 239*t*

Zone-refining, 207, 243–244

{Z₂R₆}X₇, 150*f*

{ZR₆}X₁₂R type compounds, 126*t*

{ZR₆}X₁₀ type compounds, 130*t*

{Z₄R₁₆}X₂₃=ZR₄X_{5.75}, 150